Plasma Nanotexturing of Silicon for Photovoltaic Applications : Tailoring Plasma-Surface Interactions for Improved Light Management

Guillaume Fischer

▶ **To cite this version:**

Guillaume Fischer. Plasma Nanotexturing of Silicon for Photovoltaic Applications : Tailoring Plasma-Surface Interactions for Improved Light Management. Plasma Physics [physics.plasm-ph]. Université Paris Saclay (COmUE), 2018. English. NNT : 2018SACLX087 . tel-01982208

HAL Id: tel-01982208

https://pastel.hal.science/tel-01982208

Submitted on 15 Jan 2019

HAL is a multi-disciplinary open access archive for the deposit and dissemination of scientific research documents, whether they are published or not. The documents may come from teaching and research institutions in France or abroad, or from public or private research centers.

L'archive ouverte pluridisciplinaire **HAL**, est destinée au dépôt et à la diffusion de documents scientifiques de niveau recherche, publiés ou non, émanant des établissements d'enseignement et de recherche français ou étrangers, des laboratoires publics ou privés.

université PARIS-SACLAY

NNT : 2018SACLX087

Thèse de doctorat

Plasma Nanotexturing of Silicon for Photovoltaic Applications: Tailoring Plasma-Surface Interactions for Improved Light Management

Thèse de doctorat de l'Université Paris-Saclay
préparée à Ecole Polytechnique

Ecole doctorale n°573 Interfaces : approches interdisciplinaires, fondements, applications et innovation (Interfaces)
Spécialité de doctorat : Physique

Thèse présentée et soutenue à Palaiseau, le 26 novembre 2018, par

GUILLAUME FISCHER

Composition du Jury :

M. Thierry Gacoin Directeur de Recherche, Ecole polytechnique (PMC-CNRS)	Président du jury
Mme Angélique Bousquet Maître de Conférences, Université Clermont Auvergne (ICCF-CNRS)	Rapporteur
M. Rémi Dussart Directeur de Recherche, Université d'Orléans (GREMI-CNRS)	Rapporteur
M. Cédric Broussillou Ingénieur de recherche, EDF ENR PWT (Photowatt)	Examinateur
M. Jochen Rentsch Ingénieur de Recherche, Fraunhofer ISE	Examinateur
M. Etienne Drahi Ingénieur de Recherche, TOTAL SA - GRP	Invité
M. Erik Johnson Directeur de Recherche, Ecole polytechnique (LPICM-CNRS)	Directeur de thèse

À ma chère Sandra

REMERCIEMENTS

Le présent manuscrit de thèse constitue une synthèse de mon travail effectué au sein des projets de l'Institut Photovoltaïque d'Île-de-France (IPVF) et du Laboratoire de Physique des Interfaces et Couches Minces (LPICM). Cependant, la nature même de ce document ne permet pas de rendre compte de la large (et experte !) contribution de nombreux collègues et collaborateurs, avec qui j'ai pu nouer des relations professionnelles et amicales durant ces trois dernières années. C'est cette lacune que je souhaite combler ici en remerciant l'ensemble des personnes qui m'ont accompagné dans cette aventure.

Evidemment, tout ce travail n'aurait pu se faire sans la supervision pédagogue et impliquée de mon directeur de thèse *Erik Johnson* : je m'estime chanceux d'avoir pu bénéficier durant ces trois années de ton expertise et de ta passion scientifique (et un peu de ton humour – canadien ?). C'est principalement à travers nos nombreuses interactions que j'ai progressé dans ma formation de chercheur. Selon ma propre expérience, une thèse consiste en une succession de réussites et d'échecs : tu as partagé mon enthousiasme pour les premiers, mais surtout tu m'as démontré, à de nombreuses reprises, que les « échecs » n'étaient qu'apparents et contenaient en réalité de précieuses leçons. Ainsi, j'abordais parfois nos réunions avec lassitude mais grâce à toi je retrouvais rapidement ma motivation ! Pour cela et bien plus, je souhaite ici te remercier chaleureusement.

Je tiens ensuite à remercier mes collègues de l'IPVF (j'entends ici l'entreprise IPVF !) : j'ai intégré cet institut alors qu'il était tout juste naissant et en construction (littéralement et métaphoriquement), une période à la fois intense et chahutée. Mon premier obstacle fût l'éclatement des chercheurs dans différents laboratoires, loin des équipes administratives et de direction. Heureusement, j'avais en face de moi des collègues motivés et engagés, qui ont su se rendre disponibles. En premier lieu, ma reconnaissance va à *Denis Jahan*, qui m'a accordé sa confiance dès le lancement de ce projet et m'a ensuite accompagné sur de longs mois et offerts ses conseils avisés (je me souviens encore du premier d'entre eux : « Tu dois apprendre à dire non ! »). Le témoin est ensuite passé à *Christophe Bonelli*, qui a su à son tour me donner beaucoup d'autonomie pour la réalisation de mes travaux, tout en me permettant de m'impliquer sur de nombreux aspects de la construction de l'institut, une expérience précieuse pour mon avenir professionnel. À ce titre, je remercie également *Bruno Carlotti* et *Daniel Lincot*.

Ma gratitude va aussi à tous mes autres collègues de l'IPVF. Je pense d'abord à *Sonia Haouka* et *Bérengère Larue* et leurs équipes, dont *Ariana Salemi* et *Liying Zhou-Ducret* : c'est toujours avec beaucoup de joie que je vous rendais visite (d'abord à Antony, puis au 2^{e} étage du bâtiment à Palaiseau). En effet, j'ai rapidement compris que mes questions et demandes trouvaient toujours des réponses (parfois accompagnées de chocolats) grâce à vous. Je remercie aussi *Olivier Roussel*, *Alexis Denis* et *Côme Cabriel* : je vous ai peu sollicités (n'ayant au final passé que quelques mois dans le bâtiment IPVF) mais j'ai toujours bénéficié de votre écoute et de votre aide. Merci également aux nombreux ingénieurs et chercheurs IPVF qui m'ont accompagné ces dernières années,

et m'ont partagé leur expertise, leurs conseils ou simplement leur bonne humeur : *Thomas Blévin* et *Anaïs Loubat* (super souvenirs d'Amsterdam !), mais aussi *Ahmed Ben Slimane*, *Baljeet Goraya*, *Jonathan Langlois*, *Matthieu Leroy*, *Salim Mejaouri*, *Amelle Rebai*...

En second lieu, je souhaite remercier les équipes du LPICM, à commencer par le directeur *Pere Roca i Cabarrocas*, qui m'a encouragé à multiplier les chances d'interactions autant scientifiques qu'extra-professionnelles. Grâce à des équipes passionnées, j'ai eu la chance d'évoluer dans une atmosphère de travail intense mais somme toute décontractée ! Ma reconnaissance va en particulier aux équipes qui font véritablement « tourner » le laboratoire : d'abord l'administration de *Laurence Gérot*, *Gabriela Medina* et *Fabienne Pandolf*, je sais à présent que sans vous les chercheurs dépériraient ! Un grand merci également aux équipes de la comm', du BEER (parce qu'ils ne sont jamais à court de jeux de mots !) et du G2I : *Jérôme Charliac* (cobureau de la dernière heure, dealer de caféine), *Frédéric Farci*, *Cyril Jadaud* (ré-initialisateur d'alarme gaz pour doctorants en perdition), *Frédéric Liège*, *Jean-Luc Moncel*, *Eric Paillassa*, *François Silva*, *Jacqueline Tran*, *Jean-Charles Vanel*. Mention spéciale pour *Nacib Benmammar* qui m'a accordé beaucoup de son temps alors que je découvrais encore les subtilités des systèmes plasma : merci de ton aide bienvenue lorsque j'ai dû « mettre les mains dans le cambouis », je garde un souvenir amusé de nos heures passées sur cette satanée RIE (notamment quand nous avons failli transformer la salle de manip' en piscine, mais chut !).

Je remercie également tous les chercheurs et post-docs du LPICM qui ont collaboré avec moi de diverses manières ou avec qui j'avais simplement la chance de partager du temps en salle de manip' : *Pavel Bulkin* (expert plasma et vins, un accord gagnant !), *Wanghua Chen*, *Martin Foldyna* (référant mesures optiques et consultant en slides de soutenance), *Lukas Halagacka*, *Karim Ouaras*, *Nicolas Vaissière* (recordman du labo en nombre d'entretiens pour en partir)... J'en profite pour remercier également *Thomas Germer* du National Institute of Standards and Technology (NIST) qui a collaboré sur ce projet par son expertise en caractérisations optiques.

Je dois également remercier particulièrement l'équipe du projet A (Silicium) de l'IPVF. C'est dans ce projet que j'ai « fais mes armes » pour ainsi dire : présenter mes résultats devant de nombreux experts m'a permis d'affiner ma compréhension physique, mais surtout d'affuter mes arguments pour présenter et défendre mes résultats de manière cohérente et convaincante. A ce titre, il me faut bien sûr commencer par remercier l'actuel "project leader", *Etienne Drahi* : je souhaite ici t'assurer de ma profonde gratitude pour ton aide amicale et ta générosité, et te confier mon admiration pour la ténacité dont tu fais preuve dans ton rôle éprouvant. Dans ce projet, en plus de nombreux chercheurs IPVF et LPICM déjà cités, j'ai également eu la chance de côtoyer de nombreux chercheurs issus d'horizons variés que je souhaite remercier : *Sylvain Pouliquen*, *Peter Uhlig* et *Andy Zauner*, coté Air Liquide, ainsi que *Julien Dupuis* et *Pierre-Philippe Grand* côté EDF.

Je n'oublie pas les équipes de recherche Total, avec qui j'ai passé presque trois années (en comptant un stage antérieur) dans des préfabriqués mal isolés ! Une mention particulière pour *Gilles Poulain*, qui m'a initialement encadré lors d'un stage puis a suivi une partie de mes travaux de thèse : j'ai beaucoup appris grâce à ta vision « industrielle » (pour dire les choses grossièrement) mais surtout grâce à ton sens aiguisé de la critique (dans toute la noblesse du terme). Je tiens également à remercier l'ensemble de l'équipe Total, qui a beaucoup évolué au fil du temps et à qui je n'ai que trop peu rendu visite au 3^{e} étage du bâtiment IPVF : *Jean-François Besniers*, *Fabrice Devaux*, *Amjad Deyine*, *Jara Fernandez Martin*, *Sergej Filonovich* (Pinterest addict comme moi), *Ludovic Hudanski*, *Perine Jaffrennou*, *Vincent Maillard*, *Julien Penaud*, *Patricia Prod'homme*, *Christoph Sachs*, *Martin Sander*. Je garde un souvenir (nostalgique) de nombreuses discussions (scientifiques ou non, mais toujours passionnées !) dans notre toute petite salle café du bâtiment 404A. J'ai aussi une pensée pour les différents stagiaires qui se sont succédés dans l'équipe, notamment *Billal Faryssy* (que j'ai eu la chance d'encadrer et qui a partagé mes galères sur la RIE !), ainsi que *Katia Allaoua* (pâtissière prolifique).

J'ai volontairement omis jusqu'ici de remercier mes collègues doctorants de toutes affiliations, pour beaucoup déjà devenus docteurs, mais surtout devenus des amis. Je souhaitais en effet vous remercier plus spécifiquement : ce fût un atout précieux dans ma thèse que de pouvoir partager doutes, questionnements et états d'âme avec vous (et c'était encore mieux autour de quelques bières !). J'ai eu beaucoup de chance de croiser la route de nombreux doctorants durant ces trois années et j'espère ne pas en oublier au passage. Je remercie tout particulièrement *Fabien Lebreton*, lève-tôt invétéré avec qui j'ai souvent eu le plaisir de partager « les Algécos » entre 7h et 8h (le meilleur horaire pour une discussion autour d'un café), mais aussi *Rafaël Peyronnet*, arrivé presque en même temps que moi à l'IPVF et avec qui j'ai pu partager autant les galères que les victoires. Mention spéciale également pour *Marta Chrostowski* et *Chloé Dindault* (serial relectrice de chapitres), avec qui j'ai eu le plaisir de partager de nombreux déjeuners sur les derniers mois, m'offrant des pauses bienvenues (et des rires) dans une période intensive de rédaction puis de préparation de soutenance. Je suis aussi très reconnaissant envers les nombreux autres doctorants qui se sont succédés : *Valentin Achard*, *Mutaz Al-Ghzaiwat*, *Linda Assam*, *Bastien Bruneau*, *Julien Couderc*, *Jean-Christophe Dornstetter*, *Salomé Forel*, *Gwenaëlle Hamon* (guitare-voix de 17h aux Algécos), *Rasha Khoury*, *Ronan Léal* (abonné au bureau des objets trouvés), *Harold Le Tulzo*, *Arvid Lindberg*, *Amadéo Michaud*, *Cécile Molto*, *Paul Narchi* (recruteur officiel du SCOP et du festival du rire), *Mengkoing Sreng* (travailleur de nuit), *Junkang Wang*, *Thomas Yoo*...

Il me faut également remercier mes amis du Student Chapter of Optics Paris (SCOP) : *Olivier Lefebvre*, *Benjamin Madon*, *Joséphine Morizet*, *Lipsa Nag*, *Seonyong Park*, *Alexandra Petreto*, *Samuel Serna*... avec qui j'ai passé de nombreuses heures pour l'organisation de la conférence IONS Paris 2017 (expérience inoubliable !). Merci aussi à mes collaborateurs rencontrés sur le tard (après déménagement à l'IPVF), issus des équipes d'EDF et du CNRS, et avec qui j'aurais aimé pouvoir interagir plus longuement. J'en profite également pour remercier les membres du jury qui m'ont fait l'honneur d'évaluer et critiquer mon travail de thèse.

Enfin, je souhaite remercier ma famille, au premier rang mes parents et ma soeur : même si vous ne vous en rendez peut-être pas compte, vous avez largement participé à ce travail car c'est auprès de vous que j'ai commencé à forger mon regard sur moi-même et sur le monde qui m'entoure. Je garde mes derniers mots pour *Sandra*, qui a partagé mes moments de joie (durant ces trois ans mais aussi depuis bien plus longtemps) et que je veux remercier ici pour son soutien sans faille lors de mes moments de doute.

Merci à vous tous !

CONTENTS

Remerciements v

Contents ix

List of Figures xi

List of Tables xvii

List of Abbreviations and Symbols xix

Photovoltaic Electricity for Sustainable Development 1
1 Energy Enables Human Development . . . 2
1.1 A Global Look at Energy Needs . . . 2
1.2 The Haunting Issue of Global Climate Change . . . 4
2 Aim for the Sun! . . . 6
2.1 PV Systems Deliver Electricity . . . 6
2.2 Unique Attributes of Photovoltaic Energy . . . 7
2.3 Photovoltaic is not the Sole and Universal Solution . . . 8
3 Thesis Aim and Outline . . . 10
Bibliography . . . 11

I Theoretical and Experimental Background 13
I.1 Reactive Ion Etching of Crystalline Silicon . . . 16
I.1.1 Fundamentals of CCP-RF Discharges . . . 16
I.1.2 TVWs: a Multi-frequency Extension of the RF Domain . . . 22
I.1.3 Process Description and Monitoring . . . 27
I.1.4 Silicon Etching . . . 30
I.2 Black Silicon: Theory and Characterization . . . 35
I.2.1 Silicon Nanostructure Formation . . . 35
I.2.2 Optical Properties of Nanostructured Surfaces . . . 44
I.2.3 Implementation of b-Si in Solar Cells . . . 48
I.2.4 Characterization Methods . . . 52
Conclusion . . . 56
Bibliography . . . 62

II Tailored Voltage Waveforms Excitation in the SF_6/O_2 Discharge 63
II.1 Implementation of Tailored Voltage Waveforms . . . 64
II.1.1 Electrical Calibration . . . 65
II.1.2 Validating Calibration using Amplitude Asymmetry Effect in Ar . . . 67
II.2 Amplitude and Slope Asymmetry Effects in the SF_6/O_2 discharge . . . 75
II.2.1 Comparison of SF_6/O_2 with Ar and O_2 . . . 75
II.2.2 Power Coupling Mode Transitions in SF_6/O_2 . . . 77
II.3 Tuning Ion Energy and Flux using Tailored Voltage Waveforms in SF_6/O_2 . . . 81
II.3.1 Tuning Ion Flux Energy Distributions in SF_6/O_2 . . . 81
II.3.2 Effects of Power Mode Transitions in Decoupling Ion Energy and Flux . . . 85
II.3.3 Ion Flux Non-uniformity in SF_6/O_2 Discharge . . . 89
Summary . . . 94
Bibliography . . . 96

III Plasma-Surface Interaction: Self-Organization at the Nanoscale during SF_6/O_2 Etching 97
III.1 Baseline Process using Single-frequency Excitation . . . 99
III.1.1 Nanotexturing "Process Window" . . . 99
III.1.2 Dynamic Aspects of Nanotexturing . . . 107
III.2 Texturing Uniformity at Full Wafer Scale . . . 113
III.2.1 Initial Tests and Influence of SF_6 Content . . . 113
III.2.2 Uniform Final Reflectance, Non-uniform Process Conditions . . . 116
III.3 Influence of Ion Flux and Ion Energy on Nanotexturing . . . 120
III.3.1 Influence of Ion Flux . . . 120
III.3.2 Energy Dependent Etching Yield . . . 124
III.3.3 Special Cases . . . 131
Summary . . . 134
Bibliography . . . 136

IV Tailoring Optoelectronic Properties of Plasma Nanotextured Silicon Surfaces 137
IV.1 Optical Properties of Nanotextured Silicon Surfaces . . . 139
IV.1.1 Broadband Anti-reflection Properties . . . 140
IV.1.2 Light-Trapping in Near-IR Range . . . 146
IV.1.3 Synthesis: light management through front side nanotexturing . . . 156
IV.2 Passivation of Nanotextured Silicon Surfaces . . . 158
IV.2.1 ALD Al_2O_3 Surface Passivation . . . 158
IV.2.2 Passivation of Plasma Nanotextured Silicon Surfaces . . . 160
Summary . . . 166
Bibliography . . . 168

Conclusion and Perspectives 169

A Retarding Field Energy Analyzer: Basic Theory and Measurement Analysis I

B State of the Art Black Silicon Solar Cells IX

Motifs & Reliefs XXVII

List of Communications XXIX

Résumé en français XXXI

Abstract / Résumé XXXIV

List of Figures

1 Human development index versus energy use for 2014 in 129 countries 3
2 Vulnerability versus readiness for 2014 in 180 countries 5
3 Number and repartition of people lacking access to electricity in the world 6
4 World map of solar horizontal irradiation 7
5 Lifecycle GHG emissions for the major electricity supply technologies 8

I.1 PERC solar cell schematic, model I-V and AM1.5g solar photon flux 15
I.2 Basic schematic of a CCP reactor 17
I.3 Schematic of the voltage distribution in the CCP discharge 19
I.4 IEDF at powered electrode of CCP-RF CF_4 plasma; Evolution of IEDF with discharge pressure at powered electrode in a CCP-RF Ar plasma 21
I.5 Peak ion energy versus ion flux in a CCP-RF Ar discharge (at 15 mTorr) with varying voltage amplitude and three different frequencies 22
I.6 Examples of TVWs used in the present work, shown with normalized peak-to-peak amplitudes and harmonic decompositions 23
I.7 Evolution of $(|V_{min}| - V_{max})/V_{PP}$ as a function of Θ for different numbers of harmonic frequencies in the TVWs. Illustration of peaks waveforms for different numbers of harmonic frequencies 24
I.8 Evolution of the mean ion energy and ion flux at the grounded electrode in an Ar discharge powered by TVWs (13.56 MHz plus one upper harmonic) with θ 24
I.9 Evolution of self-bias voltage and ratio of ion fluxes at the powered and grounded electrodes as a function of Θ in an Ar discharge 25
I.10 Comparison of spatiotemporal excitation rate from experiments (PROES) and PIC simulations for Ar and CF_4 discharges 26
I.11 Picture of the RIE reactor used in the present work; Schematic of the reactor and powering systems 28
I.12 Example of an I-V measurement obtained with the RFEA placed on the powered electrode for an SF_6/O_2 discharge; IFEDF derived from the smoothed I-V curve . . 29
I.13 3D stick-and-ball view of the unit cell of the diamond structure of c-Si; 2D schematic of the (100) and (111) planes in the unit cell 30
I.14 Description of basic etching processes: sputtering, pure chemical etching, ion-assisted etching, and ion-enhanced inhibitor etching 31
I.15 Synergetic effect in silicon etching by XeF_2 and Ar^+ ion bombardment; Silicon etching yield as a function of the ion energy with various species 33
I.16 Evolution of the Si etch rate and F atom density in a SF_6/O_2 discharge with the O_2 content in the feed gas 34

I.17 Picture of an un-etched reference c-Si sample and a “black silicon” sample processed as part of the present work . . . 35
I.18 Oxygen content threshold versus substrate temperature for the formation of b-Si . 37
I.19 SEM images of various b-Si surfaces obtained by SF_6/O_2 RIE (and prior any other process) from different groups illustrating the diversity of scales and morphologies 38
I.20 SEM images of alkaline textured silicon and acidic textured silicon; Comparison of reflectance for different wet etchants on mono-Si and mc-Si . . . 39
I.21 SEM images of various b-Si surfaces (prior any other process) obtained by: MACE, PIII, ADE, Pulsed femtosecond laser and colloidal lithography . . . 41
I.22 SEM images of b-Si surfaces obtained by ICP-RIE in SF_6/O_2 with varying etching time; Evolution of the total hemispherical reflectance of the samples with etching time . . . 45
I.23 Schematic of light reflection and transmission at the c-Si surface with large and small structures compared to the wavelength of incoming light . . . 46
I.24 Optical properties of c-Si at 300 K . . . 46
I.25 Model light-trapping structures; Corresponding theoretical absorptance; Theoretical photogenerated current density versus absorber thickness . . . 47
I.26 Chronology of record efficiencies and reported b-Si solar cells efficiencies for mono-Si and mc-Si cells . . . 51
I.27 Schematic of the spectrophotometer with the 150 mm integrating sphere . . . 53
I.28 SEM images of an RIE textured sample: cross-section view and top view; Circularly averaged autocorrelation function obtained from top view image . . . 54
I.29 Example of five step profiles obtained on a textured sample with a masked area used to compute the etched thickness . . . 54

II.1 Electrical schematic of RIE setup; Illustration of two challenges tackled in this section 64
II.2 Picture of the substrate electrode in the RIE reactor . . . 65
II.3 Gain and phase-shift between the feedthrough and electrode of the RIE . . . 66
II.4 Examples of waveforms required at the feedthrough to obtain target model waveforms at the electrode . . . 68
II.5 Comparison of experimental feedthrough waveforms with target values for an Ar discharge in the three test cases . . . 70
II.6 Comparison of $V_{DC}/V_{e,PP}$ from experimental measurements with theoretical AAE model for the three discharge conditions investigated with Ar . . . 72
II.7 Theoretical AAE model results obtained with ideal waveforms compared with results obtained with erroneous correction factors in the calibration method . . . 73
II.8 Evolution of V_{PP}, V_{DC}, and V_{DC}/V_{PP} with single frequency RF excitation and for TVWs when spanning voltage waveforms for Ar, O_2 and SF_6/O_2 . . . 76
II.9 Ideal sawtooth waveforms and their truncated Fourier decompositions . . . 77
II.10 Evolution of V_{PP}, V_{DC}, and V_{DC}/V_{PP} with SF_6 content in total incoming gas flux for sawtooth-down, sawtooth-up and RF excitation . . . 78
II.11 Evolution of V_{DC}/V_{PP} as a function of the discharge pressure for different incoming gas composition and power . . . 79
II.12 Schematics of the RIE substrate electrode with the RFEA probe . . . 81
II.13 Evolution of IFEDFs with applied voltage waveform in Ar and SF_6/O_2 in single-frequency and TVW excitation . . . 82
II.14 Variations of total collected ion flux with applied voltage waveform for Ar and SF_6/O_2 83
II.15 Variations of average, maximal and calculated ion bombardment energy with applied voltage waveform for Ar and SF_6/O_2 . . . 84
II.16 Influence of applied waveform on ion bombardment energy and total collected ion flux for different values of SF_6 content in an SF_6/O_2 discharge . . . 85
II.17 IFEDFs, ion energy and total ion flux measured in SF_6/O_2 (single-frequency excitation) with increasing coupled power from 5 to 45 W . . . 87

II.18 Influence of applied waveform on ion bombardment energy and total collected ion flux for different values of applied power in an SF_6/O_2 discharge 88
II.19 Average ion bombardment energy versus total collected ion flux for an SF_6/O_2 discharge for different types of applied waveforms and values of coupled power . . . 89
II.20 Measured radial profiles for DC self-bias voltage, average ion bombardment energy and total collected ion flux in Ar and SF_6/O_2 discharges with various applied voltage waveforms 90
II.21 Comparison of IFEDFs with SF_6/O_2 for different applied voltage waveforms obtained at the center or at the edge of the powered electrode 91
II.22 Evolution of total ion flux and self-bias voltage with excitation voltage waveform in an SF_6/O_2 discharge at the center or the edge of the electrode 92

III.1 Illustration of surface nanotexturing process with relevant input and output parameters 98
III.2 Surface profiles (obtained by confocal microscopy) of unetched SWS, DWS and LPD samples 101
III.3 Total hemispherical reflectance spectra for initial SWS, DWS, DSP and LPD samples 102
III.4 Influence of SF_6 content and pressure on the effective reflectance for samples A and B 104
III.5 Influence of SF_6 content and pressure on the self-bias voltage 105
III.6 Reflectance spectra of unetched SWS surface and 15 min textured samples 107
III.7 Photographs of four types of samples without texturing and after various RIE etching times 108
III.8 Top-view SEM images of four types of samples before process and after various RIE etching times (2, 10, 15 and 30 min). 109
III.9 Evolution of average nanostructure width as a function of RIE etching time for the four sample types 110
III.10 Evolution of reflectance spectra of samples having undergone different RIE etching time 111
III.11 Effective reflectance evolution with etching time for four types of sample 112
III.12 Photograph of 6” pseudo-square wafer (and SEM images from center and corner) processed for 20 min and corresponding effective reflectance profile 114
III.13 Effective reflectance profiles obtained on the diagonal of the wafers after 20 min process with different SF_6 contents and corresponding evolution of $\bar{R}_{\text{eff}}$ and MAD 115
III.14 Effective reflectance profiles obtained on the diagonal of the wafers after different process times and corresponding evolution of $\bar{R}_{\text{eff}}$ and MAD 117
III.15 Photograph of 6” pseudo-square wafer processed for 30 min with $P_w = 35$ W, $P_r = 35$ mTorr, 140 sccm SF_6/O_2 input gas flux (with 64 % SF_6 content) 118
III.16 Evolution of average nanostructure width and height versus etching time at the center and edge of the wafers; Selected SEM top view images 118
III.17 Ion flux and average ion energy profiles on the substrate electrode for three types of excitation voltage waveforms 120
III.18 Evolution of nanostructures average width and effective reflectance versus time for different sample positions and excitation voltage waveforms 122
III.19 Evolution of nanostructures average width and height, effective reflectance and etched depth as a function of ion fluence for different excitation voltage waveforms 123
III.20 Ion flux and average ion energy profiles on the substrate electrode for single-frequency excitation with varying values of power 125
III.21 Contour maps showing influence of ion flux and average ion energy on the final effective reflectance and nanostructure average width 125
III.22 Results of non-linear least square fitting: etch depth as a function of the energy weighted ion fluence; Etch yield dependence on ion energy 127

III.23 Evolution of nanostructures average width and height, effective reflectance and etched depth as a function of energy weighted ion fluence for different excitation voltage waveforms and values of applied power . . . 127
III.24 Schematic of nanotexturing evolution with energy weighted ion fluence and selected cross section view SEM images illustrating the influence of etching time, ion flux and ion energy . . . 129
III.25 Cross section view schematic of the nanotexturing phenomenon; close-up view illustrating the major species, with the SiO_xF_y inhibitor layer and the angle of unobstructed plasma exposure . . . 129
III.26 Nanostructure average height versus average width (color-mapping as a function of the instantaneous ion flux during the process); Top and cross-section view SEM images of selected samples . . . 131
III.27 SEM images of a nanotextured c-Si sample showing the dependence of the nanostructures morphology on the crystalline orientation of the substrate . . . 132
III.28 SEM top view images of selected nanotextured c-Si samples obtained at low ion bombardment energy compared to samples obtained with a similar ion flux but higher average ion energy . . . 133

IV.1 Schematic of a c-Si absorber illustrating incoming light, reflection and transmission; Solar light photon flux and contributions of loss mechanisms for a perfectly flat 180 µm thick c-Si absorber . . . 139
IV.2 Schematic of geometric model for plasma nanostructured surface; Multilayer effective medium approximation 1D model . . . 140
IV.3 Examples of profiles for c-Si material filling factor, refractive index, and extinction coefficient for different values of N; Evolution of the calculated front reflectance with N for different values of λ_0 . . . 142
IV.4 Evolution of reflectance (at $\lambda_0 = 300$, 600 and 900 nm) with nanostructure average height: comparison of experiments with proposed multilayer model . . . 142
IV.5 Evolution of effective reflectance with nanostructure average height: comparison of experiments with proposed multilayer model; Reflectance spectra for five selected samples: measurements and multilayer model results . . . 144
IV.6 BRDF measured for four surface types and for five etching times . . . 145
IV.7 Evolution of absorptance spectra with etching time for SWS and LPD samples; Corresponding evolution of photogenerated current density . . . 147
IV.8 Absorptance and reflectance spectra at normal incidence for a nanotextured c-Si sample; Corresponding computed values for $A_{tot}/(1-R_f)$ and pathlength enhancement factor from Equation (IV.4) . . . 148
IV.9 Examples of model pathlength enhancement factor curves from Equation (IV.7); Corresponding theoretical absorptance curves . . . 149
IV.10 Comparison of experimental absorptance measurements and model results for initial and nanotextured SWS and LPD samples . . . 150
IV.11 Light pathlength enhancement factor computed for SWS and LPD samples . . . 150
IV.12 Evolution of light path enhancement factor parameters (Z_∞, Z_0, Z_p) with nanostructure average width on SWS and LPD samples . . . 151
IV.13 Measured and fitted absorptance spectra for 287 µm thick samples (with corresponding fitted light path length enhancement); Measured and predicted absorptance spectra for 83 µm thick sample (with corresponding predicted light pathlength enhancement) . . . 153
IV.14 Schematics of the five types of light-trapping schemes; SEM tilted view images of plasma nanotextured surface, pyramid microstructures and nanotextured pyramids 154
IV.15 Measured absorptance spectra and corresponding light path enhancement factor for different light-trapping schemes . . . 155

IV.16 Normal incidence absorption and losses in solar photon flux for 180 µm thick absorbers with: planar surfaces, pyramid textured surfaces and front ARC, or front nanotextured surface . . . 157
IV.17 Schematic of ALD process . . . 158
IV.18 Performed process flow for passivation of plasma nanotextured c-Si surfaces . . . 159
IV.19 Effective minority carrier lifetime of unetched samples; Effective minority carrier lifetime for best, median and worst reference samples . . . 160
IV.20 Evolution of effective reflectance and front SRV with etching time for different nanotexturing process conditions . . . 162
IV.21 SEM images of samples A and B, textured for 10 min at P_w = 35 W, with E_{calc} = 85 and 115 eV, respectively . . . 162
IV.22 Evolution of local front surface recombination velocity with ion bombardment energy for 21 textured samples . . . 163
IV.23 Effective front surface recombination velocity versus effective reflectance for all passivated samples . . . 165
IV.24 Reflectance spectrum and lifetime measurement for identified "best trade-off" nanotextured sample, compared to reference samples . . . 165

A.1 Schematic of the RFEA probe on the powered electrode . . . II
A.2 RFEA current as a function of the discriminator voltage . . . VI
A.3 Comparison of IVDF, IEDF and IFEDF . . . VII

B.1 Simplified schematics of different c-Si solar cells architectures . . . XI
B.2 History of black silicon solar cells efficiencies compared to overall records . . . XVII
B.3 History of black silicon solar cells efficiencies for mono- and mc-Si absorbers depending on cell architecture and nanotexturing technique . . . XVIII
B.4 Short circuit current density vs open-circuit voltage for homojunction black silicon solar cells . . . XIX
B.5 Comparison of large-scale black silicon mc-Si cell results from literature for different nanotexturing methods . . . XX

List of Tables

I.1 Comparison of silicon texturing techniques 43
I.2 Detailed electrical properties of the current record efficiency c-Si solar cells 52

II.1 Correction factors applied to the TVW signal at the feedthrough of the RIE reactor . 67

III.1 Available range of discharge parameters for c-Si nanotexturing in the RIE setup . . 99
III.2 Labels and description of the c-Si samples used in this study 100
III.3 c-Si nanotexturing process parameters used for study presented section III.1.1.c . . 103
III.4 Baseline process parameters for SF_6/O_2 nanotexturing of c-Si in the RIE setup . . . 106
III.5 c-Si nanotexturing process parameters used for study presented section III.1.2 . . . 107
III.6 c-Si nanotexturing process parameters used for initial upscaling test 113
III.7 c-Si nanotexturing process parameters used for study presented section III.3.1 . . 121
III.8 c-Si nanotexturing process parameters used for study presented section III.3.2.a . 124

IV.1 Light-trapping parameters obtained from fitting of absorptance curves shown in Figure IV.13(a) 154
IV.2 Light-trapping parameters obtained from fitting of absorptance curves measured on samples with various surface textures 156
IV.3 c-Si nanotexturing process parameters used for study presented section IV.2.2 . . . 160
IV.4 Voltage excitation parameters used for c-Si nanotexturing step in study presented section IV.2.2.b 161

B.1 Reported global record efficiency solar cells. XII
B.2 Reported black silicon (n-type monocrystalline) solar cell results XIII
B.3 Reported black silicon (n-type multicrystalline) solar cell results XIII
B.4 Reported black silicon (p-type monocrystalline) solar cell results XIV
B.5 Reported black silicon (p-type multicrystalline) solar cell results XV
B.6 End of Table B.5 XVI

List of Abbreviations and Symbols

Abbreviations & Acronyms

AAE	Amplitude Asymmetry Effect
ACF	Autocorrelation Function
ADE	Atmospheric Dry Etching
AFG	Arbitrary Function Generator
AlBSF	Aluminium Back Surface Field (solar cell architecture)
ALD	Atomic Layer Deposition
AM1.5g	Global solar radiation spectrum standard at Air Mass 1.5
BRDF	Bidirectional Reflectance Distribution Function
b-Si	Black silicon
c-Si	Crystalline silicon
CCP	Capacitively Coupled Plasma
CVE	Chemical Vapor Etching
DSP	Double Side (mirror) Polished (surface finish)
DWS	Diamond Wire Sawn (surface finish)
EAE	Electrical Asymmetry Effect
GHG	Greenhouse Gas
GWP	Global Warming Potential
HV	High Voltage (probe)
IBC	Interdigitated Back Contacts (solar cell architecture)
ICP	Inductively Coupled Plasma
IFEDF	Ion Flux Energy Distribution Function
ISM	Industry Science and Medicine (radio frequency band)
LPD	Lapped (surface finish)
mc-Si	Multicrystalline silicon
mono-Si	Monocrystalline silicon
MACE	Metal-Assisted Chemical Etching
NS	Nanostructures
PECVD	Plasma Enhanced Chemical Vapor Deposition
PERC	Passivated Emitter and Rear Cell (solar cell architecture)
PERL	Passivated Emitter and Rear Locally diffused (solar cell architecture)
PERT	Passivated Emitter and Rear Totally diffused (solar cell architecture)
PIII	Plasma Immersion Ion Implantation
PV	Photovoltaic

Abbreviations & Acronyms (continued)

RF	Radio-Frequency
RFEA	Retarding Field Energy Analyzer
RIE	Reactive Ion Etching
SAE	Slope Asymmetry Effect
SEM	Scanning Electron Microscopy
SHJ	Silicon Heterojunction
SRV	Surface Recombination Velocity
SWS	Slurry Wire Sawn (surface finish)
TVW	Tailored Voltage Waveform
Wp	Watt-peak

Symbols

α_{Si}	Absorption coefficient of crystalline silicon [m^{-1}]
$\Delta\theta_{\mathrm{fe}}$	Phase-shift introduced by feedthrough/electrode connection [rad]
ε	Symmetry parameter (plasma)
$\boldsymbol{\epsilon}$	Permittivity (complex) of a material [$\mathrm{F}\cdot\mathrm{m}^{-1}$]
η	Efficiency (solar cell parameter) [%]
Θ	Phase-shift (between frequency components of voltage waveforms) [rad]
κ_{Si}	Extinction coefficient of crystalline silicon
λ	Wavelength of light [nm]
λ_0	Free space wavelength of light [nm]
Λ_{NS}	Nanostructures average pseudo-period [nm]
Σ_{NS}	Nanotextured surface area enhancement factor
τ_{eff}	Effective minority carrier lifetime [ms]
$\tau_{\mathrm{i,s}}$	Ion sheath transit time [ns]
ϕ_{tot}	Total ion flux [$\mu\mathrm{A}\cdot\mathrm{cm}^{-2}$] or [$\mathrm{ions}\cdot\mathrm{cm}^{-2}\cdot\mathrm{s}^{-1}$]
$\phi_{\mathrm{AM1.5g}}$	Global solar spectral photon flux at Air Mass 1.5 [$\mathrm{s}^{-1}\cdot\mathrm{m}^{-2}\cdot\mathrm{nm}^{-1}$]
ϕ_E	Ion energy distribution function [$\mu\mathrm{A}\cdot\mathrm{cm}^{-2}\cdot\mathrm{eV}^{-1}$] or [$\mathrm{ions}\cdot\mathrm{cm}^{-2}\cdot\mathrm{s}^{-1}\cdot\mathrm{eV}^{-1}$]
Φ	Ion fluence [$\mathrm{ions}\cdot\mathrm{cm}^{-2}$]
Φ_E	Energy weighted ion fluence [$\mathrm{ions}\cdot\mathrm{eV}^{1/2}\cdot\mathrm{cm}^{-2}$]
A_{g}	Grounded electrode area [cm^2]
A_{p}	Powered electrode area [cm^2]
A_{tot}	Total absorptance [%]
AR_{NS}	Nanostructures aspect ratio
d	Etched thickness [µm]
d_{Si}	Atomic density of crystalline silicon [m^{-3}]
E	Ion bombardment energy [eV]
E_{th}	Ion energy etching threshold [eV]
f_0	Basis frequency (of voltage waveforms) [MHz]
FF	Fill factor (solar cell parameter)
G_{fe}	Gain in voltage amplitude introduced by feedthrough/electrode connection
H_{NS}	Nanostructures average height [nm]
J_{ph}	Photogenerated current density [$\mathrm{mA}\cdot\mathrm{cm}^{-2}$]
J_{sc}	Short-circuit current density (solar cell parameter) [$\mathrm{mA}\cdot\mathrm{cm}^{-2}$]

Symbols (continued)

n	Number of frequency components in voltage waveforms
$\boldsymbol{n}_{\mathrm{Si}}$	Refractive index (complex) of crystalline silicon
$\bar{n}_{\mathrm{sg}}$	Time-averaged charge density in grounded electrode sheath [cm^{-3}]
$\bar{n}_{\mathrm{sp}}$	Time-averaged charge density in powered electrode sheath [cm^{-3}]
P_{r}	Discharge pressure [mTorr] (NB: 1 mTorr ≈ 0.133 Pa and 1 mTorr ≈ 1.33 µbar)
P_{w}	Total coupled power to the discharge [W]
q	Electrical charge [C]
R_{eff}	Effective reflectance [%]
R_{f}	Front reflectance [%]
S_{eff}	Effective minority carrier surface recombination velocity [$\mathrm{cm}\cdot\mathrm{s}^{-1}$]
S_{f}	Front surface minority carrier recombination velocity [$\mathrm{cm}\cdot\mathrm{s}^{-1}$]
t_{e}	Etching time [min]
$T_0 = 1/f_0$	Period of voltage waveforms [ns]
V_{DC}	DC self-bias voltage [V]
$\tilde{V}$, $\tilde{V}_{\mathrm{e}}$	Voltage waveform at the electrode [V]
$\tilde{V}_{\mathrm{f}}$	Voltage waveform at the feedthrough [V]
V_{max}	Maximal voltage (of excitation waveforms) [V]
V_{min}	Minimal voltage (of excitation waveforms) [V]
V_{oc}	Open-circuit voltage (solar cell parameter) [V]
$\bar{V}_{\mathrm{pl}}$	Time-averaged plasma potential [V]
V_{PP}	Peak-to-peak voltage (of excitation waveforms) [V]
w	Absorber thickness [µm]

Constants

e	Elementary charge (1.602×10^{-19} C)
ϵ_0	Vacuum permittitivity ($8.854 \times 10^{-12}\,\mathrm{F}\cdot\mathrm{m}^{-1}$)
k_{B}	Boltzmann constant ($1.381 \times 10^{-23}\,\mathrm{J}\cdot\mathrm{K}^{-1}$)
m_{e}	Electron mass (9.109×10^{-31} kg)

INTRODUCTION

PHOTOVOLTAIC ELECTRICITY FOR SUSTAINABLE DEVELOPMENT

"*But there is always the sun [...]. From a power standpoint the outlook for the future is not too dark for optimism.*"

Leslie A. White, 1943 [1]

Contents

1 Energy Enables Human Development **2**
1.1 A Global Look at Energy Needs 2
1.2 The Haunting Issue of Global Climate Change 4
2 Aim for the Sun! **6**
2.1 PV Systems Deliver Electricity 6
2.2 Unique Attributes of Photovoltaic Energy 7
2.3 Photovoltaic is not the Sole and Universal Solution 8
3 Thesis Aim and Outline **10**
Bibliography **11**

Introduction

The link between human development and access to energy is fundamental to describe the evolution of humankind and, maybe even more importantly, to define policies for a brighter future. In order to tangibly characterize this relationship, one can first look at the works of Leslie A. White, an American anthropologist from the mid-20th century. Adhering to the cultural evolution theory, White had been trying to comprehensibly describe the development of humankind from its early stages up to the technological advancements of the last century. His theory is extensively described in the paper "Energy and the Evolution of Culture" [1] published in 1943, which starts with an eloquent statement: "Everything in the universe may be described in terms of energy".

In [1], White studies the evolution of culture with respect to access to energy. To him, culture is a kind of behavior associated to symbolism [2], which "man [...] is the only creature to possess [and which] purpose is to serve the needs of man". Two "law[s] of cultural development" are exposed: "cultural development varies directly as the amount of energy per capita per year harnessed and put to work" and "as the efficiency of the technological means with which the harnessed energy is put to work". Crudely transposing these statements to current concepts, White has demonstrated that human development progresses due to increased total primary energy supply per capita (TPES) and improved energy efficiency. These laws are then applied by White to identify several stages of development, from the state of "savagery", when people only had food energy to put to work, until the "civilization" that emerged in the late 18^{th} century and relies on fuels and engines.

White's theories on cultural development are still subject to debate. However, the link between access to energy and human development (in terms of progress, quantified using well documented indexes adapted to our current society) is unarguably accepted, as this introductory chapter will first investigate on the global scale. The emerging threats to human development originating from climate change, strongly associated with the production and use of energy, will then be shortly discussed. Secondly, the potential benefits of increased renewable and especially solar energy from photovoltaics (PV) in the world energy mix will be introduced, as well as the current shortcomings of PV. Finally, this thesis aims and outline will be introduced.

1 Energy Enables Human Development

1.1 A Global Look at Energy Needs

The link between human development and energy use has been notably investigated by Goldemberg *et al.* [3] in 1985. The authors showed at that time that the physical quality of life (PQLI, an index based on infant mortality rate, life expectancy and literacy) was directly linked to the energy use per capita in a given country, up to 1 kWh (per hour per capita, i.e. 8.8 MWh/year/capita). Above this threshold, only marginal gains in PQLI were observed for further increases of primary energy use per capita.

A more up-to-date analysis can be made using data from the World Bank [4] and the United Nations (UN) [5]. Figures for the year 2014 (last extensively documented year available) are used from now on. The Human Development Index (HDI) is chosen as an indicator for the quality of life. HDI is computed based on life expectancy at birth, gross national income per capita and education level, and HDI values lie in the interval [0,1], the higher the better. The energy requirements are quantified by the "energy use" provided by the International Energy Agency (IEA, [6]) and which corresponds to the total primary energy supply (TPES) per capita per year for a given country. Figure 1 shows the HDI for 129 countries from 7 different geographical regions as a function of the energy use.

First, let us have a look at some global figures, the dashed lines in Figure 1 show the world averages for energy use and HDI. In 2014, the world population was about 7.27 billion people, which were using a total of approximately 1.6×10^5 TWh per year of primary energy, so an average human on planet Earth required about 22 MWh of energy per year (a number close to the average in Croa-

tia or in Thailand for instance). As a comparison, French people require 43 MWh per year, while in the US the average lies at 81 MWh per year per person. Concerning HDI, the global average in 2014 was 0.702, a value which lies in the "high development" classification of the UN but obviously hides tremendous inequalities, most African countries lying far below this value.

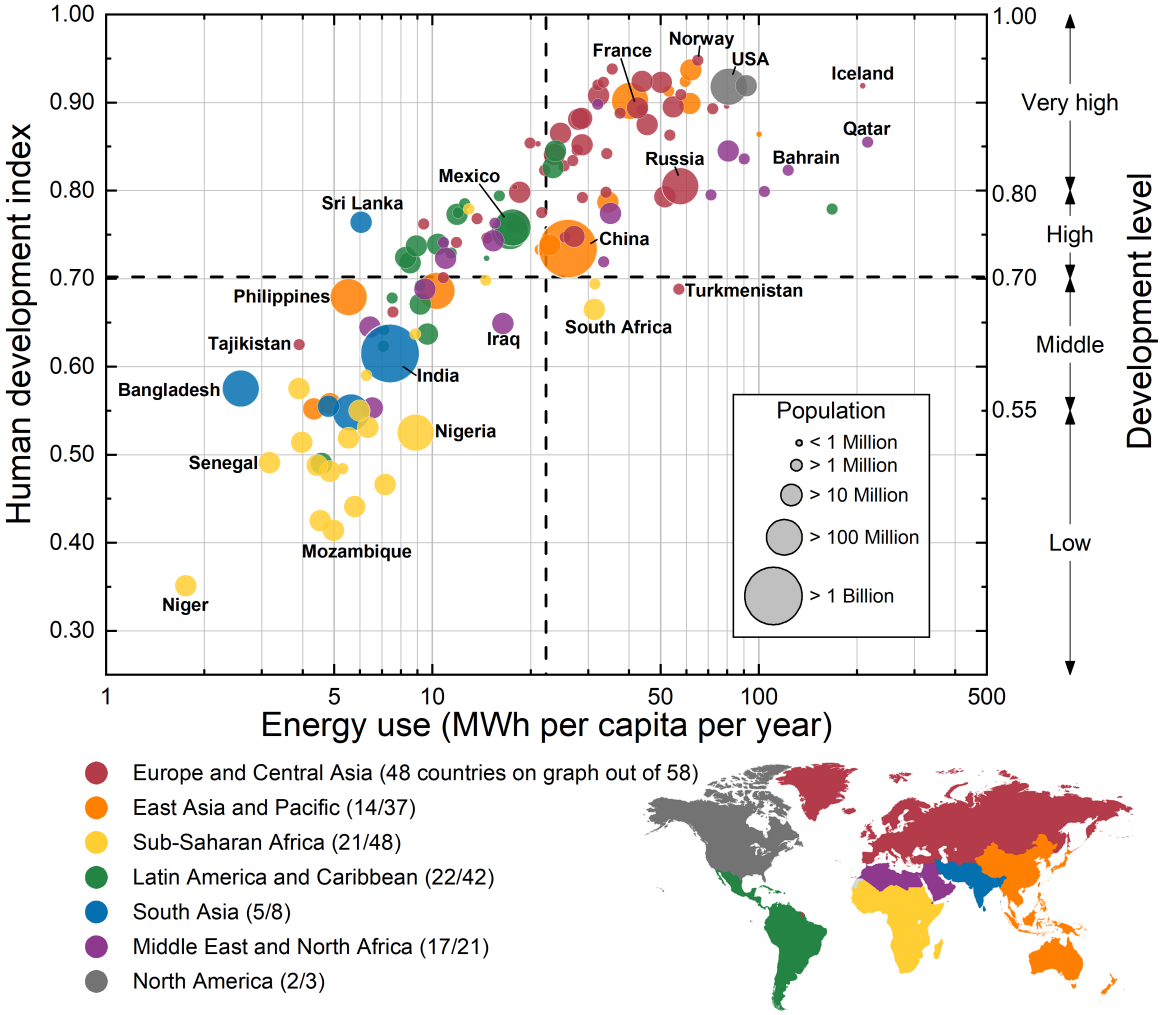

Fig. 1: Human development index versus energy use for 2014 in 129 countries. Countries are sorted by geographical regions as defined by the World Bank (see inset map). Dashed lines show the world average for HDI (0.702) and energy use per capita (22.3 MWh per year) in 2014 [4, 5].

Looking now at the distribution of situations for the data shown in Figure 1, the analysis is quite similar to the one drawn by Goldemberg *et al.* more than 30 years earlier: HDI is directly linked to the energy use per capita, at least until a threshold value (roughly 30 MWh/year/capita), above which most countries are in a high to very high development state and the correlation between HDI and energy use vanishes. The UN recognized the key role of energy for human development when setting the 17 Sustainable Development Goals [7]: goal number 7 is entitled "Affordable and clean energy" especially targeting "universal access to affordable, reliable and modern energy services" by 2030. From these values and in a (utopic) naive analysis, a global increase of the energy use per capita and a better repartition of energy would allow all countries to obtain high development, according to the standards of the UN.

However, the previous analysis fails to properly describe the energy requirements for human development, as has been pointed out by Arto *et al.* [8]. Indeed, aggregating the energy supplied in a geographical region does not express a country's real energy footprint: our globalized economy implies that for most developed countries, a large amount of energy needed to produce food or goods is actually produced and consumed in other parts of the world. The study by Arto *et al.*

shows that the threshold to achieve very high development (HDI> 0.8) is higher by 13% when considering energy footprint instead of energy use. Moreover, refinements in the quality of life index to better describe the situation in low human development countries, as recently attempted by Nadimi and Tokimatsu [9], shows that increases in energy use does not immediately prompt improvements in quality of life.

Finally, studies at the scale of entire countries do not capture inequalities among the countries' own population, and these inequalities are not restricted to developing countries. As an example, one can have a look at data for France, although it is a wealthy country. In 2013 according to a study by the French Service for observation and statistics [10], 3.2 million households (representing around 7.8 million people), where affected by "fuel poverty" according to the "Low income/high costs" indicator developed for the government of the United Kingdom in 2012 [11]. These households mostly consist in tenants, families with children and unemployed people. The study reflects that in developed countries, although most people benefit from access to energy, related expenses (e.g. fuels for heating or transportation) negatively affect vulnerable people.

1.2 The Haunting Issue of Global Climate Change

Global climate change due to human activities is a scientifically demonstrated fact, as it has been stated by the Intergovernmental Panel on Climate Change (IPCC, 5th assessment report, Summary for policymakers" of the Working Group I "The Physical Science Basis" [12]). It has been recognized as a global threat by almost all countries, and policies are being implemented to reduce the magnitude of global warming and its potential effects around the world, notably through the Paris climate agreement [13]. While both the causes and effects of climate change are too numerous to even evoke in this short introduction (and have most certainly not all been identified yet), let us focus on the basics: global warming is mostly driven by a raise in "anthropogenic radiative forcing". In other words, the net energy balance in the Earth's atmosphere is increasing, mostly due to enormous emissions of greenhouse gases from human activities.

Continuing on the issue discussed in this introduction, let us rapidly highlight how global climate warming constitutes a tangible threat to human development (just one of the many consequences that are foreseen or already set in motion).

In its 2007 "Human Development Report" [14], the UN identified five intertwined challenges coming from the effects of global warming on developing countries or, more generally, on the poorest and most vulnerable people in the world's population: (i) agricultural productivity will drop in many regions due to amplified and more frequent extreme climate events such as drought and floods, threatening poor population relying directly on local agriculture. Similarly, (ii) water resources will be redistributed on global and regional scales, threatening supplies for both irrigation and consumption. (iii) Both the sea level and the surface water temperature are rising, thus endangering coastal populations (sometimes whole insular countries) who will suffer even more from extreme weather events like hurricanes. (iv) Local ecosystems, which represent a large (sometimes unique) source of food and income, will be destroyed. (v) Diseases, especially in tropical regions, will likely affect a growing number of people. In a recent report [15], the World Bank predicts that climate change and its effects will lead to the greatest internal migrations in human history, leading up to 140 million people to move to more habitable areas in their respective countries.

In order to assess the level of threat that countries are facing due to global climate change, instructive insights are given by the Notre-Dame Global Adaptation Initiative (ND-GAIN) [16]. This program has been launched in 2013 and evaluates vulnerability and readiness for adaptation in the context of global warming, based on numerous statistical data. Vulnerability is computed through an aggregation of threats in the "life-supporting sector", namely water, food, health, ecosystem services, human habitat and infrastructures. All these sectors are indeed threatened and overlap well with the risks pointed out by the UN, as synthesized in the last paragraph. For each sector, the exposure of a given country to climate change threats are assessed, as well as the sensitivity and adaptive capacity of the country to these pressures. On the other hand, a country's readiness

is computed from three aspects: economic strength (ability to invest in new adaptive infrastructures), a favorable governance system (willing to impulse the required changes through strong policies) and a favorable social context (e.g. high education level or innovation capabilities) encouraging equitable use of investments.

These scales are used to classify countries in four categories as represented in Figure 2. A correlation between vulnerability and readiness is observed as the statistical data aggregated by both index is interrelated. Countries in the upper-left quadrant (most sub-Saharan and south Asian countries) are the most threatened by climate change: they show both a high vulnerability and low readiness, and international support should be focused on these populations to avoid potential major humanitarian disasters.

On the contrary, most countries from Europe, Central Asia and North America fall in the lower right quadrant. This distribution reflects the idea that most developed countries generated a global threat that will mostly impact populations from the economic South. The ND-GAIN analysis may help international bodies decide where efforts should be focused in order to secure the futures of as many people as possible.

Promoting human development at the global scale thus requires mankind to address big challenges, and two of them have been highlighted: providing energy to all and reducing the magnitude of climate change and its effects.

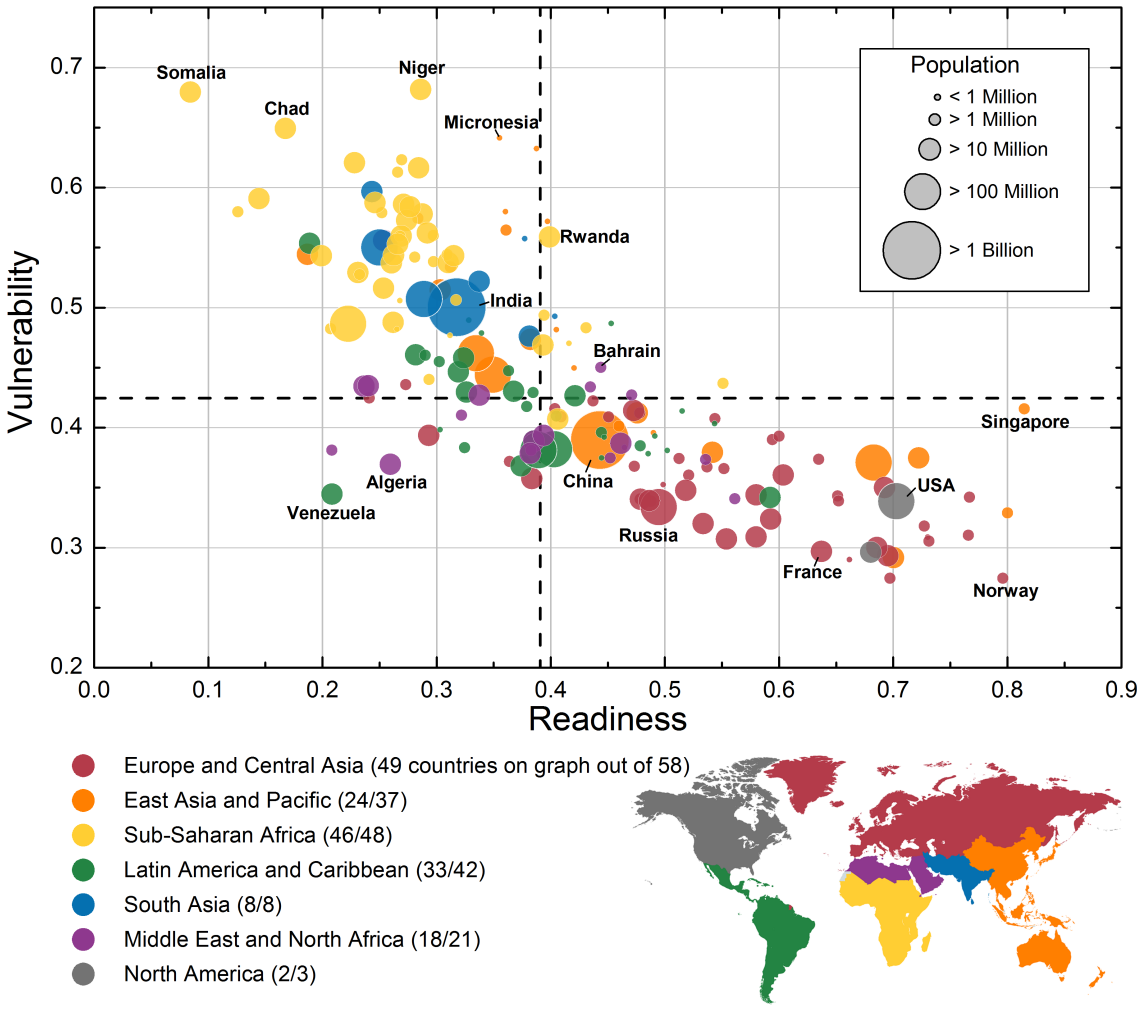

Fig. 2: Vulnerability versus readiness for 2014 in 180 countries. Countries are sorted by geographical regions as defined by the World Bank (see inset map). Dashed lines show the median values among countries [16].

2 Aim for the Sun!

Let us now go back to the works of Leslie White – who, in 1943, could obviously not have been aware of climate change. In his aforementioned paper [1], two remarkable possibilities for future stages of development for mankind are envisioned. Indeed, White first assumes that this next stage could rely on the emerging (at that time) atomic energy. However, as atomic energy was only in its emergence in the early 40s, White highlights the abundancy of another source of energy that might become "our chief source of power in the future": solar energy.

To support this idea, White cites the work of Clifford C. Furnas, professor in chemical engineering at Yale University. Furnas gave one of the earliest review of modern sources of energy in 1941 [17]. The possibility for "Direct utilization of solar energy" is in particular discussed, and Furnas gives the following order of magnitude: "the average intensity of solar energy in this latitude [41°] amounts to about 0.1 of a horse power per square foot", or around 800 W/m^2 in SI units. Then, "photoelectric cells" are debated – as a tool to directly convert solar energy to electricity, but Furnas recalls that photovoltaic cells where at that time operating at "microscopic efficiency", and that "revolutionary improvements" were required to improve this technology.

These revolutionary improvements have taken place: at the end of 2017, the global cumulative PV capacity was 403 GWp [18], and 25% of it was installed during 2017, indicative of a colossal growth of the market pushed by China. The annual electricity production over the same year was close to 500 TWh, accounting for 2% of worldwide generation.

A possible solution to our challenges, even if incomplete, can be envisioned using solar energy harnessed through PV systems.

2.1 PV Systems Deliver Electricity

It is sometimes valuable to restate the obvious: PV systems directly convert solar energy to electricity, a very important property to address the problem of energy poverty. Indeed, energy poverty not only reflects the lack of access to energy (in terms of energy use per capita as discussed previously for instance), but also to the difficulties encountered to access affordable, reliable and high-grade energy. In his overview of energy poverty [19], Gonzalez-Eguino stresses that energy poverty is usually characterized by a lack of choice: the only available resources for cooking and heating often consist of solid or liquid fuels, which affect the safety and health of population (especially in

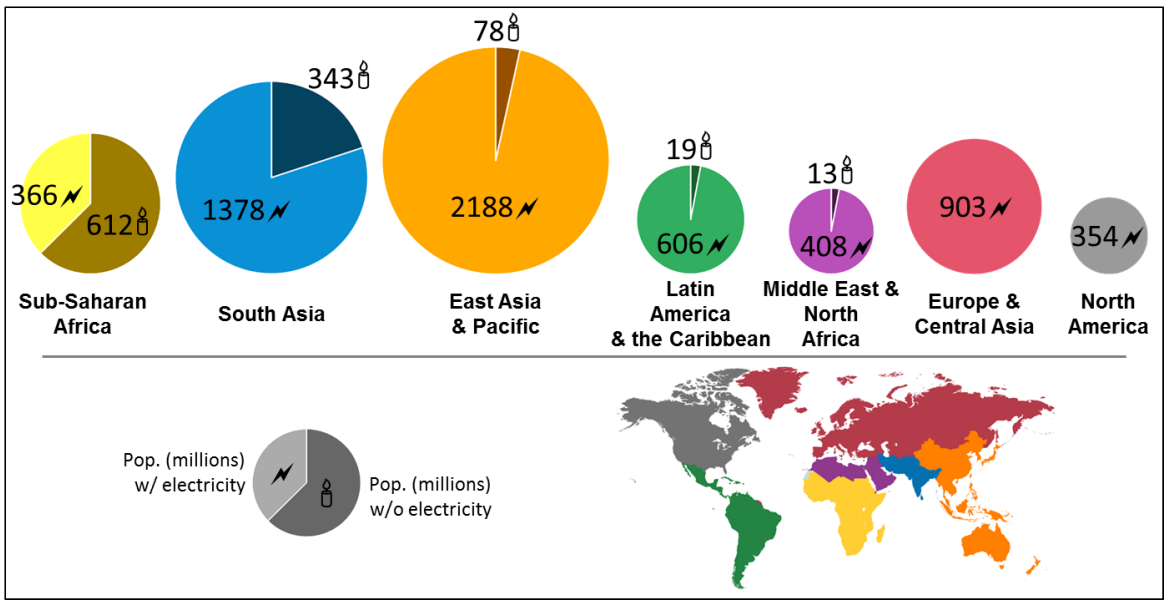

Fig. 3: Number and repartition of people lacking access to electricity in the world. Area of color pies proportional to total population. Data for 2014 from the World Bank [4].

rural areas) and are not always cheaper than other potential sources. In this perspective, access to electricity represents an essential step forward: electrification is an enabler for education (lighting in schools, access to modern media), health and safety (water pumping, refrigeration, electrical heaters for reduced indoor pollution, modern medical services and facilities), and economic development (emergence of local micro-businesses, upgraded tools for farming or transforming raw materials).

In 2014, 1.1 billion people had no access to electricity, according to the data from the "Sustainable Energy for All" program run by the World Bank [4]. The current electrification rate in different geographical regions is depicted in Figure 3. Unsurprisingly, the electrification rate in Europe, Central Asia and North America is essentially 100%. On the other hand, the worst situations are found in South Asia and sub-Saharan Africa, where respectively 20 and 63% of the population still lacks access to electricity, accounting for a total of 955 million people. For other regions, around 3% of people are deprived of access to electricity. Globally, most of the people lacking electricity (90%) live in rural regions. Tremendous work is still required to electrify these regions, where the population is expected to substantially grow in the next decades according to projections from the UN [20]. For most of these countries, renewable energies – such as solar energy converted with PV systems – represent a solution to achieve a higher level of development.

2.2 Unique Attributes of Photovoltaic Energy

Besides the fact that PV technologies deliver electricity, a few other unique properties of this energy have to be highlighted with respect to the challenges raised by energy needs and climate change.

Solar energy is dispersed at the global scale. Yearly solar energy at ground level exceeds the total annual energy demand of mankind by orders of magnitude [21]. However, the most prominent advantage of solar energy may come from its distribution at the global and local scale. The world map in Figure 4 (obtained from the "Global Solar Atlas" [22]) shows the global solar irradiation: countries from the economic South actually benefit from a high potential. Therefore, PV systems can provide electricity to large portions of the world population still lacking energy. In addition, while large electric networks may require major public investments (and therefore strong governance and economic conditions), PV systems may be deployed locally, to self-sufficiently power a household or a village for instance.

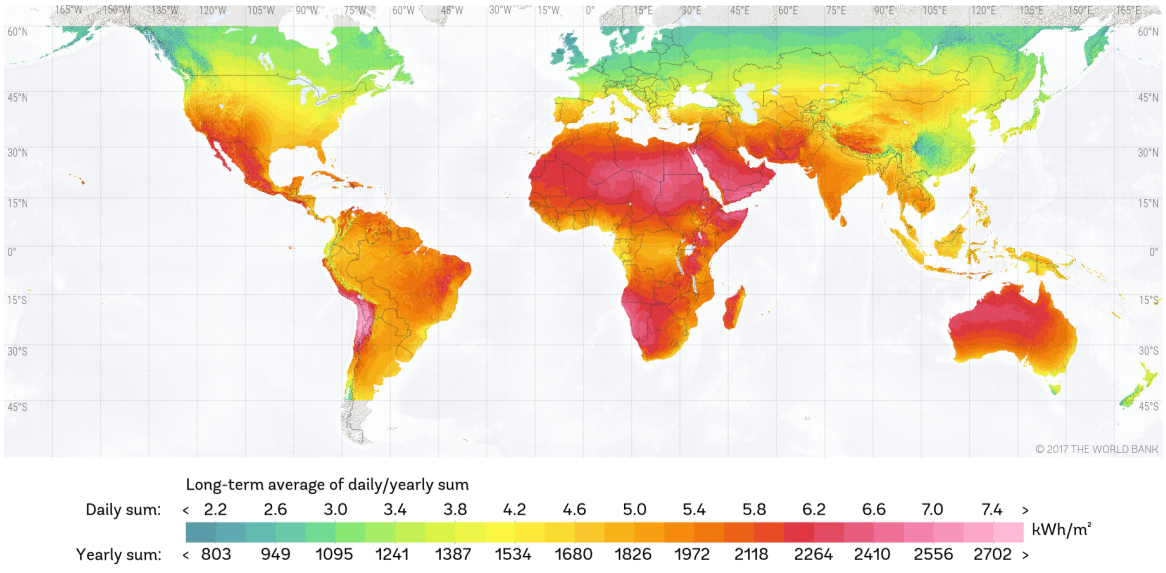

Fig. 4: World map of solar horizontal irradiation with a spatial resolution of 1 km [22].

PV technologies deliver low-carbon electricity at competitive costs. Let us first rapidly discuss the competitiveness of PV electricity. High prices of PV installations have for a long time required many countries to support their development through feed-in tariffs or capital subsidies [23]. However, the prices of PV systems (and consequently of the levelized cost of electricity, LCOE) have considerably decreased in recent years. The observed "learning curve" of PV industry (from 1976 to 2017) shows that each doubling of cumulative PV module shipments has been accompanied by a 22.8% decrease in average module sales price [25]. In 2017, the average crystalline silicon solar cell module price lay at only 0.34 \$/Wp. Recent years have however seen large fluctuations of the market: production overcapacities in China have pushed module prices far below the long-term trend and future evolutions might become more moderate. Moreover, module costs now represent only a mere half of the total costs (for large PV systems, above 100 kWp): decreasing module prices will ultimately have much less effect on the LCOE.

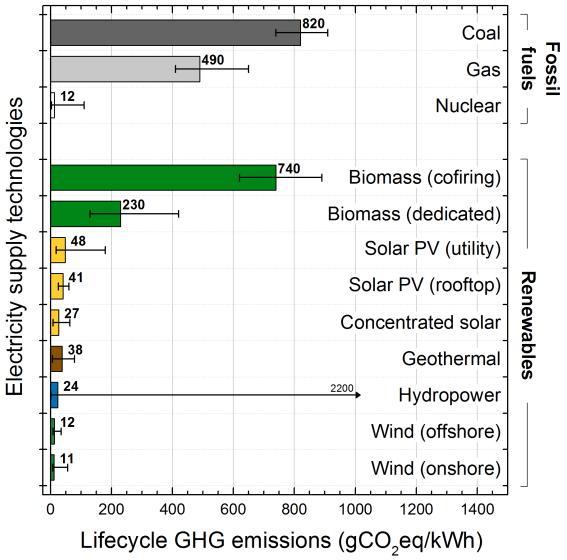

Fig. 5: Lifecycle GHG emissions for the major electricity supply technologies, adapted from the IPCC 5th assessment report [24].

Finally, the advantages of photovoltaic energy have to be discussed with respect to the issue of global climate change. Indeed, in 2014 the energy sector alone accounted for 68% of greenhouse gases emissions, essentially through carbon dioxide (CO_2) according to the IEA [26], and a substantial decrease of emissions can only be envisioned through a radical conversion to low-carbon energy sources. Obviously, such change would be beneficial to reduce the extent of global warming and its consequences for our societies.

Figure 5 shows the lifecycle greenhouse gas (GHG) emissions for the main electricity supply technologies [24]. Coal and gas, which account for 60% of the world electricity generation [27], emit respectively 820 and 490 gCO_2eq per kWh of electricity (median value), and most of this comes directly from direct emissions. These values are one order of magnitude higher than the median values for all renewables resources (with the exception of biomass). For renewable resources, none of the GHG emissions are direct but rather come from indirect sources (e.g. methane release from hydropower reservoirs) or from the infrastructure and supply chain.

Focusing on renewable resources, PV technologies are considered low-carbon electricity sources with median values of lifecycle GHG emissions at 48 gCO_2eq/kWh for utility scale installations and 41 gCO_2eq/kWh for rooftop PV. However, these values make PV twice as carbon-intensive than hydropower and four times more than wind power.

2.3 Photovoltaic is not the Sole and Universal Solution

The dark picture of the world's situation previously depicted in terms of unequal energy access, and unequal levels of threats from global climate warming is alarming. However, global and local solutions are within reach, provided that policymakers recognize the current emergency. Large improvements in human development, in particular for the poorest populations, can be expected from the development of renewable energy in general, and notably photovoltaic electricity through decentralized systems for underdeveloped or remote areas. Obviously, the large-scale development of photovoltaic energy is not the only solution to address the highlighted challenges. From the figures previously emphasized, making PV a major contributor in the global energy mix requires this industry to reach the terawatt-scale. Several challenges have to be addressed to achieve this level, as illustrated by two current limitations: (i) material scarcity and (ii) solar intermittence.

The first limit comes from PV technologies themselves: expansion of technologies currently on the market is limited by one or more of their components [28]. Focusing on the case of crystalline silicon solar cells, which represent more than 90% of the market [23], the current limiting material is silver, used for electrical contacts. Assuming some hypotheses on module production and without technological shifts, full silver depletion would occur in less than 20 years. Other technologies could continue growing for a longer time, but would eventually lead to lower maximum wattage. Lowering silver consumption per kWp in the next years therefore appears essential to ensure continued large-scale deployment of crystalline silicon solar cells.

On the other hand, the challenge of intermittence is intrinsic to the solar resource. For grid-connected PV systems, the challenge lies in the management of the electric grid. Indeed, large variations in total PV electric production need to be matched with complementary variations from other sources, or with a balance from storage systems both on a short- (minutes or hours) and long-term timescale (days or weeks). Studies on the large evolutions of the world energy mix have been launched for a long time to define the adequate shares of PV production, even up to 100% renewable energy mixes. In one scenario [29], the Lappeenranta University of Technology envisions a total installed capacity of 12.7 TWp of PV worldwide in 2030, supplying around 40% of the forecasted total energy demand. Meanwhile, this large share of PV relies on large amounts of storage with various technologies, in particular batteries for a total capacity of 9.9 TWh (accounting for 75% of the stored electricity). However, 100% renewable energy mix scenarios are raising concerns on the grounds of feasibility evaluations [30]. Off-grid installations are of greater interest regarding the previous analysis of electricity needs for development. Even though off-grid systems represent niche markets in developed countries, they are of tremendous importance in developing countries, where traditional grids are not yet deployed nor reliable [23]. Scalable off-grid PV (from pico-systems to regional grids) now represent a solution for universal electricity access [31], but require adapted storage technologies, as well as support from policy-makers to motivate investments from the private sector.

As a conclusion, sustainable development for all through large-scale PV deployment requires continued technological improvements both in PV and storage systems. Efforts currently focus, in particular, on raising the energy density of PV systems through increased solar cell efficiency. As an example (among many others), photogeneration of electrical carriers in silicon solar cells can be promoted by improving the optical properties of the front absorber surface, for instance through nanotexturing.

3 Thesis Aim and Outline

This thesis has been executed in the framework of the Project A "Silicon solar cells" of the Institut Photovoltaïque d'Île-de-France (IPVF) and in collaboration with the Laboratoire de Physique des Interfaces et Couches Minces (LPICM, CNRS, Ecole polytechnique). Project A aims to develop and implement innovative building blocks for high-efficiency silicon based solar cells, with the potential to be included in tandem structures with an efficiency above 30%.

The aim of the thesis was to develop, understand and optimize plasma texturing of silicon at the nanoscale for light management in PV applications, using an innovative plasma excitation method named Tailored Voltage Waveforms. This document is structured in the following manner:

- Chapter I first gives a brief state of the art for the theoretical and experimental background on reactive ion etching and nanoscale texturing of silicon for PV applications. The main processing and characterization tools used during this thesis will also be rapidly depicted.
- Chapter II focuses on the use of Tailored Voltage Waveforms excitation in a capacitively coupled radiofrequency discharge reactive ion etching system. The effects of Tailored Voltage Waveforms in the case of an SF_6/O_2 discharge will be especially investigated, this chemistry being later used for silicon texturing.
- Chapter III explores the plasma-surface interactions taking place during etching of silicon using an SF_6/O_2 discharge, and elucidates some universal trends using tailored voltage waveforms excitation. Finally, a demonstration of the interest of using TVWs for texturing is given.
- Chapter IV further investigates the optical and electronical properties of silicon surfaces nanotextured using the developed plasma process. Again, some universal trends are observed and together with the observations made in the previous chapter can be translated to design rules for dry texturing processes applied to PV technologies.

General conclusions are finally drawn from this thesis work, and possibilities for further research are outlined.

Bibliography (Introduction)

[1] L. A. White, Energy and the Evolution of Culture, *Am. Anthropol.* **1943**, 45(3), 335–356, doi:10.1525/aa.1943.45.3.02a00010. 1, 2, 6

[2] L. A. White, The Concept of Culture, *Am. Anthropol.* **1959**, 61(2), 227–251, doi:10.1525/aa.1959.61.2.02a00040. 2

[3] J. Goldemberg, T. B. Johansson, A. K. N. Reddy and R. H. Williams, Basic Needs and Much More with One Kilowatt per Capita, *Ambio* **1985**, 14(4/5), 190–200. 2

[4] World Bank Open Data, URL `data.worldbank.org`. 2, 3, 6, 7

[5] United Nations, Human Development Data, URL `hdr.undp.org/en/data`. 2, 3

[6] International Energy Agency, URL `www.iea.org`. 2

[7] United Nations, Sustainable Development Goals, URL `www.un.org/sustainabledevelopment`. 3

[8] I. Arto, I. Capellán-Pérez, R. Lago, G. Bueno and R. Bermejo, The energy requirements of a developed world, *Energy Sustain. Dev.* **2016**, 33, 1–13, doi:10.1016/j.esd.2016.04.001. 3

[9] R. Nadimi and K. Tokimatsu, Modeling of quality of life in terms of energy and electricity consumption, *Appl. Ener.* **2018**, 212, 1282–1294, doi:10.1016/j.apenergy.2018.01.006. 4

[10] Les ménages et la consommation d'énergie, Tech. rep., Service de l'Observation et des Statistiques, **2017**, URL `www.statistiques.developpement-durable.gouv.fr`. 4

[11] An Assessment Tool for Low Income/High Costs Fuel Poverty, Research Summary, Tech. rep., Eaga Charitable Trust, **2015**, URL `www.eagacharitabletrust.org`. 4

[12] T. Stocker *et al.* (Eds.), Climate Change 2013: The Physical Science Basis. Contribution of Working Group I to the Fifth Assessment Report of the Intergovernmental Panel on Climate Change, Cambridge University Press, Cambridge, United Kingdom and New York, NY, USA, **2013**. 4

[13] United Nations, The Paris Agreement, URL `unfccc.int/paris_agreement/items/9485.php`. 4

[14] UNDP (Ed.), Fighting climate change: human solidarity in a divided world, no. 2007/08 in Human development report, Palgrave Macmillan, Houndmills, **2007**, ISBN 978-0-230-54704-9, URL `www.un.org`. 4

[15] K. Kumari Rigaud *et al.*, Groundswell: Preparing for internal climate migration, Tech. rep., The World Bank, Washington DC, **2018**, URL `www.worldbank.org`. 4

[16] Notre Dame Global Adaptation Initiative, University of Notre Dame, URL `gain.nd.edu`. 4, 5

[17] C. C. Furnas, Future Sources of Power, *Science* **1941**, 94(2445), 425–428, doi:10.1126/science.94.2445.425. 6

[18] 2018 Snapshot of Global Photovoltaic Markets, Tech. rep., International Energy Agency, **2018**. 6

[19] M. González-Eguino, Energy poverty: An overview, *Renew. Sust. Energ. Rev.* **2015**, 47, 377–385, doi:10.1016/j.rser.2015.03.013. 6

[20] World Population Prospects: The 2017 Revision, Key Findings and Advance Tables, Tech. Rep. ESA/P/WP/248, United Nations, **2017**, URL `www.un.org`. 7

[21] R. Perez and M. Perez, The World's energy reserves, a fundamental look, *IEA-SHC - Solar Update* **2009**, 50, 2–3. 7

[22] Global Solar Atlas, URL `globalsolaratlas.info`. 7

[23] Trends 2017 in Photovoltaic Applications, Tech. Rep. 22, International Energy Agency, Photovoltaics Power Systems Programme, **2018**, URL `www.iea-pvps.org`. 8, 9

[24] O. Edenhofer *et al.* (Eds.), Climate Change 2014: Mitigation of Climate Change. Contribution of Working Group III to the Fifth Assessment Report of the Intergovernmental Panel on Climate Change, Cambridge University Press, Cambridge, United Kingdom and New York, NY, USA, **2014**, URL `www.ipcc.ch/report/ar5/wg3/`. 8

[25] International Technology Roadmap for Photovoltaic Ninth Edition, March 2018, Tech. Rep. 9, ITRPV, **2018**, URL `www.itrpv.net`. 8

[26] CO_2 Emissions from Fuel Combustion 2017, Highlights, Tech. rep., International Energy Agency, **2017**, URL `www.iea.org`. 8

[27] International Energy Outlook 2017, Tech. rep., U.S. Energy Information Administration, **2017**, URL `www.eia.gov`. 8

[28] C. S. Tao, J. Jiang and M. Tao, Natural resource limitations to terawatt-scale solar cells, *Sol. Energy Mater. Sol. Cells* **2011**, 95(12), 3176–3180, doi:10.1016/j.solmat.2011.06.013. 9

[29] C. Breyer *et al.*, On the role of solar photovoltaics in global energy transition scenarios: On the role of solar photovoltaics in global energy transition scenarios, *Prog. Photovolt. Res. Appl.* **2017**, 25(8), 727–745, doi:10.1002/pip.2885. 9

[30] B. P. Heard, B. W. Brook, T. M. L. Wigley and C. J. A. Bradshaw, Burden of proof: A comprehensive review of the feasibility of 100% renewable-electricity systems, *Renew. Sustain. Energy Rev.* **2017**, 76, 1122–1133, doi:10.1016/j.rser.2017.03.114. 9

[31] P. Alstone, D. Gershenson and D. M. Kammen, Decentralized energy systems for clean electricity access, *Nat. Clim. Change* **2015**, 5(4), 305–314, doi:10.1038/nclimate2512. 9

CHAPTER I

THEORETICAL AND EXPERIMENTAL BACKGROUND

Contents

I.1 Reactive Ion Etching of Crystalline Silicon **16**
I.1.1 Fundamentals of CCP-RF Discharges 16
I.1.1.a What is a plasma? 16
I.1.1.b Ion bombardment on the powered electrode 20
I.1.2 TVWs: a Multi-frequency Extension of the RF Domain 22
I.1.2.a Employed waveforms and sources of asymmetries 22
I.1.2.b Amplitude asymmetry effect 23
I.1.2.c Slope asymmetry effect 25
I.1.2.d TVWs at process level: uses and limitations 26
I.1.3 Process Description and Monitoring 27
I.1.3.a Description of the reactor 27
I.1.3.b Limitations of the experimental setup 28
I.1.3.c Power monitoring and in-situ characterization 29
I.1.4 Silicon Etching 30
I.1.4.a Crystalline silicon: basic properties 30
I.1.4.b Plasma etching mechanisms 31
I.1.4.c The particular case of fluorine etching of silicon 32
I.2 Black Silicon: Theory and Characterization **35**
I.2.1 Silicon Nanostructure Formation 35
I.2.1.a Silicon surface texturing by SF_6/O_2 plasma 36
I.2.1.b Common “wet” texturing techniques 38
I.2.1.c Other nanotexturing techniques 39
I.2.1.d Synthesis 41
I.2.2 Optical Properties of Nanostructured Surfaces 44
I.2.2.a Anti-reflection 44
I.2.2.b Light-trapping 46
I.2.2.c Angular acceptance 48
I.2.3 Implementation of b-Si in Solar Cells 48
I.2.3.a Challenges from electronic properties 48
I.2.3.b State of the art black silicon solar cells 50

I.2.4 Characterization Methods 52
I.2.4.a Spectrophotometry 52
I.2.4.b Scanning Electron Microscopy 53
I.2.4.c Stylus profilometry 54
I.2.4.d Photoconductance decay 55
Conclusion **56**
Bibliography **62**

Introduction

Before detailing the specific scientific background, it is useful to give a very synthetic description of a silicon solar cell, both to link the work with the previously outlined context and to clarify its purpose.

A solar cell is primarily an energy conversion system: it converts electromagnetic energy into electrical energy and relies on the photovoltaic effect. This effect has first been described in 1839 by the physicist Alexandre-Edmond Becquerel: photons are absorbed into a material creating electron-hole pairs that are separated and transmitted to an external load. Let us rapidly remind how current standard silicon solar cells are designed and operate, with a focus on optical aspects relevant to the present work. More details on the physics of solar cells can be found in [1].

Most silicon solar cells in the market are based on the "Aluminium Back Surface Field" (AlBSF) architecture, with a gradual shift to an upgraded version [2], namely the "Passivated Emitter and Rear Cell" (PERC), schematically described in Figure I.1(a). The cell is composed by a p-doped silicon absorber (around 200 µm thick) with a thin n+ emitter and rear p+ region creating a back-surface field near contacts. The front surface is textured (for anti-reflection and light-trapping purposes), and covered by passivation layers (to prevent carrier recombination at the surface) and anti-reflective coatings (ARC). A passivation layer is also present at the rear side (absent in the AlBSF architecture). Silver contacts arranged in fingers and busbars are present at the top surface (facing the Sun) and the back surface is covered by an aluminium contact with local openings of the dielectric passivation layer.

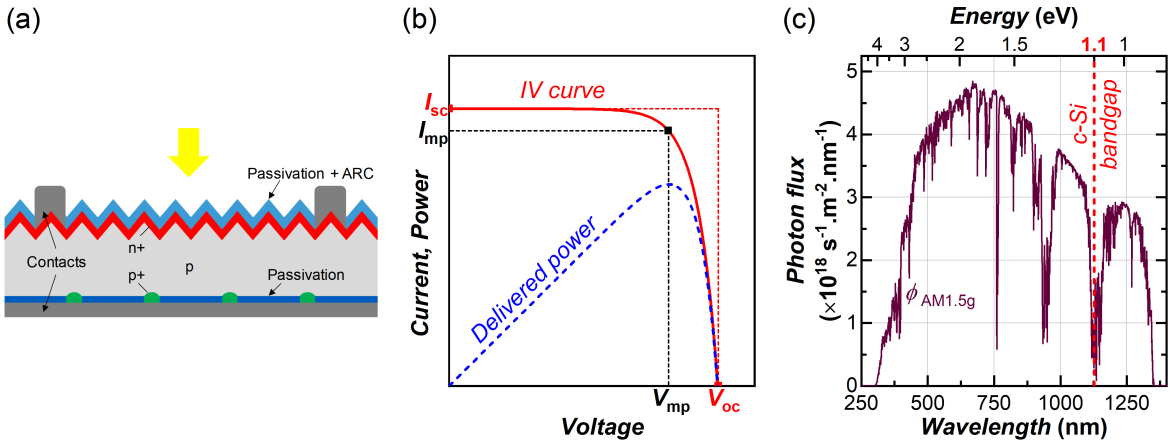

Fig. I.1: (a) Simplified schematic of a PERC solar cell; (b) model I-V characteristic under illumination and (c) AM1.5g solar spectral photon flux.

Photons absorbed in the silicon create electron-hole pairs, which are separated and extracted respectively at the front and back contacts. The operation of a solar cell is commonly described by its I-V characteristic under illumination, see Figure I.1(b). Four important metrics are derived from this curve: the open-circuit voltage V_{oc} (mV), the short-circuit current I_{sc} (mA), the fill factor FF (%) and finally the efficiency η (%), with the following relationship:

$$\eta = \frac{V_{mp} I_{mp}}{P_{in}} = \frac{V_{oc} I_{sc} FF}{P_{in}} \tag{I.1}$$

where P_{in} is the input solar power and V_{mp} (respectively I_{mp}) is the voltage (respectively current) at maximal power.

For non-concentrating photovoltaics (PV), the input power only depends on the solar spectral irradiance defined by the AM1.5g standard depicted in Figure I.1(c) [3]. The crucial challenge to obtain the highest efficiency from a device lies therefore in the minimization of losses. The present work is dedicated to the study and improvement of an innovative solution to reduce optical losses (i.e. taking place before photon absorption) in silicon solar cells, using plasma texturing of sil-

icon at the nanoscale. Implementation of the building block into a device additionally requires studying the influence of this new process on subsequent manufacturing steps.

This chapter will therefore give an overview of the state of the art in two specific fields. In section I.1, capacitively coupled plasma radio-frequency (CCP-RF) discharges, a type of plasma processing reactor, will be described with an emphasis on the case of silicon etching. Section I.2 will then detail fabrication methods and properties of "black silicon" (b-Si), a type of nanostructured silicon surface. The focus will be put on optoelectronic properties, particularly of interest for PV applications. In both parts, descriptions of the main processing and characterization tools used in this work will be given.

I.1 Reactive Ion Etching of Crystalline Silicon

Reactive ion etching (RIE) is a surface processing method in which a substrate is exposed to a plasma. The discharge provides chemical species (including ions and radicals) that interact with the substrate surface in different manners and lead to the removal of a controlled material volume. The most important feature in this type of process is the possibility to achieve highly selective and anisotropic etching. In particular, RIE plays a paramount role in the field of microelectronics as it has allowed continued reduction of component sizes in electronic chips [4].

I.1.1 Fundamentals of CCP-RF Discharges

I.1.1.a What is a plasma?

Plasma is often called the "fourth state of matter": in its earliest definition, it is a fully ionized gas comprising both positive and negative particles. By extension, partially ionized gases are also called plasmas and most common applications fall in this category, including capacitively coupled radio-frequency (CCP-RF) discharges. This state of matter has first been described by Irving Langmuir at the beginning of the 20th century [4, 5] and is characterized by the collective behavior of free charged particles moving in random directions, the medium remaining quasi-neutral. Plasmas usually contain many different types of species: neutral atoms or molecules (background gas), ions, radicals and free electrons. All the species can interact, usually through many different reactions.

It is interesting to recall that stars, nebulae, auroras or lightning are naturally occurring plasmas. On the other hand, numerous artificial applications use plasmas, even in our daily life. However, as it may be expected, these plasmas have very different properties and a first sorting can be made as a function of the density of charges and electron temperature [4]. Naturally occurring plasmas can be found at both extremes of these scales: star cores are both high temperature (around 10^7 K) high density (above 10^{28} electrons $\cdot$ m^{-3}) plasmas. In contrast, interstellar plasmas have a very low density (around 10^6 electrons $\cdot$ m^{-3}) and low temperature (below 1000 K). On the other hand, artificial plasmas are usually low temperature (except for fusion plasma), but cover a wide range of densities, from around 10^{16} electrons $\cdot$ m^{-3} for glow discharges up to 10^{24} electrons $\cdot$ m^{-3} for "thermal" plasmas like electrical arcs.

Crudely speaking, plasmas are especially used for three peculiar properties: (i) plasma discharges emit photons through de-excitation of metastable neutral particles (e.g. fluorescent lamps or plasma displays); (ii) they contain charged particles that can be driven in a precise manner through the application of electric and/or magnetic fields (e.g. etching, fusion) and (iii) they generate a wide variety of chemically active species (suitable for etching or deposition).

In the following, some basic features of capacitively coupled plasma (CCP) discharges powered by a radio frequency (RF) voltage signal will be recalled without demonstration. Thorough explorations of RF discharge plasmas can be found for instance in the books by Lieberman and Lichtenberg [6] and in Chabert and Braithwaite [7].

Focusing on the matter of interest for the present work, glow discharges are obtained by applying a continuous (DC) or alternating (AC) electrical excitation to a neutral gas. A few free electrons

are created inside the neutral gas at any time (due to cosmic rays): this initial charge is then accelerated by the electrical field (induced by the applied voltage), and may collide with another neutral particle, creating an avalanche breakdown – provided proper conditions of pressure and power especially. After this event, the discharge can be sustained with the applied electrical excitation which supplies the discharge with energy lost in collisions of charged species with walls or neutrals.

Basic reactor design. CCP discharges powered by an RF electrical excitation are widespread in both research and industry. A simplified schematic of a basic system is shown in Figure I.2. Single frequency CCP-RF reactors typically consist of two parallel electrodes, one being powered by an RF voltage (powered electrode, PE), while the other one is grounded (GE). A gas mixture is introduced in the reactor chamber to supply species that will later be ionized. The RF domain covers the range from approximately 1 to 500 MHz, and these frequencies are mostly used for radio communications. However, specific frequencies (bands around 13.56, 27.12 and 40.68 MHz in particular) have been set aside by the International Telecommunication Union for industrial, scientific and medical applications (ISM band [8]).

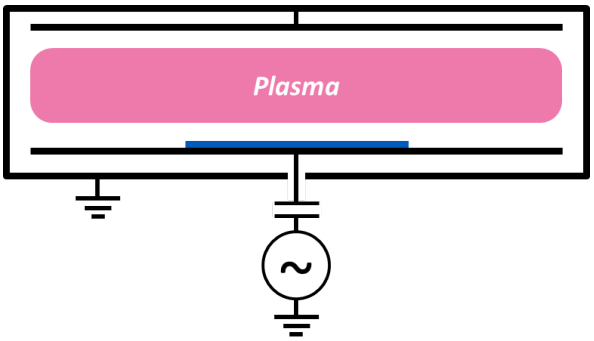

Fig. I.2: Basic schematic of a CCP reactor (vacuum components are in particular not depicted).

A last important feature of low-density CCP plasmas: they are not in thermodynamic equilibrium. Indeed, electrons are heated due to the applied RF voltage (mechanisms discussed in the next section) typically up to 3-5 eV. In turn, they exchange thermal energy through collisions with other particles, both inelastic (e.g. ionization) and elastic. In the latter case, energy exchange is most efficient between particles of similar masses. Since electrons are at least three orders of magnitude lighter than ions, the latter are not efficiently heated. However, an equilibrium can be reached between particles of similar nature, so that it is possible to define a temperature for electrons T_e and ions T_i taken separately. Ions remain at a temperature close to the temperature of the background gas (room temperature, i.e. around 30 meV, with no other source of heating). The bottom line is that in low-density discharges: $T_e \gg T_i \sim T_R$ (with T_R the room temperature).

RF sheaths. The plasma itself is present between the two electrodes and is quasi-neutral: the densities of positive ions n_i (here we consider electropositive discharges with single charged ions) and electrons n_e are approximately equal. However, the neutrality is broken near walls (electrodes or processed substrate): the space comprised between the plasma and the surface is called space charge "sheath". The latter is present in all plasma discharges due to the difference of velocity between electrons and ions. The origin of the sheath is the difference of velocity between electrons and ions: a simplified explanation of its creation can be attempted. Without considering how the plasma is produced, let us consider a uniform neutral plasma between two grounded electrodes, the potential will be uniformly zero across the domain. Electrodes act as sinks for the randomly moving charged particles. Particles will first move only due to their thermal energy, i.e. $(k_B T_e/m_e)^{1/2}$ for electrons (mass m_e) and $(k_B T_i/m_i)^{1/2}$ for ions (mass m_i), assuming Maxwell-Boltzmann energy distributions, where k_B is the Boltzmann constant. Ions move much slower

than electrons since $m_e/m_i \ll 1$ and $T_e \gg T_i$. Thus, a small positively charged region will rapidly be created between the plasma bulk and the electrodes. An electric field pointing from the plasma to the walls forms and confines the electrons inside the plasma while attracting the ions to the electrodes: the sheath is the region where this electric field builds up. Due to this electric field, positive ions are extracted from the plasma bulk and accelerated towards the walls: thus, the kinetic energy of ions in the sheath becomes much larger than their average energy inside the plasma bulk. The expansion of the sheath is limited to a few Debye lengths, λ_{De}, corresponding to the distance of electrical screening of an electrostatic potential in the plasma region:

$$\lambda_{De} = \sqrt{\frac{\epsilon_0 k_B T_e}{n_e e^2}} \tag{I.2}$$

where ϵ_0 is the vacuum permittivity, k_B the Boltzmann constant and e the elementary charge.

As has already been pointed out, the large mass difference between ions and electrons induces very different behaviors. In particular, a response time to variations of the electric field can be defined for each type of particles (for ions this characteristic time is relevant in the vicinity of the sheath edge):

$$\tau_{e,i} = 2\pi\sqrt{\frac{m_{e,i}\epsilon_0}{ne^2}} \tag{I.3}$$

Taking a simple case for numerical applications, we consider an Ar plasma, with a density $n_e = 1\times10^{16}\,\mathrm{m}^{-3}$ and an electron temperature $k_B T_e/e = 5\,\mathrm{V}$. In this case, we obtain $\lambda_{De} \approx 0.16\,\mathrm{mm}$ (to be compared with the inter-electrode distance, usually in the order of several centimeters), and the characteristic response times are: $\tau_e \approx 1\,\mathrm{ns}$ and $\tau_i \approx 300\,\mathrm{ns}$. For a 13.56 MHz RF voltage, the characteristic electric field variation time is $T_0 = 1/f_0 \approx 73\,\mathrm{ns}$, and we have $\tau_e \ll T_0 \ll \tau_i$. The electrons will therefore be able to respond to instantaneous variations of the electric field while the ions will respond to the average value.

DC self-bias. In CCP-RF discharges, due to the grounding of the reactor walls, the area of the powered electrode is usually smaller than the total grounded area. A negative DC self-bias, V_{DC}, thus builds up on the powered electrode – provided the presence of a blocking capacitor. A simple computation can be made to obtain V_{DC} using Kirchhoff's law as has been done by Schulze *et al.* [9], at any time t:

$$\widetilde{V}(t) + V_{DC} = \widetilde{V}_{sp}(t) + \widetilde{V}_{sg}(t) + \widetilde{V}_b(t) \tag{I.4}$$

where $\widetilde{V}$ is the voltage waveform (i.e. RF component on the voltage on the powered electrode), $\widetilde{V}_{sp}$ (respectively $\widetilde{V}_{sg}$) the voltage drop at the powered (respectively grounded) sheath and $\widetilde{V}_b$ the voltage drop in the bulk.

Taking the extreme cases in consideration – maximal and minimal values of $\widetilde{V}$ as illustrated in Figure I.3(a,b) – the following set of equations is derived (assuming an identical - absolute - bulk voltage drop V_{b0}):

$$V_{max} + V_{DC} = V_{sp}^{min} + V_{sg}^{max} + V_{b0} \tag{I.5}$$

$$V_{min} + V_{DC} = V_{sp}^{max} + V_{sg}^{min} - V_{b0} \tag{I.6}$$

It is now possible to isolate V_{DC} – also illustrated in the time-averaged situation in Figure I.3(c) – by introducing the symmetry parameter defined as the absolute ratio of the maximal voltage drops in the grounded and powered sheaths, $\varepsilon = |V_{sg}^{max}/V_{sp}^{max}|$. Using Equations (I.5) and (I.6), the final expression for V_{DC} is therefore:

$$V_{DC} = -\frac{V_{max} + \varepsilon V_{min}}{1+\varepsilon} + \frac{V_{sp}^{min} + \varepsilon V_{sg}^{min}}{1+\varepsilon} + \frac{1-\varepsilon}{1+\varepsilon}V_{b0} \tag{I.7}$$

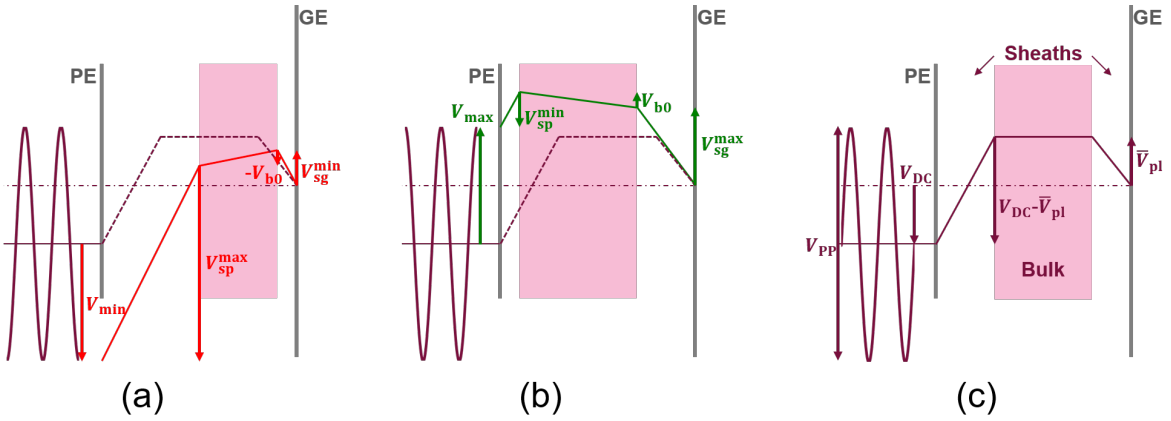

Fig. I.3: Schematic of the voltage distribution in the CCP discharge: (a) at minimal or (b) at maximal applied RF voltage and (c) in time-averaged situation.

In a first approximation, the last two terms on the right-hand side of Equation (I.7) may be considered small relatively to the first term [9]. The sheath voltage at maximal sheath collapse on both electrodes is therefore assumed negligible, as well as the voltage drop in the bulk, i.e. a high bulk conductivity is assumed. Equation (I.7) therefore simplifies to:

$$V_{DC} \approx -\frac{V_{max} + \varepsilon V_{min}}{1+\varepsilon} \tag{I.8}$$

Equation (I.8) shows that in the case of a sinusoidal RF voltage excitation ($V_{max} = |V_{min}|$) the DC self-bias only depends on the amplitude of the applied voltage V_{PP} and on the symmetry parameter, ε. While the physical meaning of ε will later be clarified, this parameter depends in particular on the ratio of electrode areas: in an asymmetric reactor, the voltage drop on the smallest electrode is always higher and V_{DC} is negative. This is typically the case for RIE reactors where high ion energy on the processed surface is usually required as will be detailed in the next section I.1.4.b.

Electron heating. Before investigating the ion bombardment, a short discussion on the root mechanisms responsible for sustaining the discharge has to be carried out. Indeed, since charges are perpetually being lost to the walls (or by recombination directly in the gas phase), ionization has to take place to compensate for the losses. To this aim, the impact energy in electron-neutral collisions needs to overcome the ionization threshold (for instance around 15 eV for Ar): electrons have to be accelerated (or "heated") enough to provoke enough ionization. In low-pressure RF discharges, the electrical power is delivered to the electrons that interact with the varying electric field, and several "heating" mechanisms have to be considered.

Collisional or "ohmic" heating takes place in the plasma bulk and becomes significant only if the bulk conductivity is low, so that a significant part of the voltage drop across the discharge occurs in the bulk. In low-pressure CC-RF discharges, these conditions are, however, not usually met and other heating mechanisms have to be considered, occurring at the sheaths where most of the voltage drop occurs.

Stochastic heating comes from the interaction of electrons with the oscillating sheaths. As it is illustrated in Figure I.3, the powered sheath thickness periodically varies 180° out of phase with the alternating RF voltage: the sheath is at its maximal expansion when the RF voltage is minimal and vice-versa. In contrast, the sheath thickness is in phase with the RF voltage near the grounded electrode. From the point of view of electrons located near the sheath region, the sheath edge can be considered as a moving wall, from which the electron will be specularly reflected (hard wall model). If an electron travels to the wall with a velocity $-v$ (we consider velocity in the frame of the fixed reactor and only components parallel to the sheath motion direction), and reaches the wall that is moving at a velocity v_w, the final electron velocity will be $v_r = -v + 2v_w$. It can be observed here that electrons can be either accelerated or slowed down due to the alternating

motion of the sheath edge. From this mechanism, strong ionization takes place when the sheath is rapidly expanding. If stochastic heating is the dominant power delivery mechanism, the discharge is said to be operated in "α -mode".

Another source of heating comes from secondary electron emission: ion bombardment on the electrodes may result in the emission of electrons from the surface. These secondary electrons freed in the sheath are then accelerated to the bulk due to the large electric field. This heating mechanism is notably important in DC glow discharges. In the case of RF discharges, if ionization is primarily due to secondary electrons, the discharge is said to be operated in "γ -mode".

Finally, a last important source of electron heating has been identified more recently in the case of low bulk conductivity, as found in electronegative discharges. In the latter case, strong ionization may take place close to the collapsing sheath due to electron heating by a combination of a high drift electric field in the bulk (due to low conductivity) and a high ambipolar electric field (accelerating electrons towards the electrode) [10]. Depending on the discharge conditions, this mechanism can become the dominant source of ionization in electronegative plasmas, in which case the discharge is operated in "DA-mode".

I.1.1.b Ion bombardment on the powered electrode

From a plasma process point of view, the energy of ions arriving at the surface is of fundamental importance, in particular in the case of etching (see section I.1.4.b). Simple considerations can be used to evaluate the ion flux energy distribution at an electrode (often named Ion Energy Distribution Function, IEDF, although this denomination may lead to confusion, see Appendix A). The aspects relevant for the present work are recalled here, see for instance Kawamura *et al.* [11] for a more complete overview of IEDF models.

Until now, it has been assumed that due to their inertia, ions only respond to the DC voltage components in the discharge, a condition synthesized by $\tau_i \gg T_0$ (reminder: τ_i designates the response time of ions and T_0 the period of the RF signal). Considering ion bombardment, it is here useful to define a new temporal quantity: the ion transit time in the sheath, $\tau_{i,s}$. Strictly speaking, it can actually be shown that $\tau_{i,s} \propto \tau_i$, however, in typical conditions both quantities are very similar and sometimes assimilated in literature [11]. Therefore in the case $\tau_{i,s} \gg T_0$, ions leave the plasma bulk with a small velocity (Bohm speed [7]) and are accelerated in the sheath by the time-averaged voltage $|\bar{V}_s|$ (valid if the sheath is non-collisional and no ionization happens inside of it). In this case, the IEDF is a Dirac function: all ions (with a charge q) reach the surface with an energy $E \sim q|\bar{V}_s|$, in the case of the powered electrode, $|\bar{V}_{sp}| = \bar{V}_{pl} - V_{DC}$ and for the grounded electrode $|\bar{V}_{sg}| = \bar{V}_{pl}$, where $\bar{V}_{pl}$ is the plasma potential (time-averaged potential in the bulk). The computation of the plasma potential is therefore of great importance to obtain an estimation of the ion energy on the electrodes.

As demonstrated by Bruneau *et al.* [12], the plasma potential can be derived for any type of periodic excitation voltage using several assumptions: (i) the potential in the plasma bulk is a linear function of the applied RF voltage (ii) the potential drop in the plasma bulk is negligible; (iii) the sheaths fully collapse at some point in the RF period; (iv) there is no field reversal. Under these hypotheses, and using notations adopted in the previous section, the plasma potential is given by:

$$\bar{V}_{pl} = \frac{-V_{min}}{V_{PP}} \left(\frac{V_{max}}{V_{PP}} V_{PP} + V_{DC} \right) \tag{I.9}$$

In the simple case of a sinusoidal voltage excitation $V_{max} = -V_{min}$, Equation (I.9) simplifies to $\bar{V}_{pl} = 1/2(V_{PP}/2 + V_{DC})$, and the ion energy at the powered electrode is:

$$E = q(V_{PP}/4 - V_{DC}/2) \tag{I.10}$$

However, the condition $\tau_{i,s} \gg T_0$ is not always satisfied (if the ions are light or the RF frequency low). Time-variations of the sheath voltage can therefore modify the IEDF, and the time at which the ions enter the sheath is of importance. Indeed, if ions enter the sheath at (or near) its full

expansion, the instantaneous sheath voltage is maximal, and the ions are highly accelerated. Conversely, ions entering the sheath near full contraction will only be modestly accelerated. The IEDF becomes bimodal: the peaks are centered around the value $q|\bar{V}_s|$, and separated by a difference ΔE. An attempt at evaluating the spacing between the peaks of the bimodal distribution has for instance been made by Benoit-Cattin and Bernard [13]. Assuming a constant sheath thickness and a sinusoidal sheath voltage with an amplitude V_{s0}:

$$\Delta E = \frac{3eV_{s0}}{\pi}\frac{T}{\tau_i} \tag{I.11}$$

ΔE therefore increases if the frequency is lowered or the amplitude of the applied RF voltage increases (if we further assume $V_{s0} = V_{PP}/2$). The computation also shows that the separation of the peaks ΔE scales with $m_i^{-1/2}$: if ions with different masses are present, the IEDF will consist of several superimposed bimodal distributions. Kuypers and Hopman for instance used this property to identify the contribution of different ions in the IEDF for an O_2 and a CF_4 discharge, the latter case being shown in Figure I.4(a).

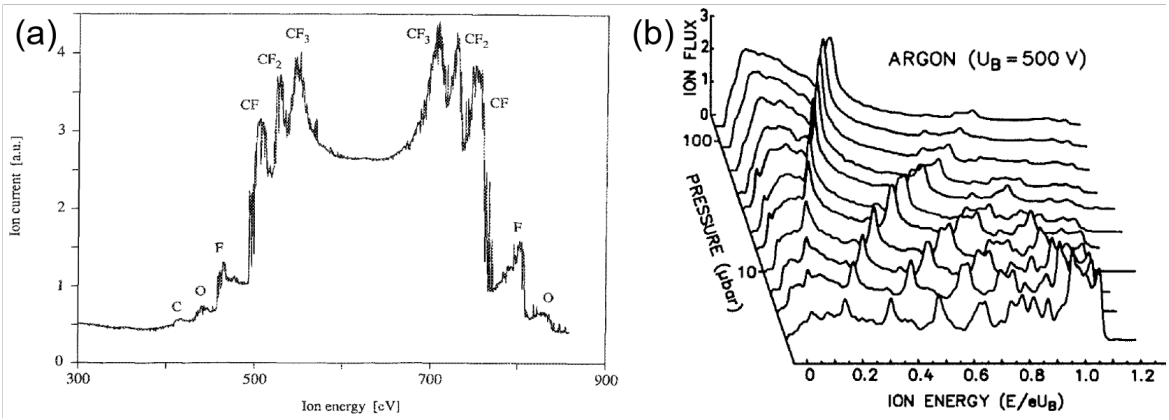

Fig. I.4: (a) IEDF at powered electrode of a CCP-RF CF_4 plasma, extracted from [14]. (b) Evolution of IEDF with discharge pressure at powered electrode in a CCP-RF Ar plasma, from [15].

If the sheath is slightly collisional, some of the ions will arrive at the electrode with a lower velocity and the distribution will be smoothed to lower energies, as shown by Wild and Koidl in the case of an Ar discharge, see Figure I.4(b) [15]. If the pressure is drastically increased, the entire distribution is shifted to low energies and only a few ions reach the electrode without collision. In the same figure, secondary peaks (i.e. at energies below the two peaks at maximal energy explained by RF modulation) in the distribution are also observed. Wild and Koidl have demonstrated that these peaks appear due to creation of secondary ions inside the sheath.

Decoupling ion flux and ion energy. Given the previous summaries of the ionization mechanisms and the computation of the ion bombardment energy, it appears that, in single frequency CCP discharges, both phenomena are connected. In turn, the ion flux and ion energy on the electrodes will be correlated, as they are both controlled by the amplitude of the applied RF voltage. This effect has for instance been highlighted by Perret *et al.* in an Ar discharge as seen in Figure I.5.

It is also observed in Figure I.5 that increasing the discharge frequency allows one to increase the ion flux at a given energy. Dual-frequency approaches were therefore proposed: powering the substrate electrode with a low frequency voltage to allow tuning of the ion energy, while a high frequency voltage on the counter electrode helps increase the ion flux. This concept of functional separation is analogous to ICP reactors for instance where inductive coupling induces high density, while an independent capacitive coupling on the substrate controls the ion energy.

As it will be highlighted in the next section, applying several voltage frequencies at the same electrode can also lead to a decoupling of flux and energy.

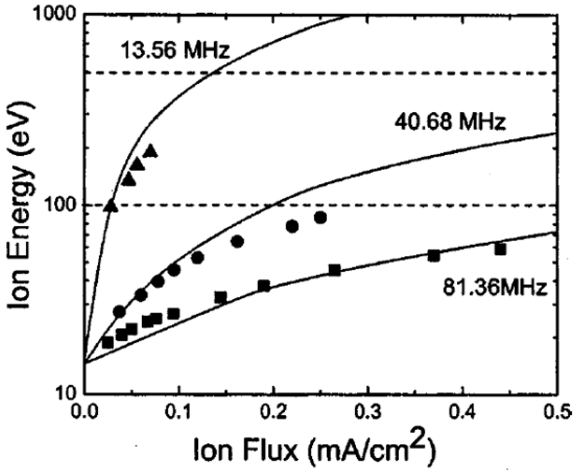

Fig. I.5: Peak ion energy versus ion flux in a CCP-RF Ar discharge (at 15 mTorr) with varying voltage amplitude and three different frequencies. Symbols show experimental data while solid lines show theoretical computations, extracted from [16].

I.1.2 TVWs: a Multi-frequency Extension of the RF Domain

Tailored Voltage Waveform (TVW) excitation was proposed in 2009 by Heil *et al.* [17] as another solution to decouple the ion flux and ion energy in CCP discharges, due to the so-called electrical asymmetry effect (EAE). The root principle is quite simple as it implies the application of an excitation voltage composed of a basis frequency and several upper harmonics with controlled relative amplitudes and phase-shifts. A complete review of the development of TVWs, with the latest associated models and numerous experimental results, is available in the thesis of B. Bruneau [18]. In the framework of this manuscript, only the fundamentals will be recalled, as well as illustrations on the use of TVWs for plasma process tuning.

I.1.2.a Employed waveforms and sources of asymmetries

While several types of voltage waveforms have been proposed in literature, the present work uses in particular the proposition by Bruneau *et al.* [19], where the supplied voltage is expressed as:

$$\widetilde{V}(t) = V_0 \sum_{k=1}^{n} \frac{n-k+1}{n} \cos\left(2\pi k f t + \Theta\right) \tag{I.12}$$

where n is the total number of frequencies, f_0 the basis frequency (13.56 MHz in the present work), Θ a constant phase-shift, and V_0 a pre-factor allowing to tune the peak-to-peak voltage (therefore the coupled power). Examples of typical waveforms obtained with Equation (I.12) are given in Figure I.6 for various values of Θ. In order to give a first classification of the waveforms, one can first discriminate:

- "pulse-like" waveforms such as peaks and valleys waveforms for which $V_{\max} \neq -|V_{\min}|$,
- "sawtooth-like" waveforms for which $V_{\max} = -|V_{\min}|$, but showing a large difference in rise and fall times.

In the previous section, the DC self-bias at the powered electrode was derived in Equation (I.8) (in the general case of a periodic voltage excitation oscillating between a maximal value $V_{\max}$ and a minimum, negative, $V_{\min}$) under the assumptions of negligible sheath potential at maximal collapse and high bulk conductivity, expression recalled here:

$$V_{DC} \approx -\frac{V_{\max} + \varepsilon V_{\min}}{1+\varepsilon} \tag{I.13}$$

where ε is the symmetry parameter of the discharge.

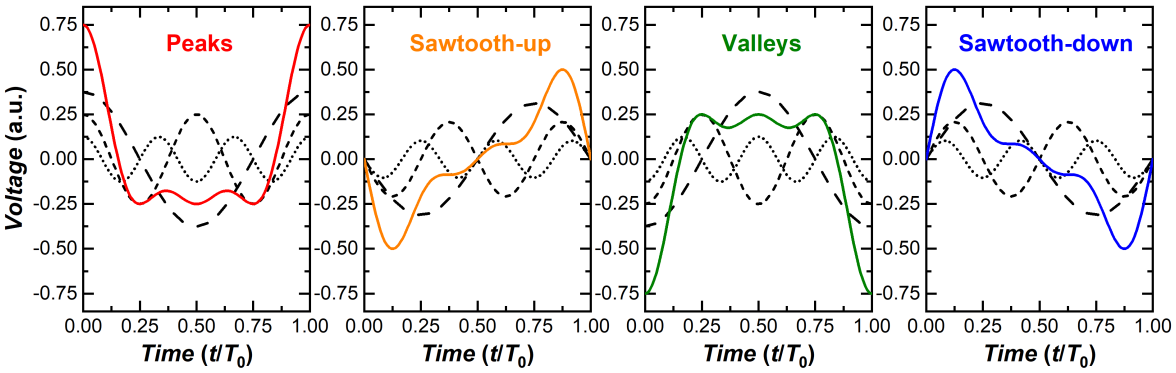

Fig. I.6: Examples of TVWs (solid color curves) used in the present work, shown with normalized peak-to-peak amplitudes and harmonic decompositions (dashed black curves).

Moreover, from simple approximations of electron and ion distributions close to the sheaths, the following scaling for the symmetry parameter has been derived [17]:

$$\varepsilon \propto \left(\frac{A_\mathrm{p}}{A_\mathrm{g}}\right)^2 \frac{\bar{n}_\mathrm{sp}}{\bar{n}_\mathrm{sg}} \tag{I.14}$$

where A_p and A_g are respectively the areas of powered and grounded walls, while $\bar{n}_\mathrm{sp}$ and $\bar{n}_\mathrm{sg}$ respectively designate the average ion densities in the powered and grounded sheaths. Using the above expression of V_DC and the scaling of ε in Equation (I.14), it is therefore possible to discern at least three different sources of asymmetries – i.e. inducing a non-zero self-bias voltage – in a CCP discharge:

- a geometrical asymmetry when $A_\mathrm{p} \neq A_\mathrm{g}$;
- an "amplitude asymmetry" when $V_\mathrm{max} \neq |V_\mathrm{min}|$;
- a "chemical" asymmetry when $\bar{n}_\mathrm{sp} \neq |\bar{n}_\mathrm{sg}|$.

The geometrical asymmetry is very common as it arises in most reactors since the powered electrode area is usually smaller than the grounded wall area; in this typical case (and neglecting other asymmetry sources) the self-bias voltage becomes negative. Notice that the scaling with the square of the area ratio is not exact as, in particular, the ratio of average ion densities in the sheaths may also depend on the ratio of electrode areas.

In contrast, the two other sources of asymmetries may be controlled using TVWs, as will now be explained. As a simplification for theoretical explanations (and unless otherwise stated), the next two sections will assume a geometrically symmetric reactor ($A_\mathrm{p} = A_\mathrm{g}$).

I.1.2.b Amplitude asymmetry effect

The first electrical asymmetry effect appears when $V_\mathrm{max} \neq V_\mathrm{min}$ and is therefore hereafter named "Amplitude Asymmetry Effect" (AAE). Assuming $\varepsilon \approx 1$ (independent of the applied waveform) so that AAE is the only source of asymmetry, V_DC will scale as $|V_\mathrm{min}| - V_\mathrm{max}$. For the waveforms used in this work, the evolution of $(|V_\mathrm{min}| - V_\mathrm{max})/V_\mathrm{PP}$ versus Θ is shown in Figure I.7(a) for different numbers n of applied frequencies. It is here observed that extrema for the self-bias voltage arise with pulse-like waveforms: V_DC will be minimal for peaks waveforms ($\Theta/\pi = 0$, case illustrated in Figure I.7(b)) and maximal for valleys waveforms ($\Theta/\pi = 1$). In contrast, V_DC is obviously null for sawtooth-like waveforms ($\Theta/\pi = 0.5$ or 1.5) since $V_\mathrm{max} = |V_\mathrm{min}|$. It should however be highlighted that the scaling of $|V_\mathrm{DC}/V_\mathrm{PP}|$ with Θ may be different in practice due to the dependence of ε on the applied waveforms. In particular, a self-amplification mechanism can be obtained: in this case a "chemical" asymmetry due to the difference in average ion densities is superimposed onto the AAE and $|V_\mathrm{DC}/V_\mathrm{PP}|$ is greater than predicted by the previously detailed (simplified) model [17].

The initial objective of the TVW method proposed in Heil *et al.* [17] was to decouple the ion energy from the ion flux. From the previous analysis, it has been shown that a continuous sweep in V_{DC} values can be obtained by varying Θ in Equation (I.12) in the range $[0,\pi]$ for instance. In turn, a gradual increase (respectively decrease) of ion bombardment energy on the powered (respectively grounded) electrode can therefore be obtained. Moreover, the range of V_{DC} values that can be achieved (at a given V_{PP}) can be extended by increasing the total number of frequencies in the applied waveforms. However, as can be inferred from both graphs in Figure I.7, the "marginal gain" (increase in $|V_{DC}/V_{PP}|$ for pulse-like waveforms) with the number of frequencies rapidly decreases. Nevertheless, one can therefore expect to easily tune the ion bombardment energy on the electrodes using TVWs. However, the evolution of the ion flux cannot be predicted with this simple approach and experiments were required to demonstrate a potential decoupling.

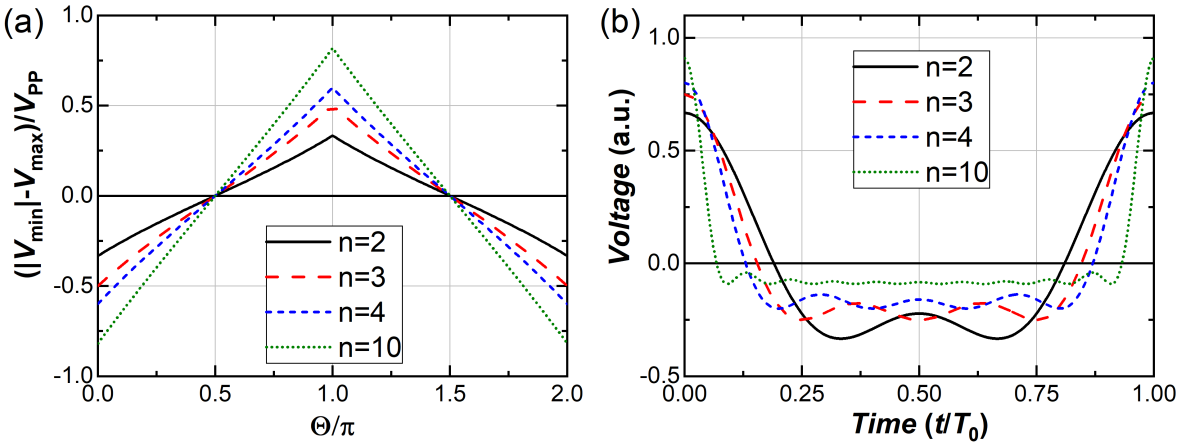

Fig. I.7: (a) Evolution of $(|V_{min}| - V_{max})/V_{PP}$ as a function of Θ for different numbers, n, of harmonic frequencies in the TVWs. (b) Illustration of peaks waveforms ($\Theta/\pi = 0$) for different values of n (with normalized peak-to-peak amplitude).

The experimental proof of a decoupling between ion energy and ion flux using the AAE was first obtained by Schulze *et al.* with an Ar plasma [20]. As shown in Figure I.8, the team successfully tuned the average ion energy (with extrema differing by approximately a factor two) at the grounded electrode of an Ar discharge for various values of pressure and inter-electrode distances. In the meantime, the ion flux was observed to remain almost constant. This "nearly perfect" decoupling is however not achievable in all conditions nor all gas discharges, as for instance observed in CF_4 [21] or O_2 [22] plasma.

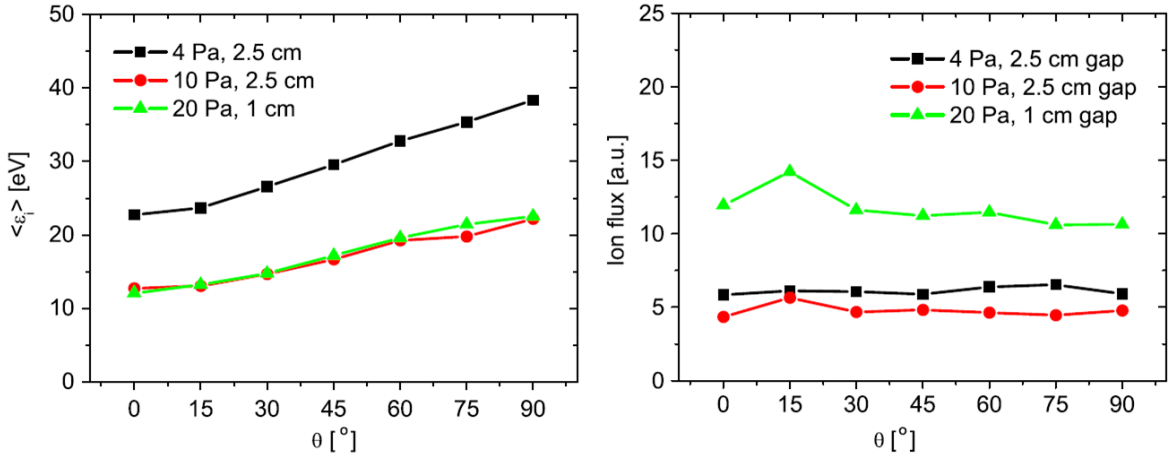

Fig. I.8: Evolution of the mean ion energy (left) and ion flux (right) at the grounded electrode in an Ar discharge powered by TVWs (13.56 MHz plus one upper harmonic) with θ, extracted from [20]. NB: the waveforms used in this study are different from the one expressed by Equation (I.12).

I.1.2.c Slope asymmetry effect

A second type of electrically induced asymmetry has been discovered due to the use of TVWs. Indeed, a non-zero self-bias could be obtained (both experimentally and in simulations) in some conditions using sawtooth-like waveforms: this effect could not be explained by the AAE since in these cases $V_{max} = |V_{min}|$. The first investigation has been made by Bruneau *et al.* [18] with Particle-In-Cell (PIC) simulations of an electropositive Ar discharge, as seen in Figure I.9. Despite the geometrical symmetry of the simulated discharge, non-zero values of self-bias were obtained for sawtooth-like waveforms. In addition, the sign of V_{DC} depends on the applied waveform: it is here positive for sawtooth-up and negative for sawtooth-down waveforms.

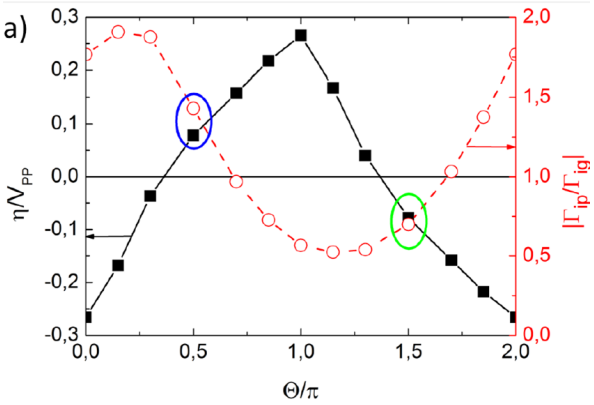

Fig. I.9: Evolution of self-bias voltage (normalized by V_{PP}) and ratio of ion fluxes at the powered and grounded electrodes as a function of Θ in an Ar discharge (PIC simulation, 400 mTorr, $V_{PP} = 200$ V), extracted from [18].

It was concluded that the non-zero self-bias was induced by a "chemical asymmetry" (i.e. $\bar{n}_{sp} \neq \bar{n}_{sg}$), and the root cause attributed to the difference in sheath motions in front of the electrodes. As an example, if the powered electrode is fed with a sawtooth-up waveform, the powered sheath will rapidly expand and then slowly collapse within an RF period. Meanwhile, the grounded sheath will, in contrast, collapse rapidly but expand slowly. In the case of the Ar discharge, electron-heating is predominantly due to sheath expansion, and ionization is more effective when the sheath motion is rapid: as a consequence, the average ion density in the powered sheath will be higher in front of the powered electrode ($\bar{n}_{sp} > \bar{n}_{sg}$ so that $\varepsilon > 1$), and a positive self-bias appears. The situation is reversed (i.e. the roles of the powered and grounded electrode are switched) when using sawtooth-down waveforms.

The difference in sheath motions is therefore the root cause of the asymmetry, and comes from the difference in rise and fall time of the input voltage. This effect is therefore referred to as the "Slope Asymmetry Effect" (or SAE, sometimes called "temporal asymmetry").

As can be inferred from the previous explanations, the dominant electron-heating mode in the discharge plays an important role in the SAE. In [23], Bruneau *et al.* compare several gas discharges, in particular Ar and CF_4, in the case of sawtooth-like waveform excitation. The excitation rate in the discharge was obtained experimentally from Phase-Resolved Optical Emission Spectroscopy (PROES) and compared to Particle-In-Cell simulations, see Figure I.10. In the case of the Ar discharge, a peak in excitation is observed close to the grounded sheath at the time of rapid expansion (red spots in top graphs Figure I.10); as expected, sheath expansion heating is dominant (discharge in α-mode). Secondary peaks of excitation are still observed both in experiment and simulation in front of the powered sheath during its slow expansion but are of much lesser intensity. In contrast, the situation is reversed for the CF_4 discharge: a high excitation rate is observed near the powered sheath during its rapid collapse (red spots in bottom graphs Figure I.10). In the electronegative CF_4 discharge (for the conditions here investigated), it was shown that drift-ambipolar electron heating dominates, in particular due to the low bulk conductivity.

As a consequence of the different electron-heating modes, the SAE switches direction depend-

ing on the dominant electron-heating mode: for sawtooth-down waveforms, the self-bias was observed to be positive in the case of CF_4 and positive for Ar.

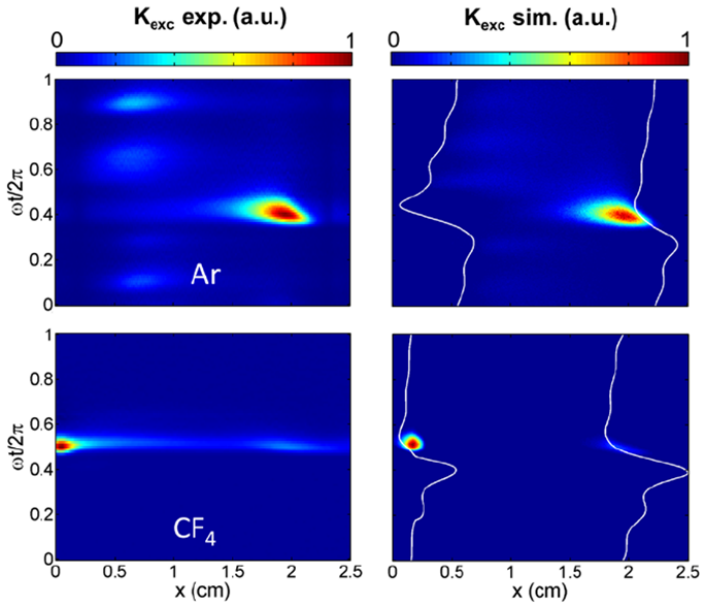

Fig. I.10: Comparison of spatiotemporal excitation rate from experiments (left column, obtained by PROES) and PIC simulations (right column) for Ar (top) and CF_4 (bottom) discharges. The horizontal axis shows the position between electrodes (powered electrode at $x = 0$, fed with a sawtooth-down waveform), the vertical axis spans one RF period. Extracted from [23].

I.1.2.d TVWs at process level: uses and limitations

Process tuning with TVWS: examples from literature. As has been shown, powering a CCP discharge with TVWs may give rise to two types of asymmetries: the Amplitude Asymmetry Effect (AAE) that allows one to tune the voltage drop on both electrodes, and the Slope Asymmetry Effect (SAE) that locally modifies the "chemistry" of the plasma depending on the sheath motion. The situation can become even more complex as these effects can be combined. Thus, a complete decoupling between ion energy and ion flux is out of reach in most conditions and discharges types. However, in all cases, the playground available to tune the process conditions is widely expanded with TVWs compared to single frequency excitation. It can be used both to optimize the process conditions (e.g. for deposition or etching), or to investigate physicochemical processes.

The first investigations of TVWs "at process level" were performed by the team of Johnson *et al.* for the deposition of microcrystalline silicon layers [24, 25]. Several studies on deposition of amorphous, microcrystalline or epitaxial silicon layers followed: a recent synthesis is for instance available in the thesis of B. Bruneau [18]. In particular, ion bombardment energy thresholds for the nucleation of microcrystalline phases [12]. 2014), or on the contrary for epitaxy breakdown [26], were identified by varying the ion bombardment energy on the growing layer using TVWs.

More recently, the effect of TVWs on the deposition of amorphous silicon by SiH_4/H_2 plasma was investigated by Wang *et al.* [27]. It was demonstrated that the ion bombardment energy on the deposited layer could indeed be tuned by varying the waveforms (due to the AAE): the film stability (under light-soaking) was observed to be decreased when the ion energy is too low. Although they did not induce the highest ion energy, sawtooth-like waveforms lead to the most stable films with higher carrier transport properties: although the mechanisms were not fully understood, this trend was attributed to the difference in plasma chemistry due to the SAE.

Finally, the most outstanding example of the SAE at process level was later reported by Wang and Johnson [28] in the deposition of amorphous and microcrystalline silicon with an $SiF_4/H_2/Ar$ plasma. Indeed, the team was able to demonstrate an "electrode-selective deposition". This plasma

chemistry either leads to deposition or etching of amorphous silicon depending on the balance of species near the electrodes. Making use of the SAE, a strong chemical asymmetry was induced by sawtooth-like waveforms on both sheaths of the reactor, so that deposition of amorphous silicon was obtained on one electrode while the other remained pristine.

Process tuning with TVWs: limitations. The TVW approach can in theory be applied to any existing CCP reactor, as it only requires a modification of the powering system. However, several limitations inherent to the use of TVWs for low-temperature plasma processing have to be recalled. First, from a technological point of view, at least two important challenges must be addressed:

- **Power matching**: for an efficient power coupling (to the plasma), the total load downstream of the amplifier has to be fully resistive (and generally close to 50 Ω) at the frequency of the input signal. Matching networks with tunable impedances are therefore inserted between the powering system and the reactor: systems are usually designed for single frequency matching. In the case of TVWs, the basis frequency can therefore be well coupled, but a strong mismatch will arise for upper harmonics. This issue may be tackled by separately amplifying and matching the different harmonics, in which case the powering system cost scales with the number of frequencies. Another solution has however recently been proposed with the design of a multi-frequency matching networks [29].

- **Monitoring of waveforms on the electrode**: in general, it is not possible to directly measure the voltage waveform at the electrode. As an alternative, the waveform is monitored at the feedthrough of the reactor, and the impedance of the electrical line (between feedthrough and electrode) may alter the phase-shifts and amplitudes of the different harmonics. Different methods can be employed to address this issue, as will be shown in Chapter II.

Secondly, more "fundamental" (or physical) limitations still exist using TVW excitation. Indeed, as it has been explained previously, a full decoupling between ion flux and ion energy is usually out of reach: in general, both the AAE and SAE effects arise simultaneously (although one effect may strongly dominate over the other). Moreover, transitions in dominant electron-heating mode may occur [30, 31] (e.g. when varying other plasma parameters such as pressure or gas mixture), and predictions of the best conditions for a given process are thus made difficult. Consequently, extensive studies may be required to first characterize the available range of parameters, followed by the choice of optimized conditions.

I.1.3 Process Description and Monitoring

I.1.3.a Description of the reactor

For the experiments described in this thesis, a Nanomaster NRE 3500 parallel plate RIE system has been used both for plasma studies and processing of silicon surfaces – a picture of the reactor is shown in Figure I.11 along with a simplified schematic. The reactor is composed of circular anodized aluminum electrodes with diameters of 20 cm. The discharge pressure can be varied between 0.03 and 1 Torr. Four different gases can be introduced: Ar (flow range: [20, 200 sccm]), H_2 [20, 200 sccm], SF_6 + 20% O_2 [20, 200 sccm] and O_2 [10, 100 sccm]. Gases are introduced through the showerhead top electrode, the exhaust being placed below the bottom electrode.

Both electrodes may be powered: applying the RF voltage to the bottom electrode with the top electrode grounded corresponds to a "RIE mode", conversely a "PECVD mode" may be obtained by inverting the roles of the electrodes.

The supplied power is monitored using an RF power probe (labeled VPM, see also section I.1.3.c) while the RF voltage is measured using a high-voltage probe (HV, at the feedthrough of the powered electrode) connected to an oscilloscope. The power is supplied by either of two separate systems:

- **Standard power supply**: including a 100 W RF voltage generator (13.56 MHz), an amplifier and a matching system integrating a blocking capacitor.

- **TVW power supply**: composed of an arbitrary function generator (AFG), a 1 kW amplifier with a frequency range [0.1, 200 MHz] and a 4.7 nF blocking capacitor. An in-house developed software is used to generate the desired voltage waveform and then perform incremental corrections to account for the impedance of the power system and changes in the impedance of the load (reactor and plasma).

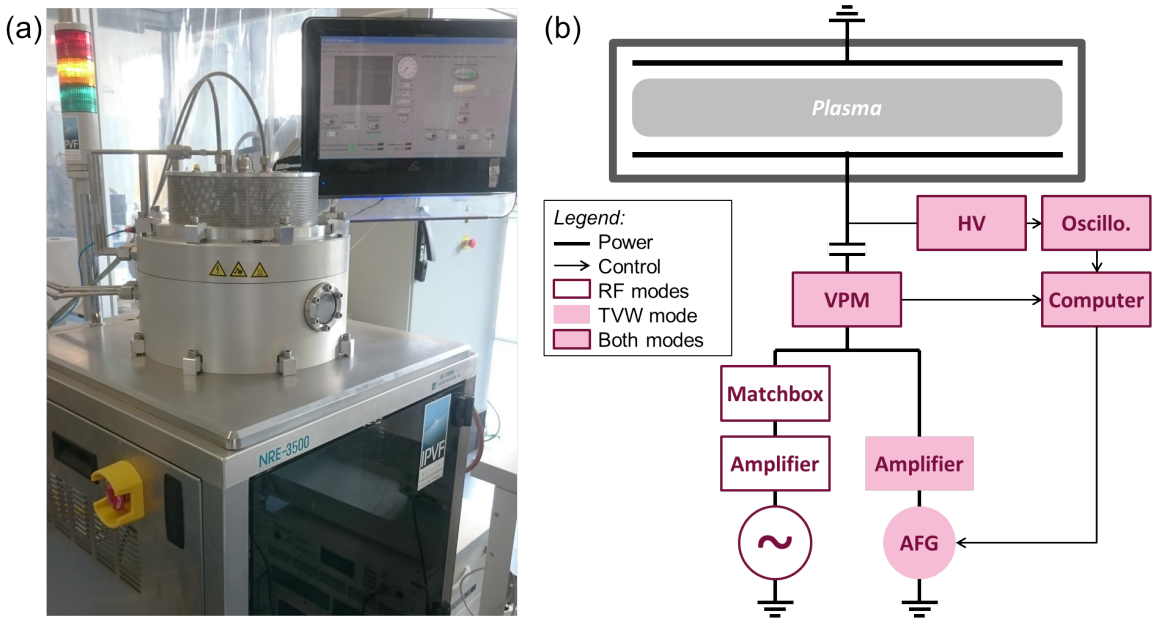

Fig. I.11: (a) Picture of the RIE reactor used in the present work, installed at LPICM (Ecole polytechnique, CNRS, Université Paris-Saclay). (b) Schematic of the reactor (vacuum and gas circuits not shown) and powering systems.

I.1.3.b Limitations of the experimental setup

Some built-in experimental limitations exist for the current implementation of the setup and are described below:

- **SF_6/O_2 gas ratio**: this mixture of gases will be of paramount importance for the present work, however, the SF_6 gas being already mixed with 20% O_2 inside the bottle, values of SF_6 content in an SF_6/O_2 mixture cannot exceed 80%. Furthermore, values in]0, 13%] cannot also be studied due to the operating ranges of the mass flow controllers.

- **Geometrical asymmetry**: although the bottom and top electrodes have the same diameter, the reactor is geometrically asymmetric due to the grounded reactor walls (the ratio of powered to grounded area is estimated around 1/2), and so V_{DC} is always negative in the investigated conditions (even in TVW mode).

- **Power coupling**: due to the absence of an impedance matching box, high values of power reflection coefficient (between 85 and 95%) are present for all plasma conditions. Power values reported in this manuscript always represent the actual coupled power, unless otherwise specifically stated.

I.1.3.c Power monitoring and in-situ characterization

Power probe. The actual value of power coupled to the plasma P_w is measured with a current-voltage probe inserted in the circuit as close as possible to the electrical feedthrough of the powered electrode. The probe is a Vigilant Power Monitor (VPM) purchased from Solayl, its operation is detailed in [32]. P_w can be expressed as:

$$P_w = P_{fwd} - P_{ref} \tag{I.15}$$

where P_{fwd} is the forward power (at the output of the matchbox – or amplifier, in the absence of a matching system) and P_{ref} the power reflected from the reactor.

Retarding Field Energy Analyzer. A commercial system from Impedans (Semion Single Sensor) is used to measure the Ion Flux Energy Distribution Function (IFEDF) in various conditions.

The sensing part of the Retarding Field Energy Analyzer (RFEA) system consists of a button probe, embedded in a 50 mm diameter holder with an anodized aluminium surface. This probe is placed on the powered or grounded electrode of the reactor. The back surface of the holder comprises a metallic part which allows the probe to take on the potential of the electrode on which it is placed. Positively charged ions enter the probe through a series of grids and are filtered in energy by applying a sweeping potential difference between two grids. A description of the probe and its theory of operation are available in [33] (see also Appendix A).

The total thickness of the button probe (placed inside the holder) is 5 mm, which is reasonably small compared to the inter-electrode distance of 35 mm. The presence of the probe is assumed to not significantly affect the orders of magnitude nor the relative variations of the IFEDFs with the plasma conditions. In order to characterize the homogeneity of the discharge, the same probe has been placed on different locations of the powered electrode.

The I-V curve measured by the RFEA represents the cumulative complementary ion flux distribution, which is then differentiated to obtain the IFEDF. A typical example of a measured I-V curve and the corresponding IFEDF, ϕ_E, are shown in Figure I.12 the example measurement has been obtained at the powered electrode of an SF_6/O_2 discharge (P_r = 30 mTorr, 100 sccm input gas flow with 57% SF_6, P_r = 25 W). The I-V curve is smoothed and derived using a Savitzky-Golay

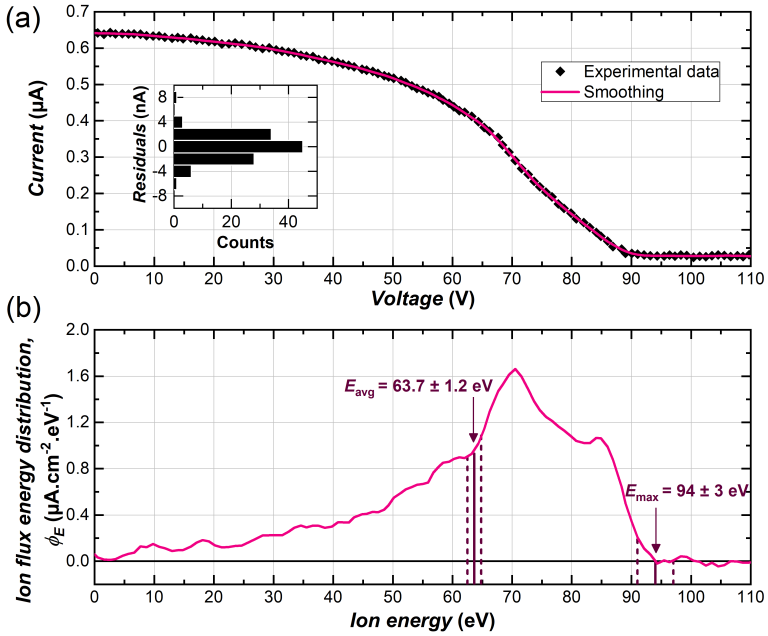

Fig. I.12: (a) Example of an I-V measurement obtained with the RFEA placed on the powered electrode for an SF_6/O_2 discharge (P_r = 30 mTorr, 100 sccm input gas flow with 57 % SF_6, P_w = 25 W). The inset graph shows the distribution of residuals from the smoothing. (b) IFEDF derived from the smoothed I-V curve.

method [34]. Notice that the current does fall to a (positive) offset value when all the ions are repelled (above $E_{max} = (94 \pm 3)$ eV here).

Besides the IFEDF, three global parameters are also extracted: the total ion flux ϕtot, the mean ion bombardment energy E_{avg} and the maximal ion bombardment energy E_{max}. The total ion flux is computed as the integral of the IFEDF. The maximal ion bombardment energy is computed as the energy where the IFEDF falls to zero (notice that large uncertainties may be obtained when the tail of the IFEDF is relatively long, e.g. highly collisional sheath). Finally, the average ion energy E_{avg} is computed from:

$$E_{avg} = \frac{\int_0^{E_{max}} E\phi_E(E)\,dE}{\int_0^{E_{max}} \phi_E(E)\,dE} \tag{I.16}$$

I.1.4 Silicon Etching

I.1.4.a Crystalline silicon: basic properties

Basic physical properties. Silicon is the chemical element with atomic number 14, it belongs to group IV (conventional designation in semiconductor physics, or group 14 in the IUPAC classification) in the periodic table. Silicon is the second most abundant element in the Earth's crust [35] although it is most commonly found associated with oxygen (in the form of silica, SiO_2, for instance). From different processes, highly pure silicon compounds can be produced: the thermodynamically stable state of pure silicon (at room temperature and under atmospheric pressure) is crystalline with a diamond cubic structure. In this form, silicon is a metalloid with semiconducting properties. A "pure" crystalline silicon solid can be either multi-crystalline (mc-Si) or monocrystalline (mono-Si). In the following, in cases where the multi- or monocrystalline nature of the material is inconsequential, the abbreviation "c-Si" will be favored. The electronic energy gap between the valence and conduction bands has a value of 1.12 eV for c-Si at 300 K.

Crystalline structure. A schematic view of the unit cell of c-Si, arranged in a diamond lattice structure, is shown in Figure I.13(a). The lattice parameter a is 5.43 Å and the atomic density $d_{Si} = 5.02 \times 10^{22}$ at$\cdot$cm^{-3}. Mono-Si wafers are commonly cut along (100) or (111) planes, see 2D sections Figure I.13(b,c), depending on the application.

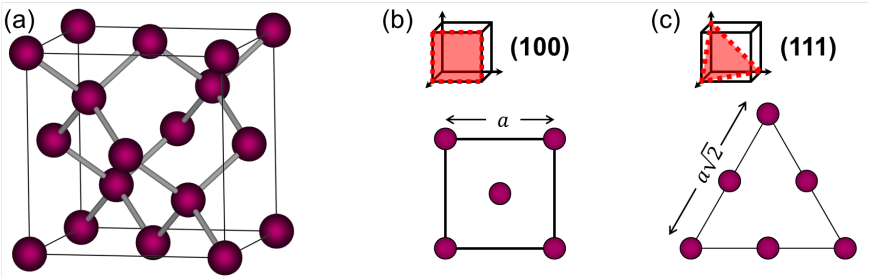

Fig. I.13: (a) 3D stick-and-ball view of the unit cell of the diamond structure of c-Si. (b) and (c) respectively show 2D schematic of the (100) and (respectively) (111) planes in the unit cell.

Doping. c-Si can be doped by inserting impurities in the crystalline network. Replacing a silicon atom with a group III atom (trivalent atom, e.g. boron) creates an electron vacancy, while introducing a group V atom (pentavalent atom, e.g. phosphorus) induces an extra valence electron. Bulk silicon doping is usually achieved by introducing the impurities in the silicon melt during ingot fabrication, and base doping in the range of 10^{15} to 10^{16} cm^{-3} (i.e. one atom of silicon out of one or ten million is replaced by an impurity). Bulk silicon doping is usually characterized by the resistivity: the higher the doping, the lower the resistivity (e.g. with phosphorous, a bulk resistivity around 5 $\Omega\cdot$cm is obtained for a doping level of 10^{15} cm^{-3}).

I.1.4.b Plasma etching mechanisms

Let us now go back to plasma processing, of which silicon etching is a paramount example, and detail the basic mechanisms leading to the two important features highlighted at the beginning of this chapter: the possibility to achieve highly selective and anisotropic etching. First, plasma etching may occur through four fundamental mechanisms [6], detailed below and illustrated in Figure I.14.

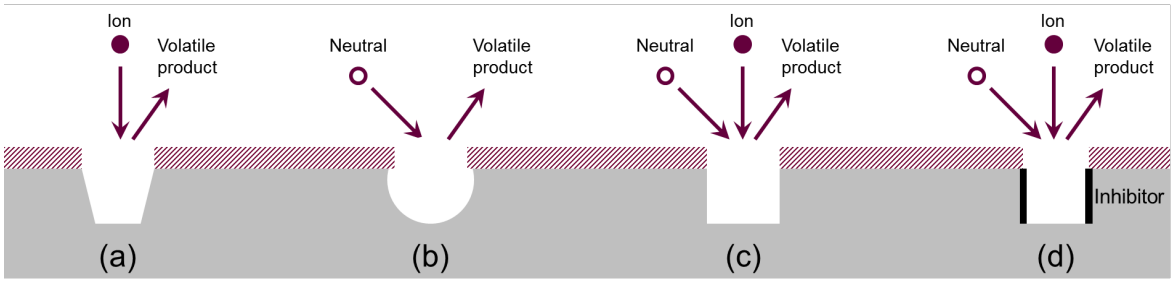

Fig. I.14: Description of basic etching processes: (a) sputtering, (b) pure chemical etching, (c) ion-assisted etching, and (d) ion-enhanced inhibitor etching.

Sputtering. Upon bombardment from positive ions, atoms can be ejected from a solid surface, leading to a physical etching phenomenon named sputtering. As an example, Ar^+ ions can be used to bombard a metallic target facing a substrate: in turn, metal atoms will be ejected and deposit on the substrate to form a thin metallic coating. The sputtering yield (i.e. number of ejected atoms per incoming ion) depends on the ion incident angle and kinetic energy (and weakly on the masses of the ions and surface atoms), therefore this process is not very selective but can lead to highly anisotropic etching due to the narrow angular distribution of ions incident on the surface.

Pure chemical etching. It corresponds to a chemical reaction between radicals (produced in the plasma and diffusing to the surface) and atoms at the surface. This mechanism, if spontaneous, can only be made efficient if the reaction between radicals and the surface atoms lead to the formation of thermodynamically stable products that are volatile at the considered temperature (i.e. the binding energy is small enough to be overcome through thermal desorption). These conditions are verified in the case of silicon etching by halogens. The process can be highly chemically selective but is isotropic as radicals diffuse in random directions. Anisotropy may still occur in case of crystalline orientation dependent etch rates [36].

Ion-assisted etching. This mechanism is a synergistic combination of the last two and one of its earliest demonstrations has been carried out by Coburn and Winters in a famous experiment [37]. The authors have shown that exposing a silicon (amorphous) substrate to a simultaneous flow of XeF_2 gas and 1 kV Ar^+ ions, the etching rate was much higher (about eightfold) than the sum of the rate obtained with XeF_2 or Ar^+ separately. Similar effects have been demonstrated for substrates exposed to a plasma, which simultaneously provides neutral etchants and a directional flux of ions. Ion-assisted etching therefore combines both the high anisotropy of physical etching and the selectivity of chemical etching. More detailed explanations on the root causes for ion-assisted etching will be given in the context of c-Si interactions with fluorine etchants in the next subsection.

Ion-enhanced inhibitor etching. This last process involves an additional actor: the inhibitor layer. SF_6/O_2 plasma etching of silicon is a very well-known example of such a mechanism. Both F* and O* radicals are produced in the plasma and diffuse to the surface where they may chemically react with the silicon surface: F* reacts to eventually form SiF_4 (volatile) molecules, while

the competing O* particles induce the formation of SiO_xF_y non-volatile species. The latter form an inhibitor layer protecting underlying Si from further etching by F*. However, this layer may be sputtered by ions to uncover the substrate. This process has been widely studied for deep-trench etching in silicon [38]: the inhibitor layer forms on both the bottom and the flanks of trenches but will only be efficiently sputtered at the bottom, where further etching is then allowed.

I.1.4.c The particular case of fluorine etching of silicon

The mechanisms leading to silicon etching using halogen species, in particular fluorine, are among the most widely investigated in the field of plasma processing. Since the earliest studies in the late 70s, many attempts at fully understanding the plasma-surface interactions have been carried out [39–41], and some basic features, including the nature of products leaving the surface, are still being debated nowadays [42]. Nevertheless, the most important qualitative aspects in the case of the F/Si system are here synthesized, first concerning pure chemical etching, then mechanisms explaining ion-assisted etching.

Pure chemical etching. The first important experimental result is the existence of spontaneous etching of c-Si by fluorine (either as F atoms or in the form of neutral molecules, e.g. XeF_2 or SF_6) in the absence of ion bombardment. This phenomenon leads mainly to the formation of SiF_4 as the final volatile product. To account for these observations, two main mechanisms based on sequential reactions have been postulated:

- The first set of reactions corresponds to successive fluorination of Si atoms through an Eley-Rideal mechanism (see sequential reactions (I.17) below, first proposed by Flamm and Donnelly in the case of c-Si etching using fluorine [40]). Incoming neutral atoms directly react with surface Si atoms.

$$\begin{aligned} Si(s) + F(g) &\longrightarrow SiF(s) \\ SiF(s) + F(g) &\longrightarrow SiF_2(s) \\ SiF_2(s) + F(g) &\longrightarrow SiF_3(s) \\ SiF_3(s) + F(g) &\longrightarrow SiF_4(g) \end{aligned} \tag{I.17}$$

- The alternative pathway, proposed by Petit and Pelletier [41], corresponds to a Langmuir-Hinshelwood mechanism: after initial halogenation of the first monolayer, formation of the final volatile product is obtained by associative desorption (reaction (I.18), where X is a halogen atom). In the case of fluorine the reactions can also involve SiF_3 species. This mechanism additionally assumes diffusion of adatoms onto the surface and rearrangements due to repulsive interactions between neighboring SiX_2 species, associative desorption taking place when sufficient coverage of the surface by SiX_2 species is attained.

$$SiX_2(s) + SiX_2(s) \longrightarrow SiX_4(g) + Si(s) \tag{I.18}$$

The Eley-Rideal mechanism is only proposed in the case of the F/Si system because the formation of SiF_3 requires breaking Si-Si bonds below the first monolayer, whereas other halogens (Cl or Br for instance) do not penetrate the crystalline lattice due to steric hindrance. In contrast, the Langmuir-Hinshelwood mechanism can also be applied to halogens other than fluorine since it is valid for monolayer adsorption.

In fact, the diffusion of fluorine into c-Si has been shown to far exceed the first monolayer even in the absence of ion bombardment (multilayer adsorption): a fluorosilyl (SiF_x) intermediate layer is formed at the surface, with a graded F density from the surface to the bulk. This layer is stable below temperatures around 200 °C [43]: if the etchant flux is stopped, already bonded F species do not further react with c-Si. Moreover, the SiF_x layer thickness and composition depend in particular on the nature of etchants, on the etch rate and on the c-Si doping (type and level). Fluorine has for instance been identified up to 20 nm inside the c-Si lattice [44] and the SiF_x layer

thickness decreases with increased etch rates. The increased etch rate for thinner SiF_x layer and the dependance on the silicon doping are actually explained by the fact that F^- ions (rather than F atoms) are diffusing into the c-Si. Indeed, due to the high electronegativity of fluorine, electrons are able to tunnel from the Si bulk through the SiF_x layer and ionize F atoms approaching the surface. The negative ions at the surface of the SiF_x layer generate an electric field across the SiF_x layer and directed from the silicon to the , which in turn "pulls" the negative ions into the c-Si layer where they react with silicon. In this model, the etch rate is positively linked to the surface density of negative ions, which both depends on the SiF_x layer thickness and silicon Fermi energy (therefore doping nature and level). In particular, the negative ion concentration increases with decreasing SiF_x layer thickness [45].

Ion enhanced etching. The synergetic effect obtained from chemical etching with simultaneous ion bombardment is illustrated in Figure I.15(a) from the experiments by Coburn and Winters: the etch rate during simultaneous XeF_2 exposure and Ar^+ ion bombardment is an order of magnitude larger than the sum of the etch rates during separate exposure to XeF_2 or Ar^+ bombardment. Several hypotheses explaining this behavior have been proposed, while some causes have been ruled out, the remaining hypotheses (see below) are likely to all contribute to the synergetic effect [6, 43].

A first effect involves bombardment by chemically reactive ions: the latter impact the substrate and benefit from both their kinetic energy and their chemical nature to break bonds. However this effect is not believed to be dominant: first, it does not explain synergetic effects in experiments where ions are chemically inert (e.g. the original study from Winters and Coburn [37] where Ar^+ beams are used). Secondly, experiments comparing bombardment by rare gas ions and reactive ions (for instance Ar^+ and CF_3^+ ions in the case of Si etching [46]) do not demonstrate very large etch yield differences. Anecdotally, the term "reactive ion etching", commonly used to designate plasma reactors dedicated to substrate etching, is actually not representative of the dominant occuring physical processes.

A second mechanism stems from enhanced chemical etching. As previously mentioned, it has been experimentally shown that, for pure chemical etching, a thinner SiF_x layer leads to an increased etch rate (in the steady-state, owing to a higher surface density of negative fluorine ions on the SiF_x layer according to the model from [45]). Ion bombardment will additionally reduce the SiF_x thickness through sputtering, therefore further promoting chemical etching.

Finally, a third explanation is linked to chemical reactions (and desorption) due to ion bombardment, sometimes called "chemical sputtering", this mechanism is believed to have the most important effect in increasing the etching rate [6, 43]. Energetic ions hitting the surface provoke "collision cascades" (displacing adatoms or atoms at the surface or in the bulk, provided sufficient

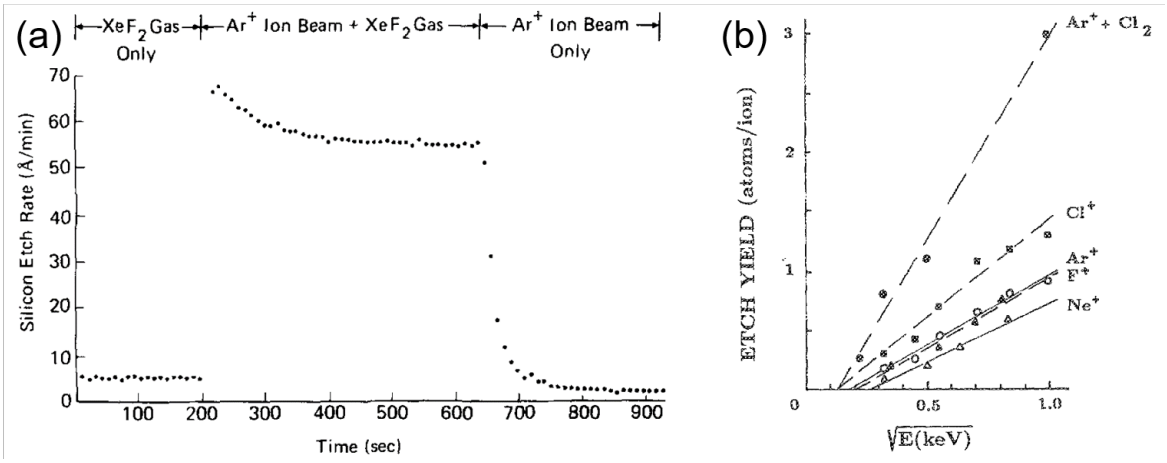

Fig. I.15: (a) Synergetic effect in silicon etching by XeF_2 and Ar^+ ion bombardment, extracted from [37]. (b) Silicon etching yield as a function of the ion energy with various species, extracted from [47].

energy). In this context, formation of volatile products is favored by the local rearrangement. For instance, in the case of the Langmuir-Hinshelwood mechanism described below, the rearrangement will induce product formation even below the threshold surface coverage needed in the absence of ion bombardment. Moreover, in the presence of ion bombardment, a significant quantity of SiF_2 molecules is also identified to leave the surface in conditions where pure chemical etching mainly leads to SiF_4 products.

The above-mentioned mechanisms imply that the ion bombardment energy is an important parameter determining the etching yield. In the case of silicon etching with relatively low ion energies, Steinbrüchel has shown a universal scaling for etching yield with the square-root of the ion energy [47], as shown in Figure I.15(b) for several types of ions. Moreover, an energy threshold, Eth, was observed in most cases.

Focus on the SF_6/O_2 mixture. In microelectronics, a challenging issue in c-Si etching rapidly emerged with fluorine etchants: despite ion-enhanced etching, the anisotropy is too low to efficiently etch vertical patterns [48, 49]. Besides shifting to other halogen etchants, solutions were found by decreasing the temperature of the substrate (cryogenic etching) and/or adding inhibitor forming species in the mixture. Crudely speaking, the idea behind cryogenic etching is to "freeze" chemical reactions on vertical walls by cooling the substrate (with liquid nitrogen for instance), while ion-enhanced etching still takes place at the bottom of the trench, see for instance [38] for a review on these methods. Regarding the addition of inhibitor forming species, it could be achieved by directly using fluorocarbons (e.g. CF_4 or CHF_3) or a mixture of gases, including the SF_6/O_2 case.

Investigations on the SF_6/O_2 mixture were first carried out by d'Agostino and Flamm in 1981 [50]. The authors observed that, similarly to CF_4/O_2 discharges, the addition of a small percentage of O_2 in the feedstock gas drastically increased the etching rate of silicon (up to a factor 3 at 40% O_2, Figure I.16). However, further increasing the O_2 content had an opposite effect and the etching rate became very low. The initial increase is explained by a higher density of F* radicals in the gas phase, due to the reaction of O_2 and O* with SF_6 and SF_x (x< 5) radicals, favoring the formation of F* and preventing their recombination. However, O* radicals also compete with F* for reactions at the surface, leading to the formation of an SiO_xF_y layer: too large a proportion of oxygen therefore oxidizes the surface and slows the etching rate [48]. As it will be detailed in section I.2.1.a, these mechanisms are of paramount importance for texturing.

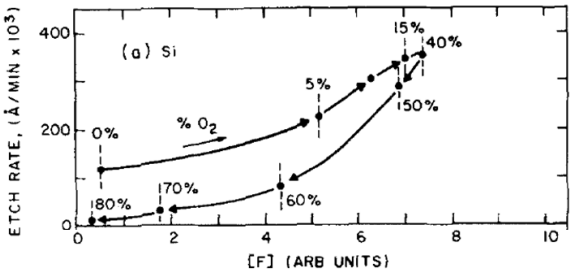

Fig. I.16: Evolution of the Si etch rate and F atom density in a SF_6/O_2 discharge with the O_2 content in the feed gas. Adapted from [50].

Finally, a combination of the two proposed method (cryogenic condition and inhibitor layer formation) can be used to achieve very high anisotropy for deep trench etching, and SF_6/O_2 is especially used to this aim.

The anisotropic behavior of silicon etching with SF_6/O_2 plasma (based on ion-enhanced inhibitor etching) is intimately linked with the emergence of nanostructures. This short summary will therefore help in the understanding of silicon plasma texturing described in the next section, and in the interpretation of experimental observations reported in following chapters.

I.2 Black Silicon: Theory and Characterization

Simply put, black silicon is a silicon surface which appears "visually" black as observed from the picture in Figure I.17, i.e. the reflection of light by the silicon surface (in the visible wavelength range, approximately [400, 700 nm]) is very low. A clear definition of "black silicon" (b-Si) has not been proposed in the scientific literature, neither on the basis of the fabrication method nor on a threshold optical metric. For instance, reflectance values (usually reported as effective reflectance, R_{eff}, see definition in section I.2.4.a) ranging from 0.5 to 15% can be found, and the wavelength range over which it is characterized is variable and depends on the application.

As a common denominator, the term "black silicon" is used for surfaces that exhibit "subwavelength" structures – roughly the nanoscale for PV applications. This property implies specific optical behaviors, especially in terms of anti-reflection, as it will be highlighted in section I.2.2. These particular types of surfaces will therefore be interchangeably named "black silicon", "nanotextured silicon" or "nanostructured silicon" in this manuscript.

In the field of PV, the processes leading to nanotexturing differ from conventional wet etching techniques (i.e. alkaline or acidic etching, see section I.2.1.b) which rather lead to microstructuring. However, a review of existing literature shows that so-called black silicon surfaces may exhibit a wide range of characteristic sizes, and various morphologies (like cones, columns, or holes). However, all black silicon surfaces often exhibit relatively high aspect ratios ranging from 1 to 10 [51].

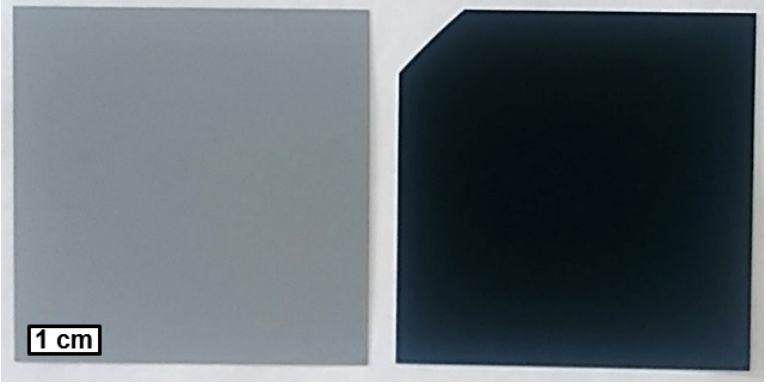

Fig. I.17: Picture of an un-etched reference c-Si sample (left) and a "black silicon" sample processed as part of the present work (right).

I.2.1 Silicon Nanostructure Formation

Various techniques may be used to form nano- or microstructures on surfaces. In order to limit the range of the following review, let us set some constraints. We focus on "pure" c-Si structures with the same crystalline orientation as the substrate, showing a 2D organization (1D or 3D patterns are excluded) and obtained from top-down approaches. The latter correspond to methods where structures are formed by removal of a certain amount of c-Si material from the initial substrate. Bottom-up approaches (where c-Si material is epitaxially grown on the substrate from an external material source, e.g. nanowires formation from vapor-liquid-solid (VLS) methods) are therefore excluded. Details on bottom-up techniques can be found in [52], while applications of plasma-assisted VLS method for PV are reviewed in [53].

Several top-down techniques are currently used for the formation of black silicon surfaces; the interested reader may consult the reviews by Otto et al [54] and Liu *et al.* [51] for a general overview over these techniques applied to PV. From an initial silicon surface, structuring can occur either directly through self-organization, or indirectly by the formation of a patterned mask and its transfer to silicon (lithography-based techniques). We will first focus on the process at stake in the present work, i.e. plasma texturing, and then describe alternative techniques.

I.2.1.a Silicon surface texturing by SF_6/O_2 plasma

Short chronology. Spontaneous formation of nanostructures during silicon etching by plasma is a well-known phenomenon firstly identified in the field of microelectronics. The first report on the formation of "black silicon" in literature was made by Schwartz and Schaible from IBM in 1979 [55]. In this paper, nanostructuring of silicon was observed when performing RIE with Cl_2/Ar plasma. The authors point out a large quantity of oxygen (characterized by Auger spectroscopy, value not reported) present in black silicon areas after the process, but the nanostructure formation was not repeatable. A similar phenomenon was later observed during etching with HCl plasma [56]. At that time, the undesirable nanostructure formation was again attributed to the presence of oxygen (from water vapor or incomplete chamber evacuation for instance), but no details on the exact mechanism were proposed. Potential solutions to avoid black silicon formation were suggested such as improving base pressure or adding fluorinated gases into the mixture.

However, roughening was also observed later during etching with fluorine containing gases such as CF_4 [57]. In this specific case, a first explanation for the roughening phenomenon was given: namely, that it was induced by redeposition of electrode material (aluminium) on the silicon sample in the form of non-volatile islets (AlF_x) that protect the underlying silicon from etching. Going back to chlorine-based RIE, a second explanation for the formation of nanostructures was given by Oehrlein *et al.* in 1990 [58] in the case of etching by $HCl/O_2/BCl_3$ plasma: the formation of non-volatile species can be directly induced by the etching process itself due to the presence of oxygen, and is intimately related to ion-enhanced inhibitor etching.

The formation of black silicon was first reported by Jansen *et al.* in the case of SF_6/O_2 (with or without the addition of CHF_3) in 1995 [59]. The authors similarly point out the role of inhibitor species for the formation of nanostructures and notice that the appearance of black silicon nanostructures coincides to the conditions (gas mixture, power, pressure...) that lead to vertical walls around masks. This effect is explained by the balance between chemical etching and passivation layer formation and is for instance dependent on the SF_6/O_2 gas flux ratio: when the flux of SF_6 is too high, the etching is in "under-passivating" mode and becomes less anisotropic (formation of negatively tapered walls). On the contrary if too much O_2 is used, the regime becomes "over-passivating" and the walls are positively tapered. There exists a middle point where the balance between all the microscopic mechanisms (etching, passivation and removal of the passivation layer by ion sputtering) leads to nearly vertical walls and formation of nanostructures.

The authors therefore propose the so-called "Black silicon method" to quickly optimize etching of trenches in a reactor by finding the conditions that lead to black silicon formation (which is easily visually observed). Then, a small shift in the process conditions is made just enough so that the b-Si does not form: these new conditions are deemed to be best for the etching of patterns with vertical walls. Several papers have been published by the same team on this method [48, 59–67], investigating the effect of the mask composition, loading, or temperature for instance, and mostly applied to manufacturing of microelectromechanical systems (MEMS). The authors actually claim that "every plasma mixture which consists of a chemical etchant, passivator and an ion source can be used for the black silicon method".

Finally, Jansen *et al.* more recently proposed a last possible source of c-Si nanostructure formation in SF_6/O_2 plasma etching, namely the formation of dust (made of $(SiO_xF_y)_n$ species) inside the plasma from SiF_4 products and oxygen. However, this effect is debated as dust nanoparticles are usually trapped inside the plasma bulk because they are negatively charged [38].

Summary of the mechanisms. The basic phenomena behind nanotexturing of silicon surface during plasma etching may now be synthesized in the particular case of mixtures containing fluorine as etchant species and oxygen as passivator [68, 69]:

- Etching of c-Si by fluorine radicals and ion enhanced etching (formation of volatile SiF_4);
- Formation of non-volatile SiO_xF_y on the surface (due to O* radicals that compete with F*) acting as in-situ micro-masking species and preventing etching of underlying c-Si;

- Sputtering of the micro-masking species (partial removal of the micro-mask).

As it has already been highlighted, an adequate balance between the c-Si etch rate, the passivation layer formation rate and sputtering rate is required to obtain black silicon (it constitutes the core of the "Black silicon method"). A rather simple Monte-Carlo model [70] taking these three mechanisms into account has successfully modeled the experimentally observed evolution of nanostructures during SF_6/O_2 plasma.

Experimental investigations have shown that the adequate balance is in particular controlled by the volatility of SiO_xF_y species (and therefore the passivation layer formation rate) which depends on the substrate temperature: in-situ micro-masking is more efficient at cryogenic conditions (e.g. using nitrogen cooling) [71]. The effect of the substrate temperature on black silicon formation was already observed by Jansen *et al.* [65]: they observed a U-shaped curve (with a minimum around 130 K, as seen in Figure I.18) for the O_2 threshold content in the feed gas required to obtain black silicon. A same trend has been observed by Dussart *et al.* [72] in different conditions with a minimum around 160 K. The increase of oxygen content required for temperature below the observed minimum threshold is not well understood but may stem from lower diffusion of physisorbed oxygen on the surface (and thus a less efficient formation of the passivation layer). In contrast the behavior above the minimal threshold value is more easily explained: it stems from the increased volatility of the SiO_xF_y layer, so that a higher quantity of O* radicals (compared to F*) is required to efficiently form the passivating layer. This effect is related to the passivation of sidewalls in deep silicon etching: the oxidation threshold (i.e. threshold oxygen content above which the passivation layer is formed) increases with the substrate temperature [71]. Ion bombardment increases the threshold (layer desorption is favored by kinetic energy transferred by the ions): the bottom of the trenches is therefore below the oxidation threshold while the walls (not subjected to ion bombardment) are passivated.

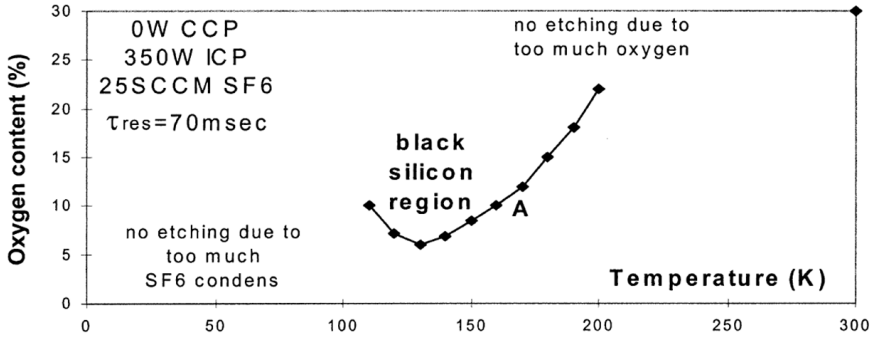

Fig. I.18: Oxygen content threshold versus substrate temperature for the formation of b-Si, extracted from [65].

However, black silicon can also be obtained with SF_6/O_2 at higher (room) temperature [73] although the suitable process conditions become more restrictive. Volatility of the passivation layer may also be controlled by adding other gases in the mixture: Lee *et al.* added Cl_2 to optimize the texturing step for silicon solar cell fabrication claiming that the passivating layer was less volatile. For the same purpose, Murias *et al.* [74] included CH_4 in the feed gas to additionally form a polymer passivating layer, which is in turn etched by oxygen. However, they found an optimum recipe with the methane addition.

Roughening initiation and nanostructure morphology. The initiation of nanoscale roughening during plasma etching is still not well understood. Indeed, the initial stages of nanostructure formation are difficult to grasp, in particular because their direct observation would require in-situ real-time probing at the nanoscale.

In the cases where nanostructures are generated by redeposition of either mask or electrode material (or nanoparticles in dusty plasmas), the initiation may be understood by a stochastic redeposition of particles, with a distribution depending on potential inter-particulate interactions and a density depending on the particles formation rate. The final nanostructure density and

size (at least shortly after the initiation) are here controlled by the initial particles. However, if nanostructuring stems from the formation of micro-masking species directly on the surface, their distribution and initial (lateral) size is more challenging to interpret. Qualitatively, the initiation in this case is sometimes explained by variations of the native oxide thickness: this layer is removed faster on locations where it is thinner, and a higher etching rate for Si induces the initial roughness. If the oxide is removed prior etching (e.g. by HF dip), small local variations in the deposition rate of micro-masking SiO_xF_y species might explain the initiation of roughening.

Once created, the nanostructures "grow" vertically and horizontally by removal of material, and the final size and morphology of the nanostructures strongly depends on the process conditions. From the literature, it is possible to give the following common characteristics for nanostructures obtained by plasma etching from in-situ micro-masking: (i) the NS size is distributed and comprised (in the lateral direction) between 10 nm and 10 µm; (ii) the aspect ratio may vary in a large range as shallow structures as well as very sharp "needle-like" structures have been obtained; (iii) the NS locations on the surface are usually correlated: a typical distance between the nanostructures can be quantified and in most cases corresponds to the base width of the NS (i.e. the structures are "neighboring"); (iv) the nanostructures are circularly symmetric (along the normal to the surface), and if not, their shape depends on the crystalline orientation of the c-Si surface and therefore the nanostructures are uniformly "oriented". Examples of b-Si surfaces from literature are shown in Figure I.19 to illustrate the diversity of possible morphologies.

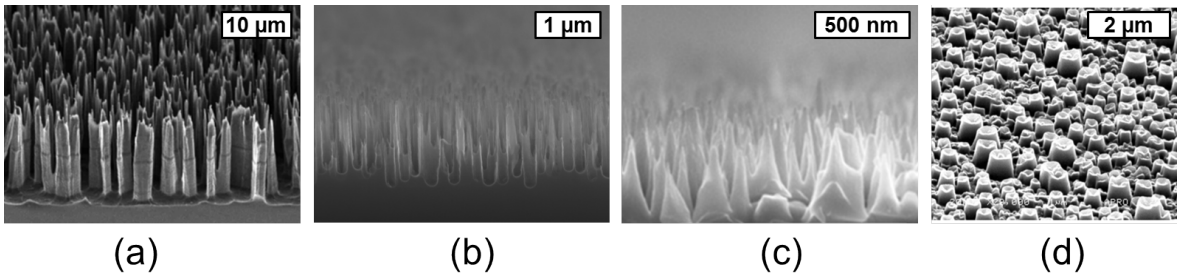

Fig. I.19: SEM images of various b-Si surfaces obtained by SF_6/O_2 RIE (and prior any other process) from different groups illustrating the diversity of scales and morphologies. Extracted (in this order) from [67], [75], [76] and [68].

I.2.1.b Common "wet" texturing techniques

As it has been previously mentioned, black silicon processes for PV applications are usually compared to the two standard chemical texturing processes, namely alkaline and acidic etching. However, nanotexturing techniques may also be combined with prior conventional texturing to obtain dual-scale structures. These "conventional" chemical techniques shall now be rapidly described before detailing competing nanotexturing methods.

Alkaline etching for mono-Si. The etching rate with a diluted alkaline solution (e.g. aqueous solutions of KOH or tetramethylammonium hydroxide – TMAH) is anisotropic: the etch rate is the slowest along <111> directions [77]. Therefore, this process is suitable for the texturing of (100) wafers: direct immersion into the solution will lead to the formation of randomly located "upright pyramids" with (111) facets, as shown in Figure I.20(a). This process is now well-established in the industry for monocrystalline solar cells and leads to an effective reflectance in the range of 9-10% without ARC. In contrast, one can obtain "inverted pyramids", for instance by defining a photolithographic pattern prior etching [78].

Acidic etching for mc-Si. The crystal orientation dependence for alkaline texturing prevents its application to multi-crystalline solar cells, for which acidic texturing is typically used instead

(more than 85% of the mc-Si solar cell in the market in 2017 [2]). This process, usually performed using an aqueous mixture of HF/HNO_3 [79], is isotropic in nature (also sometimes called "iso-texturing") and leads to rounded microstructures, Figure I.20(b). The final reflectance of acidic textured surfaces is always significantly higher (above 15% without ARC) than for alkaline etched structures, as shown in Figure I.20(c). Moreover, the effectiveness of the technique depends on the initial surface finish, and has led to challenges for new wafer sawing processes, as will be detailed in section I.2.3.b.

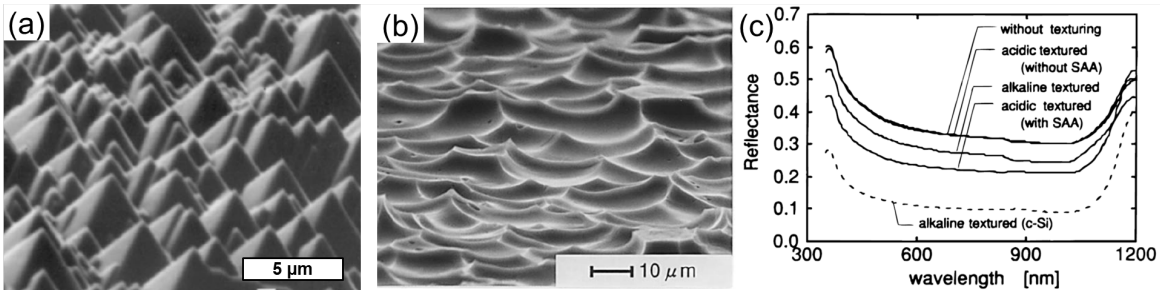

Fig. I.20: SEM images of (a) alkaline textured silicon (extracted from [77]) and (b) acidic textured silicon, extracted from [79]. (c) Comparison of reflectance for different wet etchants on mono-Si (dashed lines) and mc-Si (solid lines), extracted from [79]. SAA: surface active agents.

I.2.1.c Other nanotexturing techniques

Replacement of conventional wet texturing techniques by nanotexturing has been attempted successfully using other methods than RIE. A synthetic description of these competing approaches is given in this section. SEM images of b-Si surfaces obtained by the different methods are shown as illustration in Figure I.21 at the end of this section.

Metal Assisted Chemical Etching. MACE (sometimes shortened MCCE for Metal Catalyzed Chemical Etching) is one of the leading techniques in industry for the formation of b-Si. The market share of MACE-textured mc-Si solar cells is expected to rapidly grow in the next years: the ITRPV expects a 50% share by 2028, while it was around 10% in 2017 [2]. This process has first been proposed by Koynov *et al.* [80] in 2006, and the first AlBSF mc-Si solar cell including a front MACE textured surface was reported by the same team the next year with an efficiency of 13% [81]. The current record efficiency for similar devices using MACE texturing of the front surface is 20.19% (mono c-Si cell, [82]) and 19.06% for mc-Si [83]. Detailed reviews on the MACE process are available in [84, 85].

The technique involves the creation of a metallic layer - often in the form of nanoparticles (NP) - on the surface of the Si wafer. Different metals can be used such as Ag, Au or Cu. The etching is then performed by immersing the substrate in a solution containing HF and an oxidizing agent such as peroxide: the metallic NP then act as catalysts for localized electrochemical reactions where H_2O_2 is reduced and silicon is dissolved into H_2SiF_6 [86]. These reactions occur preferentially where metal is in contact with Si, and the metal "sinks" into the c-Si, leading to the formation of pores or nanowires.

The final morphology of MACE b-Si thus depends in particular on the nature and morphology of the initial metallic layer or NPs, on the concentrations in reactive species in the solutions, and on the etching time. Using all these "control knobs" the morphology of the nanotextured surface can easily be tailored. The texturing time is usually short (a few minutes), but also requires the recycling of the chemicals and the removal of the metal catalysts from the surface (once the texturing is finished, in order to recover the properties of the semiconductor [87]). Although the morphology of the obtained structure might depend on the crystalline orientation, this process is viable on large-scale multi-crystalline silicon wafers.

Chemical Vapor Etching. CVE is a derivation of acidic etching: wafers are placed on top of a heated bath of acidic etchant and vapor deposited onto the surface in the form of "micro-droplets" locally etches the silicon. This technique was initially tested in 2008 by Ju *et al.* after standard acidic etch to obtain a dual-scale texturing [88]: the team obtained a 16% efficiency mc-Si AlBSF cell. More recently, Zhou et al tested this technique as a method to texture diamond wire sawn mc-Si wafers and achieved 18.24% efficiency (also AlBSF cell) [89].

Plasma Immersion Ion Implantation. PIII was initially used for semiconductor doping. However, Xia *et al.* [90] demonstrated in 2011 that nanoscale texturing of c-Si by PIII was also possible using a SF_6/O_2 mixture. The team fabricated a 15.7% efficiency AlBSF solar cell.

As one may expect, this technique has similarities with RIE: the main difference lies in the very high (negative) DC voltage applied – independently from the plasma generating power – to the substrate holder (0.5 to several kilovolts). The large voltage drop in front of the substrate accelerates the ions that are thus implanted deeply into the c-Si bulk: the implantation depth depends on the applied DC voltage and on the nature of the ions but may reach several tens of nanometers. The exact mechanisms leading to nanotexturing by PIII with an SF_6/O_2 plasma have not been thoroughly studied. However, Xia *et al.* give the following interpretation: F^+ and SF_x^+ ($x< 5$) ions are implanted and react with the surrounding Si atoms, while O* radicals induce the formation of a passivation layer, similarly to the mechanisms in RIE. The chemical reactions are thus not strictly happening on the surface.

Similarly to the RIE texturing, the final morphology of the b-Si surface depends on the competition between the etching of Si by fluorine, the passivation with SiO_xF_y and the ion bombardment [90]. However, the high ion energy required for PIII may induce a high density of defects and contaminants in the c-Si that have to be removed. Applying an adequate damage removal etching post b-Si formation using a $NaNO_2/HF/H_2O$ solution, a team from the same lab achieved a record 17.46% efficiency AlBSF solar cell [91].

Atmospheric Dry Etching. ADE uses thermally activated F_2 (diluted in N_2) molecules for the nanotexturing of c-Si at atmospheric pressure. The process has first been reported by Kafle *et al.* in 2013 [92], the team fabricated AlBSF solar cells with an efficiency of 15.2%. In 2015, a record of 18% efficiency was achieved by the same team (similar cell structure), while in 2017 the same process has been used to fabricate 20.3% efficiency PERC solar cells [93]. While etching by F_2molecules at atmospheric pressure was already demonstrated and showed an isotropic behavior, the nanotexturing mechanism obtained by the ADE method is not understood for now.

Pulsed femtosecond laser. Silicon surface treatment using pulsed laser in the presence of a fluorinated background gas has been shown to generate structures. The formation mechanisms, as well as the scale and morphology of the final structures depend on numerous factors (e.g. background gas, fluence, scanning velocity) [94]. Moreover, the defects created in the silicon surface have to be mitigated with a chemical damage removal etching to achieve reasonable efficiency. Applying this method, Nayak *et al.* obtained self-assembled microscale high aspect ratio conical structures on the front surface of mono-Si AlBSF cells, and have demonstrated an efficiency of 14.2% [95], while Chen *et al.* later reached an efficiency of 15.6% for the same type of cell [96].

Lithography-based approaches. This last category aggregates several "indirect" nanotexturing techniques, where the creation of the pattern and its transfer to silicon are obtained in two separate steps. First, the pattern is formed in a masking layer deposited onto the silicon, it has for instance been achieved using: (i) colloidal lithography, [97, 98]; (ii) laser-interference lithography [99]; (iii) or nanoimprint lithography [100, 101]. The pattern is then transferred to silicon using wet or dry etching methods. Notice that these techniques are not always classified as "b-Si techniques" as they sometimes lead to microscale structures. Moreover, lithography-based ap-

proaches are the only ones that can achieve the formation of periodic structures with identical sizes, also pseudo-random arrangements are usually obtained from colloidal lithography.

A few results at solar cell level (here all on mono-Si AlBSF cells) should be highlighted. Cheon *et al.* obtained 17.2% efficiency using colloidal lithography with spin-coated silica beads (diameter of 520 nm) and subsequent etching by SF_6/O_2 plasma [97]. Using nanoimprint lithography (pattern transfer also made by SF_6/O_2 plasma), Volk *et al.* obtained 17.8% efficiency [100]. However, the "honeycomb" surface they manufactured showed structures at the microscale (around 10 µm deep for a diameter of approximately 8 µm). Finally, Cornago et al realized 15.6% efficiency cells using laser interference lithography and pattern transfer by CF_4/O_2 plasma [99]. Notice that in all cases, several additional cleaning or etching steps (in addition to the mask layer deposition and pattern transfer) are required, making the manufacturing process much more complex.

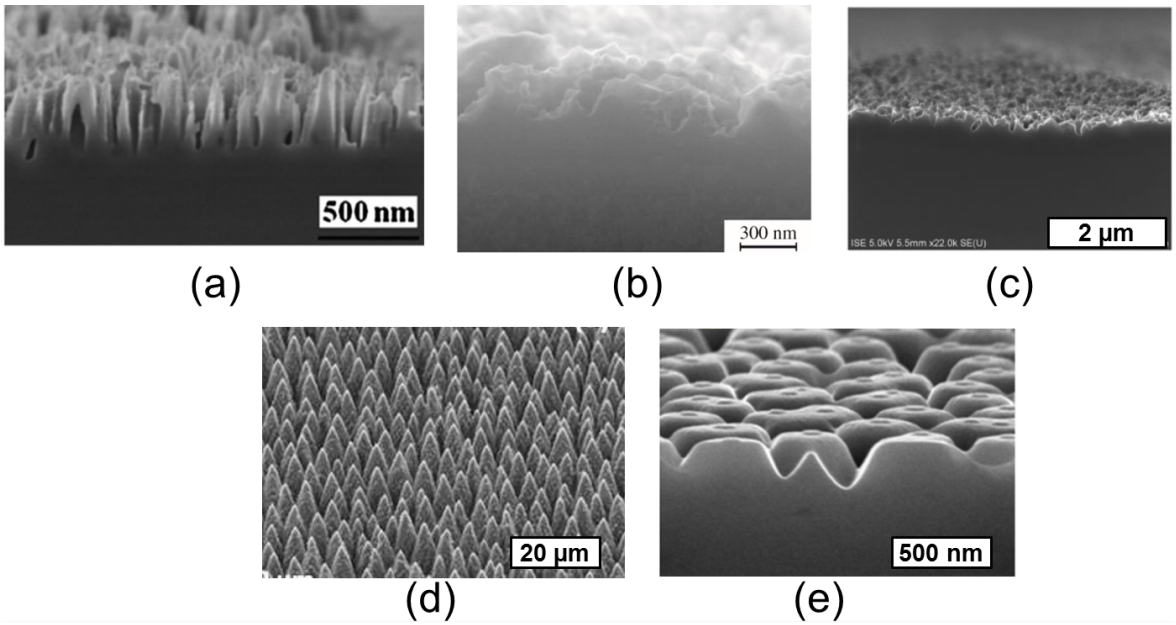

Fig. I.21: SEM images of various b-Si surfaces (prior any other process) obtained by: (a) MACE, extracted from [102]; (b) PIII, from [103]; (c) ADE, from [104]; (d) Pulsed femtosecond laser [95] and (e) Colloidal lithography [97].

I.2.1.d Synthesis

A rapid synthesis of the various texturing techniques is here proposed, with their advantages and drawbacks for implementation in PV devices evaluated regarding several criteria. This comparison is given in Table I.1. Notice that the lithography-based approaches are excluded as their characteristics may be limited both by the pattern formation step or the transfer method. For instance, if the pattern transfer is done by RIE the limitations will be similar as for direct RIE nanotexturing.

As detailed in Table I.1, a first common denominator for nanotexturing techniques is the very low reflectance that is achievable without an additional ARC, in contrast to conventional chemical etching. Values below 5% (average in the visible spectrum) have been reported for all b-Si techniques, and reflectance values in the order of 1% are common. Secondly, these techniques are all applicable on both mono- and mc-Si wafers, although crystalline orientation dependence has been observed in the case of RIE and MACE texturing. However, some teams use a chemical etching step after etching to form inverted nanopyramids, in which case the technique may not be viable for mc-Si.

A difference appears in the need for additional chemical etching steps after texturing. In the case of MACE, metal particles have to be removed from the Si surface and this step is unavoidable (and one might argue that it is "part of the process"). For ADE this step is not required as gas-

surface interaction involve only very low particle kinetic energies. In the case of RIE, DRE may be avoided if ion bombardment energy is kept low. In contrast, DRE is required for PIII and pulsed laser techniques since both techniques create a large density of defects on the silicon surface.

Regarding the issues coming from the etchants and by-products, wet techniques (conventional or MACE) are characterized by the use of a large quantity of liquid chemicals that require recycling or elimination. On the other hand, dry techniques often involve halogen etchants which sometimes have very high global warming potential (GWP). The example of F_2 and SF_6 are striking as the former has no GWP, while the latter holds the record of the highest GWP, i.e. around 22 thousand times the GWP of CO_2. The management of chemicals, gases and by-products is problematic as it might reveal costly (both financially and environmentally) but can be mitigated by recycling and careful elimination.

Finally, the viability of the nanotexturing techniques at the industrial scale is more difficult to assess. Based on the current market shares and predicted trends (for instance from the ITRPV), it is possible to state that both RIE and MACE are viable since these techniques are already employed by some companies and their market share is expected to grow. For the other methods, the evaluation is based on the author's own understanding of the technical and scientific literature, and is therefore rightfully arguable.

Tab. I.1: Comparison of silicon texturing techniques regarding various criteria.

	Method	Crystal-orient. dependent	Achievable R_{eff} (w/o ARC)	Need for DRE	Issues from etchants & by-products	Viability (industrial level)
"Standard" methods	**Alkaline etch.**	Yes, only mono-Si	High (10%)	No	Disposal of chemicals	**Yes**, dominant for mono-Si (inexpensive, high throughput and scalability)
	Acidic etch.	No	Very high (>15%), not possible on DWS mc-Si	No	Disposal of chemicals	**Yes** (inexpensive, high throughput and scalability) but gradually replaced
Black silicon methods	**RIE**	No (w/ exceptions)	Very low	Avoidable	High GWP of SF_6, treatment of by-products	**Yes for mc-Si** (but low expected share [2])
	MACE	No (w/ exceptions)	Very low	No (but removal of metal catalysts)	Disposal of chemicals, recycling of metal catalysts	**Yes for mc-si** (expected dominant within 10 years [2])
	CVE	No	Very low	No	Disposal of chemicals	**Yes?** (possibly low cost, scalability and throughput unknown)
	PIII	No	Very low	Unavoidable	High GWP of SF_6, treatment of by-products	**Unlikely?** (possibly high investment costs, issues of throughput?)
	ADE	No	Very low	No	Treatment of by-products, recycling of F_2	**Yes?** (inline system with high scalability and throughput, but costs unknown [104])
	Pulsed laser	No	Very low	Unavoidable	Potential issues from background gas (SF_6)	**Unlikely?** (good scalability but limited throughput, possibly high investment costs)

I.2.2 Optical Properties of Nanostructured Surfaces

I.2.2.a Anti-reflection

The reflection at an interface between two materials is due to the difference in refractive index and may be described by Fresnel's equations (derived from electromagnetics). The propagation of light inside a material can be described by the complex refractive index $\boldsymbol{n}(\lambda_0) = n(\lambda_0) + \mathrm{i}\kappa(\lambda_0)$. n is the refractive index and characterizes the light propagation velocity in a given material, and κ is the extinction coefficient. The latter is linked to the absorption coefficient α and both depend on the wavelength (here we consider the wavelength in vacuum λ_0, but from now we will drop this dependence in the notations for simplification):

$$\alpha = \frac{4\pi\kappa}{\lambda_0} \tag{I.19}$$

where the absorption coefficient characterizes the exponential decay of light intensity with the distance d traveled inside the material (Beer-Lambert law) with $I(d) = I(0)e^{-\alpha d}$.

Let us now consider a planar interface between air and c-Si. Air is a transparent medium (no absorption) with a near unity refractive index $n_0 = 1$. In contrast, c-Si is an absorbing material with a refractive index $n_1 + \mathrm{i}\kappa_1$. For the simple case of normal incidence, Fresnel's coefficient for reflection and transmission (in intensity) can be computed by:

$$R_\mathrm{f} = \frac{(n_1 - n_0)^2 + {\kappa_1}^2}{(n_1 + n_0)^2 + {\kappa_1}^2} \tag{I.20}$$

$$T_\mathrm{f} = 1 - R_\mathrm{f} = \frac{4n_1}{(n_1 + n_0)^2 + {\kappa_1}^2} \tag{I.21}$$

For non-normal incidence, polarization of light has to be taken into account but the transition to a higher refractive index material still induces reflection of part of the light (with the notable exception of total transmission at Brewster's angle for p-polarized light). From these very simple considerations, we notice that drastically decreasing reflectance at a given wavelength (for a flat interface) requires an adaptation of the refractive index between the two materials, i.e. index matching. This approach is for instance used when applying to anti-reflection coatings (ARC) which exhibit intermediate refractive index between air and c-Si.

If we now remove the constraint of a flat interface, another technique to reduce reflectance can be attempted by structuring at a scale much larger than the considered wavelength (for the geometric optics interpretation to be valid). Now the complex interface geometry induces multiple reflections which are as many opportunities for light to be transmitted inside the material. This second approach corresponds for instance to standard "microstructuring" for c-Si solar cells, e.g. pyramid texturing on monocrystalline (100) wafers where the pyramids usually exhibit sizes in the range of 2 to 10 µm. In most solar cells, both approaches (ARC and microstructuring) are applied simultaneously.

Back to black silicon. Nanotextured silicon surfaces exhibit very low reflectance in a broadband wavelength range, as illustrated in Figure I.22 showing results from Steglich *et al.* [105]. The team fabricated b-Si surface with SF_6/O_2 plasma texturing. Figure I.22(a) shows SEM images of the obtained structures: the average structure depth is around 0.5, 1 and 2 µm after 2, 3 and 10 min etching respectively. Meanwhile, the average nanostructure width lay respectively at 50, 75 and 225 nm. The reflectance of the samples decreases in the whole measurement range [300,1500 nm] as a function of the etching time, as shown in Figure I.22(b). After 10 min of etching, the reflectance drops to around 1% in the range from 300 to 1000 nm.

From this example, it should first be highlighted that comparison with literature may be made difficult due to the lack of a standard metric. For PV applications, the most common metric is the AM1.5g weighted average reflectance value, sometimes named "effective reflectance" (detailed in

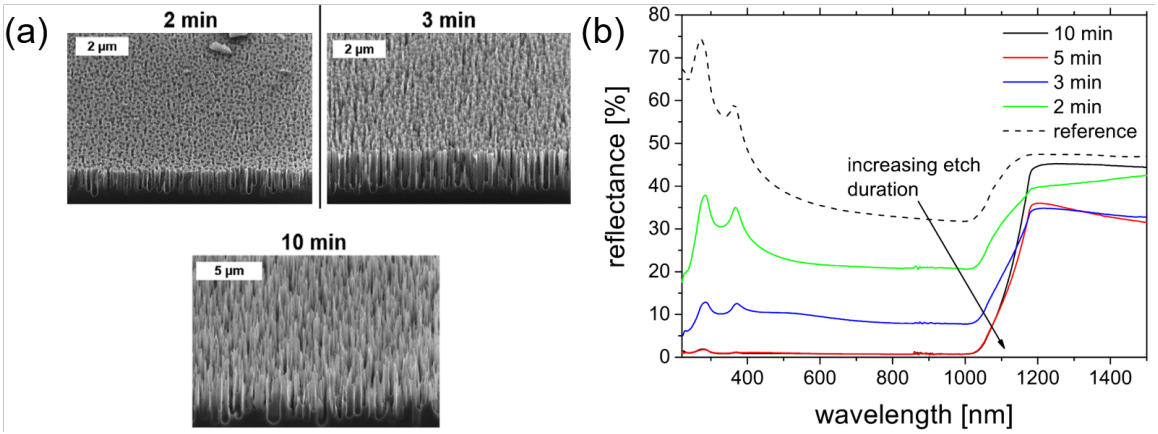

Fig. I.22: (a) SEM images of b-Si surfaces obtained by ICP-RIE in SF_6/O_2 with varying etching time. (b) Evolution of the total hemispherical reflectance of the samples with etching time. Adapted from [105].

section I.2.4.a). However, the choice of wavelengths range over which this average is computed also depends on the authors.

The broadband anti-reflective behavior obtained with "aperiodic" nanostructured silicon surfaces can be analyzed (and optimized) using full electromagnetic approaches. Some attempts have been made using for instance Rigorous Coupled Wave Analysis (RCWA, see for instance [106, 107]) or Finite Difference Time Domain (FDTD, e.g. [75, 108]) techniques to solve Maxwell's equations and model the optical properties of nanostructured surfaces. However, both techniques are computer-intensive and their validity is limited in the case of random structures.

Alternatively, a first interpretation can be made from two simplified models that depend on the characteristic lateral size Λ_{NS} of the nanostructures, the free space light wavelength λ_0 and the refractive index of the material n_{Si} [109, 110].

- If $\lambda_0/n_{Si} \ll \Lambda_{NS}$, we go back to the previously mentioned "multiple reflections" approach. Due to the complex morphology of the b-Si surface, an initial beam of light that is reflected has a great probability to impinge the silicon surface again and to be finally transmitted, as illustrated in Figure I.23(a). However, this interpretation is simplified; in particular, transmitted light might also exit the substrate if the absorption is weak. Nevertheless, simple ray-tracing simulations can in particular be used to model the reflectance in this case.

- If $\lambda_0/n_{Si} \gg \Lambda_{NS}$ (subwavelength regime), the situation becomes similar to refractive index matching. Indeed, when the characteristic lateral size of the nanostructures is very small compared to the wavelength of light, the interface becomes "optically flat". Thus, the nanotextured surface acts as graded refractive index layer, i.e. the refractive index gradually increases from air to silicon, as depicted in Figure I.23(b), a case which can again be modeled in a simple manner (see Chapter IV, section IV.1.1 in particular). While the condition for the graded-refractive index interpretation is set on the lateral size of the nanostructures, the magnitude of the effect depends on the thickness of the equivalent layer and on the refractive index profile. The anti-reflective effect of a graded refractive index layer was first theoretically demonstrated by Lord Rayleigh [111] and extensively investigated since then (see for instance [110, 112]). In the case of nanotextured c-Si surfaces, Branz *et al.* have shown experimentally that the decay of reflectance is exponential with a characteristic depth of $\lambda_0/8$: to decrease the reflectance at an air/c-Si interface by more than $95\%_{rel}$ (and up to a wavelength of 1000 nm), the graded layer thickness should be higher than 250 nm [113].

The two interpretations (geometrical optics and gradient refractive index) give a first description - in limited ranges - of the anti-reflective properties of nanotextured surfaces. However, in the case of c-Si PV applications, the studied wavelengths ($\lambda_0 \in [250, 1300\,\text{nm}]$) and the lateral size

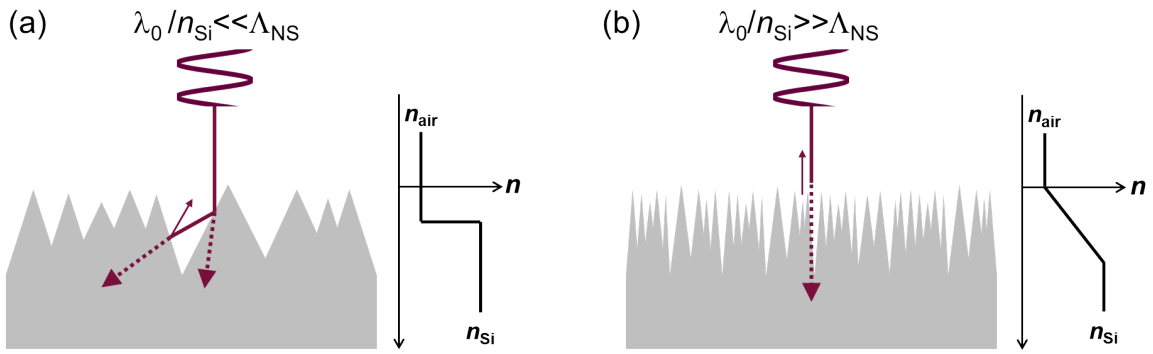

Fig. I.23: Schematic of light reflection and transmission at the c-Si surface with (a) large structures and (b) small structures compared to the wavelength of incoming light.

of the b-Si nanostructures often have a similar order of magnitude (as in the previous example, $\Lambda_{NS} \in [50, 225\,\text{nm}]$), so that neither of the two interpretations can be considered totally valid. In particular, diffraction phenomena may appear if the nanostructures have a periodic (or correlated "pseudo-random") arrangement, similarly to what is observed for "structural colors" [114].

I.2.2.b Light-trapping

Figure I.24 shows the real and imaginary components of the refractive index for c-Si at 300 K, as well as the absorption depth $1/\alpha$ (corresponds to the propagation distance where the intensity of light falls to $1/\exp(1) = 37\%$ of its initial value) as a function of the wavelength in vacuum. Typical solar cells (current industrial standard [2]) have an absorber thickness around 200 µm: above 1000 nm the absorption length of c-Si becomes much greater than the solar cell thickness and a large amount of light might be lost if it exits from the absorber. Light-trapping strategies (i.e. methods to prevent light from escaping the absorber) are required to avoid these losses in the near-IR range.

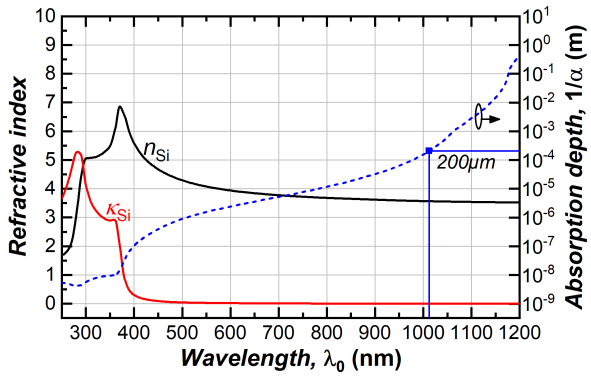

Fig. I.24: Optical properties of c-Si (at 300 K, data adapted from [115]): real and imaginary part of the refractive index and absorption depth.

A first technique to improve light-trapping is to coat the back surface of the cell with a metal which will act as a mirror (assumed perfect, a model reference situation for monofacial solar cells). In this case ("perfect rear mirror"), with no ARC on the front surface, a simple computation for normal light incidence on a slab of thickness w placed into air can be done. In this case (schematically depicted in Figure I.25(a)), the total absorptance is expressed by:

$$A_{\text{tot}} = 1 - R_{\text{f}} - \frac{(1 - R_{\text{f}})^2\, e^{-2\alpha w}}{1 - R_{\text{f}} e^{-2\alpha w}} \tag{I.22}$$

To better grasp how light-trapping is a critical property, a second case ("2 paths" in Figure I.25)

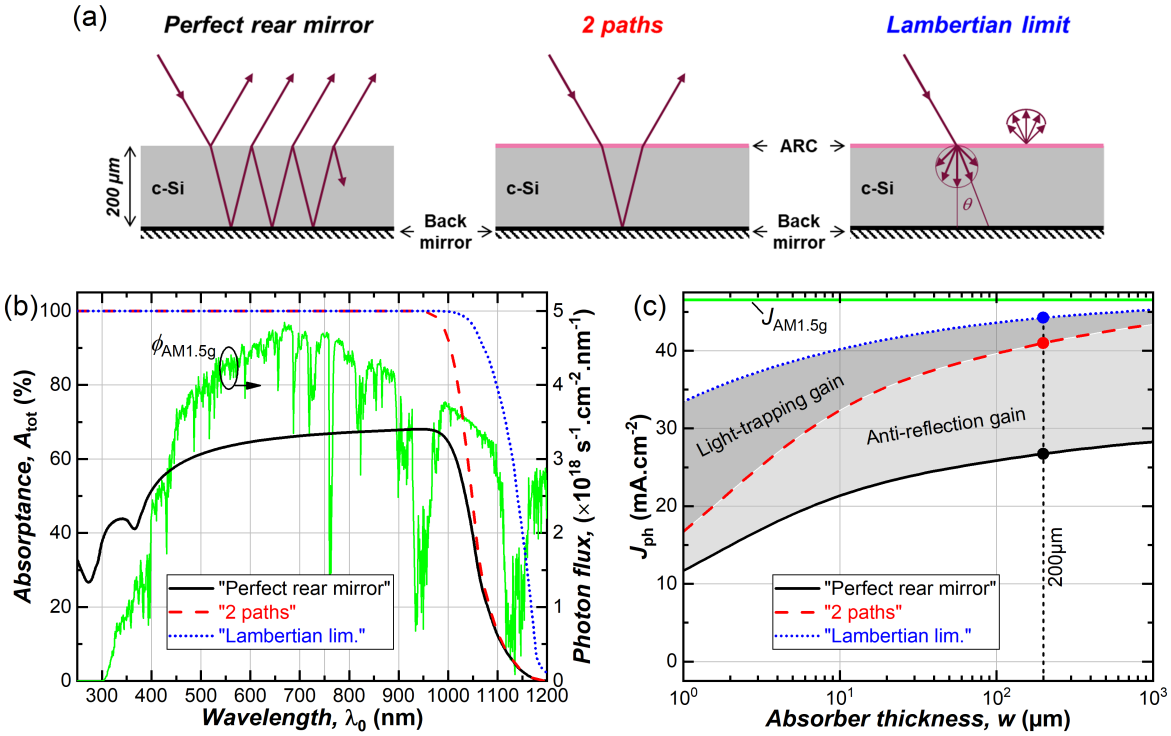

Fig. I.25: (a) Model light-trapping structures. (b) Corresponding theoretical absorptance (absorber thickness 200 µm) shown together with the AM1.5g spectral photon flux. (c) Theoretical photogenerated current density versus absorber thickness.

including a perfect rear mirror and a perfect ARC coating ($R_f = 0$ for all wavelengths) at the front surface is considered. Only escape reflectance remains, so that:

$$A_{tot} = 1 - e^{-2\alpha w} \tag{I.23}$$

Figure I.25 also shows the "Lambertian limit" case. It has first been established by Yablonovitch [116] in the limit of weak absorption and then extended to absorbing media by Green [117]. The best light-trapping efficiency (achievable with the scattering phenomenon) is obtained when the surface acts as a Lambertian scatterer, i.e. light is equally diffused in all directions. Following the computation from [118], for a system with a Lambertian front surface with perfect ARC and perfect back mirror, absorptance is expressed by:

$$A_{tot} = 1 - \left(1 + \frac{n^2(1 - T_r^2)}{T_r^2}\right)^{-1} \tag{I.24}$$

where T_r is the transmission coefficient for an "average ray" after complete randomization through the Lambertian scatterer:

$$T_r(w) = 2\int_0^{\pi/2} \cos\theta e^{-\alpha w/\cos\theta} \sin\theta d\theta \tag{I.25}$$

Notice that all the above computations on light trapping neglect any potential interference phenomena. In all the considered cases, the absorptance spectra are shown in Figure I.25(b) for a 200 µm thick absorber. Comparing the "Perfect rear mirror" and the "2 paths" cases, one can observe the gain from a perfect front ARC for wavelengths below 1000 nm, where the flat air/c-Si interface induces strong reflection in the "Perfect rear mirror" case. In the two cases, the absorptance curves rapidly join above 1000 nm where the losses are mostly due to weak absorptance. The "Lambertian limit" case gives an idea of the possible gain when scattering leads to randomization of light and drastically increases the distance traveled by light in the device: at 1100 nm, absorptance can be improved by a factor 8. Although the Lambertian limit is theoretical it may

be approached, as shown for thin (20 µm) c-Si absorbers using a b-Si front surface and a pyramid textured back side with a Bragg reflector [119].

To quantify the absorption in these systems in a global (relevant for c-Si solar cells) manner, let us compute the photogenerated current density for a given absorber thickness $J_{\mathrm{ph}}(w)$ (similarly to the approach proposed by Schuster *et al.* [118] and neglecting parasitic absorption):

$$J_{\mathrm{ph}}(w) = e \int_{250\ \mathrm{nm}}^{1200\ \mathrm{nm}} A_{\mathrm{tot}}(w,\lambda)\phi_{\mathrm{AM1.5g}}(\lambda)\lambda \mathrm{d}\lambda \tag{I.26}$$

where $\phi_{\mathrm{AM1.5g}}$ is the global solar spectral photon flux and e the electron charge. If all photons were absorbed in the [250,1200 nm] range, the photogenerated current would amount to around $J_{\mathrm{AM1.5g}} = 46.5\,\mathrm{mA}\cdot\mathrm{cm}^{-2}$.

The importance of light-trapping surges when considering thinner absorbers as can be seen from the evolution of photogenerated current density with the absorber thickness in Figure I.25(c). Below 200 µm, potential losses in case of poor light-trapping become greater than than 20% and light-trapping becomes more crucial than anti-reflection for substrates thinner than around 10 µm, although the relevance of c-Si material as a very thin absorber becomes questionable.

I.2.2.c Angular acceptance

A last important bonus achievable using front surface nanotexturing is an enhanced angular acceptance. Indeed, nanotexturing can lead to a decrease of reflectance for a broad range of light incident angles, as it has been shown in [120] for bare b-Si. Moreover, nanotextured solar cells have been shown to be less reflective compared to solar cells with pyramid texturing up to very large incidence angles (> 70°) [121]. This property is particularly interesting since the wide majority of c-Si solar cells are currently installed on static structures (more than 85% in 2017 [2]), so that the angle of incidence of light varies with the Sun's path in the sky (variations during the day and with the seasons). Due to the increased angular acceptance alone, a $2\%_{\mathrm{rel}}$ potential increase in annual power output for fixed optimally tilted cells has been evaluated for installations at latitudes below 60° [121] – corresponding approximately to the latitude of the city of Saint Petersburg in Russia. However, a more recent experimental study has shown that the enhanced angular acceptance at cell level obtained through nanotexturing is almost fully lost at module level [122]. The authors explain that the difference in angular absorption between cells with different front surface textures occurs mainly at high angles of incidence. However, integration in a module leads to a maximal angle of incidence around 43° on the cell, due to the presence of the encapsulant and glass. Moreover, losses in angular absorption were actually dominated by the reflectance at glass/encapsulant interface. The omnidirectional absorptance in nanostructured solar cells may therefore not be beneficial for PV applications.

I.2.3 Implementation of b-Si in Solar Cells

I.2.3.a Challenges from electronic properties

Having introduced several advantageous optical properties of nanotextured silicon surfaces, we now have to discuss the challenges faced when implementing such surfaces in solar cells.

Surface passivation. It is here useful to clearly highlight that the word "passivation" holds two different meanings in this work, depending on the context. Regarding plasma etching, passivation is linked to the formation of an inhibitor layer on the surface of a material during specific processes. Passivation therefore means "inhibition of chemical reactions". In the context of semiconductor device physics, passivation is used in the sense of "inhibition of carrier recombination".

Photogenerated carriers (electrons and holes) in a PV device may recombine before being collected at contacts. Different mechanisms lead to recombination, and this phenomenon can take place in the bulk (due to defects, e.g. impurities) or near interfaces with other materials (for instance due to dangling bonds). The latter phenomenon may in particular become dominant if

the surface to volume ratio is high, and c-Si solar cells are here a perfect example: a typical cell is $15.6 \times 15.6\,\mathrm{cm}^2$ wide with an absorber thickness of only $200\,\mu\mathrm{m}$. Recombination near interfaces can be mitigated by surface passivation, through two methods: (i) chemical passivation, which consists in reducing the areal density of dangling bonds and active defects; (ii) field effect passivation, which consists in repelling one type of carriers from the surface to impede recombination. Passivation for c-Si solar cells has been studied previously at the LPICM [123], and more details can be found for instance in Aberle *et al.* [124].

The quality of passivation on a sample can be evaluated by the minority carrier lifetime τ_{eff}, i.e. the characteristic delay between free carrier generation and recombination, which can be measured and expressed in the following equation:

$$\tau_{\mathrm{eff}} = \left(\frac{1}{\tau_{\mathrm{bulk}}} - \frac{2S_{\mathrm{eff}}}{w} \right)^{-1} \tag{I.27}$$

where τ_{bulk} is the "bulk lifetime" which can be theoretically computed [125], w the absorber thickness, and S_{eff} the surface recombination velocity (SRV). Equation (I.27) thus clearly separates the contribution of the bulk and the surfaces to the recombination. S_{eff} can then be isolated and gives a quantitative evaluation of the surface passivation quality.

After nanotexturing of the c-Si surface, passivation becomes more challenging due to several factors. The first and most obvious influence of nanotexturing is the high increase of the surface area [126]. Due to the high aspect ratio of the nanostructures, the real area, A_{NS}, of the surface becomes much large than the projected area A_{proj}, i.e. the surface area enhancement factor $\Sigma_{\mathrm{NS}} = A_{\mathrm{NS}}/A_{\mathrm{proj}}$ becomes high. A simple computation can be made for considering close-packed identical cones (base diameter Λ, height H) on a surface and neglecting the area between the cones. If we define the aspect ratio as $AR = H/\Lambda$, $\Sigma_{\mathrm{NS}} = (1 + 4AR^2)^{1/2}$. In the limit of high aspect ratio, the area enhancement factor is twice the aspect ratio, and values of AR up to 10 are sometimes reported in the case of PV applications [51]. Independently from the surface passivation quality (i.e. if the local SRV, S_{local}, remains identical), an increased surface area will induce higher surface recombination densities:

$$S_{\mathrm{eff}} = \Sigma_{\mathrm{NS}} S_{\mathrm{local}} \tag{I.28}$$

A second issue related to high aspect ratio has also emerged experimentally: the presence of nanostructures makes the deposition of a passivation layer more challenging. Although conventional PECVD SiN_x coatings have proven to be effective (e.g. [127]), they are not always conformally deposited: voids between the c-Si surface and the layer are present and leave unpassivated areas [128]. Other passivation materials and deposition methods are therefore investigated for black silicon solar cells. Numerous laboratory studies are for instance focusing on the use of Al_2O_3 grown by Atomic Layer Deposition (ALD) [121, 129], which is also known to improve field-effect passivation on p-type c-Si due to the presence of negative fixed charges [130].

Other issues may also pile up due to the employed nanostructuring method. Focusing on the case of plasma texturing, ion bombardment generates defects in the uppermost atomic layers (and to depths of several nanometers for high ion energies [131]): recombination is therefore favored in this damaged region. In order to tackle this issue, damage removal etching (DRE) steps are often used in the case of plasma texturing. This step follows several objectives: (i) remove the uppermost layer of c-Si where the density of defects (in the case of RIE or PIII b-Si) may be high in order to avoid recombination on this location [132, 133]; (ii) reduce the area enhancement factor of the b-Si surface (as well as its aspect ratio) in order to improve the quality of the following surface passivation; (iii) and smooth the apexes of the nanostructures to diminish their doping level (see next paragraph). Damage free plasma texturing processes are tested as well to avoid the chemical etch step after texturing [134, 135].

Doping. We here consider solar cell architectures where the front (nanotextured) surface has to be strongly doped, for instance AlBSF (that require a front emitter, in contrast with IBC cells for

instance). The doping process is almost always carried out after b-Si formation, and so the doping level is strongly dependent on the surface nanostructure. In the case of dopant diffusion (dominant technique used for emitter formation), if the nanostructures have a characteristic size smaller than the diffusion length, a large "over doping" occurs at the summit of structures. Consequently, Auger recombination (a three-particle non-radiative recombination process) is favored due to the high carrier density and the nanostructures act as a "dead layer". Since high-energy photons (in the blue range) are absorbed very close to the surface of the absorber, the overdoping especially affects the "blue response" of the cell. Some studies have shown that a chemical etching after b-Si formation (similarly as a DRE) may mitigate this issue by smoothing the apexes of the nanostructures before diffusion [136, 137].

Another solution would be to perform the diffusion prior to texturing [138, 139] to obtain a more uniform doping level in the nanostructures. In Shen *et al.* [138], the blue response of the solar cells was indeed improved if the diffusion process was applied before texturing. The authors attributed this effect to the absence of a "dead layer" and reduced lateral electric fields. However, this approach requires a simultaneous optimization of the texturing and doping processes. As shown by Shen *et al.*, the morphology of the nanostructures (obtained by PIII with SF_6/O_2) depends on the surface doping level. As well, if the texturing process removes a large thickness of silicon the diffused layer may be totally removed.

Contact deposition. While surface passivation and (to a lesser extent) doping of nanotextured surfaces have drawn a lot of attention, investigations on the challenges of front contact opening and metal deposition onto such surfaces are rare. As a notable exception, the influence of the nanotexturing on the contact formation by screen-printing (the dominant technique for front-contacted b-Si cells reported in literature) has been investigated by Kafle *et al.* [140]. The authors have shown that the formation of the Ag crystallites was favored on the tip of the structures. Regardless of the nanostructure dimensions, the overall contact resistivity was kept approximately constant on the nanotextured and acidic textured surfaces.

I.2.3.b State of the art black silicon solar cells

Already in 1995 when the team of Jansen *et al.* first depicted their "black silicon method" the authors pointed out that such surfaces could be applied to "sunlight collectors" [59]. Since then, a lot of effort has been put into the development of nanotexturing methods to maximize light collection in silicon solar cells.

The record efficiency for black silicon solar cells are synthesized in Figure I.26, together with the overall records (data from NREL, [141]). In order to set the constraints for this literature review, we have focused on solar cells with the following properties: (i) they include a front nanotextured side (and therefore discarded studies on rear surface texturing – used for light-trapping); (ii) they have thick absorbers (above approximately 50 µm: below this threshold silicon solar cells are usually called "ultra-thin" and other aspects such as the fabrication of such thin absorbers become important); (iii) they have been characterized under standard one-sun illumination (AM1.5g spectrum, without concentration). A more exhaustive account of solar cell results in the literature is available in Appendix B.

The cell types are separated in several categories: mono- or multicrystalline cells (respectively mono-Si and mc-Si in Figure I.26), and a subdivision for mono-Si cells is adopted whether the architecture includes a silicon heterojunction (SHJ). While 107 results for black silicon solar cells have been identified in literature, only independently certified cells are recognized as "historical records". Overall, around 50% of the reported results use direct MACE and almost 30% direct RIE texturing. Efficiency above 19% (on both mono-Si and mc-Si solar cells) has been shown only for these two techniques, and both current record efficiencies (for mono-Si and mc-Si cells including a b-Si front surface) involve nanotexturing by RIE. Table I.2 gives further details on the current record solar cells.

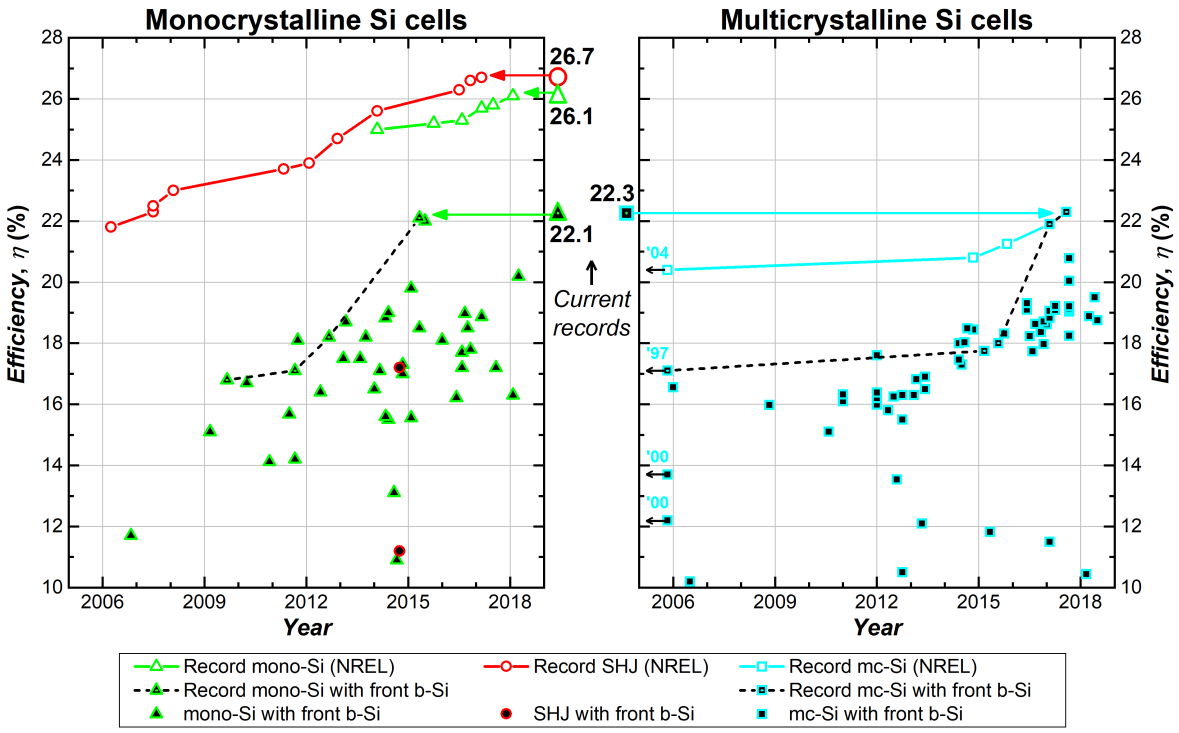

Fig. I.26: Chronology of record efficiencies and reported b-Si solar cells efficiencies for mono-Si (left) and mc-Si (right) cells.

Mono-crystalline silicon solar cells. From the values in Figure I.26, it is observed that black silicon has not proven able to achieve the highest conversion efficiency in monocrystalline solar cells for now, as only a few values higher than 20% have been shown. Moreover, the highest efficiency of 22.1% for monocrystalline b-Si solar cells is far from the overall records.

The current global record has been obtained in 2017 by Kaneka Corporation (Japan) [142, 145] with an interdigitated back-contacts silicon heterojunction (IBC-SHJ) cell at 26.7% efficiency. The front surface is therefore free of contacts and its surface is pyramid textured with an amorphous silicon passivation layer topped with an ARC. The short-circuit current is $42.65\,\mathrm{mA\cdot cm^{-2}}$, and an analysis of the experimental result (relatively to the theoretical limit of 29.1% assessed by Richter *et al.* [146]) has shown that optical losses only explain $0.1\%_{\mathrm{abs}}$ of the gap. The record for homojunction solar cells is held by the Institute for Solar Energy Research Hamelin (ISFH, Germany) since early 2018, with the efficiency of 26.1% and a short-circuit current density of $42.62\,\mathrm{mA\cdot cm^{-2}}$. Again, the front side is pyramid textured and the solar cell includes interdigitated back contacts (IBC) that reduce shading losses [143].

In contrast, the record for black silicon monocrystalline solar cells is held by a collaborative team from Aalto University (Finland) and Universitat Politècnica de Catalunya (Spain), reported in Savin *et al.* [121], also for an IBC architecture. The front surface has been textured using cryogenic ICP-RIE (substrate temperature of $-120\,^{\circ}\mathrm{C}$) with SF_6/O_2 plasma. No damage removal etching subsequent to texturing has been applied. The efficiency of the solar cell was certified at 22.1%, i.e. a similar efficiency (given the uncertainties) as the reference pyramid textured cell measured at 22.0% manufactured by the same team. The short-circuit current was only $0.2\,\mathrm{mA\cdot cm^{-2}}$ superior to the reference: the improvement in light management from nanotexturing is therefore very weak, and decreases in other sources of losses would be needed to close the large gap ($4\%_{\mathrm{abs}}$) between the record b-Si and the overall record IBC cell from ISFH.

These records show that conventional microtexturing by wet techniques with an additional ARC is therefore very effective in mitigating optical losses: for mono-Si solar cells, the interest for nanotexturing becomes debatable in terms of efficiency.

Tab. I.2: Detailed electrical properties of the current record efficiency c-Si solar cells. Uncertainties given when available.

	Cell type	Team	Area (cm^2)	V_{oc} (mV)	J_{sc} ($mA \cdot cm^{-2}$)	FF (%)	η (%)
mono-Si	n-type IBC-SHJ	Kaneka [142]	79	738	42.65	84.9	26.7 ± 0.5
	p-type IBC	ISFH [143]	4	726.6 ± 1.8	42.62 ± 0.40	84.28 ± 0.59	26.10 ± 0.31
	n-type IBC front b-Si	Aalto Univ. & Univ. Politècnica Catalunya [121]	9	677.8 ± 2.3	41.03 ± 0.78	79.48 ± 0.52	22.10 ± 0.44
mc-Si	n-type TOPcon	FhG-ISE [144]	4	674.2	41.08	80.5	22.3 ± 0.4

Multi-crystalline silicon solar cells. The situation for multicrystalline solar cells is quite different and more encouraging for black silicon solar cells. As it can be observed in the right graph in Figure I.26, most black silicon multicrystalline solar cells reported in literature have efficiency below 20%. However, the latest records obtained by the Fraunhofer Institut für Solare Energiesysteme (FhG-ISE, Germany) altered the perspective. Indeed, their most recent records (21.9% and 22.3% efficiency [144, 147]) have been obtained using front surface nanotexturing by ICP-RIE with a SF_6/O_2 plasma. Similarly as for the record cell by Savin *et al.* no subsequent damage removal etching was required as the ion bombardment energy was kept low. The main difference from previous b-Si mc-Si cell actually comes from the "high-performance" mc-Si wafer and the TOPcon approach for rear contacts (crudely speaking, it consists of an advanced surface passivation method).

The fact that the record efficiency for mc-Si solar cells has been obtained using nanotexturing is actually not entirely surprising. As it has been pointed out previously, conventional isotropic (wet) texturing techniques for mc-Si are not quite as effective as alkaline texturing on monocrystalline wafers.

The emergence of diamond wire sawing (DWS) has made texturing even more challenging for mc-Si wafers. In a few words, this technique employs metallic wires coated with diamond particles to cut the wafers, in contrast to slurry wire sawing, where the metallic wires are continuously dipped in a solution containing abrasive particles (e.g. diamond or SiC particles). DWS is gradually replacing SWS as the dominant cutting method for solar-grade silicon wafers, as shown by the ITRPV [2], due to drastic reductions in material losses. In 2017, the market of mono-Si wafers was already dominated by DWS, while for mc-Si, it represented about 30% of the market, but this share is expected to grow rapidly in the next years (exceeding 90% by 2022). However, the surface finish obtained by both techniques is very different. SWS leads to a very rough surface with a relatively thick damaged layer comprising a high density of cracks. In contrast, DWS c-Si wafers show smooth parallel grooves and partial amorphization, with a thinner damaged layer. All these factors are believed to be responsible for a much less effective acidic texturing on DWS mc-Si wafers [148] and the need for alternatives pushes investigations on nanotexturing techniques. As a consequence, MACE and RIE texturing are expected to gradually replace acidic texturing for solar cells in the next years [2].

I.2.4 Characterization Methods

I.2.4.a Spectrophotometry

Total hemispherical reflectance as well as absorptance has been measured for wavelengths λ_0 between 250 and 1250 nm, with a PerkinElmer Lambda 950 spectrophotometer equipped with a 150 mm integrating sphere, as depicted in Figure I.27. Reflectance is measured at near-normal

incidence: an angle of 8° is necessary to avoid specular reflected light to escape the integrating sphere. Absorptance has been measured by placing the sample inside the integrating sphere with a variable angle center-mount sample holder. Two types of light sources as well as two different detectors in the integrating sphere allow measurements for wavelengths from 200 to 2500 nm.

In order to quantitatively compare the reflectance of the samples, the effective reflectance, R_{eff}, is computed, Equation (I.29), by integrating the reflectance spectrum $R(\lambda_0)$ and weighting it by the AM1.5g solar spectral photon flux $\phi_{\text{AM1.5g}}$ according to the ASTM G173-03(2012) standard [3]:

$$R_{\text{eff}} = \frac{\int_{280\text{ nm}}^{1000\text{ nm}} R(\lambda)\phi_{\text{AM1.5g}}(\lambda)\mathrm{d}\lambda}{\int_{280\text{ nm}}^{1000\text{ nm}} \phi_{\text{AM1.5g}}(\lambda)\mathrm{d}\lambda} \tag{I.29}$$

The upper limit at 1000 nm is chosen to cut off the escape reflectance contribution in the region where silicon is partially transparent. Beyond this wavelength, multiple reflections can occur inside the material: thus, $R_{\text{eff}}$is representative of the external reflectance at the top surface and decorrelated from light-trapping. The measurement uncertainty is mainly attributed to the quality of the reference used for calibration of the instrument, so that relative comparisons of $R(\lambda_0)$ or $A(\lambda_0)$ between samples measured in a row are deemed valid down to differences of 0.2% absolute. In contrast, the uncertainty on absolute values of reflectance at a given wavelength is estimated at 1% absolute in the full measurement range (data from the tool manufacturer), so that the same uncertainty is evaluated for averaged values (like R_{eff}).

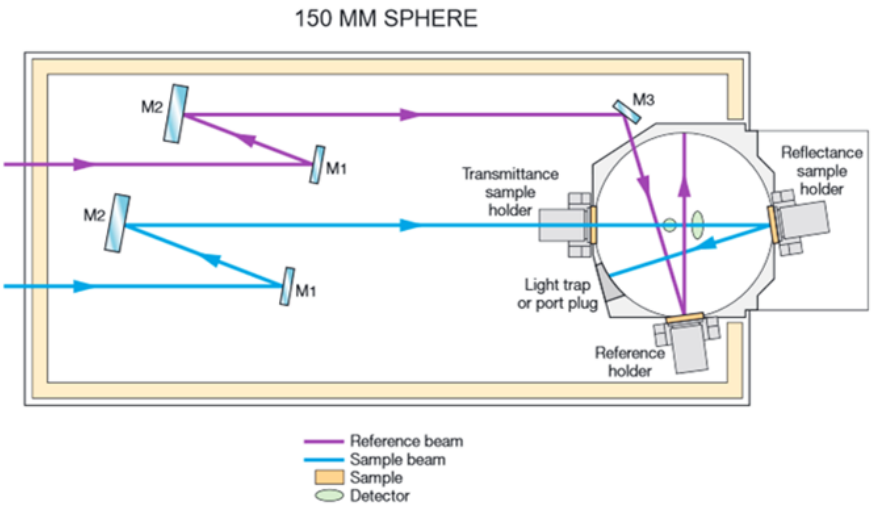

Fig. I.27: Schematic of the spectrophotometer with the 150 mm integrating sphere. Extracted from the website of the manufacturer.

I.2.4.b Scanning Electron Microscopy

A Hitachi S-4800 scanning electron microscope has been used to characterize the surface morphology of initial and nanotextured silicon samples. While the technique gives qualitative characterizations of surface nanostructures (shape, apparent size), it is useful to highlight how SEM images can be used to extract quantitative information on pseudo-random nanostructured surfaces.

Cross-section view SEM images. To obtain an estimate of the nanostructure height, cross-section views have been used: in this case the height of several tens of features is manually measured in order to obtain a statistically representative average. An example of such an image is shown in Figure I.28(a).

Top view SEM images. Grayscale top-view SEM images can provide estimates of the nanostructure lateral dimensions. In particular, it can be seen in Figure I.28(b) that the nanostructures are closely packed on the surface. The characteristic distance between nanostructures has been determined from the normalized and circularly averaged radial autocorrelation function (ACF_r) [149] computed from the grayscale SEM images:

$$ACF_r(r) = \frac{1}{2\pi}\int_0^{2\pi}\iint f(x,y)\, f\left(x + r\cos\varphi, y + r\sin\varphi\right) \mathrm{d}x\mathrm{d}y\mathrm{d}\varphi \tag{I.30}$$

where f is the grayscale image and (x,y) (respectively (r,φ)) designate the Cartesian (respectively polar) coordinates of the pixels. A typical example is shown in Figure I.28(c) as a function of the radius r. The estimated pseudo-period Λ_{NS} corresponds to twice the value of the first local minimum of the autocorrelation function as seen in the example of Figure I.28(c). Λ_{NS} is here numerically determined by fitting the ACF in the region near the minimum to a cubic polynomial in order to reduce the contribution of noise. Furthermore, it should be noted that SEM images show a distribution of structure sizes on the surface, and therefore the pseudo-period Λ_{NS} only represents an average nanostructure width.

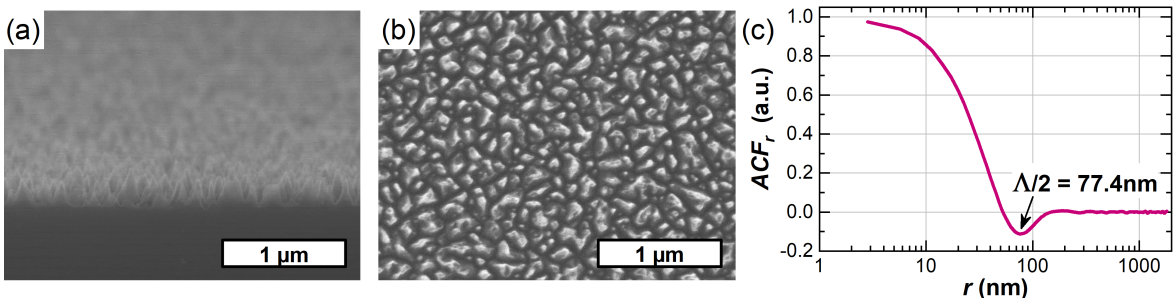

Fig. I.28: SEM images of an RIE textured sample: (a) cross-section view (b) top view, and (c) circularly averaged autocorrelation function obtained from image (b).

I.2.4.c Stylus profilometry

In order to assess the etched depth or the etching rate for a given etching process, stylus profilometry has been carried out using a Dektak XT system. To this aim, part of the considered sample is masked during the etching, so that a step is created between the etched area and the pristine part, as schematically depicted in Figure I.29. Several profiles are measured at different locations perpendicularly to the step edge. The profile is leveled assuming a horizontal pristine area, and the difference in average height in the pristine and etched area is measured, Figure I.29.

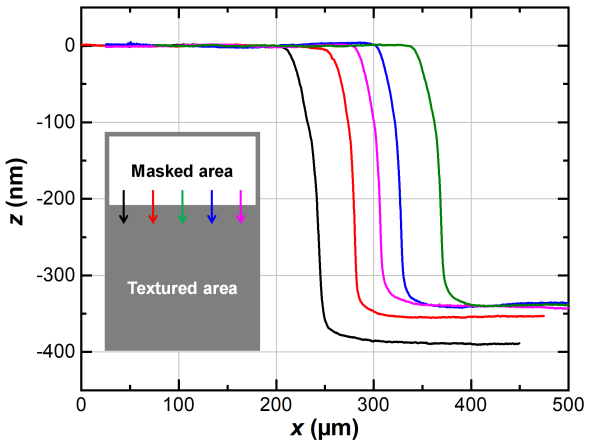

Fig. I.29: Example of five step profiles obtained on a textured sample with a masked area (schematic in inset) used to compute the etched thickness.

I.2.4.d Photoconductance decay

The quality of surface passivation has been investigated using "photoconductance decay" which measures the effective lifetime of minority carriers, τ_{eff}: the carriers are created by illumination and an inductive coil present below the sample monitors the time-variation of the conductance. This technique has been carried out using a Sinton WCT-120 system. The surface recombination velocity S_{eff} can then be computed. As customarily done in literature, both the effective lifetime and surface recombination velocity are evaluated at an injection level of 10^{15} cm^{-3}.

In the present work, asymmetric passivated samples have been used: only the front surface was textured while the back surface was not. In this case, it is not possible to isolate the different contributions from the front and rear surfaces by a single PCD measurement. Therefore, reference un-etched samples were also passivated (with the same recipe and sometimes in the same batch). The effective surface recombination velocity (SRV) of the reference samples $S_{\text{eff}}^{\text{ref}}$ was measured separately, and the front SRV, S_{f}, of textured samples was evaluated by:

$$S_{\text{f}} = \left(\frac{1}{\tau_{\text{eff}}} - \frac{1}{\tau_{\text{bulk}}} \right) w - S_{\text{eff}}^{\text{ref}} \tag{I.31}$$

where τ_{bulk} is the bulk recombination velocity computed theoretically [125] and $S_{\text{eff}}^{\text{ref}}$ is the contribution of the back surface, assumed identical to the reference samples.

Conclusion

A review of the state of the art in two fields has been carried out in this chapter. First on the current knowledge on plasma processes development for silicon etching. Some basics of capacitively coupled radio-frequency discharges have been recalled, as well as the possibility for an extended playground offered by Tailored Voltage Waveforms. The tools used in the present work to perform and monitor plasma processes have been introduced. The physicochemical mechanisms involved in plasma-surface interaction applied to silicon etching have been exposed, with an emphasis on SF_6/O_2 plasma as an important example of ion-enhanced inhibitor etching.

Secondly, nanotexturing of silicon surfaces has been detailed. Initially stimulated by research in microelectronics, SF_6/O_2 plasma texturing of silicon by reactive ion etching has then extended to photovoltaics. Nanotexturing of silicon surfaces indeed leads to remarkable anti-reflection and light-trapping properties, as illustrated by the adoption of the term "black silicon" to describe such surfaces. These properties are obviously attractive in the field of photovoltaics to improve light management in silicon-based devices. Competing "black silicon" methods (either based on wet or dry processes) have been introduced, as well as the current efficiency records at cell level. Finally, methods to characterize the optical and electrical properties of textured surfaces have been recalled.

As a conclusion, and from a pragmatic approach, continued investigations on light management in silicon solar cells are required due to both technological and economic evolutions of the market. First, improvements or breakthroughs in optical management can make new processes economically viable or competitive, because they will ultimately lead to a decrease of the dollar per watt-peak cost of solar systems. Second, other shifts of the market may indirectly free an evolution of the technology. Room for improvement is very limited in the case of monocrystalline silicon solar cells as optical losses have almost been entirely eliminated using existing "conventional" techniques (microstructuring associated with anti-reflection coatings). On the other hand, the latest record efficiencies in multi-crystalline solar cells have been obtained using RIE etching, and the current shift in sawing technologies has made nanotexturing even more attractive for industrials.

Bibliography (Chapter I)

[1] J. Nelson, The physics of solar cells, Imperial College Press, London, reprinted ed., **2010**, ISBN 978-1-86094-349-2. 15

[2] International Technology Roadmap for Photovoltaic Ninth Edition, March 2018, Tech. Rep. 9, ITRPV, **2018**, URL www.itrpv.net. 15, 39, 43, 46, 48, 52

[3] ASTM G173 - 03(2012), Standard Tables for Reference Solar Spectral Irradiances: Direct Normal and Hemispherical on 37° Tilted Surface, URL www.astm.org/Standards/G173.htm. 15, 53

[4] Plasma Processing of Materials: Scientific Opportunities and Technological Challenges, National Academies Press, Washington, D.C., **1991**, doi:10.17226/1875. 16

[5] I. Langmuir, Oscillations in Ionized Gases, *PNAS* **1928**, 14(8), 627–637, doi:10.1073/pnas.14.8.627. 16

[6] M. A. Lieberman and A. J. Lichtenberg, Principles of plasma discharges and materials processing, Wiley-Interscience, Hoboken, NJ, 2. ed ed., **2005**, ISBN 978-0-471-72001-0. 16, 31, 33

[7] P. Chabert and N. S. J. Braithwaite, Physics of radio-frequency plasmas, Cambridge Univ. Press, Cambridge, **2011**, ISBN 978-0-521-76300-4. 16, 20

[8] Radio Regulations Articles, Edition of 2016, Tech. rep., International Telecommunications Union, URL itu.tind.io/record/25397?ln=en. 17

[9] J. Schulze, E. Schüngel, Z. Donkó and U. Czarnetzki, The electrical asymmetry effect in multi-frequency capacitively coupled radio frequency discharges, *Plasma Sources Sci. Technol.* **2011**, 20(1), 015017, doi:10.1088/0963-0252/20/1/015017. 18, 19

[10] J. Schulze, A. Derzsi, K. Dittmann, T. Hemke, J. Meichsner and Z. Donkó, Ionization by Drift and Ambipolar Electric Fields in Electronegative Capacitive Radio Frequency Plasmas, *Phys. Rev. Lett.* **2011**, 107(27), 275001, doi:10.1103/PhysRevLett.107.275001. 20

[11] E. Kawamura, V. Vahedi, M. A. Lieberman and C. K. Birdsall, Ion energy distributions in rf sheaths; review, analysis and simulation, *Plasma Sources Sci. Technol.* **1999**, 8(3), R45, doi:10.1088/0963-0252/8/3/202. 20

[12] B. Bruneau, J. Wang, J.-C. Dornstetter and E. V. Johnson, Growth mechanisms study of microcrystalline silicon deposited by SiH4/H2 plasma using tailored voltage waveforms, *J. Appl. Phys.* **2014**, 115(8), 084901, doi:10.1063/1.4866693. 20, 26

[13] P. Benoit-Cattin and L.-C. Bernard, Anomalies of the Energy of Positive Ions Extracted from High-Frequency Ion Sources. A Theoretical Study, *J. Appl. Phys.* **1968**, 39(12), 5723–5726, doi:10.1063/1.1656039. 21

[14] A. D. Kuypers and H. J. Hopman, Measurement of ion energy distributions at the powered rf electrode in a variable magnetic field, *J. Appl. Phys.* **1990**, 67(3), 1229–1240, doi:10.1063/1.345721. 21

[15] C. Wild and P. Koidl, Ion and electron dynamics in the sheath of radio-frequency glow discharges, *J. Appl. Phys.* **1991**, 69(5), 2909–2922, doi:10.1063/1.348601. 21

[16] A. Perret, P. Chabert, J. Jolly and J.-P. Booth, Ion energy uniformity in high-frequency capacitive discharges, *Appl. Phys. Lett.* **2005**, 86(2), 021501, doi:10.1063/1.1848183. 22

[17] B. G. Heil, U. Czarnetzki, R. P. Brinkmann and T. Mussenbrock, On the possibility of making a geometrically symmetric RF-CCP discharge electrically asymmetric, *J. Phys. D: Appl. Phys.* **2008**, 41(16), 165202, doi:10.1088/0022-3727/41/16/165202. 22, 23, 24

[18] B. Bruneau, Control of radio frequency capacitively coupled plasma asymmetries using Tailored Voltage Waveforms, Ph.D. thesis, Ecole polytechnique, **2015**, URL tel.archives-ouvertes.fr/tel-01247986v1. 22, 25, 26

[19] B. Bruneau, T. Novikova, T. Lafleur, J. P. Booth and E. V. Johnson, Ion flux asymmetry in radiofrequency capacitively-coupled plasmas excited by sawtooth-like waveforms, *Plasma Sources Sci. Technol.* **2014**, 23(6), 065010, doi:10.1088/0963-0252/23/6/065010. 22

[20] J. Schulze, E. Schüngel and U. Czarnetzki, The electrical asymmetry effect in capacitively coupled radio frequency discharges – measurements of dc self bias, ion energy and ion flux, *J. Phys. D Appl. Phys.* **2009**, 42(9), 092005, doi:10.1088/0022-3727/42/9/092005. 24

[21] J. Schulze, A. Derzsi and Z. Donkó, Electron heating and the electrical asymmetry effect in dual-frequency capacitive CF 4 discharges, *Plasma Sources Sci. Technol.* **2011**, 20(4), 045008, doi:10.1088/0963-0252/20/4/045008. 24

[22] A. Derzsi, T. Lafleur, J.-P. Booth, I. Korolov and Z. Donkó, Experimental and simulation study of a capacitively coupled oxygen discharge driven by tailored voltage waveforms, *Plasma Sources Sci. Technol.* **2016**, 25(1), 015004, doi:10.1088/0963-0252/25/1/015004. 24

[23] B. Bruneau *et al.*, Effect of gas properties on the dynamics of the electrical slope asymmetry effect in capacitive plasmas: comparison of Ar, H_2 and CF_4, *Plasma Sources Sci. Technol.* **2016**, 25(1), 01LT02, doi:10.1088/0963-0252/25/1/01LT02. 25, 26

[24] E. V. Johnson, T. Verbeke, J.-C. Vanel and J.-P. Booth, Nanocrystalline silicon film growth morphology control through RF waveform tailoring, *J. Phys. D: Appl. Phys.* **2010**, 43(41), 412001,

doi:10.1088/0022-3727/43/41/412001. 26

[25] E. Johnson, S. Pouliquen, P. Delattre and J. Booth, Hydrogenated microcrystalline silicon thin films deposited by RF-PECVD under low ion bombardment energy using voltage waveform tailoring, *Journal of Non-Crystalline Solids* **2012**, 358(17), 1974–1977, doi:10.1016/j.jnoncrysol.2012.01.014. 26

[26] B. Bruneau, R. Cariou, J. C. Dornstetter, M. Lepecq, J. L. Maurice, P. R. i. Cabarrocas and E. V. Johnson, Ion Energy Threshold in Low-Temperature Silicon Epitaxy for Thin-Film Crystalline Photovoltaics, *IEEE J. Photovolt.* **2014**, 4(6), 1361–1367, doi:10.1109/JPHOTOV.2014.2357256. 26

[27] J. Wang, C. Longeaud, F. Ventosinos, D. Daineka, M. E. Yaakoubi and E. V. Johnson, Deposition of a-Si:H thin films using tailored voltage waveform plasmas: impact on microstructure and stability, *Phys. Status Solidi C* **2016**, 13(10-12), 735–739, doi:10.1002/pssc.201600024. 26

[28] J. K. Wang and E. V. Johnson, Electrode-selective deposition/etching processes using an SiF4/H2/Ar plasma chemistry excited by sawtooth tailored voltage waveforms, *Plasma Sources Sci. Technol.* **2017**, 26(1), 01LT01, doi:10.1088/0963-0252/26/1/01LT01. 26

[29] F. Schmidt *et al.*, Multi frequency matching for voltage waveform tailoring, *Plasma Sources Sci. Technol.* **2018**, doi:10.1088/1361-6595/aad2cd. 27

[30] S. Brandt *et al.*, Electron power absorption dynamics in capacitive radio frequency discharges driven by tailored voltage waveforms in CF_4, *Plasma Sources Sci. Technol.* **2016**, 25(4), 045015, doi:10.1088/0963-0252/25/4/045015. 27

[31] A. Derzsi *et al.*, Power coupling mode transitions induced by tailored voltage waveforms in capacitive oxygen discharges, *Plasma Sources Sci. Technol.* **2017**, 26(3), 034002, doi:10.1088/1361-6595/aa56d6. 27

[32] T. Lafleur, P. A. Delattre, J. P. Booth, E. V. Johnson and S. Dine, Radio frequency current-voltage probe for impedance and power measurements in multi-frequency unmatched loads, *Rev. Sci. Instr.* **2013**, 84(1), 015001, doi:10.1063/1.4773540. 29

[33] D. Gahan, B. Dolinaj and M. B. Hopkins, Retarding field analyzer for ion energy distribution measurements at a radio-frequency biased electrode, *Rev. Sci. Instr.* **2008**, 79(3), 033502, doi:10.1063/1.2890100. 29

[34] A. Savitzky and M. J. E. Golay, Smoothing and Differentiation of Data by Simplified Least Squares Procedures., *Analyt. Chem.* **1964**, 36(8), 1627–1639, doi:10.1021/ac60214a047. 30

[35] S. R. Taylor, Abundance of chemical elements in the continental crust: a new table, *Geochimica et Cosmochimica Acta* **1964**, 28(8), 1273–1285, doi:10.1016/0016-7037(64)90129-2. 30

[36] M. A. Blauw, T. Zijlstra, R. A. Bakker and E. van der Drift, Kinetics and crystal orientation dependence in high aspect ratio silicon dry etching, *J. Vac. Sci. Technol. B* **2000**, 18(6), 3453, doi:10.1116/1.1313578. 31

[37] J. W. Coburn and H. F. Winters, Ion- and electron-assisted gas-surface chemistry—An important effect in plasma etching, *J. Appl. Phys.* **1979**, 50(5), 3189, doi:10.1063/1.326355. 31, 33

[38] R. Dussart, T. Tillocher, P. Lefaucheux and M. Boufnichel, Plasma cryogenic etching of silicon: from the early days to today's advanced technologies, *J. Phys. D Appl. Phys.* **2014**, 47(12), 123001, doi:10.1088/0022-3727/47/12/123001. 32, 34, 36

[39] H. F. Winters, J. W. Coburn and T. J. Chuang, Surface processes in plasma-assisted etching environments, *J. Vac. Sci. Technol. B* **1983**, 1(2), 469–480, doi:10.1116/1.582629. 32

[40] D. L. Flamm and V. M. Donnelly, The design of plasma etchants, *Plasma Chem. Plasma Process* **1981**, 1(4), 317–363, doi:10.1007/BF00565992. 32

[41] B. Petit and J. Pelletier, Mécanismes d'anisotropie dans la gravure du silicium en plasma SF6. Modèle de gravure, *Rev. Phys. Appl. (Paris)* **1986**, 21(6), 377–399, doi:10.1051/rphysap:01986002106037700. 32

[42] V. M. Donnelly, Review Article: Reactions of fluorine atoms with silicon, revisited, again, *J. Vac. Sci. Technol. A* **2017**, 35(5), 05C202, doi:10.1116/1.4983922. 32

[43] H. F. Winters and J. W. Coburn, Surface science aspects of etching reactions, *Surf. Sci. Rep.* **1992**, 14(4), 162–269, doi:10.1016/0167-5729(92)90009-Z. 32, 33

[44] H. F. Winters, D. B. Graves, D. Humbird and S. Tougaard, Penetration of fluorine into the silicon lattice during exposure to F atoms, F2, and XeF2: Implications for spontaneous etching reactions, *J. Vac. Sci. Technol. A* **2007**, 25(1), 96–103, doi:10.1116/1.2400680. 32

[45] H. F. Winters and D. Haarer, Influence of doping on the etching of Si(111), *Phys. Rev. B* **1987**, 36(12), 6613–6623, doi:10.1103/PhysRevB.36.6613. 33

[46] Y.-Y. Tu, T. J. Chuang and H. F. Winters, Chemical sputtering of fluorinated silicon, *Phys. Rev. B* **1981**, 23(2), 823–835, doi:10.1103/PhysRevB.23.823. 33

[47] C. Steinbrüchel, Universal energy dependence of physical and ion-enhanced chemical etch yields at low ion energy, *Appl. Phys. Lett.* **1989**, 55(19), 1960, doi:10.1063/1.102336. 33, 34

[48] H. Jansen, H. Gardeniers, M. d. Boer, M. Elwenspoek and J. Fluitman, A survey on the reactive ion etching of silicon in microtechnology, *J. Micromech. Microeng.* **1996**, 6(1), 14–28, doi:10.1088/0960-1317/6/1/002. 34, 36

[49] S. Gomez, R. Jun Belen, M. Kiehlbauch and E. S. Aydil, Etching of high aspect ratio structures in Si using SF6/O2

plasma, *J. Vac. Sci. Technol. A* **2004**, 22(3), 606, doi:10.1116/1.1710493. 34

[50] R. d'Agostino and D. L. Flamm, Plasma etching of Si and SiO2 in SF6–O2 mixtures, *J. Appl. Phys.* **1981**, 52(1), 162, doi:10.1063/1.328468. 34

[51] X. Liu, P. R. Coxon, M. Peters, B. Hoex, J. M. Cole and D. J. Fray, Black silicon: fabrication methods, properties and solar energy applications, *Energy Environ. Sci.* **2014**, 7(10), 3223–3263, doi:10.1039/C4EE01152J. 35, 49

[52] V. Schmidt, J. V. Wittemann, S. Senz and U. Gösele, Silicon Nanowires: A Review on Aspects of their Growth and their Electrical Properties, *Adv. Mater.* **2009**, 21(25-26), 2681–2702, doi:10.1002/adma.200803754. 35

[53] S. Misra, L. Yu, W. Chen, M. Foldyna and P. R. i. Cabarrocas, A review on plasma-assisted VLS synthesis of silicon nanowires and radial junction solar cells, *J. Phys. D: Appl. Phys.* **2014**, 47(39), 393001, doi:10.1088/0022-3727/47/39/393001. 35

[54] M. Otto *et al.*, Black Silicon Photovoltaics, *Adv. Opt. Mater.* **2015**, 3(2), 147–164, doi:10.1002/adom.201400395. 35

[55] G. C. Schwartz and P. M. Schaible, Reactive ion etching of silicon, *J. Vac. Sci. Technol.* **1979**, 16(2), 410–413, doi:10.1116/1.569962. 36

[56] T. P. Chow, P. A. Maciel and G. M. Fanelli, Reactive Ion Etching of Silicon in CCl4 and HCl Plasmas, *J. Electrochem. Soc.* **1987**, 134(5), 1281–1286, doi:10.1149/1.2100658. 36

[57] G. S. Oehrlein, R. G. Schad and M. A. Jaso, Mechanism of silicon surface roughening by reactive ion etching, *Surf. Interface Anal.* **1986**, 8(6), 243–246, doi:10.1002/sia.740080604. 36

[58] G. S. Oehrlein, Study of sidewall passivation and microscopic silicon roughness phenomena in chlorine-based reactive ion etching of silicon trenches, *J. Vac. Sci. Technol. B* **1990**, 8(6), 1199, doi:10.1116/1.584896. 36

[59] H. Jansen, M. d. Boer, R. Legtenberg and M. Elwenspoek, The black silicon method: a universal method for determining the parameter setting of a fluorine-based reactive ion etcher in deep silicon trench etching with profile control, *J. Micromech. Microeng.* **1995**, 5(2), 115–120, doi:10.1088/0960-1317/5/2/015. 36, 50

[60] R. Legtenberg, H. Jansen, M. de Boer and M. Elwenspoek, Anisotropic Reactive Ion Etching of Silicon Using SF6/O2/CHF3 Gas Mixtures, *J. Electrochem. Soc.* **1995**, 142(6), 2020, doi:10.1149/1.2044234.

[61] H. Jansen, M. de Boer, B. Otter and M. Elwenspoek, The black silicon method. IV. The fabrication of three-dimensional structures in silicon with high apect ratios for scanning probe microscopy and other applications, IEEE, ISBN 978-0-7803-2503-6, **1995** 88, doi:10.1109/MEMSYS.1995.472548.

[62] M. de Boer, H. Jansen and M. Elwenspoek, The Black Silicon Method V: A Study Of The Fabricating Of Movable Structures For Micro Electromechanical Systems, vol. 1, IEEE, **1995** 565–568, doi:10.1109/SENSOR.1995.717287.

[63] H. Jansen, M. de Boer and M. Elwenspoek, The black silicon method. VI. High aspect ratio trench etching for MEMS applications, IEEE, ISBN 978-0-7803-2985-0, **1996** 250–257, doi:10.1109/MEMSYS.1996.493989.

[64] H. Jansen, M. de Boer, R. Wiegerink, N. Tas, E. Smulders, C. Neagu and M. Elwenspoek, RIE lag in high aspect ratio trench etching of silicon, *Microelectro. Eng.* **1997**, 35(1-4), 45–50, doi:10.1016/S0167-9317(96)00142-6.

[65] H. Jansen, M. de Boer, H. Wensink, B. Kloeck and M. Elwenspoek, The black silicon method. VIII. A study of the performance of etching silicon using SF6/O2-based chemistry with cryogenical wafer cooling and a high density ICP source, *Microelectron. J.* **2001**, 32(9), 769–777, doi:10.1016/S0026-2692(01)00039-8. 37

[66] M. de Boer *et al.*, Guidelines for etching silicon MEMS structures using fluorine high-density plasmas at cryogenic temperatures, *J. Microelectrochem. Sys.* **2002**, 11(4), 385–401, doi:10.1109/JMEMS.2002.800928.

[67] H. V. Jansen, M. J. de Boer, S. Unnikrishnan, M. C. Louwerse and M. C. Elwenspoek, Black silicon method: X. A review on high speed and selective plasma etching of silicon with profile control: an in-depth comparison between Bosch and cryostat DRIE processes as a roadmap to next generation equipment, *J. Micromech. Microeng.* **2009**, 19(3), 033001, doi:10.1088/0960-1317/19/3/033001. 36, 38

[68] J. Yoo *et al.*, RIE texturing optimization for thin c-Si solar cells in SF_6 /O_2 plasma, *J. Phys. D Appl. Phys.* **2008**, 41(12), 125205, doi:10.1088/0022-3727/41/12/125205. 36, 38

[69] M. Schnell, R. Ludemann and S. Schaefer, Plasma surface texturization for multicrystalline silicon solar cells, IEEE, ISBN 0-7803-5772-8, **2000** 367–370, doi:10.1109/PVSC.2000.915841. 36

[70] D. Abi Saab, P. Basset, M. J. Pierotti, M. L. Trawick and D. E. Angelescu, Static and Dynamic Aspects of Black Silicon Formation, *Physical Review Letters* **2014**, 113(26), doi:10.1103/PhysRevLett.113.265502. 37

[71] T. Tillocher *et al.*, Oxidation threshold in silicon etching at cryogenic temperatures, *J. Vac. Sci. Technol. A* **2006**, 24(4), 1073–1082, doi:10.1116/1.2210946. 37

[72] R. Dussart *et al.*, Silicon columnar microstructures induced by an SF_6 /O_2 plasma, *J. Phys. D Appl. Phys.* **2005**, 38(18), 3395–3402, doi:10.1088/0022-3727/38/18/012. 37

[73] M. Gaudig, J. Hirsch, T. Schneider, A. N. Sprafke, J. Ziegler, N. Bernhard and R. B. Wehrspohn, Properties of black silicon obtained at room-temperature by different plasma modes, *J. Vac. Sci. Technol. A* **2015**, 33(5), 05E132, doi:10.1116/1.4929540. 37

[74] D. Murias *et al.*, Black Silicon formation using dry etching for solar cells applications, *Mater. Sci. Eng. B* **2012**, 177(16), 1509–1513, doi:10.1016/j.mseb.2012.03.038. 37

[75] M. Kroll *et al.*, Optical modeling of needle like silicon surfaces produced by an ICP-RIE process, vol. 7725, **2010**

772505–772505–10, doi:10.1117/12.854596. 38, 45

[76] J. Hirsch, M. Gaudig, N. Bernhard and D. Lausch, Optoelectronic properties of Black-Silicon generated through inductively coupled plasma (ICP) processing for crystalline silicon solar cells, *Appl. Surf. Sci.* **2015**, doi:10.1016/j.apsusc.2015.11.241. 38

[77] E. Vazsonyi *et al.*, Improved anisotropic etching process for industrial texturing of silicon solar cells, *Sol. Energy Mater. Sol. Cells* **1999**, 57(2), 179–188, doi:10.1016/S0927-0248(98)00180-9. 38, 39

[78] Y. Fan, P. Han, P. Liang, Y. Xing, Z. Ye and S. Hu, Differences in etching characteristics of TMAH and KOH on preparing inverted pyramids for silicon solar cells, *Appl. Surf. Sci.* **2013**, 264, 761–766, doi:10.1016/j.apsusc.2012.10.117. 38

[79] Y. Nishimoto, Investigation of Acidic Texturization for Multicrystalline Silicon Solar Cells, *J. Electrochem. Soc.* **1999**, 146(2), 457, doi:10.1149/1.1391628. 39

[80] S. Koynov, M. S. Brandt and M. Stutzmann, Black nonreflecting silicon surfaces for solar cells, *Appl. Phys. Lett.* **2006**, 88(20), 203107, doi:10.1063/1.2204573. 39

[81] S. Koynov, M. S. Brandt and M. Stutzmann, Black multi-crystalline silicon solar cells, *physica status solidi (RRL) – Rapid Research Letters* **2007**, 1(2), R53–R55, doi:10.1002/pssr.200600064. 39

[82] C. Zhang, L. Chen, Y. Zhu and Z. Guan, Fabrication of 20.19% Efficient Single-Crystalline Silicon Solar Cell with Inverted Pyramid Microstructure, *Nanoscale Res Lett* **2018**, 13(1), 91, doi:10.1186/s11671-018-2502-9. 39

[83] J. Zha, T. Wang, C. Pan, K. Chen, F. Hu, X. Pi and X. Su, Constructing submicron textures on mc-Si solar cells via copper-catalyzed chemical etching, *Appl. Phys. Lett.* **2017**, 110(9), 093901, doi:10.1063/1.4977191. 39

[84] F. Toor *et al.*, Metal assisted catalyzed etched (MACE) black Si: optics and device physics, *Nanoscale* **2016**, 8(34), 15448–15466, doi:10.1039/C6NR04506E. 39

[85] Z. Huang, N. Geyer, P. Werner, J. de Boor and U. Gösele, Metal-Assisted Chemical Etching of Silicon: A Review: In memory of Prof. Ulrich Gösele, *Adv. Mater.* **2011**, 23(2), 285–308, doi:10.1002/adma.201001784. 39

[86] D. Z. Dimitrov, C.-H. Lin, C.-H. Du and C.-W. Lan, Nanotextured crystalline silicon solar cells, *Phys. Status Solidi A* **2011**, 208(12), 2926–2933, doi:10.1002/pssa.201127150. 39

[87] F. Toor, J. Oh and H. M. Branz, Efficient nanostructured 'black' silicon solar cell by copper-catalyzed metal-assisted etching: Efficient nanostructured 'black' silicon solar cell, *Prog. Photovolt. Res. Appl.* **2014**, doi:10.1002/pip.2562. 39

[88] M. Ju *et al.*, A new vapor texturing method for multicrystalline silicon solar cell applications, *Mater. Sci. Eng. B* **2008**, 153(1-3), 66–69, doi:10.1016/j.mseb.2008.10.030. 40

[89] L. Zhou *et al.*, A Micro-Droplet Etching Approach for Texturization of Diamond Wire Sawn Multi-Crystalline Silicon Wafers, in *33rd European Photovoltaic Solar Energy Conference and Exhibition*, **2017** 952–954, doi:10.4229/EUPVSEC20172017-2CV.2.73. 40

[90] Y. Xia, B. Liu, J. Liu, Z. Shen and C. Li, A novel method to produce black silicon for solar cells, *Sol. Energy* **2011**, 85(7), 1574–1578, doi:10.1016/j.solener.2011.03.012. 40

[91] G. Xiao, B. Liu, J. Liu and Z. Xu, The study of defect removal etching of black silicon for solar cells, *Mater. Sci. Semicond. Proc.* **2014**, 22, 64–68, doi:10.1016/j.mssp.2014.01.030. 40

[92] B. Kafle *et al.*, Industrial Screen Printed Solar Cells with Novel Atmospheric Pressure Dry Texturing Process, Tech. rep., WIP, **2013**, doi:10.4229/28thEUPVSEC2013-2BV.2.40. 40

[93] L. Clochard *et al.*, Industrial Plasma-Less Dry Texturing Method for Diamond Wire Cut mc-Si Wafers - the universal ADE texturing process **2017**. 40

[94] Y. Ma, J. Si, X. Sun, T. Chen and X. Hou, Progressive evolution of silicon surface microstructures via femtosecond laser irradiation in ambient air, *Appl. Surf. Sci.* **2014**, 313, 905–910, doi:10.1016/j.apsusc.2014.06.105. 40

[95] B. K. Nayak, V. V. Iyengar and M. C. Gupta, Efficient light trapping in silicon solar cells by ultrafast-laser-induced self-assembled micro/nano structures, *Prog. Photovolt. Res. Appl.* **2011**, 19(6), 631–639, doi:10.1002/pip.1067. 40, 41

[96] H. Y. Chen *et al.*, Enhanced performance of solar cells with optimized surface recombination and efficient photon capturing via anisotropic-etching of black silicon, *Appl. Phys. Lett.* **2014**, 104(19), 193904, doi:10.1063/1.4878096. 40

[97] S. Cheon, D. S. Jeong, J.-K. Park, W. M. Kim, T. S. Lee, H. Lee and I. Kim, Enhanced blue responses in nanostructured Si solar cells by shallow doping, *J. Phys. D: Appl. Phys.* **2018**, 51(12), 125102, doi:10.1088/1361-6463/aaaee4. 40, 41

[98] P. R. Pudasaini, D. Elam and A. A. Ayon, Aluminum oxide passivated radial junction sub-micrometre pillar array textured silicon solar cells, *J. Phys. D Appl. Phys.* **2013**, 46(23), 235104, doi:10.1088/0022-3727/46/23/235104. 40

[99] I. Cornago *et al.*, Periodic nanostructures on unpolished substrates and their integration in solar cells, *Nanotechnology* **2015**, 26(9), 095301, doi:10.1088/0957-4484/26/9/095301. 40, 41

[100] A.-K. Volk *et al.*, Honeycomb Structure on Multi-crystalline Silicon Al-BSF Solar Cell With 17.8% Efficiency, *IEEE J. Photovolt.* **2015**, 5(4), 1027–1033, doi:10.1109/JPHOTOV.2015.2402757. 40, 41

[101] C. Trompoukis *et al.*, Passivation of photonic nanostructures for crystalline silicon solar cells: Passivation of photonic nanostructures, *Prog. Photovolt. Res. Appl.* **2015**, 23(6), 734–742, doi:10.1002/pip.2489. 40

[102] Z. Yue *et al.*, Large-scale black multi-crystalline silicon solar cell with conversion efficiency over 18 %, *Applied Physics A* **2014**, 116(2), 683–688, doi:10.1007/s00339-014-8414-3. 41

[103] J. Liu *et al.*, Characterization of PIII textured industrial multicrystalline silicon solar cells, *Sol. Energy* **2012**, 86(10), 3004–3008, doi:10.1016/j.solener.2012.07.006. 41

[104] B. Kafle, J. Seiffe, M. Hofmann, L. Clochard, E. Duffy and J. Rentsch, Nanostructuring of c-Si surface by F2-based atmospheric pressure dry texturing process, *Phys. Status Solidi A* **2015**, 212(2), 307–311, doi:10.1002/pssa.201431372. 41, 43

[105] M. Steglich, T. Käsebier, M. Zilk, T. Pertsch, E.-B. Kley and A. Tünnermann, The structural and optical properties of black silicon by inductively coupled plasma reactive ion etching, *J. Appl. Phys.* **2014**, 116(17), 173503, doi:10.1063/1.4900996. 44, 45

[106] A. J. Bett, J. Eisenlohr, O. Höhn, P. Repo, H. Savin, B. Bläsi and J. C. Goldschmidt, Wave optical simulation of the light trapping properties of black silicon surface textures, *Opt. Express, OE* **2016**, 24(6), A434–A445, doi:10.1364/OE.24.00A434. 45

[107] S.-E. Cheon *et al.*, Fabrication of parabolic Si nanostructures by nanosphere lithography and its application for solar cells, *Sci. Rep.* **2017**, 7(1), doi:10.1038/s41598-017-07463-7. 45

[108] T. Rahman, R. S. Bonilla, A. Nawabjan, P. R. Wilshaw and S. A. Boden, Passivation of all-angle black surfaces for silicon solar cells, *Sol. Energy Mater. Sol. Cells* **2017**, 160, 444–453, doi:10.1016/j.solmat.2016.10.044. 45

[109] A. Gombert *et al.*, Subwavelength-structured antireflective surfaces on glass, *Thin Solid Films* **1999**, 6. 45

[110] S. Chattopadhyay, Y. Huang, Y. Jen, A. Ganguly, K. Chen and L. Chen, Anti-reflecting and photonic nanostructures, *Materials Science and Engineering: R: Reports* **2010**, 69(1-3), 1–35, doi:10.1016/j.mser.2010.04.001. 45

[111] L. Rayleigh, On Reflection of Vibrations at the Confines of two Media between which the Transition is Gradual, *Proc. London Math. Soc.* **1879**, s1-11(1), 51–56, doi:10.1112/plms/s1-11.1.51. 45

[112] R. Jacobsson, V Light Reflection from Films of Continuously Varying Refractive Index, in *Progress in Optics* (edited by E. Wolf), vol. 5, 247–286, Elsevier, **1966**, doi:10.1016/S0079-6638(08)70454-2. 45

[113] H. M. Branz, V. E. Yost, S. Ward, K. M. Jones, B. To and P. Stradins, Nanostructured black silicon and the optical reflectance of graded-density surfaces, *Appl. Phys. Lett.* **2009**, 94(23), 231121, doi:10.1063/1.3152244. 45

[114] A. R. Parker, 515 million years of structural colour, *J. Opt. A Pure Appl. Opt.* **2000**, 2(6), R15–R28, doi:10.1088/1464-4258/2/6/201. 46

[115] M. A. Green, Self-consistent optical parameters of intrinsic silicon at 300 K including temperature coefficients, *Sol. Energy Mater. Sol. Cells* **2008**, 92(11), 1305–1310, doi:10.1016/j.solmat.2008.06.009. 46

[116] E. Yablonovitch, Statistical ray optics, *J. Opt. Soc. Am.* **1982**, 72(7), 899, doi:10.1364/JOSA.72.000899. 47

[117] M. A. Green, Lambertian light trapping in textured solar cells and light-emitting diodes: analytical solutions, *Prog. Photovolt. Res. Appl.* **2002**, 10(4), 235–241, doi:10.1002/pip.404. 47

[118] C. S. Schuster, A. Bozzola, L. C. Andreani and T. F. Krauss, How to assess light trapping structures versus a Lambertian Scatterer for solar cells?, *Optics Express* **2014**, 22(S2), A542, doi:10.1364/OE.22.00A542. 47, 48

[119] A. Ingenito, O. Isabella and M. Zeman, Experimental Demonstration of 4n2 Classical Absorption Limit in Nanotextured Ultrathin Solar Cells with Dielectric Omnidirectional Back Reflector, *ACS Photonics* **2014**, 1(3), 270–278, doi:10.1021/ph4001586. 48

[120] Y.-F. Huang *et al.*, Improved broadband and quasi-omnidirectional anti-reflection properties with biomimetic silicon nanostructures, *Nature Nanotechnol.* **2007**, 2(12), 770–774, doi:10.1038/nnano.2007.389. 48

[121] H. Savin, P. Repo, G. von Gastrow, P. Ortega, E. Calle, M. Garín and R. Alcubilla, Black silicon solar cells with interdigitated back-contacts achieve 22.1% efficiency, *Nature Nanotechnol.* **2015**, doi:10.1038/nnano.2015.89. 48, 49, 51, 52

[122] I. Haedrich, M. Ernst, A. Thomson, P. Zheng, X. Zhang, H. Jin and D. Macdonald, How cell textures impact angular cell-to-module ratios and the annual yield of crystalline solar modules, *Sol. Energy Mater. Sol. Cells* **2018**, 183, 181–192, doi:10.1016/j.solmat.2018.04.006. 48

[123] F. Lebreton, Silicon surface passivation properties of aluminum oxide grown by atomic layer deposition for low temperature solar cells processes, thesis, Université Paris Saclay, **2017**, URL `http://www.theses.fr/2017SACLX109`. 49

[124] A. G. Aberle, Surface passivation of crystalline silicon solar cells: a review, *Prog. Photovolt. Res. Appl.* **2000**, 8(5), 473–487, doi:10.1002/1099-159X(200009/10)8:5<473::AID-PIP337>3.0.CO;2-D. 49

[125] A. Richter, S. W. Glunz, F. Werner, J. Schmidt and A. Cuevas, Improved quantitative description of Auger recombination in crystalline silicon, *Phys. Rev. B* **2012**, 86(16), doi:10.1103/PhysRevB.86.165202. 49, 55

[126] J. Oh, H.-C. Yuan and H. M. Branz, An 18.2%-efficient black-silicon solar cell achieved through control of carrier recombination in nanostructures, *Nature Nanotechnol.* **2012**, 7(11), 743–748, doi:10.1038/nnano.2012.166. 49

[127] Y. Jiang *et al.*, High efficiency multi-crystalline silicon solar cell with inverted pyramid nanostructure, *Sol. Energy* **2017**, 142, 91–96, doi:10.1016/j.solener.2016.12.007. 49

[128] X. Ye *et al.*, 18.45%-Efficient Multi-Crystalline Silicon Solar Cells with Novel Nanoscale Pseudo-Pyramid Texture, *Advanced Functional Materials* **2014**, 24(42), 6708–6716, doi:10.1002/adfm.201401589. 49

[129] M. Otto, M. Kroll, T. KŠsebier, R. Salzer and R. Wehrspohn, Conformal Al2O3 Coatings on Black Silicon by Thermal ALD for Surface Passivation, *Energy Procedia* **2012**, 27, 361–364, doi:10.1016/j.egypro.2012.07.077. 49

[130] G. Dingemans and W. M. M. Kessels, Status and prospects of Al2O3-based surface passivation schemes for silicon solar cells, *J. Vac. Sci. Technol. A* **2012**, 30(4), 040802, doi:10.1116/1.4728205. 49

[131] K. Eriguchi, Modeling of defect generation during plasma etching and its impact on electronic device performance—plasma-induced damage, *J. Phys. D Appl. Phys.* **2017**, 50(33), 333001, doi:10.1088/1361-6463/aa7523. 49

[132] B. Damiani, R. Ludemann, D. Ruby, S. Zaidi and A. Rohatgi, Development of RIE-textured silicon solar cells, IEEE, ISBN 978-0-7803-5772-3, **2000** 371–374, doi:10.1109/PVSC.2000.915843. 49

[133] J. Yoo, G. Yu and J. Yi, Black surface structures for crystalline silicon solar cells, *Mater. Sci. Eng. B* **2009**, 159-160, 333–337, doi:10.1016/j.mseb.2008.10.019. 49

[134] S. Schaefer and R. Lüdemann, Low damage reactive ion etching for photovoltaic applications, *J. Vac. Sci. Technol. A* **1999**, 17(3), 749–754, doi:10.1116/1.581644. 49

[135] M. M. Plakhotnyuk *et al.*, Low surface damage dry etched black silicon, *J. Appl. Phys.* **2017**, 122(14), 143101, doi:10.1063/1.4993425. 49

[136] L. Yang *et al.*, Optimization of silicon pyramidal emitter by self-selective Ag-assisted chemical etching, *RSC Adv.* **2014**, 4(47), 24458, doi:10.1039/c4ra03120b. 50

[137] M. Hong *et al.*, Control carrier recombination of multi-scale textured black silicon surface for high performance solar cells, *Appl. Phys. Lett.* **2014**, 104(25), 253902, doi:10.1063/1.4884899. 50

[138] Z. Shen, B. Liu, Y. Xia, J. Liu, J. Liu, S. Zhong and C. Li, Black silicon on emitter diminishes the lateral electric field and enhances the blue response of a solar cell by optimizing depletion region uniformity, *Scripta Mater.* **2013**, 68(3-4), 199–202, doi:10.1016/j.scriptamat.2012.10.023. 50

[139] Y. Jiang, H. Yang, W. Cao, G. Wang, H. Ma and F. Chang, Post-black etching on emitter to improve performance of multi-scale texture silicon solar cells, *Applied Physics A* **2014**, 116(3), 1409–1414, doi:10.1007/s00339-014-8247-0. 50

[140] B. Kafle *et al.*, On the Nature of Emitter Diffusion and Screen-Printing Contact Formation on Nanostructured Silicon Surfaces, *IEEE J. Photovolt.* **2017**, 7(1), 136–143, doi:10.1109/JPHOTOV.2016.2626921. 50

[141] NREL, Best Research Cell Efficiencies, URL `www.nrel.gov/pv/assets/images/efficiency-chart.png`. 50

[142] K. Yoshikawa *et al.*, Silicon heterojunction solar cell with interdigitated back contacts for a photoconversion efficiency over 26%, *Nature Energy* **2017**, 2, 17032, doi:10.1038/nenergy.2017.32. 51, 52

[143] F. Haase *et al.*, Laser contact openings for local poly-Si-metal contacts enabling 26.1%-efficient POLO-IBC solar cells, *Sol. Energy Mater. Sol. Cells* **2018**, 186, 184–193, doi:10.1016/j.solmat.2018.06.020. 51, 52

[144] J. Benick *et al.*, Approaching 22% Efficiency with Multicrystalline n-Type Silicon Solar Cells, in *Proceedings of the 33rd European Photovoltaic Solar Energy Conference and Exhibition*, WIP, Amsterdam, **2017** 460–464, doi:10.4229/EUPVSEC20172017-2DO.3.1. 52

[145] M. A. Green, Y. Hishikawa, E. D. Dunlop, D. H. Levi, J. Hohl-Ebinger and A. W. Y. Ho-Baillie, Solar cell efficiency tables (version 51), *Prog. Photovolt. Res. Appl.* **2018**, 26(1), 3–12, doi:10.1002/pip.2978. 51

[146] A. Richter, M. Hermle and S. W. Glunz, Reassessment of the Limiting Efficiency for Crystalline Silicon Solar Cells, *IEEE J. Photovolt.* **2013**, 3(4), 1184–1191, doi:10.1109/JPHOTOV.2013.2270351. 51

[147] J. Benick *et al.*, High-Efficiency n-Type HP mc Silicon Solar Cells, *IEEE J. Photovolt.* **2017**, 7(5), 1171–1175, doi:10.1109/JPHOTOV.2017.2714139. 52

[148] F. Cao, K. Chen, J. Zhang, X. Ye, J. Li, S. Zou and X. Su, Next-generation multi-crystalline silicon solar cells: Diamond-wire sawing, nano-texture and high efficiency, *Sol. Energy Mater. Sol. Cells* **2015**, 141, 132–138, doi:10.1016/j.solmat.2015.05.030. 52

[149] M. Steglich, T. Käsebier, F. Schrempel, E.-B. Kley and A. Tünnermann, Self-organized, effective medium Black Silicon for infrared antireflection, *Infrared Physics & Technology* **2015**, 69, 218–221, doi:10.1016/j.infrared.2015.01.033. 54

CHAPTER II

TAILORED VOLTAGE WAVEFORMS EXCITATION IN THE SF_6/O_2 DISCHARGE

Contents

II.1 Implementation of Tailored Voltage Waveforms **64**
II.1.1 Electrical Calibration 65
II.1.1.a Feedthrough/electrode connection in the RIE reactor 65
II.1.1.b Application of correction factors 66
II.1.2 Validating Calibration using Amplitude Asymmetry Effect in Ar 67
II.1.2.a Amplitude Asymmetry Effect model 68
II.1.2.b Study of the Ar discharge 69
II.1.2.c Impact of calibration errors 73
II.2 Amplitude and Slope Asymmetry Effects in the SF_6/O_2 discharge **75**
II.2.1 Comparison of SF_6/O_2 with Ar and O_2 75
II.2.2 Power Coupling Mode Transitions in SF_6/O_2 77
II.2.2.a Influence of SF_6 content 77
II.2.2.b Influence of discharge pressure and power 79
II.3 Tuning Ion Energy and Flux using Tailored Voltage Waveforms in SF_6/O_2 . . . . . **81**
II.3.1 Tuning Ion Flux Energy Distributions in SF_6/O_2 81
II.3.1.a Comparison of SF_6/O_2 and Ar 82
II.3.1.b Comparison of estimated ion bombardment energy with experiments 83
II.3.2 Effects of Power Mode Transitions in Decoupling Ion Energy and Flux . 85
II.3.2.a Effect of SF_6 content 85
II.3.2.b Extended process conditions “playground” in SF_6/O_2 86
II.3.3 Ion Flux Non-uniformity in SF_6/O_2 Discharge 89
II.3.3.a Effect of excitation waveform and comparison with Ar 89
II.3.3.b Elements of elucidation 92
Summary **94**
Bibliography **96**

Introduction

This chapter is dedicated to investigating the effect of Tailored Voltage Waveforms (TVWs) excitation in the SF_6/O_2 discharge. More precisely, a method for rapid implementation of TVWs – on the reactor used for silicon nanotexturing – will first be detailed using the (known) behavior of an Ar discharge as a validation tool. Next, TVWs will be applied to the SF_6/O_2 discharge in a range of plasma conditions relevant for silicon nanotexturing, and particular attention will be paid to the identification of the power coupling mode. Finally, the influence of TVWs (and the discharge operating mode) on the ion energy and ion flux at the powered electrode will be characterized in the SF_6/O_2 discharge.

II.1 Implementation of Tailored Voltage Waveforms

As it has been explained in the previous chapter, Tailored Voltage Waveforms (TVWs) excitation may be implemented in any CCP reactor by a relatively simple upgrade of the excitation system. However, a monitoring of the waveform set at the electrode, $\widetilde{V}_e(t)$, is required. In the RIE reactor used for the present work, introducing a high-voltage probe on the electrode is not realizable without significant mechanical alterations of the reactor. A versatile alternative solution consists of monitoring the waveform $\widetilde{V}_f(t)$ at the feedthrough, i.e. the RF input on the reactor as seen in the schematic Figure II.1(a). In the schematic, Z corresponds to the impedance of the electrical circuit between the amplifier and the feedthrough cable, Z_{fe} the impedance of the feedthrough/electrode connection, Z_R the reactor impedance and Z_{pl} the plasma impedance. With this solution, two challenges actually have to be tackled, as summarized in Figure II.1(b). First, if we choose a target waveform $\widetilde{V}_e(t)$ that has to appear at the electrode, how should the waveform monitored at the feedthrough $\widetilde{V}_f(t)$ be set? Second, once the feedthrough waveform has been defined, how good is the "prediction" of the waveform appearing at the electrode?

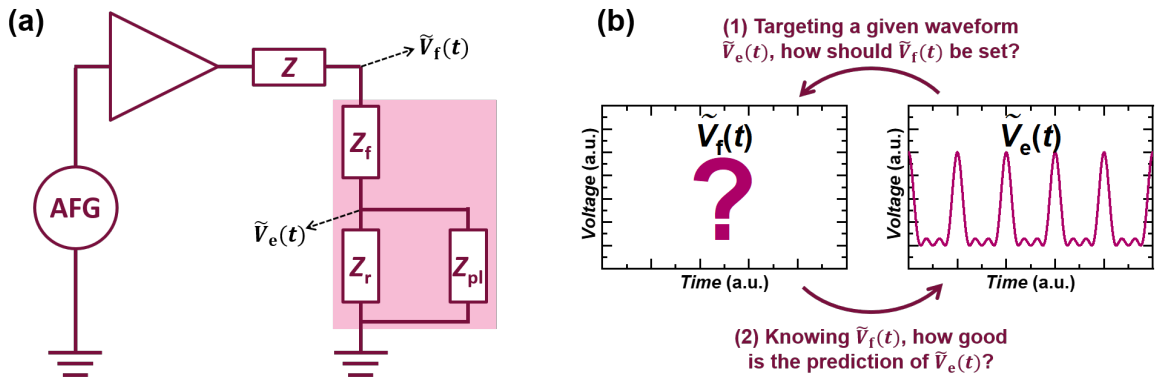

Fig. II.1: (a) Electrical schematic of RIE setup. (b) Illustration of two challenges tackled in this section.

In order to tackle these challenges, a rather simple method is here proposed. A careful electrical characterization of the connection between the feedthrough and the electrode is primarily carried out as a calibration. As will be shown here, this study can be made in open-chamber conditions (no plasma, electrode acting as an open-circuit): this method has for instance been successfully applied by Schulze *et al.* [1, 2]. Then, verification can be underdone to check that the effect of the additional impedance introduced when lighting the plasma can be neglected: to this aim, the behavior of an argon discharge excited by TVWs will be investigated. This careful study is required to ensure the validity of subsequent experimental results obtained in the present work.

It should be clearly highlighted that in this first section (where the focus switches back and forth between what happens at the feedthrough or at the electrode), mathematical notations using subscript "f" (e.g. $\widetilde{V}_f$) will refer to parameters "at the feedthrough," while subscript "e" (e.g. $\widetilde{V}_e$) correspond to parameters "at the electrode."

II.1.1 Electrical Calibration

To characterize the electrical connection between the feedthrough and the electrode, the former is fed with a sinusoidal voltage signal in open-circuit conditions, with an open chamber (see picture in Figure II.2). The voltage signals at the feedthrough and the electrode are simultaneously measured using two identical high-voltage probes (model P5100A from Tektronix, DC to 500 MHz bandwidth). The gain in signal amplitude and the phase-shift between the two signals $\widetilde{V}_\mathrm{f}$ and $\widetilde{V}_\mathrm{e}$ are then evaluated as a function of the applied frequency.

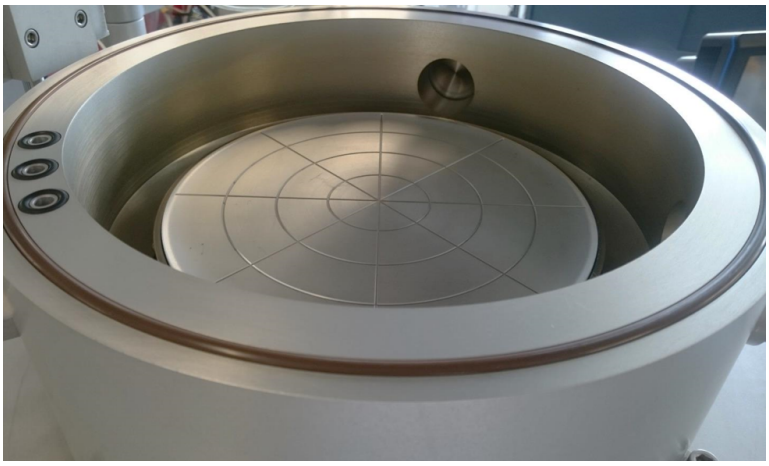

Fig. II.2: Picture of the substrate electrode in the RIE reactor (open chamber), the electrode has an external diameter of 8 inches (20.3 cm)

II.1.1.a Feedthrough/electrode connection in the RIE reactor

Figure II.3 shows the gain G_fe and phase-shift $\Delta\theta_\mathrm{fe}$ introduced by the feedthrough/electrode connection on the RIE reactor, measured in the frequency range from 1 to 80 MHz. The electrical connection is seen to act as a low-pass filter: actually, the strongly peaked gain curve and the approximate $-\pi$ phase-shift at high frequencies point to a second order passive filter behavior. Such a filter can be modeled by a complex transfer function $\boldsymbol{H}$ of the later form:

$$\boldsymbol{H}_\mathrm{fe}(\mathrm{i}f) = \frac{K}{1 + \frac{\mathrm{i}f}{Qf_\mathrm{n}} + \left(\frac{\mathrm{i}f}{f_\mathrm{n}}\right)^2} \tag{II.1}$$

where i is the imaginary unit, f the frequency, K the DC gain, Q the quality factor and f_n the undamped natural frequency of the filter. Fitting the experimental data (fit made on the gain data $G_\mathrm{fe}(f) = |H_\mathrm{fe}(\mathrm{i}f)|$ with this model leads to the following results: $K = 1$, $Q = 17.2$ and $f_\mathrm{n} = 24.5$ MHz. The peaked gain curve explains the large quality factor: a resonant frequency ($f_\mathrm{r} = f_\mathrm{n}\sqrt{1/2Q^2} \approx f_\mathrm{n}$) exists, for which the gain is maximal and very high ($G_\mathrm{fe}(f_\mathrm{r}) \approx Q$). The result of the model fitting is shown with dashed curves in graphs Figure II.3. The chosen model fits the experimental data relatively well for the gain, but rather poorly in the case of the phase-shift for frequencies above f_n (which is not surprising as the minimal phase-shift for a second order passive filter is $-\pi$ although measurements go to significantly lower values).

Nevertheless, it can be easily understood from these electrical measurements that, when feeding the RF input with a multi-frequency signal, the waveform at the electrode may be strongly altered: all harmonic components with frequencies in the range from 10 MHz to 26 MHz (approximately) are strongly amplified. On the contrary, components above 26 MHz will be attenuated, with an additional phase-shift delay of around $-\pi$.

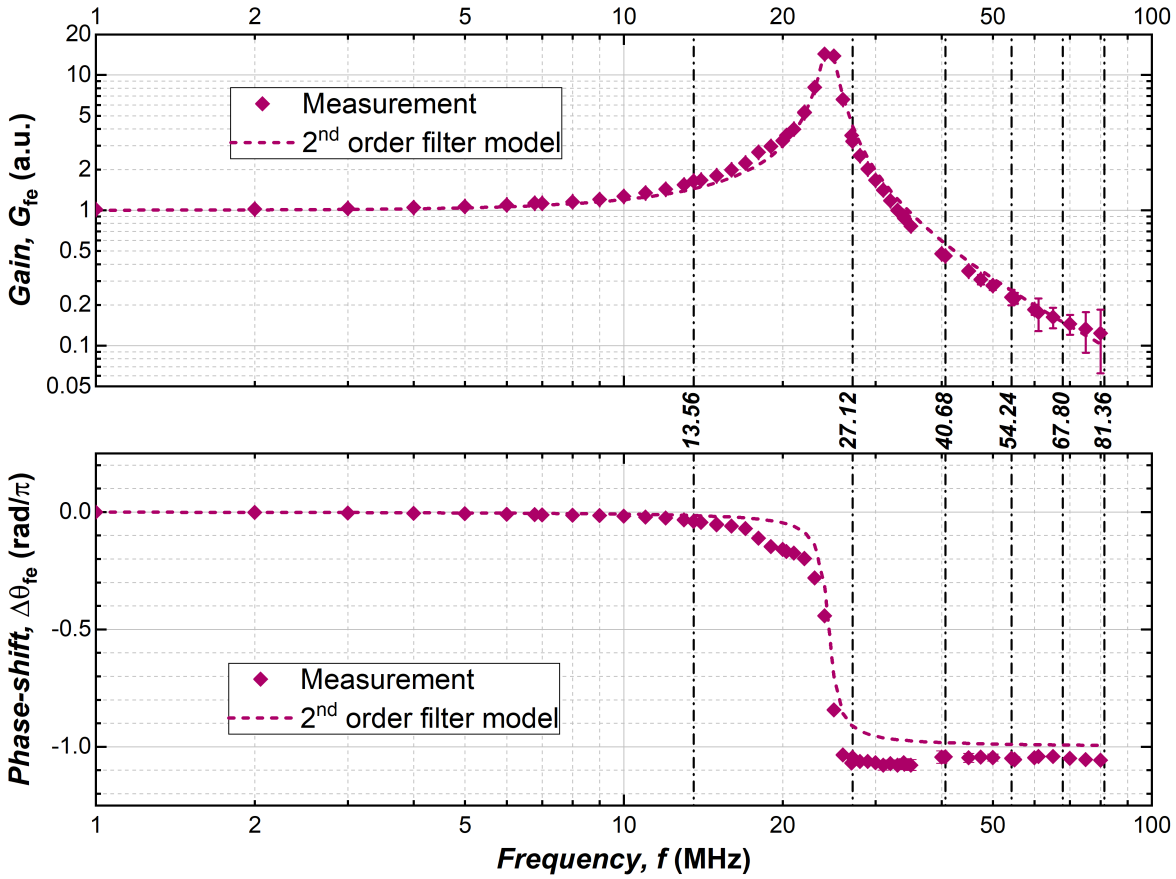

Fig. II.3: Gain (top) and phase-shift (bottom) between the feedthrough and electrode of the RIE measured in open-circuit conditions with an open chamber, dashed curves show the 2nd order passive filter model fit.

II.1.1.b Application of correction factors

Now that the feedthrough/electrode connection has been characterized in open-circuit conditions, a strong assumption has to be introduced: it is here assumed that the gain and phase-shift values measured in the previous study are still valid when a discharge is ignited, i.e. the electrode acts as an open-circuit even when introducing the additional impedance from the plasma.

Following this assumption, one could choose to apply TVWs with frequency components in the range [1,10 MHz] where $G_{\mathrm{fe}} \approx 1$ and $\Delta\theta_{\mathrm{fe}} \approx 0$. We will, however, dismiss this possibility for several reasons: (i) in the RF regime, the plasma density scales with the square of the frequency: working at very low frequency would lead to a very limited ion flux range; (ii) the RF period would possibly become significantly lower than the ion response time to variations in the electric field; (iii) the available RF domain for industrial purposes is constrained by regulators to the ISM band (in the range of interest, only components with center frequencies at 13.56, 27.12 and 40.68 MHz are available, [3]).

The alternative method requires a calibration and the use of "correction factors." Indeed, in the most general case, the AC component of the desired (target) TVW at the electrode is expressed by:

$$\widetilde{V}_{\mathrm{e}}(t) = \sum_{k=1}^{n} V(kf_0)\cos\left[2\pi k f_0 t + \Theta(kf_0)\right] \tag{II.2}$$

where f_0 is the basis frequency, n the total number of harmonic components, $V(kf_0)$ and $\Theta(kf_0)$ respectively the desired voltage amplitude and phase-shift for each component. In this case, the waveform set at the feedthrough should be:

$$\widetilde{V}_{\mathrm{f}}(t) = \sum_{k=1}^{n} \frac{V(kf_0)}{G_{\mathrm{fe}}(kf_0)} \cos\left[2\pi k f_0 t + \Theta(kf_0) - \Delta\theta_{\mathrm{fe}}(kf_0)\right] \tag{II.3}$$

where $G_{\mathrm{fe}}(kf_0)$ and $\Delta\theta_{\mathrm{fe}}(kf_0)$ are respectively the gain and phase-shift "correction factors" introduced to take the influence of the feedthrough/electrode connection into account. Notice that the "phase-shifts correction factors" $\Delta\theta_{\mathrm{fe}}(kf_0)$ depend on the chosen time scale origin, and only the differences in phase-shift between upper harmonics and basis frequency, i.e. $\Delta\theta_{\mathrm{fe}}(kf_0) - \Delta\theta_{\mathrm{fe}}(f_0)$ for $k > 1$, need to be known. For a given number of frequencies, n, in the TVW signal, the evaluation of $2n-1$ factors is therefore required.

Even with this alternative, the low-pass filter behavior and the presence of a resonant frequency further constrain the choice of the basis frequency and the number of harmonics for the TVW excitation. First, components with frequencies above 60 MHz would be attenuated by at least a factor five: the required amplification at the feedthrough will make the monitoring rather difficult (as lower harmonics will have significantly smaller amplitudes relatively to the highest harmonic). On the contrary, components close to the resonant frequency would have to be strongly attenuated at the feedthrough, and a large uncertainty on their phase relative to the basis frequency would apply: monitoring would again be made difficult.

Fortunately, when considering all the aforementioned constraints, it appears that choosing the frequencies of the ISM band – i.e. 13.56 MHz and two upper harmonics – is actually a fairly reasonable choice. In particular, the 27.12 MHz component is relatively far from the resonant frequency. Additional measurements (with the same method as previously depicted) have been carried out at these frequencies to obtain good estimates of the associated correction factors. The values are gathered in Table II.1.

Tab. II.1: Correction factors applied to the TVW signal at the feedthrough of the RIE reactor, a $10\%_{\mathrm{rel}}$ uncertainty is assumed for the gain correction factors.

Component	Frequency (MHz)	Gain, G_{fe}	Phase-shift, $\Delta\theta_{\mathrm{fe}}$ (rad)
f_0	13.56	1.68	-0.09 ± 0.05
$2f_0$	27.12	2.54	-3.19 ± 0.05
$3f_0$	40.68	0.46	-3.19 ± 0.05

Notice that in Table II.1, the announced uncertainties for gain and phase-shift correspond to measurement uncertainties and are valid in open-chamber conditions. Upon igniting the plasma, uncertainties are expected to be larger and dominated by the influence of the plasma impedance.

The first problematic introduced by the experimental constraint for waveform monitoring is therefore solved: under the proposed assumptions, it is now possible to set the waveform at the feedthrough $\widetilde{V}_{\mathrm{f}}(t)$ to obtain a given target waveform at the electrode $\widetilde{V}_{\mathrm{e}}(t)$.

II.1.2 Validating Calibration using Amplitude Asymmetry Effect in Ar

The proposed calibration method (and associated "correction factors") relies on a rather strong hypothesis, namely the assumption that the electrode acts as an open-end even in the presence of a plasma, i.e. that the voltage divider between the feedthrough cable and the reactor (previously shown in Figure II.1(a)) is not modified by the plasma impedance. In [1], Schulze *et al.* use a similar calibration method and compare the reactance of the feedthrough/electrode connection to the much higher reactance of the plasma to demonstrate that this hypothesis is valid. In the same paper, Schulze *et al.* first experimentally demonstrated the electrical asymmetry effect (more precisely the amplitude asymmetry effect, AAE) in low-pressure Ar discharge. Here, the idea is to reverse the approach and use the experimentally observed behavior of an Ar discharge as a validation tool for the calibration.

Indeed, the behavior of Ar discharges excited by TVWs in CCP reactors has been extensively investigated in recent years by means of either simulations or experiments [2, 4–8]. At relatively low power and pressure, CCP Ar discharges are operated in α-mode (sheath expansion heating) and the AAE is dominant.

II.1.2.a Amplitude Asymmetry Effect model

As explained in the previous chapter, the DC self-bias voltage on the powered electrode is given by Equation (II.4) as a function of the symmetry parameter ε and the waveform $\widetilde{V}_e$:

$$V_{DC} = -\frac{V_{e,max} + \varepsilon V_{e,min}}{1+\varepsilon} \tag{II.4}$$

where $V_{e,max}$ (respectively $V_{e,min}$) is the maximal (respectively minimal) value of $\widetilde{V}_e$. Two hypotheses are required for the previous expression to be valid: the sheath potential at maximal sheath collapse, as well as the voltage drop in the plasma bulk are assumed negligible, [9].

It should here be recalled that the primary objective behind the TVW approach, as introduced in [4], was to vary the ion bombardment energy independently from the ion flux in a CCP discharge. Regardless of the excitation waveform, the average ion bombardment energy at the powered electrode scales with V_{DC} (in the case of a collisionless sheath). Furthermore, for single frequency excitation, both V_{DC} and the ion flux scale directly with $V_{e,PP}$ (the peak-to-peak amplitude of $\widetilde{V}_e$), hence the correlation between ion flux and energy [10]. It follows that, a necessary condition to achieve a decoupling (with the additional constraints that only one electrode is powered, and the basis frequency kept constant) is to be able to vary V_{DC} independently from $V_{e,PP}$. From Equation (II.4), if variations of ε are considered negligible, this is achieved in particular by tailoring the difference $V_{e,max} - |V_{e,min}|$ with TVWs.

To this aim, the chosen set of TVWs used in this work (except when otherwise stated) are similar to the ones introduced by Bruneau *et al.* in [8] and can be expressed by:

$$\widetilde{V}_e(t) = V_0 \sum_{k=1}^{n} \frac{n-k+1}{n} \cos(2\pi k f_0 t + \Theta) \tag{II.5}$$

with the phase-shift parameter Θ constant. In this case, the "shape" of the waveform can be chosen by varying Θ in [0,2π], as shown in Figure II.4 for four values of Θ that lead to typical "pulse-like" waveforms (peaks and valleys) or "sawtooth-like" waveforms (sawtooth-up and sawtooth-down). As an illustration, graphs in Figure II.4 also show the waveforms that must be set at the feedthrough according to the correction factors introduced in the previous section.

The waveforms expressed by Equation (II.5) are chosen because they correspond to an optimum AAE: for a given number of harmonics in the signal n, the range of achievable $V_{DC}/V_{e,PP}$ values is maximized. This can be shown theoretically but has also been demonstrated experimentally by Schulze *et al.* [2] in the case $n = 2$.

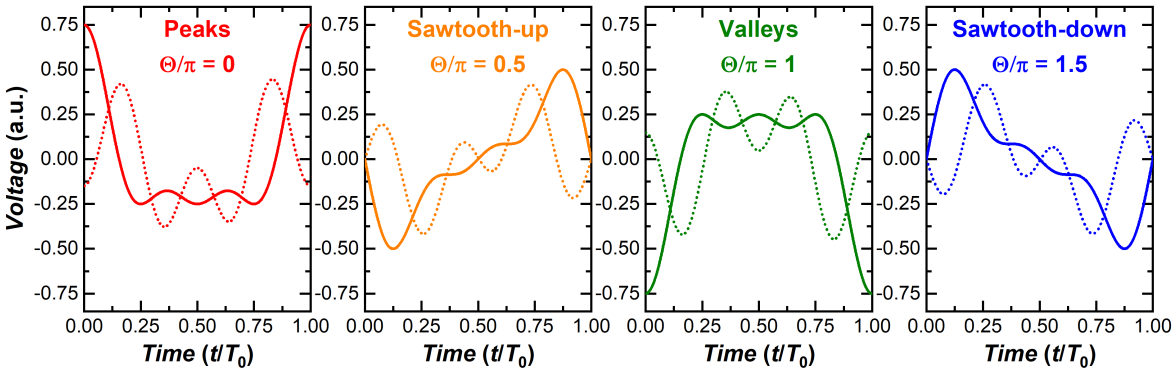

Fig. II.4: Examples of waveforms required at the feedthrough (dotted curves) to obtain target model waveforms at the electrode (solid curves).

Taking advantage of the AAE, it is therefore possible to use the Ar discharge to experimentally evaluate the validity of the calibration method and the estimated correction factors. When comparing the AAE model with the experimental results, discrepancies can be explained by at least three sources of uncertainties (in addition to metrological sources):

1. **Imperfect control of the waveforms set at the feedthrough:** experimentally, due to non-linear electrical properties of the amplifier and the plasma, the waveform set at the feedthrough may significantly diverge from the target waveform $\widetilde{V}_{\mathrm{f}}$, from Equation (II.3), thus introducing discrepancies in the observed AAE.

2. **Calibration uncertainties:** errors and/or variations in the evaluated correction factors $G_{\mathrm{fe}}(kf_0)$ and $\Delta\theta_{\mathrm{fe}}(kf_0)$ may lead to deviations from theory.

3. **Variations of the symmetry factor** (e.g. from self-amplification or SAE): in other words, the theoretical AAE model presented here is too simplistic, simulations would for instance help refining it, [5].

The first two possible sources of errors (imperfect waveform control at feedthrough and calibration uncertainties) can rather easily be quantified, as will be shown in the next subsections. The objective of the current section is therefore to quantify, when possible, the sources of errors and to experimentally assess the validity of the calibration method using an Ar discharge.

II.1.2.b Study of the Ar discharge

Validation tests. Experiments are carried out using an Ar discharge, the waveform at the feedthrough is set according to Equation (II.6) below which consists in a theoretical target waveform:

$$\widetilde{V}_{\mathrm{f}}(t) = V_0(\Theta)\sum_{k=1}^{n}\frac{n-k+1}{n}\frac{1}{G_{\mathrm{fe}}(kf_0)}\cos\left[2\pi k f_0 t + \Theta - \Delta\theta_{\mathrm{fe}}(kf_0)\right] \tag{II.6}$$

In these tests, the parameters are set to $f_0 = 13.56\,\mathrm{MHz}$, $n = 2$ or 3 and the values of the correction factors $G_{\mathrm{fe}}(kf_0)$ and $\Delta\theta_{\mathrm{fe}}(kf_0)$ are taken from Table II.1. The peak-to-peak voltage at the feedthrough is kept constant, and therefore V_0 depends on Θ, the latter being varied in the range $[0,2\pi]$.

The experimental waveform measured at the feedthrough is not identical to the target expression in $\widetilde{V}_{\mathrm{f}}$: in addition to measurement uncertainties, the waveform is obtained by a feedback loop and incremental corrections to account for the varying impedance of the circuit when the plasma is ignited. The experimental voltage waveform is therefore fit to the following expression to assess the quality of the waveform control:

$$\widetilde{V}_{\mathrm{f}}^{\mathrm{exp}}(t) = \frac{1}{2}\sum_{k=1}^{n} V_{\mathrm{f}}^{\mathrm{exp}}(kf_0)\cos\left[2\pi k f_0 t + \theta_{\mathrm{f}}^{\mathrm{exp}}(kf_0)\right] \tag{II.7}$$

Results are shown in Figure II.5 the first column corresponds to measurements obtained with $n = 2$ and $V_{\mathrm{f,PP}} = 75\,\mathrm{V}$ for a pressure of 31 mTorr; for the second column, the pressure is 31 mTorr, $n = 3$ and $V_{\mathrm{f,PP}} = 125\,\mathrm{V}$; for the third column the pressure is 123 mTorr, $n = 3$ and $V_{\mathrm{f,PP}} = 75\,\mathrm{V}$. In all cases, a total input gas flux of 100 sccm (Standard Cubic Centimeters per Minute) has been used. In Figure II.5, the graphs from the first two lines show the results of fitting the waveforms measured at the feedthrough $\widetilde{V}_{\mathrm{f}}^{\mathrm{exp}}$ with Equation (II.7), while dashed curves show the targeted values for each parameter. Notice that the time scale has been chosen so that $\Delta\theta_{\mathrm{fe}}(f_0) = 0$ in the fit, and the other phase-shift parameters are expressed in the range $[0,2\pi]$. Finally, graphs in the bottom line of Figure II.5 show the measured DC self-bias voltage: at this point it is useful to recall once again that V_{DC} directly depends on $\widetilde{V}_{\mathrm{e}}$ (experimentally inaccessible), and thus only indirectly on $\widetilde{V}_{\mathrm{f}}$. Error bars are too small to show in the graphs Figure II.5: voltage values are obtained with an uncertainty of $\pm 1\,\mathrm{V}$ and phase-shift values with an uncertainty of $\pm 0.02\,\pi$.

For the first set of conditions, Figure II.5(a-c), at a pressure of 31 mTorr, the peak-to-peak amplitude of the waveform is well controlled compared to the target value ($V_{\mathrm{f,PP}} = 75\,\mathrm{V}$), although

the amplitudes of the components are in most cases a little lower than targeted (especially for the basis frequency, $V_f(f_0)$, close to $\Theta/\pi = 0$ or 2), as seen in graph (a). In addition, the peak-to-peak amplitude of the second harmonic, $V_f^{exp}(3f_0)$, is shown in the same graph. Although it should be null in this case ($n = 2$), this component is still observed (with significant amplitude around 3 to 5 V), due to the large reflected power creating non-linearities in the electrical network: this is the reason why the amplitude $V_{f,PP}$ has been kept lower in this case (75 V) than in the two others (125 V), i.e. to avoid a significant contribution from the second (uncontrolled) harmonic. These errors most certainly come from the feedback loop step by step approximation used in the experimental setup to set the feedthrough waveform. The phase-shift between components is however very well controlled – within the measurement uncertainties, graph (b). Regarding now the measured values of V_{DC} in graphs (c), it is first observed that all values are negative – this is also true for the other two sets of measurements: this can be explained by the geometrical asymmetry of the reactor. Indeed, in the experimental setup, the area of the powered electrode is about half the area of the grounded walls (including the grounded counter electrode), therefore imposing $\varepsilon < 1$

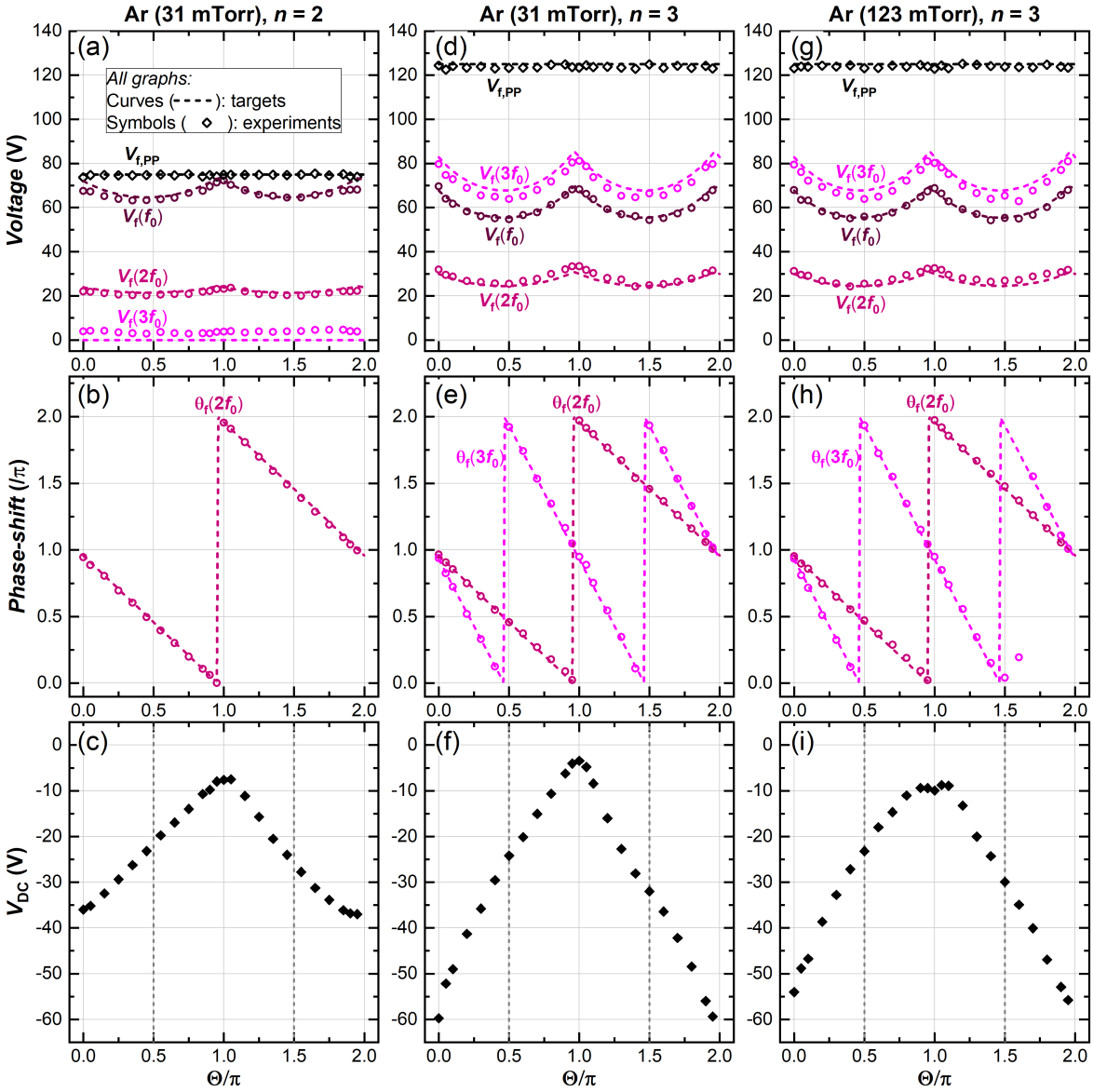

Fig. II.5: Comparison of experimental feedthrough waveforms with target values (peak-to-peak amplitudes in top line graphs and phase-shifts in center line graphs) and corresponding evolution of V_{DC} (bottom line graphs) for an Ar discharge in the three test cases: 31 mTorr, $n = 2$ (a-c), 31 mTorr, $n = 3$ (d-f) and 123 mTorr, $n = 3$ (g-i).

for all investigated conditions. Secondly, the AAE is well observed, with a typical inverted-V shape: a minimal value of −36 V is obtained for peaks waveforms ($\Theta/\pi = 0$) and a maximal value of −7.5 V for valleys waveforms ($\Theta/\pi = 1$). This demonstrates that at 31 mTorr and with only two frequency components, V_{DC} can effectively be varied in a quite large range for the Ar discharge.

In the second case, displayed in Figure II.5(d-f), an harmonic component is added ($n = 3$) and the peak-to-peak target amplitude at the feedthrough raised to $V_{f,PP} = 125$ V. Again, some systematic error seems to appear in the peak-to-peak amplitude of some components, in particular the amplitude of the second harmonic is constantly higher than the targeted values $V_f(3f_0)$ as seen in graph (d). The phase-shift of both upper harmonics are well-controlled, graph (e), and V_{DC} is again varying as expected from the AAE, in a larger range (from −60 V to −3.5 V) compared to the first investigated case (due both to the supplementary harmonic and to the increase in $V_{f,PP}$).

The third case corresponds to similar conditions ($n = 3$ and $V_{f,PP} = 125$ V) except for the pressure which is raised to 123 mTorr, Figure II.5(g-i). Similar errors are observed for the comparison of the experimental waveforms with the targeted values in terms of amplitude and phase-shift, graphs (g) and (h), except for one value of $\Delta\theta_f^{exp}(3f_0)$ which seems far from the target (for $\Theta/\pi = 1.6$). At 123 mTorr, the variation of V_{DC} again generally corresponds to the expectations from the AAE. However, there seem to be a plateau in V_{DC} for Θ in the range $[0.9\pi,1.1\pi]$ (i.e. close to valleys waveforms). This may suggest that the calibration method is becoming less appropriate at this pressure (compared to the cases at 31 mTorr), although a more detailed analysis will be attempted in the following.

Finally, it should be highlighted that a small SAE is observed in all cases: indeed, V_{DC} for sawtooth-up waveform ($\Theta/\pi = 0.5$) is significantly higher than for sawtooth-down waveform ($\Theta/\pi = 1.5$). A difference up to 8 V is in particular obtained for the Ar discharge operated at 31 mTorr with $n = 3$. These observed differences are consistent with the fact that the discharge is operated in α-mode (i.e. sheath expansion heating is dominant), and also confirm that ε is actually not perfectly constant when varying Θ.

From these measurements, it is now possible to conclude that even if the calibration method is not perfect, the observed trends are qualitatively in agreement with the AAE model, and most importantly V_{DC} can as expected be varied in a large range.

Comparison with AAE model. A quantitative comparison between experiments and model is now proposed. As previously highlighted, the symmetry factor is lower than unity as all experimental V_{DC} values are negative. If we further assume that ε is constant in the investigated conditions, a non-linear least-square fitting of Equation (II.4) with the measured V_{DC} data shows that, for all the investigated conditions, $\varepsilon \approx 0.47$ gives the best fit. Figure II.6 shows the comparison of $V_{DC}/V_{e,PP}$ obtained experimentally for the three investigated sets of conditions (as a reminder, $V_{e,PP}$ is the calculated peak-to-peak amplitude at the electrode) and the model AAE (with $\varepsilon = 0.47$ constant). Notice that in Figure II.6 the experimental data points for $\Theta/\pi = 0$ and $\Theta/\pi = 2$ come from a single measurement as the waveforms are identical: this design is especially used to highlight the continuous evolution of the measured quantities when altering the waveform by screening values of Θ/π. The same graphical process will be employed in the rest of the manuscript.

In Figure II.6, the top graphs show experimental data (black diamonds, dotted curves), as well as the result of the AAE model assuming "perfect" calibration, i.e. the prediction of the waveform at the electrode based on the measurements at the feedthrough is considered exact. In a first case (shown in solid red curves), the AAE model results are computed based on the target feedthrough waveforms, i.e. the discrepancies between the experimental feedthrough waveform and the target values (Figure II.5) are neglected. In a second case (shown by blue dashed curves), the imperfect waveform control is taken into account. In doing this, we are able to assess the influence of the first source of errors identified in section II.1.2.a, namely imperfect waveform control.

The experimental results displayed in Figure II.6 should first be analyzed: as previously explained, in all cases the experimental $V_{DC}/V_{e,PP}$ data is consistent with the AAE model as minimum values are found for peaks waveforms ($\Theta/\pi = 0$) and maximal values for valleys waveforms

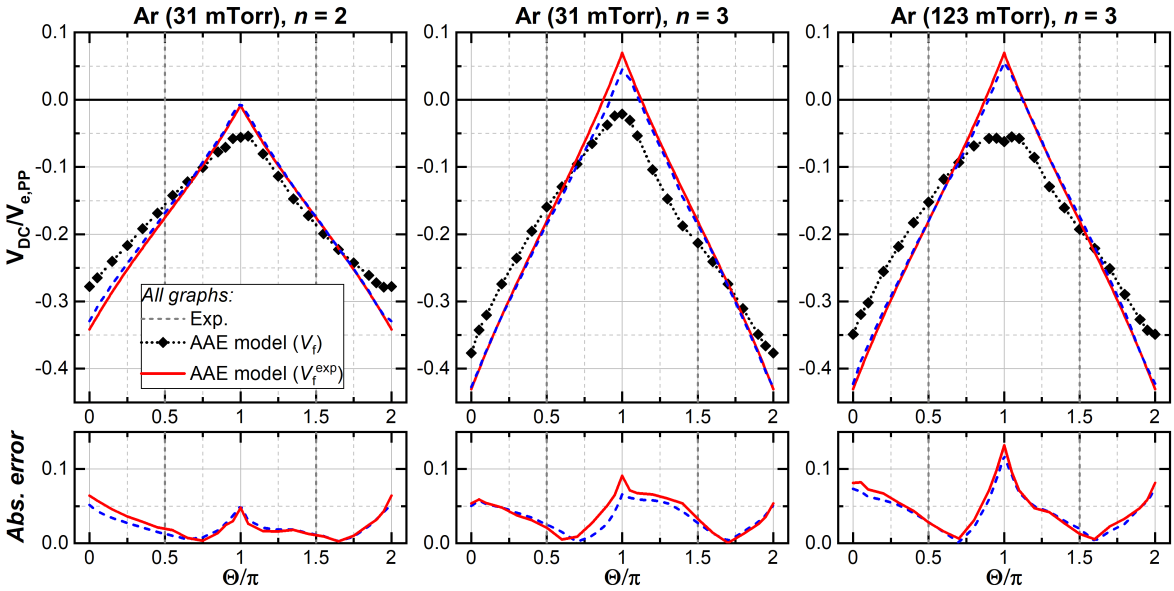

Fig. II.6: Comparison of $V_{DC}/V_{e,PP}$ from experimental measurements with theoretical AAE model for the three discharge conditions investigated with Ar. Bottom line graphs show the absolute error in $V_{DC}/V_{e,PP}$ between experiment and models.

($\Theta/\pi = 1$). Moreover, the two cases obtained at a pressure of 31 mTorr show indeed that the range in which $V_{DC}/V_{e,PP}$ can be varied is enlarged when the number of harmonics in the TVW excitation signal is increased, a phenomenon which is also predicted by the theoretical AAE model. Then, when keeping the same number of frequency components ($n = 3$) and increasing the pressure to 123 mTorr, the range of $V_{DC}/V_{e,PP}$ is again a little reduced: this may in particular be explained by a lower self-amplification effect [5, 11]. Self-amplification is due to a difference in charge densities between the powered and grounded sheaths (the highest density is found in the sheath where the voltage drop is maximal): when increasing pressure, both sheaths become more collisional and the difference in charge densities in powered and grounded sheaths shrinks, so that the variations in symmetry parameter (induced by self-amplification effect) are lowered.

Regarding now the comparison of experimental results with the AAE models shown in Figure II.6, it is observed first that even at relatively low pressure (31 mTorr), no self-amplification can be seen as the experimental values of $V_{DC}/V_{e,PP}$ are comprised within the range of the AAE model (which, as should be recalled, does not account for the self-amplification). Second, the discrepancy between the experimental results and the AAE model is maximal around pulse-like waveforms. In particular the theoretical model for $n = 3$ predicts positive values of V_{DC} for Θ in the range $[0.9\pi,1.1\pi]$ approximately, while negative values are observed experimentally. In addition, the small SAE previously pointed out (associated with the fact that the discharge is operated in α-mode) especially explains why the AAE model underestimates $V_{DC}/V_{e,PP}$ near sawtooth-up waveforms ($\Theta/\pi = 0.5$) and overestimates it near sawtooth-down waveforms ($\Theta/\pi = 1.5$).

Comparing now the two proposed models, the difference between the solid red curves and the blue dashed ones is low in all cases: hence, the imperfect control of the waveform at the feedthrough can only account for a small part of the difference between the AAE model and the experimental results. This source of error can therefore be neglected; however, results shown in the following sections of this manuscript will always rely on the measured feedthrough waveform rather than the target one. The two remaining possible sources of errors, i.e. calibration uncertainties and symmetry parameter variations, cannot be easily dissociated. The observation of the SAE shows that ε indeed varies and explains part of the deviations, however, errors in calibration may also come into play as will be shown in the next section.

II.1.2.c Impact of calibration errors

In this subsection, a theoretical study of the impact of erroneous estimations of the correction factors used for calibration will be carried out. To this aim, the evolution of $V_{DC}/V_{e,PP}$ with the waveforms will be computed theoretically and the effect of errors in the calibration will be assessed separately for each correction factor. As previously explained, the observation of the SAE (Figure II.6) shows that the theoretical AAE model is anyhow insufficient to describe the experimental data. The objective of this section is therefore solely to demonstrate that at least some of the discrepancy can also be attributed to the imperfect calibration method.

Theoretical results are shown in the graphs in Figure II.7 for the case n = 3. The evolution of $V_{DC}/V_{e,PP}$ is shown as a function of Θ, using Equation (II.4) to compute the theoretical V_{DC} and assuming $\varepsilon = 0.47$ (constant). Notice that other constant values for ε lead to identical results, all $V_{DC}/V_{e,PP}$ curves in Figure II.7 would simply be shifted vertically to higher values (if $\varepsilon > 0.47$) or lower values (if $\varepsilon < 0.47$). In all graphs, the solid red curves show the theoretical result with an ideal waveform. Other curves correspond to the expected result when misestimating one of the

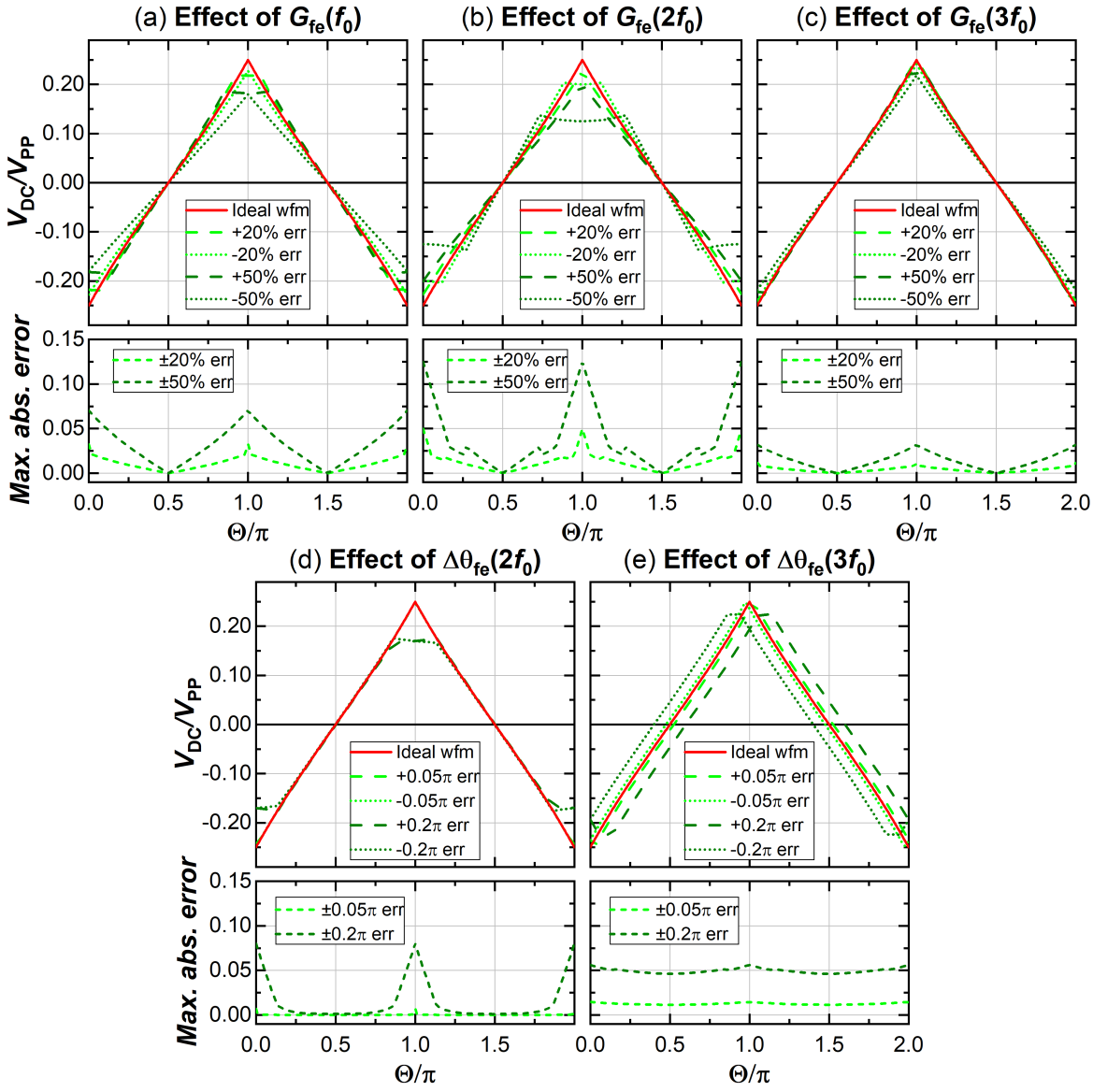

Fig. II.7: Theoretical AAE model results obtained with ideal waveforms compared with results obtained with erroneous correction factors in the calibration method. All bottom graphs show the maximal absolute error in $V_{DC}/V_{e,PP}$ introduced by errors in the corresponding correction factors.

five correction factors (assuming the other factors are exact). Notice that higher-order effects – i.e. simultaneous variations of two or more factors – are therefore not captured by this analysis. For gain factors, errors of ±20 and ±50% are assumed, while for the phase-shift correction, the effect of an over- or underestimation by 0.05π and 0.2π is shown. The bottom line graphs in Figure II.7(a-e) show the maximal absolute error that arises when misestimating each factor independently.

It should first be highlighted that the global trend is quite robust against misestimated correction factors: even with the highest considered errors, the inverted-V shape of $V_{DC}/V_{e,PP}$ is maintained to some degree for all factors. However, the propagation of errors coming from the estimation of the waveform at the electrode is not obvious. For instance, the trend for $V_{DC}/V_{e,PP}$ around pulse-like waveforms ($\Theta/\pi = 0$ or 1) is very sensitive to the gain correction factor values of the first two frequencies, as seen in Figure II.7(a-b). In contrast, a misestimated gain correction for the second harmonic, $G_{fe}(3f_0)$, is barely affecting the trend, as seen in Figure II.7(c). In the case of the phase-shift correction, a misestimated value of $\Delta\theta_{fe}(2f_0)$ only affects the $V_{DC}/V_{e,PP}$ trend locally – also near pulse-like waveforms – as shown by the graphs in Figure II.7(d). On the other hand, the trend for $V_{DC}/V_{e,PP}$ is very sensitive to errors in $\Delta\theta_{fe}(3f_0)$ for all waveforms, Figure II.7(e).

Comparing these theoretical curves with the experimental behavior of $V_{DC}/V_{e,PP}$ displayed in the previous section (Figure II.6), it appears that at least part of the discrepancies may be explained by an imperfect calibration. In particular, the largest deviations from the model have been shown to arise for pulse-like waveforms and could be attributed to erroneous estimations (or variations) of the factors $G_{fe}(f_0)$, $G_{fe}(2f_0)$ and $\Delta\theta_{fe}(2f_0)$. Nevertheless, the AAE effect (as well as a small SAE) is clearly observed and the amplitude of the experimental $V_{DC}/V_{e,PP}$ curves are large enough to obtain significant variations in ion bombardment energy.

In conclusion to this section, the calibration underdone with open-chamber conditions (no plasma) has been shown to be adequate in the case of the Ar discharge: the experimental behavior of $V_{DC}/V_{e,PP}$ is both quantitatively and qualitatively in agreement with the predictions from the simplest AAE model. Three possible sources of errors have been highlighted in the section II.1.2.a and are recalled here:

1. Imperfect control of the waveform set at the feedthrough,
2. Errors and/or variations in the correction factors $G_{fe}(kf_0)$ and $\Delta\theta_{fe}(kf_0)$,
3. Variations of the symmetry factor, ε.

From these potential sources, the first one has been shown unimportant, and most of the deviations are linked to the sources (2) and (3), which are less easily discriminated but may equally contribute.

The calibration method and the values of the correction factors might, however, not hold for other discharges, for instance when the Slope Asymmetry Effect [8, 12] becomes dominant and not theoretically predictable. In particular, the SF_6/O_2 mixture that will be investigated is known to be highly electronegative: the plasma bulk conductivity becomes low and the impedance of the plasma may significantly alter the electrical model.

Nevertheless, we will assume that the calibration is still valid in the case of the SF_6/O_2 discharge in the investigated conditions. In particular, the waveforms set at the feedthrough have not been observed to change significantly upon SF_6/O_2 plasma ignition, suggesting that the plasma impedance does not alter the waveform at the electrode. Now that the calibration method has been detailed and validated experimentally for the Ar discharge, references to “waveforms” in the following parts of this manuscript will always correspond to the voltage at the electrode.

II.2 Amplitude and Slope Asymmetry Effects in the SF_6/O_2 discharge

As explained in Chapter I, the response of plasmas to excitation by TVWs strongly depends on the discharge properties, in particular its electropositive or electronegative nature. For an electropositive Ar discharge such as investigated in section II.1, power coupling is mostly ensured by sheath expansion electron heating (discharge operated in α-mode) and the Amplitude Asymmetry Effect (AAE) is dominant. A relatively small Slope Asymmetry Effect (SAE) can still be observed, and ionization shows a maximum near the rapidly expanding sheath. The power coupling mode in electronegative discharges may, in contrast, be dominated by Drift-Ambipolar (DA) electron heating, in particular due to the low bulk conductivity, for instance demonstrated in the case of a CF_4 plasma, [13–15]. The DA power coupling mode especially leads to a strong SAE, where maximal ionization is now found near the rapidly contracting sheath (in contrast to electropositive discharges).

The primary objective of the work presented in this manuscript is the investigation of silicon nanotexturing using SF_6/O_2 plasma etching. The electronegative nature of the SF_6/O_2 plasma is well-known, but the effect of TVW excitation in such discharge has not been investigated in literature: it is the purpose of the following study. In particular, the effect of several discharge parameters (such as the pressure, coupled power and SF_6 content) on the relative importance of the amplitude and slope asymmetry effects will be examined in a range of process conditions relevant for silicon nanotexturing. These "relevant conditions" will be investigated and discussed in Chapter III, but should here be partly announced in anticipation, as they constrain the limits of the following study. Earlier experiments on silicon nanotexturing with SF_6/O_2 plasma have been carried out at the LPICM (on the same experimental setup, not published). An adequate process window, i.e. leading to satisfactory anti-reflection properties of nanotextured silicon surfaces, was identified depending on two parameters in particular: (i) discharge pressure around 30 mTorr, (i.e. the lowest achievable value in the current implementation of the setup); (ii) SF_6 content (in the input gas flux) around 50 to 60%. The range of parameters explored in the following study therefore focuses in particular on these values, which are consistent with literature [16–18].

II.2.1 Comparison of SF_6/O_2 with Ar and O_2

In order to systematically study the response of the discharge to various shapes of voltage waveform, the phase-shift Θ in Equation (II.5) has been varied from 0 to 2π, all while keeping the coupled power, discharge pressure, and incoming gas flux constant. Scanning the waveforms in this manner allows one to observe the effects of both the amplitude and slope asymmetries. Indeed, on the one hand, "pulse-like" waveforms – i.e. "peaks" (for $\Theta/\pi = 0$) and "valleys" ($\Theta/\pi = 1$) waveforms – are those with the greatest difference between V_{max} and $|V_{min}|$; the amplitude asymmetry effect should therefore be maximal for these waveforms. On the other hand, "sawtooth-up" ($\Theta/\pi = 0.5$) and "sawtooth-down" ($\Theta/\pi = 1.5$) waveforms have the feature that $V_{max} = |V_{min}|$, so any amplitude asymmetry effect is absent. However, the rising and falling slopes of the waveforms are very different, and the presence of any slope asymmetry effect will be amplified. As well, for comparison, the electrical parameters obtained with a standard RF excitation (frequency of 13.56 MHz) were also acquired.

Measurements have been made with Ar, O_2, and SF_6/O_2 discharges excited by the voltage waveforms described above. For the studies described in this section, the SF_6 content in the incoming SF_6/O_2 gas mixture is set to 57%. Figure II.8(a) shows the evolution of the peak-to-peak voltage V_{PP}, Figure II.8(b) shows the DC self-bias V_{DC}, and Figure II.8(c) shows the normalized value V_{DC}/V_{PP} for all types of waveforms and for the three gas mixtures, all for a pressure of 30 mTorr and a coupled power of 10 W.

The variation in V_{PP} observed in Figure II.8(a) is a result of the condition of keeping the coupled power constant, as the value of V_{PP} required to achieve the desired discharge power significantly varies with waveform shape. At equivalent power, the value of V_{PP} is greater for sawtooth-like waveforms ($\Theta/\pi = 0.5$ and 1.5) than for pulse-like waveforms ($\Theta/\pi = 0$ and 1). This can be intu-

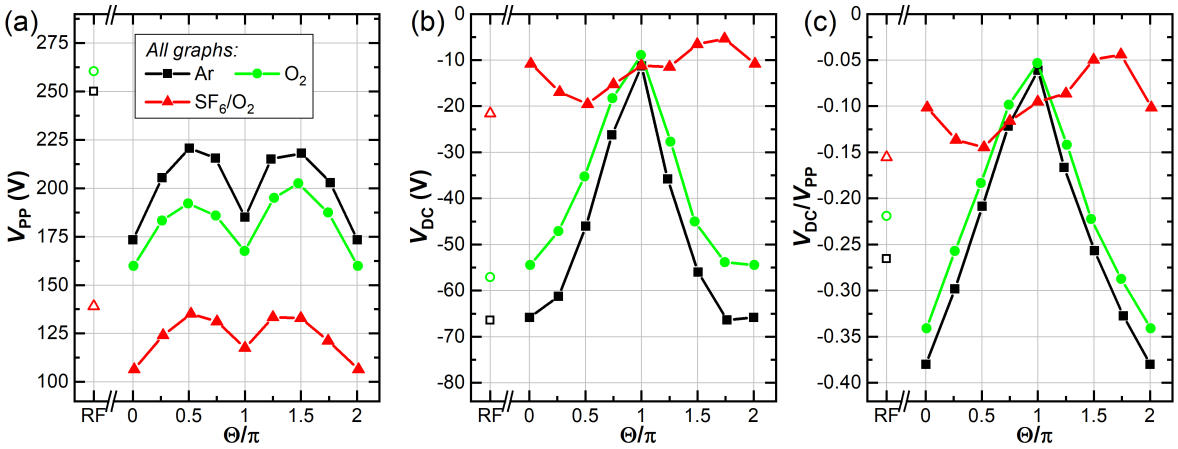

Fig. II.8: Evolution of V_{PP} (a), V_{DC} (b), and V_{DC}/V_{PP} (c) with single frequency RF excitation (open symbols) and for TVWs (solid symbols) when spanning voltage waveforms by varying Θ over $[0,2\pi]$ for Ar, O_2 and SF_6/O_2 (SF_6 flux fraction of 57%) discharges operated at constant pressure and power (respectively 30 mTorr and 10 W).

itively understood by assuming that the faster the sheath expansion, the more efficient the electron heating. Therefore, for pulse like waveforms, a peak in the electron heating is expected both in front of the grounded and powered electrode during one RF period. In contrast, for sawtooth-like waveforms, only one of the sheaths experiences a fast expansion per RF period (e.g. the powered electrode sheath in the case of sawtooth-up waveforms), requiring a greater V_{PP} to couple the same power to the plasma.

In Figure II.8(b-c), V_{DC} and V_{DC}/V_{PP} profiles typical of a situation with a dominant amplitude asymmetry is clearly observed for the Ar and O_2 discharges; V_{DC}/V_{PP} has a maximum (in absolute value) for peaks waveforms, and a minimum for valleys waveforms (Figure II.8(c)). Moreover, only a small difference in V_{DC}/V_{PP} is observed for sawtooth-up and sawtooth-down waveforms (at $\Theta/\pi = 0.5$ and 1.5, respectively), indicating that only a weak slope asymmetry effect is present for these conditions. Finally, one more element of information can be obtained from this curve, as the relative values at $\Theta/\pi = 0.5$ and 1.5 indicate whether the plasma has an electropositive or electronegative character [13, 19]. For both the Ar and O_2 mixtures, the value of V_{DC} (Figure II.8(b)) is slightly more negative for the sawtooth-up waveform, and this behavior is characteristic for an electropositive discharge where the sheath expansion electron heating (also named α-mode) is dominant. The results obtained for the pure O_2 discharge (here powered in α-mode when driven by TVWs) are consistent with what has been observed by Derzsi *et al.* [20]. However, it should be noted that a hybrid (α-DA)-mode can also be obtained for O_2 discharges under similar conditions of pressure when standard RF excitation is used. In such a case, the transition from α- to DA-mode is thought to be due to the change in sheath expansion heating efficiency when varying V_{PP}. However, it is not possible to discriminate one mode from the other by only probing electrical parameters. For the discharge conditions generated by the sawtooth TVWs, the O_2 discharge appears to be behaving as did the Ar one, giving relative values of V_{DC} consistent with an electropositive discharge.

The evolution of the DC self-bias voltage with waveform shape in the case of SF_6/O_2 is quite different from the other two cases: indeed, it is observed that the extrema for V_{DC}/V_{PP} are now found near the sawtooth-up (minimum value) and sawtooth-down (maximum value) waveforms. This strongly indicates that in this case, the slope asymmetry effect dominates over the amplitude asymmetry effect. A similar situation has previously been observed for CF_4 discharges [15], and was attributed to the strong electronegativity of the plasma. Indeed, in such cases, as explained in the introduction of this section, the electron heating is predominantly ensured through DA-mode heating: a stronger ionization is obtained in front of the rapidly contracting sheath, due to the combination of a drift electric field in the plasma bulk and to an ambipolar electric field at the sheath edge, accelerating electrons towards the electrode [21]. The balance of ion fluxes arriving

at the powered and grounded electrode is therefore modified (e.g. for sawtooth-down waveforms, the rapid sheath contraction occurs in front of the powered electrode; more ionization is obtained there and the geometrical asymmetry of the discharge is partly compensated by an increased flux of positive ions arriving at the powered electrode). It can also be noted that the DC self-bias is decreased (in absolute value) compared to its value for Ar and O_2 discharges. However, this can mainly be attributed to the condition of constant power, as the SF_6/O_2 discharge requires a much lower V_{PP} for the same coupled power.

II.2.2 Power Coupling Mode Transitions in SF_6/O_2

II.2.2.a Influence of SF_6 content

In the previous section, it has been shown that the power coupling mode for an SF_6/O_2 discharge is completely different from that of an Ar or a pure O_2 discharge (for the conditions used). One could therefore expect to observe a power coupling transition when slowly adding SF_6 to an O_2 discharge. If the plasma were driven by a sawtooth-like voltage waveform, this would involve a change in the excitation peak location, from the fast-expanding sheath to the fast-contracting one. In a perfectly geometrically **symmetric** reactor, this would cause a change in sign in V_{DC} . In a geometrically **asymmetric** reactor, observing this change through the V_{DC} would not be straightforward; the change in V_{DC} associated to a change in coupling mode would be superimposed on top of that caused by the geometrical asymmetry. Furthermore, at constant power, V_{PP} would be changing as well, masking the change.

For these reasons, in this section, we propose to instead observe the relative, normalized values of V_{DC} for mirror versions of sawtooth-like voltage waveforms. In doing so, one can remove (to a first order) the effect of both the geometrical asymmetry and any changes in V_{PP}. Conceptually, we note if when switching the fast expanding sheath from the RF electrode to the grounded electrode, the V_{DC}/V_{PP} increased or decreased in magnitude.

In order to more precisely investigate this possibility, a second type of waveform (first proposed in [8]) has been used, consisting of the truncated Fourier series of an ideal sawtooth-up (minus sign) or sawtooth-down (plus sign) signal (see Figure II.9) corresponding to:

$$\widetilde{V}(t) = \pm\, V_0 \sum_{k=1}^{n} \frac{1}{k} \sin(2\pi k f_0 t) \tag{II.8}$$

When these sawtooth-like waveforms are applied, no amplitude asymmetry effect can arise since $V_{max}$and $|V_{min}|$ are equal. Any differences in the electrical response of the plasma to sawtooth-up versus sawtooth-down waveforms can therefore only be attributed to a slope asymmetry effect. Using sawtooth-down waveforms as an example, it can be shown that the ratio of fall time over rise time (i.e. ratio of sheath expansion time over contraction time) is equal to the total number of harmonics applied, n (set to 3 in the current study).

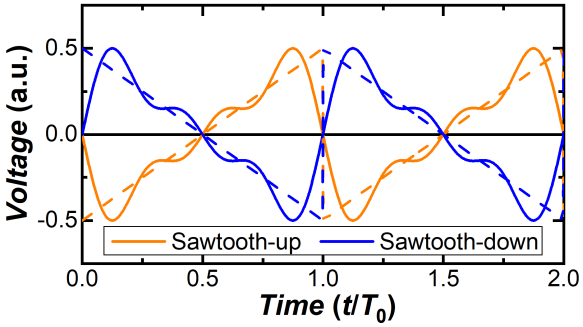

Fig. II.9: Ideal sawtooth waveforms (dashed curves) and their truncated Fourier decompositions (solid curves) obtained with Equation (II.8) and $n = 3$, the timescale is normalized by the signal period T_0.

In this section, the SF_6 content in the total SF_6/O_2 gas flux of 100 sccm has been varied at a constant discharge coupled power of 20 W for a pressure of either 30 or 120 mTorr. For the 120 mTorr conditions using TVW excitation, measurements are only provided up to a 50% mixture fraction of SF_6, as above this value, the discharge would extinguish at the targeted power. The measured electrical parameters of the obtained discharge (V_{PP}, V_{DC} and V_{DC}/V_{PP}) are shown in Figure II.10.

It may first be noted that at 30 mTorr and SF_6 content below 50%, the V_{PP} required to attain a given coupled power is higher in standard RF excitation than with TVWs. This observation is also valid at 120 mTorr for a pure O_2 discharge and is linked to the fact that collision-less electron heating scales with the square of the sheath velocity [10]; in TVW mode (including sawtooth-like waveforms), although the fundamental frequency remains identical, the higher frequency components induce a much faster sheath motion (in front of either the grounded or powered electrode).

A more difficult result to explain is the divergence between the values of V_{PP} for the sawtooth-up and –down waveforms, occurring at values of SF_6 content above 20% for the 30 mTorr case, Figure II.10(a), and at low values of SF_6 content (<30%) for the 120 mTorr case, Figure II.10(d). Ideally, one would expect these to show identical values. However, as previously stated, TVWs strongly influence energy loss per ion on each electrode in a geometrically asymmetric system, and so constant power is not a perfect proxy for plasma density. This point could be better investigated in the future in a geometrically symmetric system, or by directly measuring plasma density.

It is observed in Figure II.10(c,f) that for pure O_2 discharges at both 30 and 120 mTorr, $|V_{DC}/V_{PP}|$ is higher for sawtooth-down waveforms than for sawtooth-up waveforms. However, with an increasing fraction of SF_6 in the mix, this situation reverses itself, and $|V_{DC}/V_{PP}|$ for sawtooth-up waveforms becomes higher. At 30 mTorr (Figure II.10(c)), this crossing is observed for an SF_6 flux fraction of around 20%, while for 120 mTorr (Figure II.10(f)), the crossing occurs below the smallest SF_6 fraction that can be probed with the experimental setup (below 13%).

The change in relative value of $|V_{DC}/V_{PP}|$ for sawtooth-up vs sawtooth-down waveforms has been previously attributed to a change in the dominant heating mode in the plasma [19]. Depending on the power coupling mode, and as it has been highlighted previously, the ionization will be

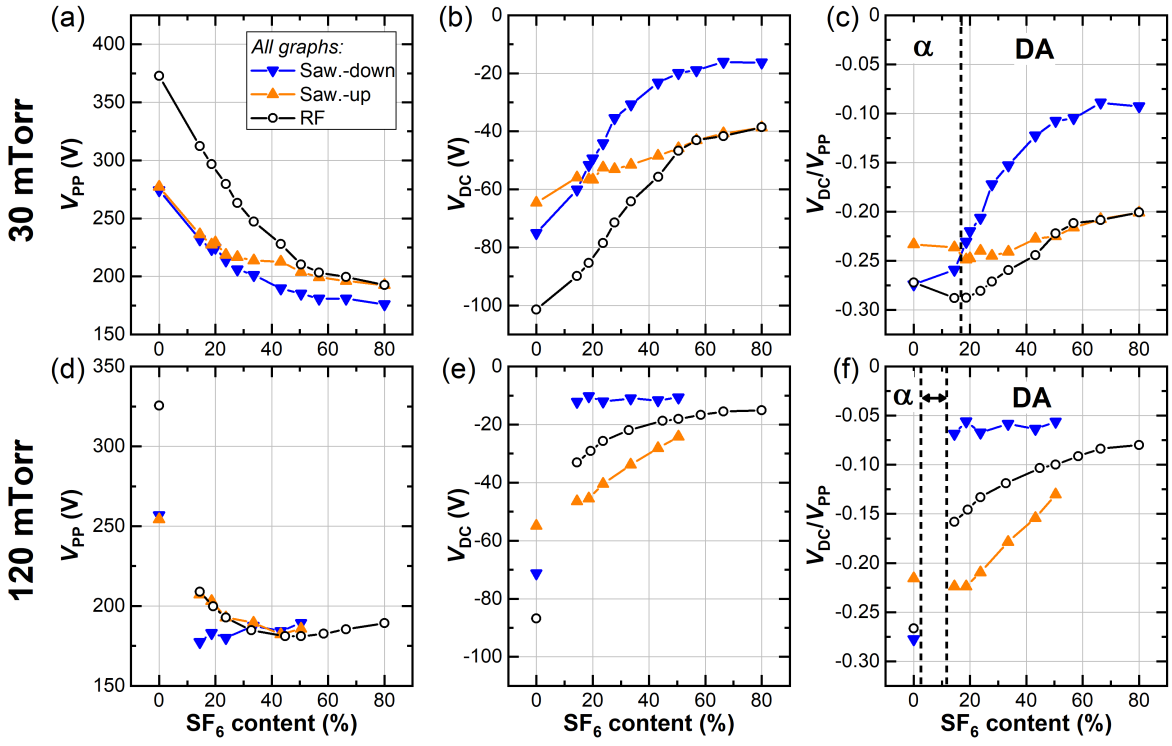

Fig. II.10: Evolution of V_{PP} (a,d), V_{DC} (b,e), and V_{DC}/V_{PP} (c,f) with SF_6 content in total incoming gas flux (100 sccm) for sawtooth-down, sawtooth-up and RF excitation. The coupled power is 20 W, and the discharge pressure 30 mTorr (a-c), and 120 mTorr (d-f). The legend is identical for all graphs.

greater in front of either the powered or grounded electrode, modifying $|V_{DC}/V_{PP}|$. For pure O_2 discharges, a higher value of $|V_{DC}/V_{PP}|$ for sawtooth-up is consistent with an electropositive behavior (dominant α-mode). However, when SF_6 is added to the discharge by increasing its fraction in the total incoming gas flux, the discharge is expected to evolve to a more electronegative behavior, as observed by Pateau *et al.* at similar pressures [22]. Undergoing such an evolution, it is expected that the DA heating-mode would become dominant.

Furthermore, the fact that the crossover occurs at a lower SF_6 content for the higher pressure is also consistent with previously observed results [21, 22] wherein increasing pressure also increased the electronegativity of the discharge, and the dominance of the DA heating mode. This dependence on pressure will be further examined in the following section.

II.2.2.b Influence of discharge pressure and power

In the previous section, a difference was noted in the gas mixture at which a change in the dominant power coupling mode occurred for two values of process pressure. In this section, this dependence on pressure is investigated in more detail. As it has been proposed that the dominant power coupling mode is indicated by the relative value of $|V_{DC}/V_{PP}|$ for the two types of sawtooth waveform, these values (V_{DC}/V_{PP}) are plotted as a function of discharge pressure in Figure II.11 for two different values of SF_6 fraction in the mixture and two values of coupled power.

When the fraction of SF_6 in the total incoming gas flux of SF_6+O_2 is 13% and for pressures below 35 mTorr (Figure II.11(a)), $|V_{DC}/V_{PP}|$ is just slightly higher for sawtooth-up than for sawtooth-down waveforms. When the pressure increases, the situation quickly reverses, and $|V_{DC}/V_{PP}|$ becomes much smaller for sawtooth-down waveforms, while it remains relatively constant for sawtooth-up waveforms (for the range of pressures investigated). This indicates a transition from a dominant

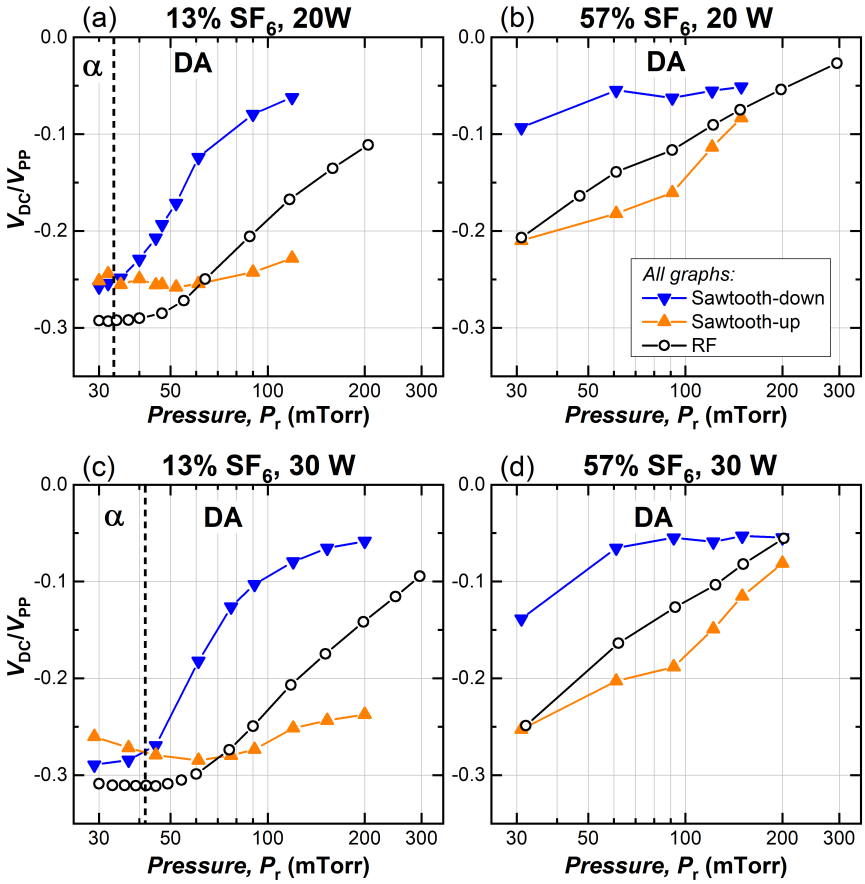

Fig. II.11: Evolution of V_{DC}/V_{PP} as a function of the discharge pressure for different incoming gas composition and power. The total incoming gas flux is 120 sccm in case (a-b) and 140 sccm in case (c-d).

α-mode (below 35 mTorr) to a DA-mode. When the SF_6 content in the gas mixture is increased to 57% (Figure II.11(b)), the power coupling is dominated by the DA-mode over the whole range of pressure investigated since $|V_{DC}/V_{PP}|$ with sawtooth-up waveforms is always higher than with sawtooth-down waveforms.

Similar experiments carried out at a higher power (30 W, Figure II.11(c-d)) demonstrate a similar behavior. Indeed, at 13% SF_6 content, a crossover (understood as a transition from α- to DA-mode) is again observed, while at 57% SF_6 the discharge is operating in DA-mode throughout the investigated range. Furthermore, at 13% SF_6 content, (Figure II.11(a,c)) an increase in the transition pressure from 35 to 40 mTorr is observed when increasing the power from 20 to 30 W. This stems from the promotion of sheath expansion heating when the voltage amplitude is raised at a fixed pressure [21].

Curiously, the difference between the relative values of $|V_{DC}/V_{PP}|$ for the two types of waveform decreases at higher pressure, although no cross-over occurs. This is a reminder of the limits of using the technique of comparing relative values of $|V_{DC}/V_{PP}|$ for the two types of sawtooth waveform. This technique relies on the fact that the difference in the sheath expansion/contraction rates for the two sides of the plasma is of non-negligible importance for the discharge conditions. Simply put, the contraction rate should appear "fast" on one side, but "slow" on the other. What is defined as "fast" and "slow" depends on the plasma conditions, principally pressure and gas mixture. At the higher pressures of Figure II.11, the difference in sheath speeds is beginning to be less important (or rather, the difference in ion generation and flux they generate is reduced), and so the differentiating nature of the voltage waveforms is fading.

II.3 Tuning Ion Energy and Flux using Tailored Voltage Waveforms in SF_6/O_2

The effects of powering the SF_6/O_2 discharge with TVWs in a CCP reactor have been investigated in detail in the previous section, close to the appropriate range of parameters for nanotexturing (as obtained previously in the lab, see introduction of section II.2). Transitions in dominant electron heating modes have been highlighted using mirror versions of sawtooth waveforms. In turn, the dominant asymmetry effect (either AAE or SAE) is modified and leads to completely responses of the discharge to the applied waveforms. In particular, the resulting DC self-bias is in particular affected, as well as the location of maximal ionization in the discharge.

In the present section, in-situ characterization using a Retarding Field Energy Analyzer (RFEA) system ([23], also described in Chapter I) is used to acquire Ion Flux Energy Distribution Functions (IFEDFs) on the powered electrode. This method will help investigate the evolution of (positive) ion bombardment energy and ion flux with the excitation signal: these variations will in particular be linked to the identified discharge powering mode. It should be highlighted that the RFEA grids cover an area of around 0.3 cm^2, and the openings consist of 37 holes (with a diameter of 800 µm). In subsections II.3.1 and II.3.1, the RFEA system will be placed at a fixed position on the powered electrode, with the sensor grids located at around 7.5 cm from the center of the electrode, as shown in the schematic of Figure II.12(a). In subsection II.3.3, the uniformity of the discharge will be assessed by moving the RFEA probe along the radius of the electrode, Figure II.12(b).

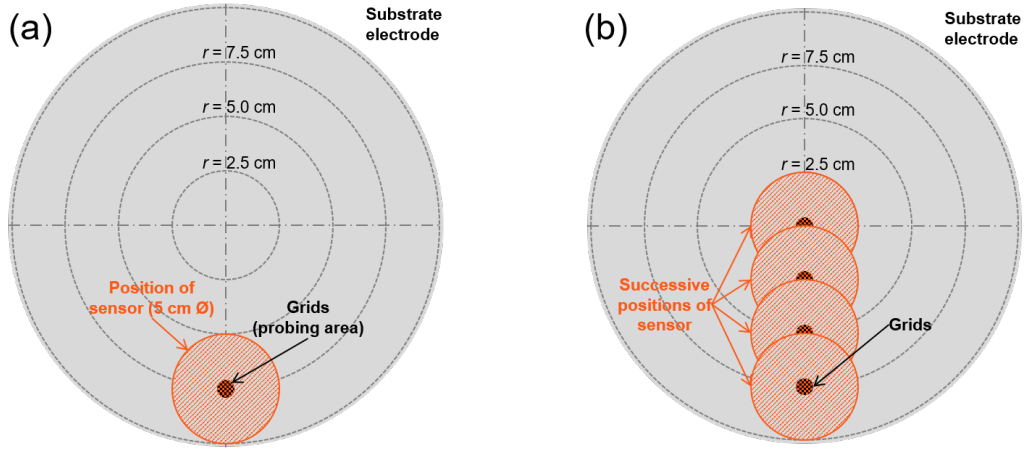

Fig. II.12: Schematics (to scale) of the RIE substrate electrode with the RFEA probe: (a) position for measurements depicted in sections II.3.1 and II.3.2, (b) its successive positions for measurements shown in section II.3.3.

II.3.1 Tuning Ion Flux Energy Distributions in SF_6/O_2

In this first section, a comparison of IFEDFs obtained with Ar and SF_6/O_2 discharges will be carried out. The underlying objective is to first demonstrate that TVWs indeed allow one to vary the process conditions at the substrate (powered) electrode (in terms of ion flux and energy) at a fixed value of coupled power (here 25 W in all conditions). Here in all cases the pressure is maintained at 30 mTorr, and the SF_6 content in the input gas flux is kept at 57% for the SF_6/O_2 discharge. Secondly, the IEDF measurements give the opportunity to definitively validate this hypothesis in the case of SF_6/O_2 by comparing the calculated "theoretical" ion bombardment energy with the experimental measurements. Indeed, the calibration method presented in section II.1.1 was for now experimentally validated with Ar only, with the assumption that it remains valid for other discharges – for which cases the plasma impedance may greatly differ.

In this section, the employed waveforms are again expressed by Equation (II.5), section II.1.2.a, with $n = 3$ (three frequency components, 13.56 MHz and two upper harmonics). These measure-

ments are again often compared to single frequency excitation (13.56 MHz) and this case is labeled "RF" as in the rest of the manuscript.

II.3.1.a Comparison of SF_6/O_2 and Ar

Graphs in Figure II.13 show the evolution of the IEDFs on the powered electrode with the applied voltage waveform in Ar and SF_6/O_2 discharges (notice that both the flux density and energy scales are different from one graph to the other). The RF case (bottom curves in both graphs) correspond to a sinusoidal voltage excitation and the TVW excitation cases are shown above, from $\Theta/\pi = 0$ (peaks waveforms) to $\Theta/\pi = 1.75$. Regarding first the results with Ar (left graph), it can be observed that all curves are relatively "flat", with a significant flux at all energies below E_{max} so that E_{avg} is much lower than E_{max} in all cases: it can thus be deduced that the sheath is relatively collisional. Finally, the qualitative evolution of E_{max} with the applied voltage waveforms corresponds to the expectation: the average sheath voltage drop is maximal for peaks waveforms ($\Theta/\pi = 0$) and minimal close to valleys waveforms ($\Theta/\pi = 1$). Notice that the actual minimal value of E_{max} with Ar is here found for $\Theta/\pi = 0.75$, but measurement uncertainties – shown later in Figure II.15 – may alter the analysis. Between peaks and valleys waveforms, it is demonstrated that E_{max} (and E_{avg}) can be varied continuously.

Regarding now the SF_6/O_2 discharge operated in the same conditions (IFEDFs shown in the

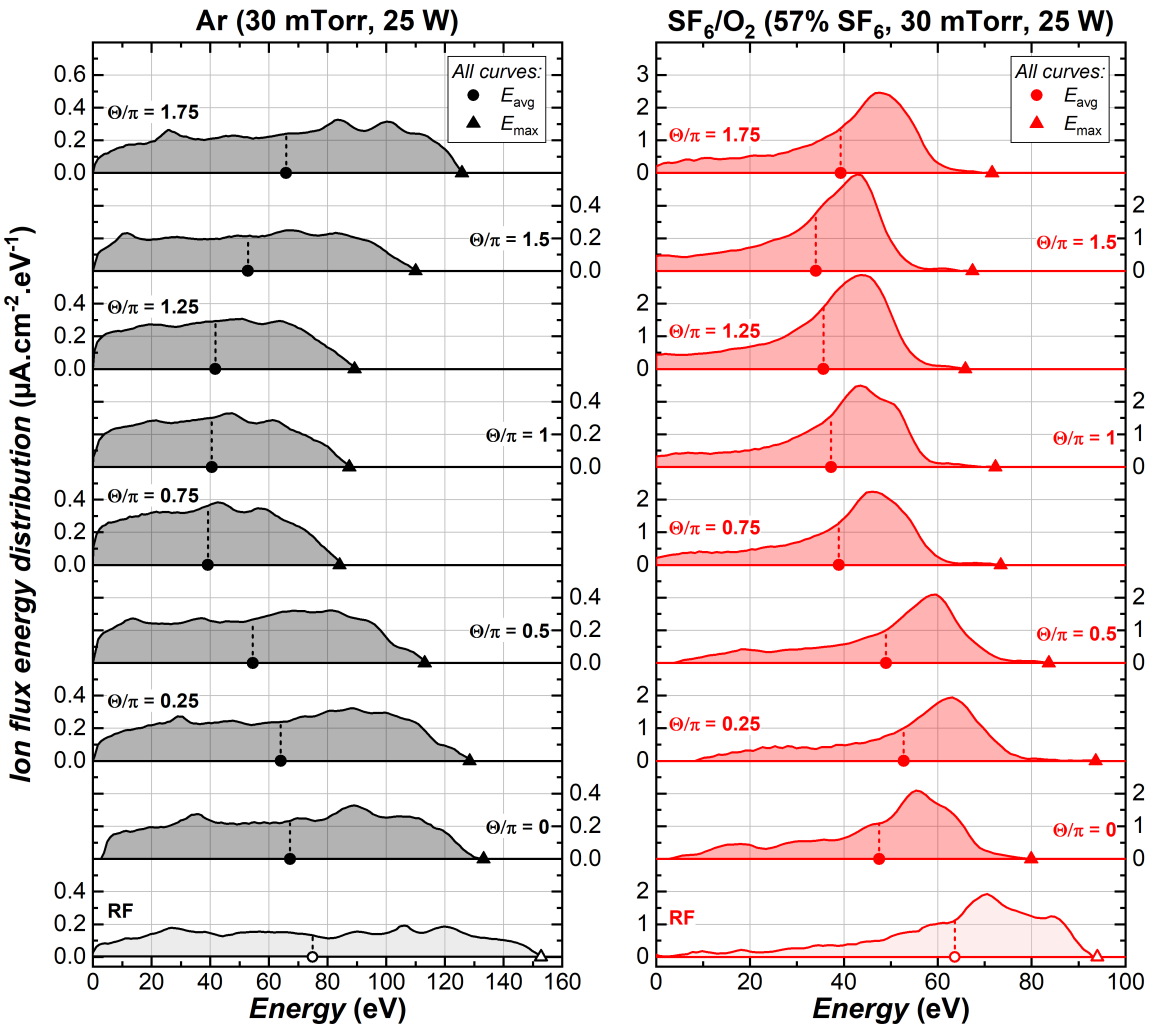

Fig. II.13: Evolution of IFEDFs with applied voltage waveform in Ar (left) and SF_6/O_2 with 57% SF_6 in input gas flux (right) at 30 mTorr and 25 W in the single-frequency RF case (bottom curves in both graphs) and with TVW excitation, from $\Theta/\pi = 0$ to $\Theta/\pi = 1.75$.

right graph in Figure II.13) the situation is quite different. First, the IFEDFs all present a significant peak (sometimes with an apparent bimodal nature, e.g. in the RF case): the sheath is therefore less collisional than in the Ar case. Moreover, the IFEDFs show quite a "long tail" at high energies compared to the case of Ar, so that the estimations of E_{max} are blurred by large uncertainties. With TVW excitation, the evolution of E_{max} and E_{avg} with the applied voltage waveforms also greatly differs from the Ar case, due to the different power coupling mode (DA-mode rather than α-mode). Indeed, in the last section, it was demonstrated than in the considered conditions, the Ar discharge is operated in α-mode and the AAE is dominant; for SF_6/O_2 in the same conditions of power and pressure, the discharge is operated in DA-mode with a dominant SAE. As a consequence, the extreme values of E_{max} are not found for pulse-like waveforms, although it is still possible to vary E_{max} continuously by slightly altering the waveforms. This behavior is consistent with the variation of V_{DC} observed for a similar discharge in the previous section.

Figure II.14 shows the evolution of the total ion flux (ϕ_{tot}, integral of IFEDF) for all the cases displayed in Figure II.13. In all cases, the total ion flux is much greater for the SF_6/O_2 discharge than for Ar. Regarding the evolution of the total flux with the applied voltage waveform, the trends are opposite in Ar and SF_6/O_2 with TVW excitation. For the SF_6/O_2 discharge, a maximal flux is observed for $\Theta/\pi = 1.25$ and a minimal value for $\Theta/\pi = 0.25$, while an opposite trend is found for Ar (although due the measurement uncertainties the actual extremes for Ar are more delicate to identify). The position of the extreme values of ion fluxes in the case of Ar and SF_6/O_2 are difficult to interpret. However, it should be recalled that for sawtooth-like waveforms ($\Theta/\pi = 0.5$ or 1.5) the location of maximal ionization in the discharge depends on the dominant electron heating mechanism. For Ar, operated in α-mode, maximal ionization is expected in front of the powered sheath for sawtooth-up waveforms ($\Theta/\pi = 0.5$), while for SF_6/O_2 due to dominant Drift-Ambipolar electron heating maximal ionization is expected in front of the powered electrode for sawtooth-down waveforms $\Theta/\pi = 1.5$. This interpretation will be further explored in the next section when observing the transition from α-mode to DA-mode in an SF_6/O_2 discharge.

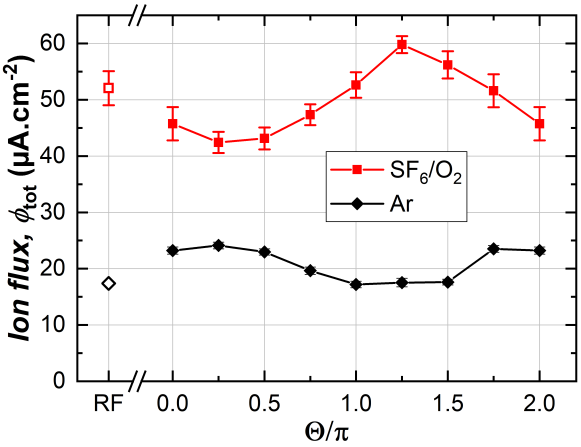

Fig. II.14: Variations of total collected ion flux with applied voltage waveform for Ar and SF_6/O_2 (with 57% SF_6 in input gas flux) at 30 mTorr and 25 W.

II.3.1.b Comparison of estimated ion bombardment energy with experiments

From an experimental point of view, rapid process developments can require an estimation of the ion bombardment energy (either average or maximal) based only on the input voltage waveform. Full IFEDFs measurements are also not always possible or simple to achieve (e.g. lack of mechanical access to the chamber, deposition conditions...). In Chapter I, a computation of the ion bombardment energy was proposed according to the following equation:

$$E_{calc} = q(\bar{V}_{pl} - V_{DC}) \tag{II.9}$$

where $\bar{V}_{pl}$ is the time-averaged plasma potential and q the (positive) ion charge. E_{calc}, from Equation (II.9), represents the theoretical ion bombardment energy for a collisionless sheath, in case the ion transit time τ_i much greater than the period of the RF voltage, T_0, and under these assumptions $E_{calc} = E_{max}$, [24]. If $\tau_i \sim T_0$ (or τ_i just a few times larger than T_0), the distribution becomes bimodal, [25], and $E_{calc} = E_{avg}$. Here, with both Ar and SF_6/O_2, the sheath is observed to be collisional, and with SF_6/O_2 a bimodal distribution has been demonstrated. In such case, E_{calc} cannot easily be quantitatively compared to either E_{max} or E_{avg}. However, even in the case of a strongly collisional sheath, the IFEDF usually presents a long tail at the high energy end due to the small fraction of ions that do not collide during their transit: E_{calc} is thus expected to underestimate E_{max} but have a similar qualitative evolution.

It has also been shown that for a periodic voltage waveform, the time-averaged plasma potential can be computed using the equation below, [26]:

$$\bar{V}_{pl} = \frac{-V_{min}}{V_{PP}} \left(\frac{V_{max}}{V_{PP}} V_{PP} + V_{DC} \right) \tag{II.10}$$

The assumptions used for Equation (II.10) are the following: (i) the potential in the plasma bulk is a linear function of the applied RF voltage; (ii) the potential drop in the plasma bulk is negligible; (iii the sheaths fully collapse at some point in the RF period; (iv) there is no field reversal. In the experiments, V_{DC} is measured while V_{min}, V_{max} and V_{PP} (reminder: at the electrode) are estimated from the measurements at the feedthrough using the calibration method presented in section II.1.1.

Experimental values of E_{avg} and E_{max} are shown in Figure II.15 below (same values as in Figure II.13, here shown with additional error bars) as a function of Θ/π, along with the estimations of E_{calc} based on Equation (II.10). As expected, it is observed that E_{calc} always significantly underestimates E_{max}. However, the qualitative evolution of E_{calc} with the applied voltage waveform is generally in agreement with the variations of E_{max} (this is not surprising as the variation in E_{max} is especially controlled by the evolution of V_{DC} which is used in the computation of E_{calc}). An exception still appears for the case of valleys waveforms ($\Theta/\pi = 1$) especially in SF_6/O_2, where E_{calc} is very low compared to the measurements: this might indicate that the control of the valleys waveform is not very good (in particular the calibration method might be failing in this case).

Nevertheless, in these two cases, the values of E_{calc} seem to give a relatively good first approximation for the order of magnitude of the ion bombardment energy and its variations with the

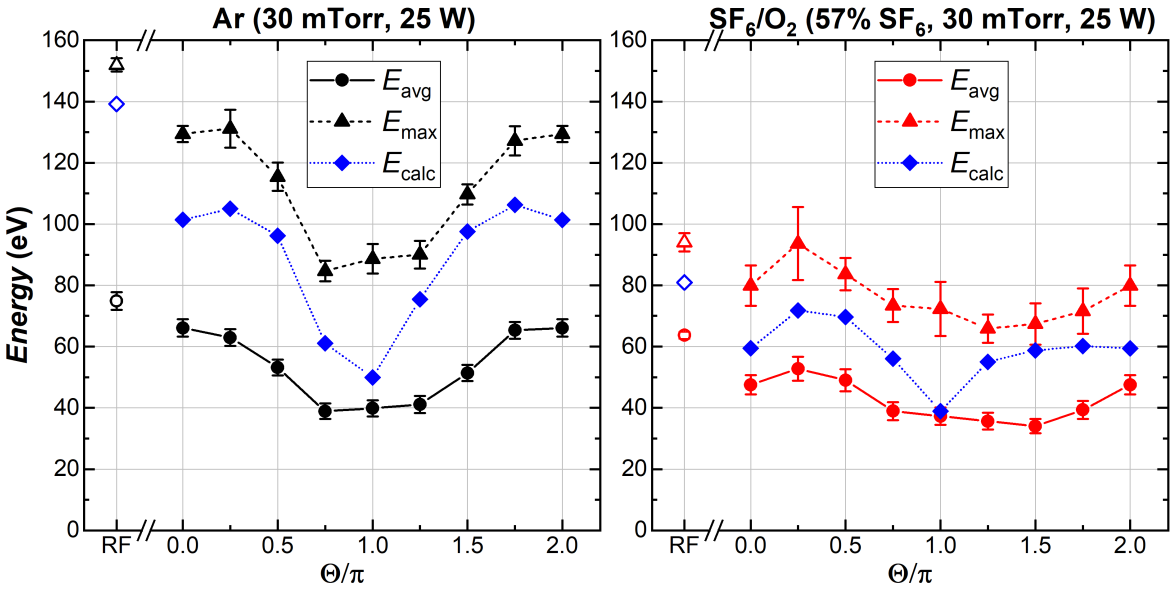

Fig. II.15: Variations of average, maximal and calculated – using Equation (II.9) – ion bombardment energy with applied voltage waveform for Ar (left) and SF_6/O_2 (right).

applied voltage waveform, and can be used as a rapid estimation method. In the following sections, we will continue plotting the values obtained for E_{calc} in comparison with E_{avg} and E_{max} to show that this statement is also valid for other conditions investigated in this work.

II.3.2 Effects of Power Mode Transitions in Decoupling Ion Energy and Flux

The comparison between Ar and SF_6/O_2 has shown the different effects of TVW excitation on IFEDFs depending on the dominant electron heating mode. In particular, the evolution of the ion flux and mean (or maximal) ion energy will vary depending on the power coupling mode. In section II.2.2, it was in particular demonstrated that, for an SF_6/O_2 discharge, a transition in dominant electron-heating was observed with the SF_6 content in the input gas flux. The discharge has indeed been shown to be operated in α-mode at low SF_6 content and in DA-mode at high SF_6 content and this transition is expected to have major effects both on the ion energy (notably due to different variations of V_{DC} with the applied waveform) and to the ion flux due to the reversal of effect in SAE.

II.3.2.a Effect of SF_6 content

From the results of section II.2, it has been shown that at 30 mTorr and a coupled power of 25 W, sheath expansion heating is dominant if the SF_6 content is low (below around 18%), while Drift-Ambipolar heating becomes preponderant above this value. IFEDFs measurements have therefore been obtained with varying waveforms for different values of SF_6 content in the input gas flux.

Results are shown in the graphs Figure II.16 (here the full IFEDFs are not shown, but only aggregate values). As expected, variations of ion energy and ion flux for a pure O_2 discharge are therefore very similar to those obtained for Ar. For an SF_6 content of 17% (i.e. a value close to the mode transition threshold), the variations of ion energy are quite similar, but the ion flux has nearly doubled for all Θ/π, and it stays quite flat. Interestingly, this is the sole case that has been

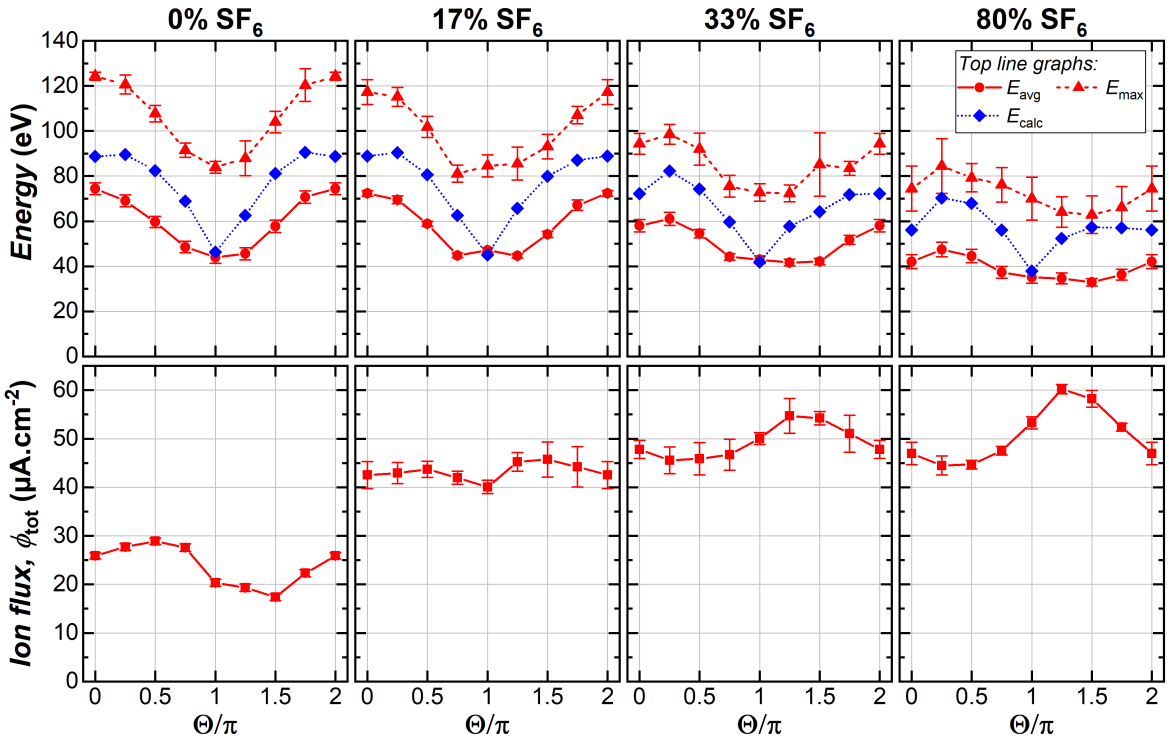

Fig. II.16: Influence of applied waveform on ion bombardment energy (top line graphs) and total collected ion flux (bottom line graphs) for different values of SF_6 content in the input gas flux of an SF_6/O_2 discharge (at 30 mTorr and 25 W).

observed in this work where the ion flux is almost constant with the waveforms (within the measurement uncertainties). A "true" – although not perfect – decoupling is here obtained, i.e. the mean (or maximal) ion bombardment energy can be varied in a large range (from 80 to 120 V for E_{max}) without significantly changing the total ion flux (around $10\%_{rel}$ difference between lowest and highest value). At 33 and 80% SF_6 content in the input gas flux the evolution of ion flux and energy are qualitatively similar (e.g. the position of maximal and minimal values versus Θ/π are unchanged for E_{avg} and ϕ_{tot}) and consistent with the measurements made with 57% SF_6 content discussed previously (section II.3.1). For these "high SF_6 content" cases only the magnitude of the ion energy and flux is changed: for all voltage waveforms, increasing the SF_6 content leads to a decreased E_{avg} or E_{max}. Regarding the ion flux, increasing the SF_6 content from 33 to 80% leads to an increased flux for $\Theta/\pi = 1.25$ and 1.5, while for other waveforms similar values are found (within uncertainties).

Finally, notice that the qualitative evolution of the calculated ion bombardment energy E_{calc} is generally in agreement with the evolution of E_{max} for SF_6 contents between 0 and 33%, as seen in the top line graphs in Figure II.16. A notable exception (already pointed out in section II.3.1) is however observed for the cases at $\Theta/\pi = 1$, where E_{calc} falls well below the general trend. At 80% SF_6 content, however, large qualitative deviations are observed and E_{calc} for instance does no longer adequately predict the position of the minimal value of E_{max}.

These results first show that a "true" decoupling of ion flux and ion bombardment energy cannot be obtained in the investigated conditions (except for a single value of 17% SF_6 content as highlighted before). Moreover, the dominant electron heating mode will have a dramatic effect on the relationship between the ion flux and energy.

II.3.2.b Extended process conditions "playground" in SF_6/O_2

Although only a partial decoupling between ion flux and ion energy has been shown using TVWs in SF_6/O_2 discharges, it is still possible to extend the available playground dictated by single-frequency RF excitation. To demonstrate this possibility, measurements are carried out with single-frequency excitation at different values of coupled power and then compared to results obtained when introducing TVW excitation in identical discharge conditions.

RF baseline. With a SF_6/O_2 discharge (57% SF_6 30 mTorr), the substrate electrode is fed with a sinusoidal RF voltage ($f_0 = 13.56$ MHz) with increasing V_{PP}: the IFEDF is recorded for different values of coupled power (from 5 to 45 W). The results are shown in Figure II.17: graph (a) presents the IFEDFs, graphs (b) and (c) respectively show the evolution of the ion energy and the ion flux with the input peak-to-peak voltage. In particular in graph (b), both the mean and average ion energy measured with the RFEA are shown, along with the result of the computation using Equation (II.9).

In Figure II.17(a), it is observed that at low coupled power (from 5 to 20 W) the measured IFEDFs show a clear maximal peak (close to the E_{max}) – the peak is either singular or the energy resolution too low. At higher values of coupled power, a bimodal distribution seems to arise at high ion energies. Although the peaks of the bimodal distribution are not always well distinguished, the local maxima are observed to split further with increasing coupled power. These observations are consistent with the aforementioned hypothesis: the sheath voltage oscillation time is lower than the ion transit time in the sheath but the difference is low, so that the final energy of an ion depends on the time (in the RF period) at which it entered the sheath. Moreover, several types of ions (with different masses) are expected to impinge on the surface, which might contribute to the multiple peaks observed in the distribution, as explained in Chapter I, section I.1.1.b. Some secondary peaks are also seen (e.g. measurement at 15 W) however their interpretation is challenging as they may in some case be explained by noisy data. Indeed, as a reminder, the RFEA measures an I-V curve which is numerically differentiated to obtain the IFEDF: even with a smoothing with a Savitzky-Golay approach [27], the numerical derivation is sensitive to the signal-to-noise ratio in the I-V data. For this reason and due to the low resolution (1 V steps in the I-V curve), interpretations will here focus on the most prominent features of the IFEDFs.

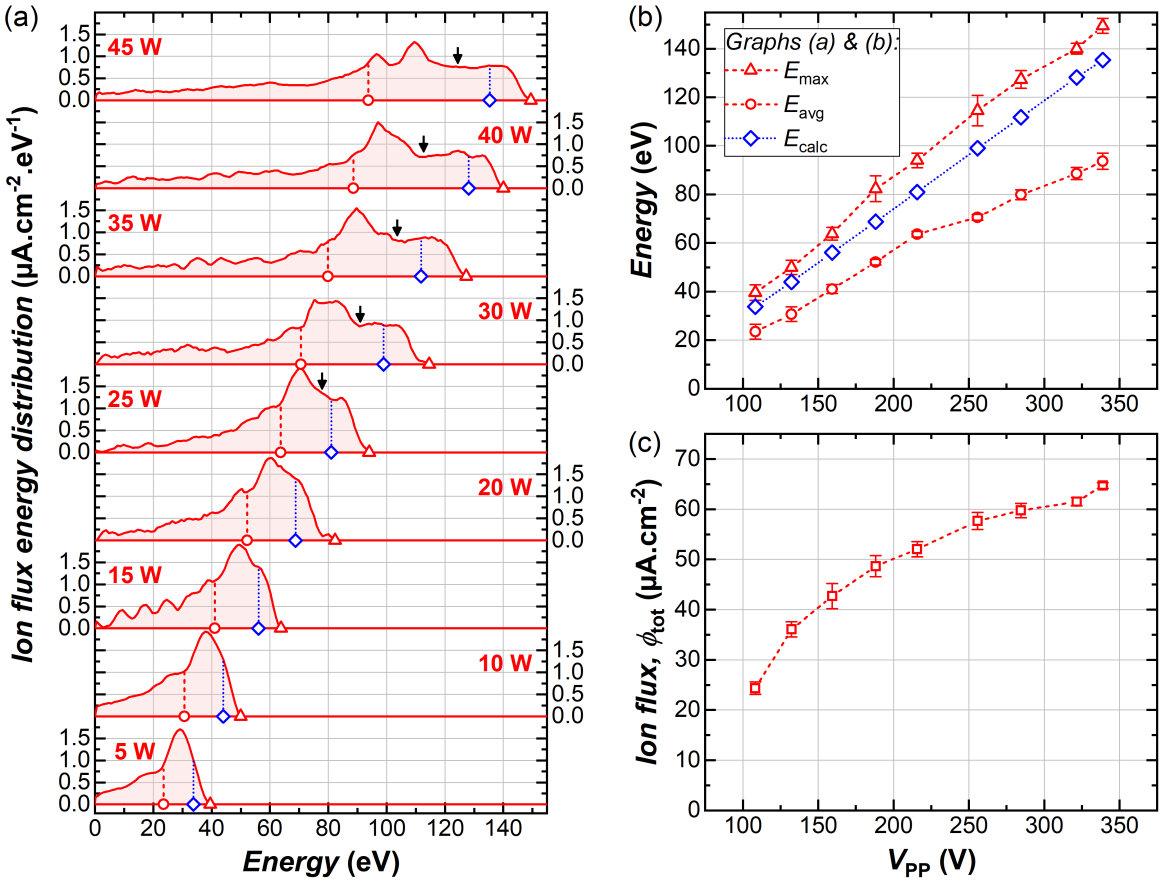

Fig. II.17: (a) IFEDFs measured in SF_6/O_2 (57% SF_6, 30 mTorr, single-frequency excitation) with increasing coupled power from 5 to 45 W. Graphs (b) and (c) respectively show the corresponding values of ion energy and total collected ion flux as a function of the applied V_{PP}.

At the low energy end of the IFEDFs, the ion flux is observed to be significant, i.e. the sheath is partly collisional. In Figure II.17(b), both the measured mean and maximal IBE are increasing almost linearly with the applied V_{PP}. The computation with Equation (II.9) is in qualitative agreement with the trends for the average and maximal ion energy, and the order of magnitude is well predicted. In the case of a bimodal distribution, E_{calc} should correspond to the center value between the two peaks (approximately shown by black arrows in Figure II.17(a), when the bimodal distribution is seen): here it appears that E_{calc} overestimates this center value. Two hypotheses may explain this effect: (i) the sheath is partly collisional, and the position of the bimodal peaks may therefore be shifted to lower energies; (ii) the computation of E_{calc} depends on the estimated gain correction factor for $f_0 = 13.56$ MHz, which may be overestimated.

Finally, and as expected, the ion flux increases with the applied V_{PP} (or equivalently with the coupled power, Figure II.17(c)): the correlation between ion flux and ion energy is well observed. This single-frequency case will serve as a baseline to which investigations using TVW excitation will be now be compared.

Extended playground using TVWs. Using identical conditions (57% SF_6 30 mTorr), measurements have been performed using TVW excitation for three different values of coupled power (15, 25 and 35 W). Results are first shown in the graphs Figure II.18 as a function of the applied waveform (again screening Θ values in the range $[0, 2\pi]$). Top line graphs in Figure II.18 show the evolution of ion bombardment energy on the powered electrode (E_{avg}, E_{max} and E_{calc}) while bottom line graphs show the total collected ion flux from the IFEDF measurements.

Measurements shown in Figure II.18 for the 25 W case are the same as previously described in section II.3.1.a, and we will therefore focus on comparisons with the two other cases. As can be ex-

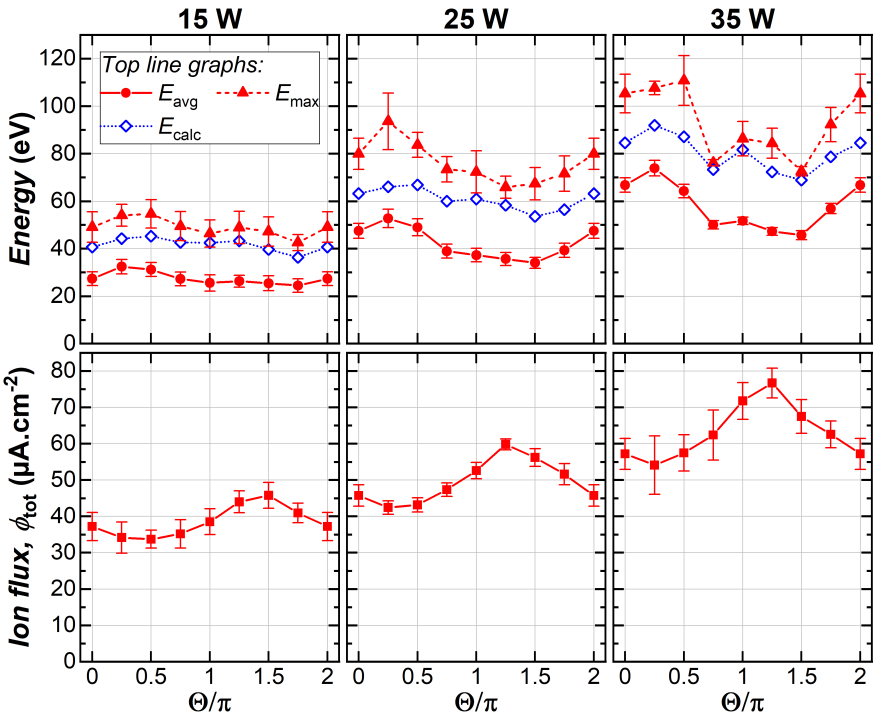

Fig. II.18: Influence of applied waveform on ion bombardment energy (top line graphs) and total collected ion flux (bottom line graphs) for different values of applied power in an SF_6/O_2 discharge (57% SF_6, 30 mTorr).

pected by analogy to single-frequency excitation, both the ion energy (either average or maximal) and ion flux can be seen to increase when the coupled power is raised (for a given Θ/π value, i.e. waveform). The qualitative evolution E_{calc} is in agreement with the measured variations of average and maximal ion energies (E_{avg} and E_{max}) at 15 and 25 W. At 35 W, variations of E_{calc} are quite similar to E_{avg} but more difficult to compare with E_{max}, possibly due to the large uncertainties obtained for some of the measurements and due to a long high-energy tail in the IFEDFs. Nevertheless, the measured variations of average ion energy and total ion flux are similar to the two cases at lower power and the TVW approach is still demonstrated to allow a significant variation of these parameters.

In addition, and similarly as detailed earlier for the 25 W case, the variations of ion energy and ion flux at 15 and 35 W are also consistent with the discharge power coupling being dominated by Drift-Ambipolar electron heating (DA-mode).

The measurements of average ion energy and total ion flux taken in single-frequency RF excitation and with TVWs (for the three values of coupled power) are plotted in a single graph in Figure II.19. In that, the solid curve is a guide to the eye to follow the correlation between ion energy and ion flux in the RF case. Similarly, the light-gray area show the extended playground made available through the use of TVWs. In particular, TVWs especially help increase the ion flux at a given energy or lower the average energy at a given flux. For instance, at an average ion energy of 50 eV, it is possible to vary the total ion flux between approximately 40 and 75 $\mu A \cdot cm^{-2}$ using TVWs, compared to a value around 48 $\mu A \cdot cm^{-2}$ for RF excitation.

This "extended playground" is of great interest from at least two points of view: (i) if the physical phenomena are well identified, the ion energy or flux can be tuned depending on the requirements for process purposes; (ii) conversely, if the physical phenomena are to be identified, using TVWs unleashes a large playground to vary parameters associated with ions independently. Of course, these measurements are limited to the behavior of positive ions: variations of other parameters (e.g. density of chemically reactive neutral species) are not captured from IFEDF characterizations.

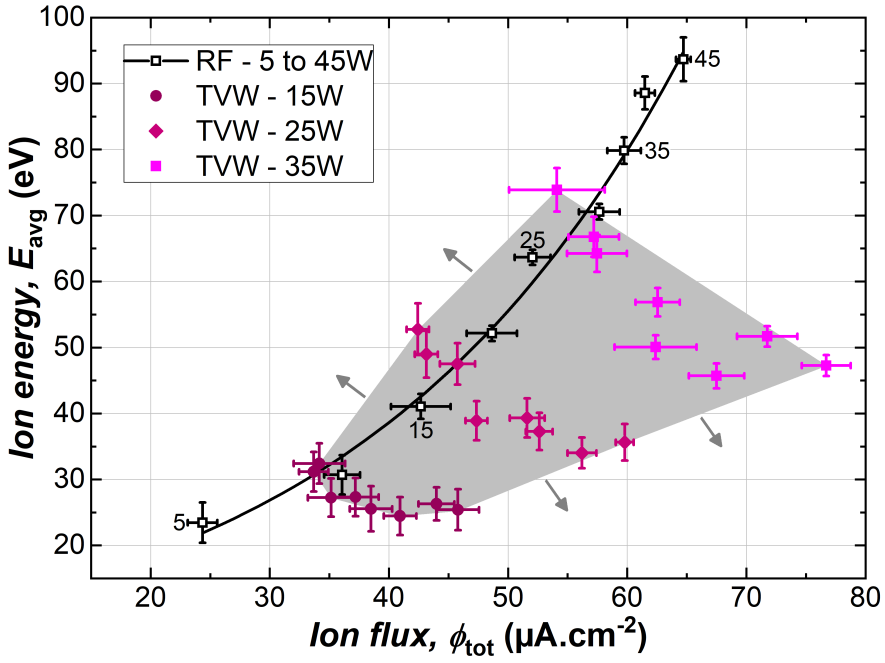

Fig. II.19: Average ion bombardment energy versus total collected ion flux for an SF_6/O_2 discharge (with 57% SF_6 in input gas flux) for different types of applied waveforms and values of coupled power. The solid black curve and the gray polygon are added as guides to the eye.

II.3.3 Ion Flux Non-uniformity in SF_6/O_2 Discharge

Up to now in this manuscript, the RFEA probe has been used to qualify how the IFEDFs on the substrate electrode can be tuned using TVW excitation, and to this aim measurements were taken with the probe located at a given (fixed) position on the electrode. As a reminder, the collection area of the RFEA grids is three orders of magnitude smaller than the area of the electrode (around 324 cm^2). At process level and especially by comparison to standard solar cell sizes, i.e. the current standard in mass production corresponds to 6 inches pseudo-square wafers (area of 243 cm^2) [28], it is interesting to look at the uniformity of the discharge in the reactor. The reactor being cylindrical (with 20 cm diameter parallel electrodes), a rotational symmetry is assumed, and measurements will be taken by placing the RFEA probe at different locations on a radius of the electrode.

II.3.3.a Effect of excitation waveform and comparison with Ar

At each chosen location, plasma conditions are varied both in Ar and SF_6/O_2, and IFEDFs are recorded. In both cases, the pressure is set to 30 mTorr and the coupled power to 25 W. Results are shown in Figure II.20, for Ar (left column) and SF_6/O_2 (right column): for each graph the abscissa spans the electrode radius. Notice that a lateral offset has been introduced in all graphs to help visualize the curves.

Top graphs show the V_{DC} measured on the powered electrode: this parameter is used as a control to check that the conditions are reasonably comparable between different locations. Indeed, changing the location of the probe implies the venting and opening of the chamber, and a slight change in masked electrode area (due to the ceramic coated cable connecting the probe to the electronic control unit). Small but significant changes in V_{DC} are observed in some cases for the Ar discharge (e.g. valleys waveforms case, $\Theta/\pi = 1$). In contrast, very small variations of V_{DC} are observed in SF_6/O_2, showing that the displacement of the probe negligibly affects the plasma. The second row of graphs in Figure II.20 shows the evolution of the average ion energy: E_{avg} is very stable along the radius of the electrode (small variations observed with the Ar discharge are linked to the variations of V_{DC}, attributed to the small change in discharge properties induced by the displacement of the probe on the electrode). This observation indicates that the DC component

of the powered sheath voltage, and thus the plasma potential near the powered electrode is fairly uniform in the discharge. Finally, the third row shows the evolution of the total ion flux along the radius of the electrode: in the Ar case, some small variations are observed again but ϕ_{tot} can be considered uniform on the area of the electrode (within the measurement uncertainties).

The SF_6/O_2 case is more surprising: the constant V_{DC} values and uniform E_{avg} across the electrode again indicate a constant DC sheath voltage drop on the electrode. However, the ion flux significantly increases from the center to the "edge" of the electrode: in the RF case, ϕ_{tot} is almost three times higher at the edge than at the center of the electrode. Notice that in this section the term "edge" is used abusively: due to experimental constraints, the most peripheral measurement was performed at $r = 7.5$ cm (while the electrode radius is 10 cm). In all TVW mode cases, the center to edge increase is less pronounced than with single-frequency RF excitation, but even in the "most uniform" case (here with sawtooth-up waveforms, $\Theta/\pi = 0.5$), the ion flux at the edge of the electrode is still around 1.6 times higher than at the center.

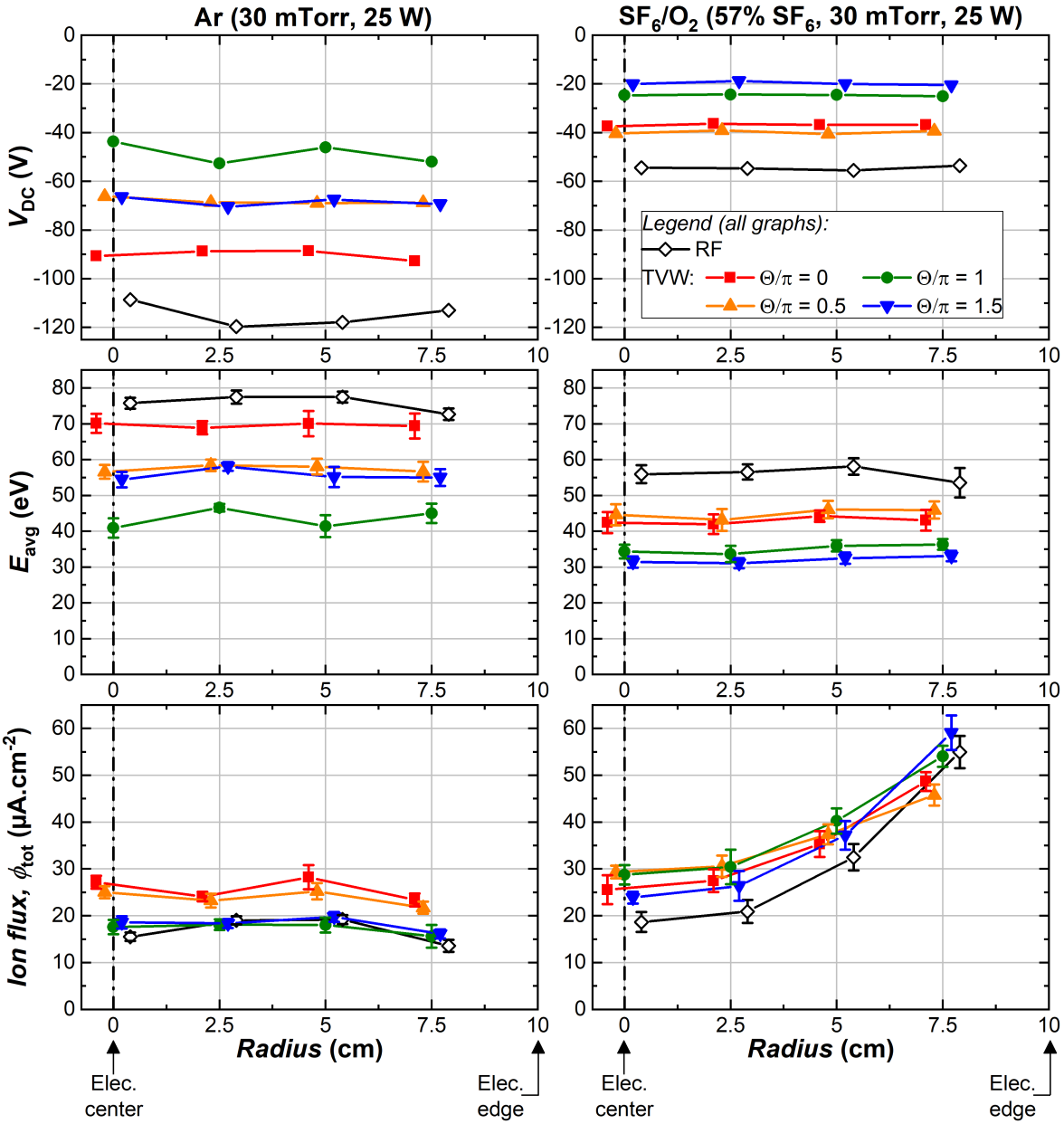

Fig. II.20: Measured radial profiles for DC self-bias voltage (top line), average ion bombardment energy (middle line) and total collected ion flux (bottom line) in Ar discharge (left) and SF_6/O_2 discharge (right) and various applied voltage waveforms. A lateral offset is introduced between curves to ease visualization.

A closer look at the results obtained with SF_6/O_2 at the center (0 cm) and edge (7.5 cm) of the electrode is supplied in Figure II.21 showing the IFEDFs for all tested excitation waveforms. The IFEDFs are shown in "true scale" in the left graph and normalized in the right graph (energy scaled by E_{max} and area of the curves normalized to unity). While E_{avg} was already shown constant along the radius of the electrode, the curves in the left graph Figure II.21, also show the maximal ion energy, E_{max}, is very similar at both locations. In addition, the normalized curves displayed in the right graph show the similarity of the distributions at each location (which is also true for the two other locations, i.e. 2.5 and 5 cm from the center, data not shown here): only the ion flux density is varying from the center to the edge of the electrode.

All this observations support the previous conclusion that the sheath voltage is constant across the electrode. In that regard, the single frequency (RF) case, bottom curves in Figure II.21 is especially interesting. Indeed, the energy gap between the two high energy peaks (associated to the bimodal distribution, see black arrows in left graph Figure II.21) is larger at the edge of the discharge (around 14 eV) then at the center (8 eV). Although weak, this effect may indicate that the powered sheath RF voltage amplitude is higher at the electrode edge than at the center, suggesting a uniform DC sheath voltage with non-uniform RF amplitude across the electrode.

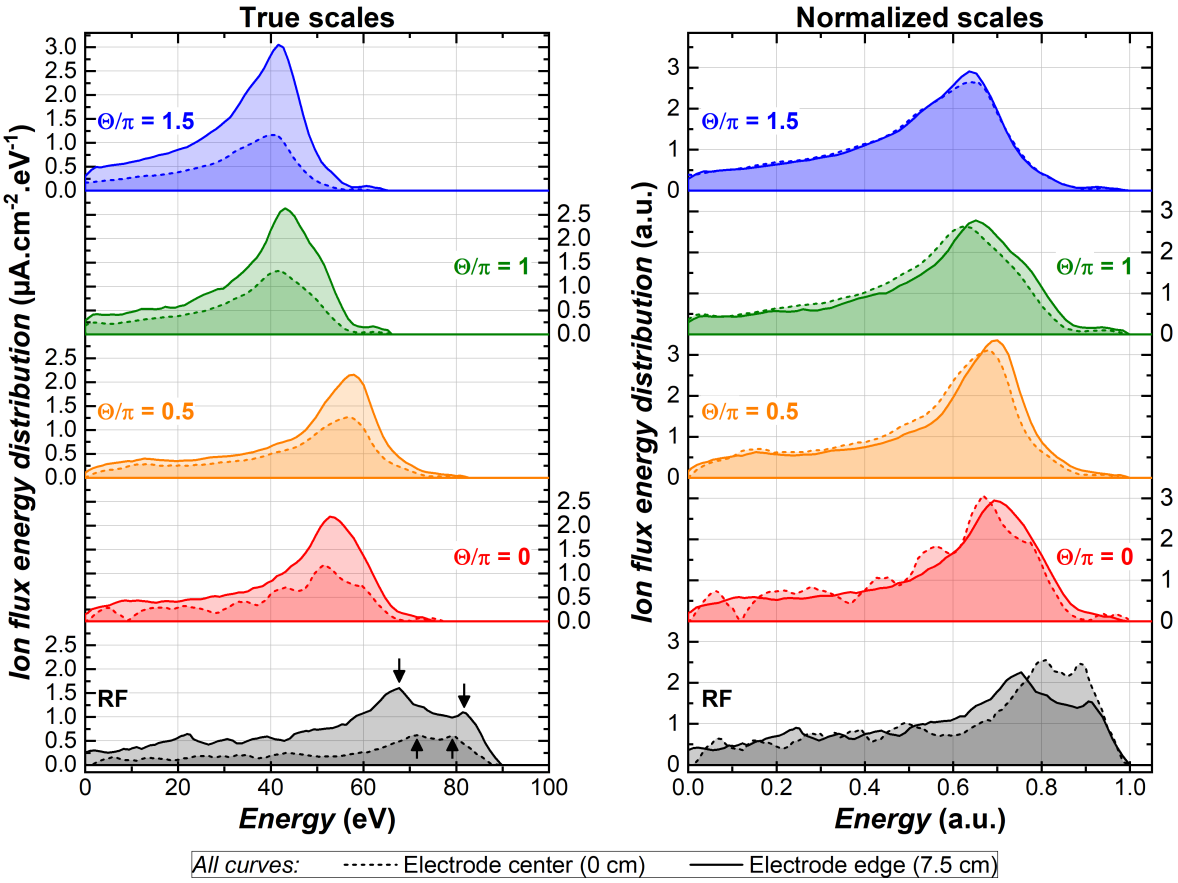

Fig. II.21: Comparison of IFEDFs with SF_6/O_2 (57% SF_6, 30 mTorr, 25 W) for different applied voltage waveforms in "true scale" (left) and normalized scales (right) obtained at the center (0 cm, dashed curves) or at the edge (7.5 cm, solid curves) of the powered electrode.

Finally, Figure II.22 shows the evolution of global discharge parameters with the excitation waveform, with the RFEA probe located at the center or at the edge of the electrode. Figure II.22(a) first shows the total ion flux evolution with the excitation voltage. The values obtained in TVW mode at the electrode edge are not surprising as they are similar to the results presented in section II.3.2.b: due to the slope asymmetry effect the ion flux is highest for sawtooth-down waveforms ($\Theta/\pi = 1.5$) and lowest for sawtooth-up waveforms ($\Theta/\pi = 0.5$). In contrast, the situation is surprisingly reversed at the electrode center, a rather surprising effect that leads to the following

discussion.

The reversal in ion flux variations (from the center to the edge of the electrode) importantly recalls that the evolution of the self-bias voltage, Figure II.22(b), only captures global information (dominant effects) on the discharge behavior. It should here be recalled that with these waveforms the amplitude asymmetry effect is absent, so that the self-bias voltage can be approximated by the following equation (under the same hypotheses as Equation (II.4), section II.1.2.a):

$$V_{DC} \approx -\frac{V_{PP}}{2}\frac{1-\varepsilon}{1+\varepsilon} \tag{II.11}$$

where the symmetry parameter ε scales in particular with the ratio of average (positive) ion density in the powered and grounded electrode sheaths, $\bar{n}_{sp}/\bar{n}_{sg}$ (see Chapter I section I.1.2.a). $\bar{n}_{sp}$ and $\bar{n}_{sq}$ are here to be considered both temporally averaged (in an RF period) and spatially averaged (over the whole electrode) densities. The comparison of V_{DC} values show that ε is lower for sawtooth-down waveforms, and this effect is attributed to a lower $\bar{n}_{sp}/\bar{n}_{sg}$ ratio: as a conclusion (and as has been deduced in section II.2 for identical discharge conditions), drift-ambipolar electron heating mode (DA-mode) is here globally dominant. However, this result conceals the local variations in absolute ion flux and a reversed behavior (from the center to the edge of the electrode) as a function of the applied waveform. Unfortunately, definitive conclusions cannot be drawn since the ion flux at the grounded electrode has not been characterized: the $\bar{n}_{sp}/\bar{n}_{sg}$ ratio remains inaccessible. As a conclusion (although unsatisfactory), the previous experimental results imply that a global description of the discharge leads to a very incomplete comprehension of the mechanisms at play.

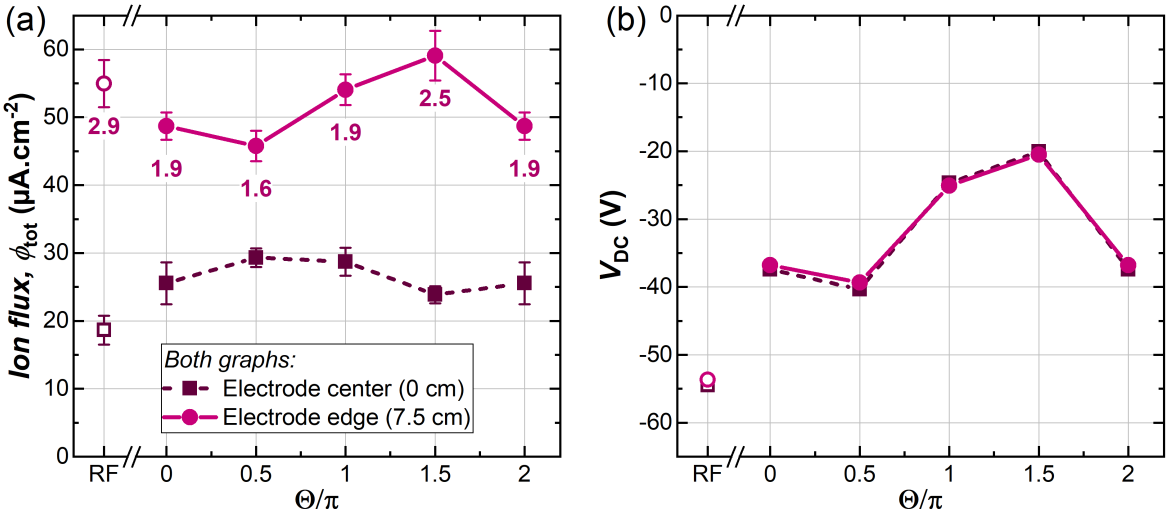

Fig. II.22: (a) Evolution of total ion flux with excitation voltage waveform, measured in identical discharge conditions (25 W, 30 mTorr, 57% SF_6) at the center or the edge of the electrode. Labels indicate the "center-to-edge" ion flux ratio. (b) Self-bias voltage evolution in the same conditions.

II.3.3.b Elements of elucidation

A first step towards a more detailed comprehension comes from the identification of the possible sources of non-uniformity. Several important observations should first be summarized: (i) in the investigated conditions of pressure (31 mTorr) and power (25 W), non-uniform ion flux is observed for the SF_6/O_2 plasma but not for Ar; (ii) in SF_6/O_2, the ion flux increases from the center to the edge of the discharge (edge-high profile) while the distribution in energy is kept almost identical (in particular E_{avg} is constant along the radius of the electrode); (iii) the ion flux uniformity is improved when using TVW excitation (i.e. the ratio between the total ion fluxes measured at 7.5 cm and 0 cm is lower) compared to the single frequency case, and depends on the applied waveform – with the best uniformity observed for sawtooth-up waveforms $\Theta/\pi = 0.5$.

The edge-high ion flux profile necessarily comes from a gradient of plasma density, with a higher power deposition close to the electrode edge. A first hypothesis to explain this effect comes from a gradient of gas composition on top of the electrode. From the results of section II.2, the possible electropositive behavior at the center of the discharge could be explained by a lower SF_6/O_2 ratio in the discharge center. In such case, the transition from α-mode to DA-mode with increasing SF_6 content (observed in section II.2) would still be valid but not representative of the whole discharge: a spatial transition would also occur, with a higher SF_6 content at the periphery of the discharge. By comparison to Figure II.10(a), section II.2.2.a, a constant V_{PP} is here present on the electrode so that a more efficient power deposition would occur at the periphery of the discharge (where the SF_6 content is larger). A confirmation of this hypothesis would in particular require an adequate modeling of SF_6/O_2 gas transport properties in the volume of the reactor.

Another explanation to the edge-high ion flux profile comes from electrostatic edge effects (with sometimes an additional electromagnetic contribution) [29, 30]. An enhanced electric field (thus an increased power deposition) appears in the vicinity of the electrode edge due to its proximity with the grounded sidewalls (and a grounded guard ring in the case of the RIE electrode). In addition, the asymmetric reactor geometry ("telegraph effect") may also be responsible for the observed radial non-uniformity [31]. In this case, the asymmetric geometry leads to higher power deposition near the edge of the plasma: this effect would be weaker in larger reactors (due to decreased geometric asymmetry) but is also affected by the presence of dielectric substrates. Interestingly, Schüngel *et al.* have shown that TVW excitation gives the ability to tune the magnitude of the "telegraph effect": they used this property to improve uniformity in an H_2 discharge [32].

In the specific case of non-magnetized CCP discharges, additional electromagnetic effects (such as the standing wave effect or skin effect) can also prove detrimental for plasma uniformity [30]. The standing wave effect appears when the electrode diameter is comparable to the standing wave wavelength (the latter decreases with the applied voltage frequency). In such case, the electric field (component perpendicular to the electrodes) is maximum at the center of the discharge and decreases towards the edge, leading to a center-high ion flux profile [29]. For the reactor used in the present work, the electrode diameter is 20 cm and the standing wave wavelength is at least one order of magnitude larger (using the calculation from the practical formula proposed by Chabert *et al.* [33] for the investigated conditions). More importantly, the standing wave effect cannot explain the edge-high profiles obtained in SF_6/O_2. The skin effect is a more suitable candidate: it appears when the inter-electrode distance is comparable or larger than the skin depth (i.e. the characteristic field penetration distance in the plasma), and leads to edge-high ion flux profiles. The skin depth decreases with increasing plasma conductivity and is therefore observed at relatively high plasma density, while the SF_6/O_2 discharge here investigated is operated at relatively low power (25 W).

While identifying the exact – or at least dominant – source of ion flux non-uniformity would require additional characterization or simulation resources, the previous analysis will help selecting possible candidates. Obviously, if the etching (or nanotexturing) process depends on the ion flux, a large non-uniformity of the surface properties will be observed when processing large scale samples (6 inches pseudo-square wafers being the current standard for photovoltaic applications), although the introduction of a dielectric substrate may drastically change the discharge behavior – and actually introduce other sources of non-uniformity. In that regard, it should be highlighted that the RIE reactor used in this study is relatively small compared to wafer sizes relevant for photovoltaic application: the influence of the reactor size on the sources of non-uniformity should therefore be taken into account. Depending on the mechanism(s) explaining the observed non-uniformity, the upscaling of the process would especially require a careful study of: (i) the reactor design to mitigate possible edge effects, (ii) gas transport properties in case of gas composition gradients, and (iii) power deposition mechanisms due to possible electromagnetic effects.

Summary

The implementation and use (in particular in the case of an SF_6/O_2 discharge) of TVW excitation in the RIE setup has been presented in this chapter. Major findings are recalled below:

- TVW excitation was successfully implemented on the RIE reactor used for nanotexturing. **Large differences between the waveform set at the feedthrough and the one measured at the electrode are observed** in open-chamber conditions. A rather **simple calibration method is used to mitigate this discrepancy** and it can also be used in the presence of plasma as shown using the (known) behavior of an Ar discharge.

- The effect of TVWs on the SF_6/O_2 discharge was investigated depending on the discharge parameters. The relative contribution of **two types of Electrical Asymmetry Effect (EAE)** was observed. The use of **mirror versions of sawtooth voltage waveforms** is used to isolate the net (positive or negative) change in V_{DC}/V_{PP} from absolute values or trends (as well as the impact of the geometrically asymmetric reactor). A **zero-crossing in the net change is interpreted as a change in the dominant electron heating mode**.

- For O_2 plasma (similarly as for Ar), the Amplitude Asymmetry Effect dominates, and only a very small impact of the Slope Asymmetry Effect can be seen, although its slight effect indicates that the plasma is electropositive and operated in α-mode (sheath expansion heating). **For small additions of SF_6, the plasma begins to act more electronegatively and Drift-Ambipolar power coupling becomes preponderant**. However, as the overall pressure increases, the differentiation between the two mirror sawtooth waveforms disappears, as the importance of the difference in the sheath velocities decreases.

- The ion flux energy distribution function on the powered electrode of an SF_6/O_2 discharge was characterized using single-frequency and TVW excitation. At fixed discharge conditions (pressure, power and SF_6 content), **the average (and maximal) ion energy is successfully varied in a large range by changing the waveform**. Meanwhile the total ion flux is also significantly varied, so that **a complete decoupling between energy and flux cannot be obtained.** The relative variations of both ion energy and ion flux with the applied waveform also strongly depend on the dominant electron heating. Nevertheless, in conditions relevant for silicon nanotexturing, **TVW excitation leads to a widely extended playground compared to single-frequency voltage**.

- Finally, in the same conditions, the **ion flux on the powered electrode of the SF_6/O_2 discharge is not uniform** in the RIE reactor, showing an **edge-high radial profile**; in addition **the magnitude of the non-uniformity depends on the applied waveform** and can be considerably improved using TVWs compared to single-frequency excitation. Several possible sources for this non-uniformity have been highlighted but the specific reason(s) at play could not be deciphered based on the available data.

Bibliography (Chapter II)

[1] J. Schulze, E. Schüngel and U. Czarnetzki, The electrical asymmetry effect in capacitively coupled radio frequency discharges – measurements of dc self bias, ion energy and ion flux, *J. Phys. D Appl. Phys.* **2009**, 42(9), 092005, doi:10.1088/0022-3727/42/9/092005. 64, 67

[2] J. Schulze, E. Schüngel, U. Czarnetzki and Z. Donkó, Optimization of the electrical asymmetry effect in dual-frequency capacitively coupled radio frequency discharges: Experiment, simulation, and model, *J. Appl. Phys.* **2009**, 106(6), 063307, doi:10.1063/1.3223310. 64, 68

[3] Radio Regulations Articles, Edition of 2016, Tech. rep., International Telecommunications Union, URL `itu.tind.io/record/25397?ln=en`. 66

[4] B. G. Heil, U. Czarnetzki, R. P. Brinkmann and T. Mussenbrock, On the possibility of making a geometrically symmetric RF-CCP discharge electrically asymmetric, *J. Phys. D: Appl. Phys.* **2008**, 41(16), 165202, doi:10.1088/0022-3727/41/16/165202. 68

[5] J. Schulze, E. Schüngel, Z. Donkó and U. Czarnetzki, Excitation dynamics in electrically asymmetric capacitively coupled radio frequency discharges: experiment, simulation, and model, *Plasma Sources Sci. Technol.* **2010**, 19(4), 045028, doi:10.1088/0963-0252/19/4/045028. 69, 72

[6] E. Schüngel, Z. Donkó and J. Schulze, A Simple Model for Ion Flux-Energy Distribution Functions in Capacitively Coupled Radio-Frequency Plasmas Driven by Arbitrary Voltage Waveforms, *Plasma Process Polym* **2017**, 14(4-5), doi:10.1002/ppap.201600117.

[7] B. Bruneau, T. Lafleur, J.-P. Booth and E. Johnson, Controlling the shape of the ion energy distribution at constant ion flux and constant mean ion energy with tailored voltage waveforms, *Plasma Sources Sci. Technol.* **2016**, 25(2), 025006, doi:10.1088/0963-0252/25/2/025006.

[8] B. Bruneau, T. Gans, D. O'Connell, A. Greb, E. V. Johnson and J.-P. Booth, Strong Ionization Asymmetry in a Geometrically Symmetric Radio Frequency Capacitively Coupled Plasma Induced by Sawtooth Voltage Waveforms, *Physical Review Letters* **2015**, 114(12), doi:10.1103/PhysRevLett.114.125002. 68, 74, 77

[9] J. Schulze, E. Schüngel, Z. Donkó and U. Czarnetzki, The electrical asymmetry effect in multi-frequency capacitively coupled radio frequency discharges, *Plasma Sources Sci. Technol.* **2011**, 20(1), 015017, doi:10.1088/0963-0252/20/1/015017. 68

[10] P. Chabert and N. S. J. Braithwaite, Physics of radio-frequency plasmas, Cambridge Univ. Press, Cambridge, **2011**, ISBN 978-0-521-76300-4. 68, 78

[11] Z. Donkó, J. Schulze, B. G. Heil and U. Czarnetzki, PIC simulations of the separate control of ion flux and energy in CCRF discharges via the electrical asymmetry effect, *J. Phys. D: Appl. Phys.* **2009**, 42(2), 025205, doi:10.1088/0022-3727/42/2/025205. 72

[12] B. Bruneau, R. Cariou, J. C. Dornstetter, M. Lepecq, J. L. Maurice, P. R. i. Cabarrocas and E. V. Johnson, Ion Energy Threshold in Low-Temperature Silicon Epitaxy for Thin-Film Crystalline Photovoltaics, *IEEE J. Photovolt.* **2014**, 4(6), 1361–1367, doi:10.1109/JPHOTOV.2014.2357256. 74

[13] B. Bruneau *et al.*, Effect of gas properties on the dynamics of the electrical slope asymmetry effect in capacitive plasmas: comparison of Ar, H_2 and CF_4, *Plasma Sources Sci. Technol.* **2016**, 25(1), 01LT02, doi:10.1088/0963-0252/25/1/01LT02. 75, 76

[14] S. Brandt *et al.*, Electron power absorption dynamics in capacitive radio frequency discharges driven by tailored voltage waveforms in CF_4, *Plasma Sources Sci. Technol.* **2016**, 25(4), 045015, doi:10.1088/0963-0252/25/4/045015.

[15] B. Bruneau *et al.*, Slope and amplitude asymmetry effects on low frequency capacitively coupled carbon tetrafluoride plasmas, *J. Appl. Phys.* **2016**, 119(16), 163301, doi:10.1063/1.4947453. 75, 76

[16] H. Jansen, M. de Boer, H. Wensink, B. Kloeck and M. Elwenspoek, The black silicon method. VIII. A study of the performance of etching silicon using SF6/O2-based chemistry with cryogenical wafer cooling and a high density ICP source, *Microelectron. J.* **2001**, 32(9), 769–777, doi:10.1016/S0026-2692(01)00039-8. 75

[17] R. Dussart *et al.*, Silicon columnar microstructures induced by an SF_6 /O_2 plasma, *J. Phys. D Appl. Phys.* **2005**, 38(18), 3395–3402, doi:10.1088/0022-3727/38/18/012.

[18] M. Gaudig, J. Hirsch, T. Schneider, A. N. Sprafke, J. Ziegler, N. Bernhard and R. B. Wehrspohn, Properties of black silicon obtained at room-temperature by different plasma modes, *J. Vac. Sci. Technol. A* **2015**, 33(5), 05E132, doi:10.1116/1.4929540. 75

[19] J. K. Wang and E. V. Johnson, Electrode-selective deposition/etching processes using an SiF4/H2/Ar plasma chemistry excited by sawtooth tailored voltage waveforms, *Plasma Sources Sci. Technol.* **2017**, 26(1), 01LT01, doi:10.1088/0963-0252/26/1/01LT01. 76, 78

[20] A. Derzsi, T. Lafleur, J.-P. Booth, I. Korolov and Z. Donkó, Experimental and simulation study of a capacitively coupled oxygen discharge driven by tailored voltage waveforms, *Plasma Sources Sci. Technol.* **2016**, 25(1), 015004, doi:10.1088/0963-0252/25/1/015004. 76

[21] J. Schulze, A. Derzsi, K. Dittmann, T. Hemke, J. Meichsner and Z. Donkó, Ionization by Drift and Ambipolar Electric Fields in Electronegative Capacitive Radio Frequency Plasmas, *Phys. Rev. Lett.* **2011**, 107(27), 275001, doi:10.1103/PhysRevLett.107.275001. 76, 79, 80

[22] A. Pateau, A. Rhallabi, M.-C. Fernandez, M. Boufnichel and F. Roqueta, Modeling of inductively coupled plasma SF6/O2/Ar plasma discharge: Effect of O2 on the plasma kinetic properties, *J. Vac. Sci. Technol. A* **2014**, 32(2), 021303, doi:10.1116/1.4853675. 79

[23] D. Gahan, B. Dolinaj and M. B. Hopkins, Retarding field analyzer for ion energy distribution measurements at a radio-frequency biased electrode, *Rev. Sci. Instr.* **2008**, 79(3), 033502, doi:10.1063/1.2890100. 81

[24] E. Kawamura, V. Vahedi, M. A. Lieberman and C. K. Birdsall, Ion energy distributions in rf sheaths; review, analysis and simulation, *Plasma Sources Sci. Technol.* **1999**, 8(3), R45, doi:10.1088/0963-0252/8/3/202. 84

[25] P. Benoit-Cattin and L.-C. Bernard, Anomalies of the Energy of Positive Ions Extracted from High-Frequency Ion Sources. A Theoretical Study, *J. Appl. Phys.* **1968**, 39(12), 5723–5726, doi:10.1063/1.1656039. 84

[26] B. Bruneau, J. Wang, J.-C. Dornstetter and E. V. Johnson, Growth mechanisms study of microcrystalline silicon deposited by SiH4/H2 plasma using tailored voltage waveforms, *J. Appl. Phys.* **2014**, 115(8), 084901, doi:10.1063/1.4866693. 84

[27] A. Savitzky and M. J. E. Golay, Smoothing and Differentiation of Data by Simplified Least Squares Procedures., *Analyt. Chem.* **1964**, 36(8), 1627–1639, doi:10.1021/ac60214a047. 86

[28] International Technology Roadmap for Photovoltaic Ninth Edition, March 2018, Tech. Rep. 9, ITRPV, **2018**, URL `www.itrpv.net`. 89

[29] A. Perret, P. Chabert, J.-P. Booth, J. Jolly, J. Guillon and P. Auvray, Ion flux nonuniformities in large-area high-frequency capacitive discharges, *Appl. Phys. Lett.* **2003**, 83(2), 243–245, doi:10.1063/1.1592617. 93

[30] P. Chabert, Electromagnetic effects in high-frequency capacitive discharges used for plasma processing, *J. Phys. D: Appl. Phys.* **2007**, 40(3), R63, doi:10.1088/0022-3727/40/3/R01. 93

[31] A. A. Howling, L. Sansonnens, J. Ballutaud, C. Hollenstein and J. P. M. Schmitt, Nonuniform radio-frequency plasma potential due to edge asymmetry in large-area radio-frequency reactors, *J. Appl. Phys.* **2004**, 96(10), 5429–5440, doi:10.1063/1.1803608. 93

[32] E. Schüngel, S. Mohr, J. Schulze and U. Czarnetzki, Prevention of ion flux lateral inhomogeneities in large area capacitive radio frequency plasmas via the electrical asymmetry effect, *Appl. Phys. Lett.* **2015**, 106(5), 054108, doi:10.1063/1.4907887. 93

[33] P. Chabert, J. L. Raimbault, J. M. Rax and M. A. Lieberman, Self-consistent nonlinear transmission line model of standing wave effects in a capacitive discharge, *Phys. Plasmas* **2004**, 11(5), 1775–1785, doi:10.1063/1.1688334. 93

CHAPTER III

PLASMA-SURFACE INTERACTION: SELF-ORGANIZATION AT THE NANOSCALE DURING SF_6/O_2 ETCHING

Contents

III.1 Baseline Process using Single-frequency Excitation **99**
III.1.1 Nanotexturing "Process Window" 99
III.1.1.a Available range of conditions 99
III.1.1.b Description of the samples 100
III.1.1.c Identification of nanotexturing process window 103
III.1.2 Dynamic Aspects of Nanotexturing 107
III.1.2.a Nanostructure size evolution and dependence on initial surface state 108
III.1.2.b Hemispherical reflectance evolution 110
III.2 Texturing Uniformity at Full Wafer Scale **113**
III.2.1 Initial Tests and Influence of SF_6 Content 113
III.2.1.a Definition of optimization parameters 113
III.2.1.b Influence of SF_6 content 115
III.2.2 Uniform Final Reflectance, Non-uniform Process Conditions 116
III.2.2.a Dynamic evolution 116
III.2.2.b Other possible sources of nanotexturing non-uniformity . . . 119
III.3 Influence of Ion Flux and Ion Energy on Nanotexturing **120**
III.3.1 Influence of Ion Flux 120
III.3.1.a Ion flux non-uniformities 120
III.3.1.b Ion fluence 121
III.3.2 Energy Dependent Etching Yield 124
III.3.2.a Influence of ion energy 124
III.3.2.b Energy weighted ion fluence 126
III.3.2.c Qualitative interpretations 128
III.3.3 Special Cases 131
III.3.3.a Tuning the aspect ratio 131
III.3.3.b Crystalline orientation dependence 132
Summary **134**
Bibliography **136**

Introduction

The process of c-Si nanotexturing using a CCP SF_6/O_2 discharge implies numerous input and output parameters. A schematic, presented in Figure III.1, helps visualize the complexity of this process. The schematic shows: the process "control knobs," the substrate properties, the plasma parameters (bulk and sheath) and finally the process outcome in terms of surface properties and, incidentally, optical properties. The most important relationships are depicted by solid arrows.

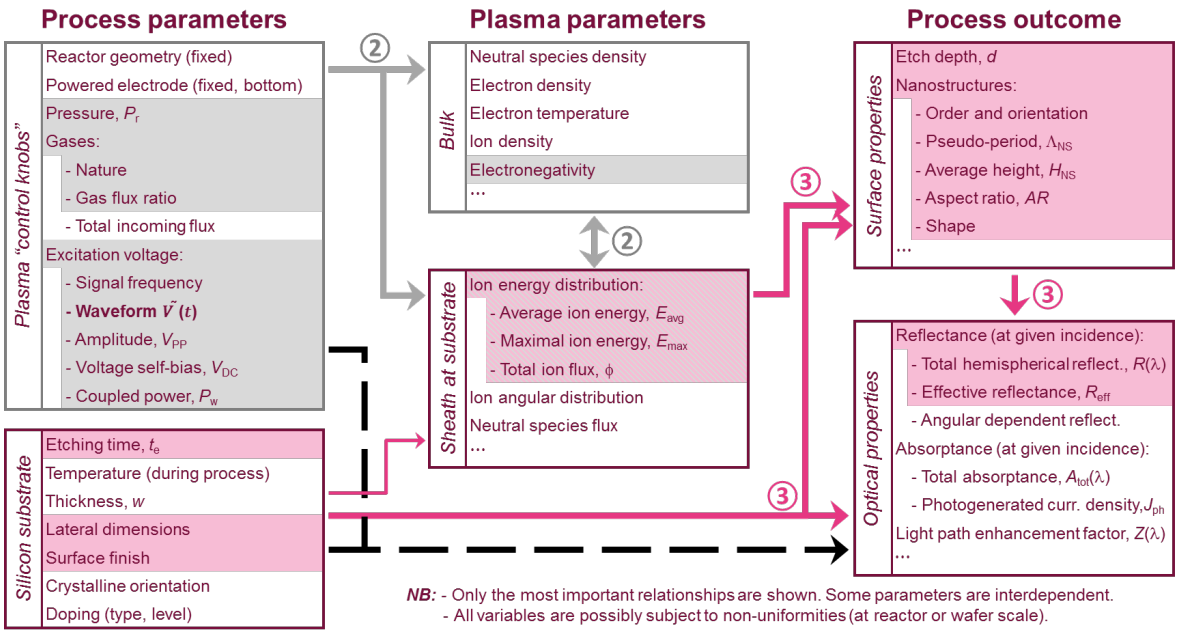

Fig. III.1: Illustration of surface nanotexturing process with relevant input and output parameters. Circled numbers and highlighted parameters correspond to the most important relationships and parameters studied in Chapter II (gray) and III (pink) of the present manuscript.

In the frame of the present work, the main objective is the development of a nanostructured c-Si surface suitable for implementation in solar cells. In other words, a maximization of photogenerated current density is sought (without jeopardizing electrical properties of the cell). Notice that for the time being, and because it represents an easily accessible "proxy" for the optimization, investigations will focus on the effective reflectance, R_{eff}, of the nanotextured samples: decreased reflectance for wavelengths above the bandgap of c-Si will obviously lead to improvements in photogenerated current density. However, obtaining a direct link (represented by the dashed arrow on the schematic in Figure III.1) between process parameters and final optical properties would be unrealistic and occult the role of intermediaries (e.g. the plasma).

Indeed, as seen in the schematic Figure III.1, process "control knobs" indirectly influence the final surface properties via the plasma sheath (which is also impacted by the properties of the plasma bulk and the substrate). In turn, the final optical properties may depend both on the initial sample characteristics and on the obtained nanostructures.

Chapter I focused on the influence of the process control knobs on the ion flux energy distribution (at the substrate electrode), in particular with the introduction of a particular "control knob," i.e. the voltage waveform, which was expanded to include Tailored Voltage Waveforms. Using this knowledge, a more direct link between the parameters of the plasma and the final properties of the textured surface will be drawn in the present chapter.

In section III.1, an adequate process window (in terms of "external" process parameters) will be identified, and the dynamic evolution of the surface properties will be explored. Section III.2 will focus on the process upscaling to full wafers (at a size compatible with photovoltaic applications in particular). Section III.3 will then more specifically focus on the influence of ion flux and energy on the obtained surface morphology and reflectance: a global (descriptive) phenomenological model will be depicted, paving the way to more comprehensive design rules for process optimization.

III.1 Baseline Process using Single-frequency Excitation

In this study, the development of the crystalline c-Si nanotexturing process with an SF_6/O_2 discharge in the RIE reactor starts with the identification of an adequate process window. After the selection of optimum process parameters, the dynamic evolution of the nanostructures during the process will be investigated with the chosen baseline recipe.

III.1.1 Nanotexturing "Process Window"

III.1.1.a Available range of conditions

The ranges for "control knobs" on the RIE setup (described in Chapter I) are listed in Table III.1, in the specific case of a mixture of SF_6 and O_2. Other gases may be added, in particular Ar, but this addition may change the available range of pressure or SF_6 content.

Tab. III.1: Available range of discharge parameters for c-Si nanotexturing in the RIE setup.

Input parameters		Values or range
Gases	**Pressure,** P_r	30 mTorr to 1 Torr
	Nature	$SF_6 + O_2$ (possible addition of Ar)
	Total input flux	30 to 300 sccm
	SF_6 content	0 to 80 %
Voltage excitation	**Signal basis frequency,** f_0	13.56 MHz
	Number of harmonics, n	1 (Single-frequency) or 3 (TVWs)
	Coupled power, P_w	Up to 60 W (0.2 W·cm^{-2})
Substrate	**Temperature,** T_S	25 to 300 °C

Similar tables stating the process conditions will be used in the following parts of the manuscript to clearly indicate the process conditions used in each study. Some comments have to be added to this list of parameters:

Gases. The pressure is controlled by the rotating speed of the turbo pump, so that the available range of pressure depends in particular on the input gas nature and total flux. The SF_6 content corresponds to its volume fraction in the incoming gas flux. The maximal limit of 80% SF_6 in the incoming gas flux comes from the use of a premixed SF_6/O_2 bottle (with 20% O_2).

Voltage excitation. The base frequency is the same, 13.56 MHz, for single-frequency and tailored voltage waveform excitation, for the latter case, two upper harmonics are used (27.12 and 40.68 MHz). Similarly as in Chapter II, the power P_w listed in Table III.1 represents the value coupled to the discharge measured by a current-voltage probe, detailed in section I.1.3.c of Chapter I. P_w corresponds to the forward power P_{fwd} at the input of the reactor minus the reflected power P_{ref}. Notice that with single-frequency excitation, power and peak-to-peak voltage are interdependent and determine the value of self-bias voltage through the interaction with the reactor geometry. In contrast, using TVWs gives an additional degree of freedom, to independently tune the self-bias voltage for instance (although in a limited range). Finally, the available range of power also depends on the nature of gases and discharge pressure.

Substrate temperature. The temperature is monitored with a thermocouple in the substrate holder electrode, only giving an estimate of the substrate temperature. The substrate holder is water-cooled when working at room temperature. The cooling is, however, not efficient enough to fully compensate plasma-induced heating (from ion bombardment and exothermic etching reactions). For a process duration above 5 min, variations in electrode temperature are observed but

low (up to 10 °C) and their effect on the etching process will therefore be neglected. Alternatively, a heating system can also be used to heat the substrate electrode up to 300 °C.

Process conditions for nanotexturing: a glimpse at literature. As it is well-documented in scientific literature, c-Si nanotexturing by SF_6/O_2 plasma can only be achieved in a limited range of discharge parameters. In particular, a strong interdependence between the substrate temperature and the SF_6/O_2 ratio has been demonstrated [1, 2]: generally, it has been shown that the higher the substrate temperature, the lower the required SF_6 content (volume fraction in input gas flux). [1] When the substrate is cooled to cryogenic temperatures (in the range from -160 to −70 °C in [1, 2]), black silicon may be obtained for an SF_6 content as high as 80 or 94%. At substrate temperatures closer to 0 °C, more oxygen is required and reported values of SF_6 content are much lower: 50% in the study of Steglich *et al.* (performed with TS around −40 °C, [3]) or 54% in the case of Gaudig *et al.* for T_S at −5 °C [4]. At "room-temperature" (between around 20 and 30 °C), a relatively large range may be available: formation of black silicon has been reported with SF_6 contents of 42% [4], 60% [5] or 72% [6] for instance.

In addition to the influence of temperature and SF_6/O_2 ratio, Jansen *et al.* [7] have shown that the process window to obtain black silicon especially depends on the applied power and discharge pressure. Regarding pressure, studies cited earlier indicate values ranging from 15 to 225 mTorr (2 to 30 Pa), i.e. the low end of the available range on the RIE setup. Conditions for the coupled power are more difficult to identify from literature: most reports only give the total injected power (and not the actual power coupled to the plasma), nor the size of the electrode, therefore making comparisons challenging. Nevertheless, studies on reactors of similar sizes as the RIE setup used in the present work show that black silicon can be obtained in the available range of power densities for our setup [5, 6].

III.1.1.b Description of the samples

In addition to discharge parameters, the type of c-Si substrate may play a role in the nanotexturing process. Several types of samples purchased from different manufacturers will be used in the course of the present work, as summarized in Table III.2, also indicating the substrate thickness and the growth method: either Czochralski (CZ) or Float-Zone (FZ).

Tab. III.2: Labels and description of the c-Si samples used in this study. All samples are cut from (100) n-type (phosphorus doped) c-Si wafers, with a resistivity in the range 1–5 Ω·cm (specifications from manufacturers). Thickness measured at the LPICM.

Label	**Surface finish (both sides)**	**Growth method**	**Thickness** (µm)
SWS	Slurry-wire-sawn	FZ	275 ± 5
DWS	Diamond-wire-sawn	CZ	177 ± 2
DSP	Mirror polished	CZ	280 ± 2
LPD	Lapped	CZ	285 ± 5

Surface finish and bulk properties. The c-Si wafers exhibit various initial finishes: slurry wire sawn (SWS), diamond wire sawn (DWS), double-side mirror-polished (DSP), and lapped (LPD) wafers are used. Confocal microscopy surface profiles of the initial morphologies are shown in Figure III.2 for SWS, DWS and LPD samples, with two extracted 2D profiles in each case.

SWS and DWS wafers are processed "as-cut," i.e. they did not undergo any other process after sawing from the ingot, and their surface properties differ according to the employed sawing technique. In slurry wire sawing, the abrasive particles are contained in the slurry solution poured on the metal wires during the cutting. In contrast, the abrasive particles are coated on the metal

1. Notice that in the available literature, analyses are most often reported in terms of O_2 content instead, but for the sake of consistency with the previous chapter, the SF_6 content will here be indicated.

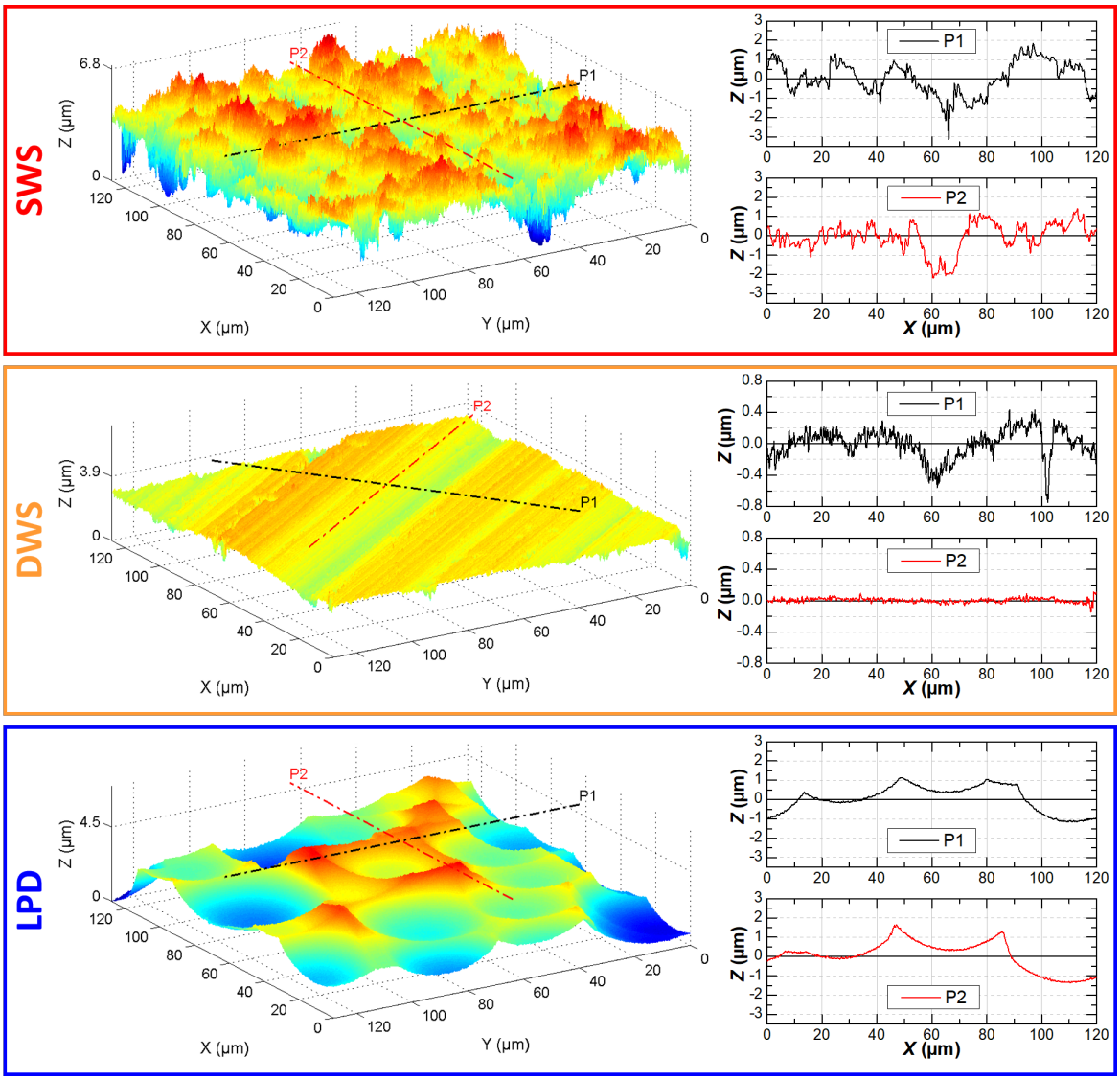

Fig. III.2: 128 × 128 µm^2 surface profiles (obtained by confocal microscopy) of unetched SWS, DWS and LPD samples. Dashed lines show the position of the extracted 2D profiles (graphs on the right, profiles normalized to zero mean, notice the different scales on the vertical axis for the DWS case).

wires in the case diamond wire sawing, leading to different modes of interaction with the silicon and therefore a different surface finish [8, 9]. SWS and DWS wafers both exhibit micrometer-sized mounds and grooves with sharp edges, however, the surface of the DWS wafer appears much smoother compared to the SWS surface: the root-mean-square (rms) roughness of the SWS sample is 0.8 µm, while a value of 0.3 µm is found for the DWS one. Moreover, SWS wafers seem to have a nearly isotropic microstructure, in contrast with DWS wafers showing strong anisotropy due to saw marks, that are observed easily in the confocal surface profiles Figure III.2. As a result, a large difference in roughness is observed for profiles taken perpendicularly (profile P1) or parallel to the saw marks, a feature characteristic of diamond wire sawing and also observable with the naked eye.

In contrast, DSP wafers underwent several mechanical and chemical etching processes inducing a very low surface roughness and a mirror-like visual appearance (the initial topography of DSP wafers has not been characterized through confocal microscopy).

Finally, LPD wafers underwent mechanical grinding with a slurry solution, followed by a chemical etching to remove the subsurface damage induced by the lapping process. LPD wafers exhibit shallow pits with square edges dispersed on the surface, with no observable long-range order. The rms roughness of LPD wafers is around 0.8 µm, similar to SWS wafers. Notice that all samples

are initially symmetric: the surface finish is similar on each side (but only the side exposed to the plasma will be modified during the nanotexturing process).

The substrates listed in Table III.2 are chosen for the diversity of initial surface topographies previously discussed, and due to several experimental constraints. It would for instance be appealing to only consider mirror-polished (DSP) samples. Indeed, the very low initial roughness would make the study of nanostructures, as well as the quantification of the etch depth (measurement relying on stylus profilometry), much easier. However, c-Si wafers used in the photovoltaic industry are not polished to a "mirror state" as this process is very expensive and of no added value for solar cells. Therefore, any potential influence of the initial surface finish on the process should be considered.

Finally, only n-type monocrystalline c-Si samples with (100) orientation are used. The doping level is known to influence the etching rate of c-Si with fluorine plasma due to electrostatic effects [7, 10]. However, this dependence is negligible for low bulk doping level (values below 10^{16} cm^{-3} are typical for solar-grade wafers), and due to the ion bombardment, this dependence on the doping type can be neglected [11]. RIE nanotexturing of c-Si using SF_6/O_2 is also known to be efficient on mc-Si wafers, and only a few studies in the literature have reported dependence on the crystalline orientation [12, 13].

Initial total reflectance. The reflectance of the initial c-Si samples surfaces is strongly influenced by the surface roughness and crystalline structure. Figure III.3 shows the total hemispherical reflectance spectra of the substrates before etching at near normal incidence, together with the theoretical Fresnel reflectance for a planar surface [14] and the AM1.5g solar photon flux spectrum [15]. DSP and LPD wafers exhibit similar reflectance from 250 to 1000 nm. Their effective reflectance R_{eff} is high (37.8% and 35.8% for DSP and LPD, respectively) due to their very low surface roughness. The increase of reflectance for wavelengths longer than approximately 1 µm is due to the substrate becoming semitransparent: part of the light entering the c-Si can escape it after being reflected at the rear surface.

Unetched DWS wafers, despite their high surface roughness, exhibit a comparable level of reflectance (R_{eff} = 37.4 %) to the unetched DSP and LPD samples, except for wavelengths below 450 nm. Indeed, the peaks at about 270 nm and 360 nm, corresponding to the Van Hove singularities in the density of states of c-Si [16], do not appear. The lack of Van Hove features is attributed to a thin layer (a few nanometers) of amorphous silicon on top of the c-Si, induced by plastic ductile

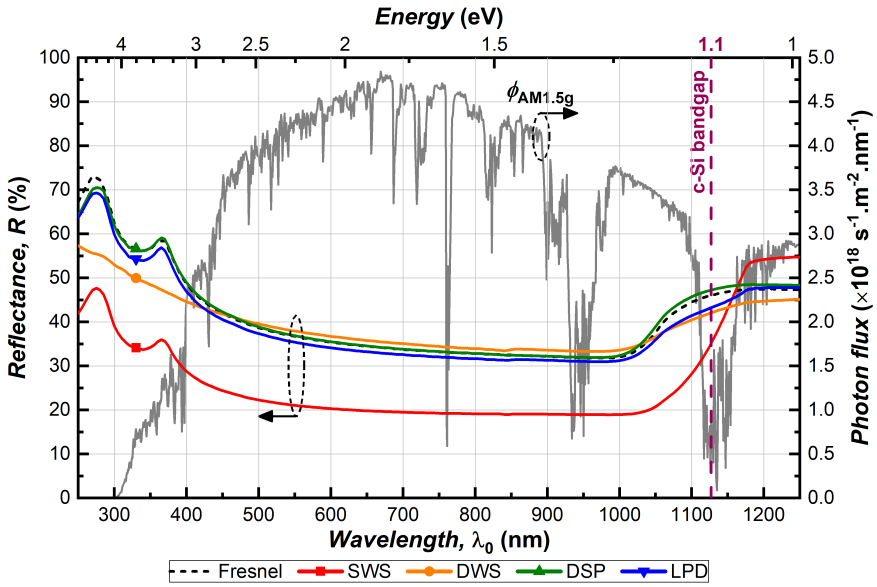

Fig. III.3: Total hemispherical reflectance spectra for initial SWS, DWS, DSP and LPD samples, as well as theoretical Fresnel reflectance for a 280 µm c-Si slab and AM1.5g photon flux spectrum.

mode cutting during diamond wire sawing, which mechanically hardens the c-Si surface [17]. In contrast, the characteristic peaks of c-Si are observed for SWS wafers, but the whole spectrum is lowered, with $R_{eff} = 21.6\,\%$. This decreased reflectance in the entire range is attributed to multiple reflections in the large topographical features found on the surface.

Finally, it is interesting to notice that the convexity of the curves near the bandgap of the material, i.e. in the approximate range [1050,1150 nm], depends on the surface finish. Indeed, for SWS wafers the reflectance curve is convex, whereas all other curves are concave. This effect is due to a much higher level of light-trapping for these samples as we will see in Chapter IV.

III.1.1.c Identification of nanotexturing process window

Benefitting from both the study of literature and previous work carried out at the LPICM (not published), a few preliminary experiments have been conducted to identify a baseline process for c-Si nanotexturing with SF_6/O_2 plasma. The conditions used for this study are summarized in Table III.3 together with a schematic of the sample locations on the substrate electrode during the process. SWS samples have been used and for each set of conditions two samples were introduced in the chamber: one at the center of the electrode (sample A) and another one at approximately 5 cm from the center (sample B). It should be highlighted that in all experiments presented in this chapter, the native oxide present at the surface of the c-Si substrate is not removed (e.g. by HF dip) before the process.

Tab. III.3: c-Si nanotexturing process parameters used for study presented section III.1.1.c. Varied parameters indicated by an asterisk. Schematic (to scale) of substrate electrode with sample locations during process.

	Input parameters		Sample locations
Gases	***Pressure,** P_r	30, 55, 100 mTorr	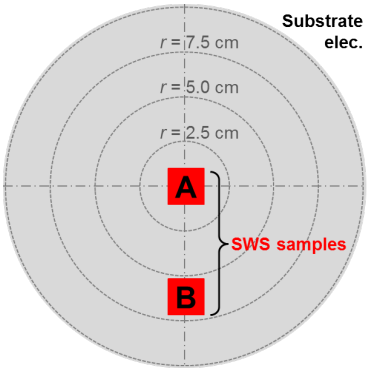
	Nature	$SF_6 + O_2$	
	***Total input flux**	70, 140, 210 sccm	
	***SF_6 content**	34, 46, 57, 69, 80 %	
Voltage	**Signal basis freq., f_0**	13.56 MHz	
	# of harmonics, n	1 (single-freq.)	
	Nominal power, P_{fwd}	100 W	
Substrates	**Sample type**	SWS	
	Sample size	2×2 cm^2	
	Temperature, T_S	25 °C	
	Etching time, t_e	15 min	

Single-frequency voltage excitation has been used, the etching time (15 min) and the substrate temperature (25 °C) were kept constant, while various values of pressure, total incoming gas flux and SF_6 contents have been used. Finally, it should be noted that for this study the nominal power ($P_{fwd} = 100$ W, indicated by the generator) was set constant rather than the coupled power P_w (see Equation (I.15) Chapter I).

Total hemispherical reflectance measurements were performed on the samples, in the wavelength range [250,1250 nm] (full spectra not shown). The experiments aim to locate an adequate baseline process for efficient c-Si surface nanotexturing: the optimization is therefore done directly by comparing "anti-reflection" performances. The effective reflectance, R_{eff}, is therefore computed in order to compare all the samples. By weighting the reflectance with the AM1.5g solar irradiance spectrum (see Equation (I.29), Chapter I), this single parameter characterizes the average decrease of reflectance achieved from nanotexturing that is relevant for photovoltaic applications.

All results are shown in the graphs of Figure III.4: absolute values of R_{eff} are given in the top line graphs while bottom line graphs show the relative difference between sample A and B. As a reminder, unetched SWS samples have an effective reflectance of 21.6%.

Evolution of effective reflectance. The top graph Figure III.4(a) shows the influence of the SF_6 content on the effective reflectance at a constant pressure of 30 mTorr for three values of total input gas flux. A clear minimum of reflectance is found: for 70 sccm gas flux, the minimal value is attained at an SF_6 content of 47%, with R_{eff} = 8.1 % for sample A (5.5% for sample B). If the SF_6 content is decreased to 35%, R_{eff} is almost similar as the unetched sample (around 20%). Increasing the SF_6 content also leads to increased effective reflectance: remarkably, for the highest SF_6 content (80%) R_{eff} reaches values much higher than the unetched sample (29.4 and 31.5% for sample A and B respectively), a phenomenon attributed to the smoothing of the surface during etching.

A similar behavior is found when the gas flux is increased to 140 or 210 sccm, except the optimum SF_6 content is shifted to 57%, and the lowest reflectance is found for sample B (around 3.0% for both values of total gas flux). From the available data, this shift in optimum SF_6 content as a function of the total gas flux is possibly only "apparent": more experiments would be needed (with intermediate SF_6 contents) to confirm that an actual shift in exists, which would be due to a different gas residence time in the reactor.

The existence of an optimum SF_6 content is interpreted as a result of the required balance between c-Si etching (by fluorinated species) and passivation layer formation acting as etch inhibitor (in the form of SiO_xF_y species, created due to the presence of oxygen). Around the optimum SF_6 content, a certain balance between etching rate and passivation layer formation rate is achieved, and SiO_xF_y species act as a micro-mask leading to the formation of nanostructures, as discussed in Chapter I, section I.2.1. Above the optimum SF_6 content, the process shifts to an "over-etching regime": the etching rate is too high for the micro-masking passivation layer to be efficiently formed on the surface. In contrast, below the optimum, the process reaches an "over-passivating regime": the passivation layer formation is promoted due to a large density of O* radicals and etching inhibited on most of the surface. At both extremes, formation of nanostructures is therefore prevented.

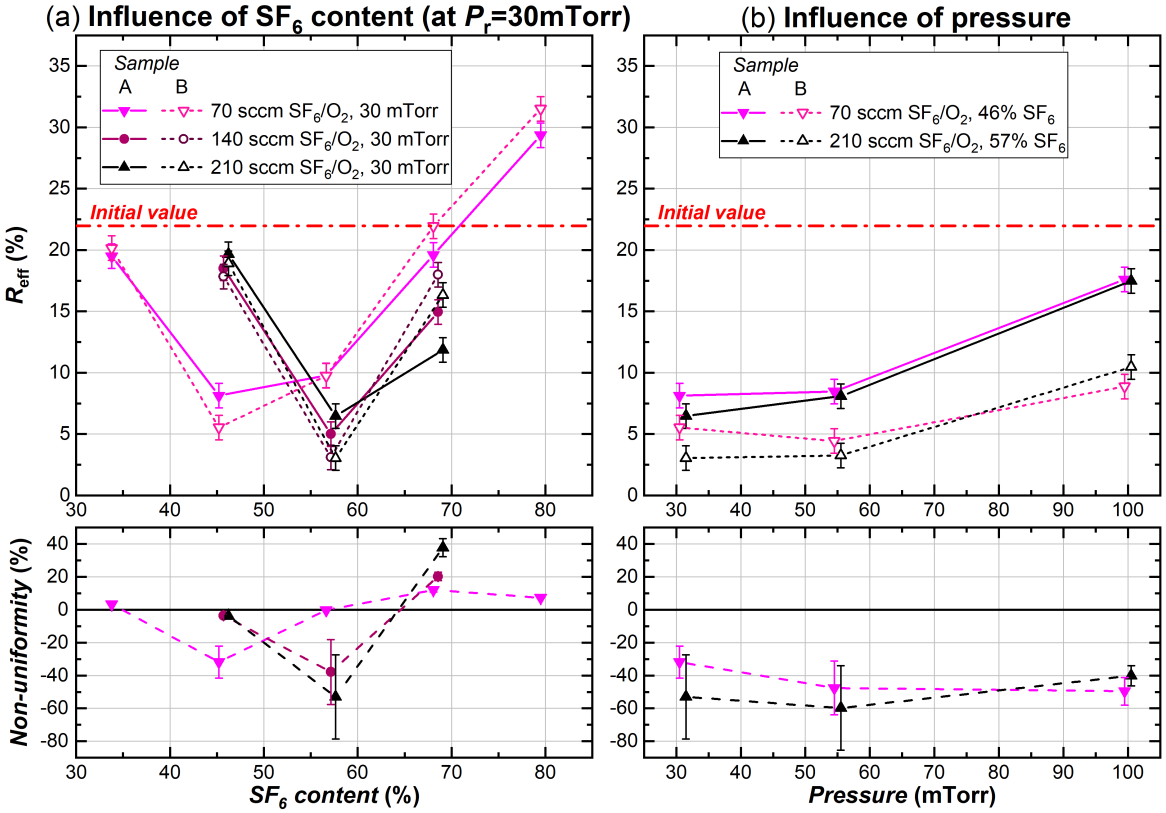

Fig. III.4: Influence of (a) SF_6 content and (b) pressure on the effective reflectance, R_{eff}, for samples A and B (top row), and inhomogeneity between the samples (bottom row), obtained for various conditions of total input gas flux. Lines shown as guides to the eye.

In the top graph Figure III.4(a) a significant difference in R_{eff} is observed in some cases between samples A and B, which were simultaneously processed but placed at different locations on the radius of the electrode. For a better visualization of this difference, the bottom graph (in the same figure) shows the "non-uniformity" of texturing, quantified by the relative difference $(R_{eff,A} - R_{eff,B})/R_{eff,A}$. It is interesting to notice that for the optimum SF_6 content (leading to the lowest R_{eff} values, i.e. 46% for 70 sccm gas flux and 57% for 140 or 210 sccm) the reflectance of sample B is much lower (30 to 55%$_{rel}$) than for sample A. For all other cases, both samples either have a similar reflectance, or the situation is reversed (sample B is more reflective).

The pressure of 30 mTorr is the lowest accessible value with the RIE setup in process conditions. For the optimum points in SF_6 content obtained at 70 and 210 sccm total input flux, additional tests were performed at a higher pressure (55 and 100 mTorr) and results are shown in Figure III.4(b). At an SF_6 content of 57% (total gas flux of 210 sccm), raising the pressure from 30 to 55 mTorr little affects R_{eff} (+1.6%$_{abs}$ for sample A and +0.3%$_{abs}$ for B), but a further increase to 100 mTorr significantly increases R_{eff} (+9.4%$_{abs}$ for sample A and +7.2%$_{abs}$ for B). A quantitatively similar behavior is found at an SF_6 content of 46% for an input flux of 70 sccm, except for sample B obtained at 55 mTorr which has a slightly lower reflectance (-1.1%$_{abs}$) compared to the result at 30 mTorr. It therefore appears that, globally, the lowest reflectance results are obtained for samples processed at the lowest discharge pressure available.

Regarding the influence of the pressure on relative differences between the samples, it is observed that for all conditions in Figure III.4(b) R_{eff} is much lower (from -30 to -60%$_{rel}$) for sample B than for sample A. A large non-uniformity in the process conditions along the radius of the electrode is therefore demonstrated, and is possibly linked to the non-uniform ion flux revealed in Chapter II for similar plasma conditions. A more detailed study of this possible effect will be carried out in sections III.2 and III.3 of the present chapter.

Evolution of self-bias voltage. While the nominal power P_{fwd} was kept constant for all the aforementioned experiments, it is interesting to have a look at the values of self-bias voltage, which may give a first indication on a possible effect of ion bombardment energy. Values are displayed in the graphs of Figure III.5 for the explored conditions.

It is first observed in Figure III.5(a) that regardless of the total input gas flux, V_{DC} decreases (in absolute value) when the SF_6 content is increased: in the 70 sccm case, the self-bias voltage goes from −193 V at an SF_6 content of 34%, to −142 V at 80% of SF_6. This effect has already been observed in the previous chapter and comes from an increase in electronegativity of the discharge: the ratio of positive ions to electrons increases, leading to a rise in self-bias voltage and a decrease in applied V_{PP} (not monitored here) required to obtain the nominal power. Moreover, a small increase of V_{DC} is observed (SF_6 content of 57 or 69%) when the total input flux is increased, maybe

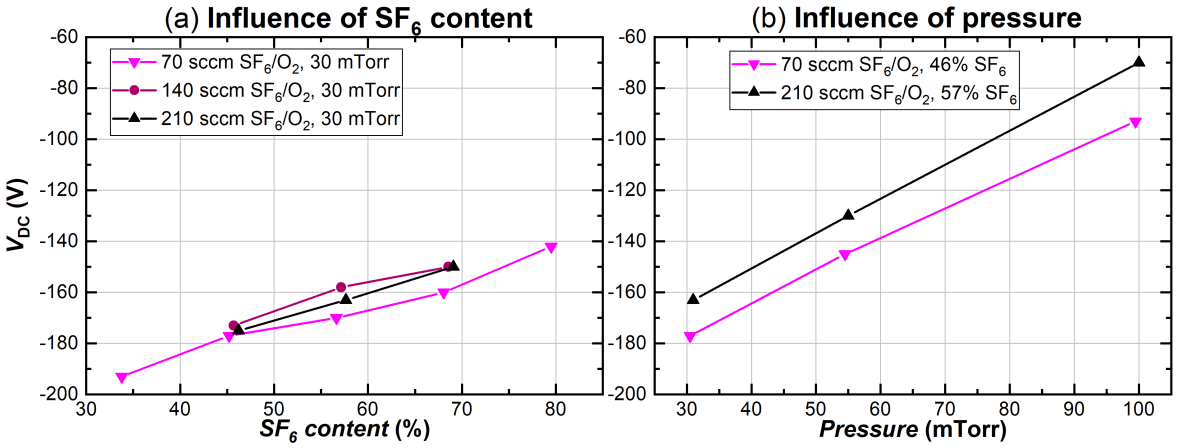

Fig. III.5: Influence of (a) SF_6 content and (b) pressure on the self-bias voltage measured in process conditions used for nanotexturing (conditions displayed in Table III.3). Lines shown as guides to the eye.

due to a change in electronegativity induced by different gas residence times for SF_6 and O_2.

Increasing the pressure at a given SF_6 content and total input flux also leads to a decrease in $|V_{DC}|$, as shown in Figure III.5(b). For instance, at an SF_6 content of 57% and a gas flux of 210 sccm, the self-bias voltage goes from −177 V at 30 mTorr to −90 V at 100 mTorr. This effect was already observed in Chapter II and is also due to an increased discharge electronegativity: with higher pressure, the electron energy drops and attachment reactions are favored.

From these observations, the influence of V_{DC} at different values of SF_6 content cannot be linked to differences (and notably the existence of an optimum) in the final effective reflectance for the processed samples. In contrast, the decrease in $|V_{DC}|$ (and therefore of ion bombardment energy) when increasing pressure could partially explain the simultaneous increase in R_{eff} although this hypothesis will require further investigations (see section III.3.2.a of the present chapter).

Baseline recipe. Obviously, more experiments would be required to identify an absolute optimum for nanotexturing (in terms of lowest R_{eff}) according to the three process parameters already investigated, namely SF_6 content, total input gas flux and discharge pressure. However, multiple other effects have to be investigated as well, e.g. the effect of discharge power or the etching time. For this reason, a baseline process is chosen at this point, with the parameters listed in Table III.4. Notice that it was later determined that the actual coupled power in these conditions is $P_w = 55$ W (for a nominal power $P_{fwd} = 100$ W indicated by the generator).

Tab. III.4: Baseline process parameters for SF_6/O_2 nanotexturing of c-Si in the RIE setup.

Baseline process parameters		
Gases	**Pressure,** P_r	30 mTorr to 1 Torr
	Nature	$SF_6 + O_2$
	Total input flux	140 sccm
	SF_6 content	57 %
Voltage excitation	**Signal basis frequency,** f_0	13.56 MHz
	Number of harmonics, n	1 (Single-frequency)
	Coupled power, P_w	55 W (P_{fwd} =100 W)
Substrate	**Temperature,** T_S	25 °C

The reflectance spectra of samples ($2 \times 2 cm^2$ SWS c-Si) processed with this baseline recipe for 15 min to samples are shown in Figure III.6 together with the measurement for a reference sample and the solar photon flux according to standard AM1.5g. A drastic decrease of reflectance is observed for samples A (placed at the center of the electrode) and B (around 6 cm from the center), in the range 250 to 1180 nm approximately. Above this value absorption drops (since the photon energy becomes lower than the optical band gap of c-Si) and the reflectance remains almost unchanged.

As previously highlighted, with this recipe, the reflectance of samples placed at different locations on the radius of the electrode is different and sample B shows a promising result. The total hemispherical reflectance of this sample lies below 3% in the range from 460 to 1010 nm, demonstrating a broadband anti-reflection property obtained by SF_6/O_2 plasma nanotexturing. In addition, these wavelengths also correspond to the range of highest photon flux in the global solar spectrum (average of $3.92 \times 10^{18}\ s^{-1} \cdot m^{-2} \cdot nm^{-1}$, corresponding to a photogenerated current density around $35\ mA \cdot cm^{-2}$, if fully absorbed). Overall, the effective reflectance of sample A is only 3.1%, i.e. $86\%_{rel}$ lower than the initial surface.

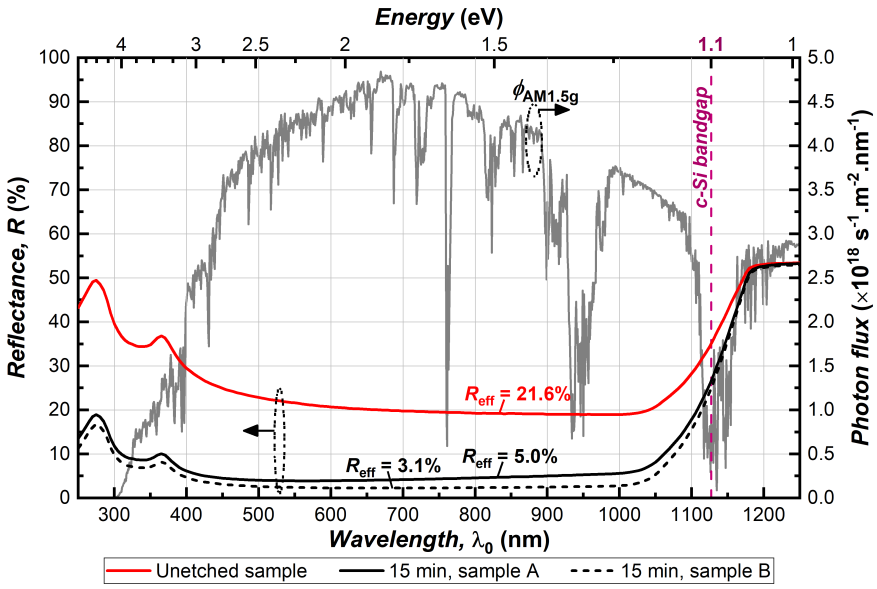

Fig. III.6: Reflectance spectra of unetched SWS surface and 15 min textured samples (baseline process, Table III.4), with AM1.5g photon flux spectrum.

III.1.2 Dynamic Aspects of Nanotexturing

Samples of all four types of wafers were nanotextured using the conditions summarized in Table III.5. Multiple processing times were used in order to gain insight into the formation of the nanostructures and the effect of the preexisting micro-morphology on their evolution. Selected values for the process times, te, were 2, 5, 10, 15, 30 and 75 min.

Tab. III.5: c-Si nanotexturing process parameters used for study presented section III.1.2. Varied parameters indicated by an asterisk. Schematic (to scale) of substrate electrode with sample locations during process.

	Input parameters		Sample locations
Gases	**Pressure,** P_r	30 mTorr	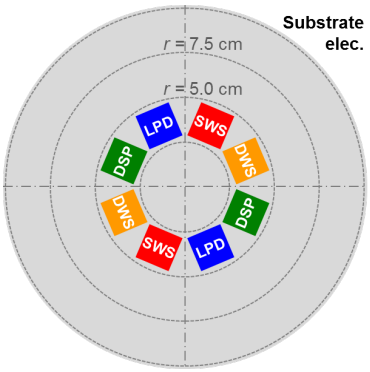
	Nature	$SF_6 + O_2$	
	Total input flux	140 sccm	
	SF_6content	57 %	
Voltage	**Signal basis freq.,** f_0	13.56 MHz	
	# of harmonics, n	1 (single-freq.)	
	Power, P_w	55 W	
Substrates	***Sample type**	SWS, DWS, DSP, LPD	
	Sample size	2×2 cm^2	
	Temperature, T_S	25 °C	
	***Etching time,** t_e	2, 5, 10, 15, 30, 75 min	

Photographs of a set of samples are shown in Figure III.7. First, large differences in unetched samples are observed: SWS, DWS and LPD samples show diffused reflectance, in contrast with DSP samples where specular reflectance is dominant. Diagonal sawing marks are especially seen on the unetched DWS sample. A dramatic change in visual appearance is then seen for 5 min textured samples: a "darkening" is observed, although the visual effect of the initial surface finish is still distinguishable. After 15 min, differences are still observed with the naked eye, but the samples appear similarly (and uniformly) black in the picture.

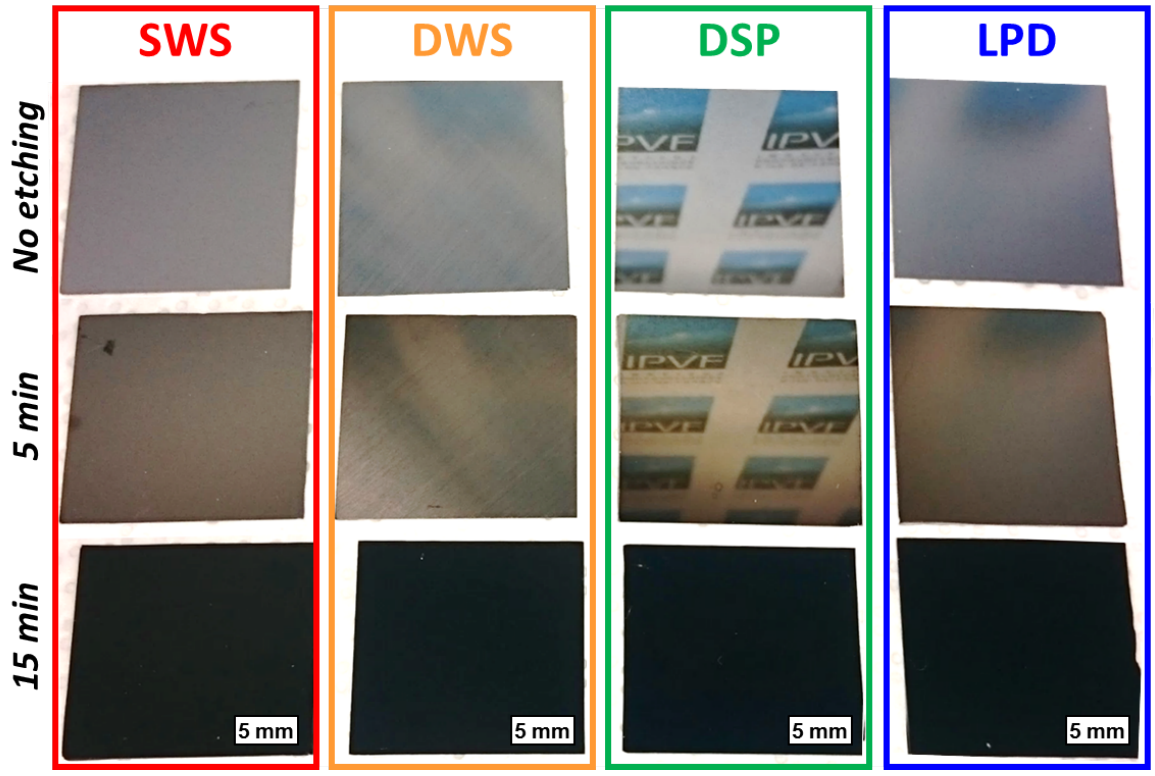

Fig. III.7: Photographs of four types of samples without texturing (top row) and after various RIE etching times (5 and 15 min). Notice the visible diagonal sawing marks on unetched DWS sample, as well as the specular reflection (IPVF logo) on the unetched DSP sample. $2 \times 2\text{cm}^2$ samples (scale only shown on bottom line).

III.1.2.a Nanostructure size evolution and dependence on initial surface state

SEM images of the processed samples are shown in Figure III.8. It can be seen – in the inset images for nanotextured LPD samples – that the nanostructures resemble cones, with an apex angle of roughly 45° (determined from side-view SEM images, not shown here).

Nanostructures appear rapidly after the beginning of the plasma process (nanostructures are already observed after only 2 min). The typical nanostructure size then continuously increases with processing time. They develop through the etching of the surrounding c-Si, so the resulting nanostructures are the negative shape of the etched volume. On DSP wafers, where the initial roughness is very low, the nanocones are vertically oriented and uniformly distributed. In contrast, nanostructure formation on SWS and DSP wafers is clearly influenced by the initial roughness; a less uniform distribution of sizes and slopes can be observed. Moreover, in the deep grooves of the SWS wafers, the growth of nanostructures seems to be hindered. On DWS samples, nanocones are aligned along the grooves, and they appear larger on the top of the grooves than on the bottom. Finally, it is noted that the shapes of the nanostructures become more complex as the processing time is increased. In particular, the cone-like structures seen after 15 min of etching exhibit multiple ridges on their sides.

The average nanostructure width, Λ_{NS}, has been computed for all nanotextured samples from series of top-view SEM images according to the method described in section I.2.4.b Chapter I. Figure III.9(b) shows the evolution of Λ_{NS} with etching time for the four different initial surface conditions. Values of Λ_{NS} very little depend on the initial surface finish of the wafer. After 2 min of etching, Λ_{NS} is about (46 ± 6) nm for all samples, and it increases with etching time following a scaling law $\Lambda_{NS} \propto t_e^{\gamma}$, where t_e is the etching time and γ an exponent. Comparable behaviors have been observed by several teams for c-Si surface roughening induced by plasma processes with SF_6 [18, 19], CF_4/O_2 [20], and Cl_2 [21]. Note that the computation of Λ_{NS} is influenced by the presence of the initial microstructure, especially on SWS wafers, once the size of the nanostructures

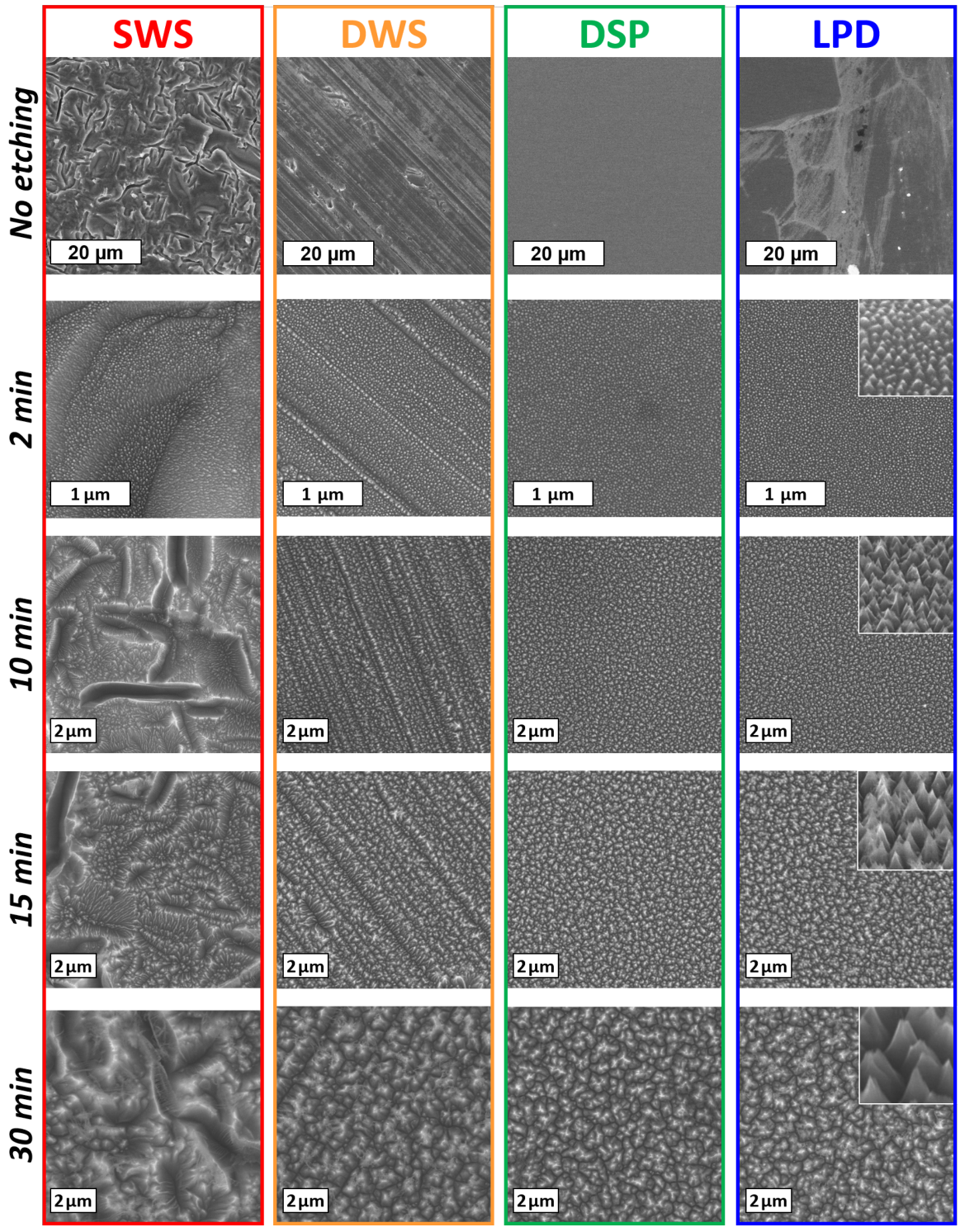

Fig. III.8: Top-view SEM images of four types of samples before process and after various RIE etching times (2, 10, 15 and 30 min). Inset images for the textured LPD samples are 40° off normal tilted views, magnified 3.5 times compared to the corresponding top views. Notice the different scales depending on etching time.

induced by RIE is of similar scale. This effect is most likely responsible for an overestimation of Λ_{NS} for the SWS sample etched for 30 min. For the DSP samples, where the initial roughness is negligible compared to the scale of the RIE induced textures, a value of $\gamma = 1.3 \pm 0.1$ is found (all stated uncertainties represent 95% confidence limits).

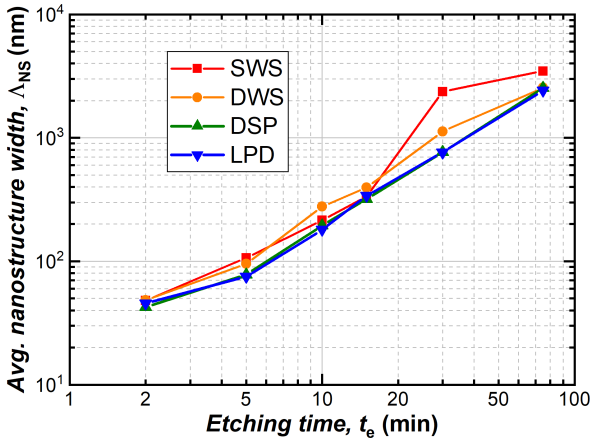

Fig. III.9: Evolution of average nanostructure width, Λ_{NS}, as a function of RIE etching time for the four sample types.

The dynamic evolution of nanostructures is intimately linked to their formation mechanism. While etchant reemission has been suggested as a possible cause for roughening [20], other experimental investigations support a mechanism linked to the formation of a passivation layer, e.g., "soft" etch-inhibitors such as SiO_xF_y species [22, 23], as previously mentioned, or to the presence of "hard" etch-inhibitors due to contamination from the reactor redepositing on the c-Si surface [19]. A recent study [24] successfully simulated the empirical dynamic evolution of black silicon by considering the formation of a passivation layer and the balance between its growth and etch rates. However, the observed scaling behavior is insufficient to definitively assess the nanostructure formation mechanism.

Nevertheless, the similar trends observed in Figure III.9(b) for all types of samples show that the initial topography on these samples has little impact on the length scales of the nanostructures. However, the initial microstructure of the SWS, DWS, and LPD samples is still observable in the SEM images of the samples for etching times below 30 min. A dual-scale structure is present and will affect their optical properties.

III.1.2.b Hemispherical reflectance evolution

Figure III.10 shows the evolution in the reflectance spectra of the four sample types during etching. The reflectance of the front surface of the c-Si samples is observed to strongly decrease with the formation of the nanostructures in the wavelength range [250,1100 nm]. For the samples processed 2 or 5 min, it is clear that the reflectance reduction is stronger for shorter wavelengths, in particular around $\lambda_0 \approx 400$ nm. The particular case of the DWS samples still stands out: after just 2 min etching, a strong decrease of reflectance is observed together with the reappearance of the Van Hove features. This phenomenon is attributed to the removal of the thin amorphous silicon layer which covered the surface, as previously discussed.

At 10 or 15 min of etching, the reflectance has dropped below $10\%_{abs}$ in the wavelength range [330,1000 nm] for all samples, while an asymptotic behavior appears to be reached after 30 min. After 75 min etching, the reflectance is similar (around $2\%_{abs}$ in the range [500,1000 nm]) for all the samples, showing that the influence of the initial microscale roughness on the hemispherical reflectance has vanished.

As explained in Chapter I, the optical properties of nanotextured surfaces can be interpreted in terms of either a gradient refractive index layer or a multiple reflection effect. As a reminder, for normal incidence, the effective medium layer effect can be used to qualitatively describe the

reflectance of nanotextured surfaces provided the characteristic lateral size of the nanostructures, here Λ_{NS} is much smaller than the scaled wavelength λ_0/n_{Si} (n_{Si} is roughly 3.5 to 4 through most of the wavelength range of interest). In this case, the black silicon layer acts as an intermediate layer of graded refractive index between air and c-Si [25]. On the other hand, for very large nanostructures (compared to λ_0/n_{Si}), geometrical optics can be used to interpret the decreased reflectance as the result of multiple reflections between the surface structures, leading to improved transmission of light to the c-Si.

Here, the gradient refractive index interpretation can be used to qualitatively interpret the broadband anti-reflective behavior in the cases of 2 and 5 min etched samples, where $\Lambda_{NS} \leq 100$ nm. In order for a gradient refractive index layer to smoothly adapt the refractive index – and therefore lower the reflectance, the layer depth (or in the case of nanotextured surfaces, the height of the nanostructures) should be similar in the order of magnitude of the wavelength [26]. The height of the nanostructures has not been characterized on these samples: however, for a given sample (e.g. for 10 min etching), the stronger anti-reflective effect observed for shorter wavelengths is explained by a larger optical depth. This effect is more pronounced for DSP and LPD samples: for SWS and DWS samples, the initial microscale roughness already leads to lower reflectance due to multiple reflections.

For 10 and 15 min etched samples, Λ_{NS} lies in the range [200,400 nm], and so the decrease of reflectance cannot be appropriately described in terms of either gradient refractive index or multiple reflection effect. In particular, diffraction phenomena have to be taken into account and iridescence is actually observable on the DSP samples. In addition, it should also be emphasized that Λ_{NS} represents an average over a distribution of sizes and does not inform on the nanostructures height, making the analysis more difficult as well.

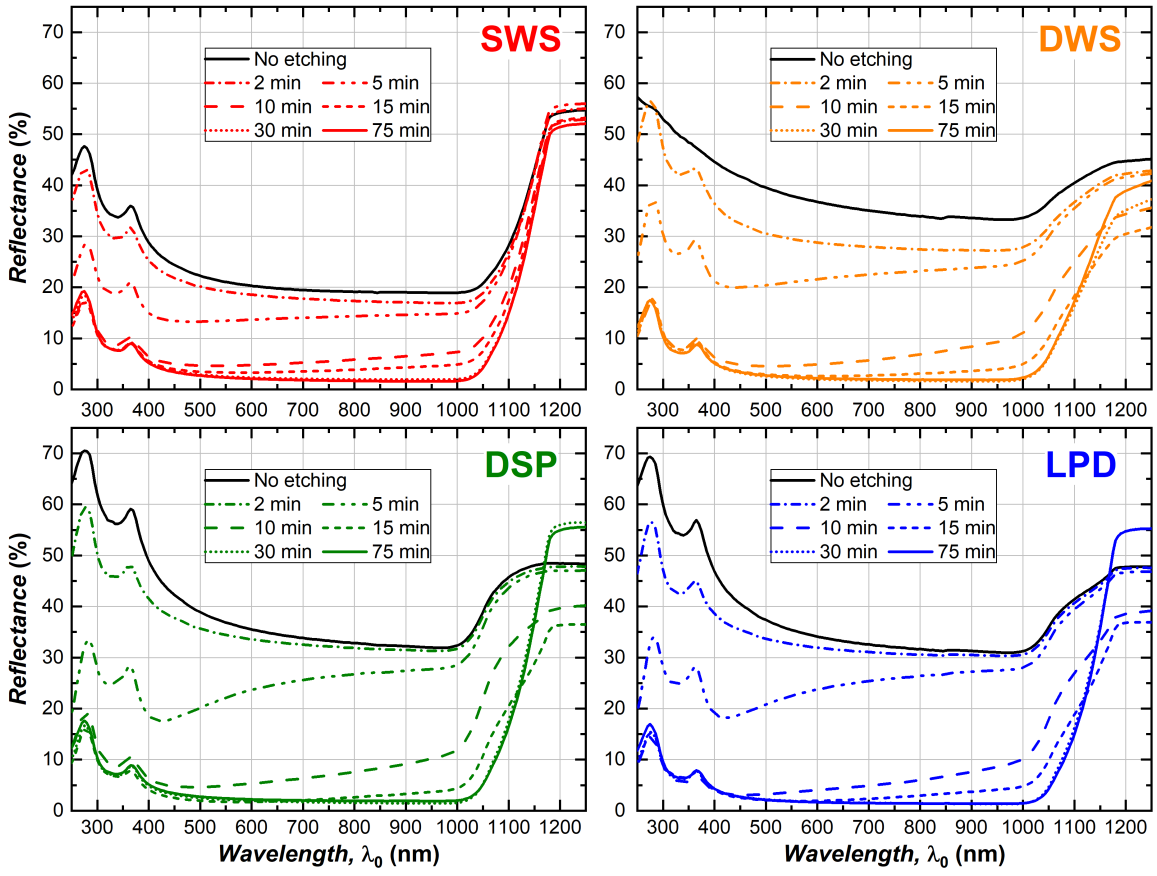

Fig. III.10: Evolution of reflectance spectra (from 250 to 1250 nm) of samples having undergone different RIE etching times.

Finally, for samples etched for 30 or 75 min, the nanostructure average width reaches the micrometer scale, so that for short wavelengths a geometrical optics approach can be used to interpret the decreased reflectance in terms of multiple-reflections.

The effective reflectance, R_{eff}, is computed for all the samples: Figure III.11 shows the evolution of R_{eff} as a function of the etching time. As expected, a monotonous decrease of R_{eff} is observed for all the samples: after only 2 min of process, R_{eff} drops by 7% to 20%$_{\text{rel}}$, and all curves converge after 10 min around $R_{\text{eff}} = 7\,\%$ showing that the nanotexturing is not as effective on SWS samples that had the lowest initial reflectance. The decrease continues until 30 min, when R_{eff} stabilizes around 2 to 3% for all samples. It should be recalled that the nanostructures average width continuously increases during the process (also between 15 and 75 min of process): it therefore appears that an optimum etching time around 15 to 20 min (corresponding to an average nanostructure width Λ_{NS} in the order of 300 nm) is sufficient to achieve excellent anti-reflection properties in the whole wavelength range of interest for photovoltaic applications. A quantitative interpretation of this optical behavior will be proposed in Chapter IV.

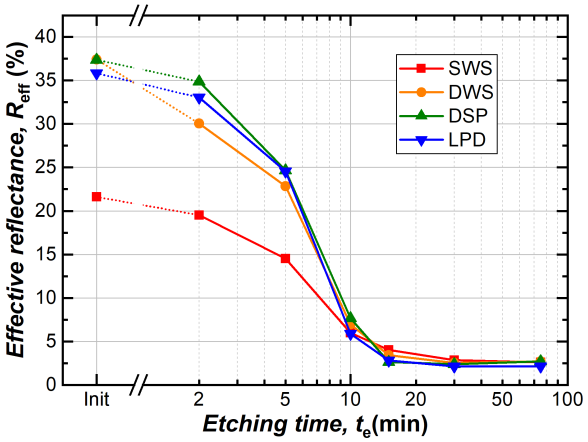

Fig. III.11: Effective reflectance evolution with etching time for four types of sample.

III.2 Texturing Uniformity at Full Wafer Scale

Due to the previously identified non-uniformity in ion flux for the SF_6/O_2 baseline discharge (see section II.3.3 Chapter II), and other possible sources of etching non-uniformity in CCP discharges [27–29], it is of interest to verify that the process may be scaled-up to a full wafer, with a size relevant for photovoltaic applications. Investigations have therefore been conducted with 6 inches pseudo-square wafers (15.6 cm large with rounded-off corners and a 20 cm diagonal, as depicted on the schematic in Table III.6). The total area of the wafer is thus around 240 cm^2 (60 times larger than the samples tested until now in the present work). These studies have been carried out with the participation of Billal Faryssy, during his internship at the LPICM.

III.2.1 Initial Tests and Influence of SF_6 Content

III.2.1.a Definition of optimization parameters

To properly analyze the following results, an appropriate method must be designed to give a global characterization of nanotextured wafers and optimize the process. The premises of the chosen scheme can be explained by a representative example: a 6" pseudo-square wafer was processed with the conditions summarized in Table III.6 below (close to the baseline recipe identified in section III.1.1.c). A schematic of the substrate electrode with the wafer is also supplied as illustration: notice that two areas of the wafer were masked during the process to measure the etch depth, although these results are not shown.

Tab. III.6: c-Si nanotexturing process parameters used for initial upscaling test. Schematic (to scale) of substrate electrode with wafer location.

	Input parameters		Sample locations
Gases	**Pressure,** P_r	35 mTorr	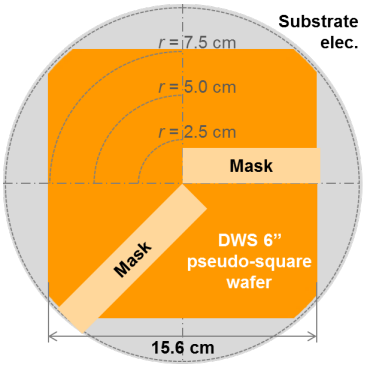
	Nature	$SF_6 + O_2$	
	Total input flux	140 sccm	
	SF_6 content	57 %	
Voltage	**Signal basis freq.,** f_0	13.56 MHz	
	# of harmonics, n	1 (single-freq.)	
	Power, P_w	$P_w = 55$ W	
Substrates	**Sample type**	DWS	
	Sample size	6" pseudo-square	
	Temperature, T_S	25 °C	
	Etching time, t_e	20 min	

A photograph of the wafer after processing is shown in Figure III.12(a): a significant non-uniformity of the reflectance can be visually observed. Indeed, while the edges and corners of the wafer (across a distance of approximately 1 to 3 cm depending on the location) look black, the center of the wafer appears almost pristine. In-between these areas, a gradient of reflectance occurs over a relatively short distance (in the order of 1 to 2 cm). These visual observations and the SEM images supplied in Figure III.12(a) demonstrate that black silicon nanostructures (with efficient anti-reflective properties) are formed at the edges and corners of the wafer but absent in the central area. In addition, it appears that the areas where black silicon is formed roughly respect the symmetries of the wafer: this observation confirms that the discharge properties also comply with these symmetries.

The upscaling tests aim at obtaining a uniform reflectance over the whole wafer area, and the optimization will therefore be exclusively done according to spectrophotometric measurements. However, these measurements are local by nature as only a small area (here around 18 mm^2) is probed by the measurement beam. Therefore, due to the observed symmetries and to avoid time-consuming measurements, the choice has been made to only perform characterizations along

half of a diagonal for all processed wafers. An example of effective reflectance profile obtained by this method is shown in Figure III.12(b). Although not representative of the whole wafer area, the proposed measurement procedure is adequate for the process optimization carried out in this study.

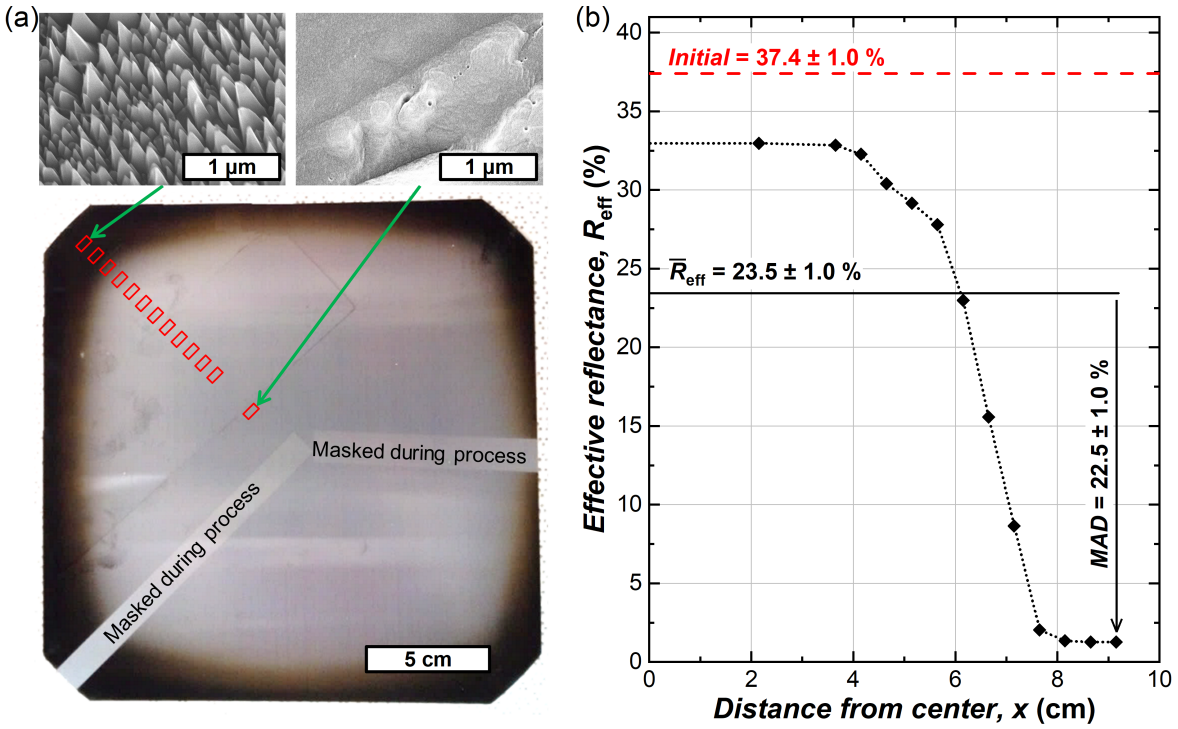

Fig. III.12: (a) Photograph of 6" pseudo-square wafer (and SEM images from center and corner) processed for 20 min with: $P_w = 35$ W, $P_r = 35$ mTorr, SF_6/O_2 gas flux: 140 sccm (57 % SF_6). Red rectangles show approximate size (around 6×3 mm^2) and positions of light spots during spectrophotometric measurements, leading to the effective reflectance profile shown in (b).

Comparison between different wafers are then made according to two global parameters: first, the "profile averaged" reflectance, $\bar{R}_{eff}$, is calculated from the local effective reflectance values obtained along the diagonal of the wafer (parametrized by the coordinate x – origin at the center of the wafer). Due to the non-uniform sampling of $R_{eff}(x)$, $\bar{R}_{eff}$ is computed as:

$$\bar{R}_{eff} = \frac{1}{x_N} \sum_{i=0}^{N} \frac{R_{eff}(x_{i+1}) + R_{eff}(x_i)}{2} (x_{i+1} - x_i) \tag{III.1}$$

where N is the number of measurements in the profile and x_i the distance from the center of the wafer (notice that in Equation (III.1) we assume $x_0 = 0$ mm and $R_{eff}(x_0) = R_{eff}(x_1)$, i.e. the value at the center of the wafer is approximated by the closest measurement). Obviously, a minimal reflectance over the entire wafer (i.e. minimal $\bar{R}_{eff}$) is here sought.

Next, a global parameter to quantify the uniformity of the effective reflectance must be chosen. Several possible quantifications exist: their relevance depends on the requirements of the envisioned application. For photovoltaic applications, in addition to the need for a low $\bar{R}_{eff}$, large absolute deviations of R_{eff} across the wafer need to be avoided. At least two reasons can be invoked: (i) it would be visible with the naked eye – an important criterion for solar cells; (ii) it would most probably come from large variations in surface morphology (at the nanoscale) across the wafer and therefore hinder uniformity in subsequent processes (e.g. deposition of passivation layers). From this analysis, the maximal absolute deviation (MAD) to $\bar{R}_{eff}$ is therefore selected, and expressed by:

$$MAD = \max_{i \in [1,N]} |R_{eff}(x_i) - \bar{R}_{eff}| \tag{III.2}$$

For the previously shown wafer the results are: $\bar{R}_{\text{eff}} = (23.5 \pm 1.0)\,\%$ and $MAD = (22.5 \pm 1.0)\,\%$, values also illustrated in Figure III.12(b). Obtaining such a high average reflectance and an MAD in the same order of magnitude successfully summarizes that the tested process is not suitable for upscaling to 6" pseudo-square wafers in the RIE reactor.

III.2.1.b Influence of SF_6 content

The behavior observed in the initial upscaling test (center-high profile of reflectance) is analog to a "bull's eye" effect described for c-Si etching experiments, where the etch rate monotonically increases from the center to the edge of the wafer [27, 28, 30].

In these cases, the presence of a large wafer (i.e. a large etchable area) has been shown to especially induce large gradients of neutral etchants in the plasma: fluorine is largely depleted at the center of the discharge compared to the edges of the wafer. The interpretation is made more complex in the case of nanotexturing due to the presence of additional oxygen that acts as an inhibitor layer source.

The effect of the SF_6 content in the input gas flux is therefore investigated. Additionally, this parameter was especially identified (see section III.1.1.c) to significantly influence the difference of final reflectance for 2×2 cm^2 samples disposed at different locations on the radius of the electrode. Notice that, however, the comparison with these experiments is made difficult due to the large difference of "macro-loading": with two 2×2 cm^2 samples, less than 2% of the electrode area is covered by (etchable) c-Si, while almost 75% is covered with a 6" pseudo-square wafer.

In a first series of tests, several wafers are therefore processed with various SF_6 contents (from 50 to 69%), all other conditions are kept identical as in Table III.6. Results of reflectance measurements are shown in Figure III.13. It is directly seen from the reflectance profiles in Figure III.13(a) that relatively small variations of SF_6 content are responsible for dramatic evolutions of the reflectance map. For an SF_6 content between 50 and 60%, the nanotexturing process is only efficient (in terms of anti-reflection) at the edge of the wafer where the effective reflectance decreases as low as 1% (60% SF_6 case). However, the central area of these wafers (up to a distance of around 40 to 60 mm from the center) shows a much higher value (between 27 and 34% for an SF_6 content of respectively 60 and 50%). Consequently, the average reflectance value $\bar{R}_{\text{eff}}$ for these wafers is comprised between 20 and 30%, as seen in Figure III.13(b).

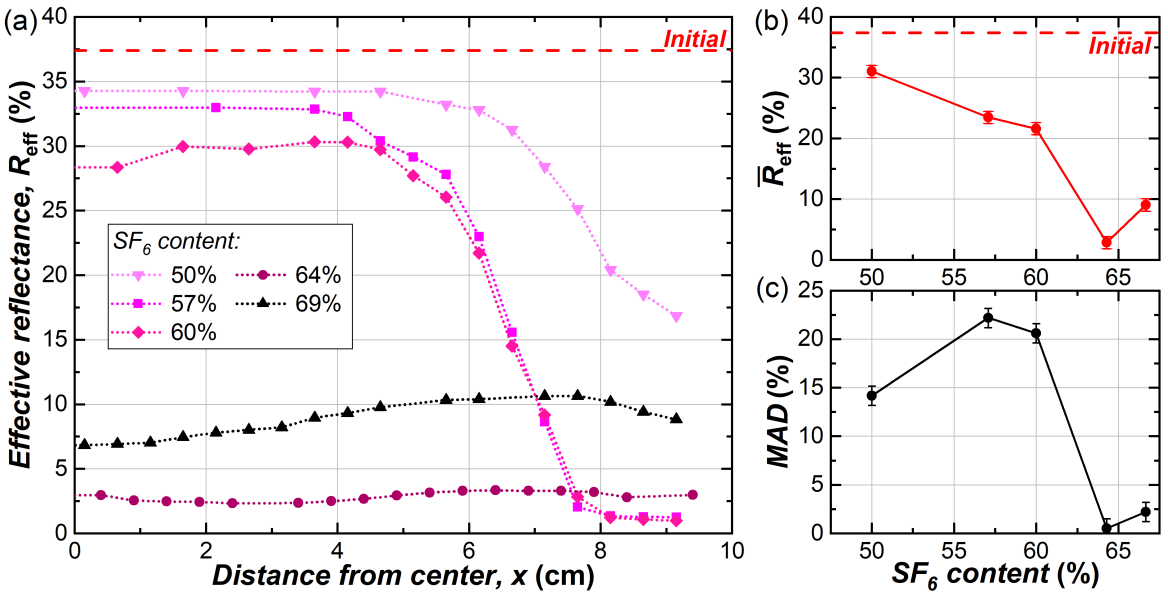

Fig. III.13: (a) Effective reflectance profiles obtained on the diagonal of the wafers after 20 min process with different SF_6 contents. (b) Corresponding "profile averaged" effective reflectance and (c) maximal absolute deviation from $\bar{R}_{\text{eff}}$ vs SF_6 content. Constant parameters: $P_r = 35$ mTorr, $P_w = 35$ W, input gas flux: 140 sccm.

Quite unexpectedly, a further increase to 64% of SF_6 leads to a much lower $\bar{R}_{eff}$ (around 2%), and a maximal absolute deviation, MAD, of less than 1%, as seen in Figure III.13(c). The corresponding profile is indeed much more promising: despite some undulation, the reflectance is very uniform over the whole diagonal of the wafer. This result seems to be close to an optimum as $\bar{R}_{eff}$ and MAD increase again when going to 69% SF_6 in the input gas. However, it is interesting to notice that in this case, the reflectance shows a maximum around 7 cm and decreases towards both the center and the edge.

In order to interpret these results, one must recall that, as explained in section III.1.1.c, the formation of nanostructures is the result of a competition between c-Si etching (by fluorinated species), local inhibitor layer formation (of type SiO_xF_y formed due to the presence of oxygen) and sputtering of the inhibitor layer by ions. A possible interpretation for the obtained results with different SF_6 contents therefore comes from the previously suggested hypothesis of reactive species depletion at the wafer center, where the c-Si substrate acts as a sink for etchants. For this qualitative analysis, the ion bombardment conditions (in terms of flux and energy) are supposed to be constant for all SF_6 contents and across the electrode: any possible radial variation of the ion flux, as demonstrated in Chapter II, is neglected for now. This hypothesis is supported by the fact that only relatively low variations of V_{DC} (below $10\%_{rel}$) have been observed for the considered SF_6 content range (50 to 69% SF_6).

Variations in ion bombardment being neglected, the etching rate and the inhibitor layer formation rate are assumed to only depend on the local density of neutral species (either etchant or inhibitor forming species). Under these assumptions, the formation of nanostructures only depends on the local ratio between fluorine and oxygen neutral densities.

Regarding now the results obtained at the lowest value of SF_6 content (50%): nanotexturing only occurs close to the wafer edges, and it is concluded that, in this area, the adequate balance between fluorine and oxygen neutrals densities is achieved and nanostructures formed. Meanwhile, fluorine is highly depleted in the center of the wafer so that the passivation layer covers most of the surface and etching is almost fully inhibited. If the SF_6 content is continuously increased, the fluorine depletion is gradually compensated, and texturing becomes more and more efficient at the wafer center. Fortunately, at an SF_6 content of 64%, the conditions for texturing are met on the whole surface of the wafer: the densities of fluorine and oxygen (as well as their ratio) may not be completely uniform, but enough for the full surface to be exposed to conditions adequate for texturing.

The observed reflectance profile at an SF_6 content of 69% (with a maximum of reflectance located at around $x = 7$ cm from the wafer) is more difficult to interpret. One possibility could come from simultaneous variations of the O* and F* species density along the electrode radius: it is conceivable that both evolve in a manner such that the center and the edges of the wafer are simultaneously in a regime adequate for texturing, while some inner area is in a slightly shifted regime.

III.2.2 Uniform Final Reflectance, Non-uniform Process Conditions

III.2.2.a Dynamic evolution

Additional tests have been performed with the best recipe for upscaling identified in the previous section, using different process times (1, 5, 10, 20 and 30 min): $P_w = 35$ W, $P_r = 35$ mTorr, 140 sccm SF_6/O_2 input gas flux (with 64% SF_6 content). Reflectance results are first shown in Figure III.14.

For an etching time of 1 or 5 min, center-high profiles of reflectance are again observed, Figure III.14(a): for 1 min, the effective reflectance barely decreases in the center of the wafer (-1.1%$_{abs}$ compared to the unetched wafer), while a large drop is observed at the extreme edge (-14.4%$_{abs}$), with a monotonic profile in-between. Consequently, the average reflectance is high $\bar{R}_{eff} = 32.5\%$, with a large maximal absolute deviation of $MAD = 9.5\%$ – see Figure III.14(b,c). When increasing the process time to 5 min, the reflectance continues to drop on the whole wafer, and becomes almost uniform over a distance of 5 cm at the edge: both $\bar{R}_{eff}$ and MAD significantly decrease.

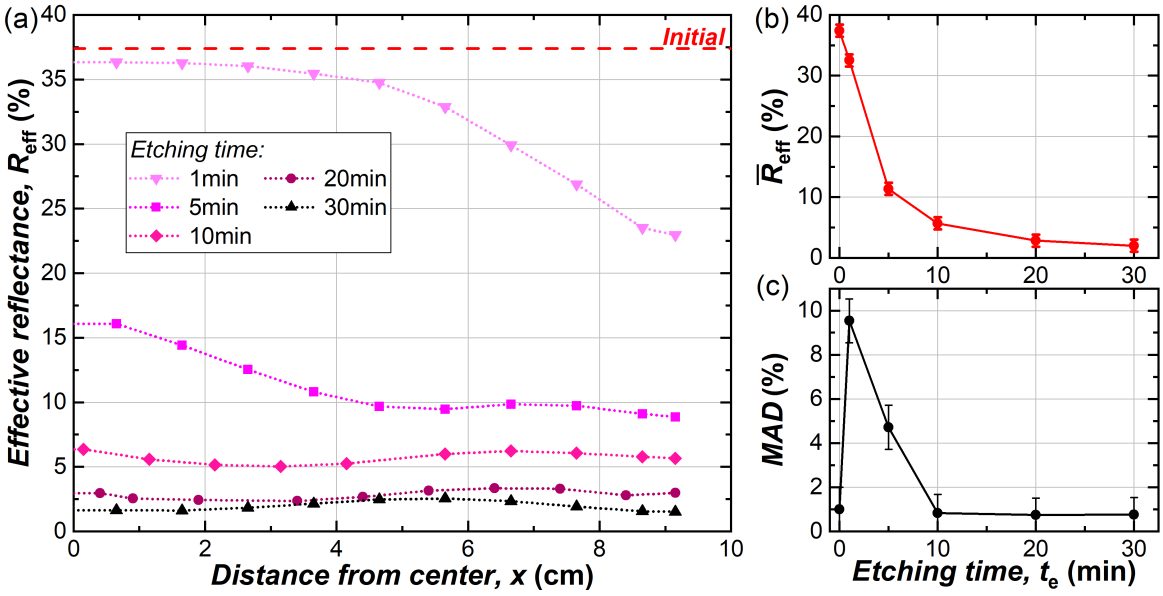

Fig. III.14: (a) Effective reflectance profiles obtained on the diagonal of the wafers after different process times. (b) Corresponding "profile averaged" effective reflectance and (c) maximal absolute deviation from $\bar{R}_{eff}$ vs etching time. Constant parameters: $P_r = 35$ mTorr, $P_w = 35$ W, input gas flux: 140 sccm (64 % SF_6).

After 10 min of process, the reflectance profiles become almost flat, although a small "waviness" can be observed. Therefore, MAD reaches a lower plateau with a value around 1%. Meanwhile, the average reflectance of the wafer continues to decrease, reaching $\bar{R}_{eff} = (2.0 \pm 1.0)$ % after 30 min: a photograph of the wafer is supplied as illustration in Figure III.15. These observations confirm that while the final effective reflectance may be almost uniform (after 10 to 30 min of process), the nanotexturing conditions are not uniform and leading to different "rates" of R_{eff} decrease at the center and edge of the wafer.

A closer look at the nanostructures formed at the center and the edge of the processed wafer is then revealed using scanning electron microscopy images (approximate locations where the images were taken are shown by green circles in the picture of the 30 min processed sample, Figure III.15). Both top and cross-section view images are taken to assess the average nanostructure width and height. Results and selected SEM images are supplied in Figure III.16 (notice missing data for 1 min case: nanostructures could not be observed by SEM at the wafer center).

At the wafer center, the average nanostructure height and width, shown in Figure III.16(a,b), increase almost linearly with time, up to values of $\Lambda_{NS} = (94 \pm 6)$ nm and $H_{NS} = (560 \pm 30)$ nm. Meanwhile, the evolution of nanostructures formed at the edge of the wafer is significantly different compared to the center: wider structures are obtained for etching times below 10 min, at which point Λ_{NS} achieves a plateau value (around 70 nm). In contrast, H_{NS} steadily increases with values continuously higher (between 100 and 200 nm taller) than the results found at the wafer center, until an etching time of 30 min where both trends converge (within uncertainties).

SEM images in Figure III.16(c) show that, in addition to differences in size, the morphologies of nanostructures observed at the two investigated areas on the wafer appear very different. "Cone-shaped" structures are formed at the wafer edge, similarly to observations made in section III.1.2.a, the nanocones being closely packed but "disconnected" from each other and distributed in pseudo-random location (except when formed on protruding saw marks where they are aligned). In contrast, nanostructures formed at the wafer center resemble interconnected vertical "walls," with some also following the orientation of the saw marks. Despite these differences, both areas have a similar effective reflectance since, as it has been previously highlighted, this property especially depends on the nanostructures height (this link will be further explored in Chapter IV).

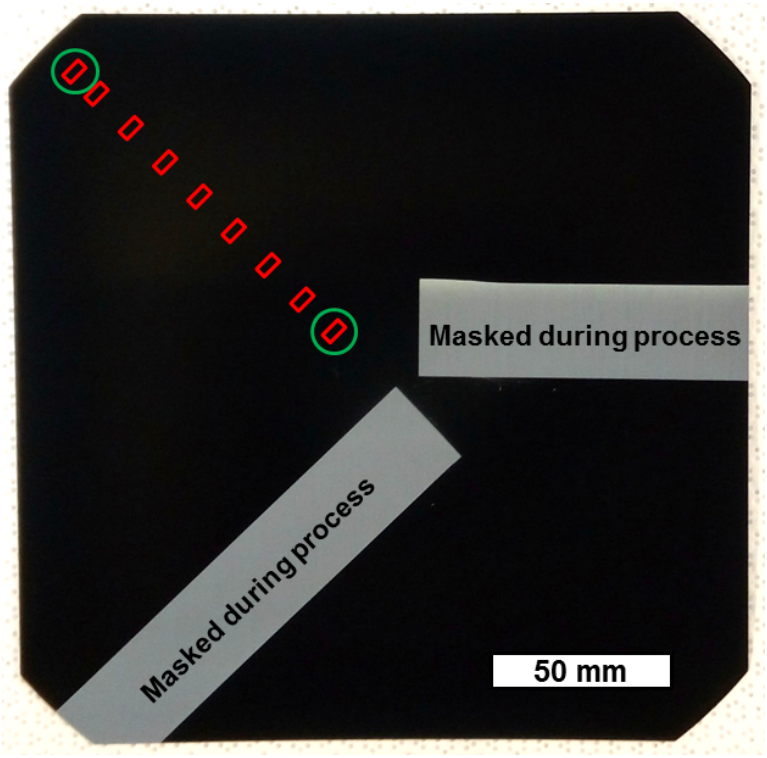

Fig. III.15: Photograph of 6" pseudo-square wafer processed for 30 min with $P_w = 35$ W, $P_r = 35$ mTorr, 140 sccm SF_6/O_2 input gas flux (with 64 % SF_6 content). Red rectangles show approximate size (around 6×3 mm^2) and positions of light spots during spectrophotometric measurements. Green circles show approximate areas where SEM images are taken.

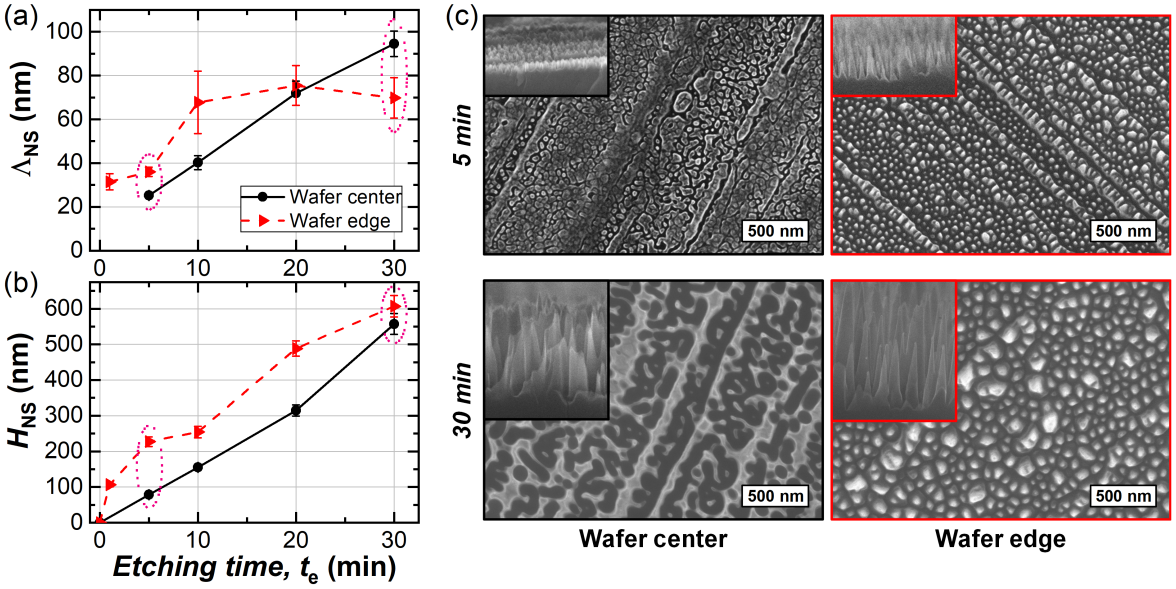

Fig. III.16: Evolution of (a) average nanostructure width and (b) average nanostructure height versus etching time at the center and edge of the wafers. (c) Selected SEM top view images (cross-section views in insets) for a process time of 5 and 30 min.

III.2.2.b Other possible sources of nanotexturing non-uniformity

The important differences in the dynamic evolution of the surface and optical properties between the center and the edge of the wafer demonstrate that significant variations in the plasma-surface interactions occur across the wafer surface. Several possible sources of non-uniformity can still be (non-exhaustively) enumerated – see list below, as well as propositions to test and mitigate them. Notice that these possible sources are introduced by the presence of the wafer, and come in supplement to the effects affecting the discharge (without a substrate), already suggested in Chapter I.

- **Gradient of neutral species density:** this possibility was discussed in section III.2.1.b to explain the difference in effective reflectance profiles obtained for different SF_6 contents in the input gas flux. Despite the final uniform effective reflectance obtained with this plasma recipe, this hypothesis is still valid, and simulation models for the discharge could help identify such non-uniformities.

- **Ion-flux non-uniformity:** an important radial variation of the ion flux on the substrate electrode was demonstrated in Chapter II: this phenomenon was observed with an empty chamber (no substrate) but may still occur when introducing a wafer in the chamber. Assuming that the total ion flux has an influence on the nanostructures formation, it could explain the difference in nanostructures obtained at the center and edge of the wafer: this phenomenon will actually be confirmed in section III.3 (although it cannot be definitively concluded that it is the main source of non-uniformity observed in the current study).

- **Gradient in wafer temperature:** the wafer is not clamped to the substrate electrode and the thermal contact conductance may therefore be poor. A large variation of temperature (with a maximum at the wafer center) could lead to non-uniform nanotexturing since the process has been shown dependent on the substrate temperature (as discussed from literature, section III.1.1.a). A clamping system, associated to a more efficient cooling, could help reduce this possible temperature gradient.

III.3 Influence of Ion Flux and Ion Energy on Nanotexturing

The important role of ion flux (and its energy distribution) in plasma etching processes is quite well-documented, as well as the underlying physicochemical phenomena, discussed in Chapter I (see section I.1.4.b). In contrast, the influence of ion flux and energy in the particular case of nanotexturing of c-Si using SF_6/O_2 plasma has mostly been investigated through variations in process "control knobs" such as the power or the DC bias voltage [2, 4, 7, 31, 32].

Previous investigations on the SF_6/O_2 discharge, reported in Chapter II, have shown that both the total ion flux and the ion flux energy distribution on the powered electrode can be tuned by tailoring the excitation voltage waveform. Additionally, the presence of a non-uniform ion flux profile along the radius of the electrode further widens the range of ion flux values that can be probed. Taking advantage of both the "extended playground" and the non-uniform ion flux profile, the influence of the ion flux and ion energy on plasma-surface interaction can therefore be identified, and it is the objective of the following study.

III.3.1 Influence of Ion Flux

III.3.1.a Ion flux non-uniformities

The spatial non-uniformity of the ion flux has been assessed with the following conditions (corresponding to the study from Chapter II): $P_w = 25$ W, $P_r = 30$ mTorr, 105 sccm total incoming gas flux (57% SF_6). It has in particular been shown that, regardless of the tested excitation waveforms, the ion flux varies in a large range along the radius of the electrode (with an edge-high profile). The center to edge variation in ion flux is as high as a factor three in the RF case, as seen in Figure III.17(a) (data from Chapter II shown again for clarity, notice the ion flux scale is now expressed in [ions $\cdot$ cm$^{-2}\cdot$s^{-1}]), while it is lower when using TVWs: between 1.6 for sawtooth-up and 2.5 for sawtooth-down waveforms. In contrast, the distribution in energy of the ions, and in particular E_{avg} is constant (within the uncertainties) along the electrode radius in all conditions, Figure III.17(b). The highest values (around 56 eV) are obtained for the RF case. The average energy is lower (around 44 eV) for sawtooth-up waveforms, and lowest (around 32 eV) for sawtooth-down waveforms.

Silicon samples have been processed for various times in the same conditions (summarized in Table III.7) that were used for the ion flux energy distribution functions (IFEDF) measurements. For each condition, 2×3 cm^2 c-Si samples were placed along a radius of the powered electrode, as shown in the schematic Table III.7, at the same locations as the IFEDF measurements, i.e. at the center of the electrode or at a distance of 2.5, 5 and 7.5 cm from the center.

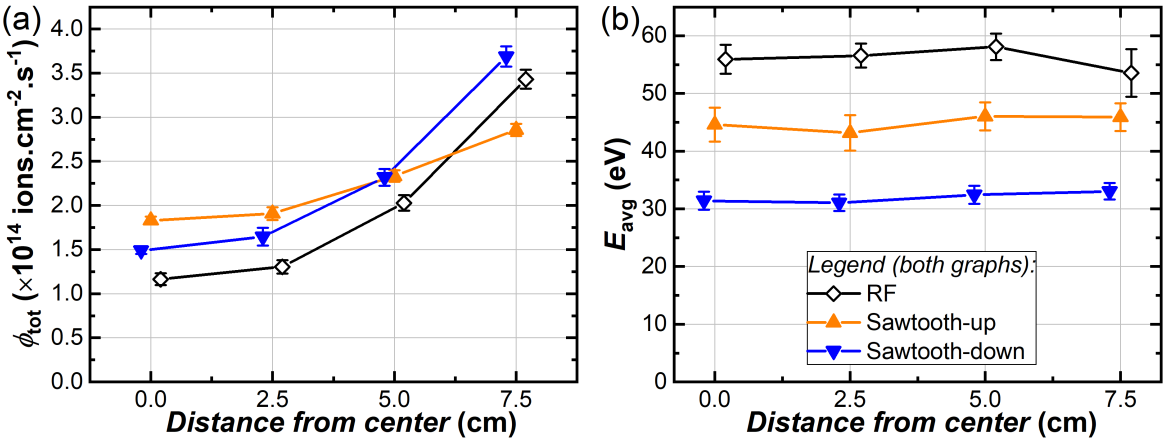

Fig. III.17: (a) Ion flux and (b) average ion energy profiles on the substrate electrode for three types of excitation voltage waveforms. Constant parameters: $P_w = 25$ W, $P_r = 30$ mTorr, SF_6/O_2 total incoming gas flux: 105 sccm (SF_6 content of 57 %). Data shown previously in Chapter II, recalled here for clarity.

Tab. III.7: c-Si nanotexturing process parameters used for study presented section III.3.1. Varied parameters indicated by an asterisk. Schematic (to scale) of substrate electrode with sample locations during process and positions of IFEDF measurements – carried out in the absence of substrates.

	Input parameters		Sample locations
Gases	**Pressure,** P_r	30 mTorr	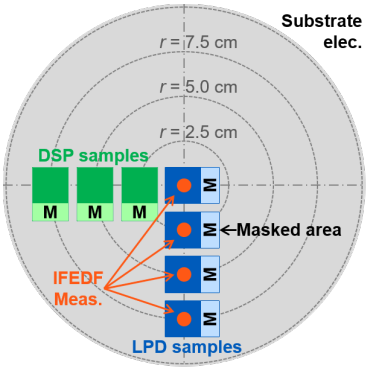
	Nature	$SF_6 + O_2$	
	Total input flux	105 sccm	
	SF_6 content	57 %	
Voltage	**Signal basis freq.,** f_0	13.56 MHz	
	***# of harmonics,** n	1 (single-freq.), 3 (TVWs)	
	Power, P_w	25 W	
Substrates	***Sample type**	DSP, LPD	
	Sample size	2×3 cm^2	
	Temperature, T_S	25 °C	
	***Etching time,** t_e	3, 5, 10, 20, 40 min	

Four LPD and three DSP samples were etched simultaneously (for each set of conditions), obviously only one sample (LPD) could be placed at the center of the electrode. LPD samples were then characterized by SEM and spectrophotometry (measurement of total hemispherical reflectance spectrum). The etched thickness, d, is measured by stylus profilometry on the DSP wafers only. Indeed, due to the initial roughness of the LPD samples (root mean square roughness of 0.8 µm measured by confocal microscopy), reliable estimates of the etched depth cannot be obtained by stylus profilometry.

Due to this constraint, two additional assumptions are made: (i) the properties of the discharge are axisymmetric because of the cylindrical geometry of the chamber, i.e. at a given distance, r, from the center, the process conditions (ion flux and ion energy in particular) are assumed constant; (ii) the texturing process leads to the same removal of material on the LPD and DSP samples. Both assumptions are in particular supported by the study presented in section III.1.2: no difference in the evolution of the nanostructures has been observed depending on the sample initial surface finish on samples disposed at different positions on the electrode but at the same distance from the center.

III.3.1.b Ion fluence

As in the study of section III.1.2, the evolution of the nanostructure width and surface effective reflectance are first characterized for all samples and plotted versus process time in Figure III.18, here distinguishing the various samples positions (on the substrate electrode) and the excitation waveforms.

Regarding the evolution of the nanostructures average width, it should first be highlighted that nanostructures appear on all samples, independent of the excitation voltage waveform and the sample position on the substrate electrode (notice, however, that in the case of RF excitation and 3 min of etching, a reasonable estimate of Λ_{NS} could only be obtained for one of the samples). Moreover, the trends are all qualitatively similar, as seen in the top row of graphs Figure III.18: the nanostructures average width is estimated to be in the range 40 to 55 nm for the lowest tested etching time, and it then increases when the process duration is increased. Significant differences in the "growth rate" of the nanostructures are observed depending on the location of the samples during the process: the rate is highest for the samples located at 7.5 cm from the center of the electrode, and lowest for the samples placed at 0 or 2.5 cm from the center. In addition, differences depending on the excitation waveform also appear: the highest nanostructure growth rate is found for RF excitation while the lowest value is obtained for sawtooth-down excitation. Interestingly, the differences in Λ_{NS} for different sample locations (and at a given etching time) are lowest in the case of sawtooth-up waveform. Finally, another peculiar behavior is observed for sawtooth-down

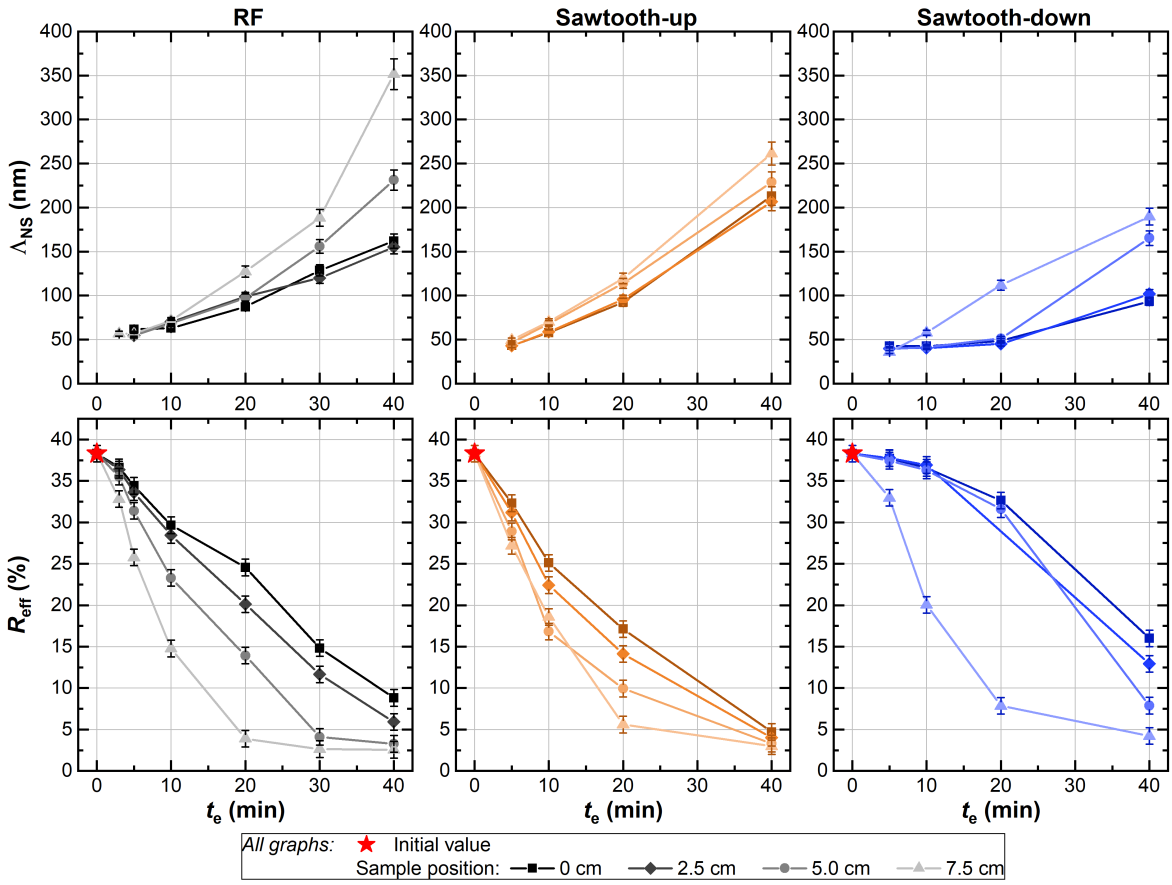

Fig. III.18: Evolution of nanostructures average width, Λ_{NS} (top graphs), and effective reflectance, R_{eff} (bottom graphs), versus time for different sample positions and excitation voltage waveforms. Constant parameters: $P_r = 30$ mTorr, $P_w = 25$ W, SF_6/O_2 incoming gas flux: 105 sccm (SF_6 content of 57 %).

excitation: while the nanostructures average width seems to grow almost linearly with time on the sample located at 7.5 cm, an apparent "delayed onset" seems to occur for the other positions: the nanostructures average width is almost constant (around 40 to 50 nm) between 5 and 20 min, before a sharp increase after 40 min etching.

A very similar discussion can be made for the evolution of the effective reflectance with the process time – except the trends are here decreasing, as shown on the bottom row of graphs Figure III.18. Indeed, for all conditions, R_{eff} steadily decreases with the etching time, and comparisons between various sample positions and waveform excitations are totally analogous to the analysis made for Λ_{NS}This behavior is not surprising as a clear (negative) link between nanostructures average width and reflectance has previously been demonstrated.

In fact, all measurements are consistent with a prominent influence of the total ion flux, ϕ_{tot}, on the development of the nanostructures (and therefore on the effective reflectance): the higher the flux, the faster the nanostructures grow (and the faster the reflectance decreases). The ion fluence, Φ, therefore seems to represent an representative global parameter to give a phenomenological model of the nanostructure evolution, with:

$$\Phi = t_e \phi_{tot} = t_e \int_0^{E_{max}} \phi_E(E) \mathrm{d}E \tag{III.3}$$

where t_e is the etching time, ϕ_E is the IFEDF and E_{max} is the maximal ion bombardment energy. Results for Λ_{NS}, H_{NS}, d and R_{eff} are shown versus Φ in Figure III.19.

As expected, clear trends seem to appear from the graphs in Figure III.19, however, for the sake of the demonstration, only qualitative behaviors will be analyzed in this section, a more complete discussion of the quantitative trends will be given in section III.3.2.b.

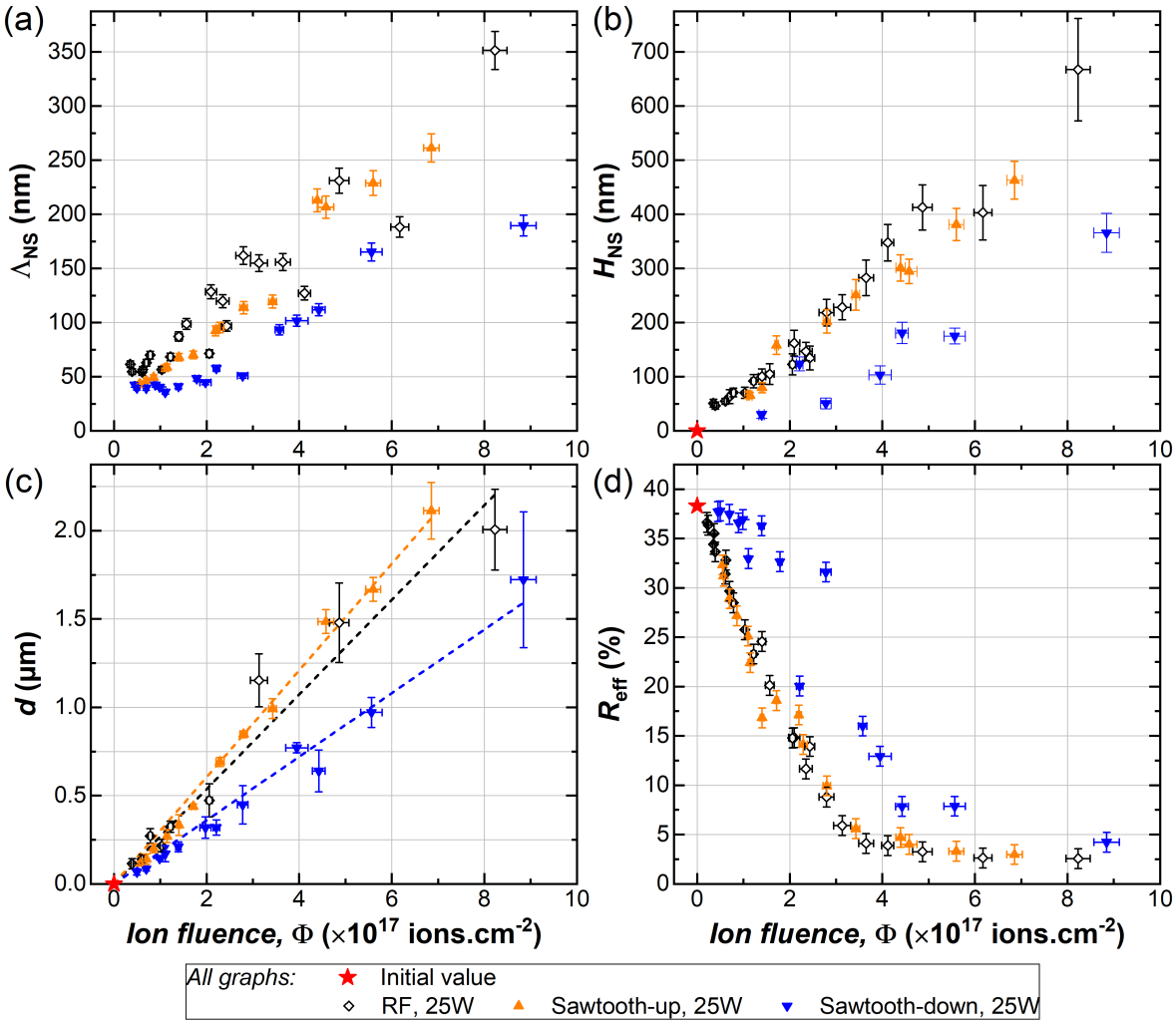

Fig. III.19: Evolution of (a) nanostructures average width and (b) height, (c) effective reflectance and (d) etched depth as a function of ion fluence for different excitation voltage waveforms. Dashed lines in (c) show linear fit of the data points for the three types of voltage excitation. Constant parameters: $P_r = 30$ mTorr, $P_w = 25$ W, SF_6/O_2 incoming gas flux: 105 sccm (SF_6 content of 57 %).

Growth of the average lateral and vertical nanostructure dimensions with the ion fluence – respectively shown in Figure III.19(a) and (b) – is first observed. Values for Λ_{NS} are somehow scattered around a general upward trend. In contrast, the average height of the nanostructures, H_{NS}, clearly follows a linear increase with the ion fluence. For both nanostructures dimensions (Λ_{NS} and H_{NS}), separate tendencies seem to emerge for each excitation type: in particular, at a given value of ion fluence, sawtooth-down voltage excitation leads to smaller (both in width and height) nanostructures than RF or sawtooth-up voltage excitation.

In addition, Figure III.19(c) also shows the evolution of the etched depth, d, with the ion fluence. Here, linear trends are observed for all three types of excitation: the etching yield only depends on the type of excitation. Dashed lines in the same graph show the results of linear regressions, leading to the following "average" etching yields values: 13.4 atoms$\cdot$ion^{-1} for RF excitation, 15.1 atoms$\cdot$ion^{-1} for sawtooth-up voltage waveform, and 9.0 atoms$\cdot$ion^{-1} for sawtooth-down voltage waveform. Notice that the "average" etching yield values are probably overestimated: indeed, and as it was pointed out in section I.1.3.c of Chapter I, the imperfect collection efficiency of the RFEA used for IFEDF measurements leads to underestimations of the total ion flux.

Finally, the evolution of R_{eff} is shown in Figure III.19(d): the reflectance of the nanostructured c-Si surface steadily decreases when the ion fluence is increased. Samples etched in RF

and sawtooth-up excitation conditions fall on a very robust trend. The reflectance of samples obtained with sawtooth-down excitation, however, still seem to diverge from the other two cases. In fact, this behavior is not surprising in view of the previous analysis of the nanostructures average dimensions – Figure III.19(a,b): in the case of sawtooth-down waveforms and for a given ion fluence, the values of Λ_{NS} and H_{NS} are lower compared to the two other cases. Indeed, as discussed previously and in the wavelength range presently of interest, the total hemispherical reflectance of nanostructured c-Si surfaces especially depends on the nanostructures dimensions. This relationship will be further investigated in Chapter IV.

From the analysis of the surface property change with ion fluence for the three investigated types of waveforms, a possible explanation for the diverging trends comes from the ion energy. Indeed, it should here be recalled that the average ion flux energy distribution is almost identical for each type of excitation voltage (regardless of the position of the sample on the electrode). The following average energies were obtained for the three types of voltage excitation: 56 eV for single-frequency waveform, 44 eV for sawtooth-up waveform, and 32 eV for sawtooth-down voltage waveform. The hypothesis of the importance of ion energy will be further explored in the next section.

III.3.2 Energy Dependent Etching Yield

III.3.2.a Influence of ion energy

In order to distinguish the specific role of ion bombardment energy from the already discussed important role of ion fluence, a few more experiments have been conducted. In particular, the average ion energy obtained at a coupled power of 25 W is relatively low (E_{avg} below 60 eV for all investigated excitation voltage waveforms). More tests are therefore added with single-frequency RF excitation at a coupled power of 35 and 45 W. All other parameters are kept constant, i.e. the total incoming SF_6/O_2 gas flux is kept at 105 sccm, with an SF_6 content of 57%, and the pressure set again to $P_r = 30$ mTorr.

Ion flux energy distribution functions have been measured at the same positions on the substrate electrode (center and at 2.5, 5 and 7.5 cm from the center). The total ion flux and average ion energy are shown respectively in Figure III.20(a) and Figure III.20(b) (notice missing data for the center of the discharge at $P_w = 45$ W).

Similarly to the 25 W power case, an edge-high ion flux profile is observed at 35 and 45 W, while relatively constant energy distribution (data not shown), and therefore average energy, are found across the electrode. When increasing the coupled power from 25 to 35 and 45 W, the ion flux profile experiences a small rise over the whole electrode, while a large increase in average ion

Tab. III.8: c-Si nanotexturing process parameters used for study presented section III.3.2.a. Varied parameters indicated by an asterisk. Schematic (to scale) of substrate electrode with sample locations during process and positions of IFEDF measurements – carried out in the absence of substrates.

	Input parameters		Sample locations
Gases	**Pressure,** P_r	30 mTorr	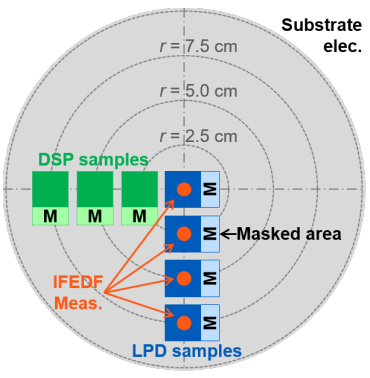
	Nature	$SF_6 + O_2$	
	Total input flux	105 sccm	
	SF_6 content	57 %	
Voltage	**Signal basis freq.,** f_0	13.56 MHz	
	# of harmonics, n	1 (single-freq.)	
	***Power,** P_w	25, 35, 45 W	
Substrates	***Sample type**	DSP, LPD	
	Sample size	2×3 cm^2	
	Temperature, T_S	25 °C	
	Etching time, t_e	10 min	

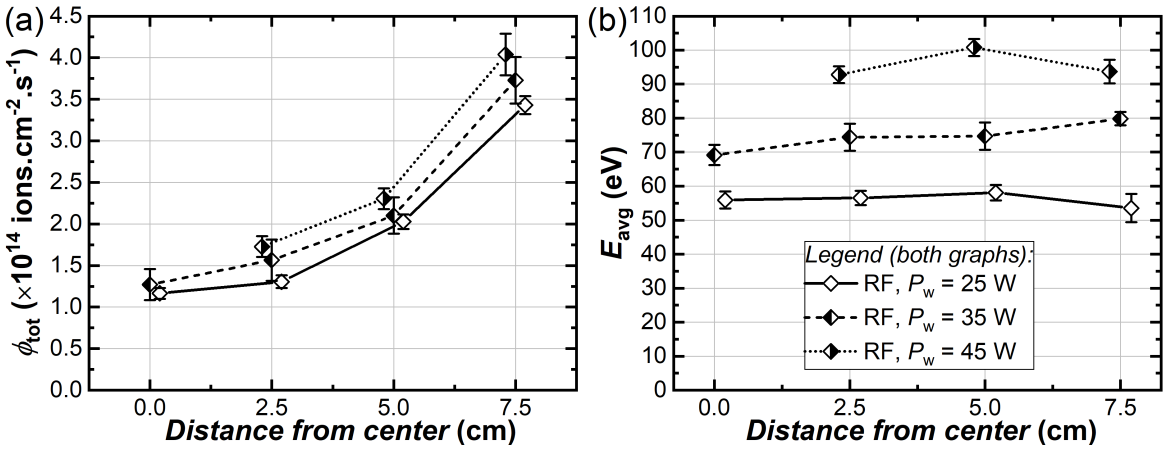

Fig. III.20: (a) Ion flux and (b) average ion energy profiles on the substrate electrode for single-frequency excitation with varying values of P_w. Constant parameters: $P_r = 30$ mTorr, SF_6/O_2 total incoming gas flux: 105 sccm (SF_6 content of 57 %). Data for $P_w = 25$ W shown again for comparison.

energy is found (mostly driven by the self-bias voltage): E_{avg} is around 75 eV for $P_w = 35$ W, and around 95 eV for $P_w = 45$ W.

Etching processes are then performed (same method as for section III.3.1.b), for a single value of 10 min etching time – the full set of process conditions is summarized in Table III.8. Results are compared in Figure III.21 (together with data obtained for the same etching time at $P_w = 25$ W and different excitation voltages). These graphs present contour maps of the nanostructure average width, Figure III.21(a), and surface effective reflectance, Figure III.21(b), as a function of the total ion flux ϕ_{tot} (horizontal axis) and the average ion energy E_{avg} (vertical axis).

Unsurprisingly, the contour map for Λ_{NS} again shows the importance of the ion flux, Figure III.21(a): at a given average ion energy, the higher the ion flux, the larger the nanostructures. The opposite trend is found again for the reflectance, which decreases with increasing ion flux, Figure III.21(b). More interestingly, an influence of the average ion energy is also demonstrated, although the scaling seems weaker than for the ion flux. Indeed, it is observed that at a given ion flux, increasing the ion energy also leads to an increase in the average nanostructure width, and conversely, to a decrease of effective reflectance.

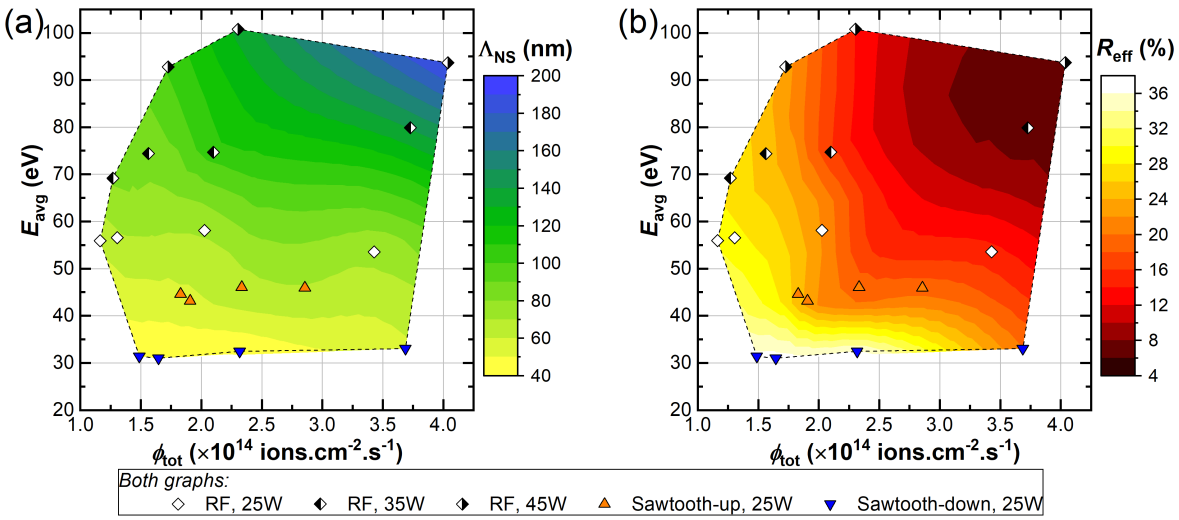

Fig. III.21: Contour maps showing influence of ion flux and average ion energy on (a) the final effective reflectance and (b) nanostructure average width. Symbols show the locations of experimental data. Constant parameters: $t_e = 10$ min, $P_r = 30$ mTorr, SF_6/O_2 incoming gas flux: 105 sccm (SF_6 content of 57 %).

III.3.2.b Energy weighted ion fluence

Phenomenological model for the etching yield. Aiming at a global (predictive) description of the previous results, a phenomenological model is adopted: the etching yield is assumed to increase linearly with the square root of the ion energy, above an etching threshold E_{th}. This model was first proposed by Steinbrüchel, in particular for the ion-enhanced chemical etching of silicon [33], and shown to depend on both the nature of the substrate and of the etchant. It was later used to successfully model the etching of c-Si with an SF_6/O_2 plasma [34, 35]. The etching yield, $Y(E)$, is expressed as follows:

$$Y(E) = Y_0 \left(E^{1/2} - E_{\text{th}}^{1/2}\right) \tag{III.4}$$

where Y_0 is a proportionality constant. In agreement with this model, the energy weighted ion fluence Φ_E is also defined and linked to the etched depth:

$$\Phi_E = t_e \int_{E_{\text{th}}}^{E_{\text{max}}} \phi_E(E) \left(E^{1/2} - E_{\text{th}}^{1/2}\right) \mathrm{d}E \tag{III.5}$$

$$d = \frac{Y_0 \Phi_E}{d_{\text{Si}}} \tag{III.6}$$

where $d_{\text{Si}} = 5.02 \times 10^{22}\,\text{at}\cdot\text{cm}^{-3}$ is the atomic density of c-Si. This model can be used to fit the data from the previous results: a non-linear least-square regression is performed with E_{th} and Y_0 as the fitting parameters. The best fit ($R^2 = 0.96$) is found for $E_{\text{th}} = 13\,\text{eV}$, and $Y_0 = 4.6\,\text{atoms}\cdot\text{ion}^{-1}\cdot\text{eV}^{-1/2}$. Uncertainties have not been estimated for these parameters, but due to the uncertainties in the RFEA measurements the uncertainty in etching threshold is at least in the order of 2 eV, while Y_0 is most probably overestimated due to an underestimation of the total ion flux. Results are shown in Figure III.22: graph (a) shows the etch depth versus energy weighted ion fluence Φ_E after fitting (notice that one data point has been excluded), and graph (b) shows the energy dependent etch yield.

From this phenomenological model, two findings have to be highlighted: (i) ions bombarding the surface with an energy below 13 eV seem to have no effect on the nanotexturing process, as their etching yield is null; (ii) above the threshold of 13 eV, the higher the energy of the bombarding ion, the more atoms are removed from the surface: the etch yield at 30 eV is around 8 $\text{atoms}\cdot\text{ion}^{-1}$, while above 65 eV more than 20 atoms are removed per incoming ion. From a process point of view, it is also interesting to note that Y_0/d_{Si}, here around $92\,\text{nm}/(10^{17}\,\text{ions}\cdot\text{eV}^{1/2}\cdot\text{cm}^{-2})$, can be interpreted as an etch rate when working at constant ion flux and energy conditions.

Remarkably, the energy threshold found in this study is very close to the value ($E_{\text{th}} = 15\,\text{eV}$) obtained by Belen *et al.* for trench etching of c-Si in an SF_6/O_2 discharge, in similar conditions of substrate temperature, pressure and SF_6 content [34]. However, the value obtained by this team for the proportionality constant, $Y_0 = 7\,\text{atoms}\cdot\text{ion}^{-1}\cdot\text{eV}^{-1/2}$, is significantly higher: their study focused on an ICP discharge, leading to both much higher ion fluxes and neutral densities compared to a CCP discharge, possibly explaining this discrepancy. In particular, the etching yield also increases with the fluorine to ion flux ratio at the surface [36]: this dependence is not accounted for in the present study.

This model efficiently describes the "bulk etching" that occurs during the nanotexturing process, but has now to be confronted to the other characteristic parameters of the processed samples, i.e. the nanostructures dimensions Λ_{NS}, H_{NS} and the reflectance R_{eff}. Therefore, the experimental dataset is now shown against the energy weighted ion fluence, Φ_E from Equation (III.5), in Figure III.23. Notice that error bars have here been removed to facilitate visualization.

Self-organization at the nanoscale. Graphs in Figure III.23 demonstrate the relevance of the chosen model for the etching yield, Equation (III.4): clear trends versus the energy weighted ion fluence are obtained for all the parameters of interest. In particular, the average nanostructure width and height, Figure III.23(a,b), follow quite robust trends versus Φ_E.

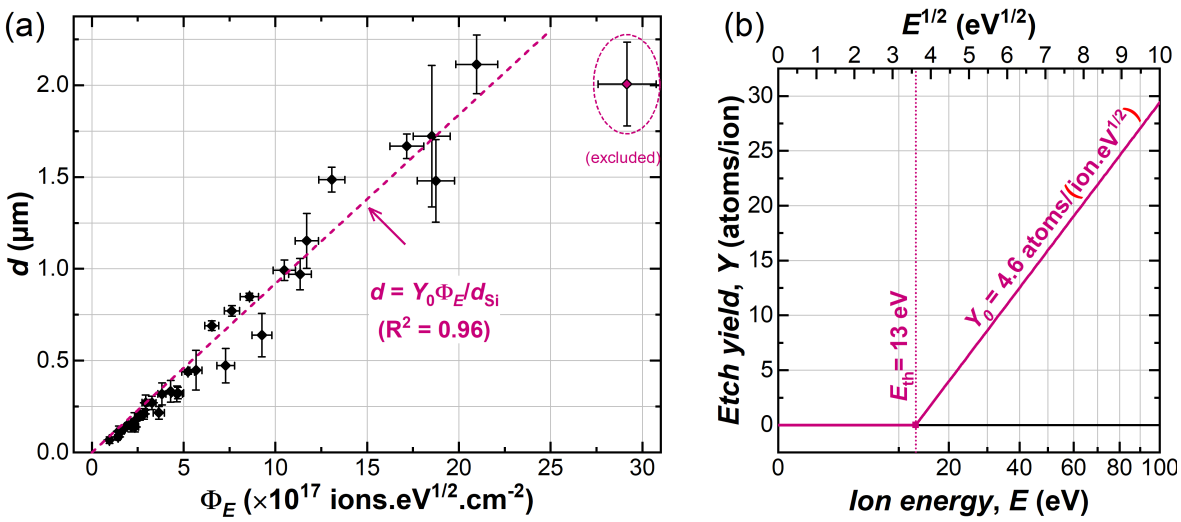

Fig. III.22: Results of non-linear least square fitting: (a) etch depth as a function of the energy weighted ion fluence; (b) Etch yield dependence on ion energy (notice the different top and bottom horizontal scales).

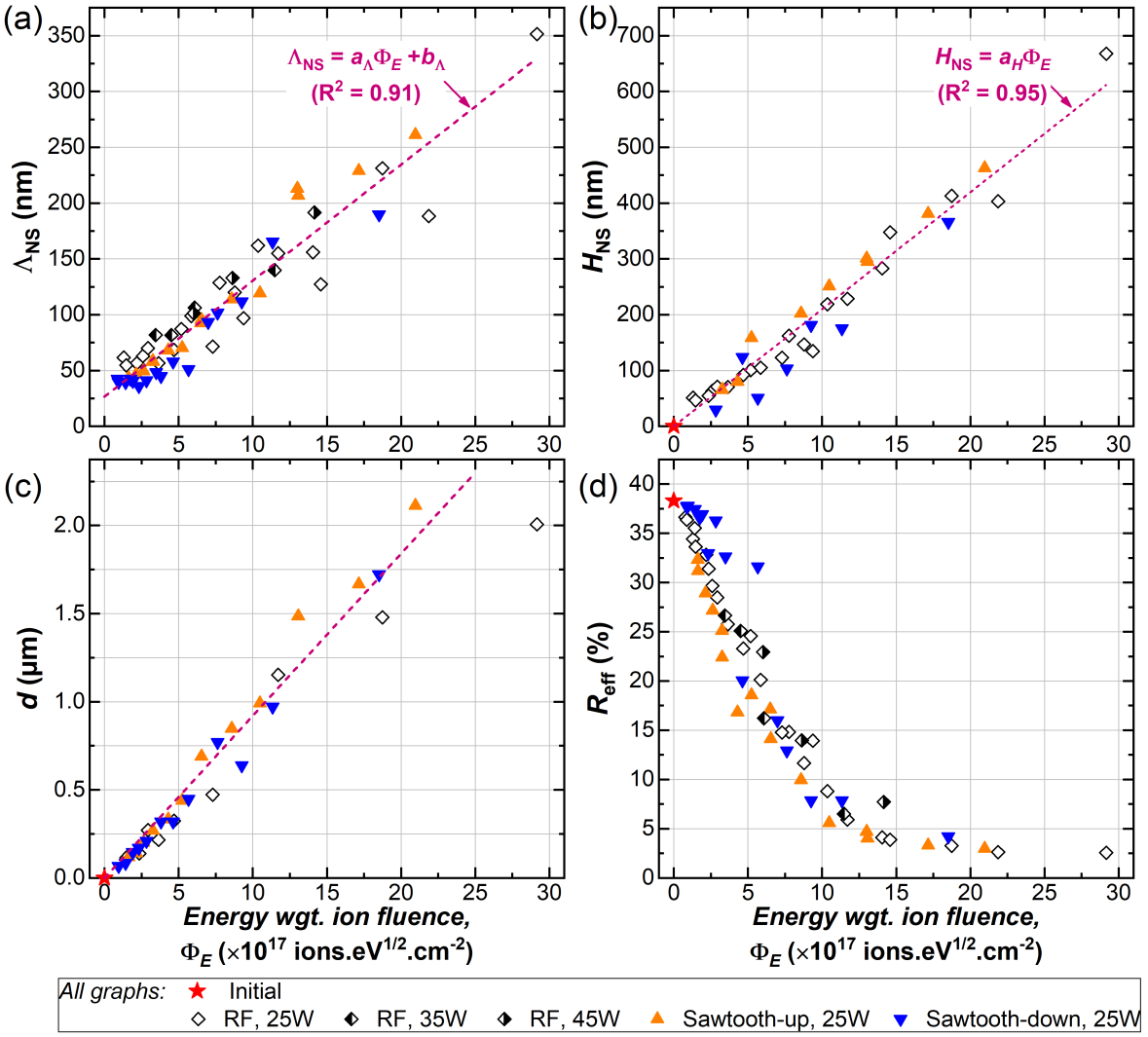

Fig. III.23: Evolution of (a) nanostructures average width and (b) height, (c) effective reflectance and (d) etched depth as a function of energy weighted ion fluence, Equation (III.5), for different excitation voltage waveforms and values of applied power. Fitting curves (full dataset) shown by dashed lines for Λ_{NS}, H_{NS} and d versus Φ_E. Constant parameters: $P_r = 30$ mTorr, 105 sccm SF_6/O_2 incoming gas flux (57 % SF_6).

For Λ_{NS}, an affine fitting (over the full dataset) in the form $\Lambda_{NS} = a_\Lambda \Phi_E + b_\Lambda$ is chosen. From this regression, $a_\Lambda = 10\,\text{nm}/(10^{17}\,\text{ions}\cdot\text{eV}^{1/2}\cdot\text{cm}^{-2})$ and $b_\Lambda = 27\,\text{nm}$, with a relatively low coefficient of determination ($R^2 = 0.91$), due to a significant scattering of the data around the affine trend. Notice that this scaling is much more general as the one identified in section III.1.2 (with $\Lambda_{NS} \propto t_e^\gamma$), as it here includes and demonstrates the significant influence of the ion flux and energy – in addition to the process time. The scaling parameter a_Λ may be interpreted as a "growth rate" in the horizontal direction, directly linking the energy weighted ion fluence the c-Si surface is subjected to during the process to the average nanostructure width. In addition, b_Λ can be interpreted as an offset due to a possible transient "initiation" phase (not captured by the affine fitting) in the nanostructuring phenomenon: this parameter is therefore not relevant for low values of Φ_E, as the smallest values observed for Λ_{NS} lie in the range from 40 to 50 nm. The existence of a non-zero initial nanostructure width will be discussed in the paragraph "Qualitative interpretations" below.

For H_{NS} a similar fitting procedure is used except a linear fitting is adopted, with $H_{NS} = a_H \Phi_E$. Here the regression leads to $a_H = 21\,\text{nm}/(10^{17}\,\text{ions}\cdot\text{eV}^{1/2}\cdot\text{cm}^{-2})$, with a more robust scaling (coefficient of determination $R^2 = 0.95$) compared to the evolution of Λ_{NS}. Again, a_H may be interpreted as a "growth rate" of the nanostructures in the vertical direction.

A clear trend linking R_{eff} to Φ_E is also observed in Figure III.23(d): this trend is a direct consequence of the evolution of H_{NS} and Λ_{NS}. Indeed, as it will be further investigated in the next chapter, the nanotextured c-Si surface can be approximated to a gradient refractive index layer between air and c-Si, provided $\Lambda_{NS} \ll \lambda_0 / n_{Si}$: this hypothesis can be considered valid in the range $\lambda_0 \in [280, 1000\,\text{nm}]$ for $\Lambda_{NS} < 150\,\text{nm}$. In this limit, the reflectance of the surface (and therefore effective reflectance) decreases with the thickness of the gradient refractive index layer, i.e. in the order of the average nanostructure height.

Finally, a major result of this study has to be highlighted: the importance of the ion flux and ion energy has been demonstrated and aggregated in the form of the energy weighted ion fluence, Φ_E. The results prove that increasing either the ion flux or energy will accelerate the nanotexturing process, which is of great interest for process development. It can therefore be inferred that the ion flux is rate-limiting for the etching process (although it is here not possible to determine if the neutral etchants flux is also limiting). However, it also demonstrates that, in the explored range of parameters, it is not possible to escape the "universal" trend. This phenomenon is depicted in the schematic in Figure III.24 showing the general evolution of the nanostructures during the process for increasing Φ_E. In addition, SEM images are displayed to illustrate the evolution of the nanostructures when varying Φ_E by either increasing the etching time, the total ion flux or the ion energy (keeping other parameters constant).

III.3.2.c Qualitative interpretations

To analyze the previous results, the assumption of a micro-masking phenomenon (in the form SiO_xF_y, as previously suggested) will again be adopted, and the formation of nanostructures interpreted as the consequence of different etch rates on "pristine" c-Si and on areas covered by inhibitor species. Actually, the dichotomy between "pristine" c-Si and precipitates of inhibitor species is an oversimplification: the full surface is likely made defective by ion bombardment and covered by an intermediate layer in the form of SiF_x or SiO_xF_y, with local variations in composition (both in the lateral and vertical directions) and in thickness [37]. Nevertheless, this simplification will be made in the following analysis as it does not significantly affect the comprehension of the phenomena. Schematics of the nanostructures during the process is supplied for illustration, Figure III.25, and will be used for the analysis.

First, the observation of a "bulk etching" demonstrates that the inhibitor layer only "slows down" the etching – rather than fully stopping it. The micro-mask may indeed prevent (or drastically slow) etching of the underlying c-Si by neutrals, but the inhibitor species are still sputtered by energetic ions, releasing silicon atoms from the surface. A significant etching can therefore also be obtained on the apex of the nanostructures (depending on the balance between the passivation layer formation rate and the sputtering rate). Nevertheless, the inhibitor layer has to reduce

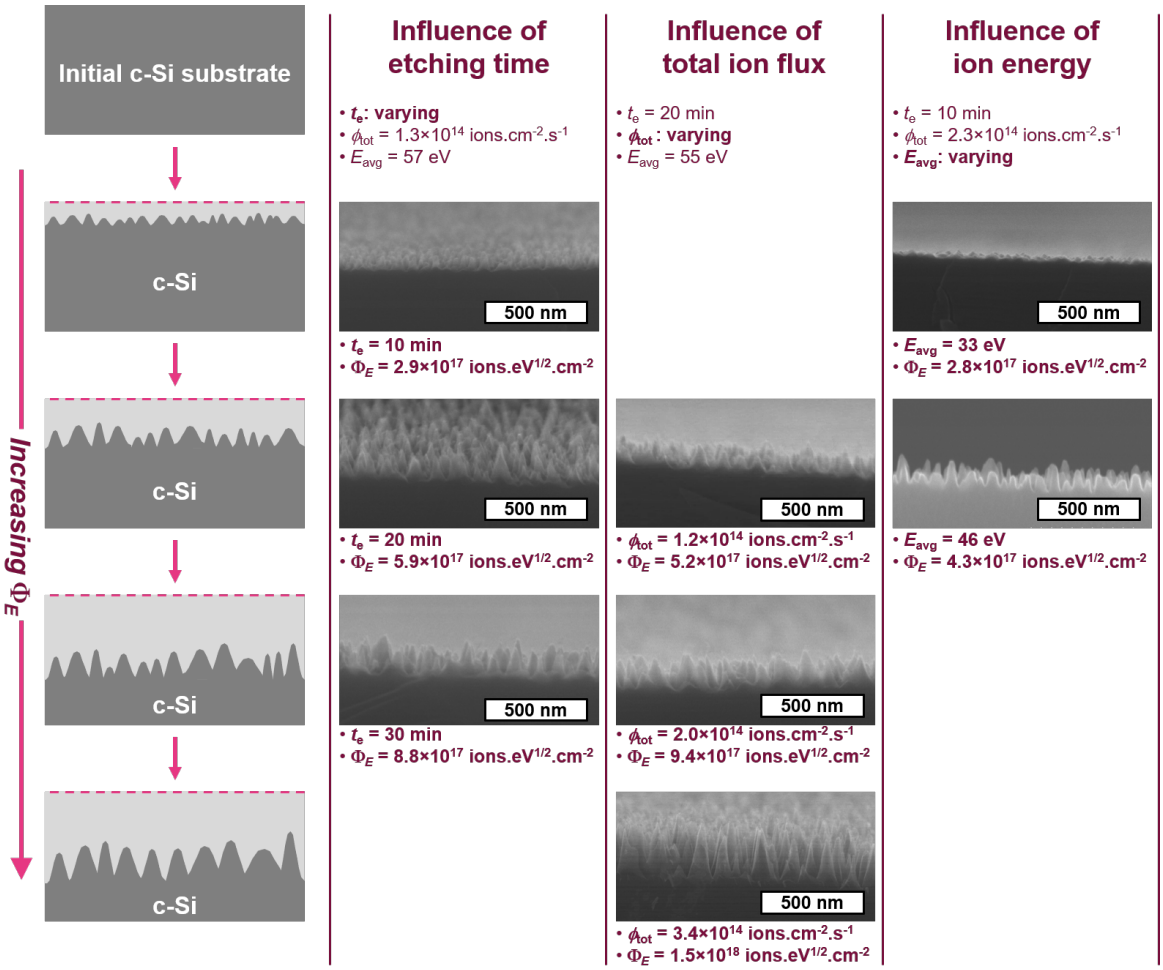

Fig. III.24: Schematic (left column, not to scale) of nanostructure evolution with energy weighted ion fluence, Φ_E, and selected cross section view SEM images illustrating influence of etching time, ion flux and ion energy (in each column, varying parameters in bold). SEM images grouped so that Φ_E values are in the same order of magnitude in each row. Constant parameters: $P_r = 30$ mTorr, 105 sccm SF_6/O_2 (57 % SF_6).

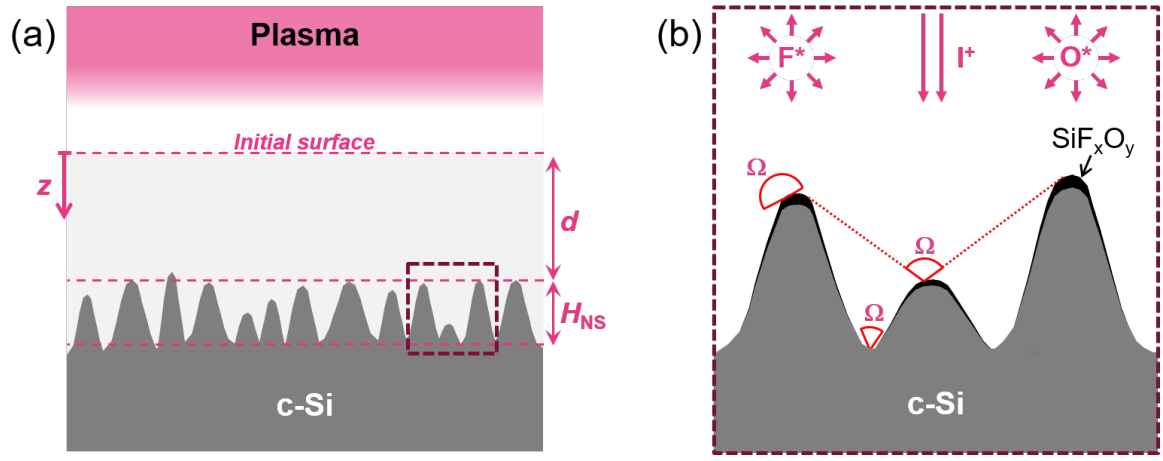

Fig. III.25: (a) Cross section view schematic (not to scale) of the nanotexturing phenomenon. (b) Close-up view illustrating the major species (positive ions I^+, fluorine F* and oxygen O* radicals), with the SiO_xF_y inhibitor layer and the angle of unobstructed plasma exposure Ω in three locations on the surface.

the etch rate enough for nanostructures to appear: in fact, the difference of etch rates between the apexes and grooves of the nanostructures can be estimated. Indeed, the apex of the nanostructures is in average located at a distance d from the initial c-Si surface, see the z axis in the schematic Figure III.25(a), so that the etch rate is here proportional to Y_0/d_{Si}.

A similar analysis for the bottom of the nanostructures (located in average at a distance $d + H_{NS}$) can be made, and in this case the etch rate is proportional to $Y_0/d_{Si}+a_H$. In the explored conditions, the inhibitor layer slows the etching by: $a_H/(Y_0/d_{Si} + a_H) \approx 20\%_{rel}$. Notice that this interpretation also underlines the fact that the (energy dependent) etching yield previously quantified is only valid for the apexes of the nanostructures, while it locally increases in the trenches.

Regarding the evolution of the nanostructures width, two regimes have to be distinguished: an initiation phase and a steady-state regime. Indeed, it has been observed that for very low values of energy weighted ion fluence (or equivalently low etching times), nanostructures appear with a characteristic lateral size in the order of 40 to 50 nm. If confirmed, this initiation phase could actually be understood as the consequence of the distribution of micro-masking species on the surface during the early stages of the process. The diffusion length of neutral adatoms on the c-Si surface (e.g. O* or F*, depending on the rate-limiting factor for the formation of SiO_xF_y) should therefore be in the same order as the initial average nanostructure width.

After this initiation phase, a steady-state regime is observed, during which the nanostructures average width continuously increases. In other words, a selection of nanostructures occurs during the process: while the largest nanostructures are conserved, their neighbors are progressively "etched away." This behavior can be understood from a "shadowing" phenomenon, as proposed in [24]. Assuming that the mean free path of neutrals is much larger than the characteristic nanostructure size (valid at low discharge pressure), the incoming flux of neutrals at a given point of the surface is proportional to the solid angle Ω of unobstructed exposure to the plasma – illustrated (in 2D) in the schematic Figure III.25(b). Hence, the passivation layer formation rate (induced by F* and O*) is positively linked with Ω. Due to the surface morphology, Ω is, of course, much higher at the apexes of the surface than in the trenches, due to shadowing by neighboring nanostructures. In the end, an adequate balance is achieved with the apexes of the largest nanostructures in "over-passivating" regime, whereas the trenches and the smallest nanostructures are in "over-etching" regime.

Finally, it should be underlined that all the major trends have been qualitatively explained by monitored parameters (ion flux and ion energy in particular). Hence, possible variations in uncontrolled parameters (e.g. variations in neutral species densities along the radius of the discharge for instance) have been neglected.

III.3.3 Special Cases

III.3.3.a Tuning the aspect ratio

In addition to the absolute vertical and horizontal sizes of the nanostructures, their aspect ratio can be of great importance depending on the application. For instance, a high aspect ratio will possibly affect subsequent conformal deposition of thin films (e.g. passivation layers) on top of the c-Si surface. In addition, a high aspect ratio may significantly increase the surface area enhancement factor (i.e. the ratio of real to projected area), and in turn increase the defect density at the surface (defined in terms of projected area).

In the frame of this study, the average nanostructure height and width have been characterized, although it has been shown that a distribution of sizes (for a given surface) exists. Thus, the average aspect ratio, AR_{NS}, may be different from the ratio of average height and width: however, the approximation $AR_{NS} \sim H_{NS}/\Lambda_{NS}$ has been validated by comparing the two quantities on a subset of twelve samples (data not shown). In section III.3.2.b, the nanostructure average width and height have been shown to comply with the following scaling as a function of the energy weighted ion fluence: $\Lambda_{NS} = a_\Lambda \Phi_E + b_\Lambda$, and $H_{NS} = a_H \Phi_E$ (with the constant parameters a_λ, b_Λ and a_H determined experimentally). Therefore, the following average trend is expected for AR_{NS}:

$$AR_{NS} = \frac{a_H}{a_\Lambda}\left(1 - \frac{b_\Lambda}{\Lambda_{NS}}\right), \text{ valid for } \Lambda_{NS} \geq b_\Lambda \tag{III.7}$$

Since Λ_{NS} increases with Φ_E, the nanostructure aspect ratio is expected to increase as well, tending to an asymptotic value $a_H/a_\Lambda \approx 2$. However, some scattering in the values of H_{NS} and Λ_{NS} versus Φ_E was previously pointed out. Figure III.26(a) therefore shows AR_{NS} versus Λ_{NS} for the full available dataset, with a color-mapping corresponding to the instantaneous ion flux during the process. While the dataset indeed follows the average trend (from Equation (III.7), shown by the dashed curve), an apparent splitting of the data points is observed – despite the large uncertainties – depending on the instantaneous ion flux during the process. Indeed, in most cases, a relatively

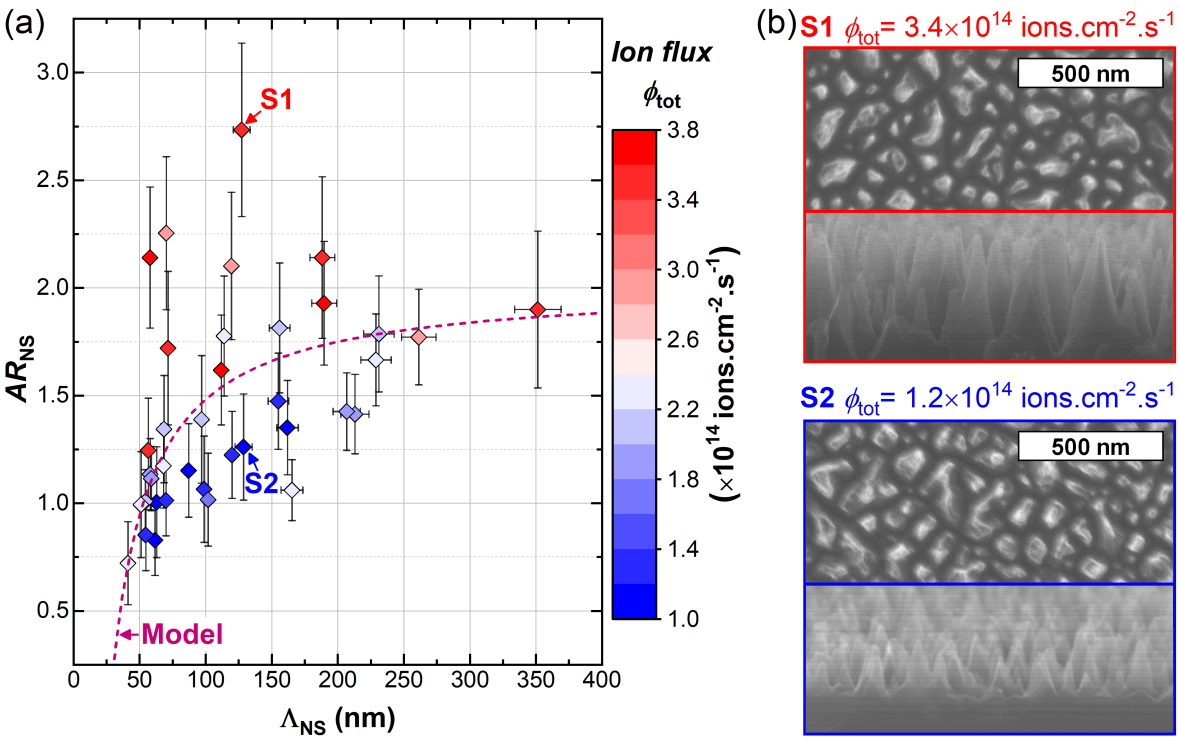

Fig. III.26: (a) Nanostructure average height versus average width: color-mapping as a function of the instantaneous ion flux during the process. AR_{NS}: aspect ratio. (b) Top and cross-section view SEM images of selected samples.

high ion flux (here above 2.4×10^{14} ions$\cdot$cm$^{-2}\cdot$s^{-1}) leads to the formation of high aspect ratio nanostructures (taller than the average trend predicts), while an opposite situation is found when the ion flux is below 2.4×10^{14} ions$\cdot$cm$^{-2}\cdot$s^{-1}.

This phenomenon is illustrated by the SEM images in Figure III.26(b): two samples (S1 and S2) with a similar nanostructure average width ($\Lambda_{NS} \approx 160$ nm) have been selected. Sample S1 was processed with an ion flux of 3.4×10^{14} ions$\cdot$cm$^{-2}\cdot$s^{-1}: the nanostructures on its surface have an average aspect ratio around 2.7 (i.e. $H_{NS} \approx 350$ nm for this sample). In contrast, sample S2 was exposed to a much lower instantaneous ion flux of 1.2×10^{14} ions$\cdot$cm$^{-2}\cdot$s^{-1}, and the final nanostructures are significantly smaller: $AR_{NS} \approx 1.3$ and $H_{NS} \approx 160$ nm.

In section III.3.2.b, it was already demonstrated that the (energy dependent) etching yield slightly increases in the trenches of the nanostructures compared to the apexes (hence the nanotexturing), but that in all locations, intensifying the instantaneous ion flux increases the yield. However, it appears that this increase is slightly more pronounced at the bottom of the nanostructures (leading to a higher average aspect ratio). This may be understood by different dominant etching mechanisms: in the proposed model for texturing, the apexes of the nanostructures are covered by micro-masking species, so that ions act mostly by sputtering of the inhibitor layer. In contrast, inhibitor species are supposed to be almost absent from the trenches of the nanostructures, where ions therefore mainly act through ion-enhanced chemical etching.

While the values of aspect ratios are comprised in a relatively small range – between 1 and 2 for most samples, the dependence on the ion flux opens a (small) degree of freedom to tune the nanostructures morphology.

III.3.3.b Crystalline orientation dependence

In all the previous discussions, the crystalline orientation of the substrate has been neglected as on most samples no influence of this parameter could be observed from SEM images. However, a few samples stood out: top view SEM images have revealed an influence of the crystalline orientation on the nanostructures morphology, as illustrated in Figure III.27. The c-Si samples were cleaved from a (100) wafer: a careful alignment of the sample was achieved to ensure that the horizontal axis of the top view SEM images in Figure III.27 is aligned with the [011] crystalline direction. These images, and their cross section counterparts, reveal that the nanostructures consist of interconnected walls with steep flanks, that are in numerous cases (although not always) approximately

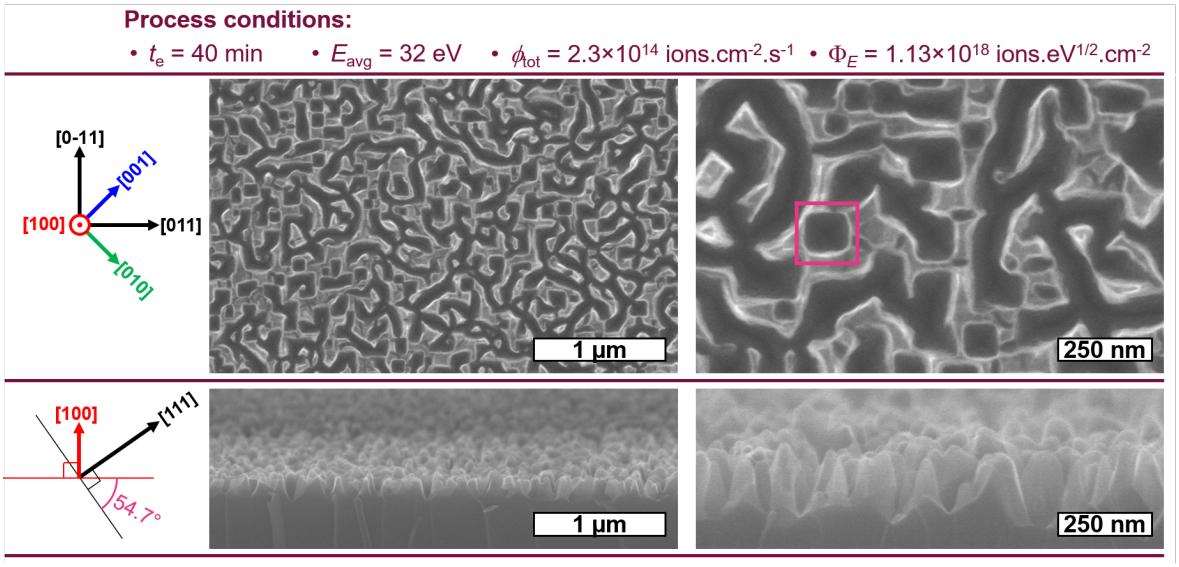

Fig. III.27: SEM images (top views and cross section views) of a nanotextured c-Si sample (cleaved from a (100) wafer) showing the dependence of the nanostructures morphology on the crystalline orientation of the substrate (see for instance the red square in the top right image, added to facilitate identification).

aligned with [0-11] or [011] directions. In particular, this morphology generates holes with "square edges" (one example is highlighted by a red square in the top right image in Figure III.27).

Notice that the structures observed in Figure III.27 are not "inverted pyramids" such as the ones obtained by chemical etching (usually using a patterned etching mask, e.g. [38]) where the flanks consist of (111) facets with an angle of 54.7° relative to the (100) plane, as illustrated in the schematic in the bottom left corner of Figure III.27. Indeed, cross section views show that the flanks of the holes are actually steeper (in the range from 65 to 85° relative to the (100) plane).

Dependence of nanostructure morphology on the crystalline orientation has been reported in previous studies on plasma nanotexturing [12, 13], or on trench etching [39]. This behavior arises from a different etch rate depending on the crystalline orientation of the c-Si substrate: in particular, it has been shown that for SF_6/O_2 plasma etching, the etch rate is higher for (100) planes than for (111) planes, although the difference in etch rate is relatively weak at room temperature [40]. Due to the higher atomic surface density on (111) planes compared to (100) planes, fewer dangling bonds are available for chemical reactions (one dangling bond per atom on (111) planes and two per atom on (100) planes). Consequently, the lower etch rate on (111) planes is interpreted by a promotion of passivation and a limitation of chemical etching. The analysis is, however, made more complex due to the ion bombardment that will contribute to the etching: in particular, the etching yield depends on the ion incidence angle, and may be highest in off-normal incidence [41], reducing the "apparent" etch rate difference.

In the present study, crystalline orientation dependence has only been observed on 4 samples (out of a total of 64): too few to deduce precise conditions for this morphology to arise. In addition, the crystalline orientation dependence does not immediately appear during the process: as shown on the two SEM images on the left of Figure III.28 the "inverted-pyramid-like" morphology is not seen for an etching time of 10 min. Nevertheless, it should be pointed out that crystalline orientation dependence has been observed only with the lowest average ion bombardment energy (E_{avg} = 32 eV) obtained in the study. For similar conditions of ion flux and identical etching times, a higher ion energy gives rise to the formation of more classical (in the present study) cone-shaped structures, as seen on the two SEM images on the right in Figure III.28. The disappearance of crystalline orientation dependence with increased ion energy can be understood from an increased contribution of the ions to the etching (evolving from a dominant chemical nature to an ion-enhanced behavior), leading to a reduced difference in etch rates between (100) and (111) planes.

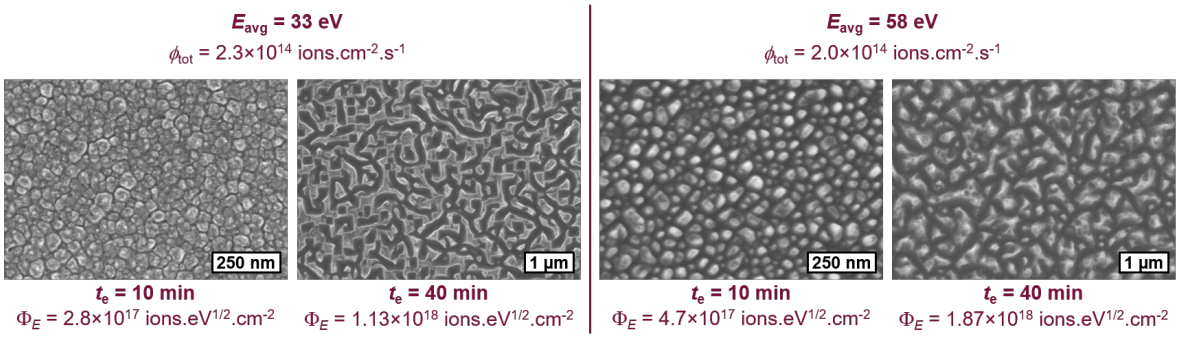

Fig. III.28: SEM top view images of selected nanotextured c-Si sample: (left) samples obtained at low ion bombardment energy (E_{avg} = 32 eV) for 10 and 40 min of etching. The crystalline orientation dependence of nanostructures morphology is only observed at t_e = 40 min (same sample as in Figure III.27). As a comparison, the two images on the right show samples obtained with a similar ion flux but higher average ion energy.

Summary

In this chapter, the analysis of experimental results has revealed important effects and "universal" trends (in the explored range of process conditions). The main findings should be recalled:

- Nanotexturing of c-Si in a SF_6/O_2 CCP discharge has been obtained at room temperature.
- The f**ormation of nanostructures strongly depends on the SF_6 content** in the input gas flux, but also on the **total input gas flux and discharge pressure**. A broadband decrease of reflectance has been demonstrated, leading to effective reflectance values below 2%.
- **Nanostructures "grow" by etching of surrounding material**, with a pseudo-random arrangement, from an average width around 40 nm to micrometric sizes (extreme values observed in the present study). The **nanostructure average size and its evolution are independent from the initial surface finish** but a preferential arrangement along salient points (e.g. saw marks) has been demonstrated. Additionally, a **significant "bulk etching" occurs simultaneously** to the formation of structures, i.e. a substantial volume of c-Si is removed from the whole surface.
- Upscaling tests have demonstrated that a **uniform effective reflectance across a 6" pseudo-square wafer** could be achieved, although in a very narrow process window. In addition, a difference in nanostructure sizes (from the center to the edge of the wafer) was still identified, indicating that **etching conditions are not totally uniform**. A possible gradient in the neutral species densities in the plasma could possibly explain this phenomenon.
- Tailored voltage waveforms have been used to tune the ion flux energy distribution function at the substrate electrode and therefore the nanotexturing conditions. The **available range has been further expanded by taking advantage of radial ion flux non-uniformities** on the electrode.
- A phenomenological model successfully describes the "bulk etching" phenomenon: the **etching yield increases linearly with the square root of the ion energy, above an etching threshold of 13 eV**. Moreover, this model efficiently describes the evolution of the **nanostructure average width and height as well: both parameters evolve linearly with the energy weighted ion fluence**, demonstrating the importance of both the ion flux and ion energy on the final surface properties.
- Two observations indicate possible deviations from the "universal trend": (i) the **aspect ratio** of the nanostructures seems to **depend on the applied ion flux** (increasing the ion flux leads to higher aspect ratios); (ii) a **crystalline orientation dependence may be obtained** (altering the nanostructure morphology) and possibly arises in conditions of relatively low ion bombardment energy.

Finally, the energy weighted ion fluence also effectively predicts the effective reflectance of the surface for a given process: this direct link between process conditions and final optical properties is helpful for process development. However, this descriptive model conceals at least two important features: (i) the clear trend in the evolution of the effective reflectance hides the quite complex optical behavior of SF_6/O_2 plasma nanotextured c-Si surfaces; (ii) the effective reflectance (computed from total hemispherical reflectance spectra measured at normal light incidence) does not account for other important optical properties, such as light scattering or light-trapping in the near-IR range. For these reasons, a more detailed investigation of the optical properties will be carried out in the next chapter.

Bibliography (Chapter III)

[1] H. Jansen, H. Gardeniers, M. d. Boer, M. Elwenspoek and J. Fluitman, A survey on the reactive ion etching of silicon in microtechnology, *J. Micromech. Microeng.* **1996**, 6(1), 14–28, doi:10.1088/0960-1317/6/1/002. 100

[2] R. Dussart *et al.*, Silicon columnar microstructures induced by an SF_6 /O_2 plasma, *J. Phys. D Appl. Phys.* **2005**, 38(18), 3395–3402, doi:10.1088/0022-3727/38/18/012. 100, 120

[3] M. Steglich, T. Käsebier, M. Zilk, T. Pertsch, E.-B. Kley and A. Tünnermann, The structural and optical properties of black silicon by inductively coupled plasma reactive ion etching, *J. Appl. Phys.* **2014**, 116(17), 173503, doi:10.1063/1.4900996. 100

[4] M. Gaudig, J. Hirsch, T. Schneider, A. N. Sprafke, J. Ziegler, N. Bernhard and R. B. Wehrspohn, Properties of black silicon obtained at room-temperature by different plasma modes, *J. Vac. Sci. Technol. A* **2015**, 33(5), 05E132, doi:10.1116/1.4929540. 100, 120

[5] Y. Huang, W. Yan, X. Tan and L. He, Study on silicon nanopillars with ultralow broadband reflectivity via maskless reactive ion etching at room temperature, *Mater. Sci. Eng. B* **2017**, 223, 153–158, doi:10.1016/j.mseb.2017.06.013. 100

[6] J. Pezoldt, T. Kups, M. Stubenrauch and M. Fischer, Black luminescent silicon, *Phys. Status Solidi C* **2011**, 8(3), 1021–1026, doi:10.1002/pssc.201000388. 100

[7] H. Jansen, M. d. Boer, R. Legtenberg and M. Elwenspoek, The black silicon method: a universal method for determining the parameter setting of a fluorine-based reactive ion etcher in deep silicon trench etching with profile control, *J. Micromech. Microeng.* **1995**, 5(2), 115–120, doi:10.1088/0960-1317/5/2/015. 100, 102, 120

[8] A. Bidiville, K. Wasmer, R. Kraft and C. Ballif, Diamond Wire-Sawn Silicon Wafers – from the Lab to the Cell Production **2009**, doi:10.4229/24thEUPVSEC2009-2CV.1.86. 101

[9] Bidiville, A., Heiber, J., Wasmer, K., Habegger, S. and Assi, F., Diamond Wire Wafering: Wafer Morphology in Comparison to Slurry Sawn Wafers **2010**, doi:10.4229/25thEUPVSEC2010-2CV.1.78. 101

[10] Y. H. Lee, M.-M. Chen and A. A. Bright, Doping effects in reactive plasma etching of heavily doped silicon, *Appl. Phys. Lett.* **1985**, 46(3), 260–262, doi:10.1063/1.95918. 102

[11] E. Dilonardo, G. Valerio Bianco, M. Michela Giangregorio, M. Losurdo, P. Capezzuto and G. Bruno, Silicon doping effect on SF6/O2 plasma chemical texturing, *J. Appl. Phys.* **2011**, 110(1), 013303, doi:10.1063/1.3603051. 102

[12] M. Moreno, D. Daineka and P. Roca i Cabarrocas, Plasma texturing for silicon solar cells: From pyramids to inverted pyramids-like structures, *Sol. Energy Mater. Sol. Cells* **2010**, 94(5), 733–737, doi:10.1016/j.solmat.2009.12.015. 102, 133

[13] L. Schneider, N. A. Feidenhans'l, A. Telecka and R. J. Taboryski, One-step Maskless Fabrication and Optical Characterization of Silicon Surfaces with Antireflective Properties and a White Color Appearance, *Sci. Rep.* **2016**, 6, 35183, doi:10.1038/srep35183. 102, 133

[14] M. A. Green, Self-consistent optical parameters of intrinsic silicon at 300 K including temperature coefficients, *Sol. Energy Mater. Sol. Cells* **2008**, 92(11), 1305–1310, doi:10.1016/j.solmat.2008.06.009. 102

[15] ASTM G173 - 03(2012), Standard Tables for Reference Solar Spectral Irradiances: Direct Normal and Hemispherical on 37° Tilted Surface, URL `www.astm.org/Standards/G173.htm`. 102

[16] F. Stern, Elementary Theory of the Optical Properties of Solids, in *Solid State Physics* (edited by D. Turnbull and F. Seitz), vol. 15, 299–408, Academic Press, **1963**. 102

[17] W. Chen, X. Liu, M. Li, C. Yin and L. Zhou, On the nature and removal of saw marks on diamond wire sawn multicrystalline silicon wafers, *Mater. Sci. Semicond. Proc.* **2014**, 27, 220–227, doi:10.1016/j.mssp.2014.06.049. 103

[18] R. Pétri, P. Brault, O. Vatel, D. Henry, E. André, P. Dumas and F. Salvan, Silicon roughness induced by plasma etching, *J. Appl. Phys.* **1994**, 75(11), 7498–7506, doi:10.1063/1.356622. 108

[19] G. Kokkoris, V. Constantoudis, P. Angelikopoulos, G. Boulousis and E. Gogolides, Dual nanoscale roughness on plasma-etched Si surfaces: Role of etch inhibitors, *Phys. Rev. B* **2007**, 76(19), 193405, doi:10.1103/PhysRevB.76.193405. 108, 110

[20] Y.-P. Zhao, T. Jason, G.-C. Drotar, S. Wang and T.-M. Lu, Roughening in Plasma Etch Fronts of Si(100), *Phys. Rev. Lett.* **1999**, 82(24), 4882–4885, doi:10.1103/PhysRevLett.82.4882. 108, 110

[21] N. Nakazaki, H. Tsuda, Y. Takao, K. Eriguchi and K. Ono, Two modes of surface roughening during plasma etching of silicon: Role of ionized etch products, *J. Appl. Phys.* **2014**, 116(22), 223302, doi:10.1063/1.4903956. 108

[22] E. Gogolides, C. Boukouras, G. Kokkoris, O. Brani, A. Tserepi and V. Constantoudis, Si etching in high-density SF6 plasmas for microfabrication: surface roughness formation, *Microelectro. Eng.* **2004**, 73–74, 312–318, doi:10.1016/j.mee.2004.02.059. 110

[23] M. Martin and G. Cunge, Surface roughness generated by plasma etching processes of silicon, *J. Vac. Sci. Technol. B* **2008**, 26(4), 1281–1288, doi:10.1116/1.2932091. 110

[24] D. Abi Saab, P. Basset, M. J. Pierotti, M. L. Trawick and D. E. Angelescu, Static and Dynamic Aspects of Black Silicon Formation, *Physical Review Letters* **2014**, 113(26), doi:10.1103/PhysRevLett.113.265502. 110, 130

[25] D. H. Raguin and G. M. Morris, Analysis of antireflection-structured surfaces with continuous one-dimensional

surface profiles, *Appl. Opt.* **1993**, 32(14), 2582–2598, doi:10.1364/AO.32.002582. 111

[26] W. H. Southwell, Pyramid-array surface-relief structures producing antireflection index matching on optical surfaces, *J. Opt. Soc. Am. A, JOSAA* **1991**, 8(3), 549–553, doi:10.1364/JOSAA.8.000549. 111

[27] A. G. Nagy, Radial Etch Rate Nonuniformity in Reactive Ion Etching, *J. Electrochem. Soc.* **1984**, 131(8), 1871–1875, doi:10.1149/1.2115981. 113, 115

[28] D. J. Economou, Uniformity of Etching in Parallel Plate Plasma Reactors, *J. Electrochem. Soc.* **1989**, 136(1), 188, doi:10.1149/1.2096584. 115

[29] V. M. Donnelly and A. Kornblit, Plasma etching: Yesterday, today, and tomorrow, *J. Vac. Sci. Technol. A* **2013**, 31(5), 050825, doi:10.1116/1.4819316. 113

[30] H. V. Jansen, M. J. de Boer, S. Unnikrishnan, M. C. Louwerse and M. C. Elwenspoek, Black silicon method: X. A review on high speed and selective plasma etching of silicon with profile control: an in-depth comparison between Bosch and cryostat DRIE processes as a roadmap to next generation equipment, *J. Micromech. Microeng.* **2009**, 19(3), 033001, doi:10.1088/0960-1317/19/3/033001. 115

[31] H. Jansen, M. de Boer, H. Wensink, B. Kloeck and M. Elwenspoek, The black silicon method. VIII. A study of the performance of etching silicon using SF6/O2-based chemistry with cryogenical wafer cooling and a high density ICP source, *Microelectron. J.* **2001**, 32(9), 769–777, doi:10.1016/S0026-2692(01)00039-8. 120

[32] D. Murias *et al.*, Black Silicon formation using dry etching for solar cells applications, *Mater. Sci. Eng. B* **2012**, 177(16), 1509–1513, doi:10.1016/j.mseb.2012.03.038. 120

[33] C. Steinbrüchel, Universal energy dependence of physical and ion-enhanced chemical etch yields at low ion energy, *Appl. Phys. Lett.* **1989**, 55(19), 1960, doi:10.1063/1.102336. 126

[34] R. J. Belen, S. Gomez, D. Cooperberg, M. Kiehlbauch and E. S. Aydil, Feature-scale model of Si etching in SF6/O2 plasma and comparison with experiments, *J. Vac. Sci. Technol. A* **2005**, 23(5), 1430–1439, doi:10.1116/1.2013317. 126

[35] V. Ishchuk, D. L. Olynick, Z. Liu and I. W. Rangelow, Profile simulation model for sub-50 nm cryogenic etching of silicon using SF6/O2 inductively coupled plasma, *J. Appl. Phys.* **2015**, 118(5), 053302, doi:10.1063/1.4927731. 126

[36] S. Gomez, R. Jun Belen, M. Kiehlbauch and E. S. Aydil, Etching of high aspect ratio structures in Si using SF6/O2 plasma, *J. Vac. Sci. Technol. A* **2004**, 22(3), 606, doi:10.1116/1.1710493. 126

[37] K. Eriguchi, Modeling of defect generation during plasma etching and its impact on electronic device performance—plasma-induced damage, *J. Phys. D Appl. Phys.* **2017**, 50(33), 333001, doi:10.1088/1361-6463/aa7523. 128

[38] Y. Fan, P. Han, P. Liang, Y. Xing, Z. Ye and S. Hu, Differences in etching characteristics of TMAH and KOH on preparing inverted pyramids for silicon solar cells, *Appl. Surf. Sci.* **2013**, 264, 761–766, doi:10.1016/j.apsusc.2012.10.117. 133

[39] R. Dussart, T. Tillocher, P. Lefaucheux and M. Boufnichel, Plasma cryogenic etching of silicon: from the early days to today's advanced technologies, *J. Phys. D Appl. Phys.* **2014**, 47(12), 123001, doi:10.1088/0022-3727/47/12/123001. 133

[40] T. Zijlstra, E. van der Drift, M. J. A. de Dood, E. Snoeks and A. Polman, Fabrication of two-dimensional photonic crystal waveguides for 1.5 μm in silicon by deep anisotropic dry etching, *J. Vac. Sci. Technol. B* **1999**, 17(6), 2734, doi:10.1116/1.591054. 133

[41] R. J. Belen, S. Gomez, M. Kiehlbauch and E. S. Aydil, In situ measurement of the ion incidence angle dependence of the ion-enhanced etching yield in plasma reactors, *Journal of Vacuum Science & Technology A* **2006**, 24(6), 2176–2186, doi:10.1116/1.2362725. 133

CHAPTER IV

TAILORING OPTOELECTRONIC PROPERTIES OF PLASMA NANOTEXTURED SILICON SURFACES

Contents

IV.1 Optical Properties of Nanotextured Silicon Surfaces **139**
IV.1.1 Broadband Anti-reflection Properties 140
IV.1.1.a Multilayer effective medium approximation model 140
IV.1.1.b Confrontation with experimental results 141
IV.1.1.c Angle-resolved reflectance measurements 144
IV.1.2 Light-Trapping in Near-IR Range 146
IV.1.2.a Quantification using the light pathlength enhancement factor 147
IV.1.2.b Improvement of light-trapping through nanotexturing 150
IV.1.2.c Comparison with different light-trapping designs 151
IV.1.3 Synthesis: light management through front side nanotexturing 156
IV.2 Passivation of Nanotextured Silicon Surfaces **158**
IV.2.1 ALD Al_2O_3 Surface Passivation 158
IV.2.1.a Short description of the ALD process 158
IV.2.1.b Samples and texturing process 159
IV.2.2 Passivation of Plasma Nanotextured Silicon Surfaces 160
IV.2.2.a Baseline passivation results 160
IV.2.2.b Dynamics of passivation degradation 161
IV.2.2.c Disentangling the effects of plasma induced defects and surface area enhancement 163
Summary **166**
Bibliography **168**

Introduction

In Chapter III, SF_6/O_2 plasma etching process conditions have been linked to the final nanostructure morphology of the c-Si surface, although the process was primarily optimized as a function of the final effective reflectance. Indeed, the achievement of broadband anti-reflective properties is the original motive for studying nanoscale texturing of silicon surfaces for photovoltaic applications. However, the nanotexturing process modifies the optical properties of c-Si absorbers in various ways: sectionIV.1 of the present chapter will therefore be dedicated to in-depth investigations of the optics of nanotextured absorbers. Two complementary objectives are sought from this study: (i) to obtain a better description and comprehension of the optical properties of nanotextured c-Si absorbers; (ii) to define relevant criteria to further optimize developments of black silicon processes.

Regarding photovoltaic applications, the optical properties of the absorber will play a fundamental role in the generation of electrical carriers. The operation of solar cells also relies on the collection of the electrical carriers to an external network or load, as it has been quickly recalled in the introduction of ChapterI. In that respect, the "material properties" (e.g. bulk quality, presence of defects) of the c-Si absorber, as well as its interfaces with other constituents of solar cells (e.g. metal contacts), will be of great importance. Challenges have in particular been identified in the literature regarding the passivation of plasma nanotextured c-Si surfaces: owing notably to the ion bombardment during the process, a large density of defects may be present at the surface (or in the subsurface region) of the absorber and act as strong recombination centers. Section IV.2 of this chapter will therefore focus on the influence of ion bombardment on the passivation of nanotextured c-Si surfaces.

IV.1 Optical Properties of Nanotextured Silicon Surfaces

The premises behind the study of silicon surface nanotexturing in the context of photovoltaic applications can be recalled with the basic case of a planar c-Si slab, as depicted in Figure IV.1(a). Increasing photogeneration of electrical carriers per unit area is equivalent to increasing the absorption of incoming photons (flux normalized to unity) in the c-Si, i.e. maximize the absorptance, A_{tot}. With this aim, two sources of losses have to be mitigated, as synthesized in the following expression:

$$A_{\text{tot}} = 1 - R_{\text{f}} - (R_{\text{esc}} + T) \tag{IV.1}$$

where R_{f} is the front reflectance, R_{esc} the escape reflectance and T the transmittance, and where all quantities depend on the properties of incoming light (angle of incidence in particular) and on the (complex) refractive index of the absorber. Reflection at the front air/c-Si interface is due to the abrupt difference of refractive index between the two media: front reflectance corresponds to the fraction of photons that do not penetrate the c-Si absorber. In contrast, escape reflectance and transmittance characterize the fraction of incoming photons penetrating the silicon but escaping before being absorbed: both phenomena are due to weak absorption (and therefore only significant in a limited wavelength range).

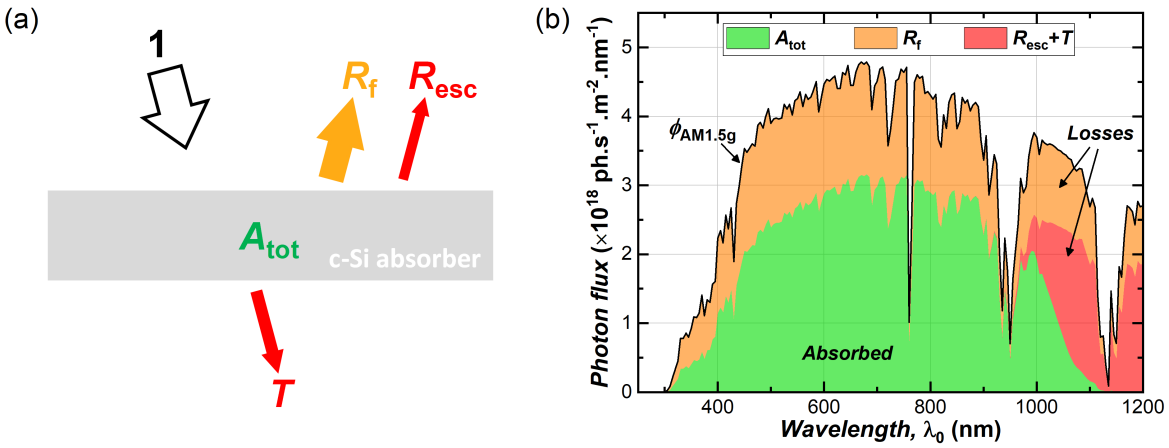

Fig. IV.1: (a) Schematic of a c-Si absorber illustrating incoming light, reflection and transmission. (b) Solar light photon flux (computed from the AM1.5g spectrum) and contributions of loss mechanisms for a perfectly flat 180 µm thick c-Si absorber (assuming normal light incidence).

The contributions of the different loss mechanisms are shown in Figure IV.1(b), here computed theoretically for the AM1.5g solar spectrum, in the simple case of normal light incidence on a 180 µm thick absorber. This case is intentionally simplistic, but it illustrates the importance of mitigating optical losses using appropriate light management techniques:

- Front reflectance represents the largest share in the overall losses: for $\lambda_0 \in [250, 1200\,\text{nm}]$ the total "available" photogenerated current density amounts to $46.3\,\text{mA}\cdot\text{cm}^{-2}$, while the losses due to front reflection correspond to $16.2\,\text{mA}\cdot\text{cm}^{-2}$. A drastic reduction of reflectance at the front surface of the absorber is therefore essential to improve carrier generation. In that respect, the broadband anti-reflective properties of nanotextured samples have been shown and rapidly discussed in Chapter III: in the following, a more in-depth investigation of the relationship between nanostructure morphology and the final front reflectance of the surface will first be carried out.

- Escape reflectance and transmittance also induce large losses for $\lambda_0 > 1000\,\text{nm}$ (amounting to an equivalent photogenerated current density loss of $4.5\,\text{mA}\cdot\text{cm}^{-2}$), illustrating the additional need for light-trapping. To this aim, plasma nanotexturing of the front surface of the absorber can also prove to be very efficient, owing to a promotion of light-scattering, as will be demonstrated in the second subsection.

IV.1.1 Broadband Anti-reflection Properties

In this manuscript, the link between the nanostructure morphology (after SF_6/O_2 etching) and the total hemispherical reflectance of black silicon samples has, up to now, only been qualitatively explained. In particular, it has been shown in Chapters I and III that, due to the complex morphologies and varying sizes, an adequate and simple optical model describing the reflectance of black silicon surfaces in a large range of wavelengths is still missing. However, in the case of a very small nanostructure width (compared to the wavelength in c-Si, $\lambda_{Si} = \lambda_0/n_{Si}$), the nanostructured surface may be approximated by a gradient refractive index layer, and a simple implementation of this approach is here proposed to quantitatively describe (even in a limited range) the normal incidence reflectance of the black silicon samples. Here, the analysis is made using the results obtained in section III.3 of Chapter III: as a reminder, these samples were obtained from LPD wafers, which have a relatively smooth initial surface so that their initial reflectance – before nanotexturing – is close to that of a perfectly flat c-Si slab (see also initial sample description, section III.1.1.b Chapter III).

IV.1.1.a Multilayer effective medium approximation model

Description of the model. In order to understand the evolution of the reflectance of nanotextured c-Si surfaces, the nanostructures are geometrically modeled by a tiling of upright c-Si pyramids with base width L_{MM} and height H_{MM}, as illustrated in Figure IV.2(a), on a c-Si bulk and surrounded by air.

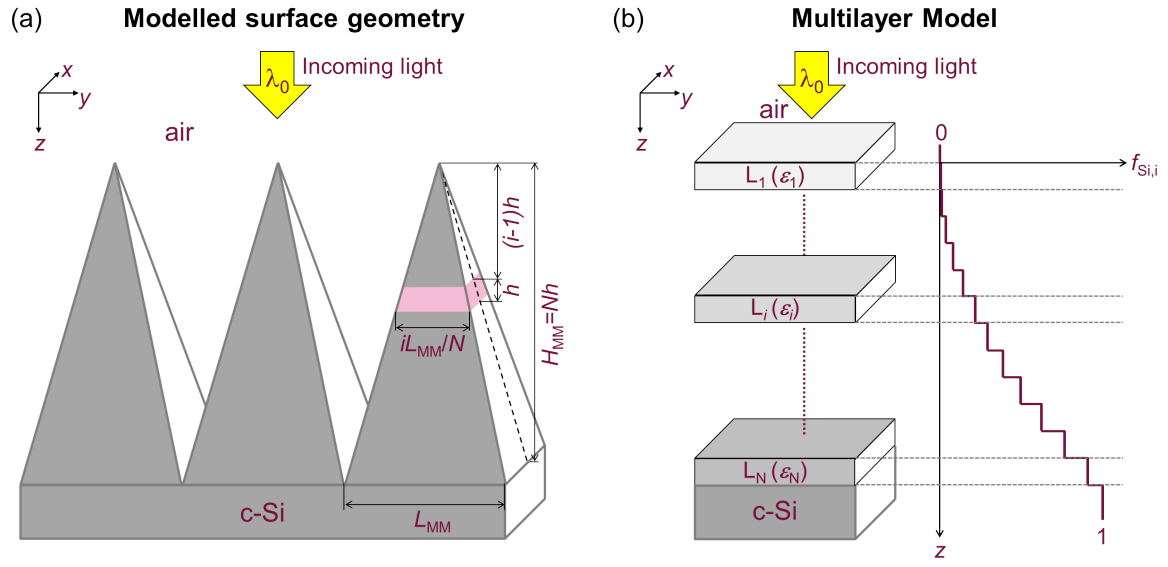

Fig. IV.2: (a) Schematic of geometric model (pavement of upright pyramids) for plasma nanostructured surface. (b) Multilayer effective medium approximation 1D model with graph of c-Si filling factor.

The optical properties of this surface are modeled by approximating it by a stratified film of N successive layers (L_i for $i \in [1,N]$, expanding infinitely in directions x and y) with an identical thickness $h = H_{MM}/N$ and a complex permittivity $\boldsymbol{\epsilon}_i$, as shown in Figure IV.2(b). In the limit of very large N, this model is equivalent to approximate the nanostructured surface as a gradient refractive index layer. The permittivity of each layer is obtained using Bruggeman's effective medium approximation [1]. In this model, the complex permittivity $\boldsymbol{\epsilon}_i$ of each layer of composite material (here a mixture of c-Si and air) is derived from the following equation:

$$f_{Si,i}\frac{\boldsymbol{\epsilon}_{Si}-\boldsymbol{\epsilon}_i(\lambda_0)}{\boldsymbol{\epsilon}_{Si}+2\boldsymbol{\epsilon}_i(\lambda_0)}+(1-f_{Si,i})\frac{\epsilon_{air}-\boldsymbol{\epsilon}_i(\lambda_0)}{\epsilon_{air}+2\boldsymbol{\epsilon}_i(\lambda_0)}=0 \tag{IV.2}$$

where $\boldsymbol{\epsilon}_{Si}(\lambda_0)$ is the relative permittivity of crystalline silicon and $\epsilon_{air} = \epsilon_0$ the permittivity of air.

$f_{\mathrm{Si},i}$ is the c-Si material filling factor for each layer L_i, i.e. the volume fraction of silicon in the layer. Using the geometry of the modeled nanostructures, the filling factor is easily derived:

$$f_{\mathrm{Si},i} = \left(\frac{i-1/2}{N}\right)^2 \tag{IV.3}$$

Notice that this quadratic behavior could actually be generalized to any type of conical structures fully tiling the plane (where a cone is understood mathematically as being formed by a set of straight segments connecting to a common point, the apex). In addition, while the periodic structure suggested in Figure IV.2(a) is convenient to easily represent a full tiling of the surface, the 1D model will actually not account for diffraction phenomena (the modeled geometry is only introduced here to describe the computation of the c-Si material filling factor).

In the end, the nanostructured c-Si surface is modeled by a system composed of the multilayer stack comprised between air and c-Si – both treated as semi-infinite media. The transfer matrix method [2] is then used to compute the front reflectance (in *intensity*) of the system at normal incidence, R_{MM} (the bulk being assumed semi-infinite; escape reflectance is not taken into account by the model). Crudely speaking, the transfer matrix method simply consists of using a matrix structure to represent the link between the *amplitudes* of electromagnetic waves entering and exiting a thin-film (in forward and backward directions). For a full stack, the product of all the matrices (obtained for each component layer) will directly link the *amplitudes* of the incoming, reflected, and transmitted waves and allow the computation of the reflectance (and transmittance) in *intensity*. In the model, all materials are assumed nonmagnetic, and the complex permittivity of the c-Si material is derived from [3].

Choice of the number of layers. In order to choose an optimum number of layers in the multilayer model, a few preliminary computations have been performed, with examples illustrated in Figure IV.3: graph (a) shows examples of profiles (for f_{Si}, n and κ) in the multilayer model, while (b) gives the results of some computations with $H_{\mathrm{MM}} = 200\,\mathrm{nm}$, $\lambda_0 = 300, 600, 900\,\mathrm{nm}$ and for N in the range [5,1000].

Figure IV.3(b) shows that, in the investigated conditions, the computation rapidly converges with only a few tens of layers, and above $N = 250$, increasing (by a factor 2 or 4) the number of layers in the model leads to changes of less than $1 \times 10^{-4}\,\%_{\mathrm{abs}}$ in R_{MM}. A few complementary tests have shown that this level of convergence is valid in the full range (both for $H_{\mathrm{MM}} \in [10, 1000\,\mathrm{nm}]$ and $\lambda_0 \in [250, 1250\,\mathrm{nm}]$) of interest. Consequently, further computations (presented in the next section) will be made with $N = 250$.

Notice that the choice of a uniform layer thickness $h = H_{\mathrm{MM}}/N$ is arbitrary, but other approaches (e.g. keeping the optical thickness of each layer constant) would lead to identical results – except the convergence of R_{MM} as a function of N would differ.

IV.1.1.b Confrontation with experimental results

Influence of the nanostructure height. In order to understand the effect of the nanostructure height on the reflectance, the total effective medium layer thickness is varied in the multilayer model. For comparison with experiments, only wavelengths below 1000 nm may be considered, as escape reflectance – not taken into account in the multilayer model – only becomes significant above this value for the approximately 285 µm thick samples used experimentally. In a first analysis, the reflectance will therefore be computed with the multilayer model at $\lambda_0 = 300, 600, 900\,\mathrm{nm}$ (i.e. close to the lower limit, center and higher limit of the range of interest), and is compared to the experimental results in Figure IV.4. Notice that the comparison is done by assuming that the experimental results are best modelled with $H_{\mathrm{MM}} = H_{\mathrm{NS}}$, i.e. the *total* thickness of the effective medium multilayer is taken identical to the nanostructures *average* height.

First, it should be highlighted that, regardless of the wavelength, the multilayer model predicts a continuous decrease of the reflectance with the effective multilayer total thickness (except for small oscillations), as seen in the graphs Figure IV.4. For this reason, a fair comparison between

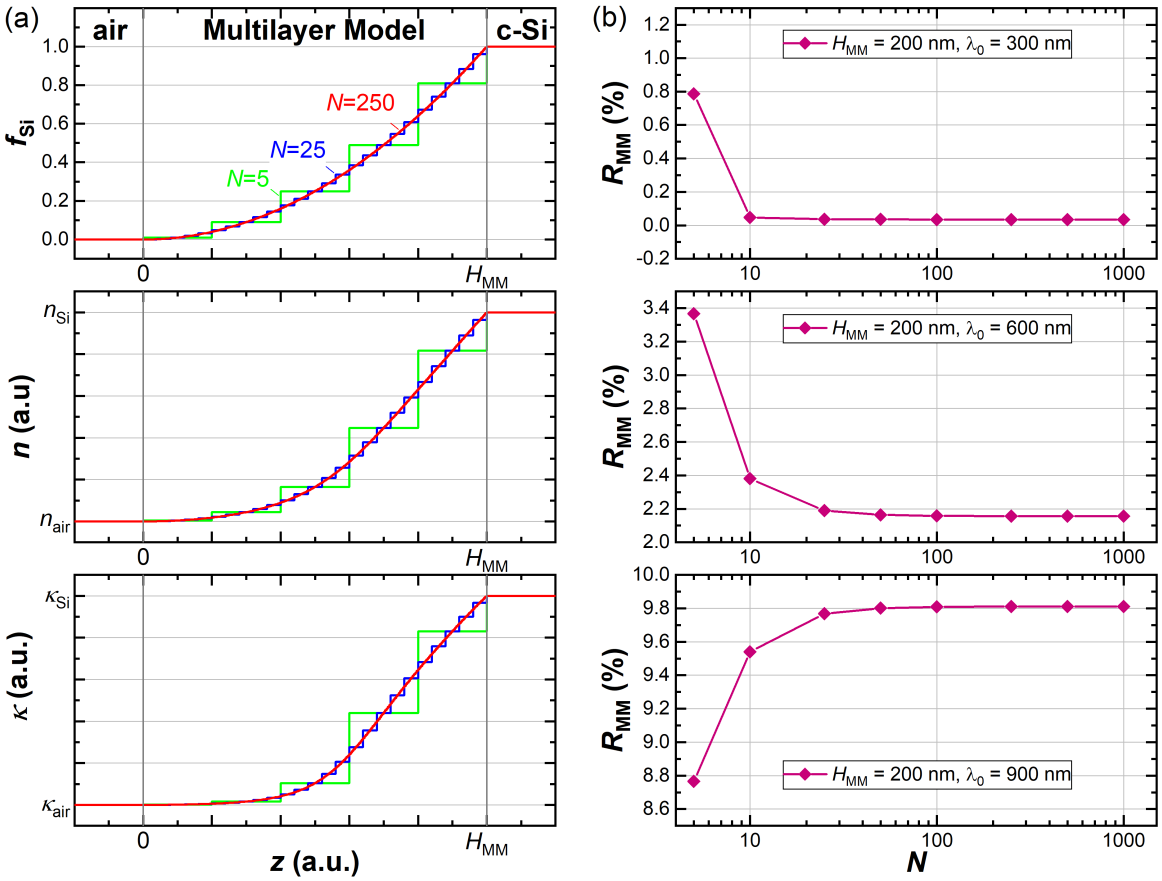

Fig. IV.3: (a) Examples of profiles for c-Si material filling factor, f_{Si}, refractive index, n, and extinction coefficient, κ, for $N = 5, 25, 250$. (b) Evolution of calculated front reflectance, R_{MM} with N in $[5, 1000]$ and for $\lambda_0 = 300, 600, 900$ nm.

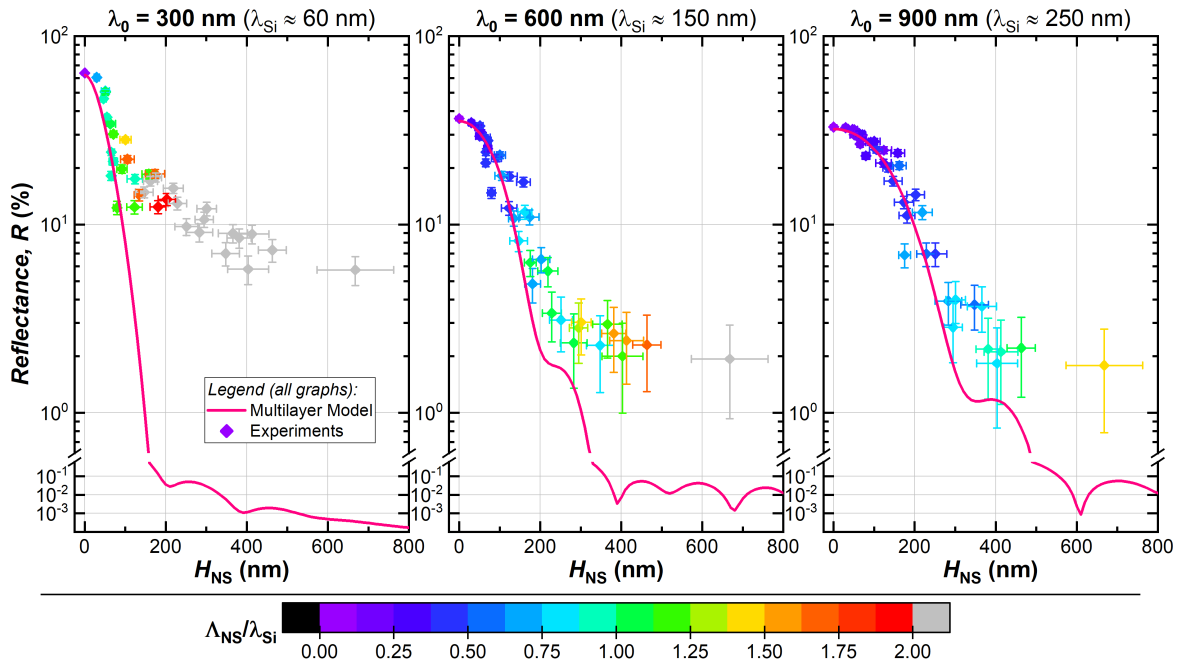

Fig. IV.4: Evolution of reflectance (at $\lambda_0 = 300$, 600 and 900 nm) with nanostructure average height: comparison of experiments with proposed multilayer model. Colormap (identical for all graphs) showing parameter $\Lambda_{NS}/\lambda_{Si}$.

model and experimental results is better obtained using a logarithmic vertical-axis scale (notice the break introduced for better visualization). In addition, the decrease of reflectance obtained from the model is more rapid for $\lambda_0 = 300\,\text{nm}$ than for $\lambda_0 = 600\,\text{nm}$ (than for $\lambda_0 = 900\,\text{nm}$) because at a given thickness H_{MM}, the transition appears "smoother" for shorter wavelength. Indeed, as it has been recalled in Chapter I section I.2.2.a, the thickness of the inhomogeneous layer has to be - at least - similar to the light wavelength for the reflectance to be significantly reduced. For the modelled profiles and the three value of wavelengths under investigation, the reflectance of the surface decreases to less than a percent of the initial value when H_{MM} is larger than approximately $\lambda_0/2$.

Comparing the model with experimental results, it should be recalled that the "effective medium approximation" (here in the form of a multilayer model) is only valid in the limit of a nanostructure width much smaller than the scaled wavelength λ_0/n_{Si}. For this reason, experimental results are differentiated as a function of this criterion: in Figure IV.4, a colormap shows the value $\Lambda_{NS}/\lambda_{Si}$ for all samples (at 300, 600 and 900 nm, λ_{Si} is approximately equal to 60, 150 and 250 nm respectively). It should be reminded (from Chapter III) that values of H_{NS} and Λ_{NS} are positively correlated for our plasma nanotextured c-Si samples.

At $\lambda_0 = 300\,\text{nm}$, the model predicts the absolute (front) reflectance of the surface relatively well until approximately $H_{NS} = 100\,\text{nm}$, corresponding to samples for which $\Lambda_{NS} < \lambda_{Si}$. Above this threshold the multilayer model becomes invalid and diverges from the experimental results. As a result, when H_{NS} increases, the model predicts a much lower reflectance (up to several orders of magnitude) compared to experimental results.

At $\lambda_0 = 600$ or $900\,\text{nm}$, a similar analysis can be made: reflectance values are satisfactorily predicted until $H_{NS} = 200$ or $300\,\text{nm}$, respectively. Again, the model significantly diverges from experimental results when $\Lambda_{NS} \geq \lambda_{Si}$ approximately. Notice that, even in the range of validity of the model ($\Lambda_{NS} < \lambda_{Si}$), some scattering of the experimental data around the model curve can be observed. This may be partly due to the uncertainties in the estimation of the nanostructure average height and surface reflectance (as suggested from the error bars), but also to possible differences in nanostructure morphologies, which may in some cases significantly deviate from the modelled geometry (i.e. neighboring cones with a quadratic c-Si material filling factor).

Effective reflectance. Regarding photovoltaic applications, a broadband anti-reflective behavior of nanotextured c-Si surfaces is sought in order to improve carrier generation in the absorber. In that respect, the effective reflectance, R_{eff}, computed from Equation (I.29) Chapter I, represents a relevant parameter to globally assess the anti-reflective properties of a textured surface. As a consequence, it is of interest to evaluate the range of validity of the multilayer model for the prediction of R_{eff} as a function of the nanostructure sizes. To this aim, the multilayer model has been used to compute the full reflectance spectra (in the range [250,1000 nm]) for $H_{MM} \in [0, 800\,\text{nm}]$, and the effective reflectance has been extracted from these theoretical spectra. Results are shown in Figure IV.5(a) together with experimental data – here using linear scales and with a color-mapping according to the nanostructure average width, Λ_{NS}. In Figure IV.5(b), full reflectance spectra are shown for selected samples with the corresponding multilayer model results.

Figure IV.5(a) shows that the experimental trend is well predicted by the proposed multilayer model, despite its relative simplicity, when nanostructures have an average width lower than approximately 125 nm. Above this threshold, the model becomes inaccurate in a large part of the wavelength range, as illustrated with the spectra shown in Figure IV.5(b). For the initial surface, sample A ($H_{NS} = 0\,\text{nm}$), the measured reflectance is actually slightly higher than the model – here corresponding simply to the Fresnel formula for a single air/c-Si interface. This discrepancy may be due to the fact that the measurement is actually performed at a small incidence angle (around 8°), to the presence of the native oxide or to a small error in the spectrophotometer calibration.

Regarding nanotextured samples B, C and D ($\Lambda_{NS} < 125\,\text{nm}$), the agreement between the experimental reflectance and the multilayer model spectra is fairly good for $\lambda_0 > 450\,\text{nm}$ approximately, while large differences are seen below this value. As previously highlighted, this discrep-

ancy comes from the fact that the multilayer model actually becomes invalid to describe the reflectance of the nanotextured surface. Despite this deviation and since the fraction of photon flux in the AM1.5g solar spectrum is relatively low in this range – see Figure IV.5(b) - the computed effective reflectance for samples B to D is very close to the multilayer model value, as seen in Figure IV.5(a). In contrast, for sample E (with $\Lambda_{NS} = 210\,nm$), the experimental reflectance is much higher than the model spectrum in the whole wavelength range, explaining the difference between the experimental and modelled effective reflectance.

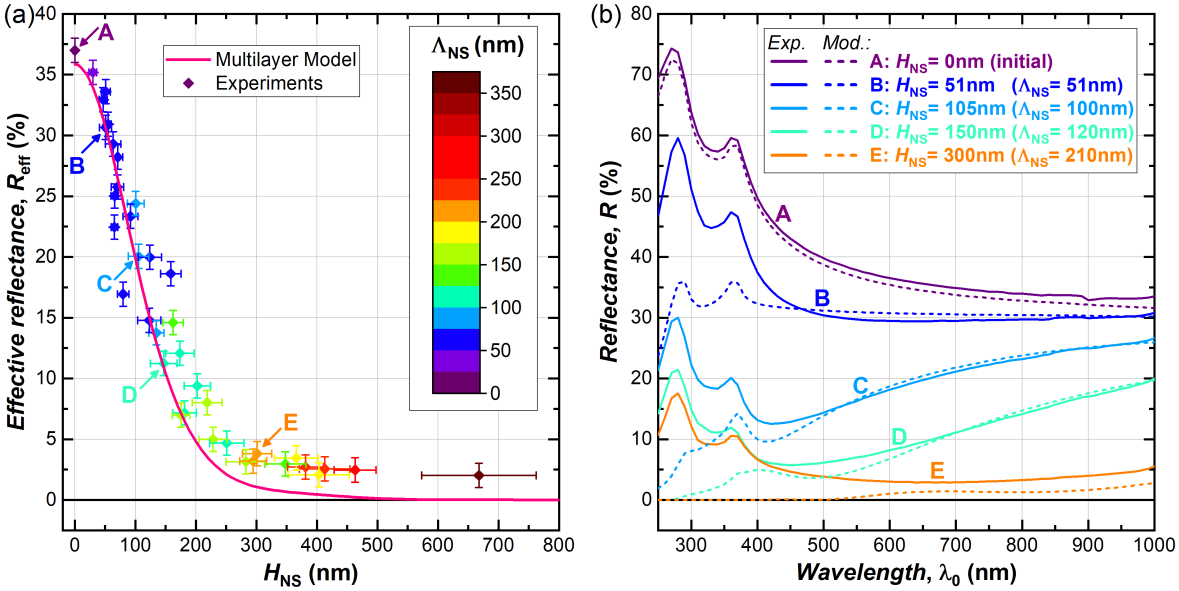

Fig. IV.5: (a) Evolution of effective reflectance with nanostructure average height: comparison of experiments with proposed multilayer model. Colormap showing nanostructure average width for experimental results. (b) Reflectance spectra for five selected samples: measurements (solid curves) and multilayer model results (dashed curves).

Despite the relative simplicity of the proposed multilayer model, the effective reflectance of the nanostructured samples can be accurately predicted, although for a limited range of nanostructures sizes. Some refinements, for instance in the c-Si material filling factor profile, could help improve the quality of the prediction in its range of validity.

As previously recalled, during the SF_6/O_2 etching process (regardless of the plasma conditions in the investigated process window), an increase in average nanostructure height H_{NS} always goes with an increase in average nanostructure width Λ_{NS}. The proposed multilayer model indicates that lower front reflectance can be obtained by increasing H_{NS}, however, the simultaneous increase in Λ_{NS} inevitably makes the model irrelevant. Additionally, the lateral growth of the nanostructures will also induce the initiation of light-scattering in the investigated wavelength range.

IV.1.1.c Angle-resolved reflectance measurements

It has been previously stated that the lateral growth of the nanostructures (increased Λ_{NS}) causes the onset of light scattering. Obviously, this phenomenon cannot be directly detected from total hemispherical measurements that only characterize the total reflected light intensity. However, light scattering will induce large modifications of the angular distribution of reflected light in the hemisphere above the surface. In order to investigate this effect, measurements of angle-resolved diffuse scattering were performed on selected unetched and nanotextured samples (here corresponding to samples obtained in the study of section III.1.2 Chapter III) with various initial surface morphologies. These characterizations have been carried out in collaboration with Dr. Thomas Germer, researcher at the National Institute of Standards and Technology (NIST).

The bidirectional reflectance distribution function (BRDF, f_r), quantified as the radiance scattered into a specific direction normalized by the incident irradiance [4], was measured using 633 nm radiation at an incident angle of 5° and scanning directions evenly spaced in a directional cosine space centered on the surface normal [5, 6]. Figure IV.6 shows the results of these measurements.

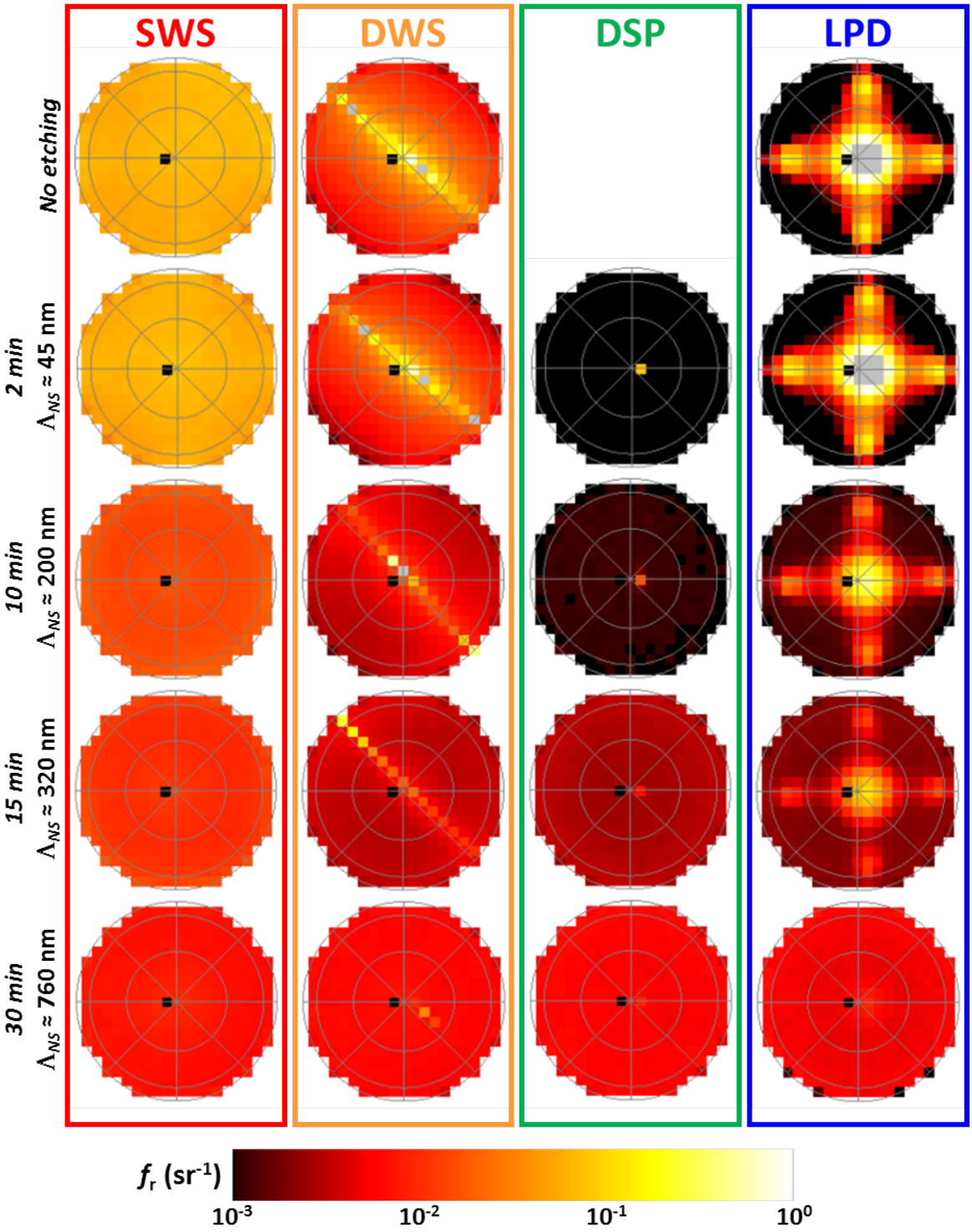

Fig. IV.6: BRDF, f_r, measured for four surface types and for five etching times. The data are shown in projected cosine space, and a grid (30° in polar angle and 45° in azimuth angle) is overlaid on top of the data. The black point in each data to the left of the surface normal is due to the detector blocking the incident beam. The incident angle was 5° and the wavelength was 633 nm. The samples are aligned so that the (110) crystal direction is horizontal. Λ_{NS} values (computed in the DSP case) are also given for reference.

Each of the surfaces has a distinctive scatter pattern prior to any etching. For the lowest etching times, the DSP sample had a BRDF that was below the instrument noise floor, as the instrument was configured, except near the specular direction (one of the samples was not characterized for this reason).

Regarding the measurements on unetched samples, the SWS sample had a relatively uniform BRDF, the DWS sample shows a distinctive diffraction pattern from the wire saw marks at approximately 45° to the (110) crystal direction, and the LPD sample showed a distinctive four-fold symmetric pattern that was correlated to a large number of 113 surface planes.

As the samples are etched, their scatter patterns evolve towards a common behavior: while remnants of their original structure are still observed after 15 min, their behaviors remarkably converge for 30 min of etching. The scattering from the SWS samples remain uniform but decrease in value. The diffuse part of scattering from the DWS samples decreases, while the distinctiveness of the saw mark diffraction is reduced. The scattering from the DSP and LPD samples rise in directions having low initial scatter, while the distinctiveness of its original scattering pattern is reduced. The DSP samples continue to exhibit specularity until 15 min of etching, albeit much reduced from that of the unetched surface, and totally disappears after 30 min.

The emergence of light-scattering with the formation of nanostructures (in cases where light-scattering is initially low, such as the DSP or LPD samples) is clearly observed in the angle-resolved reflectance measurements. In the context of photovoltaic applications, one might actually be more interested by the influence of scattering on the light transmitted into the silicon. In particular, light-scattering will have a key role on the "light-trapping" properties of the absorber. The influence of the nanotexturing process on the light-trapping properties will therefore be more specifically investigated in the next subsection.

IV.1.2 Light-Trapping in Near-IR Range

As explained in Chapter I section I.2.2.b, light-trapping can be understood as the ability of the optical system to prevent incoming light from escaping. In the case of a c-Si absorber, this property becomes especially important for near-IR light, where the absorption depth becomes longer than the absorber thickness: as shown in the introduction of this chapter, for a 180 µm thick planar absorber, poor light-trapping represents 20% of the optical losses in photogenerated current density. It is therefore of great interest to investigate the evolution of light absorption in c-Si samples with front nanotextured surfaces.

As a starting example, total absorptance spectra have been measured (at normal incidence) on initial and nanotextured SWS and LPD samples (one side, baseline recipe from Chapter III section III.1.1.c, samples illuminated from the nanotextured side for absorptance measurements). The reflectance of these samples has already been shown and discussed in Chapter III. These samples have similar thicknesses: (275 ± 5) µm for SWS and (285 ± 2) µm for LPD samples. Results are shown in Figure IV.7(a,b), while graph (c) shows the evolution of the photogenerated current density J_{ph} in the c-Si substrate – calculated from the absorptance spectra, Equation (I.26) in Chapter I. As a theoretical reference, the Yablonovitch limit (for a 280 µm thick c-Si substrate) is also shown in the graphs Figure IV.7: this limit is often considered as the maximal absorptance achievable through light-scattering, although it has been computed in the limit of weak absorption and is therefore not practically achievable for c-Si [7, 8].

For both SWS and LPD substrates, the absorptance increases in the whole wavelength range owing to the nanotexturing process. For wavelengths below 1000 nm (where silicon is strongly absorbing), this rise is mainly due to the decrease of reflectance at the front surface. On the other hand, above 1000 nm, enhancement of absorptance may both be due to lower reflectance and to improved light-trapping inside the silicon. Notice that some samples also show significant absorptance values above 1180 nm (exceeding the Yablonovitch limit): this phenomenon is attributed to free carrier absorption due to metallic impurities, likely originating from wafer slicing.

For the initial SWS sample, absorptance is already relatively high (with an average of 51%) in the range from 1000 to 1200 nm, as seen in Figure IV.7(a), suggesting a high initial light-trapping. In

addition, the "shape" of the absorptance spectra in this range is actually not evolving significantly when the front surface is nanotextured. The initial texture of both rear and front surfaces of SWS samples has been shown (section IV.1.1.c) to induce a high level of scattering, which is also preserved during the nanotexturing of the front surface, and explains a very good light-trapping for all the SWS samples. In the same wavelength range, absorptance is comparatively very low (25% average in [1000,1200 nm]) for the unetched LPD sample, Figure IV.7(b), that therefore seems to have less efficient light-trapping than the initial SWS sample. This apparently poor light-trapping can be explained by a low level of scattering at both interfaces. In contrast, the absorptance significantly increases with texturing time (especially after 15 or 30 min): the convexity of the curve reverses and the absorptance spectrum of the 30 min textured LPD samples becomes very similar to the SWS counterpart.

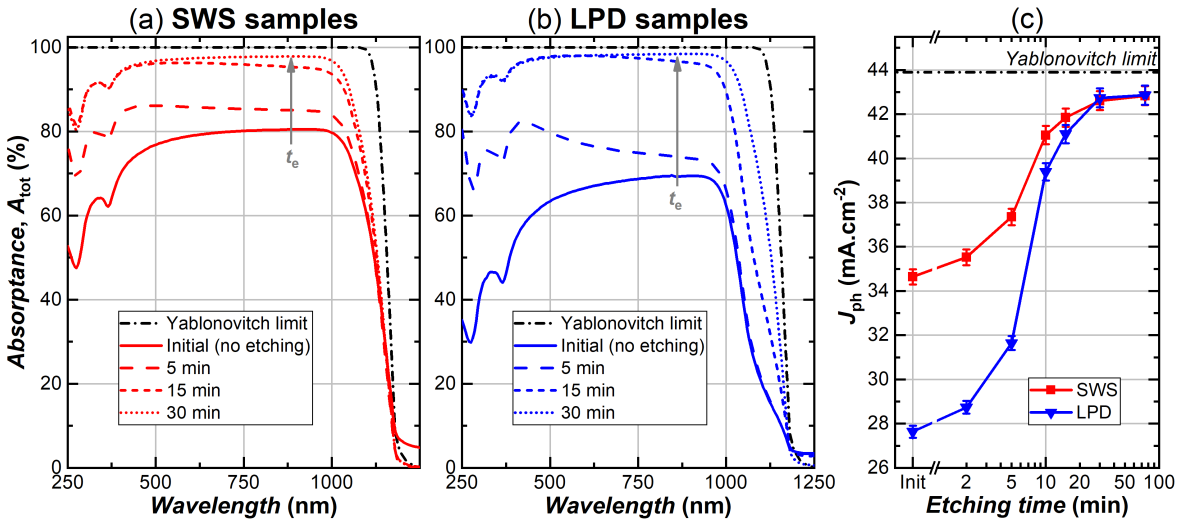

Fig. IV.7: Evolution of absorptance spectra with etching time (at 0, 5,15 and 30 min) for (a) SWS and (b) LPD samples. (c) Corresponding evolution of photogenerated current density, J_{ph}. Dash-dot black curves show theoretical Yablonovitch limit for a 280 µm thick c-Si substrate.

Figure IV.7(c) shows the evolution of the theoretical photogenerated current density, J_{ph}, computed from the absorptance spectra and neglecting parasitic absorption. Due to high initial front reflectance and poor light-trapping, J_{ph} is very low (around 28 mA·cm^{-2}) for the initial LPD samples compared to the SWS samples (initial value $J_{ph} = 34.5$ mA·cm^{-2}). As the samples are etched and their absorptance increases, J_{ph} rises, reaching an identical asymptotic value after 30 min for both SWS and LPD samples, around 42.8 mA·cm^{-2}, close to the 43.9 mA·cm^{-2} theoretical value obtained from the Yablonovitch limit.

This analysis of the absorptance spectra and estimation of the photogenerated current density give a global idea of the light-trapping quality. However, the contribution of the anti-reflective properties cannot easily be discerned, and the absorptance also depends on the properties of the rear surface and on the sample thickness. The previous method only qualitatively informs on the influence of nanotexturing on light-trapping properties, and a more specific (and quantitative) approach is to be sought.

IV.1.2.a Quantification using the light pathlength enhancement factor

Definitions and methods. A more specific quantification of the light-trapping properties may be obtained thanks to the "light pathlength enhancement factor", Z, [9]. Primarily, this factor can be considered as the optical depth of the absorber at a given wavelength, and is usually obtained from internal quantum efficiency measurements to only account for band-to-band absorption (leading to carrier generation). Nevertheless, for the purpose of comparing light-trapping abilities for absorbers with different surface textures, a satisfactory estimation of Z may be obtained using only photometric measurements. In particular, free carrier absorption may be neglected in

first approximation when the samples are weakly doped (here below 1×10^{16} cm^{-3}). Under this assumption and with $1 - R_f$ being the intensity of light actually entering the absorber, Z is obtained from:

$$\frac{A_{tot}(\lambda_0)}{1 - R_f(\lambda_0)} = 1 - e^{-\alpha_{Si}(\lambda_0) Z(\lambda_0) w} \tag{IV.4}$$

The right-hand side of the previous equation corresponds to the theoretical absorption of light after a pathlength Zw in an ideal c-Si absorber: for a given absorber, the higher the light pathlength enhancement, the higher the absorptance. From Equation (IV.4), the estimation of Z therefore requires the measurement of both the total absorptance and the front reflectance. In practice, only the total reflectance $R_{tot} = R_f + R_{esc}$ may be measured by spectrophotometry, and the front reflectance needs to be isolated from escape reflectance. In the range [250,950 nm], where the absorption length of c-Si is much shorter than the substrate thickness (above 180 µm for the samples used here), escape reflectance is neglected and $R_f = R_{tot}$. In the range]950,1250 nm], a simple extrapolation based on a linear fitting of $R_{tot} = r_1 \lambda_0 + r_0$ in [900,950 nm] is proposed. This simple extrapolation is supported first by the small variations in refractive indices of c-Si in the range [900,1300 nm], and, for nanotextured samples, by the pseudo-random distribution of the nanostructures on the surface. Finally, the following approximation of R_f is thus made:

$$R_f(\lambda_0) = \begin{cases} R_{tot}(\lambda_0), & \text{if } \lambda_0 \leq 950 \text{ nm} \\ r_1 \lambda_0 + r_0, & \text{if } \lambda_0 > 950 \text{ nm} \end{cases} \tag{IV.5}$$

Combining Equations (IV.4) and (IV.5), an estimation of Z can be obtained for all samples in the wavelength range of interest (here approximately in [900,1200 nm], where light-trapping plays an important role). However, a direct computation will give rise to non-physical values, as demonstrated in Figure IV.8 for an example case: graph (a) shows the measured spectra for A_{tot}, $R_{tot}$and R_f, graph (b) shows $A_{tot}/(1 - R_f)$ and graph (c) the light pathlength enhancement factor computed using Equation (IV.4).

At very weak absorption ($\lambda_0 > 1200$ nm), A_{tot} should rapidly tend to zero: in the case of a small deviation in measured absorptance (here A_{tot} remains positive possibly due to free carrier absorption), Z will take very high (non-physical) values. On the other hand, for $\lambda_0 < 1000$ nm, $A_{tot}/(1-R_f)$ should rapidly tend to 1 as absorption becomes very strong. Here, values above 1 are computed from experimental measurements below 980 nm: due to the measurement uncertainties, Z cannot be computed in this range.

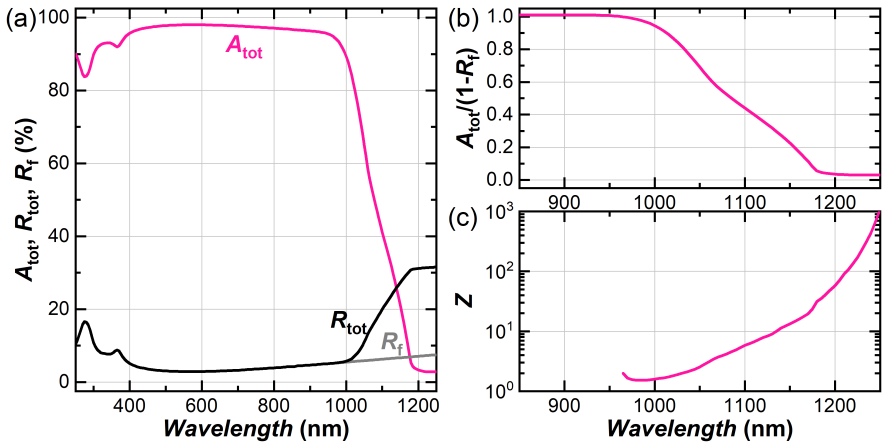

Fig. IV.8: (a) Absorptance and reflectance spectra at normal incidence for a nanotextured c-Si sample (LPD, 15 min etching). (b) Computed values for $A_{tot}/(1 - R_f)$ and (c) pathlength enhancement factor computed from Equation (IV.4) for the same sample.

Parametrization of light pathlength enhancement factor. To circumvent the demonstrated issues in the direct computation of Z, Equation (IV.4) is modified to:

$$\frac{A_{\text{tot}}(\lambda_0)}{1-R_{\text{f}}(\lambda_0)} = \Delta a_\infty + (\Delta a_0 - \Delta a_\infty)\, e^{-\alpha_{\text{Si}}(\lambda_0) Z(\lambda_0) w} \tag{IV.6}$$

where Δa_∞ and Δa_0 are constant parameters which will account for the deviations in experimental measurements respectively in the limits of very strong and very weak absorption. In addition, a parametrization of the light pathlength enhancement factor based on the method proposed by McIntosh and Baker-Finch [10] will be adapted to our study. In this model, Z is expressed as a function of the absorption coefficient, α_{Si}, the thickness of the substrate, w, and three independent (dimensionless) parameters Z_∞, $Z_0$and Z_{p}, as follows:

$$Z_{\text{mod}}(\lambda_0) = Z_\infty + \frac{1}{\alpha_{\text{Si}}(\lambda_0) Z_{\text{p}} w} \ln\left[\frac{Z_0}{Z_\infty} - \left(\frac{Z_0}{Z_\infty} - 1\right) e^{-\alpha_{\text{Si}}(\lambda_0) Z_\infty Z_{\text{p}} w}\right] \tag{IV.7}$$

Within this model, Z_∞ corresponds to the pathlength enhancement factor in the limit of very strong absorption (below 1000 nm), while Z_0 corresponds to the limit at very weak absorption (above 1200 nm): the higher Z_∞ and Z_0, the higher the absorptance (and the better the light-trapping).

On the other hand, Z_{p} has been introduced as a degree of freedom defining the evolution of Z_{mod} in the transition range. This effect is illustrated in Figure IV.9: graph (a) shows examples of Z_{mod} curves as a function of the wavelength for a 100 µm and a 280 µm thick absorber, with $Z_0 = 10$, $Z_\infty = 1.2$ and different values of Z_{p}. Figure IV.9(b) depicts the corresponding theoretical absorptance curves (assuming $R_{\text{f}} = 0$). It is observed that, at a given substrate thickness, the lower Z_{p} the higher Z and the higher the absorptance.

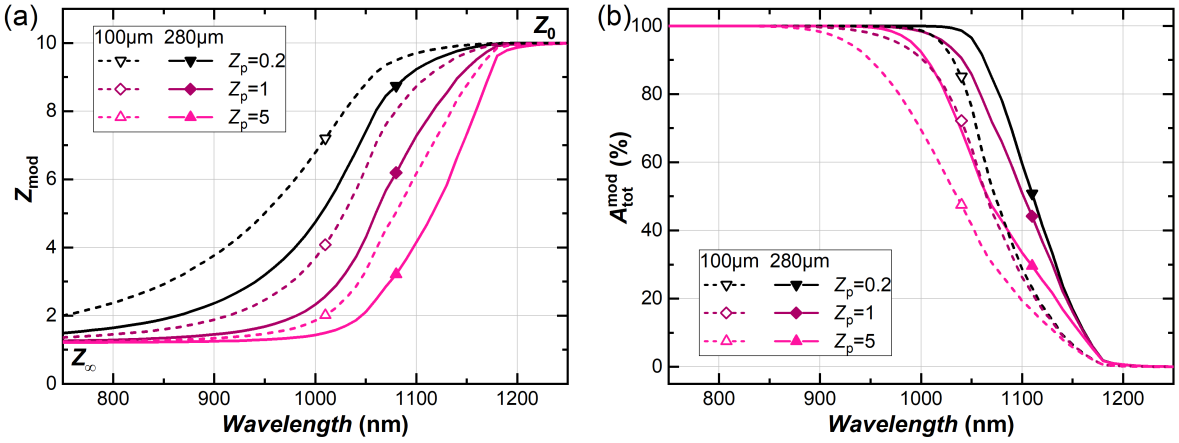

Fig. IV.9: (a) Model pathlength enhancement factor curves from Equation (IV.7) with $Z_\infty = 1.2$, $Z_0 = 10$ and different values of Z_{p} for 100 and 280 µm absorbers. (b) Corresponding theoretical absorptance curves (assuming $R_{\text{f}} = 0$).

In cases where this parametrization satisfactorily fits experimental data, the triplet of parameters $(Z_\infty, Z_0, Z_{\text{p}})$ is independent from the substrate thickness [10, 11]. That is, two absorbers with different thicknesses will have similar light-trapping properties if they have a similar triplet $(Z_\infty, Z_0, Z_{\text{p}})$ – which is not equivalent to having the same absorptance spectra $A_{\text{tot}}(\lambda_0)$ or same light pathlength enhancement factor $Z(\lambda_0)$. Reciprocally, once the triplet of parameters is evaluated for a given substrate, it should be possible to "predict" A_{tot} for any other substrate having similar front and rear surface morphologies but a different thickness.

IV.1.2.b Improvement of light-trapping through nanotexturing

The proposed model for the light pathlength enhancement factor is now used to fit the absorptance spectra shown in the introduction of this section, for SWS and LPD samples. Notice that the fit is performed in the wavelength range [900,1250 nm]. Results are shown in Figure IV.10(a,b): for both types of samples, the experimental spectra are shown (open circles) in the top graphs together with the fitting results (solid curves).

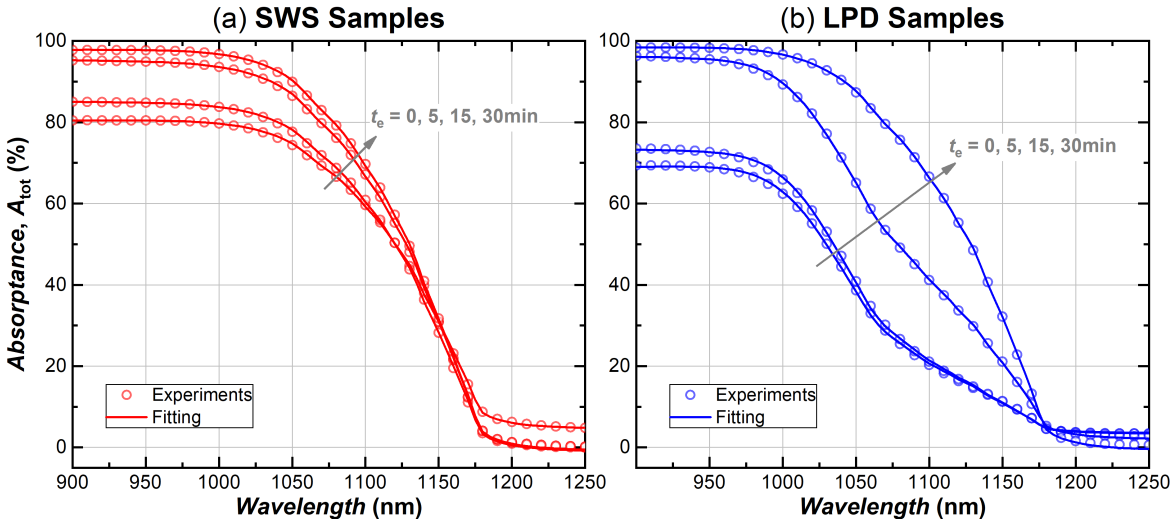

Fig. IV.10: Comparison of experimental absorptance measurements and model results for initial and nanotextured (a) SWS and (b) LPD samples.

The absolute difference between the measured absorptance and the fitting is less than 1% in the full range, i.e. below the uncertainties in the absorptance measurements. The proposed parametrization of the light pathlength enhancement factor is therefore relevant to model the absorptance of nanotextured samples.

The resulting light pathlength enhancement factor is shown in Figure IV.11. The unetched SWS sample originally has strong light-trapping properties, as expected from the analysis in introduction of this section: this property is explained by the initial texture of both rear and front surfaces, inducing a high level of scattering. As they are etched, the light-trapping properties of SWS samples slightly decline: for wavelengths above 1150 nm, Z_{mod} decreases with the etching time.

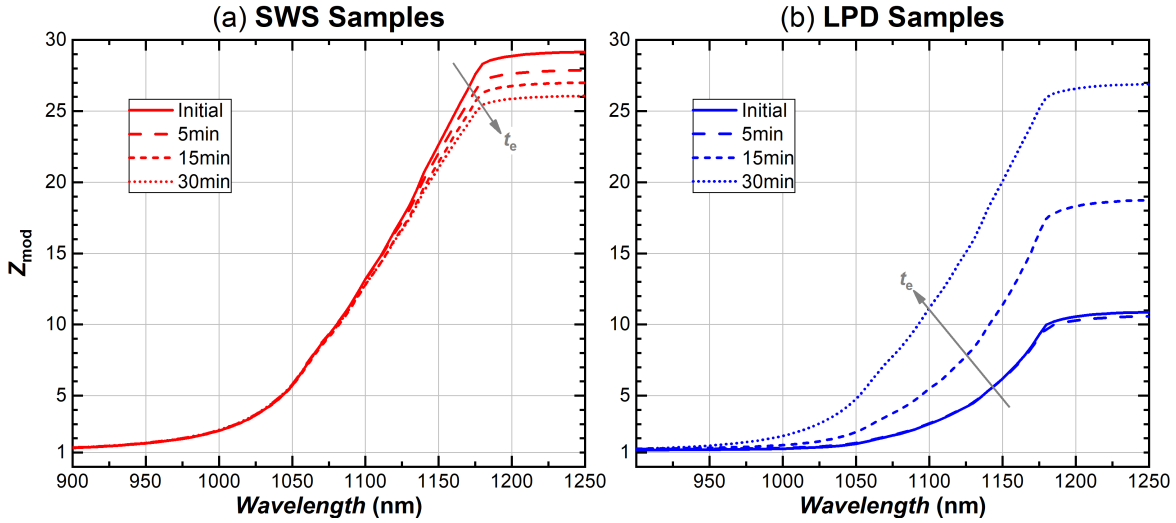

Fig. IV.11: Light pathlength enhancement factor computed for (a) SWS and (b) LPD samples.

In contrast, Z_{mod} is relatively low in the full wavelength range for the initial LPD sample, confirming its poor initial light-trapping properties, due to a low level of scattering at both interfaces. After 5 min of texturing, almost no change can be observed, however, after 15 and 30 min of etching, the light pathlength enhancement factor increases significantly up to values similar to the SWS samples (here the comparison is valid because the absorbers have similar thicknesses). It can be concluded that, after 30 min of nanotexturing, the scattering from the front (nanotextured) surface of LPD samples becomes high enough for light-trapping to be effective, even with a weakly scattering rear-surface.

In order to link the light-trapping properties to the nanotextured surface morphology, Figure IV.12 shows the evolution of Z_0, Z_∞ and Z_p with the nanostructure average width for SWS and LPD samples. As expected, the light-trapping properties of the SWS samples are only slightly affected by the presence of nanostructures on the front surface: Z_∞, and Z_p stay constant (close to 1), while Z_0 decreases but remains relatively high: from 29 initially to 25 when large structures ($\Lambda_{\mathrm{NS}} \approx 3.5\,\mu\mathrm{m}$) are formed on the front surface by plasma etching.

In contrast, the light-trapping properties of the LPD samples remain relatively constant until the nanostructures attain an average width above 100 nm. Above that, Z_0 increases and Z_p decreases significantly (as a reminder for the proposed model: the lower Z_p, the better the light trapping). Interestingly, the light-trapping properties of the LPD samples become similar to the SWS samples when the nanostructures have an average width above 750 nm.

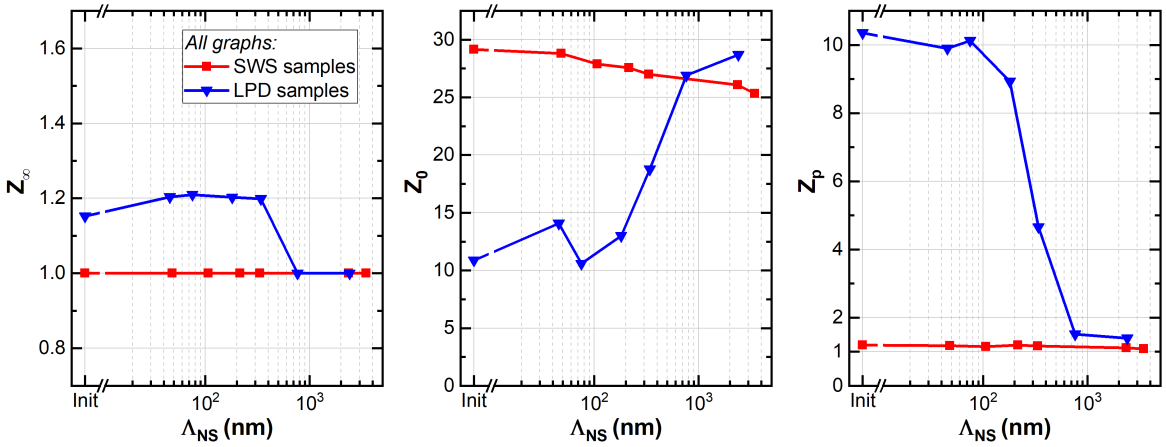

Fig. IV.12: Evolution of light path enhancement factor parameters (Z_∞, Z_0, Z_p) with nanostructure average width on SWS and LPD samples.

IV.1.2.c Comparison with different light-trapping designs

The absorptance of nanotextured c-Si samples has been appropriately modelled by parametrizing the light pathlength enhancement factor with Equation (IV.7). Significant improvements of light-trapping properties have been demonstrated using front surface plasma nanotexturing of c-Si absorbers (with initially poorly scattering surfaces). However, the performances of nanotextured surfaces have still to be compared to other structures, in particular, pyramid microstructures obtained by alkaline etching which have been shown to induce strong light-trapping [12] and represent the industrial standard for monocrystalline c-Si solar cells. For a fair comparison with absorbers of different thicknesses, it is first required to demonstrate that the triplet of parameters (Z_∞, Z_0, Z_p) is indeed independent from the absorber thickness in the case of nanotextured samples.

Clarification of sample designation. Apart from demonstrating the strong influence of nanotexturing on the light-trapping properties of c-Si absorbers, previous results have importantly recalled that absorptance (and therefore light-trapping) strongly depends on the morphology of

both the front and rear sides of the absorber. For the sake of clarity, the designation of samples will therefore be detailed in the present section, taking the form: "front surface morphology / thickness (in µm) / back surface morphology".

As an example, a double-side mirror polished sample with a thickness of 280 µm will be designated by "P/280/P" ("P" for "planar"). Nanotextured samples will for instance be labelled by "NS/280/P" ("NS" for "nanostructures"), designating a 280 µm thick absorber with a nanotextured front side and a planar rear surface. Notice that for asymmetric samples, the order of the surfaces will become meaningful when detailing absorptance measurements, which may be taken by illuminating either the front or back side of the samples. In addition, all the nanotextured samples used in this study have been obtained with the same recipe (baseline process defined in section III.1.1.c Chapter III, with an etching time of 30 min and leading to $\Lambda_{NS} \approx 750$ nm), which has been shown to induce strong light-trapping on LPD samples (see section IV.1.2.b).

Moreover, only the absorptance has been measured in this study: the fitting is therefore made using the additional assumption that the front surface reflectance, R_f, is constant over the wavelength range, according to the following equation:

$$A_{tot}(\lambda_0) = 1 - R_f + [\Delta a_0 - (1 - R_f)]\, e^{-\alpha_{Si}(\lambda_0) Z(\lambda_0) w} \tag{IV.8}$$

where R_f becomes a fitting parameter and Δa_0 represents the deviation of the absorptance measurement in the weak absorption limit, as in Equation (IV.6): this parameter is interpreted as a discrepancy in the measurements (which is not significant when characterizing the optical properties of the samples).

Independence from absorber thickness. In order to verify that the parametrization is indeed independent from the absorber thickness for nanotextured samples, tests have been performed using samples of different thicknesses: (287 ± 2) µm and (83 ± 2) µm. For each case, total absorptance has been measured on reference (unetched) samples and on samples with a nanotextured front side.

Measurements are shown in the top row of graphs in Figure IV.13(a,b) (symbols corresponding to experimental results). Regardless of the absorber thickness, the absorptance is lowest for the planar samples (P/287/P and P/83/P) since both surfaces of these samples are highly reflective and non-diffusing. In contrast, single side nanotextured samples (NS/287/P and NS/83/P) have the highest absorptance when illuminated from the front side, which is both anti-reflective and strongly diffusing. For the same samples, the absorptance is lower when illuminating the back surface than the front (due to the high reflectivity of the planar back surface) but much larger than the absorptance on corresponding planar samples – for wavelengths below 1150 nm and down to 1000 nm (for sample NS/287/P) or 900 nm (for sample NS/83/P). It can therefore be concluded that light-trapping is strongly promoted regardless of the location (front or back) of the diffusing surface.

The experimental results for the 287 µm thick samples have been **fitted** using Equations (IV.7) and (IV.8), and the results shown by the solid curves in Figure IV.13(a). The middle row of graph shows that the difference between the experiments and the fitting curves is lower than $1.3\%_{abs}$ in the whole range. The result fitting light pathlength enhancement is shown in the bottom graph Figure IV.13(a), while the corresponding parameters (Z_∞, Z_0, Z_p) are gathered in Table IV.1. The light pathlength enhancement curves in the bottom graph of Figure IV.13(a) show the large improvement of light-trapping obtained by nanotexturing. Actually, comparing the parameters in Table IV.1, it can be seen that from the triplet (Z_∞, Z_0, Z_p) only Z_0 is affected (going up to 22 for the nanotextured sample with front illumination, compared to 1.2 for the planar c-Si slab), while Z_∞ and Z_p are essentially unaffected.

Interestingly, the light pathlength enhancement factor is very similar for front or back illumination, demonstrating that the light-trapping performances obtained through nanotexturing do not significantly depend on the side where light first penetrates the absorber. In fact, the small difference depending on the illuminated side comes from the importance of the first path through

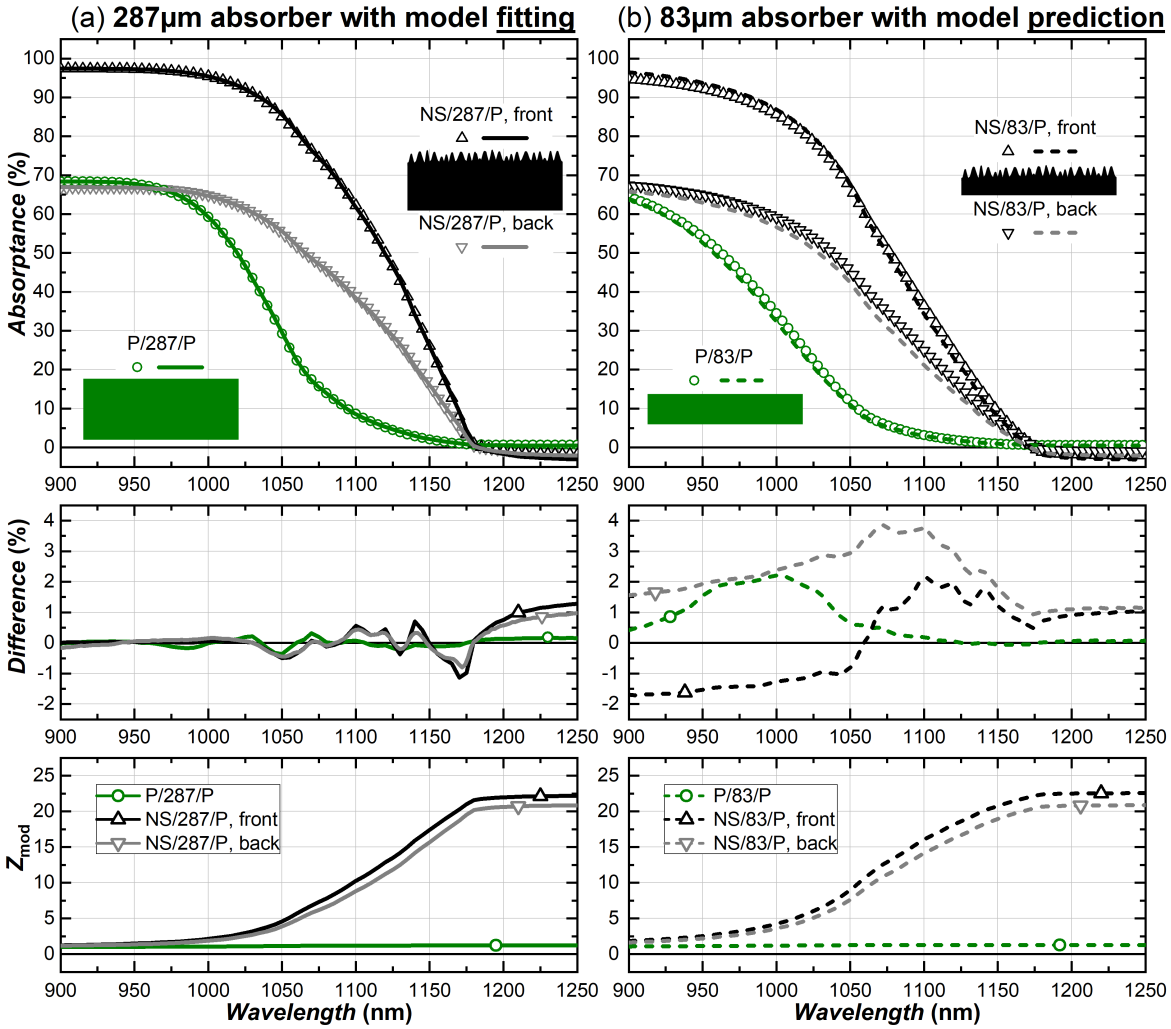

Fig. IV.13: (a) Measured absorptance spectra for 287 µm thick samples: (top) symbols show experimental data and solid curves correspond to fittings; (middle) difference between fit and measurement; (bottom) corresponding light pathlength enhancement factor. (b) Results for 83 µm thick samples with identical surface morphologies: dashed curves here show predicted absorptance and light path enhancement factor (using light trapping parameters obtained for the 287 µm thick samples).

the absorber [10]. Sample NS/287/P has a strongly diffusing front side and a planar (specularly reflecting) back side: if the front side is illuminated, light is diffused immediately upon entry; in contrast, if the back side is illuminated (at normal incidence), all light will first travel in a normal direction through the absorber, and only be scattered when reflected at the front side.

The method is now reversed for 83 µm: rather than fitting the absorptance measurements on these samples, we instead use the values of R_f and (Z_∞, Z_0, Z_p) obtained for the 287 µm samples to **predict** the absorptance on the thinner samples. To this aim, Equations (IV.7) and (IV.8) are used: Figure IV.13(b) compares the **predicted** spectra (dashed curves) with the experimental results. It can be observed that the model computation satisfactorily predicts the absorptance of the 83 µm samples regardless of the sample surface morphologies or illuminated side. The difference between the experiment and the model – shown in the middle row of graph in Figure IV.13(b) – is lower than $2\%_{abs}$ for samples P/83/P and NS/83/P with front illumination. For sample NS/83/P illuminated from the back side, a larger deviation (up to $4\%_{abs}$) is observed, but seems to mostly correspond to a constant offset, therefore rather attributed to a deviation of R_f.

Given these results, it can be concluded that the proposed parametrization of the light pathlength enhancement factor is indeed independent from the absorber thickness in the case of single side nanotextured samples. Two important implications should therefore be highlighted: (i) other

Tab. IV.1: Light-trapping parameters obtained from fitting of absorptance curves shown in Figure IV.13(a). NA: not applicable.

Sample	Illuminated side	Fitting results			
		R_f (%)	Z_∞	Z_0	Z_p
P/287/P	NA	32	1.0	1.2	1.7
NS/287/P	Front	4.8	1.0	22.2	1.5
	Back	*33.1*	*1.0*	*20.9*	*1.9*

light-trapping schemes can be compared to nanotextured samples by direct comparison of the triplet (Z_∞, Z_0, Z_p) regardless of the thickness of the absorbers; (ii) once the triplet (Z_∞, Z_0, Z_p) has been determined for a given structure (e.g. including a plasma nanotextured surface), the absorptance of samples having identical surface morphologies but different thicknesses can easily be predicted (and for instance used in a model).

Comparison with different light-trapping schemes. Lastly, light-trapping performances achievable through nanotexturing are compared to other schemes. For this analysis, five types of samples will be used, as schematized in Figure IV.14(a). The previously studied structures – i.e. double side mirror polished samples (P/287/P) and single side plasma nanotextured samples (NS/287/P) – will be compared to: double side nanotextured samples (NS/287/NS), double side alkaline textured samples with microscale pyramids (Pyr/238/Pyr) and finally double side pyramid textured samples with one plasma nanotextured side (Pyr+NS/238/Pyr). These five different light-trapping schemes involve three types of textured surfaces: SEM images of the surface morphologies are displayed in Figure IV.14(b).

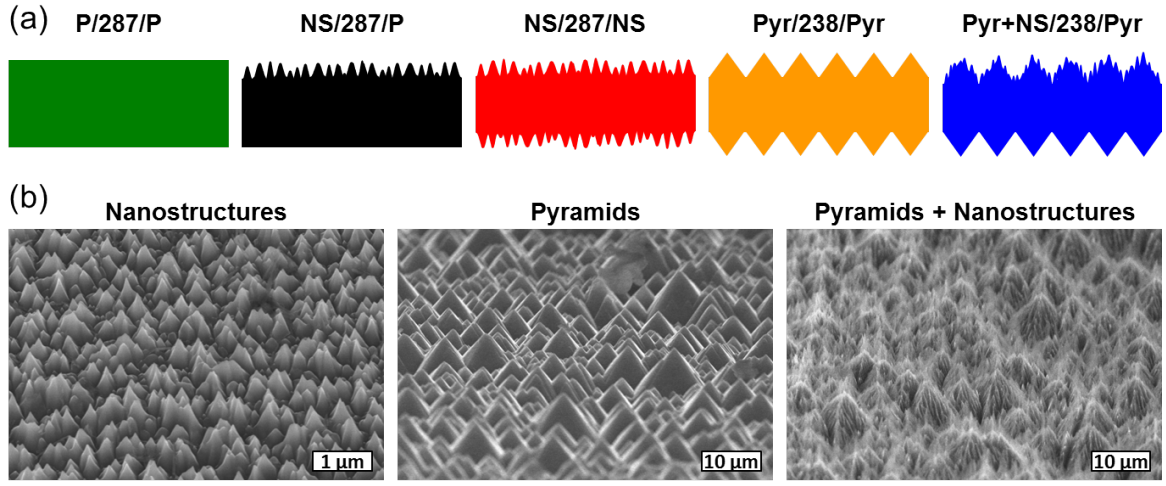

Fig. IV.14: (a) Schematics of the five types of light-trapping schemes. Colors will be used as keys in Figure IV.15. (b) SEM tilted view images of plasma nanotextured surface, pyramid microstructures obtained by alkaline etching and nanotextured pyramids.

Absorptance has been measured for all samples (with illumination from the front or the back side for asymmetric samples) and the results fitted using Equations (IV.7) and (IV.8). Results are shown in Figure IV.15(a,b): top graphs show the experimental absorptance spectra while bottom graphs show the light pathlength enhancement obtained from the fitting. The results obtained for planar and nanotextured samples are voluntarily separated from the pyramid textured samples due to the different thicknesses: a direct comparison of the absorptance or the light pathlength enhancement factor would be irrelevant, as previously highlighted. For a fair comparison of light-trapping properties between samples of different thicknesses, one has to rely on the values of the fitting parameters, R_f and the triplets (Z_∞, Z_0, Z_p), which are gathered in Table IV.2.

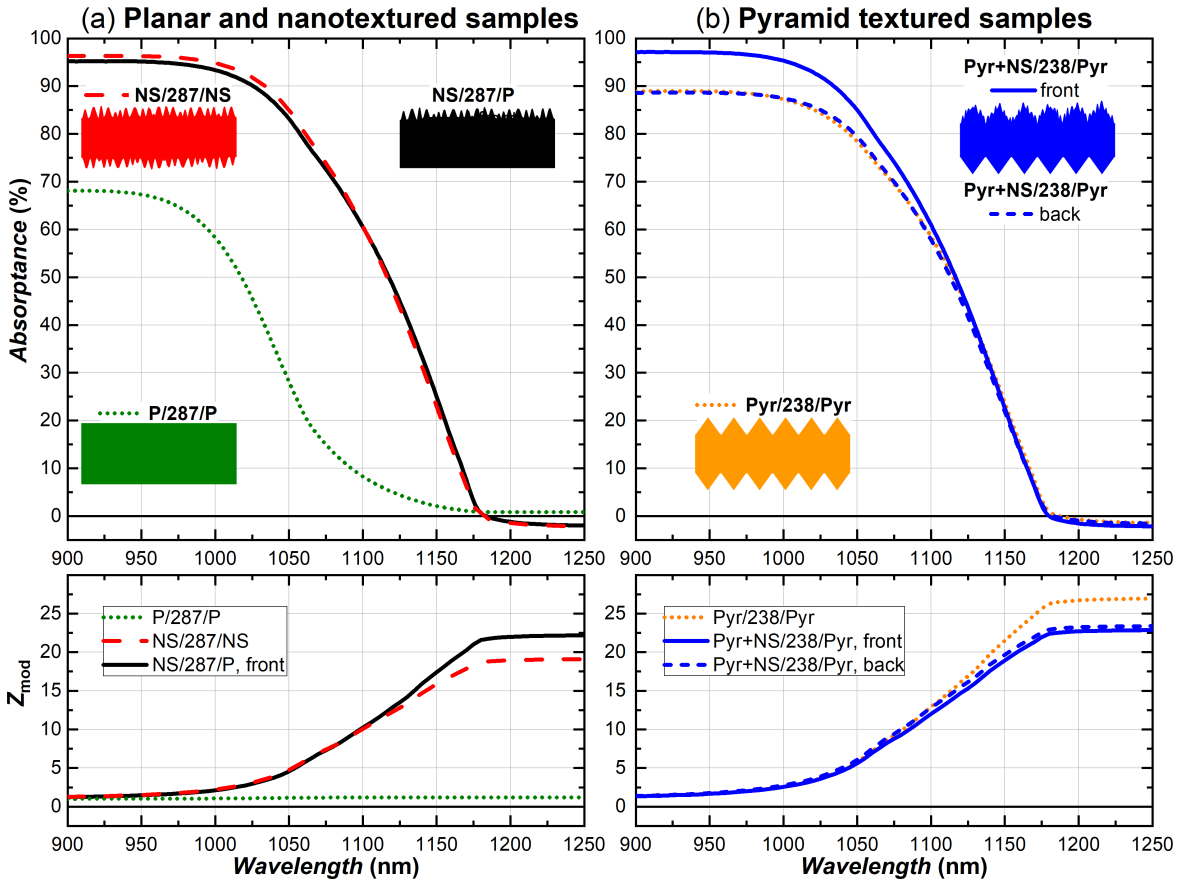

Fig. IV.15: Measured absorptance spectra (top) and corresponding light path enhancement factor (bottom) for different light-trapping schemes: (a) planar and nanotextured samples, (b) pyramid textured samples.

First, Figure IV.15(a) shows that the absorptance spectra obtained for samples NS/287/NS and NS/287/P (measured with front illumination) are similar, although a small deviation is observed for $\lambda_0 < 1050\,\text{nm}$, possibly due to a small difference of front reflectance. This observation suggests identical light-trapping properties, however, the light pathlength enhancement factor in the bottom row of graphs show that light-trapping is slightly diminished (especially in the limit of weak absorption) for the double side nanotextured sample (as a reminder, the direct comparison of Z_{mod} is here valid because the absorbers have an identical thickness). For both samples, light is scattered directly upon penetration (at the first path): for sample NS/287/P the back surface will reflect a large part of the light, while on sample NS/287/NS the back surface is also anti-reflective and a large portion of light will escape and the light pathlength enhancement will be comparatively lower.

We then consider the results for pyramid textured samples (Pyr/238/Pyr and Pyr+NS/238/Pyr) displayed in Figure IV.15(b). From the values at the shortest wavelength (see also values of R_f in Table IV.2), it is observed that the front reflectance of the pyramid textured surface lies around 11%, i.e. higher than the value obtained for nanotextured surface (around 4%). When "superimposing" nanostructures on the pyramids by plasma texturing, the reflectance of the surface decreases further to around 3%.

A very high light pathlength enhancement factor is obtained for the double side pyramid textured sample, demonstrating that these structures induce strong light-trapping, owing to the scattering properties of both surfaces. In the case of sample Pyr+NS/238/Pyr (illuminated either from the back or the front), the light pathlength enhancement factor is significantly decreased for $\lambda_0 > 1100\,\text{nm}$ compared to sample Pyr/238/Pyr. This effect is again attributed to the anti-reflective properties of the nanotextured surface: while both surfaces remain highly scattering, light within the c-Si can more easily escape on the nanotextured side.

Lastly, the fitting results in Table IV.2 conclusively demonstrate that pyramid texturing leads to superior light-trapping than single (or even double) side nanotexturing. In particular, the light pathlength enhancement factor in the limit of weak absorption (represent by the value of Z_0) is significantly higher for sample Pyr/238/Pyr ($Z_0 = 27$) than for sample NS/287/P (illuminated from the front, $Z_0 = 22$), for similar values of Z_∞ and Z_p.

Tab. IV.2: Light-trapping parameters obtained from fitting of absorptance curves measured on samples with various surface textures. In all cases, the coefficient of determination of the fitting is higher than 0.9998. NA: not applicable.

Type	Sample	Thickness (µm)	Illuminated side	Fitting results R_f (%)	Z_∞	Z_0	Z_p
Symmetric	**P/287/P**	287	NA	32	1.0	1.2	1.7
	Pyr/238/Pyr	238	NA	11.1	1.0	27.0	1.3
	NS/287/NS	287	NA	3.6	1.0	19.1	1.3
Asymmetric	**NS/287/P**	287	Front	4.8	1.0	22.2	1.5
			Back	*33.1*	*1.0*	*20.9*	*1.9*
	Pyr+NS/238/Pyr	238	Front	2.8	1.0	22.9	1.3
			Back	*11.3*	*1.0*	*23.4*	*1.1*

IV.1.3 Synthesis: light management through front side nanotexturing

As a conclusion to this investigation on optical properties, it has been shown that single side plasma nanotexturing significantly enhances absorptance in c-Si substrates, owing both to broadband anti-reflection and light-trapping in the near-IR range. These properties are notably valuable for photovoltaic applications, but should be compared to other light management schemes. In particular, for monocrystalline solar cells, the current standard corresponds to double side pyramid texturing with a front anti-reflective coating.

The comparison will be done using graphs in Figure IV.16, showing the absorption and losses of photon flux (in the AM1.5g spectrum) for different structures, at normal incidence. Graph (a) illustrates the base case of a perfectly flat 180 µm thick absorber (theoretical computation). Graph (b) corresponds to a double side pyramid textured structure with a front ARC (optical properties computed using the "wafer ray tracer" online tool from PV Lighthouse [13], with the following parameters: 180 µm absorber, double side random upright pyramids with an angle of 54.74° and a base width of 5 µm, 75 nm SiN_x front coating, no rear coating). Finally, graph (c) corresponds to a single-side nanotextured 180 µm thick c-Si slab (absorptance and front reflectance computed using the properties of sample NS/287/P: front reflectance has been used directly – and extrapolated in the near IR range using Equation (IV.5), while absorptance has been estimated using the light pathlength enhancement factor parameters from Table IV.2 and Equations (IV.6) and (IV.7)).

The planar c-Si slab case in Figure IV.16(a) has been discussed in introduction of this section, and leads to large losses due to both high front reflection and poor light-trapping. In comparison, the implementation of either pyramid texturing (with an additional ARC) or nanotexturing greatly reduces optical losses. Interestingly, both structures lead to very similar values of photogenerated current densities. Indeed, in both cases the losses in photogenerated current density due to front reflectance are cut by a factor of 10 (from 16.2 $mA \cdot cm^{-2}$ in the planar case to around 1.5 $mA \cdot cm^{-2}$). Concomitantly, losses due to weak absorption in the near-IR range are reduced by 22%$_{rel}$ (from 4.5 $mA \cdot cm^{-2}$ to around 3.5 $mA \cdot cm^{-2}$). Overall, the expected photogenerated current density is increased by more than 60%$_{rel}$ (from 25.6 $mA \cdot cm^{-2}$ to around 41.5 $mA \cdot cm^{-2}$). In any case, it should be recalled that the absolute values of photogenerated current densities obtained here are still not representative of the photogeneration in a solar cell, as several contributions are not included. For instance in the case of a monofacial PERC cell, the shading from front contacts or the contribution of the rear contacts to light-trapping are not taken into account.

Nevertheless, it can be concluded that front surface nanotexturing leads to improved light management in c-Si absorbers. In the case of monocrystalline solar cells, no added value (in terms of optical properties) can, however, be demonstrated compared to pyramid texturing - except the absence of a need for an ARC. In contrast, for multicrystalline solar cells, reduction of front reflectance through chemical texturing has been shown less effective (see Chapter I section I.2.3.b), and plasma nanotexturing represents a promising alternative.

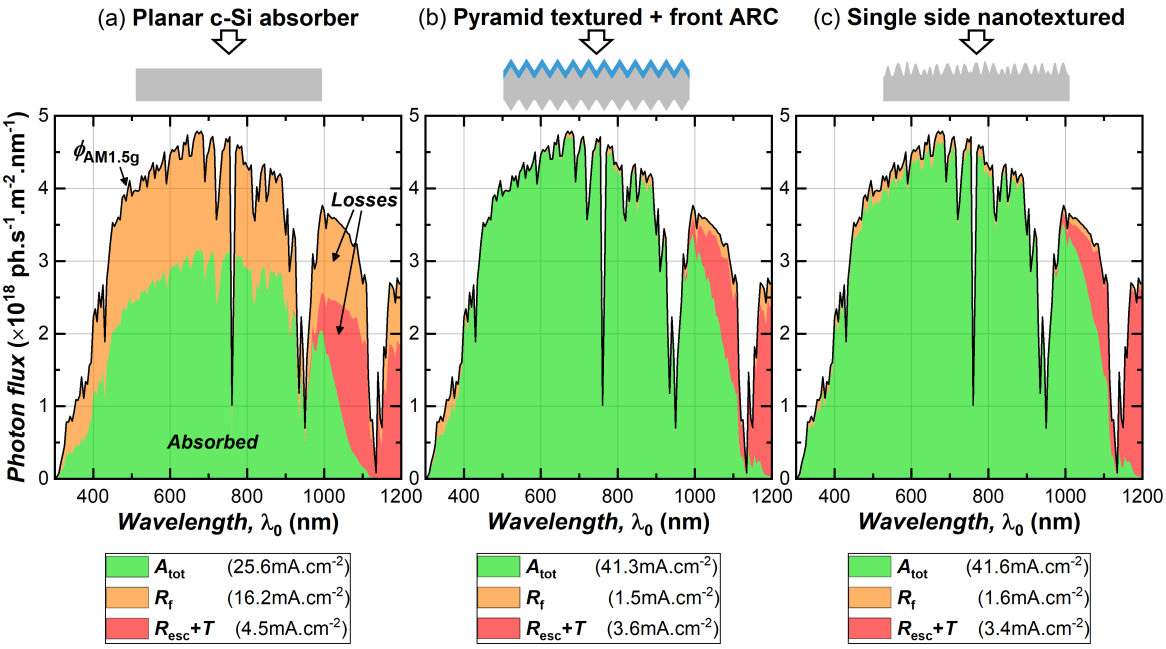

Fig. IV.16: Normal incidence absorption and losses in solar photon flux (AM1.5g spectrum) for 180 µm thick absorbers with: (a) planar surfaces (theoretical computation), (b) double side pyramid texturing and front ARC (simulated by ray tracing), (c) front nanotextured surface (computation based on experimental results for sample NS/287/P).

Finally, the enhanced optical properties obtained through plasma nanotexturing often come at the expense of reduced electrical properties [14, 15]: front surface nanotexturing indeed leads to enhanced surface area, while defects may additionally be created by plasma etching, both effects leading to enhanced recombination of electrical carriers close to the surface. The passivation of plasma nanotextured c-Si surfaces has therefore been investigated, and these results will be presented in the next section.

IV.2 Passivation of Nanotextured Silicon Surfaces

Outstanding optical properties, both in terms of anti-reflection and light-trapping, have been achieved using SF_6/O_2 plasma nanotexturing of c-Si surfaces. Nevertheless, the implementation of plasma texturing in the fabrication of high efficiency c-Si solar cells still proves challenging: indeed, both ultraviolet light and ion bombardment from the plasma can induce defects in the c-Si, such as vacancies or impurities [16, 17], which may act as strong recombination centers without the application of a proper passivation technique. In addition, the high aspect ratio of the nanostructures prevents the conformal deposition of passivation layers, such as plasma enhanced chemical vapor deposited amorphous silicon nitride (SiN_x) and leads to high values of surface area enhancement factor (ratio between the real surface area and the projected surface area). This area enhancement intrinsically increases recombination events at the surface [18]. While the conformality issue can be solved using Atomic Layer Deposition (ALD) of amorphous alumina (Al_2O_3) for instance, the surface area enhancement cannot be avoided.

The passivation of SF_6/O_2 plasma nanotextured surfaces has therefore been investigated using ALD-Al_2O_3 deposition [19]. In the following, a short description of the experimental methods will first be given. Then, the dynamic evolution of passivation quality will be investigated for different process conditions. The contribution of ion bombardment on the degradation of the surface passivation will be distinguished from the effect of enhanced surface area. Finally, attempts at mitigating the effect of ion bombardment will be made by the application of a dry "damage removal etching".

IV.2.1 ALD Al_2O_3 Surface Passivation

IV.2.1.a Short description of the ALD process

ALD is a thin-film deposition technique based on the sequential pulsing of precursors in the reactor, as schematically described in Figure IV.17. Many reviews on the ALD process are available in the literature (see for instance [20]) and only the key features of ALD deposition will here be recalled. Starting from an initial (functionalized) surface, a first precursor is introduced in the reactor (pulse 1): owing to self-limiting chemical reactions with the surface, a first molecule or atom (red circles on the schematic), will be deposited conformally and uniformly until saturation of all available sites on the surface. The reactor is then purged to remove remaining precursor molecules and by-products. A second precursor is introduced (pulse 2), and another molecule or atom is deposited (blue circles), forming a complete monolayer of the desired material. Another purge is performed and the ALD cycle can be repeated for the deposition of subsequent monolayers. The process is actually effective in a limited range of substrate temperature called the "ALD window", where the growth per cycle (and therefore the final layer thickness) can be finely controlled.

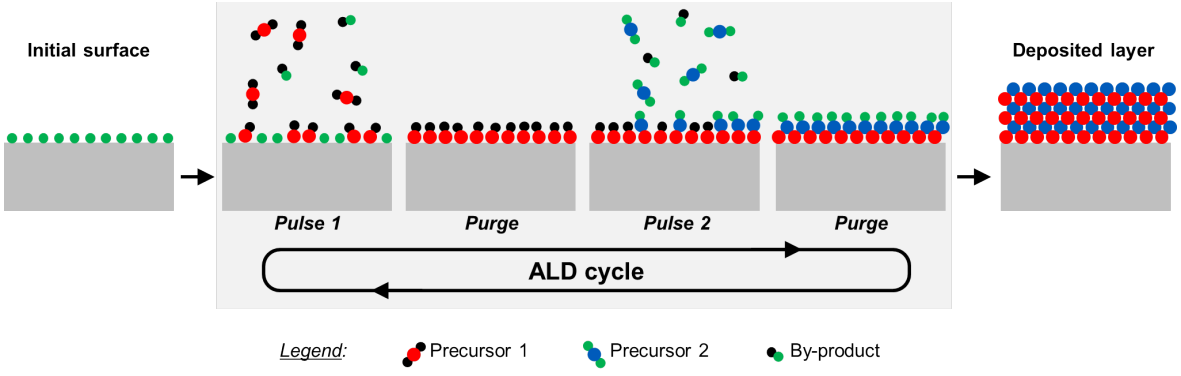

Fig. IV.17: Schematic of ALD process showing initial surface, ALD cycle and deposited layer (here after 3 cycles). Layer stoichiometry and details of molecules (precursors and by-product) are fictitious.

In the present study, a Picosun R-200 reactor has been used for the simultaneous front and rear deposition of Al_2O_3 layers on c-Si samples. Trimethylaluminium (TMA) and H_2O have been used as precursors, and the process was performed at a temperature of 150 °C. A total of 60 cycles was performed for each coating, corresponding to the deposition of an Al_2O_3 layer approximately 7 nm thick. After deposition, the sample is annealed at 350 °C during 30 min. This process recipe (ALD deposition and annealing) has been developed by Fabien Lebreton, as part of his PhD thesis carried out in the LPICM on the passivation of c-Si surfaces [21].

IV.2.1.b Samples and texturing process

In this study, 180 µm thick n-type doped c-Si CZ (100) samples, with a resistivity of 4.5 Ω·cm and an area of 5×5 cm^2, have been used (cut from DWS wafers, see also description of the initial surface morphology in Chapter III). As described in Figure IV.18, a saw damage removal (SDR) process has first been applied (outsourced), and a total of 26 samples has been processed, plus ten reference (i.e. untextured) samples.

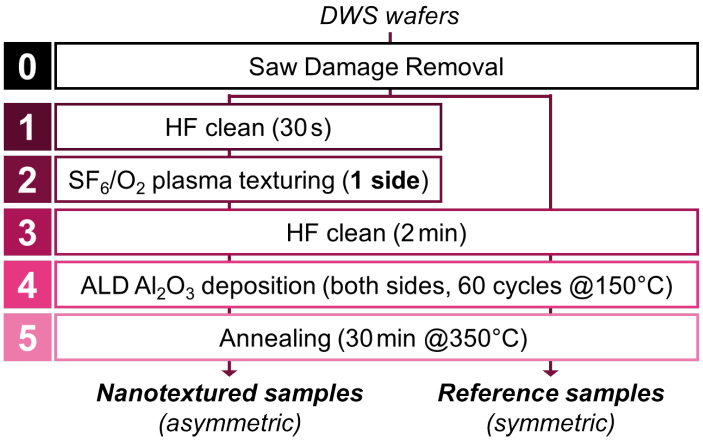

Fig. IV.18: (a) Performed process flow for passivation of plasma nanotextured c-Si surfaces. Step 0 has been outsourced; all other steps are performed at the LPICM. In study of section IV.2.2, conditions are varied only for step 2 (nanotexturing), see Table IV.3.

Afterwards, the samples were HF cleaned (step 1), then textured on one side using an SF_6/O_2 plasma (step 2). The range of parameters for the nanotexturing process is given in Table IV.3: the gas composition and pressure correspond to the baseline recipe defined in Chapter III, and only the coupled power and excitation voltage were varied. Also notice that three samples were processed simultaneously although only one of them was then passivated: to avoid large non-uniformities across the samples (due to the ion flux non-uniformity identified in Chapter II), the samples were placed as close as possible to the center of the electrode. Reference samples for passivation did not go through steps 1 and 2. Notice that no chemical "Damage Removal Etching" (DRE) step has been performed after texturing.

After texturing, another HF dip is performed (step 3), before the samples are loaded in the ALD reactor. The Al_2O_3 layer is deposited (step 4) and annealed (step 5) using the recipe described in the previous section, and the samples are subsequently illuminated at 1 mW·cm^{-2} overnight to ensure trap saturation in Al_2O_3 [22].

After the full process, the effective minority carrier lifetime, τ_{eff}, of the passivated samples has been measured by photo-conductance decay using a WCT-120 from Sinton instruments. For reference (symmetric) samples, this measurement can be used to compute the effective surface recombination velocity with:

$$S_{eff}^{ref} = \left(\frac{1}{\tau_{eff}} - \frac{1}{\tau_{bulk}}\right)\frac{w}{2} \tag{IV.9}$$

where τ_{bulk} is the bulk lifetime (computation from [23]) and w the sample thickness.

Tab. IV.3: c-Si nanotexturing process parameters used for study presented section IV.2.2. Varied parameters are indicated by an asterisk. Schematic (to scale) of substrate electrode with sample locations during process.

	Input parameters		Sample locations
Gases	**Pressure,** P_r	30 mTorr	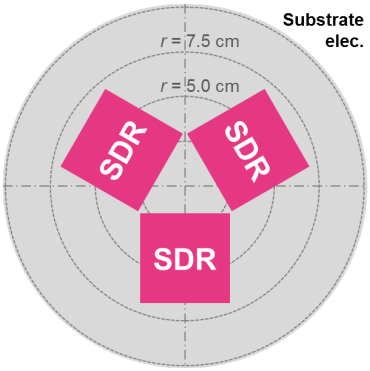
	Nature	SF_6+ O_2	
	Total input flux	105 sccm	
	SF_6content	57 %	
Voltage	**Signal basis freq.,** f_0	13.56 MHz	
	***# of harmonics,** n	1 (single-freq.), 3 (TVWs)	
	***Power,** P_w	35 or 55 W	
Substrates	**Sample type**	DWS (SDR)	
	Sample size	5×5 cm^2	
	Temperature, T_S	25 °C	
	***Etching time,** t_e	2, 5, 10, 20 min	

IV.2.2 Passivation of Plasma Nanotextured Silicon Surfaces

IV.2.2.a Baseline passivation results

Before studying the effect of plasma nanotexturing, the quality of surface passivation is evaluated on unetched samples which serve as (symmetric) reference samples. A total of ten unetched samples has been passivated: all samples (except the first two) have been obtained in different ALD runs. Results are displayed in Figure IV.19: the minority carrier lifetime for each reference sample is shown in graph (a) at an injection level of 10^{15} cm^{-3}, while the full minority carrier lifetime curves are shown in graph (b) for the best, median and worst samples amongst the ten references.

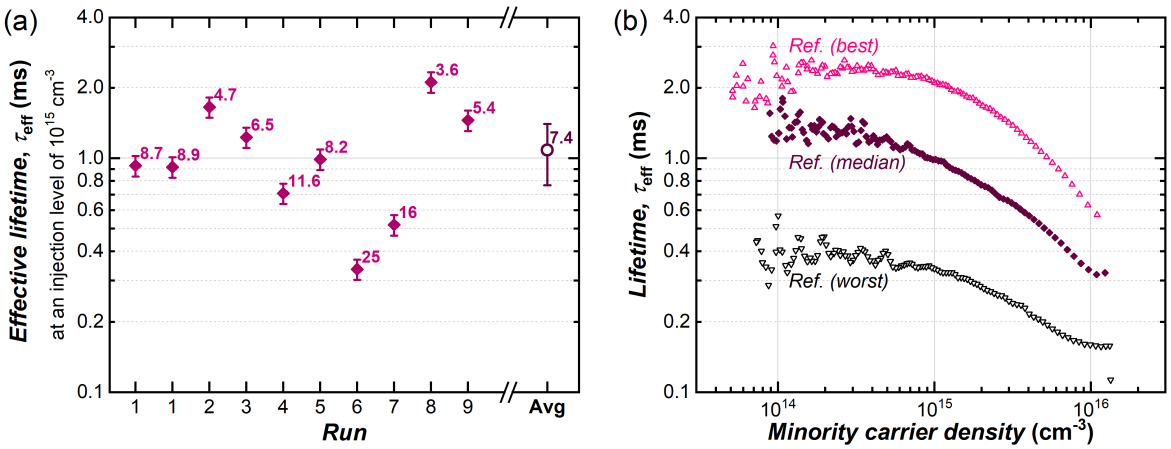

Fig. IV.19: (a) Effective minority carrier lifetime (at an injection level of 10^{15} cm^{-3}) of unetched samples. Labels indicate the effective SRV value (cm·s^{-1}). (b) Effective minority carrier lifetime for best, median and worst reference samples. Notice logarithmic vertical scale on both graphs.

A relatively large distribution of τ_{eff} is observed in Figure IV.19(a): values ranging from 0.35 to 2 ms have been obtained, i.e. almost an order of magnitude of difference. Interestingly, the only two reference samples processed in the same run (#1) have very similar passivation properties (τ_{eff} close to 900 µs). Since the samples undergo several process steps (in particular an HF dip and an annealing), the main cause(s) for the dispersion in the results cannot be identified. However, the distribution seems to be centered on a value close to 1 ms (corresponding to an average effective SRV of 7.4 cm·s^{-1}), which will be considered as the baseline. However, due to the relatively large distribution of values for reference samples, the measured SRV values obtained on single nanotextured samples will be considered to be reliable within only ±20%$_{rel}$.

For nanotextured samples, the texturing process will only affect the passivation quality on the processed (front) side of the sample: in order to isolate this contribution, the "front SRV", S_f, will be computed [24]:

$$S_f = \left(\frac{1}{\tau_{eff}} - \frac{1}{\tau_{bulk}}\right) w - S_{eff}^{ref} \tag{IV.10}$$

where S_{eff}^{ref} is the contribution of the back surface, which will here be taken as the effective SRV corresponding to the average effective lifetime for the symmetric reference samples, i.e. $7.4\,cm \cdot s^{-1}$. In the following sections, all the results and analyses will be made based solely on the front SRV.

IV.2.2.b Dynamics of passivation degradation

In a first set of tests, the dynamical evolution of the sample properties is investigated for four different process conditions, detailed in Table IV.4. For these experiments, the ion bombardment energy at the substrate electrode was varied at an identical coupled power ($P_w = 35\,W$) by applying different voltage waveforms (TVW mode). Since the ion energy could not be increased to values higher than around 115 eV, a supplementary case was added using single-frequency excitation (RF mode) at $P_w = 55\,W$ (corresponding to the baseline recipe introduced in Chapter III section III.1.1.c). Notice that the ion flux energy distribution was not measured in these cases so that the analysis will only rely on the calculated ion bombardment energy E_{calc}, which represents a reasonable proxy for the maximal ion bombardment energy on the substrate electrode, as shown in Chapter II.

Tab. IV.4: Voltage excitation parameters used for c-Si nanotexturing step in study presented section IV.2.2.b. Constant parameters: $P_r = 30\,mTorr$, 105 sccm SF_6/O_2 incoming flux (57% SF_6). NA: not applicable.

Coupled power, P_w (W)	**Basis freq.,** f_0 (MHz)	**Number of harmonics,** n	**Phase-shift** Θ/π (rad/π)	**Self-bias voltage,** V_{DC} (V)	**Ion energy,** E_{calc} (eV)
35	13.56	3 (TVW)	0.5	-81 ± 2	115 ± 8
35	13.56	3 (TVW)	0.75	-65 ± 2	105 ± 8
35	13.56	3 (TVW)	1	-35 ± 1	85 ± 4
55	13.56	1 (single-freq.)	NA	-145 ± 3	190 ± 12

Results are shown in Figure IV.20: graph (a) first shows the evolution of the effective reflectance as a function of the process time. Notice that the displayed values correspond to the reflectance measured after the deposition of the Al_2O_3 layer which has a (small) additional anti-reflective effect, due to a refractive index intermediate (around 1.6 at $\lambda_0 = 633\,nm$, [21, 25]) between the indices of air and c-Si. The effective reflectance of the samples continuously decreases with a rate depending on the process conditions, in particular only a slight – barely significant – decrease is observed for samples textured at $E_{calc} = 85\,eV$. From the samples etched in TVW excitation mode, it appears that the higher the ion bombardment, the faster the decrease (which is consistent with the results of Chapter III): after 10 min, the reflectance of these samples is about 35%, 7% and 3% for $E_{calc} = 85$, 105 and 115 eV, respectively. The samples textured in RF mode (at 55 W, $E_{calc} = 190\,eV$ and $R_{eff} = 11\%$ after 10 min) do not fall within this trend. Based on the results of Chapter III, the hidden parameter is possibly the total ion flux (not measured here).

The evolution of the front SRV during the process is shown in Figure IV.20(b). At $E_{calc} = 85\,eV$, the evolution is not significant until a process time of 10 min where S_f increases to around $20\,cm \cdot s^{-1}$ compared to the initial value of $7.4\,cm \cdot s^{-1}$. The situation is quite different when the ion bombardment energy is higher than 100 eV: the surface recombination velocity jumps after 2 min of texturing, and the magnitude of the rise is directly correlated to the ion bombardment energy. At 105 eV, S_f increases to $40\,cm \cdot s^{-1}$, while at 190 eV, S_f rises by almost two orders of magnitude. This effect is attributed to the rapid formation of a plasma-induced damaged layer and the simultaneous increase in surface area (both contributions will be further discussed in the next section). The

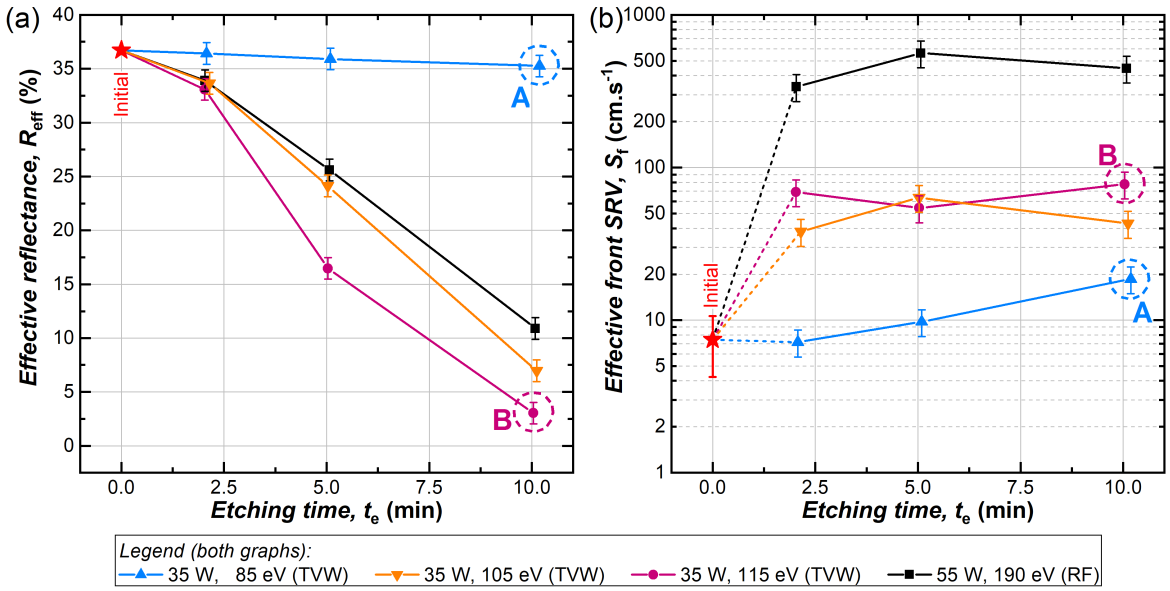

Fig. IV.20: Evolution of (a) effective reflectance and (b) front SRV with etching time for different nanotexturing process conditions. Circled data points in the graphs correspond to SEM images shown in Figure IV.21.

dependence on the ion bombardment energy suggests that the depth of the damaged layer and/or the density of electrically active defects mostly depend on the energy of incoming ions. As the process continues, S_f remains fairly stable relative to the observed initial jump, showing that at an ion bombardment energy higher than 100 eV a large density of electrically active defects are created in less than 2 min. Afterwards, the damaged layer properties (e.g. depth or density of electrically active defects) are either constant or do not sufficiently evolve to affect the surface passivation quality.

Regarding the samples processed at E_{calc} = 85 eV, the very small reduction of R_{eff} and the slow increase in S_f suggests that the texturing is not operating similarly as in the other three cases. This is confirmed by comparing SEM images of samples A (10 min, 85 eV) and B (10 min, 115 eV), in Figure IV.21: while nanocones are indeed observed on sample B, the surface of sample A seems relatively smooth with only the presence of isolated "nanoholes" (indicated by white arrows in the SEM images) that appear similar to the ones observed in section III.3.3.b Chapter III.

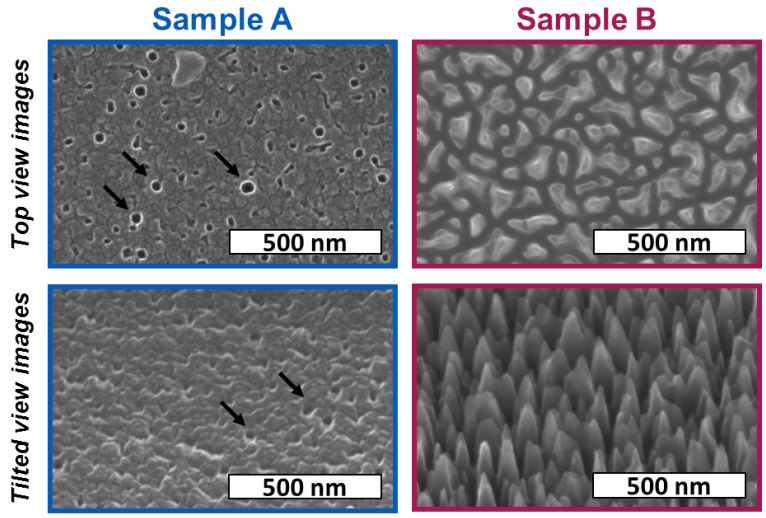

Fig. IV.21: SEM images of samples A and B (circled points in Figure IV.20), textured for 10 min at P_w = 35 W, with E_{calc} = 85 and 115 eV, respectively. See other process conditions in Tables IV.3 and IV.4.

IV.2.2.c Disentangling the effects of plasma induced defects and surface area enhancement

The energy of ions bombarding the surface has been shown to strongly influence the final passivation quality of nanotextured samples. However, the increasing surface area will simultaneously affect the front SRV value. In order to discriminate between both contributions, additional tests have been performed at different ion bombardment energies, and the surface area enhancement due to the texturing will be estimated for all samples.

To this aim, corona-voltage measurements (using a Semilab PV-2000A tool) have been performed on the passivated samples. This method allows the measurement of the surface potential (more precisely the contact voltage difference between the surface and the Kelvin-probe) while incrementally depositing electric charges using a corona discharge. The dielectric capacitance of the Al_2O_3 layer can be computed from the slope in the corona-voltage measurement [26, 27]. Thus, assuming the Al_2O_3 layer electrical properties and thickness are constant on the surface and between the samples, the dielectric layer capacitance only depends on the "real" area of the surface. The surface area enhancement factor, Σ_{NS}, is finally estimated by the ratio of the slopes obtained on corona-voltage curves measured for unetched and textured samples. By definition, $\Sigma_{NS} = 1$ for reference samples, and for nanotextured samples, measurement uncertainties for Σ_{NS} are estimated at $\pm 10\%_{rel}$.

Figure IV.22 shows the evolution of the local front SRV, S_f/Σ_{NS}, values as a function of E_{calc} for the 21 available passivated samples (with an etching time comprised between 2 and 20 min). Despite the relatively large uncertainties, the SRV is observed to drastically increase with increasing ion bombardment energy, while the etching time has no obvious effect. This observation is consistent with the dynamical study from section IV.2.2.b: the damaged layer is formed within less than 2 min, after what the passivation quality is not significantly evolving. A relatively robust trend is actually obtained, represented by the dashed fitting line corresponding to an exponential law: above 85 eV, increasing the ion bombardment energy by 40 eV corresponds to a three-fold upsurge in local SRV. It can therefore be concluded that increasing the ion bombardment energy directly leads to higher local densities of electrically active defects, acting as recombination centers.

Ion bombardment energies below 85 eV have not been probed with the tested conditions: however, it appears that at 85 eV, it is possible to obtain local SRV values close to the reference samples, even after 10 or 20 min of process. This observation suggests that, at 85 eV, the electrically active defects created by plasma texturing have a very low density, and are only moderately degrading surface passivation.

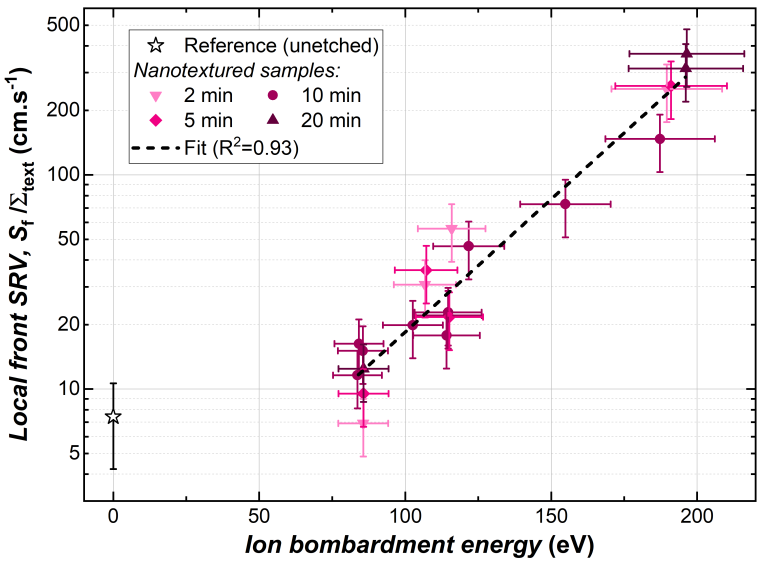

Fig. IV.22: Evolution of local front surface recombination velocity with ion bombardment energy for 21 samples textured during 2, 5, 10 or 20 min.

While the computation of a local SRV helps one to understand the phenomena at play, the surface area enhancement is unavoidable when reducing reflectance through texturing (but Σ_{NS} should be kept as low as possible in order to achieve low effective SRV values). Therefore, a synthesis of the sample properties is proposed in Figure IV.23 showing the effective SRV as a function of the effective reflectance for all available samples. In this graph, labels indicate the surface area enhancement factor, Σ_{NS}, for all nanotextured samples. It should be recalled that the final goal is to simultaneously obtain a low SRV and a low effective reflectance.

Figure IV.23 first shows that effective reflectance values below 5% have been obtained for samples with surface area enhancement factors ranging roughly from 2.3 to 4.2. Consequently, strong anti-reflective behavior can be obtained through plasma nanotexturing while keeping the surface area enhancement relatively low (and therefore mitigating its contribution to the degradation of the passivation quality).

The "apparent" best trade-off obtained during this study seems to correspond to sample C (indicated by the black arrow in Figure IV.23) with the following characteristics: $R_{eff} = (4.5 \pm 1.0)\,\%$ and $S_f = (38 \pm 7)\,cm \cdot s^{-1}$. The reflectance spectrum and lifetime measurement corresponding to this sample are shown in Figure IV.24(a) and (b) respectively, together with the measurements obtained for reference samples. This result is very promising as the local SRV of this sample is around $12\,cm \cdot s^{-1}$, i.e. close to the reference value of $7.4\,cm \cdot s^{-1}$. If confirmed, this result would suggest that the nanotexturing is not limiting the passivation quality, however, additional tests would be needed for definitive validation (due especially to the large uncertainties).

Finally, it should be highlighted that sample C has been obtained by a 10 min process at $P_w = 35\,W$, using TVW excitation (basis frequency $f_0 = 13.56\,MHz$, number of harmonics $n = 3$, phase-shift $\Theta/\pi = 1.5$ – corresponding to "sawtooth-down" waveforms). The ion bombardment energy during the process was estimated at $E_{calc} = (84 \pm 8)\,eV$. Interestingly, sample A (obtained in the dynamical study in section IV.2.2.b) was processed in similar conditions (same power and ion bombardment energy) except with "sawtooth-up" waveforms ($\Theta/\pi = 1.5$), but the nanotexturing process was shown to be much less effective. Given the results of Chapter III, a difference in ion flux may explain the very different final properties between samples A and C: the influence (if any) of this parameter on the final passivation quality should also be investigated more carefully.

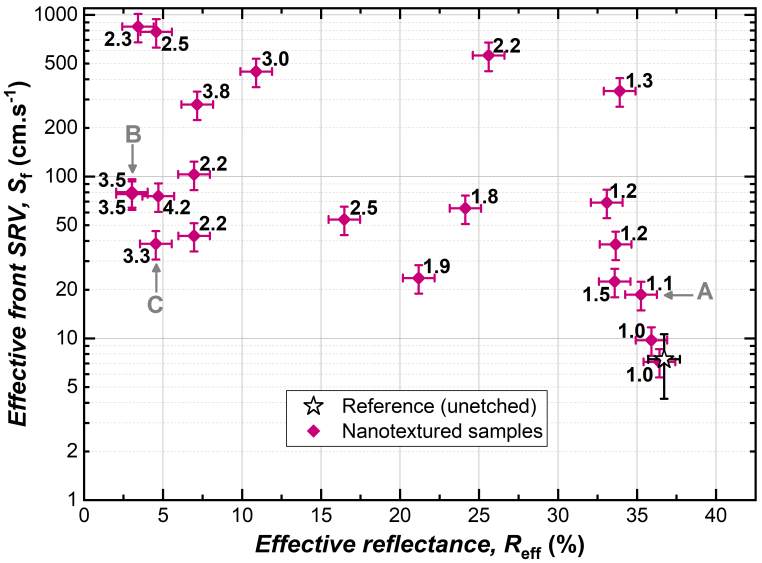

Fig. IV.23: Effective front surface recombination velocity versus effective reflectance for all passivated samples. Labels indicate surface area enhancement factors for nanotextured samples.

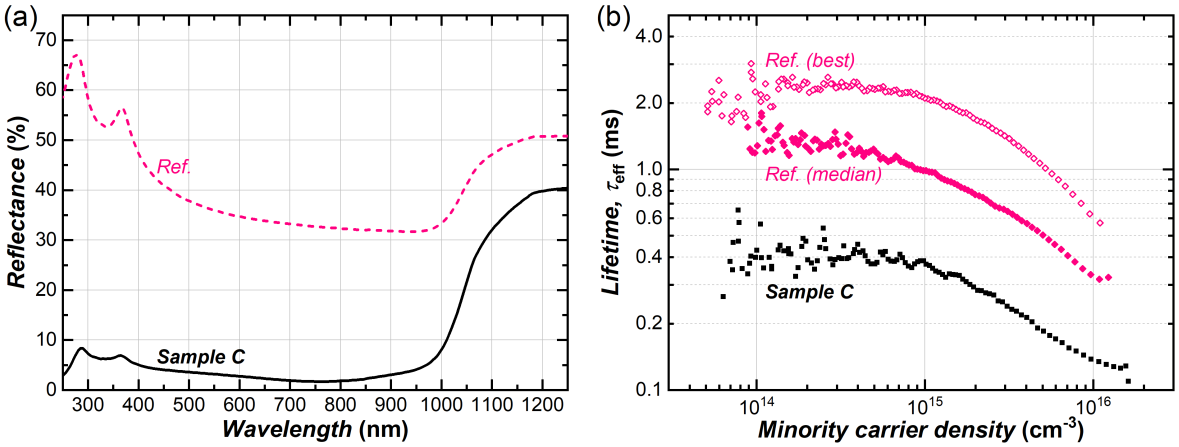

Fig. IV.24: (a) Reflectance spectrum and (b) lifetime measurement for nanotextured sample C (identified as "best trade-off" in section IV.2.2.c), compared to reference samples. Reminder: $5 \times 5\,\mathrm{cm}^2$ CZ (100) n-type substrates, resistivity of $4.5\,\Omega\cdot\mathrm{cm}$, thickness $w = 180\,\mu\mathrm{m}$.

Summary

The optical properties of SF_6/O_2 plasma nanotextured c-Si surfaces have been investigated in-depth as a function of the nanostructure morphology, and the most important findings are recalled below:

- The broadband anti-reflective properties of nanotextured c-Si surfaces (in the wavelength range [250,1000 nm]) lead to **effective reflectance values below 2%**, and are **explained both by the nanostructure average height H_{NS} and width Λ_{NS}** .

- A simple **1D multilayer effective medium model reliably describes the effective reflectance** (at normal incidence) of plasma nanotextured surfaces, **for Λ_{NS} below approximately 125 nm** (corresponding to $H_{NS} \approx 200$ nm – due to the positive correlation between both dimensions). Above this threshold, the 1D multilayer model becomes inaccurate. Above $H_{NS} = 200$ nm, higher aspect ratio nanostructures would lead to lower effective reflectance.

- The **appearance of light-scattering** for nanotextured surfaces has first been **characterized by angle-resolved reflectance** measurements at $\lambda_0 = 633$ nm (and near normal incidence): nanotexturing has been shown to dramatically alter the directional reflectance of initially specularly reflecting surfaces. **For large nanostructures ($\Lambda_{NS} \approx 750$ nm), reflection becomes relatively uniform in all directions** regardless of the initial surface finish.

- To further investigate the influence of nanotexturing on light-trapping performances, the absorptance (at normal incidence in the range [900,1250 nm]) of c-Si samples has been characterized. A **simple parametrization of the light pathlength enhancement factor has been successfully applied to model the absorptance spectra** of c-Si samples with different front and back surface morphologies. For single-side nanotextured samples with initially poor light scattering, **light-trapping has been shown to dramatically improve for $\Lambda_{NS} \approx 750$ nm**.

- Finally, the proposed **parametrization has been shown to be independent from the absorber thickness** for nanotextured samples, allowing comparison (and prediction) of absorptance for absorbers with identical surface morphologies but different thicknesses. Using this property, it has been shown that single side **nanotextured c-Si absorbers achieve comparable but still weaker light-trapping properties than double side pyramid textured structures** (obtained by alkaline etching).

Surface passivation of plasma nanotextured c-Si surfaces has been investigated experimentally as a function of the ion bombardment energy during the process. Samples have been passivated using ALD-Al_2O_3 and the nanotexturing process conditions have especially been varied using Tailored Voltage Waveforms to obtain different ion bombardment energies at constant plasma power. Important findings revealed by this study are summarized below:

- The passivation recipe leads to high effective lifetime on **reference (untextured) samples**, with an **effective lifetime around 1 ms** (at an injection level of 10^{15} cm^{-3}, averaged over ten samples) corresponding to an effective surface recombination velocity (SRV) around 7.4 cm $\cdot$ s^{-1}. The effective reflectance of these samples is, however, very high (36.7%).

- On nanotextured samples, both the increase of the surface area and the creation of defects due to the ion bombardment induced much higher effective SRV values (roughly between 40 and 800 cm $\cdot$ s^{-1} for samples with an effective reflectance below 5%). The contribution of surface area enhancement has been successfully isolated, and a **positive link between the ion bombardment during the process and the final SRV of the textured surface** has been demonstrated: above around 85 eV, increasing the ion bombardment energy by 40 eV leads to a threefold rise in local SRV, therefore dramatically decreasing the electronic properties.

- An apparent acceptable trade-off (although confirmation on complete devices would be required) has been identified with the following properties: an effective reflectance of 4.5% and an effective SRV around $38\,cm \cdot s^{-1}$. This sample was obtained by a 10 min process at relatively low ion bombardment energy (around 85 eV) and has a surface area enhancement factor around 3.3: as a consequence, the local SRV of this sample is close to the reference value ($12\,cm \cdot s^{-1}$ compared to $7.4\,cm \cdot s^{-1}$). Although further experiments would be required for confirmation, this result promisingly suggests that **passivation quality is not drastically limited by plasma nanotexturing if ion bombardment energy is kept below 85 eV**.

Bibliography (Chapter IV)

[1] G. A. Niklasson, C. G. Granqvist and O. Hunderi, Effective medium models for the optical properties of inhomogeneous materials, *Appl. Opt.* **1981**, 20(1), 26, doi:10.1364/AO.20.000026. 140

[2] R. Jacobsson, V Light Reflection from Films of Continuously Varying Refractive Index, in *Progress in Optics* (edited by E. Wolf), vol. 5, 247–286, Elsevier, **1966**, doi:10.1016/S0079-6638(08)70454-2. 141

[3] M. A. Green, Self-consistent optical parameters of intrinsic silicon at 300 K including temperature coefficients, *Sol. Energy Mater. Sol. Cells* **2008**, 92(11), 1305–1310, doi:10.1016/j.solmat.2008.06.009. 141

[4] J. C. Stover, Optical Scattering: Measurements and Analysis, Third Edition, Society of Photo-Optical Instrumentation Engineers, **2012**, ISBN 978-0-8194-9251-7. 145

[5] T. A. Germer and C. C. Asmail, Goniometric optical scatter instrument for out-of-plane ellipsometry measurements, *Rev. Sci. Instr.* **1999**, 70(9), 3688–3695, doi:10.1063/1.1149950. 145

[6] H. J. Patrick, L. M. Hanssen, J. Zeng and T. A. Germer, BRDF measurements of graphite used in high-temperature fixed point blackbody radiators: a multi-angle study at 405 nm and 658 nm, *Metrologia* **2012**, 49(2), S81–S92, doi:10.1088/0026-1394/49/2/S81. 145

[7] E. Yablonovitch, Statistical ray optics, *J. Opt. Soc. Am.* **1982**, 72(7), 899, doi:10.1364/JOSA.72.000899. 146

[8] M. A. Green, Lambertian light trapping in textured solar cells and light-emitting diodes: analytical solutions, *Prog. Photovolt. Res. Appl.* **2002**, 10(4), 235–241, doi:10.1002/pip.404. 146

[9] J. A. Rand and P. A. Basore, Light-trapping silicon solar cells-experimental results and analysis, in *The Conference Record of the Twenty-Second IEEE Photovoltaic Specialists Conference - 1991*, **1991** 192–197 vol.1, doi:10.1109/PVSC.1991.169207. 147

[10] K. R. McIntosh and S. C. Baker-Finch, A Parameterization of Light Trapping in Wafer-Based Solar Cells, *IEEE J. Photovolt.* **2015**, 5(6), 1563–1570, doi:10.1109/JPHOTOV.2015.2465175. 149, 153

[11] A. Fell, K. R. McIntosh and K. C. Fong, Simplified Device Simulation of Silicon Solar Cells Using a Lumped Parameter Optical Model, *IEEE J. Photovolt.* **2016**, 6(3), 611–616, doi:10.1109/JPHOTOV.2016.2528407. 149

[12] P. Campbell and M. A. Green, Light trapping properties of pyramidally textured surfaces, *J. Appl. Phys.* **1987**, 62(1), 243–249, doi:10.1063/1.339189. 151

[13] Wafer ray tracer, URL `www.pvlighthouse.com.au`. 156

[14] X. Liu, P. R. Coxon, M. Peters, B. Hoex, J. M. Cole and D. J. Fray, Black silicon: fabrication methods, properties and solar energy applications, *Energy Environ. Sci.* **2014**, 7(10), 3223–3263, doi:10.1039/C4EE01152J. 157

[15] M. Otto *et al.*, Black Silicon Photovoltaics, *Adv. Opt. Mater.* **2015**, 3(2), 147–164, doi:10.1002/adom.201400395. 157

[16] S. Samukawa, B. Jinnai, F. Oda and Y. Morimoto, Surface Reaction Enhancement by UV irradiation during Si Etching Process with Chlorine Atom Beam, *Jap. J. Appl. Phys.* **2007**, 46(3), L64–L66, doi:10.1143/JJAP.46.L64. 158

[17] G. S. Oehrlein, Dry etching damage of silicon: A review, *Mater. Sci. Eng. B* **1989**, 4(1), 441–450, doi:10.1016/0921-5107(89)90284-5. 158

[18] J. Oh, H.-C. Yuan and H. M. Branz, An 18.2%-efficient black-silicon solar cell achieved through control of carrier recombination in nanostructures, *Nature Nanotechnol.* **2012**, 7(11), 743–748, doi:10.1038/nnano.2012.166. 158

[19] G. Dingemans and W. M. M. Kessels, Status and prospects of Al2O3-based surface passivation schemes for silicon solar cells, *J. Vac. Sci. Technol. A* **2012**, 30(4), 040802, doi:10.1116/1.4728205. 158

[20] R. L. Puurunen, Surface chemistry of atomic layer deposition: A case study for the trimethylaluminum/water process, *J. Appl. Phys.* **2005**, 97(12), 121301, doi:10.1063/1.1940727. 158

[21] F. Lebreton, Silicon surface passivation properties of aluminum oxide grown by atomic layer deposition for low temperature solar cells processes, thesis, Univ. Paris Saclay, **2017**, URL `www.theses.fr/2017SACLX109`. 159, 161

[22] F. Lebreton, R. Lachaume, P. Bulkin, F. Silva, S. A. Filonovich, E. V. Johnson and P. R. i. Cabarrocas, Deleterious electrostatic interaction in silicon passivation stack between thin ALD Al2O3 and its a-SiNX:H capping layer: numerical and experimental evidences, *Energy Procedia* **2017**, 124, 91–98, doi:10.1016/j.egypro.2017.09.328. 159

[23] A. Richter, S. W. Glunz, F. Werner, J. Schmidt and A. Cuevas, Improved quantitative description of Auger recombination in crystalline silicon, *Phys. Rev. B* **2012**, 86(16), doi:10.1103/PhysRevB.86.165202. 159

[24] S.-Y. Lien, C.-H. Yang, K.-C. Wu and C.-Y. Kung, Investigation on the passivated Si/Al2O3 interface fabricated by non-vacuum spatial atomic layer deposition system, *Nanoscale Res. Lett.* **2015**, 10(1), doi:10.1186/s11671-015-0803-9. 161

[25] P. Kumar, M. K. Wiedmann, C. H. Winter and I. Avrutsky, Optical properties of Al_2O_3 thin films grown by atomic layer deposition, *Appl. Opt.* **2009**, 48(28), 5407–5412, doi:10.1364/AO.48.005407. 161

[26] M. Wilson, COCOS (corona oxide characterization of semiconductor) non-contact metrology for gate dielectrics, in *AIP Conf. Proc.*, vol. 550, AIP, Gaithersburg, Maryland (USA), **2001** 220–225, doi:10.1063/1.1354401. 163

[27] M. Wilson, Z. Hameiri, N. Nandakumar and S. Duttagupta, Application of non-contact corona-Kelvin metrology for characterization of PV dielectrics on textured surfaces, in *2014 IEEE 40th Photovoltaic Specialist Conference (PVSC)*, **2014** 0680–0685, doi:10.1109/PVSC.2014.6925012. 163

CONCLUSION AND PERSPECTIVES

SF_6/O_2 plasma etching of crystalline silicon surfaces has been investigated in a capacitively coupled reactive ion etching system, focusing on the prospect of implementation to front surface nanotexturing of c-Si solar cells. The major findings of this work are hereafter summarized together with their possible implications for future research.

Tailoring SF_6/O_2 plasma properties

Different electrical asymmetries have been shown to arise when powering an SF_6/O_2 discharge with Tailored Voltage Waveforms. The nature of the dominant effect (either Amplitude or Slope Asymmetry) has been identified in various discharge conditions using particular types of waveforms as an innovative probing tool. Consequently, the predominant electron heating mechanism has been determined, and its influence on ion bombardment at the powered electrode investigated. In discharge conditions relevant for c-Si nanotexturing, large variations in both ion flux and ion energy have been achieved using TVWs.

The discharge properties have been analyzed on the basis of external electrical parameters (e.g. self-bias voltage) and the measurement of the ion flux energy distributions at the powered electrode. Important discharge characteristics are therefore not captured by this method. A more in-depth understanding could be obtained using additional probing tools (e.g. optical emission spectroscopy to gain more information on neutral species in the discharge). Alternatively, simulation approaches could prove more helpful as they would allow a prediction of the electrical asymmetries depending on discharge parameters, and therefore accelerate the optimization of etching processes for instance. In particular, the root causes of non-uniformities in ion flux along the radius of the electrode (as well as the later identified non-uniformities in nanotexturing) could be better understood and mitigated.

Understanding plasma-surface interactions

In this work, the contribution of ion bombardment on the nanotexturing of c-Si surface during SF_6/O_2 etching has been established. A "universal trend" (in the investigated range of conditions) has been demonstrated: the "bulk etching" yield increases with the ion energy, above an threshold energy close to 13 eV. Meanwhile, nanostructures are formed and both their average width and height are controlled by the energy weighted ion fluence during the process. A strong correlation between the etch depth and the nanostructure height is demonstrated, with a (lost) material thickness equivalent to four times the nanostructure height. In addition, the nanostructure aspect ratio weakly depends on the instantaneous ion flux but remains constrained to a limited range.

These findings are of great interest for process development but imply restrictions in the range of available surface properties. Consequently, future investigations should focus on ways to escape the observed trends. In particular, the relative contribution of ions and neutral etchants to the etching yield should be evaluated. Such an analysis could first be qualitatively attempted by

varying the SF_6 content in the discharge. However, a better knowledge of the chemical nature of incoming neutrals and ions could also be required: both parameters may affect the etching yield, and concomitantly the nanostructures evolution. The initiation of the nanotexturing phenomenon also remains to be understood. It has for instance been suggested that adatom diffusion on the surface could be linked to the initial nanostructure width (here around 40 nm): variations in the substrate temperature or in the nature of inhibitor species (e.g. through addition of CH_4) could lead to variations in adatom diffusion lengths and translate into different initial nanostructure width. Finally, from a process standpoint, the c-Si material loss simultaneous to nanotexturing could actually prove useful by combining the nanotexturing step to the "saw damage removal" usually required after c-Si wafer sawing.

Improving light management

Two major effects obtained through front surface nanotexturing of c-Si substrates have been studied. A broadband anti-reflective behavior (with an effective reflectance falling below 2%) has first been shown, while an enhanced light-trapping in the near-IR range has also been demonstrated. Both properties have been linked to the nanostructure sizes and their combination shown to drastically decrease optical losses in c-Si absorbers. In the investigated nanotexturing regime, optimization of light management could be supported by an adequate optical model, but stay restricted due to the demonstrated process limitations (e.g. in terms of achievable nanostructure morphology).

The improved optical properties obtained through plasma nanotexturing come at the expanse of increased recombination of photogenerated electrical carriers at the surface, due to defects induced by ion bombardment. This effect can still be mitigated (on Al_2O_3 passivated samples) by keeping the ion bombardment energy below around 85 eV. In that respect, the chemical nature of electrically active defects remains to be identified, as well as their distribution on the surface (or in the subsurface).

In view of the previously highlighted findings, design rules can be drawn to optimize SF_6/O_2 plasma nanotexturing of c-Si surfaces for PV applications. First, regarding the surface morphology: (i) nanostructures with a height superior to 200 nm are required to decrease effective reflectance below 5% at normal incidence; (ii) on initially poorly scattering substrates, nanostructures should be larger than 750 nm to significantly improve light-trapping in the near-IR range. Second, from a process standpoint: (iii) both ion flux and ion energy have to be maximized to hasten nanostructure growth; (iv) ion energy should however be kept below 85 eV to avoid formation of electrically deleterious defects (but above the etching threshold - around 13 eV). These requirements are conflicting in the case of a single frequency CCP discharge, but the trade-off may be resolved (at least partly) using TVWs, or other types of plasma reactors (e.g. inductively coupled plasma systems).

APPENDIX A

RETARDING FIELD ENERGY ANALYZER: BASIC THEORY AND MEASUREMENT ANALYSIS

Contents

A.1 Basic Theory of Operation . . . . . **II**
A.1.1 Probe Description and Computation of the RFEA Current II
A.1.2 How is it Linked to the IEDF? III
A.2 Supplementary Definitions . . . . . **IV**
A.2.1 Average Ion Energy IV
A.2.2 Energy Weighted Ion Fluence IV
A.3 Different Ion Charges and/or Masses . . . . . **V**
A.4 Illustration with an Example . . . . . **V**
Bibliography . . . . . **VII**

As it has been underlined in Chapter I, section I.1.3.c, some confusion may arise from the available literature reporting results obtained with a Retarding Field Energy Analyzer (RFEA). In many cases, this confusion arises from the difference between the **Ion Energy Distribution Function** (**IEDF**) and the **Ion Velocity Distribution Function** (**IVDF**). This appendix therefore clarifies the theory of operation of the employed RFEA system and recalls the definition of the computed quantities. In this work, a "Semion single sensor" from Impedans has been used: a description of this system is for instance available in [1].

As a foreword (and because it may also lead to misinterpretation), some elements of vocabulary have to be detailed:

- a "flux density" here corresponds to a vector field that is integrated over a surface to obtain a "flux" (consequently, an ion flux density is expressed in $[\text{ions}\cdot\text{m}^{-2}\cdot\text{s}^{-1}]$ while a flux is expressed in $[\text{ions}\cdot\text{s}^{-1}]$);
- a "fluence" is the integral of a flux over time (dimensionless, it simply corresponds to a number of ions), and similarly a "fluence density" is the integral of a flux density over time (units $[\text{ions}\cdot\text{m}^{-2}]$).

A.1 Basic Theory of Operation

A.1.1 Probe Description and Computation of the RFEA Current

Basic probe design. The schematic of the RFEA probe is displayed in Figure A.1 the probe consists of a chassis placed in the reactor (here on the powered electrode), with an entrance hole and a series of grids facing the plasma. The RFEA chassis and grid G0 are electrically connected to the powered electrode so that they take a DC potential equal to V_{DC}: in the following, the self-bias voltage V_{DC} will be considered as the reference potential.

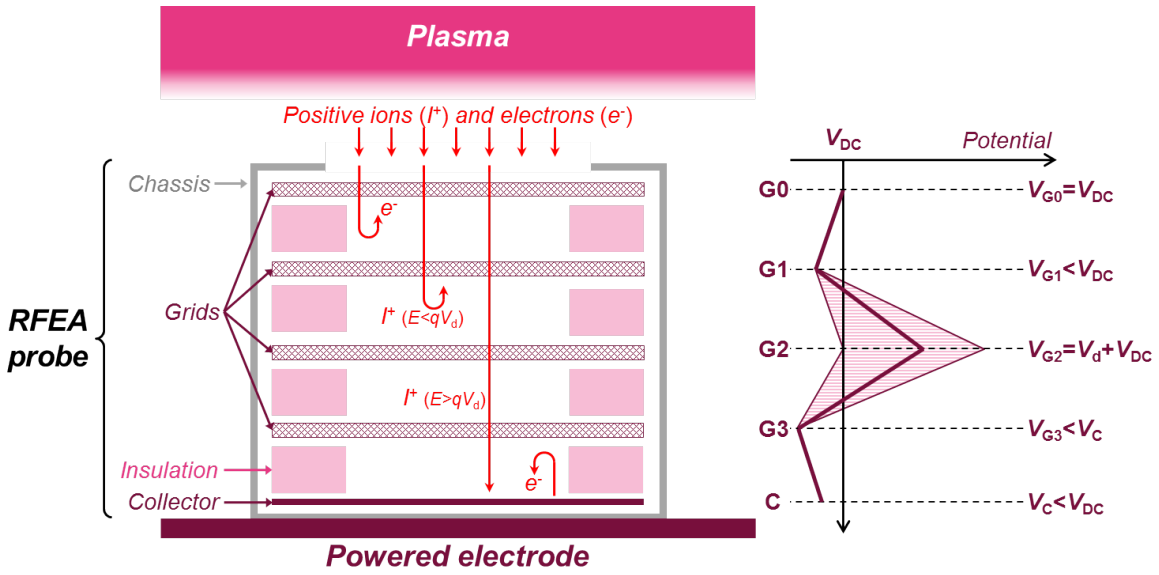

Fig. A.1: Schematic of the RFEA probe (not to scale) on the powered electrode showing the details of the grids and collection parts (electric potential illustrated in the right graph relative to V_{DC}).

During operation, both positive ions (kinetic energy E, charge q) and electrons enter the probe. In the configuration used to obtain the distribution of positive ions, Grid G1 is placed at a negative potential (relative to V_{DC}) in order to repel electrons. Then, positive ions are filtered in kinetic energy thanks to the varying potential of grid G2, V_{G2}, defining the discriminator voltage $V_d = V_{G2} - V_{DC}$: ions with a kinetic energy (at the entrance of the probe) higher than qV_d are transmitted to the collector C, while lower energy ions are repelled. V_d is increased incrementally in

a user-defined range, usually from $V_d = 0$ ($V_{G2} = V_{DC}$, there is no potential barrier, i.e. all ions are collected) to some value V_{max} (at least enough to repel all ions and acquire the full ion distribution). In addition, grid G3 is inserted before the collector with a potential $V_{G3} < V_C$ to avoid injection of secondary electrons (created by ions bombarding the collector) in the plasma.

Finally, for the RFEA used in the present work, the entrance aperture in fact consists of several holes with a total opening area $A = 1.86 \times 10^{-5}\,m^2$, and each grid has a transmission factor of $T = 0.5$ (according to the manufacturer specifications).

Computation of the RFEA current. The density of positive ions in the volume facing the RFEA (and just above it) is n_{ions}, defined as a function of the **Ion Velocity Distribution Function** (**IVDF**):

$$n_{ions} = \int_0^{v_{max}} f_v(v)\mathrm{d}v \tag{A.1}$$

where v is the ion velocity and v_{max} the maximal velocity in the **IVDF**. Notice that the present analysis only considers the velocity component perpendicular to the powered electrode, and that for convenience the distribution is NOT normalized: $f_v(v)$ is expressed in $[\text{ions}\cdot\text{s}\cdot\text{m}^{-4}]$. In addition, all quantities are assumed constant across the opening area of the RFEA.

The total ion flux density (expressed in $[\text{ions}\cdot\text{m}^{-2}\cdot\text{s}{-}1]$) passing through the entrance surface of the RFEA probe is therefore:

$$\phi_{tot} = \int_0^{v_{max}} v f_v(v)\mathrm{d}v \tag{A.2}$$

If $V_d = 0$, the potential barrier imposed by Grid G2 is null, i.e. all ions can travel to the collector (with a global transmission factor T^4 due to the non-ideal transmission of the grids). The RFEA current, IRFEA, is therefore the integral over the opening area of the surface of the ion current density $q\phi_{tot}$:

$$I_{RFEA}(V = V_{DC}) = AT^4 q\phi_{tot} \tag{A.3}$$

where q is the ion charge (all ions are considered identically charged).

If $V_d > V_{DC}$, only ions arriving with a kinetic energy higher than $E_d = qV_d$ are collected, or equivalently all ions with a velocity superior to $v_d = \sqrt{2qV_d/m}$ (assuming additionally that all ions have an identical mass m), so that:

$$I_{RFEA}(V_d) = AT^4 q \int_{\sqrt{2qV_d/m}}^{v_{max}} v f_v(v)\mathrm{d}v \tag{A.4}$$

Applying the Leibniz integral rule to derive Equation (A.4), since f_v, v and v_{max} are independent of V_d:

$$\frac{\mathrm{d}I_{RFEA}}{\mathrm{d}V_d} = -\frac{AT^4 q^2}{m} f_v\left(\sqrt{2qV_d/m}\right) \tag{A.5}$$

As a result, the derivative of the RFEA current I_{RFEA} with the discriminator voltage is proportional to the **IVDF**.

A.1.2 How is it Linked to the IEDF?

With $f_E(E)$, the **Ion Energy Distribution Function** (**IEDF**, expressed in $[\text{ions}\cdot\text{m}^{-3}\cdot\text{eV}^{-1}]$), the following relationship applies: $f_v(v)\mathrm{d}v = f_E(E)\mathrm{d}E$ (i.e. the number of ions with a velocity in the infinitesimal range $\mathrm{d}v$ is equal to the number of ions with an energy in the corresponding range $\mathrm{d}E$). Recalling that $\mathrm{d}E = mv\mathrm{d}v$, we thus obtain $f_E(E) = f_v(v)/(mv)$: by setting $E = qV_d$ and replacing in Equation (A.5), the following equation gives the **IEDF** from the RFEA measurement:

$$f_E(E) = -\frac{1}{AT^4 q^2}\sqrt{\frac{m}{2E}}\frac{\mathrm{d}I_{RFEA}}{\mathrm{d}V_d} \tag{A.6}$$

As a result, the derivative of the RFEA current with the discriminator voltage is NOT directly proportional to the **IEDF**, $f_E(E)$. In addition, it is observed from Equations (A.5) and (A.6) that the computation of both the **IVDF** and the **IEDF** from the RFEA current depends on the ion mass: in the case of complex gas mixtures, retrieving these distributions is therefore impossible without additional assumptions on the ion masses.

As a practical alternative, one can define the "**Ion Flux density Energy Distribution Function**" (**IFEDF**), ϕE (expressed in $[\text{ions}\cdot\text{m}^{-2}\cdot\text{s}^{-1}\cdot\text{eV}^{-1}]$) with:

$$\phi_E(E) = \sqrt{\frac{2E}{m}} f_E(E) \tag{A.7}$$

A similar approach has for instance been used in [2, 3], and this quantity can be directly computed from the RFEA measurement (notice that the ion mass is not needed for the computation):

$$\phi_E(E) = -\frac{1}{AT^4q^2}\frac{\mathrm{d}I_{\text{RFEA}}}{\mathrm{d}V_{\text{d}}} \tag{A.8}$$

In addition, the integration of ϕE directly gives the total ion flux density in front of the RFEA probe (with $E_{\max} = mv_{\max}^2/2$ the maximal ion energy in the **IEDF**):

$$\phi_{\text{tot}} = \int_0^{E_{\max}} \phi_E(E)\mathrm{d}E \tag{A.9}$$

A.2 Supplementary Definitions

A.2.1 Average Ion Energy

The average energy of the ions passing through the opening area of the probe is here defined as a function of the **IFEDF** ϕE (here this value is noted $E_{\text{avg}}^{\phi_E}$) for clarity although the simpler notation E_{avg} has been adopted in the core of the present manuscript):

$$E_{\text{avg}}^{\phi_E} = \frac{\int_0^{E_{\max}} E\phi_E(E)\mathrm{d}E}{\phi_{\text{tot}}} \tag{A.10}$$

Notice that this definition does not match the average ion energy in the **IEDF**, which would correspond to an average energy of the ions "in the volume" of the sheath just in front of the electrode and would be expressed in the following manner:

$$E_{\text{avg}}^{f_E} = \frac{\int_0^{E_{\max}} E f_E(E)\mathrm{d}E}{n_{\text{ions}}} \tag{A.11}$$

In contrast with $E_{\text{avg}}^{f_E}$, the definition of E_{avg} in Equation (A.10) is more useful from a practical point of view: (i) in the cases of complex discharges because ϕE can be obtained from the RFEA measurements without any hypothesis on the masses of the incoming ions; (ii) when studying etching processes, the average energy of the ions hitting the surface is more relevant to analyze the etching phenomena.

A.2.2 Energy Weighted Ion Fluence

First, the etching can be considered as the result of a "flux of atoms" removed from the substrate surface, which is equal to the flux of incoming ions weighted by the energy dependent etching yield per ion, $Y(E)$ (expressed in $[\text{atoms}\cdot\text{ion}^{-1}]$). Therefore, the number of atoms (per unit area) removed from the surface, N_{etch}, during a process of duration t_{e} is expressed by:

$$N_{\text{etch}} = t_{\text{e}}\int_0^{E_{\max}} Y(E)\phi_E(E)\mathrm{d}E \tag{A.12}$$

Using the model from Chapter III (section III.3.2.b) for the etching yield $Y(E) = Y_0(E^{1/2} - E_{\text{th}}^{1/2})$, we obtain the etched depth, $d = N_{\text{etch}}/d_{\text{Si}}$ (with d_{Si} is the atomic density of crystalline silicon):

$$d = \frac{Y_0 t_{\text{e}}}{d_{\text{Si}}} \int_{E_{\text{th}}}^{E_{\text{max}}} (E^{1/2} - E_{\text{th}}^{1/2}) \phi_E(E) \mathrm{d}E \tag{A.13}$$

From the point of view of process development, it is therefore useful to define the energy weighted ion fluence density, Φ_E (expressed in $[\text{ions} \cdot \text{m}^{-2} \cdot \text{eV}^{1/2}]$):

$$\Phi_E = t_{\text{e}} \int_{E_{\text{th}}}^{E_{\text{max}}} (E^{1/2} - E_{\text{th}}^{1/2}) \phi_E(E) \mathrm{d}E \tag{A.14}$$

A.3 Different Ion Charges and/or Masses

In previous sections, a rather simple analysis was obtained by assuming that all ions have an identical nature (with a given constant mass and charge), as a final digression, one can consider the case of more complex discharges with positive ions having different natures. Let us therefore consider two populations (A and B) of positive ions (subscripts in the following Equations will indicate the respective contribution of ions A and B). In this case, the measured RFEA current corresponds to the addition of the contributions from both ion populations, using Equations (A.4) and (A.9):

$$I_{\text{RFEA}}(V_{\text{d}}) = AT^4 \left[q_{\text{A}} \int_{q_{\text{A}} V_{\text{d}}}^{E_{\text{max,A}}} \phi_{E,\text{A}}(E) \mathrm{d}E + q_{\text{B}} \int_{q_{\text{B}} V_{\text{d}}}^{E_{\text{max,B}}} \phi_{E,\text{B}}(E) \mathrm{d}E \right] \tag{A.15}$$

With the same derivation method as in section A.1, we obtain:

$$\frac{\mathrm{d}I_{\text{RFEA}}}{\mathrm{d}V_{\text{d}}} = -AT^4 \left[q_{\text{A}}^2 \phi_{E,\text{A}}(q_{\text{A}} V_{\text{d}}) + q_{\text{B}}^2 \phi_{E,\text{B}}(q_{\text{B}} V_{\text{d}}) \right] \tag{A.16}$$

Consequently, two cases must be discriminated:

Different masses ($m_{\text{A}} \neq m_{\text{B}}$) but identical charges ($q_{\text{A}} = q_{\text{B}} = q$) . in this case, the total **IFEDF** $\phi_{E,\text{A+B}}$ is simply the sum of the contributions from ions A and B (respectively $\phi_{E,\text{A}}$ and $\phi_{E,\text{B}}$), and can be computed from the RFEA measurement:

$$\phi_E(E, \text{A+B}) = -\frac{1}{AT^4 q^2} \frac{\mathrm{d}I_{\text{RFEA}}}{\mathrm{d}V_{\text{d}}} \tag{A.17}$$

In this case, all computations using the **IFEDF** are still valid: in particular the average ion energy, computed with Equation (A.10), and the energy weighted ion fluence density computed from Equation (A.14). Of course, the relative contributions cannot be discriminated from this measurement alone.

Different charges ($q_{\text{A}} \neq q_{\text{B}}$) . In this case, the **IFEDF** cannot be retrieved from a single measurement without additional assumptions on the relative density of ions A and B and on their behavior in the plasma sheath.

A.4 Illustration with an Example

The RFEA probe is here placed on the powered electrode of the RIE setup and an Ar discharge is produced using a TVW excitation signal (basis frequency $f_0 = 13.56\,\text{MHz}$, $n = 3$, peaks waveforms), with a total coupled power of $P_{\text{w}} = 15\,\text{W}$ and a pressure of $P_{\text{r}} = 30\,\text{mTorr}$. With this rather simple discharge, only one species (Ar^+) of singly charged ions (charge $q = +e$) is considered, with a mass $m_{Ar^+} \approx 40\,\text{u} \approx 6.6 \times 10^{-26}\,\text{kg}$.

The RFEA current is measured with the discriminator voltage V_{d} varied between $-2\,\text{V}$ and $140\,\text{V}$ (by steps of approximately $1\,\text{V}$) during four successive sweeps. Raw measurements are displayed

in Figure A.2: the sampling interval is not perfectly constant, and some scattering of the data is observed. The raw I-V data is therefore smoothed before further post-processing (dashed black curve in Figure A.2) using a Savitzky-Golay algorithm [4].

The I-V curve is monotonically decreasing between 0 and 95 V, and is flat afterwards, indicating that the incoming ions have a large distribution in energy (with a maximum around 95 V). Notice that the current does not fall to zero: the I-V curve is shifted vertically by a small offset of approximately 27 nA.

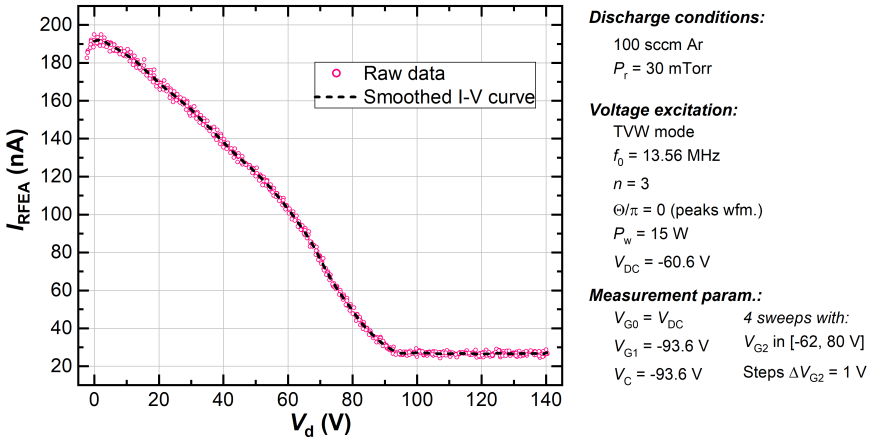

Fig. A.2: RFEA current as a function of the discriminator voltage, plasma and measurement conditions are displayed on the right.

Using the definitions from the previous sections, the **Ion Velocity Distribution Function** (**IVDF**), **Ion Energy Distribution Function** (**IEDF**), and **Ion Flux density Energy Distribution Function** (**IFEDF**) are computed and displayed in Figure A.3.

The **IVDF** is first shown in Figure A.3(a) on a velocity scale: as it had been inferred from the I-V curve, a large distribution of ion velocity exists in front of the RFEA probe. Notice that the negative values in the distribution function are due to measurement artefacts in the I-V curve: for low ion velocity (below $2.5\times10^3\,\mathrm{m\cdot s^{-1}}$) this effect comes from a small increase in RFEA current for $V_\mathrm{d}<2\,\mathrm{V}$ (see Figure A.2) that is attributed to a measurement artefact; at high ion velocity (around $22\times10^3\,\mathrm{m\cdot s^{-1}}$) the **IVDF** also takes small negative values due to the RFEA current not being completely flat above the maximal ion energy. The **IVDF** is shown again in Figure A.3(b) on an energy scale, mostly to highlight once again that the **IFEDF** (shown in Figure A.3(c) and commented in the following) is indeed proportional to the **IVDF**.

Figure A.3(c) simultaneously shows the **IEDF** and **IFEDF** (on an energy scale). The distributions are very similar for high ion energy (above 70 eV in particular), but significantly diverge for low energies: between 5 and 45 eV, the **IFEDF** is slowly increasing, while the **IEDF** is globally decreasing (although some local peaks are seen on both curves). As for the **IVDF** curve, the **IEDF** and **IFEDF** take negative values (at both ends of the distributions) due to measurement artefacts in the I-V curve.

Finally, the total ion flux density is $\phi_\mathrm{tot}=(8.7\pm0.6)\times10^{17}\,\mathrm{ions\cdot m^{-2}\cdot s^{-1}}$ and corresponds to an ion current density of $J_\mathrm{tot}=q\phi_\mathrm{tot}=(0.14\pm0.01)\,\mathrm{A\cdot m^{-2}}$. In addition the average ion energies obtained by Equations (A.10) and (A.11) are significantly different: the average energy in the **IEDF** is $E_\mathrm{avg}^{f_E}=(44\pm2)\,\mathrm{eV}$, while the average energy in the **IFEDF** is $E_\mathrm{avg}^{\phi_E}=(54\pm2)\,\mathrm{eV}$ (these values are also indicated in Figure A.3(c) for comparison).

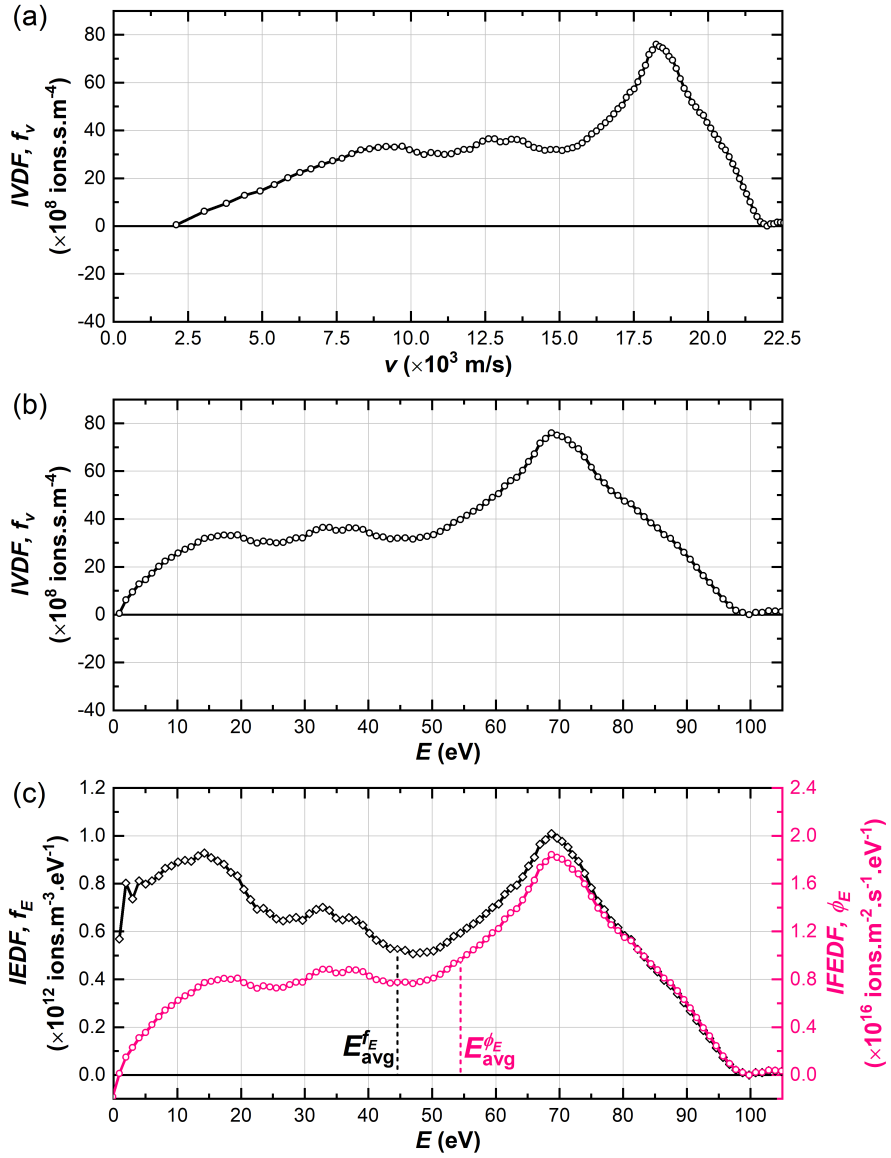

Fig. A.3: IVDF plot against (a) a velocity scale and (b) an energy scale. (c) Comparison of the **IEDF** and **IFEDF** on an energy scale.

Bibliography (Appendix A)

[1] D. Gahan, B. Dolinaj and M. B. Hopkins, Retarding field analyzer for ion energy distribution measurements at a radio-frequency biased electrode, *Rev. Sci. Instr.* **2008**, 79(3), 033502, doi:10.1063/1.2890100. II

[2] J. Schulze, E. Schüngel and U. Czarnetzki, The electrical asymmetry effect in capacitively coupled radio frequency discharges – measurements of dc self bias, ion energy and ion flux, *J. Phys. D Appl. Phys.* **2009**, 42(9), 092005, doi:10.1088/0022-3727/42/9/092005. IV

[3] E. Schüngel, Z. Donkó and J. Schulze, A Simple Model for Ion Flux-Energy Distribution Functions in Capacitively Coupled Radio-Frequency Plasmas Driven by Arbitrary Voltage Waveforms, *Plasma Process Polym* **2017**, 14(4-5), doi:10.1002/ppap.201600117. IV

[4] A. Savitzky and M. J. E. Golay, Smoothing and Differentiation of Data by Simplified Least Squares Procedures., *Analyt. Chem.* **1964**, 36(8), 1627–1639, doi:10.1021/ac60214a047. VI

APPENDIX B

STATE OF THE ART BLACK SILICON SOLAR CELLS

Contents

B.1 Scope of this synthesis . . . . . **X**
B.2 Synthesis of literature . . . . . **XII**
B.2.1 Current Record Efficiency Cells XII
B.2.2 Black Silicon Solar Cells XIII
B.3 Short analysis . . . . . **XVII**
B.3.1 Comparison of Historical Record Efficiencies XVII
B.3.2 Comparison of Cell Architectures and b-Si Methods XVIII
B.3.3 Focus on Large-scale mc-Si AlBSF cells XX
Bibliography . . . . . **XXV**

Multiple competing nanotexturing techniques are being explored at both laboratory and industrial scale for silicon solar cells. From a technological point of view, a fair evaluation of the techniques requires a comparison of achievable cell results, and one can begin by a synthesis of achievements reported in scientific literature.

B.1 Scope of this synthesis

As detailed in Chapter I of the present document, some constraints have been set to reduce the scope of this literature synthesis. Most of "black silicon solar cell" results found in scientific are here gathered, with the following restrictions:

- Reported cells present a front nanotextured silicon surface obtained through one of the nanotexturing technique classified as "black silicon methods" in Chapter I (see also list recalled below). Studies that make use of subsequent steps modifying the initial structure morphology (e.g. chemical etching after RIE) are included. Studies on cell rear surface texturing – used for light-trapping – are however discarded. Hereafter, solar cells with the previously described properties are named "black silicon solar cells".

- Reported cells have thick absorbers, i.e. above 100 µm. Indeed, below this threshold silicon solar cells are usually referred to as "thin" or "ultra-thin". In these cases, light-trapping (for near-IR wavelengths) becomes important and comparisons more difficult.

- Cells have been characterized under standard one-sun illumination ($100\,\mathrm{mW\cdot cm^{-2}}$, AM1.5g spectrum), in some cases with independent confirmation by a certified test center.

- Finally, all cell architectures are considered. However, some studies (either journal papers or conference proceedings) have also been discarded from this review due to significant deficiencies in the account of the manufacturing process and cell characteristics.

A synthesis of the results reported in literature will be given in the form of a table detailing useful information on the manufacturing process used and on the cell results (including illuminated area, open-circuit voltage V_{oc}, short-circuit current density J_{sc}, fill factor FF and efficiency η. The "black silicon techniques" that are considered are the following (details available in Chapter I):

- **MACE** Metal-Assisted Chemical Etching (also often named MCCE for Metal Catalyzed Chemical Etching), in which case the nature of the metal catalyst will be given (e.g. Ag, Cu, Au or mixtures), if available.

- **RIE** Reactive Ion Etching, in which case the etching gas mixture and type of plasma reactor will be given if available (e.g. CCP and ICP respectively for capacitively and inductively coupled plasma reactors).

- **PIII** Plasma Immersion Ion Implantation, here performed using an SF_6/O_2 discharge in all cases.

- **ADE** Atmospheric Dry Etching, performed with F_2 gas.

- **CVE** Chemical Vapor Etching.

- **fs LASER** femtosecond laser texturing, here performed in an SF_6 atmosphere in all cases.

- **Lithography** (e.g. colloidal lithography, laser induced lithography) with subsequent etching (here by RIE in all cases).

Cells are classified by type of absorber (multi- or monocrystalline silicon, respectively abbreviated mc-Si and mono-Si), and some specifics of the manufacturing process will be given if available in the original publication. Moreover, the results for black silicon solar cells are to be compared to overall record efficiency cells that have historically been reported by the NREL [1]. The "architectures" of the solar cells are in particular stated, with the following abbreviations:

- **AlBSF** Aluminium Back Surface Field cell,
- **PERC** Passivated Emitter and Rear Contacts,
- **PERL** Passivated Emitter and Rear Locally diffused,
- **TOPcon** Tunnel Oxide Passivated contact,
- **IBC** Interdigitated Back Contacts,
- **SHJ** Silicon Hetero-Junction,
- **BCB-SHJ** Back Contacts Back Silicon Hetero-Junction.

Simplified schematics of the different solar cells architectures are given in Figure B.1 (notice that some variations in the exact architectures can exist depending on the studies).

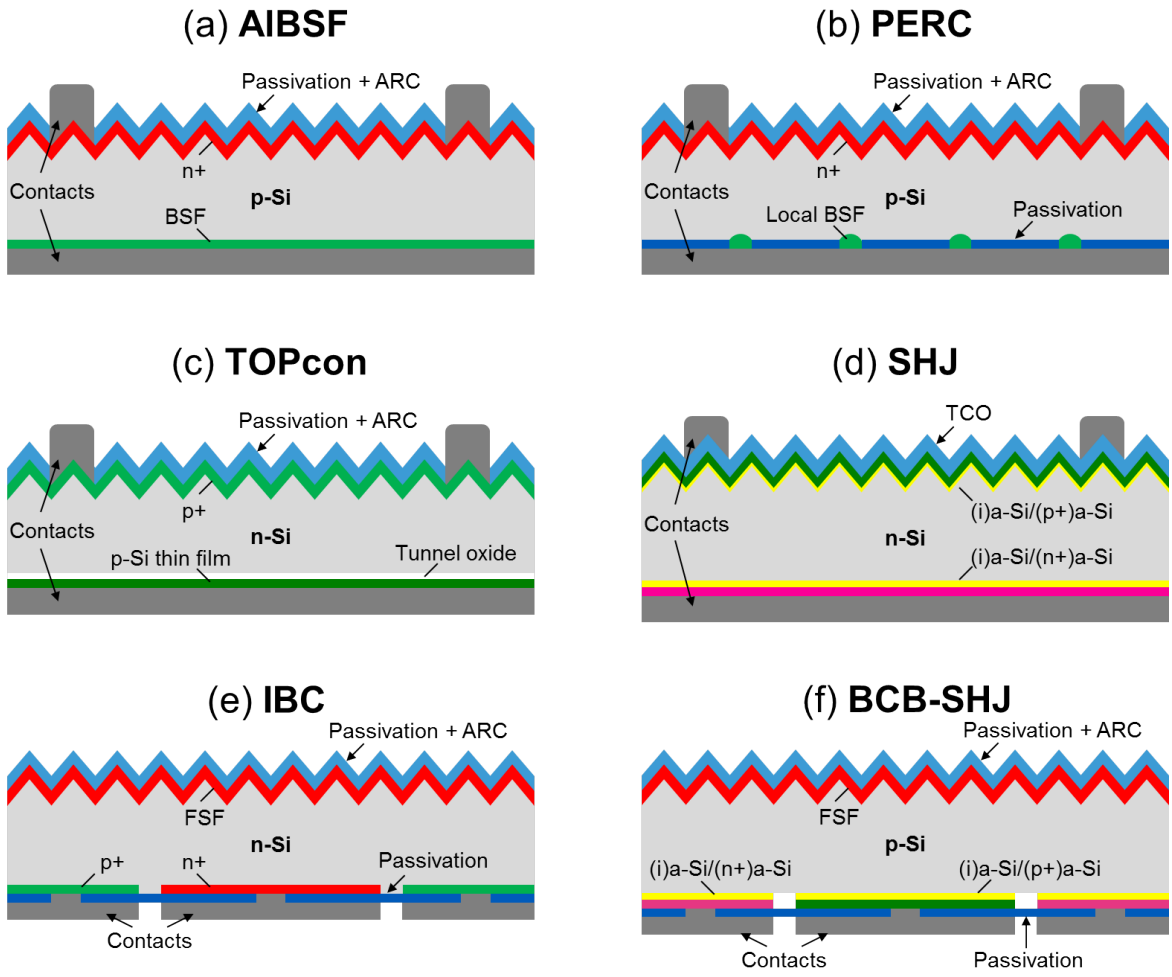

Fig. B.1: Simplified schematics of different silicon solar cells architectures.

Surface passivation of nanostructured silicon being historically a challenging issue, the type of front passivation layer will also be recalled for all cells, along with the deposition technique. Passivation layers used for black silicon solar cells are (sometimes as double-layers and with the additional role of ARC):

- **SiN_x (or a-SiN_x:H)** silicon nitride, obtained by Plasma Enhanced Chemical Vapor Deposition (PECVD),
- **Al_2O_3** aluminium oxide, by Atomic Layer Deposition (ALD),
- **SiO_2 (or a-SiO_x:H)** silicon oxide, usually grown by Thermal Oxidation (TO), unless otherwise stated,
- **a-Si (or a-Si:H)** amorphous silicon.

Finally, two more abbreviations will be used to denote specifics of black silicon solar cells:

- **DRE** Damage Removal Etching, designates an etching step (usually chemical) applied after initial nanotexturing to remove the damaged layer it may have produced, and to smoothen the nanostructures. In the present synthesis, the use of a DRE step is only reported in case it has been applied after a "dry process", i.e. RIE, PIII or fs LASER treatment. Chemical etching steps are also sometimes used after chemical texturing (e.g. after MACE) to smoothen the nanostructures, in which case it will not be accounted, but considered part of the texturing process.
- **DWS** Diamond Wire Sawn. This sawing technique is nowadays progressively replacing "slurry wire sawing", and induces challenges for the texturing of mc-Si wafers. A lot of efforts are therefore produced to efficiently texture DWS wafers, and their use (if stated in the original publication) will therefore be shown in the synthesis tables.

B.2 Synthesis of literature

B.2.1 Current Record Efficiency Cells

Before listing results of "black silicon solar cells", it is useful to have a look at current overall records, synthesized in Table B.1, for single junction silicon-based solar cells.

Tab. B.1: Reported global record efficiency solar cells.

Ref.	Year	Type	b-Si meth.	DRE	Front b-Si?	Area (cm^2)	V_{oc} (mV)	J_{sc} (mA/cm^2)	FF (%)	η (%)
[2]	17	mono-Si	n-IBC-SHJ	Kaneka Corp.	No	79	738	42.65	84.9	26.7
[3]	18	mono-Si	p-IBC	ISFH	No	4	726.6	42.62	84.28	26.1
[4]	17	mc-Si	n-TOPcon	FhG-ISE [4]	Yes	4	674.2	41.08	80.5	22.3

Monocrystalline silicon. The best confirmed efficiency, 26.7%, has been obtained in 2017 by the Kaneka Corporation (Japan) for a heterojunction solar cell with interdigitated back contacts [2]. Regarding homojunction cells, the record is held by the "Institut für Solarenergieforschung in Hameln" (ISFH) in Germany which recently reported a 26.1% cell (also with back contacts) [3]. In both cases, the front surface is pyramid textured (with alkaline etching) and coated by an ARC.

Multicrystalline silicon. In particular due to increased recombination in the bulk, efficiencies achievable for mc-Si absorbers are lower than for mono-Si: the current record (homojunction) cell lies at 22.3%, obtained in 2017 by the Fraunhofer "Institut für Solarenergie" (FhG-ISE, Germany, [4]). In contrast with the mono-Si record cells, this cell presents front contacts (with a "TOPcon architecture"). Another important difference (in the frame of this summary) comes from the front nanotexturing (by RIE) used in the manufacturing of this cell. This achievement was made possible mostly due to the high bulk material quality and surface passivation approach. However, this result demonstrates that RIE nanotexturing of the front surface is indeed an effective light management approach for high-efficiency cells.

B.2.2 Black Silicon Solar Cells

The following Tables (B.2 to B.6) give a synthesis of black silicon solar cell results found in literature regarding respectively n-type mono-Si, n-type mc-Si, p-type mono-Si and p-type mc-Si absorbers. A total of 107 studies are gathered, published as early as 1997: the first result was obtained by the team of Fukui *et al.* for a mc-Si AlBSF solar cell with a front RIE nanotextured surface, for a 17.1% efficiency. With the same nanotexturing technique (and cell architecture), the first mono-Si cell has only been reported in 2006 by Yoo *et al.* with an efficiency of 11.7%.

Globally, it is observed from the tables that most of the work (93 out of 107 reported cells) has been dedicated to the AlBSF architecture, and only 6 results have been reported for n-type absorbers, but several other architectures have been tested as well, including back contact cells and silicon heterojunctions. Regarding the type of absorber, 44 studies report cells with mono-Si and 63 with mc-Si.

Looking now at the nanotexturing technique, a majority of the cells have been textured using MACE (55), the second most studied technique being RIE (30), followed by PIII (8), and only 14 studies use other techniques. Due in particular to the focus on standard AlBSF cells, most of the cells (75) include a "classic" front surface passivation with SiN_x deposited by PECVD. The preferred alternative is SiO_2 (19 cells, with or without an additional SiN_x capping), followed by the ALD-Al_2O_3 alternative (10 cells, again with or without SiN_x capping).

Further (short) analyses are carried out based on this data in the next sections.

Tab. B.2: Reported black silicon **(n-type monocrystalline)** solar cell results under one-sun illumination (best cell results are given when available). *Independently confirmed cell results. NR: Not Reported, NA: Not Applicable.

Ref.	Year	Type	b-Si meth.	DRE	Front passiv.	Area (cm^2)	V_{oc} (mV)	J_{sc} (mA/cm^2)	FF (%)	η (%)
[5]	15	n-IBC	RIE (SF_6/O_2, ICP, cryo.)	NR	Al_2O_3	9	662	40.9	81.3	**22***
[6]	15	n-IBC	RIE (SF_6/O_2)	Yes	SiO_2/SiN_x	9	635	40.5	77.0	**19.8**
[7]	13	n-PERL	RIE (SF_6/O_2, cryo.)	NR	Al_2O_3	4	628	39.3	75.8	**18.7**
[8]	14	n-SHJ	MACE (Au)	NA	a-Si (PECVD)	NR	649	34.2	77.4	**17.2**

Tab. B.3: Reported black silicon **(n-type multicrystalline)** solar cell results under one-sun illumination (best cell results are given when available). *Independently confirmed cell results.

Ref.	Year	Type	b-Si meth.	DRE	Front passiv.	Area (cm^2)	V_{oc} (mV)	J_{sc} (mA/cm^2)	FF (%)	η (%)
[4]	17	n-TOPcon	RIE (SF_6/O_2, ICP)	No	Al_2O_3/SiN_x	4	674.2	41.1	80.5	**22.3***
[9]	17	n-TOPcon	RIE (SF_6/O_2, ICP)	No	Al_2O_3/SiN_x	4	672.6	40.8	81.6	**21.9***

Tab. B.4: Reported black silicon **(p-type monocrystalline)** solar cell results under one-sun illumination (best cell results are given when available). *Independently confirmed cell results. NR: Not Reported, NA: Not Applicable. ITO: Indium Tin Oxide. LPD: Liquid Phase Deposition.

Ref.	Year	Type	b-Si method	DRE	Front passiv.	Area (cm^2)	V_{oc} (mV)	J_{sc} (mA/cm^2)	FF (%)	η (%)	Comments
[10]	15	IBC	RIE (SF_6/O_2, ICP, cryo.)	NR	Al_2O_3	9	665	42.2	78.7	**22.1***	
[11]	18	AlBSF	MACE (Ag)	NA	SiN_x	243	647	38.5	80.9	**20.19**	
[12]	14	AlBSF	MACE (Ag)	NA	SiN_x	243	646	36.5	80.5	**19**	
[13]	16	PERC	MACE (Ag)	NA	SiO_2 (evap)	225	607	40.1	77.9	**18.97**	Front ITO contact, diff. before text.
[14]	17	AlBSF	MACE (Cu)	NA	SiN_x	243	638	37.5	78.8	**18.87**	
[15]	14	AlBSF	MACE (Ag)	NA	SiN_x	243	639	37.2	79.1	**18.83**	Diff. before text.
[16]	15	AlBSF	MACE (Ag)	NA	Al_2O_3/TiO_2 (ALD)	0.92	590	39.3	79.9	**18.5**	
[17]	16	AlBSF	MACE (Ag)	NA	SiO_2/SiN_x	243	640	37.0	78.0	**18.5**	
[18]	13	AlBSF	MACE (Ag)	NA	Al_2O_3	0.92	598	41.3	75.1	**18.2**	
[19]	12	AlBSF	MACE (Ag)	NA	SiO_2	0.81	628	36.5	79.6	**18.2***	
[20]	11	Other	RIE (HBr/O_2, ICP)	Yes	ITO contact	NR	631	35.9	80	**18.1**	Atypical cell architecture
[21]	16	AlBSF	RIE (SF_6/O_2)	NR	SiN_x	6.25	624	36.3	80.1	**18.1**	Selective emitter
[22]	16	AlBSF	MACE (Ag)	NA	SiO_2/SiN_x	100	597	38.5	77.5	**17.8**	
[23]	16	AlBSF	ADE (F_2)	NA	SiN_x	243	626	34.9	81	**17.7**	
[24]	13	AlBSF	MACE (Ag)	NA	SiN_x	156	623	35.5	79.3	**17.5**	
[25]	13	AlBSF	RIE (SF_6/O_2)	NR	SiN_x	156	620	36	78.4	**17.5**	
[26]	14	AlBSF	MACE (Ag)	NA	SiO_2	243	629	35.1	78.6	**17.3**	Avg
[23]	16	AlBSF	ADE (F_2)	NA	Al_2O_3/SiN_x	25	618	35.2	78.8	**17.2**	
[27]	17	AlBSF	Colloid. litho. + RIE (CF_4/O_2, CCP)	Yes	SiN_x	1	590	37.7	74.8	**17.2**	Avg (4 cells)
[28]	11	AlBSF	MACE (Au)	NA	SiO_2	NR	615	35.6	78.2	**17.1***	
[29]	14	AlBSF	MACE (Ag)	NA	SiO_2/SiN_x	243	623	34.6	77.8	**17.1**	
[30]	14	AlBSF	MACE (Cu)	NA	SiO_2	1	616	36.6	75.4	**17***	
[31]	09	AlBSF	MACE (Au)	NA	SiO_2	1	612	34.1	80.6	**16.8***	
[32]	10	AlBSF	RIE (SF_6/O_2, CCP)	NR	SiN_x	156	617	36.8	76	**16.7**	
[33]	14	AlBSF	MACE (Au)	NA	Al_2O_3/SiN_x	4	621	33.1	80.2	**16.5**	
[34]	12	AlBSF	MACE (Ag)	NA	SiO_2 (LPD)	1	607	34.9	77.2	**16.4**	
[35]	18	AlBSF	Colloid. litho. + RIE (SF_6/O_2)	Yes	SiN_x	9	585	36	77.2	**16.3**	
[21]	16	AlBSF	RIE (SF_6/O_2)	NR	SiN_x	100	598	35.3	76.9	**16.22**	
[36]	11	AlBSF	PIII (SF_6/O_2)	Yes	SiN_x	156	619	32	78.3	**15.68**	
[37]	14	AlBSF	fs laser (SF_6)	Yes	SiN_x	1	590	36	73.6	**15.6**	
[38]	15	AlBSF	Laser-interf. litho. + RIE (CF_4)	NR	SiN_x	65	609	33.1	77.2	**15.56**	
[39]	14	AlBSF	MACE (Ag)	NA	SiN_x	1	584	35.9	74	**15.5**	
[40]	09	AlBSF	RIE (SF_6/O_2, CCP)	Yes	SiN_x	156	611	32.5	77	**15.1**	
[41]	11	AlBSF	fs laser (SF_6)	Yes	SiO_2/SiN_x	4	507	39.2	71.4	**14.2**	
[42]	10	AlBSF	fs laser (SF_6)	Yes	SiO_2/SiN_x	1	507	39.2	72	**14.12**	
[43]	14	AlBSF	RIE (SF_6/O_2, CCP)	NR		4	570	33.0	70.0	**13.11**	SF_6/O_2 CCP w/ metal masking grid
[44]	06	AlBSF	RIE (SF_6/O_2, hollow cathode)	NR	SiO_2	98	564	28.6	73	**11.7**	
[45]	14	BCB-SHJ	RIE (SF_6/O_2, ICP)	NR	Al_2O_3	1	562	35.1	57	**11.2**	
[46]	14	AlBSF	MACE (Ag)	NA	NR	NR	550	35.6	56	**10.9**	
[46]	14	AlBSF	MACE (Ag)	NA	NR	NR	550	35.6	56	**10.9**	Diff. before text.

Tab. B.5: Reported black silicon **(p-type multicrystalline)** solar cell results under one-sun illumination (best cell results are given when available). [a]Cell area inferred from text. *Independently confirmed cell results. NR: Not Reported, NA: Not Applicable.

Ref.	Year	Type	b-Si method	DRE	Front passiv.	Area (cm^2)	V_{oc} (mV)	J_{sc} (mA/cm^2)	FF (%)	η (%)	Comments
[47]	17	PERC	RIE	Yes	SiN_x	243	661.4	39.1	80.3	**20.78***	DWS wafer, “Special technol. for front surface passiv.”
[48]	17	PERC	MACE	NA	SiN_x	243	655	38.5	80.2	**20.04**	DWS wafer
[49]	18	AlBSF	RIE ($SF_6/O_2/Cl_2$)	NA	SiN_x	243	635.4	38.1	80.5	**19.5**	
[50]	16	AlBSF	MACE (Ag)	NA	SiN_x	243[a]	642.4	37.4	80.3	**19.31**	
[51]	17	PERC	MACE	NA	SiN_x	243[a]	647	37.4	79.3	**19.22**	Avg (1000 cells)
[48]	17	AlBSF	MACE	NA	SiN_x	243	638	37.5	81.2	**19.21**	DWS wafer
[52]	17	AlBSF	MACE (Ag)	NA	SiN_x	243[a]	640	36.9	81.2	**19.2**	
[53]	17	AlBSF	MACE (Ag)	NA	SiN_x	243[a]	641	37	80.7	**19.12**	DWS wafer
[54]	16	AlBSF	RIE	Yes	SiN_x	243[a]	642.2	37.1	80.2	**19.1**	DWS wafer
[51]	17	PERC	MACE	NA	SiN_x	243	646	37.4	79.2	**19.09**	DWS wafer, avg (1000 cells)
[55]	17	AlBSF	MACE (Cu)	NA	SiN_x	243	639.3	37.4	79.6	**19.06**	DWS wafer
[56]	17	AlBSF	MACE	NA	SiN_x	243[a]	637	37.4	80.4	**19.04**	DWS wafer, avg (10 cells)
[57]	18	AlBSF	MACE (Cu)	NA	SiN_x	243	638.6	36.7	80.6	**18.88**	DWS wafer
[58]	17	AlBSF	MACE (Ag)	NA	SiN_x	243	637.2	36.9	80.2	**18.83**	Avg (20 cells)
[59]	18	AlBSF	MACE (Ag)	Yes	SiN_x	243	635	36.9	80.1	**18.75**	
[60]	16	AlBSF	MACE (Ag+Cu)	NA	SiN_x	243	632.2	36.8	80.2	**18.71**	DWS wafer
[61]	16	AlBSF	MACE (Ag)	NA	SiN_x	243	638.1	36.5	79.9	**18.63**	Avg (20 cells)
[62]	17	AlBSF	MACE (Ag)	NA	SiN_x	243	635	36.7	79.8	**18.62**	
[63]	14	AlBSF	RIE ($SF_6/O_2/Cl_2$, CCP)	NR	SiN_x	243	637	36.4	79.8	**18.49**	
[64]	14	AlBSF	MACE (Ag)	NA	SiN_x	243	634	36.7	79.3	**18.45**	
[65]	16	AlBSF	MACE (Ag)	NA	SiN_x	243[a]	629.1	37.1	78.6	**18.36**	Avg (375 cells)
[66]	15	AlBSF	MACE (Ag)	NA	SiN_x	243	634	36.9	78.3	**18.31**	DWS wafer
[67]	17	AlBSF	CVE	NA	SiN_x	243[a]	629.9	36.0	80.4	**18.24**	DWS wafer, avg (50 cells)
[68]	16	AlBSF	MACE (Ag)	NA	SiN_x	243	633	36.2	79.4	**18.23**	Avg
[69]	14	AlBSF	MACE (Ag)	NA	SiN_x	243	632	36.1	79.1	**18.03**	
[70]	15	AlBSF	ADE (F_2)	NA	SiN_x	243	627	35.7	80.4	**18***	
[12]	14	AlBSF	MACE (Ag)	NA	SiN_x	243	634	36	79.2	**18**	
[71]	16	AlBSF	RIE ($SF_6/O_2/Cl_2$)	Yes	SiN_x	243	624	36.6	78.6	**17.97**	Avg (10 cells)
[72]	15	AlBSF	MACE (Ag)	NA	SiN_x	243	629	35.6	79.2	**17.75***	
[73]	16	AlBSF	MACE (Ag)	NA	SiN_x	243	624.9	35.8	79.4	**17.74**	DWS wafer, avg (100 cells)
[74]	12	AlBSF	RIE (SF_6/O_2)	Yes	SiN_x	243	632	35.7	77.9	**17.6**	Selective emitter
[75]	14	AlBSF	PIII (SF_6/O_2)	Yes	SiN_x	243	623	36.0	77.8	**17.46**	
[76]	14	AlBSF	ADE (F_2)	NA	Al_2O_3/SiN_x	25	621	35.6	78	**17.3**	
[77]	97	AlBSF	RIE ($SF_6/O_2/Cl_2$)	NR	SiN_x	225	621	36.2	76.2	**17.1***	
[78]	13	AlBSF	MACE (Ag)	NA	SiN_x	243	624	35.2	77.2	**16.9**	Diffusion before texturing, selective emitter
[79]	13	AlBSF	RIE ($SF_6/O_2/Cl_2$, CCP)	Yes	SiN_x	243	613	36.1	76.0	**16.82**	
[80]	06	AlBSF	MACE (Ag)	NA	SiN_x	4	618	34.6	77.4	**16.56**	
[78]	13	AlBSF	MACE (Ag)	NA	SiN_x	243	617	34.1	77.8	**16.5**	
[81]	12	AlBSF	MACE (Ag)	NA	SiO_2/SiN_x	243	624	36.1	76.2	**16.38**	

Tab. B.6: End of Table B.5. [a]Cell area inferred from text. *Independently confirmed cell results. NR: Not Reported, NA: Not Applicable.

Ref.	Year	Type	b-Si method	DRE	Front passiv.	Area (cm^2)	V_{oc} (mV)	J_{sc} (mA/cm^2)	FF (%)	η (%)	Comments
[82]	11	AlBSF	RIE ($SF_6/O_2/Cl_2$, CCP)	No	SiN_x	243	614	33.8	78.6	**16.32**	In-situ DRE
[83]	12	AlBSF	PIII (SF_6/O_2)	NR	SiN_x	243	613	34.2	77.6	**16.3**	
[84]	13	AlBSF	PIII (SF_6/O_2)	NR	SiN_x	243	609	34.5	78.1	**16.3**	Diffusion before texturing
[85]	12	AlBSF	PIII (SF_6/O_2)	Yes	SiN_x	243	613	34.1	77.6	**16.25**	
[74]	12	AlBSF	RIE (SF_6/O_2)	No	SiN_x	243	619	34.0	76.9	**16.2**	
[86]	11	AlBSF	RIE (SF_6/O_2, CCP)	NR	SiN_x	243	619	33.5	77.7	**16.1**	
[87]	12	AlBSF	PIII (SF_6/O_2)	NR	SiN_x	243	614	34	76.4	**15.99**	
[88]	08	AlBSF	CVE	NA	SiN_x	156	611	33.8	77.3	**15.98**	
[89]	12	AlBSF	MACE (Ag)	NA	SiO_2/SiN_x	243	604	33.9	77.3	**15.8**	
[84]	12	AlBSF	PIII (SF_6/O_2)	NR	SiN_x	243	600	33.2	77.9	**15.5**	
[90]	12	AlBSF	PIII (SF_6/O_2)	NR	SiN_x	243	600	33.2	77.9	**15.5**	
[91]	10	AlBSF	RIE (SF_6/O_2)	Yes	SiN_x	149	600	34	73	**15.1**	
[92]	00	AlBSF	RIE (SF_6/O_2)	No	SiO_2/SiN_x	NR	591	30.6	75.9	**13.7**	
[93]	12	AlBSF	CVE	NA	SiN_x	156	597	29.6	76.6	**13.54**	EFG wafer
[94]	00	AlBSF	RIE (SF_6/O_2)	NR	SiN_x	21.2	583.7	28.9	72.5	**12.2**	
[95]	13	AlBSF	MACE (Ag)	NA	SiN_x	25	610	32.4	61.4	**12.1**	
[96]	15	AlBSF	MACE (Ag)	NA	SiO_2	5.76	552	29.6	72.4	**11.82**	
[97]	17	AlBSF	CVE-MACE (Ag)	NA	SiN_x	4	530	33	65.5	**11.5**	DWS wafer, combination of CVE and MACE
[98]	12	AlBSF	MACE (Ag)	NA	SiN_x	25	564	26.4	70.4	**10.5**	
[99]	18	AlBSF	MACE (Ag/Cu)	NA	SiN_x	243	578	25.9	69.8	**10.44**	
[44]	06	AlBSF	RIE (SF_6/O_2, hollow cathode)	NR	SiO_2	100	566	25	72	**10.2**	

B.3 Short analysis

B.3.1 Comparison of Historical Record Efficiencies

Figure B.2 compares black silicon solar cells efficiencies with historical records (data from NREL) for both mono- and multicrystalline absorbers. First let us highlight that only two tests have been carried out on silicon heterojunction cells with front nanotexturing: any comparison with overall records is therefore highly biased. In contrast, there are many studies on homojunction solar cells so that a comparison to overall records becomes more reasonable. Moreover, for both mono- and mc-Si cells and as can be expected, there is a global "upward trend" in reported efficiencies for black silicon solar cells. Besides this, the situation is however quite different for the two types of absorbers.

For mono-Si cells, there is still a large gap ($4\%_{abs}$) between the highest black silicon solar cell efficiency (22.1% obtained by Savin *et al.* in 2015) and the record from ISFH (26.1%). Furthermore, only 3 results above 20% efficiency have been reported so far, and the record efficiency for mc-Si (22.3% from FhG-ISE) actually overcomes the mono-Si record.

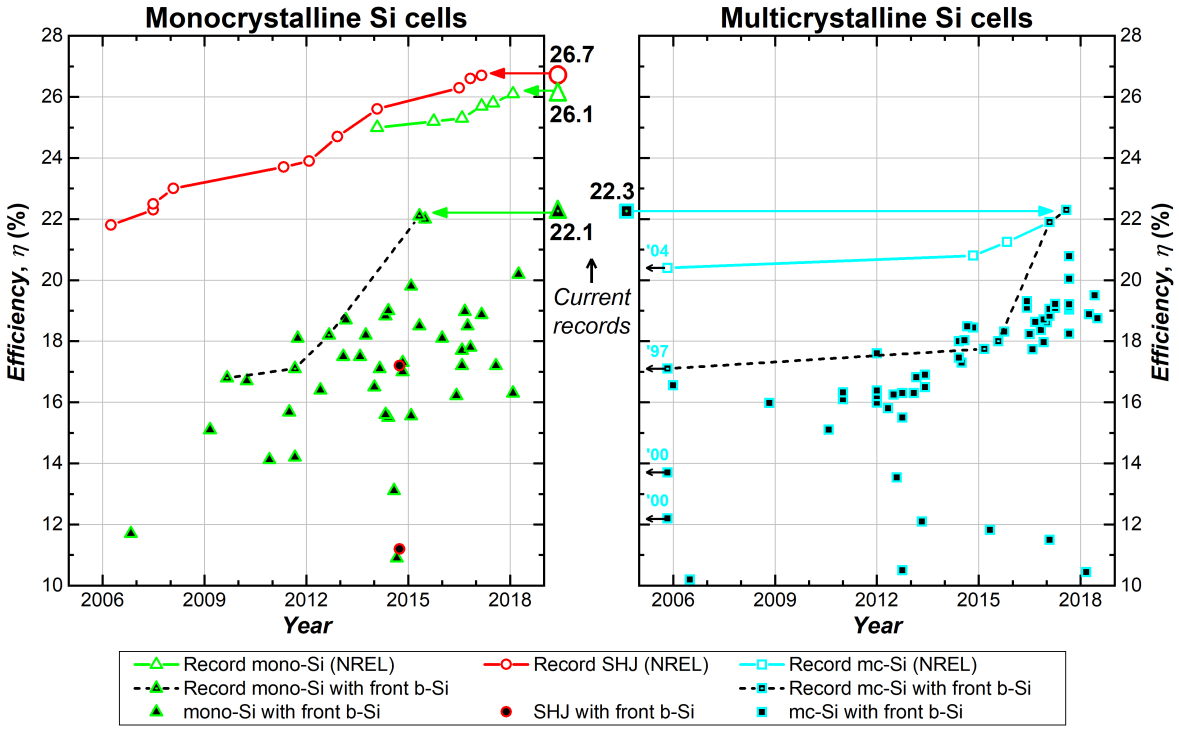

Fig. B.2: History of black silicon solar cells efficiencies compared to overall records for mono- and mc-Si absorbers.

In the case of mc-Si now: before 2017 the best (confirmed) black silicon solar cells were significantly less efficient (by around $3\%_{abs}$) than the overall records. However, the two last records have drastically changed the perspective: FhG-ISE pushed the mc-Si record efficiency above 22%, with a cell including a front nanotextured surface. As explained previously, the record 22.3% can hardly be explained by improved light management, however this result proves that nanotexturing (here by RIE) is compatible with high-efficiency. The context will certainly continue to evolve in the next years: the current shift of the wafer market to diamond wire sawing (DWS) makes nanotexturing very appealing.

It can be concluded that, taking only efficiency as a metric, nanotexturing has not proved relevant for mono-Si cells up to now, however, it can be an adequate solution for mc-Si.

B.3.2 Comparison of Cell Architectures and b-Si Methods

Figure B.3 again shows black silicon cell results throughout recent years, but now distinguishing nanotexturing techniques. A direct comparison of efficiencies would be biased: the different architectures are therefore also separated in the graph. In particular, poor rear surface passivation quality usually limits the efficiency of AlBSF cells compared to other cell types. In the case of mono-Si cells, the best AlBSF cell has an efficiency of 20.19% (obtained by Zhang *et al.* [11]), and, from the eight results on cells other than AlBSF, only two exceed this value (though by a $2\%_{abs}$ gap). The situation is different for mc-Si cells: AlBSF represent an even larger majority of the reported results (57 out of 63 cells) but the best efficiencies are clearly obtained with other architectures (here PERC and TOPcon cells), that have been more recently investigated.

Interestingly, no obvious trend can be observed depending on the nanotexturing technique (either for mono- or multicrystalline solar cells), however, a few conclusions can still be drawn. Results using MACE and RIE (leading approaches) are fairly distributed and claiming that either of the two techniques is superior (only regarding achievable efficiency) would not be substantiated by literature. However, MACE and RIE have a clear advantage compared to other nanotexturing techniques: the best efficiency reported for another technique for mono-Si cells (17.7% efficiency using ADE for an AlBSF cell, obtained by Kafle *et al.* [23]) is only ranked 17th out of 44. From a similar analysis for mc-Si the best result with a technique other than MACE and RIE is ranked 26th out of 63 (18.24% efficiency with CVE texturing on an AlBSF cell, from Xin *et al.* [67]).

Notice that in the case of mc-Si cells, the emergence of DWS wafers has driven most of the recent studies: 14 out of the 30 results reported since 2015 are obtained on DWS wafers.

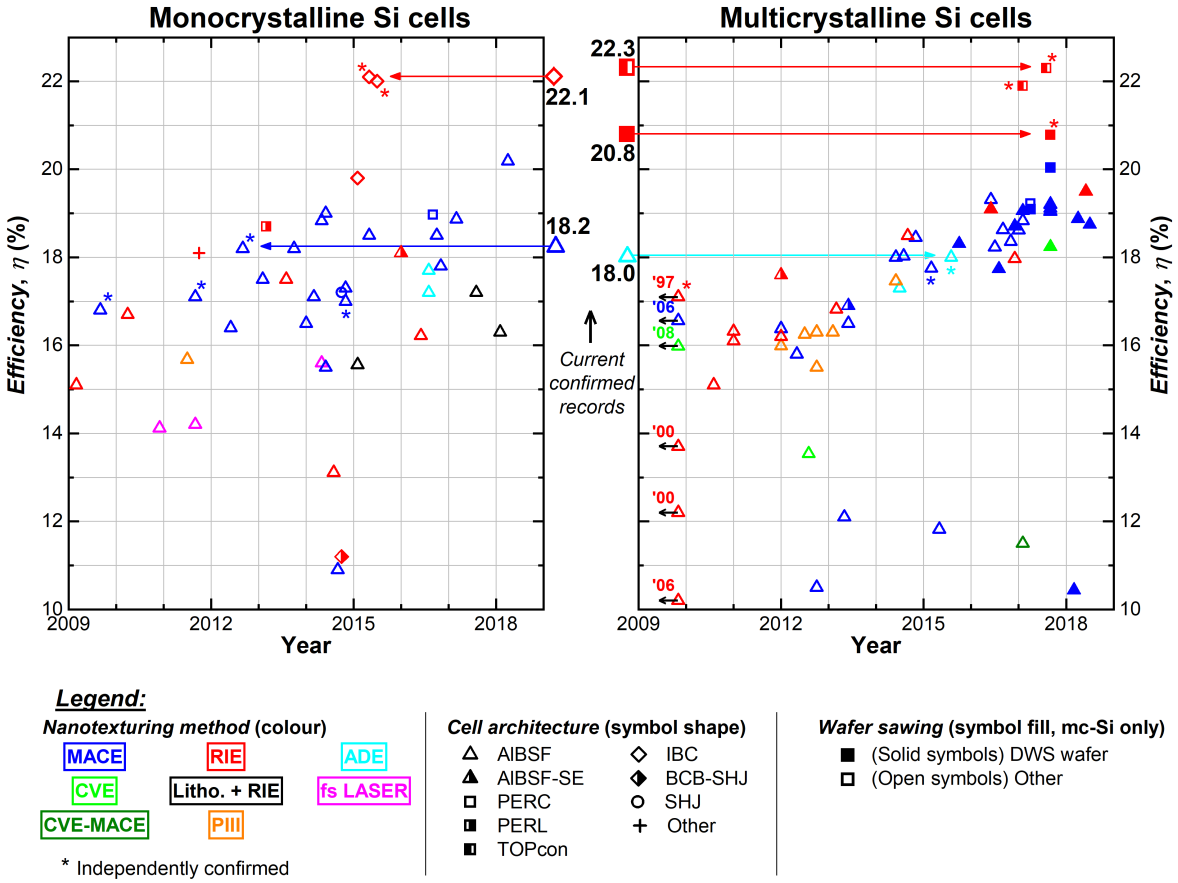

Fig. B.3: History of black silicon solar cells efficiencies for mono- and mc-Si absorbers depending on cell architecture and nanotexturing technique.

Another analysis may be carried out: black silicon is primarily implemented in solar cells to improve light management and its effectiveness can in particular be evaluated by the achievable short-circuit current density. On the other hand, nanotextured silicon surfaces represent a chal-

lenge for surface passivation: the latter notably impacts the open-circuit voltage. Figure B.4 therefore shows J_{sc} vs V_{oc} for literature results both in the case of mono- and mc-Si cells (notice that only homojunction solar cells are here present, and that the scale ranges have been restricted so that some of the poorest results are not shown). It should be recalled that V_{oc} and J_{sc} are not independent, but positively linked by the following relation:

$$V_{oc} = \frac{k_B}{e} \ln\left(\frac{J_{sc}}{J_0} + 1\right) \tag{B.1}$$

where k_B is the Boltzmann constant, e the elementary charge, T the temperature, and J_0 the reverse saturation current density. This theoretical relationship between V_{oc} and J_{sc} is shown in the graphs Figure B.4 using "iso-J_0" curves (dashed curves, labelled by values of J_0 in fA·cm^{-2}). Limiting factors for the efficiency can therefore be identified using these J_{sc} vs V_{oc} plots.

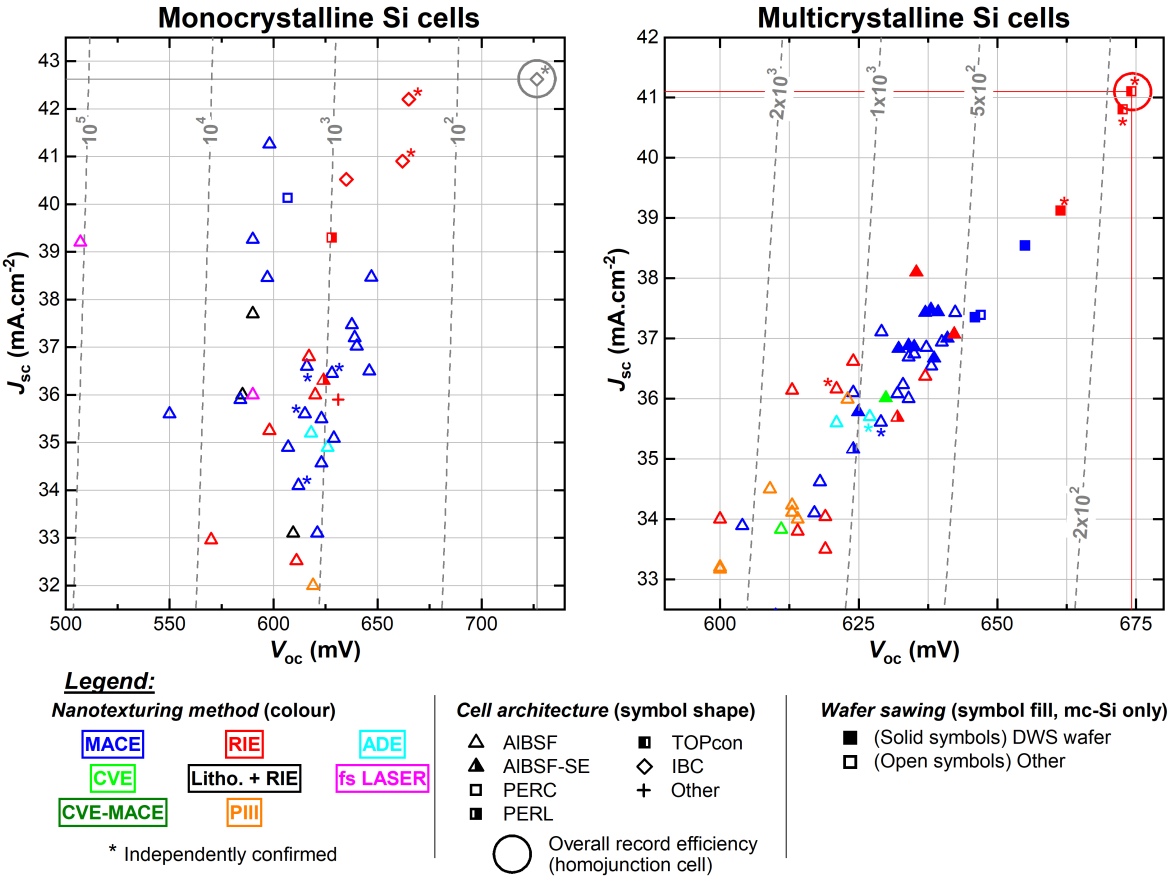

Fig. B.4: Short circuit current density vs open-circuit voltage for homojunction black silicon solar cells (some results outside of the scale ranges are not shown). "Iso-J_0 lines" are shown in dashed curves (labelled by J_0 values in fA·cm^{-2}).

Beginning here with the case of mc-Si cells, a strong (somewhat linear) correlation between J_{sc} vs V_{oc} results are observed: it cannot be explained by the fundamental relationship expressed by the previously described equation. In contrast, it shows that advances have been made in the quality of the bulk (especially for the record TOPcon cells from Benick *et al.* ([4, 9]) which have been obtained with "high performance" wafers), but also certainly in surface passivation, while simultaneously improving light management. A large – though logical – gap is observed between a cluster of the best AlBSF cells ($V_{oc} \approx 640$ mV and $J_{sc} \approx 37$ mA·cm^{-2}) and the modern architectures.

In the case of mono-Si cells, results from literature are most scattered: in particular J_{sc} values lie in a large range. Several black silicon solar cells reported in literature achieve short-circuit current densities above 40 mA·cm^{-2}, and therefore approaching the value 42.62 mA·cm^{-2} value of the record efficiency cell, but again the relevance of nanotexturing for mono-Si cells is not demonstrated. On the other hand, a limitation in V_{oc} (or similarly J_0) is observed: difficulties inherent to

surface passivation certainly explain part of the situation, and more efforts would be needed to close the gap between the value of V_{oc} = 665 mV reported for the cell obtained by Savin *et al.* [10] and the 726.6 mV of the record cell.

B.3.3 Focus on Large-scale mc-Si AlBSF cells

A last analysis will be undertaken here by comparing AlBSF cells which represent most of the black silicon solar cells reported in literature. This architecture is also the most common in the market (more than 70% of the market, [100]) and a fair comparison may be carried out by selecting "large-scale" cells results (here only cells with an area larger than 150 cm^2). Moreover, one result (with MACE) with a cell efficiency below 12% has been discarded, as well as two results for ADE nanotexturing (too few results for a fair comparison). Results are depicted in the graphs Figure B.5. Notice that most of the work has focused on MACE, so that the analysis is somewhat biased.

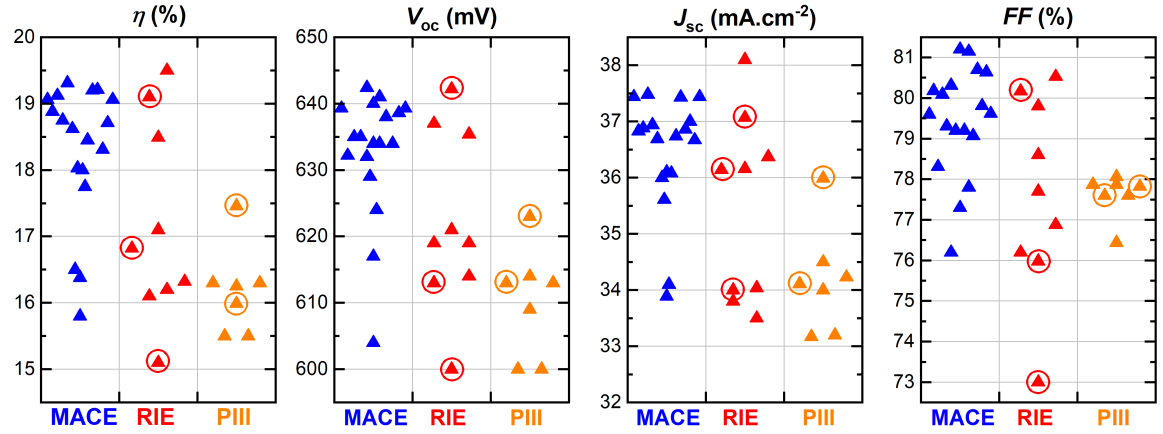

Fig. B.5: Comparison of large-scale black silicon mc-Si cell results (η, V_{oc}, J_{sc} and FF) from literature for different nanotexturing methods. Circled symbols: results using Damage Removal Etching (RIE or PIII only).

MACE leads in general to the best efficiencies for mc-Si AlBSF cells (6 results above 19%), due to high values of both V_{oc} and J_{sc}, FFvalues being scattered in a larger range. In contrast, only 2 (out of 7) cells textured by RIE achieve an efficiency above the 19% mark, while other lie mostly around 16 to 17%. However, RIE textured cells often have a relatively high J_{sc} (above 36 $mA \cdot cm^{-2}$), but the two best efficiencies are actually achieved due to a high V_{oc} (above 630 mV): this result would indicate that a good light management is achievable with RIE but that in turn good passivation is more difficult to achieve.

The situation for PIII is less encouraging: the highest efficiency lies around 17.5%, and all cells suffer from a low V_{oc} and low FF. A fairly good light management is achievable with PIII texturing as one result has demonstrated a J_{sc} above 36 $mA \cdot cm^{-2}$, however the short-circuit current density is much lower for all 6 other studies on PIII.

Finally, Damage Removal Etching (DRE) by chemical baths has been tested for several RIE and PIII textured cells (shown by circled symbols in Figure B.5): while the best efficiency reported for PIII indeed makes use of a DRE step, it is not the case for RIE. In addition, the highest efficiency mc-Si cell – for a different architecture, namely TOPcon – obtained by Benick *et al.* [4] has been achieved without DRE. From this analysis, DRE therefore does not appear to be a prerequisite to achieve high-efficiencies.

Bibliography (Appendix B)

[1] NREL, Best Research Cell Efficiencies, URL www.nrel.gov/pv/assets/images/efficiency-chart.png. XI

[2] K. Yoshikawa *et al.*, Silicon heterojunction solar cell with interdigitated back contacts for a photoconversion efficiency over 26%, *Nature Energy* **2017**, 2, 17032, doi:10.1038/nenergy.2017.32. XII

[3] F. Haase *et al.*, Laser contact openings for local poly-Si-metal contacts enabling 26.1%-efficient POLO-IBC solar cells, *Sol. Energy Mater. Sol. Cells* **2018**, 186, 184–193, doi:10.1016/j.solmat.2018.06.020. XII

[4] J. Benick *et al.*, Approaching 22% Efficiency with Multicrystalline n-Type Silicon Solar Cells, in *Proceedings of the 33rd European Photovoltaic Solar Energy Conference and Exhibition*, WIP, Amsterdam, **2017** 460–464, doi:10.4229/EUPVSEC20172017-2DO.3.1. XII, XIII, XIX, XX

[5] P. Ortega, E. Calle, G. von Gastrow, P. Repo, D. Carrió, H. Savin and R. Alcubilla, High-efficiency black silicon interdigitated back contacted solar cells on p-type and n-type c-Si substrates: High-efficiency black silicon interdigitated back contacted solar cells, *Prog. Photovolt. Res. Appl.* **2015**, doi:10.1002/pip.2664. XIII

[6] A. Ingenito, O. Isabella and M. Zeman, Nano-cones on micro-pyramids: modulated surface textures for maximal spectral response and high-efficiency solar cells: Modulated textures for maximal spectral response and high-efficiency solar cells, *Prog. Photovolt. Res. Appl.* **2015**, 23(11), 1649–1659, doi:10.1002/pip.2606. XIII

[7] P. Repo *et al.*, N-type Black Silicon Solar Cells, *Energy Procedia* **2013**, 38, 866–871, doi:10.1016/j.egypro.2013.07.358. XIII

[8] M. Mews, C. Leendertz, M. Algasinger, S. Koynov and L. Korte, Amorphous/crystalline silicon heterojunction solar cells with black silicon texture: Amorphous/crystalline silicon heterojunction solar cells with black silicon texture, *Phys. Status Solidi Rap. Res. Lett.* **2014**, 8(10), 831–835, doi:10.1002/pssr.201409327. XIII

[9] J. Benick *et al.*, High-Efficiency n-Type HP mc Silicon Solar Cells, *IEEE J. Photovolt.* **2017**, 7(5), 1171–1175, doi:10.1109/JPHOTOV.2017.2714139. XIII, XIX

[10] H. Savin, P. Repo, G. von Gastrow, P. Ortega, E. Calle, M. Garín and R. Alcubilla, Black silicon solar cells with interdigitated back-contacts achieve 22.1% efficiency, *Nature Nanotech.* **2015**, doi:10.1038/nnano.2015.89. XIV, XX

[11] C. Zhang, L. Chen, Y. Zhu and Z. Guan, Fabrication of 20.19% Efficient Single-Crystalline Silicon Solar Cell with Inverted Pyramid Microstructure, *Nanoscale Res. Lett.* **2018**, 13(1), 91, doi:10.1186/s11671-018-2502-9. XIV, XVIII

[12] M. P. Jura *et al.*, Conventionally-processed silicon nanowire solar cells demonstrating efficiency improvement over standard cells, in *2014 IEEE 40th Photovoltaic Specialist Conference (PVSC)*, **2014** 0598–0600, doi:10.1109/PVSC.2014.6924992. XIV, XV

[13] L.-X. Wang, Z.-Q. Zhou, H.-C. Hao and M. Lu, A porous Si-emitter crystalline-Si solar cell with 18.97% efficiency, *Nanonotechnology* **2016**, 27(42), 425207, doi:10.1088/0957-4484/27/42/425207. XIV

[14] L. Yang *et al.*, 18.87%-efficient inverted pyramid structured silicon solar cell by one-step Cu-assisted texturization technique, *Sol. Energy Mater. Sol. Cells* **2017**, 166, 121–126, doi:10.1016/j.solmat.2017.03.017. XIV

[15] L. Yang *et al.*, Optimization of silicon pyramidal emitter by self-selective Ag-assisted chemical etching, *RSC Adv.* **2014**, 4(47), 24458, doi:10.1039/c4ra03120b. XIV

[16] W.-C. Wang, M.-C. Tsai, J. Yang, C. Hsu and M.-J. Chen, Efficiency Enhancement of Nanonotextured Black Silicon Solar Cells Using Al_2O_3 /TiO_2 Dual-Layer Passivation Stack Prepared by Atomic Layer Deposition, *ACS Appl. Mater. Interfaces* **2015**, 150507072344001, doi:10.1021/acsami.5b00677. XIV

[17] P. Li *et al.*, Effective optimization of emitters and surface passivation for nanostructured silicon solar cells, *RSC Adv.* **2016**, 6(106), 104073–104081, doi:10.1039/C6RA20945A. XIV

[18] W.-C. Wang *et al.*, Surface Passivation of Efficient Nanonotextured Black Silicon Solar Cells Using Thermal Atomic Layer Deposition, *ACS Appl. Mater. Interfaces* **2013**, 5(19), 9752–9759, doi:10.1021/am402889k. XIV

[19] J. Oh, H.-C. Yuan and H. M. Branz, An 18.2%-efficient black-silicon solar cell achieved through control of carrier recombination in nanostructures, *Nature Nanotech.* **2012**, 7(11), 743–748, doi:10.1038/nnano.2012.166. XIV

[20] Y. Chen, Z. Xu, M. R. Gartia, D. Whitlock, Y. Lian and G. L. Liu, Ultrahigh Throughput Silicon Nanomanufacturing by Simultaneous Reactive Ion Synthesis and Etching, *ACS Nano.* **2011**, 5(10), 8002–8012, doi:10.1021/nn2024754. XIV

[21] R. S. Davidsen *et al.*, Black silicon laser-doped selective emitter solar cell with 18.1% efficiency, *Sol. Energy Mater. Sol. Cells* **2016**, 144, 740–747, doi:10.1016/j.solmat.2015.10.018. XIV

[22] F. Es, G. Baytemir, M. Kulakci and R. Turan, Metal-assisted nano-textured solar cells with SiO2/Si3N4 passivation, *Sol. Energy Mater. Sol. Cells* **2017**, 160, 269–274, doi:10.1016/j.solmat.2016.10.032. XIV

[23] B. Kafle *et al.*, On the emitter formation in nanonotextured silicon solar cells to achieve improved electrical performances, *Sol. Energy Mater. Sol. Cells* **2016**, 152, 94–102, doi:10.1016/j.solmat.2016.03.031. XIV, XVIII

[24] D. Z. Dimitrov and C.-H. Du, Crystalline silicon solar cells with micro/nano texture, *Appl. Surf. Sci.* **2013**, 266, 1–4, doi:10.1016/j.apsusc.2012.10.081. XIV

[25] J. Liu, B. Liu, S. Liu, Z. Shen, C. Li and Y. Xia, A simple method to produce dual-scale silicon surfaces for solar cells, *Surf. Coat. Technol.* **2013**, 229, 165–167, doi:10.1016/j.surfcoat.2012.06.043. XIV

[26] Z. Zhao, P. Li, Y. Wei, C. Lu, X. Tan and A. Liu, 17.3% efficient black silicon solar cell without dielectric antireflection coating, *Sol. Energy* **2014**, 110, 714–719, doi:10.1016/j.solener.2014.10.029. XIV

[27] S.-E. Cheon *et al.*, Fabrication of parabolic Si nanostructures by nanosphere lithography and its application for solar cells, *Sci. Rep.* **2017**, 7(1), doi:10.1038/s41598-017-07463-7. XIV

[28] F. Toor, H. M. Branz, M. R. Page, K. M. Jones and H.-C. Yuan, Multi-scale surface texture to improve blue response of nanoporous black silicon solar cells, *Appl. Phys. Lett.* **2011**, 99(10), 103501, doi:10.1063/1.3636105. XIV

[29] Z. Zhao, B. Zhang, P. Li, W. Guo and A. Liu, Effective Passivation of Large Area Black Silicon Solar Cells by SiO2/SiN:H Stacks, *Int. J. Photoenergy* **2014**, 2014, 1–6, doi:10.1155/2014/683654. XIV

[30] F. Toor, J. Oh and H. M. Branz, Efficient nanostructured 'black' silicon solar cell by copper-catalyzed metal-assisted etching: Efficient nanostructured 'black' silicon solar cell, *Prog. Photovolt. Res. Appl.* **2014**, doi:10.1002/pip.2562. XIV

[31] H.-C. Yuan, V. E. Yost, M. R. Page, P. Stradins, D. L. Meier and H. M. Branz, Efficient black silicon solar cell with a density-graded nanoporous surface: Optical properties, performance limitations, and design rules, *Appl. Phys. Lett.* **2009**, 95(12), 123501, doi:10.1063/1.3231438. XIV

[32] J. Yoo, Reactive ion etching (RIE) technique for application in crystalline silicon solar cells, *Sol. Energy* **2010**, 84(4), 730–734, doi:10.1016/j.solener.2010.01.031. XIV

[33] Y. Liu, A. Das, Z. Lin, I. B. Cooper, A. Rohatgi and C. Wong, Hierarchical robust textured structures for large scale self-cleaning black silicon solar cells, *Nano. Energy* **2014**, 3, 127–133, doi:10.1016/j.nanoen.2013.11.002. XIV

[34] H.-C. Yuan, J. Oh, Y. Zhang, O. A. Kuznetsov, D. J. Flood and H. M. Branz, Antireflection and SiO2 surface passivation by liquid-phase chemistry for efficient black silicon solar cells, IEEE, **2012** 000686–000689, doi:10.1109/PVSC.2012.6317702. XIV

[35] S. Cheon, D. S. Jeong, J.-K. Park, W. M. Kim, T. S. Lee, H. Lee and I. Kim, Enhanced blue responses in nanostructured Si solar cells by shallow doping, *J. Phys. D: Appl. Phys.* **2018**, 51(12), 125102, doi:10.1088/1361-6463/aaaee4. XIV

[36] Y. Xia, B. Liu, J. Liu, Z. Shen and C. Li, A novel method to produce black silicon for solar cells, *Sol. Energy* **2011**, 85(7), 1574–1578, doi:10.1016/j.solener.2011.03.012. XIV

[37] H. Y. Chen *et al.*, Enhanced performance of solar cells with optimized surface recombination and efficient photon capturing via anisotropic-etching of black silicon, *Appl. Phys. Lett.* **2014**, 104(19), 193904, doi:10.1063/1.4878096. XIV

[38] I. Cornago *et al.*, Periodic nanostructures on unpolished substrates and their integration in solar cells, *Nanonotechnology* **2015**, 26(9), 095301, doi:10.1088/0957-4484/26/9/095301. XIV

[39] M. Hong *et al.*, Control carrier recombination of multi-scale textured black silicon surface for high performance solar cells, *Appl. Phys. Lett.* **2014**, 104(25), 253902, doi:10.1063/1.4884899. XIV

[40] J. Yoo, G. Yu and J. Yi, Black surface structures for crystalline silicon solar cells, *Mater. Sci. Eng. B* **2009**, 159-160, 333–337, doi:10.1016/j.mseb.2008.10.019. XIV

[41] B. K. Nayak, V. V. Iyengar and M. C. Gupta, Efficient light trapping in silicon solar cells by ultrafast-laser-induced self-assembled micro/nano structures, *Prog. Photovolt. Res. Appl.* **2011**, 19(6), 631–639, doi:10.1002/pip.1067. XIV

[42] V. V. Iyengar, B. K. Nayak and M. C. Gupta, Optical properties of silicon light trapping structures for photovoltaics, *Sol. Energy Mater. Sol. Cells* **2010**, 94(12), 2251–2257, doi:10.1016/j.solmat.2010.07.020. XIV

[43] C. Cho, D. Kong, J.-H. Oh, B. Kim, B. Lee and J. Lee, Surface texturing method for silicon solar cell using reactive ion etching with metal mesh: Surface texturing method for silicon solar cell, *Phys. Status Solidi A* **2014**, 211(8), 1844–1849, doi:10.1002/pssa.201330545. XIV

[44] J. Yoo, I. Parm, U. Gangopadhyay, K. Kim, S. Dhungel, D. Mangalaraj and J. Yi, Black silicon layer formation for application in solar cells, *Sol. Energy Mater. Sol. Cells* **2006**, 90(18-19), 3085–3093, doi:10.1016/j.solmat.2006.06.015. XIV, XVI

[45] J. Ziegler, J. Haschke, T. Käsebier, L. Korte, A. N. Sprafke and R. B. Wehrspohn, Influence of black silicon surfaces on the performance of back-contacted back silicon heterojunction solar cells, *Opt. Exp.* **2014**, 22(S6), A1469, doi:10.1364/OE.22.0A1469. XIV

[46] Y. Jiang, H. Yang, W. Cao, G. Wang, H. Ma and F. Chang, Post-black etching on emitter to improve performance of multi-scale texture silicon solar cells, *Appl. Phys. A* **2014**, 116(3), 1409–1414, doi:10.1007/s00339-014-8247-0. XIV

[47] S. Dong *et al.*, Industrially Feasible PERC Cells on Diamond Wire Sawing Multi-Crystalline Silicon Wafers Textured by RIE towards 20.78% Efficiency, in *33rd European Photovoltaic Solar Energy Conference and Exhibition*, **2017** 290–294, doi:10.4229/EUPVSEC20172017-2AO.6.4. XV

[48] D. Liu, D. Song, J. Shi, F. Li, Y. Wang, H. Wang and Z. Xu, Industrially MCCE Textured Multi-Crystalline PERC with 20% Efficiency, in *Proceedings of the 33rd European Photovoltaic Solar Energy Conference and Exhibition*, **Nov 2017** 621–623, doi:10.4229/EUPVSEC20172017-2AV.2.11. XV

[49] W. Lu *et al.*, Enhanced optoelectronic conversion in diamond-wire sawing multi-crystalline silicon solar cells through nanonotexture-induced photon management, *Sol. Energy Mater. Sol. Cells* **2018**, 185, 439–444,

doi:10.1016/j.solmat.2018.06.001. XV

[50] S. Zou, X. Wang, F. Cao, X. Ye and G. Xing, 19.31%-efficient Multi-crystalline Silicon Solar Cell with MCCE black silicon technology, in *Proceedings of the 32nd European Photovoltaic Solar Energy Conference and Exhibition*, **2016** 816–821, doi:10.4229/EUPVSEC20162016-2AV.3.23. XV

[51] Y. Lin, F. Huang, H. Wu, C. Yeh, C. Chang and J. Chien, High Efficiency Passivated Emitter Rear Contact Solar Cells with Diamond Wire Saw Multi-crystalline Silicon wafers, *Energy Procedia* **2017**, 130, 55–59, doi:10.1016/j.egypro.2017.09.414. XV

[52] V. Hoffmann, S. Zou, J. M. Míguez and X. Su, Enhancing Performance of Upgraded Metallurgical Grade Silicon Solar Cells Nano-Textured by using Metal Catalyzed Chemical Etching, in *Proceedings of the 33rd European Photovoltaic Solar Energy Conference and Exhibition*, **2017** 613–616, doi:10.4229/EUPVSEC20172017-2AV.2.9. XV

[53] W. Jooss *et al.*, Development and Optimization of a Novel Inline Black Silicon Texturing Process for Increased Solar Cell Performance, in *Proceedings of the 33rd European Photovoltaic Solar Energy Conference and Exhibition*, **2017** 368–372, doi:10.4229/EUPVSEC20172017-2CO.9.2. XV

[54] Y. Yang *et al.*, Fabricating Nano-Texture on Diamond-Wire Saw Multi-crystalline Silicon using RIE-etch, in *Proceedings of the 32nd European Photovoltaic Solar Energy Conference and Exhibition*, **2016** 667–670, doi:10.4229/EUPVSEC20162016-2AV.1.35. XV

[55] J. Zha, T. Wang, C. Pan, K. Chen, F. Hu, X. Pi and X. Su, Constructing submicron textures on mc-Si solar cells via copper-catalyzed chemical etching, *Appl. Phys. Lett.* **2017**, 110(9), 093901, doi:10.1063/1.4977191. XV

[56] S. Fox *et al.*, Pilot Production of High Efficiency Metal Catalyzed Textured Diamond Wire Sawn mc-Si Solar Cells Combined with Nickel-Copper Plated Front Contact Processing, in *Proceedings of the 33rd European Photovoltaic Solar Energy Conference and Exhibition*, **2017** 362–367, doi:10.4229/EUPVSEC20172017-2CO.9.1. XV

[57] P. Wang, S. Xiao, R. Jia, H. Sun, X. Dai, G. Su and K. Tao, 18.88%-efficient multi-crystalline silicon solar cells by combining Cu-catalyzed chemical etching and post-treatment process, *Sol. Energy* **2018**, 169, 153–158, doi:10.1016/j.solener.2018.04.049. XV

[58] Q. Wang, C. Pan, K. Chen, S. Zou, M. Shen and X. Su, Efficient nanostructured quasi-single crystalline silicon solar cells by metal-catalyzed chemical etching, *Sol. Energy Mater. Sol. Cells* **2017**, 164, 40–46, doi:10.1016/j.solmat.2017.02.002. XV

[59] G. Su, R. Jia, X. Dai, K. Tao, H. Sun, Z. Jin and X. Liu, The Influence of Black Silicon Morphology Modification by Acid Etching to the Properties of Diamond Wire Sawn Multicrystalline Silicon Solar Cells, *IEEE J. Photovolt.* **2018**, 8(4), 937–942, doi:10.1109/JPHOTOV.2018.2829085. XV

[60] C. Zheng *et al.*, High-Efficient Solar Cells by the Ag/Cu-Assisted Chemical Etching Process on Diamond-Wire-Sawn Multicrystalline Silicon, *IEEE J. Photovolt.* **2017**, 7(1), 153–156, doi:10.1109/JPHOTOV.2016.2631304. XV

[61] F. Hu, Y. Sun, J. Zha, K. Chen, S. Zou, L. Fang and X. Su, Pre-texturing multi-crystalline silicon wafer via a two-step alkali etching method to achieve efficient nanostructured solar cells, *Sol. Energy Mater. Sol. Cells* **2017**, 159, 121–127, doi:10.1016/j.solmat.2016.08.032. XV

[62] Y. Jiang *et al.*, High efficiency multi-crystalline silicon solar cell with inverted pyramid nanostructure, *Sol. Energy* **2017**, 142, 91–96, doi:10.1016/j.solener.2016.12.007. XV

[63] X. Niu *et al.*, High Efficiency Multi-Crystalline Silicon Solar Cells with Texturing by Reactive Ion Etching, in *29th European Photovoltaic Solar Energy Conference and Exhibition*, **2014** 920–923, doi:10.4229/EUPVSEC20142014-2AV.2.51. XV

[64] X. Ye *et al.*, 18.45%-Efficient Multi-Crystalline Silicon Solar Cells with Novel Nanoscale Pseudo-Pyramid Texture, *Adv. Funct. Mater.* **2014**, 24(42), 6708–6716, doi:10.1002/adfm.201401589. XV

[65] Y. C. Niu, Z. liu, X. K. Ren, X. J. Liu, H. T. Liu and Y. S. Jiang, Fabrication of micro-nano composite textured surface for slurry sawn mc-Si wafers cell, *IOP Conference Series: Materials Science and Engineering* **2017**, 167, 012008, doi:10.1088/1757-899X/167/1/012008. XV

[66] F. Cao, K. Chen, J. Zhang, X. Ye, J. Li, S. Zou and X. Su, Next-generation multi-crystalline silicon solar cells: Diamond-wire sawing, nano-texture and high efficiency, *Sol. Energy Mater. Sol. Cells* **2015**, 141, 132–138, doi:10.1016/j.solmat.2015.05.030. XV

[67] Z. Xin *et al.*, A Micro-Droplet Etching Approach for Texturization of Diamond Wire Sawn Multi-Crystalline Silicon Wafers, in *33rd European Photovoltaic Solar Energy Conference and Exhibition*, **2017** 952–954, doi:10.4229/EUPVSEC20172017-2CV.2.73. XV, XVIII

[68] Z. Ying *et al.*, High-Performance Black Multicrystalline Silicon Solar Cells by a Highly Simplified Metal-Catalyzed Chemical Etching Method, *IEEE J. Photovolt.* **2016**, 6(4), 888–893, doi:10.1109/JPHOTOV.2016.2559779. XV

[69] Z. Yue *et al.*, Large-scale black multi-crystalline silicon solar cell with conversion efficiency over 18 %, *Appl. Phys. A* **2014**, 116(2), 683–688, doi:10.1007/s00339-014-8414-3. XV

[70] B. Kafle *et al.*, Nanotextured multicrystalline Al-BSF solar cells reaching 18% conversion efficiency using industrially viable solar cell processes, *Phys. Status Solidi Rapid Res. Lett.* **2015**, 9(8), 448–452,

doi:10.1002/pssr.201510219. XV

[71] W.-H. Chen and F. C.-N. Hong, 0.76% absolute efficiency increase for screen-printed multicrystalline silicon solar cells with nanostructures by reactive ion etching, *Sol. Energy Mater. Sol. Cells* **2016**, 157, 48–54, doi:10.1016/j.solmat.2016.05.046. XV

[72] X. X. Lin *et al.*, Realization of improved efficiency on nanostructured multicrystalline silicon solar cells for mass production, *Nanonotechnology* **2015**, 26(12), 125401, doi:10.1088/0957-4484/26/12/125401. XV

[73] Y.-C. Niu, H.-T. Liu, X.-J. Liu, Y.-S. Jiang, X.-K. Ren, P. Cai and T.-G. Zhai, Study on nano-pores enlargement during Ag-assisted electroless etching of diamond wire sawn polycrystalline silicon wafers, *Mater. Sci. Semicond. Process* **2016**, 56, 119–126, doi:10.1016/j.mssp.2016.08.004. XV

[74] J.-M. Shim *et al.*, 17.6% Conversion Efficiency Multicrystalline Silicon Solar Cells Using the Reactive Ion Etching with the Damage Removal Etching, *Int. J. Photoenergy* **2012**, 2012, 1–6, doi:10.1155/2012/248182. XV, XVI

[75] G. Xiao, B. Liu, J. Liu and Z. Xu, The study of defect removal etching of black silicon for solar cells, *Mater. Sci. Semicond. Process* **2014**, 22, 64–68, doi:10.1016/j.mssp.2014.01.030. XV

[76] B. Kafle, J. Seiffe, M. Hofmann, L. Clochard, E. Duffy and J. Rentsch, Nanostructuring of c-Si surface by F2-based atmospheric pressure dry texturing process, *Phys. Status Solidi A* **2015**, 212(2), 307–311, doi:10.1002/pssa.201431372. XV

[77] K. Fukui, K. Okada, Y. Inomata, H. Takahashi, S. Fujii, Y. Fukawa and K. Shirasawa, Surface and bulk-passivated large area multicrystalline silicon solar cells, *Sol. Energy Mater. Sol. Cells* **1997**, 48(1-4), 219–228, doi:10.1016/S0927-0248(97)00104-9. XV

[78] Y. Wang *et al.*, Selective nano-emitter fabricated by silver assisted chemical etch-back for multicrystalline solar cells, *RSC Adv.* **2013**, 3(35), 15483, doi:10.1039/c3ra43100b. XV

[79] K. M. Park, M. B. Lee, K. S. Jeon and S. Y. Choi, Reactive Ion Etching Texturing for Multicrystalline Silicon Solar Cells Using a SF_6 /O_2 /Cl_2 Gas Mixture, *Jap. J. Appl. Phys.* **2013**, 52(3S), 03BD01, doi:10.7567/JJAP.52.03BD01. XV

[80] K. Tsujino, M. Matsumura and Y. Nishimoto, Texturization of multicrystalline silicon wafers for solar cells by chemical treatment using metallic catalyst, *Sol. Energy Mater. Sol. Cells* **2006**, 90(1), 100–110, doi:10.1016/j.solmat.2005.02.019. XV

[81] W. C. Hsu, Y.-S. Lu, J.-Y. Chyan and J. A. Yeh, High-Efficiency 6" Multicrystalline Black Solar Cells Based on Metal-Nanoparticle-Assisted Chemical Etching, *Int. J. Photoenergy* **2012**, 2012, 1–7, doi:10.1155/2012/197514. XV

[82] K.-s. Lee, M.-H. Ha, J. H. Kim and J.-W. Jeong, Damage-free reactive ion etch for high-efficiency large-area multi-crystalline silicon solar cells, *Sol. Energy Mater. Sol. Cells* **2011**, 95(1), 66–68, doi:10.1016/j.solmat.2010.03.007. XVI

[83] J. Liu *et al.*, Characterization of PIII textured industrial multicrystalline silicon solar cells, *Sol. Energy* **2012**, 86(10), 3004–3008, doi:10.1016/j.solener.2012.07.006. XVI

[84] Z. Shen, B. Liu, Y. Xia, J. Liu, J. Liu, S. Zhong and C. Li, Black silicon on emitter diminishes the lateral electric field and enhances the blue response of a solar cell by optimizing depletion region uniformity, *Scr. Mater.* **2013**, 68(3-4), 199–202, doi:10.1016/j.scriptamat.2012.10.023. XVI

[85] B. Liu, S. Zhong, J. Liu, Y. Xia and C. Li, Silicon Nitride Film by Inline PECVD for Black Silicon Solar Cells, *Int. J. Photoenergy* **2012**, 2012, 1–5, doi:10.1155/2012/971093. XVI

[86] J. Yoo, G. Yu and J. Yi, Large-area multicrystalline silicon solar cell fabrication using reactive ion etching (RIE), *Sol. Energy Mater. Sol. Cells* **2011**, 95(1), 2–6, doi:10.1016/j.solmat.2010.03.029. XVI

[87] S. Zhong *et al.*, Influence of the texturing structure on the properties of black silicon solar cell, *Sol. Energy Mater. Sol. Cells* **2013**, 108, 200–204, doi:10.1016/j.solmat.2012.10.001. XVI

[88] M. Ju *et al.*, A new vapor texturing method for multicrystalline silicon solar cell applications, *Mater. Sci. Eng. B* **2008**, 153(1-3), 66–69, doi:10.1016/j.mseb.2008.10.030. XVI

[89] Y. Liu *et al.*, Nanostructure Formation and Passivation of Large-Area Black Silicon for Solar Cell Applications, *Small* **2012**, 8(9), 1392–1397, doi:10.1002/smll.201101792. XVI

[90] S. Zhong *et al.*, The study on the properties of black multicrystalline silicon solar cell varying with the diffusion temperature, *Energy Procedia* **2012**, 14, 505–511, doi:10.1016/j.egypro.2011.12.966. XVI

[91] B. Prasad, S. Bhattacharya, A. Saxena, S. Reddy and R. Bhogra, Performance enhancement of mc-Si solar cells due to synergetic effect of plasma texturization and SiNx:H AR coating, *Sol. Energy Mater. Sol. Cells* **2010**, 94(8), 1329–1332, doi:10.1016/j.solmat.2009.06.026. XVI

[92] B. Damiani, R. Ludemann, D. Ruby, S. Zaidi and A. Rohatgi, Development of RIE-textured silicon solar cells, IEEE, ISBN 978-0-7803-5772-3, **2000** 371–374, doi:10.1109/PVSC.2000.915843. XVI

[93] M. Ju, N. Balaji, Y.-J. Lee, C. Park, K. Song, J. Choi and J. Yi, Novel vapor texturing method for EFG silicon solar cell applications, *Sol. Energy Mater. Sol. Cells* **2012**, 107, 366–372, doi:10.1016/j.solmat.2012.07.015. XVI

[94] M. Schnell, R. Ludemann and S. Schaefer, Plasma surface texturization for multicrystalline silicon solar cells,

IEEE, ISBN 0-7803-5772-8, **2000** 367–370, doi:10.1109/PVSC.2000.915841. XVI

[95] J. Shi *et al.*, Refined nano-textured surface coupled with SiNx layer on the improved photovoltaic properties of multi-crystalline silicon solar cells, *Solid-State Electronics* **2013**, 85, 23–27, doi:10.1016/j.sse.2013.03.002. XVI

[96] S. K. Srivastava, P. Singh, M. Yameen, P. Prathap, C. Rauthan, Vandana and P. Singh, Antireflective ultra-fast nanoscale texturing for efficient multi-crystalline silicon solar cells, *Sol. Energy* **2015**, 115, 656–666, doi:10.1016/j.solener.2015.03.010. XVI

[97] C. Amri, R. Ouertani, A. Hamdi and H. Ezzaouia, Effect of Silver-Assisted Chemical Vapor Etching on morphological properties and silicon solar cell performance, *Mater. Sci. Semicond. Process* **2017**, 63, 176–183, doi:10.1016/j.mssp.2017.02.019. XVI

[98] J. Shi *et al.*, Nanoporous black multi-crystalline silicon solar cells: realization of low reflectance and explanation of high recombination loss, *Mater. Sci. Semicond. Process* **2013**, 16(2), 441–448, doi:10.1016/j.mssp.2012.08.006. XVI

[99] S.-D. Wang and T.-W. Chen, Texturization of diamond-wire-sawn multicrystalline silicon wafer using Cu, Ag, or Ag/Cu as a metal catalyst, *Appl. Surf. Sci.* **2018**, 444, 530–541, doi:10.1016/j.apsusc.2018.03.085. XVI

[100] International Technology Roadmap for Photovoltaic Ninth Edition, March 2018, Tech. Rep. 9, ITRPV, **2018**, URL `www.itrpv.net`. XX

MOTIFS & RELIEFS

Au cours de ce travail, j'ai passé de nombreuses heures à imager des surfaces de silicium nanotexturées par plasma, grâce à la microscopie électronique à balayage. La plupart de ces images seront maintenant perdues, peut-être sauvegardées un temps sous la forme de kilooctets de données. Ces images ont permis d'acquérir des informations – parcellaires – sur les mécanismes de formation des nanostructures. De nombreuses zones d'ombres restent à élucider, néanmoins il n'est pas nécessaire de comprendre un phénomène pour en apprécier les effets. Voici ci-dessous quelques images que je souhaitais partager pour l'esthétique particulière des motifs et reliefs formés.

Notez que seules sept images montrent des nanostructures de silicium : l'une des images ci-dessous (réponse en bas de page) correspond en effet à une photographie d'un phénomène naturel. Il s'agit de "pénitents de glace", partageant des similitudes avec les nanostructures de silicium, mais à une échelle un milliard de fois plus grande.

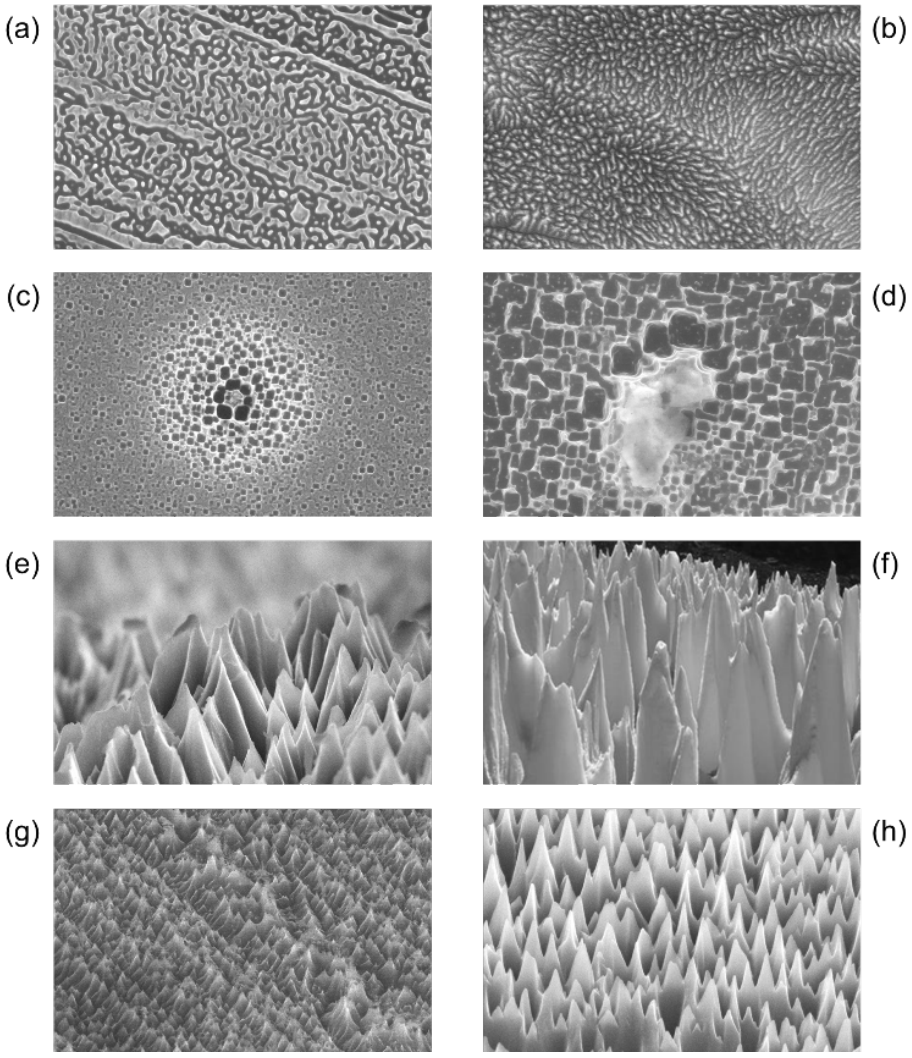

L'image (f) est une photographie (prise dans les Andes argentines) de "pénitents de glace" de 1.5 à 2 m de hauteur. Image modifiée, source : Wikipedia. Informations sur les "pénitents de glace" disponibles par exemple dans Claudin *et al.*, doi:10.1103/PhysRevE.92.033015.

List of Communications

Peer-reviewed papers

- **G. Fischer**, E. Drahi, M. Foldyna, T. A. Germer and E. V. Johnson, Plasma nanotexturing of silicon surfaces for photovoltaics applications: influence of initial surface finish on the evolution of topographical and optical properties, *Optics Express* **2017**, 25(24), A1057–A1071, doi:10.1364/OE.25.0A1057.

- **G. Fischer**, K. Ouaras, E. Drahi, B. Bruneau and E. V. Johnson, Excitation of Ar, O_2, and SF_6/O_2 plasma discharges using tailored voltage waveforms: Control of surface ion bombardment energy and determination of dominant electron excitation mode, *Plasma Sources Science and Technology* **2018**, doi:10.1088/1361-6595/aaca05.

Conference proceedings

- **G. Fischer**, E. Drahi, F. Lebreton, P. Bulkin, G. Poulain and E. V. Johnson, Nanotextured Silicon Surfaces Using Tailored Voltage Waveform Plasmas: Impact of Ion Bombardment Energy on Etching Dynamics and Passivation, *Proc. of the 33rd European Photovoltaic Solar Energy Conference and Exhibition* **2017**, 679–683, doi:10.4229/EUPVSEC20172017-2AV.2.33.

- R. Peyronnet, **G. Fischer**, T. Blévin, E. V. Johnson, E. Drahi and M. Lemiti, Texturing optimization for bifacial n-PERT: are pyramids and/or black silicon the way to go for thinner devices?, *Energy Procedia*, **2017**, 124, 250–259, doi:10.1016/j.egypro.2017.09.296.

- T. A. Germer, M. Foldyna, Z. Mrazkova, **G. Fischer** and E. Drahi, Mueller matrix bidirectional reflectance distribution function measurements and modeling of textured silicon surfaces, *Proc. SPIE 9961, Reflection, Scattering, and Diffraction from Surfaces V* **2016**, 996107, doi:10.1117/12.2236976.

Oral presentations

- (Contributed oral, Coburn & Winters student award finalist) **G. Fischer**, E. Drahi, S. A. Filonovich, and E. V. Johnson, SF_6/O_2 Plasma Nanotexturing of Silicon: Decoupling How Ion Flux and Ion Energy Matter, *65th American Vacuum Society Symposium* **2018**, Long Beach, CA (US)

- (Contributed oral) **G. Fischer**, E. Drahi, G. Poulain, B. Bruneau, and E. V. Johnson, Effect of Tailored Voltage Waveforms on surface nanotexturing of silicon in capacitively coupled SF_6/O_2 discharges, *63rd American Vacuum Society Symposium* **2016**, Nashville, TN (US)

- (Contributed oral) **G. Fischer**, E. Drahi, G. Poulain, B. Bruneau, and E. V. Johnson, Tailored Voltage Waveforms in an SF_6/O_2 discharge: slope asymmetry and its effect on surface nanotexturing of silicon, *69th Gaseous Electronics Conference* **2016**, Bochum (DE)
- (Invited oral) **G. Fischer**, E. Drahi, G. Poulain, B. Bruneau, and E. V. Johnson, Insights into Plasma Nanotexturing of Silicon Surfaces Using Tailored Voltage Waveforms Excitation, *PV-Days* **2016**, Haale(Saale) (DE)
- (Contributed oral) **G. Fischer**, G. Poulain, E. Drahi, B. Bruneau, M. Foldyna and E. V. Johnson, Plasma texturing of silicon using Radiofrequency and Tailored Voltage Waveforms excitations, *Journées Nationales du Photovoltaïque* **2015**, Dourdan (FR)

Poster presentations

- **G. Fischer**, E. Drahi, G. Poulain, B. Bruneau, and E. V. Johnson, Insights into Plasma Nanotexturing of Silicon Surfaces Using Tailored Voltage Waveforms Excitation, *Journées Nationales du Photovoltaïque* **2016**, Dourdan (FR)
- (Best poster award) **G. Fischer**, R. Léal, R. Peyronnet, E. Drahi, G. Poulain, M. Lemiti, E. V. Johnson and P. Roca i Cabarrocas, SF_6/O_2 Plasma Processing Solutions to Challenges in High-Efficiency Silicon Solar Cell Fabrication, *Workshop on Energy Transition* **2016**, Palaiseau (FR)

RÉSUMÉ EN FRANÇAIS

Nanostructuration du Silicium par Gravure Plasma pour Applications Photovoltaïques : Optimisation des Interactions Plasma-Surface pour l'Amélioration des Propriétés Optiques

Cette thèse est dédiée à l'étude de la nanotexturation de surface du silicium cristallin par un procédé de gravure ionique réactive en chimie SF_6/O_2. Ce procédé est réalisé en réacteur plasma à couplage capacitif et excitation radiofréquence simple ou multi-fréquence. Dans ce dernier cas, des asymétries électriques peuvent être générées dans le plasma, contrôlées par la forme du signal de tension radiofréquence utilisé (méthode des « forme d'ondes sur mesure », abrégé TVW, de l'anglais "Tailored Voltage Waveforms"). L'objectif général de ce travail est l'optimisation du procédé de nanotexturation en vue d'une intégration pour le traitement de la face avant de l'absorbeur de cellules photovoltaïques silicium cristallin.

L'étude se porte premièrement sur les différents mécanismes de chauffage électronique dans le plasma SF_6/O_2 à faible pression (entre 30 et 200 mTorr, i.e. environ 4 à 27 Pa). L'utilisation de l'excitation TVW permet de générer des asymétries électriques variables dans le plasma. Dans la gamme de conditions utilisées pour la nanotexturation, une asymétrie « temporelle » domine le comportement du plasma en réponse à l'excitation TVW. Ce phénomène est attribué à la forte électronégativité de la décharge SF_6/O_2. L'une des conséquences de ce phénomène est la variation du flux et de l'énergie de bombardement ioniques au niveau du substrat silicium. Cette technique permet donc d'élargir la gamme de conditions disponible pour la gravure, par rapport à une excitation simple fréquence.

Deuxièmement, une fenêtre process permettant d'obtenir une nanotexturation efficace et rapide de la surface de silicium cristallin est identifiée : la réflexion de la lumière en surface du silicium est ainsi drastiquement réduite (formant du « silicium noir » ou "black silicon" en anglais). La largeur et la hauteur des nanostructures formées augmente avec le temps de gravure, le flux d'ion et l'énergie de bombardementUn. Un modèle phénoménologique de gravure est proposé pour intégrer l'ensemble de ces paramètres : il est démontré que la taille des nanostructures est directement liée à la fluence ionique pondérée par l'énergie de bombardement. En particulier, un seuil de gravure d'environ 13 eV est identifié, au-dessus duquel le rendement de gravure augmente avec la racine carrée de l'énergie de bombardement.

Les propriétés optiques des surfaces nanotexturées sont ensuite étudiées. Lorsque la largeur des nanostructures est petite devant la longueur d'onde de la lumière (dans le silicium), la surface

nanotexturée agit comme une couche antireflet à gradient d'indice de réfraction. Une très faible réflectance (de l'ordre de 2% en incidence normale) dans une large gamme spectrale (approximativement [250,1000 nm]) peut être atteinte lorsque les nanostructures sont hautes de plus de 250 nm environ. De plus, une forte diffusion de la lumière est engendrée lorsque la largeur des nanostructures dépasse un seuil d'environ 700 nm. Ce phénomène permet d'augmenter la longueur moyenne du trajet de la lumière dans l'absorbeur, et provoque ainsi une amélioration de l'absorptance dans la gamme [1000,1200 nm].

Les propriétés optiques des surfaces nanotexturées sont très intéressantes pour améliorer la photogénération de charges électriques dans les cellules photovoltaïques en silicium cristallin. Cependant, une augmentation de la recombinaison des charges électriqes est engendrée par la nanotexturation plasma : cet effet provient en partie de l'accroissement (inévitable) de l'aire développée de la surface, mais aussi par la formation de dommages induits en surface du silicium par bombardement ionique lors du procédé de nanotexturation. Après passivation de la surface par dépôt d'une couche mince d'oxide d'aluminium (Al_2O_3), il est démontré que la vitesse de recombinaison des porteurs minoritaires en surface augmente avec l'énergie de bombardement ionique maximale (i.e. la qualité de la passivation de surface diminue).

Ainsi, des conditions optimales de nanotexturation du silicium par plasma SF_6/O_2 peuvent être obtenues par la maximisation du flux d'ions, tout en maintenant l'énergie de bombardement faible (mais supérieure au seuil de gravure). Ces spécifications peuvent se révéler antagonistes dans le cas d'une décharge à couplage capacitif et excitation simple fréquence, mais le conflit peut être (en partie) levé par l'utilisation d'une méthode multifréquence telle que l'excitation à forme d'ondes sur mesure.

université PARIS-SACLAY
ÉCOLE DOCTORALE
INTERFACES
Approches Interdisciplinaires : Fondements, Applications et Innovation

Titre : Nanostructuration du silicium par gravure plasma pour applications photovoltaïques : Optimisation des interactions plasma-surface pour l'amélioration des propriétés optiques

Mots clés : Gravure ionique réactive, Nanotexturation, Formes d'ondes sur mesure, Photovoltaïque

Résumé : Cette thèse est dédiée à l'étude de la nanotexturation de surface du silicium cristallin (c-Si) par un procédé de gravure ionique réactive en chimie SF_6/O_2. Ce procédé est réalisé en réacteur plasma à couplage capacitif (CCP), à excitation RF simple ou multi-fréquence, générant dans ce dernier cas des asymétries électriques dans le plasma (méthode des "forme d'ondes sur mesure", abrégé TVW, de l'anglais "Tailored Voltage Waveforms"). L'objectif est l'optimisation du procédé en vue d'une intégration pour le traitement de la face avant de l'absorbeur de cellules photovoltaïques c-Si.
L'étude se porte premièrement sur les différents mécanismes de chauffage électronique dans le plasma SF_6/O_2 à faible pression. L'utilisation de l'excitation TVW permet de générer des asymétries électriques variables dans le plasma, affectant ainsi le flux et l'énergie de bombardement ioniques au niveau du substrat c-Si, élargissant la gamme de conditions disponible pour la gravure. Deuxièmement, une fenêtre process permettant d'obtenir une nanotexturation efficace de la surface de c-Si est identifiée : la réflexion de la lumière en surface du c-Si est ainsi drastiquement réduite (formant du "silicium noir"). Un modèle phénoménologique de gravure est proposé, démontrant que la taille des nanostructures formées est directement liée à la fluence ionique pondérée par l'énergie de bombardement. Les propriétés optiques des surfaces nanotexturées sont ensuite étudiées. Lorsque la largeur des nanostructures est petite devant la longueur d'onde de la lumière (dans le c-Si), la surface nanotexturée agit comme une couche antireflet à gradient d'indice de réfraction. Une très faible réflectance (de l'ordre de 2% en incidence normale) dans une large gamme spectrale (approximativement [250,1000 nm]) peut être atteinte. De plus, une forte diffusion de la lumière est engendrée lorsque la largeur des nanostructures dépasse un certain seuil, permettant l'amélioration de l'absorptance dans la gamme [1000,1200 nm].
Les propriétés optiques des surfaces nanotexturées sont intéressantes pour améliorer la photogénération de charges électriques dans les cellules photovoltaïques c-Si. Cependant, les dommages induits en surface du c-Si par bombardement ionique sont responsables d'une augmentation de la recombinaison des charges en surface. Des conditions optimales de nanotexturation du c-Si par plasma SF_6/O_2 peuvent être obtenues par la maximisation du flux d'ions, en maintenant l'énergie de bombardement faible. Ces spécifications se révèlent antagonistes dans le cas d'une décharge CCP à excitation simple fréquence, mais le conflit peut être (en partie) levé par l'utilisation de l'excitation TVW.

Title: Plasma Nanotexturing of Silicon for Photovoltaic Applications: Tailoring Plasma-Surface Interactions for Improved Light Management

Keywords: Reactive Ion Etching; Silicon Nanotexturing, Tailored Voltage Waveforms; Photovoltaics

Abstract: This thesis focuses on the study of crystalline silicon (c-Si) surface texturing at the nanoscale (nanotexturing) using capacitively coupled plasma reactive ion etching (CCP-RIE). The general objective consists of tuning the nanotextured surface properties to improve light-management in c-Si solar cells through front surface texturing. To this aim, both single-frequency voltage excitation and Tailored Voltage Waveforms (TVWs), i.e. a multifrequency approach triggering electrical asymmetries in the plasma, are used.
The electron heating mechanisms and ion bombardment energy on the surface are first studied. An identification of the dominant electron heating mechanisms in low pressure SF_6/O_2 plasma is demonstrated using TVWs as an innovative probing tool. Different electrical asymmetry effects are shown to arise, affecting both the ion flux and bombardment energy on the etched surface. TVW excitation leads to an extended range of conditions for SF_6/O_2 plasma etching in CCP-RIE. The plasma-surface interaction mechanisms during SF_6/O_2 plasma nanotexturing of c-Si surfaces are then investigated. A processing window to achieve nanotextured anti-reflective c-Si surfaces ("black silicon") at room temperature is delimited. A phenomenological model is proposed to account for the roles of ion flux and energy on the etching process. From this model, a direct link between the energy weighted ion fluence and the nanostructure size is identified. Subsequently, optical properties of plasma nanotextured c-Si surfaces are studied. When the nanostructure width is small compared to the wavelength (in c-Si), the nanotextured surface acts as an anti-reflective graded refractive index layer. Very low reflectance over a broad wavelength range (in the order of 2% in [250,1000 nm] at normal incidence) can be achieved. Additionally, strong light scattering is shown to arise when the nanostructure width overcomes a given threshold: light is then more efficiently trapped in the c-Si substrate, leading to superior absorptance in the range [1000,1200 nm].
The aforementioned optical properties of nanotextured c-Si surfaces are of practical interest for improved light management in c-Si photovoltaic devices. However, plasma induced damage is responsible for increased carrier recombination, although this effect can be mitigated when ion bombardment energy is kept low. Optimized conditions for c-Si nanotexturing in SF_6/O_2 plasma can be achieved by maximizing the ion flux while keeping ion energy low (but above the etching threshold). These requirements are conflicting in the case of a single frequency CCP discharge, but the trade-off may be (at least partly) resolved using TVWs.

Université Paris-Saclay
Espace Technologique / Immeuble Discovery
Route de l'Orme aux Merisiers RD 128 / 91190 Saint-Aubin, France